

JULY 2024

AJNR

VOLUME 45 • PP 833-986

AJNR

AMERICAN JOURNAL OF NEURORADIOLOGY

Official Journal ASNR • ASFNR • ASHNR • ASPNR • ASSR
JULY 2024 | VOLUME 45 | NUMBER 7 | WWW.AJNR.ORG

THE JOURNAL OF DIAGNOSTIC AND INTERVENTIONAL NEURORADIOLOGY

Spinal CSF leak: Bridging the Gap Conference

Comparison of CT perfusion output of RapidAI and Viz.ai software for acute ischemic stroke

ASL to differentiate between progressive disease and treatment-induced effects in high-grade gliomas

7T MRI for Cushing disease





The ASNR Career Center

The Go-To Job Site for Neuroradiology Employers and Job Seekers

For Job Seekers

- Access to an expanded network of jobs via the National Healthcare Career Network
- Confidential resume posting
- Professional online profile

For Employers

- Employer resources to help you recruit top talent
- Multiple pricing options, including free Fellowship listings
- Resume search

Start here: careers.asnr.org

AJNR

AMERICAN JOURNAL OF NEURORADIOLOGY

JULY 2024
VOLUME 45
NUMBER 7
WWW.AJNR.ORG

Publication Preview at www.ajnr.org features articles released in advance of print.
Visit www.ajnrblog.org to comment on AJNR content and chat with colleagues.

REVIEW ARTICLE

-  **833** **Multimodal Neuroimaging of the Effect of Serotonergic Psychedelics on the Brain** *Paloma C. Frautschi, et al.*

NEUROPSYCHIATRIC
IMAGING

STATE OF PRACTICE

-  **841** **Perspectives from the Inaugural “Spinal CSF Leak: Bridging the Gap” Conference: A Convergence of Clinical and Patient Expertise**
Andrew L. Callen, et al.








SPINE IMAGING AND
SPINE IMAGE-GUIDED
INTERVENTIONS

RADIOLOGY-PATHOLOGY CORRELATION

- 850** **Epstein-Barr Virus–Associated Smooth-Muscle Tumor of the Brain** *Afra Alfalahi, et al.*

BRAIN TUMOR
IMAGING

GENERAL CONTENTS

-  **855** **Imaging Assessments and Clinical Significance of Brain Frailty in Moyamoya Disease** *Liuxian Wang, et al.*
-  **863** **A Comparison of CT Perfusion Output of RapidAI and Viz.ai Software in the Evaluation of Acute Ischemic Stroke** *Saif Bushnaq, et al.*
-  **871** **CTP for the Screening of Vasospasm and Delayed Cerebral Ischemia in Aneurysmal SAH: A Systematic Review and Meta-analysis**
Amer Mitchell, et al.
- 879** **Hypoperfusion Intensity Ratio Is Associated with Early Neurologic Deficit Severity and Deterioration after Mechanical Thrombectomy in Large-Vessel Occlusion Ischemic Stroke** *Małgorzata M. Miller, et al.*
-   **887** **Association between CT Perfusion Parameters and Hemorrhagic Transformation after Endovascular Treatment in Acute Ischemic Stroke: Results from the ESCAPE-NA1 Trial** *Rosalie V. McDonough, et al.*
-  **893** **Comprehensive Analysis of Post-Pipeline Endothelialization and Remodeling** *Vera Sharashidze, et al.*
-  **899** **Use of the Neuroform Atlas Stent or LVIS Jr Stent for Treatment of Unruptured Intracranial Aneurysms in Parent Arteries of <2 mm in Diameter: A Multicenter Experience** *Tengfei Li, et al.*

NEUROVASCULAR/
STROKE IMAGING

NEUROVASCULAR/
STROKE IMAGING

ARTIFICIAL
INTELLIGENCE

NEUROVASCULAR/
STROKE IMAGING

NEUROVASCULAR/
STROKE IMAGING

NEUROVASCULAR/
STROKE IMAGING

NEUROINTERVENTION

NEUROINTERVENTION

AJNR (Am J Neuroradiol ISSN 0195–6108) is a journal published monthly, owned and published by the American Society of Neuroradiology (ASNR), 820 Jorie Boulevard, Oak Brook, IL 60523. Annual dues for the ASNR include approximately 19% for a journal subscription. The journal is printed by Intellicor Communications, 330 Eden Road, Lancaster, PA 17601; Periodicals postage paid at Oak Brook, IL and additional mailing offices. Printed in the U.S.A. POSTMASTER: Please send address changes to American Journal of Neuroradiology, P.O. Box 3000, Denville, NJ 07834, U.S.A. Subscription rates: nonmember \$475 (\$560 foreign) print and online, \$320 online only; institutions \$550 (\$625 foreign) print and basic online, \$1080 (\$1160 foreign) print and extended online, \$380 online only (basic), \$825 online only (extended); single copies are \$35 each (\$40 foreign). Indexed by PubMed/MEDLINE, BIOSIS Previews, Current Contents (Clinical Medicine and Life Sciences), EMBASE, Google Scholar, HighWire Press, Q-Sensei, RefSeek, Science Citation Index, SCI Expanded, ReadCube, and Semantic Scholar. Copyright © American Society of Neuroradiology.

	906	Predictors of Aneurysm Obliteration in Patients Treated with the WEB Device: Results of a Multicenter Retrospective Study <i>Panagiotis Mastorakos, et al.</i>	NEUROINTERVENTION
		912 Reduced Diffusivity along Perivascular Spaces on MR Imaging Associated with Younger Age of First Use and Cognitive Impairment in Recreational Marijuana Users <i>Christina Andica, et al.</i>	NEUROPSYCHIATRIC IMAGING
		920 The Differentiation between Progressive Disease and Treatment-Induced Effects with Perfusion-Weighted Arterial Spin-Labeling in High-Grade Gliomas <i>Christina Maria Flies, et al.</i>	BRAIN TUMOR IMAGING
	927	Differentiating Low-Grade from High-Grade Intracranial Ependymomas: Comparison of Dynamic Contrast-Enhanced MRI and Diffusion-Weighted Imaging <i>Julio Arevalo-Perez, et al.</i>	BRAIN TUMOR IMAGING
	934	Territory-Related Functional Connectivity Changes Associated with Verbal Memory Decline in Patients with Unilateral Asymptomatic Internal Carotid Stenosis <i>Jyun-Ru Chen, et al.</i>	NEUROIMAGING PHYSICS/FUNCTIONAL NEUROIMAGING/CT AND MRI TECHNOLOGY
	943	MR Imaging Features of Critical Spinal Demyelinating Lesions Associated with Progressive Motor Impairment <i>B. Mark Keegan, et al.</i>	SPINE IMAGING AND SPINE IMAGE-GUIDED INTERVENTIONS
	951	Lateral Spinal CSF Leaks in Patients with Spontaneous Intracranial Hypotension: Radiologic-Anatomic Study of Different Variants <i>Wouter I. Schievink, et al.</i>	SPINE IMAGING AND SPINE IMAGE-GUIDED INTERVENTIONS
	957	The Spatial Relationship between Spinal Osteoarthritis and CSF Venous Fistulas in Patients with Spontaneous Intracranial Hypotension <i>Emma M.Z. Sechrist, et al.</i>	SPINE IMAGING AND SPINE IMAGE-GUIDED INTERVENTIONS
	961	Improved Cerebral Glymphatic Flow after Transvenous Embolization of CSF-Venous Fistula <i>Derrek Schartz, et al.</i>	SPINE IMAGING AND SPINE IMAGE-GUIDED INTERVENTIONS
			ULTRA-HIGH-FIELD MRI/IMAGING OF EPILEPSY/DEMYELINATING DISEASES/INFLAMMATION/INFECTION
		965 Comparison of a Whole-Brain Contrast-Enhanced 3D TSE T1WI versus Orbits Contrast-Enhanced 2D Coronal T1WI at 3T MRI for the Detection of Optic Nerve Enhancement in Patients with Acute Loss of Visual Acuity <i>David Prillard, et al.</i>	ULTRA-HIGH-FIELD MRI/IMAGING OF EPILEPSY/DEMYELINATING DISEASES/INFLAMMATION/INFECTION
	971	7T MRI for Cushing Disease: A Single-Institution Experience and Literature Review <i>Ian T. Mark, et al.</i>	ULTRA-HIGH-FIELD MRI/IMAGING OF EPILEPSY/DEMYELINATING DISEASES/INFLAMMATION/INFECTION
			HEAD AND NECK IMAGING
	977	MR Imaging Findings in Anti-Leucine-Rich Glioma Inactivated Protein 1 Encephalitis: A Systematic Review and Meta-analysis <i>Francisco C. Almeida, et al.</i>	ULTRA-HIGH-FIELD MRI/IMAGING OF EPILEPSY/DEMYELINATING DISEASES/INFLAMMATION/INFECTION

ONLINE FEATURES

LETTERS

E18 Shift Volumes *Nadja Kadom*

- E19 **CPT Codes for Quantitative MRI of the Brain: What It Means for Neuroradiology** *S. Bash, et al.*
- E20 **Correspondence on “Antithrombotic Treatment after Carotid Stenting in Patients with Concomitant Atrial Fibrillation”** *Hailong Zhong, et al.*
- E21 **Reply** *Medina-Rodriguez Manuel, et al.*
- E22 **A Note of Caution Regarding Single-Arm 1p or 19q Deletion in IDH-Mutant Gliomas** *Sohil H. Patel, et al.*
- E23 **Reply** *Arian Lasocki, et al.*
- E24 **Arterial Spin-Labeling Imaging Features of Atypical Cerebral Developmental Venous Anomaly Phenotypes** *Todd Abruzzo, et al.*
- E25 **Reply** *Dong Hyun Yoo, et al.*
- E26 **Regarding “Central Vein Sign in Multiple Sclerosis: A Comparison Study of the Diagnostic Performance of 3T versus 7T MRI”** *Onur Tuncer*
- E27 **Reply** *L. Okromelidze, et al.*

BOOK REVIEWS *R.M. Quencer, Section Editor*

Please visit www.ajnrblog.org to read and comment on Book Reviews.



Quantitative neuroimaging combining PET and fMRI can aid in the understanding of functional changes occurring in the brain following psilocybin and lysergic acid diethylamide administration in human participants. The surface rendered images demonstrate the connectivity, activation, or response in regions affected by psilocybin (*top row*) and LSD (*bottom row*): increased (*green*), decreased (*red*), or increased and decreased (*purple*).



Indicates Editor's Choices selection



Indicates Fellows' Journal Club selection



Indicates open access to non-subscribers at www.ajnr.org



Indicates article with supplemental online data



Indicates article with supplemental online video



Evidence-Based Medicine Level 1



Evidence-Based Medicine Level 2

EDITOR-IN-CHIEF

Max Wintermark, MD, MAS, FASFN, FICIS

*Frank T. McGraw Memorial Chair in the Study of Cancer
Professor and Chair of Neuroradiology
The University of Texas MD Anderson Center*

DEPUTY EDITOR

Lubdhra M. Shah, MD, MS

Professor of Radiology and Director of Spine Imaging
Department of Radiology and Imaging Sciences
University of Utah

SPECIAL ADVISORS TO THE EDITOR-IN-CHIEF

Mauricio Castillo, MD, FACR

MA Mauro Distinguished Professor of Radiology
University of North Carolina-Chapel Hill

Robert Quencer, MD

Professor Emeritus
Department of Radiology
University of Miami

ARTIFICIAL INTELLIGENCE

Senior Editor

Reza Forghani, MD, PhD

Professor of Radiology & Artificial Intelligence
Vice Chair of AI
Director, Radiomics & Augmented Intelligence Laboratory (RAIL)
Department of Radiology
University of Florida College of Medicine

Associate Editors

Andreas Rauschecker, MD, PhD

Assistant Professor-in-Residence
Co-Executive Director and Clinical Director,
Center for Intelligent Imaging (ci²)
Department of Radiology & Biomedical Imaging
University of California, San Francisco

Sam (Seyedmehdi) Payabvash, MD

Assistant Professor of Radiology
Yale School of Medicine
Connecticut

Special Editors

Greg Zaharchuk, MD, PhD

Professor of Radiology (Neuroimaging and Neurointervention)
Stanford University
California

Spyridon Bakas, PhD

Joshua Edwards Associate Professor
Department of Pathology and Laboratory Medicine
Inaugural Director of the Division of Computational Pathology
Indiana University School of Medicine

BRAIN TUMOR IMAGING

Senior Editor

Ben Ellingson, PhD

Professor and Director of MRI Research
Director, UCLA Brain Tumor Imaging Laboratory
Department of Radiological Sciences
David Geffen School of Medicine
University of California, Los Angeles

Associate Editors

Ali Nabavizadeh, MD

Assistant Professor of Radiology
Division of Neuroradiology
University of Pennsylvania

Mark S. Shiroishi, MD, MS, FASFN

Assistant Professor, Division of Neuroradiology,
Department of Radiology
Director of Neuro-Oncology Imaging – USC Brain Tumor Center
Chief of Pediatric Neuroradiology – Los Angeles General Medical Center
Affiliated Faculty – USC Imaging Genetics Center
Mark and Mary Stevens Neuroimaging and Informatics Institute
Keck School of Medicine of USC
University of Southern California

Special Editor

Susan Chang, MD

Professor, Neurological Surgery
University of California, San Francisco

EMERGENCY NEURORADIOLOGY

Senior Editor

Karen Buch, MD

Assistant Professor of Radiology
Massachusetts General Hospital

Associate Editors

Melissa A. Davis, MD, MBA

Vice Chair of Medical Informatics
Associate Professor
Department of Radiology and Biomedical Imaging
Yale School of Medicine
Connecticut

Jason Talbott, MD, PhD

Associate Professor, Neuroradiology Section
Department of Radiology and Biomedical Imaging
University of California, San Francisco and
Zuckerberg San Francisco General Hospital

Special Editor

Brian L. Edlow, MD

Neurocritical Care Faculty, Massachusetts General Hospital
Co-Director, Mass General Neuroscience

Associate Director, Center for Neurotechnology and Neurorecovery
Affiliated Faculty, Athinoula A. Martinos Center for Biomedical Imaging
Associate Professor of Neurology, Harvard Medical School
Chen Institute MGH Research Scholar
2023-2028

HEAD AND NECK IMAGING

Senior Editor

Amy Juliano, MD

Associate Professor of Radiology
Massachusetts Eye and Ear
Harvard Medical School

Associate Editors

Burce Ozgen, MD

Clinical Professor of Radiology
University of Illinois at Chicago

David Zander, MD

Assistant Professor, Radiology
University of Colorado School of Medicine

Special Editor

Stephen Y. Lai, MD, PhD, FACS

Professor of Head and Neck Surgery
The University of Texas MD Anderson Center

HEALTH POLICIES/QUALITY IMPROVEMENT/EVIDENCE-BASED NEUROIMAGING

Senior Editor

Nadja Kadom, MD, FACR, FAAP

Professor, Department of Radiology and Imaging Sciences
Emory University School of Medicine
Pediatric Neuroradiologist, Department of Radiology
Children's Healthcare of Atlanta

Associate Editors

Melissa M. Chen, MD

Associate Professor,
Department of Neuroradiology, Division of Diagnostic Imaging
The University of Texas MD Anderson Center

Ajay Malhotra, MBBS, MD, MMM

Professor of Radiology and Biomedical Imaging and Neurosurgery
Yale School of Medicine
Connecticut

MOLECULAR NEUROIMAGING/NUCLEAR MEDICINE

Senior Editor

Ana M. Franceschi, MD, PhD

Associate Professor of Radiology

Donald and Barbara Zucker School of Medicine at Hofstra/Northwell
The Feinstein Institutes for Medical Research
Neuro-PET Imaging
Lenox Hill Hospital
New York

Associate Editors

Nadya Pyatigorskaya, MD, PhD

Neuroradiology Department, Pitié-Salpêtrière Hospital
Researcher, Brain Institute (ICM)
France

Marc Daniel Benayoun, PhD, MD

Assistant Professor of Radiology
Co-Section Head of Nuclear Medicine
Medical Director of Nuclear Medicine and PET
Vice Chair of Radiation Drug Research Committee
Atrium Wake Forest Health
North Carolina

Special Editor

Satoshi Minoshima, MD, PhD

Anne G. Osborn Chair and Professor
Department of Radiology and Imaging Sciences
Spencer Fox Eccles School of Medicine
University of Utah

NEURODEGENERATIVE DISORDER IMAGING

Senior Editor

Gloria Chiang, MD

Associate Professor, Co-Director of the Brain Health Imaging Institute
Department of Radiology
Weill Cornell Medicine/NewYork-Presbyterian Hospital

Associate Editors

Fang Frank Yu, MD

Assistant Professor of Radiology
Division of Neuroradiology, Department of Radiology
Advanced Imaging Research Center
University of Texas Southwestern Medical Center

Priya Rajagopalan, MBBS, MPH

Assistant Professor of Radiology, Division of Neuroradiology
Associate Program Director, Neuroradiology Fellowship
Medical Director, Center for Image Acquisition
Mark and Mary Stevens Neuroimaging and Informatics Institute
Keck School of Medicine, University of Southern California

NEUROIMAGING PHYSICS/FUNCTIONAL NEUROIMAGING/CT AND MRI TECHNOLOGY

Senior Editor

Hongyu An, DSc

Professor, Mallinckrodt Institute of Radiology
Neurology, Biomedical Engineering, Electrical and Systems Engineering, Division of Biology and Biomedical Sciences
Director, Biomedical Magnetic Resonance Center
Associate Director, Center for Clinical Imaging Research
Washington University in St. Louis

Associate Editors

Timothy J. Carroll, PhD

Professor, Department of Radiology
University of Chicago

Hugo de Jong, PhD

Professor of Medical Physics Radiology and Nuclear Medicine
UMC Utrecht
the Netherlands

Special Editor

Roland Bammer, PhD, MEE, MBA, FISMRM

Head/Chair, Department of Radiology and Radiological Sciences
Professor of Radiology and Radiological Sciences,
Monash University
Australia

NEUROINTERVENTION

Senior Editor

Steven Hetts, MD, FACR

Co-Chief, NeuroEndovascular Surgery Service Line
Chief of Interventional Neuroradiology, Mission Bay Hospitals
Professor of Radiology, Biomedical Imaging, and Neurological Surgery
University of California, San Francisco

Associate Editors

Kristine Blackham, MD

Associate Professor
Diagnostic and Interventional Neuroradiology
Clinic for Radiology and Nuclear Medicine
University Hospital of Basel

Maksim Shapiro, MD

Clinical Associate Professor
Departments of Radiology, Neurosurgery, and Neurology
Division of Neurointerventional Radiology
NYU Langone Health and Bellevue NYCH + Hospitals
New York

Special Editor

Giuseppe Lanzino, MD

Professor of Neurosurgery
Mayo Clinic, Minnesota

NEUROPSYCHIATRIC IMAGING

Senior Editor

Jody Tanabe, MD

Professor
Chief of Neuroradiology
University of Colorado-Anschutz Medical Campus

Associate Editors

John-Paul J. Yu, MD, PhD

Assistant Professor of Radiology, Psychiatry, and Biomedical Engineering
University of Wisconsin School of Medicine and Public Health

J. Eric Schmitt, MD, PhD

Assistant Professor of Radiology and Psychiatry
Division of Neuroradiology
Perelman School of Medicine, University of Pennsylvania

Special Editor

Leanne Williams, PhD

Vincent V.C. Woo Professor of Psychiatry and Behavioral Sciences
Director of the Stanford Center for Precision Mental Health and Wellness
Stanford University
California

NEUROVASCULAR/STROKE IMAGING

Senior Editor

Ajay Gupta, MD, MS

Professor and Chair, Department of Radiology
Columbia University
New York

Associate Editors

Shalini Amukotuwa, MB BS, PhD, FRANZCR

Head of Neuroradiology and Director of MRI, Monash Health
Associate Professor of Radiology, Monash University
Australia

Mahmud Mossa-Basha, MD

Professor of Radiology, Neurology and Electrical Engineering
Vice Chair of Clinical Research and Clinical Transformation
Co-Director of the Research Vascular Imaging Lab
University of Washington School of Medicine

Special Editors

Bruce Campbell, MBBS (Hons), BMedSc, PhD, FRACP, FAHMS

Consultant Neurologist, Head of Neurology and Stroke
Department of Neurology and Melbourne Brain Centre
Royal Melbourne Hospital
Professor of Neurology, Dame Kate Campbell Fellow
University of Melbourne
Australia

David Liebeskind, MD, FAAN, FAHA, FANA, FSVIN, FWSO

Professor of Neurology
Director, Neurovascular Imaging Research Core
Director, UCLA Comprehensive Stroke Center
University of California, Los Angeles

PEDIATRIC NEUROIMAGING

Senior Editor

Caroline D. Robson, MBChB

Division Chief & Endowed Chair, Neuroradiology
Director, Head & Neck Imaging
Department of Radiology
Department of Otolaryngology
Boston Children's Hospital
Harvard Medical School

Associate Editors

Anna Trofimova, MD, PhD

Assistant Professor, Radiology and Imaging Sciences, Emory University
Pediatric Neuroradiologist, Children's Healthcare of Atlanta

Matthew Whitehead, MD

Department of Radiology, Division of Neuroradiology
Children's Hospital of Philadelphia
Associate Professor of Radiology
Perelman School of Medicine, University of Pennsylvania

Special Editor

Nomazulu Dlamini, MD, MBBS, MRCPCH, MSc (Lon), PhD

Assistant Professor, Director of Children's Stroke Program
The Hospital for Sick Children

Toronto

SPINE IMAGING AND SPINE IMAGE-GUIDED INTERVENTIONS

Senior Editor

J. Levi Chazen, MD

Associate Professor, Neuroradiology
Director, Spine Imaging
Hospital for Special Surgery
Weill Cornell Medicine
New York

Associate Editors

Jennifer McCarty, MD

UTHealth Houston

Vinil Shah, MD

Associate Professor of Radiology Neuroradiology
Division Chief
University of California, San Francisco

Special Editor

Wouter I. Schievink, MD

Professor of Neurosurgery
Director, Cerebrospinal Fluid Leak Program
Director, Vascular Neurosurgery Program
NFL Neurotrauma Consultant
Department of Neurosurgery
Cedars-Sinai Medical Center
California

ULTRA-HIGH-FIELD MRI/IMAGING OF EPILEPSY/DEMYELINATING DISEASES/INFLAMMATION/INFECTION

Senior Editor

Erik Middlebrooks, MD

Professor of Radiology
Mayo Clinic Florida

Associate Editors

Susie Y. Huang, MD, PhD

Associate Professor of Radiology, Harvard Medical School
Associate Chair, Faculty Affairs, Department of Radiology
Director of Translational Neuro MR Imaging & Connectomics, Athinoula A. Martinos Center for Biomedical Imaging
Massachusetts General Hospital

Girish Bathla, MD, FRCR

Associate Professor, Neuroradiology
Mayo Clinic
Minnesota

Special Editor

Darin T. Okuda, MD, FAAN, FANA

Professor of Neurology
Director, Neuroinnovation Program
Director, Multiple Sclerosis & Neuroimmunology Imaging Program
Director, Radiologically Isolated Syndrome Consortium
Department of Neurology
UT Southwestern Medical Center at Dallas

Founding Editor
Juan M. Taveras

Editors Emeriti
Mauricio Castillo, Robert I. Grossman,
Michael S. Huckman, Robert M. Quencer,
Jeffrey S. Ross

OUTREACH AND EDUCATION

Senior Editor

Lea Alhilali, MD

Radiology Partners, HonorHealth Research
Institute
Arizona

DIGITAL MEDIA AND ENGAGEMENT

Senior Editor

Kevin Hsu, MD

Clinical Assistant Professor
Department of Radiology
NYU Grossman School of Medicine
New York

Case Collection Editors

Matylda Machnowska, BMedSc, MD, FRCSC, ABR

Assistant Professor of Radiology, University of Toronto
Neuroradiologist, Sunnybrook Health Sciences Centre

Anvita Pauranik, MD

Clinical Assistant Professor of Radiology
BC Children's Hospital
University of British Columbia

Sandy Cheng-Yu Chen, MD

Chair, Translational Imaging Research Center
Taipei Medical University Hospital
Vice President of Taipei Medical University

Social Media Editor

Kimberly Seifert, MD, MS

Stanford University
California

Assistant Social Media Editors

Ani Hoxha, MD

Mother Theresa UHC
Albania

Maxwell Opoku, MD

Novosibirsk State Research University
Russia

Podcast Editor

Kevin Hiatt, MD

Assistant Professor, Radiology
Wake Forest University School of Medicine
North Carolina

Deputy Podcast Editor

George K. Vilanilam, MD

PGY5 Resident Physician, Department of Radiology
University of Arkansas for Medical Sciences

STATISTICS

Senior Editor

Bryan A. Comstock, MS

Senior Biostatistician, Department of Biostatistics
University of Washington

Managing Editor
Karen Halm
Assistant Managing Editor
Laura Wilhelm
Executive Director, ASNR
Mary Beth Hepp

BOOK REVIEW EDITOR

Robert Quencer, MD

Professor Emeritus
Department of Radiology
University of Miami

JUNIOR EDITORIAL BOARD

ARTIFICIAL INTELLIGENCE

Janet Mei, MD, MPH

Johns Hopkins University School of Medicine
Maryland

BRAIN TUMOR AND NEUROPSYCHIATRIC IMAGING

Richard Dagher, MD

The University of Texas MD Anderson Center

EMERGENCY NEURORADIOLOGY AND NEUROIMAGING PHYSICS/FUNCTIONAL NEUROIMAGING/CT AND MRI TECHNOLOGY

Maryam Vajdani-Jahromi, MD, PhD

Harvard Medical School, Massachusetts General Hospital

HEAD AND NECK IMAGING

Jacqueline Junn, MD

Emory University School of Medicine
Georgia

NEURODEGENERATIVE DISORDER IMAGING

Mikail Malik, BHSc, Medical Student (MD 2T6)

University of Toronto

NEUROINTERVENTION AND HEALTH POLICIES/QUALITY IMPROVEMENT/EVIDENCE-BASED MEDICINE

Alexandre Boutet, MD, PhD, Senior Editorial Fellow

Joint Department of Medical Imaging
University of Toronto

NEUROVASCULAR/STROKE IMAGING

Sebastiano Vacca, Medical Student

University of Cagliari Medical School

PEDIATRIC NEUROIMAGING

Matheus Dorigatti Soldatelli, MD, PhD, EDiNR/EDiPnR

Boston Children's Hospital, Harvard Medical School

SPINE IMAGING AND SPINE IMAGE-GUIDED INTERVENTIONS

Ian Mark, MD, MSM

Mayo Clinic, Minnesota

ULTRA-HIGH-FIELD MRI/IMAGING OF EPILEPSY /DEMYELINATING DISEASES/INFLAMMATION/INFECTION

Maram Alaffi, MBBS

University of California, San Diego Health

Scientific Editor
Theresa S. Richards, PhD
Digital Publications Senior Manager
Gwen Travis

AJNR *go green*

***AJNR* urges American Society of Neuroradiology members to reduce their environmental footprint by voluntarily suspending their print subscription.**

The savings in paper, printing, transportation, and postage directly fund new electronic enhancements and expanded content.

The digital edition of *AJNR* presents the print version in its entirety, along with extra features including:

- Publication Preview
- Case Collection
- Podcasts
- The *AJNR* News Digest
- The *AJNR* Blog

It also reaches subscribers much faster than print. An electronic table of contents will be sent directly to your mailbox to notify you as soon as it publishes.

Readers can search, reference, and bookmark current and archived content 24 hours a day on www.ajnr.org.

ASNR members who wish to opt out of print can do so by using the *AJNR* Go Green link on the *AJNR* Website (<http://www.ajnr.org/content/subscriber-help-and-services>). Just type your name in the email form to stop print and spare our ecosystem.

AJNR

Dear *AJNR* Subscriber:

Towards the end of 2024, *AJNR* is set to undergo a significant change by fully embracing an electronic format, bidding farewell to traditional paper publications. This shift is motivated by the necessity to address rising costs linked to printing, shipping, and storage, and our goal to maintain financial equilibrium.

The transition to an electronic format brings a host of advantages, presenting more personalized content and enriched visual elements. This includes additional images and diverse media types, particularly beneficial in the field of neuroradiology. Supplementary content will enhance your experience, providing easy access to materials, commentaries, and related resources.

Acknowledging the sentimental value attached to physical copies, we are compelled by both practical financial considerations and a commitment to sustainability to embrace technological progress. Our emphasis is on maintaining a positive outlook and adaptability throughout this transition. To actively engage you in this continual journey, the *AJNR* wants to hear your innovative ideas to shape our electronic platform. I have already heard from many of you through email and our online sessions throughout April.

Please reach out directly to me at mw.ajnr.eic@gmail.com with any ideas or suggestions.

Also, please immediately activate your individual subscription account and also consider registering for Publish Ahead of Print (including Preprint) and electronic Table of Contents, Case of the Week, and Keyword/Author Alerts. These links and more information can be found on the *AJNR* website (<https://www.ajnr.org/content/ajnr-update>) or using the QR code below.

Thank you for your continued engagement.

Sincerely,

Max Wintermark
Editor-in-Chief



AJNR

Moving to a fully

Electronic Format by 2025

Feedback and innovative ideas are strongly encouraged!

Contact Dr. Max Wintermark, *AJNR* Editor-in-Chief
at mw.ajnr.eic@gmail.com



Multimodal Neuroimaging of the Effect of Serotonergic Psychedelics on the Brain

Paloma C. Frautschi, Ajay P. Singh, Nicholas A. Stowe, and John-Paul J. Yu



ABSTRACT

SUMMARY: The neurobiological mechanisms underpinning psychiatric disorders such as treatment-resistant major depression, post-traumatic stress disorder, and substance use disorders, remain unknown. Psychedelic compounds, such as psilocybin, lysergic acid diethylamide, and N,N-dimethyltryptamine, have emerged as potential therapies for these disorders because of their hypothesized ability to induce neuroplastic effects and alter functional networks in the brain. Yet, the mechanisms underpinning the neurobiological treatment response remain obscure. Quantitative neuroimaging is uniquely positioned to provide insight into the neurobiological mechanisms of these emerging therapies and quantify the patient treatment response. This review aims to synthesize our current state-of-the-art understanding of the functional changes occurring in the brain following psilocybin, lysergic acid diethylamide, or N,N-dimethyltryptamine administration in human participants with fMRI and PET. We further aim to disseminate our understanding of psychedelic compounds as they relate to neuroimaging with the goal of improved diagnostics and treatment of neuropsychiatric illness.

ABBREVIATIONS: DMN = default mode network; DMT = N,N-dimethyltryptamine; FC = functional connectivity; LSD = lysergic acid diethylamide; rs-fMRI = resting-state fMRI

Classical serotonergic psychedelics, such as psilocybin, lysergic acid diethylamide (LSD), mescaline, and N,N-dimethyltryptamine (DMT), are in the midst of a resurgent wave of interest within the field of neuropsychiatry. Despite the growing interest in these drugs as a treatment option for treatment-resistant major depressive disorder, post-traumatic stress disorder, and substance use disorders, our collective understanding of the neurobiology underpinning psychedelic therapy significantly trails the enthusiastic use and claimed neuroplastic effects touted by these therapies.¹⁻³ Insight into the underlying mechanisms of this unique drug class is crucial to advance the conversation around psychedelic therapy in the context of psychiatric illness. Neuroimaging, with techniques such as fMRI and PET, can provide researchers and clinicians alike novel insights into the psychedelic-driven neurobiological changes at the individual level and help lead to a

more mechanistic understanding of the treatment effect of psychedelic therapy.

Potent serotonergic hallucinogens have been used for millennia as an adjuvant during ritual and ceremonial practices and have emerged as a novel class of potential therapeutics for psychiatric illness.⁴⁻⁷ Psilocybin is a prodrug, which, following dephosphorylation in the liver to psilocin, demonstrates agonism of 5-HT_{2A} receptors and partial agonism of 5-HT_{1A} and 5-HT_{2C} receptors.⁸ LSD, another psychedelic under active investigation for its therapeutic benefits, was first synthesized by Alfred Hoffman in 1938, and demonstrates 5-HT_{2A} agonism as well as partial agonism of dopaminergic receptors.⁹ The endogenous psychedelic substance DMT, found in plants and the human brain, mainly acts as a 5-HT_{2A} receptor agonist but shows promiscuity for other serotonergic receptors.^{10,11} Finally, mescaline, the active component of peyote, has 5-HT_{2A} receptor agonism, with some activity at adrenergic receptors.⁶ In all instances, binding and agonism of the 5-HT_{2A} receptor are thought to be responsible for the intense subjective sensations (eg, out-of-body experiences, altered consciousness, mindfulness), as well as functional changes in brain activity (eg, increased neuronal firing) and network reorganization that correspond to receptor-mediated neuroplastic regulation induced by such compounds.^{12,13} Though 5-HT_{2A} agonism is regarded as the principal method of action for hallucinogenic effects in psychedelics, there are

Received October 17, 2023; accepted after revision November 20.

From the Departments of Radiology (P.C.F., A.P.S., J.-P.J.Y.) and Psychiatry (J.-P.J.Y.), University of Wisconsin School of Medicine and Public Health, Madison, Wisconsin; and Neuroscience Training Program, Wisconsin Institutes for Medical Research (N.A.S., J.-P.J.Y.), Graduate Program in Cellular and Molecular Biology (A.P.S., J.-P.J.Y.), and Department of Biomedical Engineering (J.-P.J.Y.), University of Wisconsin-Madison, Madison, Wisconsin.

Please address correspondence to John-Paul J. Yu, MD, PhD, Division of Neuroradiology, Department of Radiology, University of Wisconsin Hospital and Clinics, Madison, WI; e-mail: jp.yu@wisc.edu



Indicates article with online supplemental data.

<http://dx.doi.org/10.3174/ajnr.A8118>

conflicting interpretations regarding how receptor polymorphism or co-agonism may influence the hallucinogenic state, and controversially, if this is necessary for positive neuroplastic and behavioral outcomes.^{14–16} This lack of consensus has hindered researchers from confidently defining the mechanistic action behind psychedelics, delaying their widespread clinical adoption.¹⁷ To synthesize findings in the primary literature, many reviews include studies that rely on subjective effects of psilocybin more so than the potential functional connectivity (FC) changes induced in the brain upon administration; others have sought to include studies utilizing measurements, such as CBF, or place their focus on psychiatric populations only.^{18,19} In this review, we address the paradigms of resting-state fMRI (rs-fMRI), task-based fMRI, or PET in the context of psilocybin, LSD, or DMT administration within a nonpsychiatric human population to focus on the baseline effect of this exciting and emerging drug class on FC in the brain. Second, we address the drug-specific neurobiological changes mediated by serotonergic receptor activation that have been measured using multimodal PET-fMRI neuroimaging. Finally, this review will address its own limitations and those of other studies and suggest future models to bridge the knowledge gap between diagnosis and prognosis in the context of psychedelic therapy.

METHODS OF LITERATURE SELECTION

For this review, studies that reported the use of rs-fMRI and task-based fMRI were selected (Fig 1). To select fMRI articles, a PubMed search was conducted by using combinations of the keywords “psilocybin,” “LSD,” “DMT,” and “mescaline” in combination with “AND fMRI.” Though some clinical, psychedelic studies have used ayahuasca, only studies using DMT were considered to avoid muddled interpretation because of ayahuasca containing both DMT and harmala alkaloids, thereby acting as both serotonin agonist and monoamine oxidase inhibitor.²⁰ A second PubMed search was conducted to select studies that used PET imaging as principal imaging technique by using the keywords “psilocybin,” “LSD,” “DMT,” and “mescaline,” also in combination with “AND PET.” No study that used mescaline fit the inclusion criteria for either fMRI or PET; thus, this review includes studies using LSD, psilocybin, and DMT, as represented in Figure 1.²¹ As the development of PET predates the development of fMRI imaging by more than 20 years, the articles included in this review regarding MR span from 2012–2023 and reflect the resurgence of psychedelic research that began in the early 2000s, whereas articles on PET span from 1997–2022 and are primarily based on studying models of psychosis.²² The imaging parameters of these studies are represented in the Online Supplemental Data, and the study design is reported in the Online Supplemental Data. This review only includes studies that strictly included nonpsychiatric human volunteers to establish a baseline understanding of how serotonergic psychedelics interact with functional brain connectivity (fMRI) and receptor biology (PET) for a higher spatiotemporal resolution.²³ A visual representation of individual ROIs most affected by psilocybin and LSD is represented in Figure 2. Studies that used other methods of neuroimaging, such as CT,

magnetoencephalography, single-photon emission CT, or electroencephalogram were excluded for a total of 34 articles.²³

DISCUSSION

Functional Neuroimaging Visualizes Psychedelic Alterations

FC can be measured by using fMRI, and together with blood oxygen level-dependent signal contrast, indirectly measure neuronal activity.²⁴ This contrast captures signal related to functional activity in the corresponding brain regions activated during a task, referred to as task-based fMRI. In contrast, rs-fMRI does not employ any task-based activities and instead aims to characterize a baseline reading of brain network activity and synchrony, referred to as the default mode network (DMN). Thus, rs-fMRI allows analysis of the DMN, which is a particularly attractive technique when scanning patients with psychiatric conditions or those who are in a current psychedelic state and unable to correctly follow a task.²⁴ The DMN has been proposed as a biomarker in fMRI studies for assessing behavioral outcomes based on initial (at-rest) brain coupling patterns.^{25,26} DMN FC alterations are featured prominently in psychedelic studies, and the clear effect of these compounds on behavior is likely to be associated with changes in the DMN. Thus, both task-based fMRI and rs-fMRI can establish the functional brain connectivity precedent of a patient by visualizing indirect spatiotemporal activity changes within and between brain networks. This enables researchers to monitor subsequent connectivity modifications, allowing for a deeper understanding of neurobiological consequences of these putative network connections following psychedelic ingestion.

Psilocybin. Several studies have attributed the therapeutic potential of psilocybin to its ability to alter brain connectivity in limbic areas of the brain linked to emotional and memory response.²⁷ This theory is supported by a 2015 study with 25 individuals, where functional imaging showed reduced activity, rather than an expected increase, in the right amygdala when presented with a negative or neutral visual cue to induce fear-based activation of the limbic system.²⁸ A second study using the same 2015 data found that psilocybin reduced connectivity from the amygdala to the primary visual cortex, thereby decreasing the visual threat response.²⁹ This decreased connection from amygdala to primary visual cortex was also observed in a follow-up study with 15 individuals, which found reduced connectivity from the frontal pole to the amygdala, and decreased connectivity between the amygdala and striatum upon a negative or neutral face visual cue.³⁰ Together, these findings display the possibility of psilocybin treatment to reduce excessive amygdala reactivity, a symptom displayed in many psychiatric disorders.^{2,3} Finally, activation patterns were altered upon psilocybin administration in a study of 12 individuals finding reduced activation between the right amygdala and anterior cingulate cortex, a functional change that lasted up to 1 month postpsilocybin administration.³¹ Of interest, despite the noted reduction in activity particular to the amygdala, a 2014 rs-fMRI study of 25 individuals found increased signaling variation in the anterior cingulate cortex and hippocampus, pointing to the need for additional in-depth analyses of how psychedelics interact with connectivity and activation pattern changes that demonstrate region-specific changes throughout the brain.³²

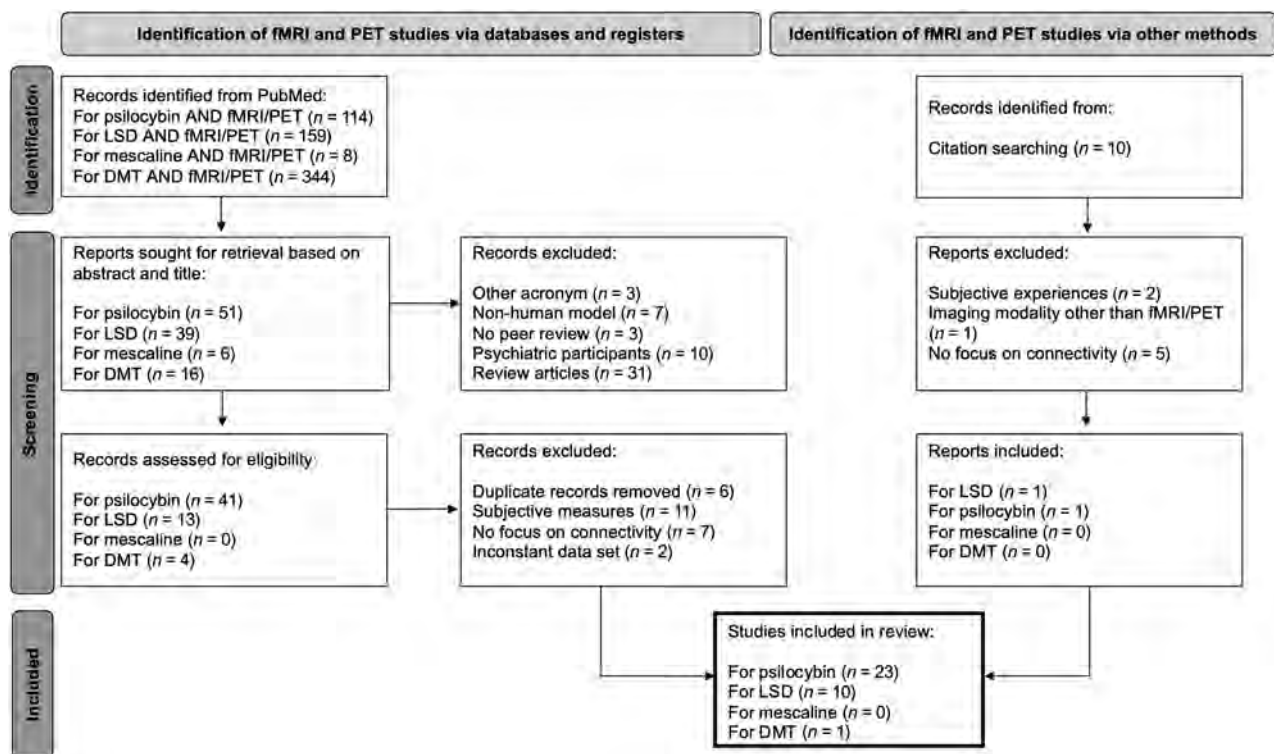


FIG 1. PRISMA 2020 flow diagram for method of selection of literature. Diagram of selection for current review, including searches of databases, registers, and other sources.

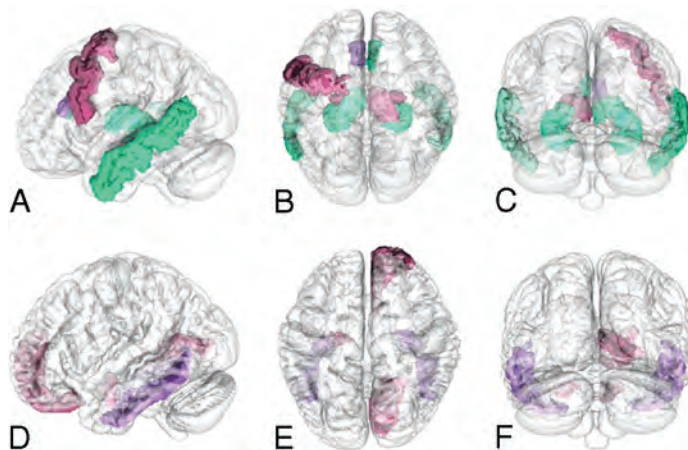


FIG 2. Visual representation of brain regions affected by psilocybin (A–C, sagittal, axial, and coronal, respectively) and LSD (D–F, sagittal, axial, and coronal, respectively). The connectivity, activation, or response of the visually represented regions is increased (green), decreased (red), or increased and decreased (purple), as figures in the selected literature. Regions affected by DMT are not represented because of insufficient ROI-based information. Figures produced by using a downloaded 4D functional human brain mask (<https://nifti.nimh.nih.gov>) and ROIs selected from DSI studio (<https://dsi-studio.labsolver.org>) human brain atlas.

In addition to these effects, psilocybin has been shown to change intranetwork functional associations. The primary hallucinogenic experience following psilocybin administration is thought to be modulated by general decreases in neural activity.³³ While a novel rs-fMRI analysis by Carhart-Harris et al³³ of 15 individuals in 2012 found reduced global FC in the DMN, an

analysis by Roseman et al³⁴ of the same data set found increased connectivity between the visual and sensorimotor networks and resting-state (default mode) networks.³³ The DMN, known for demonstrating increased activity in passive, reflective moments reveals a notably hyperactive FC in individuals with major depressive disorder.^{35,36} In addition to major depressive disorder, the DMN is also involved in social stress; psilocybin was shown to reduce feelings of social exclusion, not just by preventing them, but rather diminishing the strength of the negative experience. A 2016 rs-fMRI study by Preller et al³⁷ demonstrated that this change was modulated by altered connections in the anterior cingulate cortex and medial frontal gyrus. Psilocybin induces an overall decrease in FC in the executive control network that correlates to, and, according to McCulloch et al (2022),²⁴ predicts the positive personality changes lasting 3 months later. This decrease in executive control network connectivity is reproduced in a 2015 study that demonstrates a relationship between decreased amount of executive network nodes and increased subjective effects, measured as ego dissolution.³⁸ Furthermore, the corresponding ego dissolution was found to be

a result of psilocybin-induced decreased FC between the medial temporal lobe and other higher-level areas of the brain. Thus, the decreased connectivity seen in nonpsychiatric patients might validate a similar alteration that occurs in psychiatric patients. In a follow-up study using the 2012 data set from Carhart-Harris et al, psilocybin administration was associated with increased connectivity between the default mode and task positive networks.³⁹ A 2020 rs-fMRI study by Mason et al⁴⁰ also found increased connectivity between the DMN and salience or attention networks. Together, these reports demonstrate psilocybin can potentially alter connectivity between resting-state networks and active, task-based networks.

Madsen et al⁴¹ showed in a 2021 rs-fMRI study that the psilocin plasma level in blood negatively correlated with the level of network integration in both executive and DMNs, underscoring the role of acute effect of psilocin on the de-integration of networks. A 2020 study of 23 individuals showed 5-HT_{2A} receptor agonism was associated with desynchrony of executive control and attention networks and an increase in connectivity at sensory regions, pointing to a delicate pattern of altered connections within and between the networks.⁴² These findings were independently confirmed during a third reanalysis of the 2012 Carhart-Harris et al study, even after controlling for the confounding potential of neuronal activity and cardiovascular overlap.³² Lastly, task-based fMRI demonstrated that psilocybin affects the claustrum; a 2020 study of 12 participants found decreased connections between the claustrum and DMN but an increased connection between the claustrum and task positive network.⁴³ As the claustrum highly expresses 5-HT_{2A} receptors and is involved in connectivity to the cerebral cortex, this finding is interesting but has not been replicated. Overall, fMRI studies demonstrate that psilocybin-induced region-specific increases in network connectivity between the DMN and the claustrum, sensorimotor, visual, and task-positive networks occur in conjunction with a global decrease in FC. In addition, psilocybin was found to induce elevated brain signaling at sensory regions, while concomitantly decreasing the brain's ability to process associative input.^{33,34,44} In this case, brain signaling can be illustrated as dynamic measures of CBF and electrical activity using an fMRI-electroencephalogram or magnetoencephalogram and reflects the brain's ability to reach flexible states of disorganization, as seen from psilocybin, causing altered states of "normal" consciousness.⁴⁴ Together, this suggests that psilocybin results in an influx of sensory information along with an altered ability to effectively integrate these new inputs, thus creating intense perceptual effects.

LSD. LSD has also been shown to induce unique alterations in resting-state and task-based fMRI. Unlike psilocybin, LSD induces altered sensory information flow in the thalamocortical pathway, by improperly filtering external and internal signals, creating an excessive influx of disintegrated information.⁴⁵ This was validated in 2 rs-fMRI studies of 20 individuals where LSD administration induced hyperconnectivity between the precuneus and thalamus, and between primary sensory areas and thalamus, respectively.^{46,47} This latter finding was replicated in a 2018 rs-fMRI study of 24 individuals where increased connectivity was

observed between the posterior cingulate cortex and thalamus, an outcome dependent on 5-HT_{2A} receptor activation.⁴⁸ A 2022 rs-fMRI study of 25 individuals demonstrated not only an increase in structural and FC between the right lingual gyrus and thalamus, but a decrease between the left auditory cortex, postcentral gyrus, and thalamus. Thus, rs-fMRI can highlight the unique, LSD-induced connectivity changes between the thalamus and lingual or proprioceptive areas of the brain.⁴⁹ A generalized increase in hyperconnectivity is also demonstrated in a 2016 rs-fMRI study of 20 individuals where LSD induced increased connectivity between the primary visual cortex, prefrontal cortex and caudate.⁵⁰ Another main area that seems to be affected by LSD administration is the frontoparietal cortex, which experiences increased FC as identified in 2 studies using reanalysis of previously published data.^{48,50-52}

DMT. As with the LSD and psilocybin, the endogenous psychedelic DMT also demonstrates significant effects on human brain FC. Only 1 study was included in the present review to isolate the unique FC characteristics induced by DMT administration. A 2023 rs-fMRI study by Timmermann et al⁵³ demonstrated a notable decrease in between-network segregation in frontoparietal, salience, and DMNs. However, an increase in global FC is seen throughout the brain, specifically in the frontoparietal, salience, and DMNs. This finding demonstrates the compound's ability to cause paradoxical changes within and between functional networks.⁵³ Of interest, this was a similar connectivity pattern observed upon psilocybin administration in an rs-fMRI study from 2020, where the DMN, attention, and salience networks also become altered.⁴⁰ Though these 3 psychedelic drugs are used interchangeably in clinical treatment, the above fMRI studies suggest that each drug has unique effects on brain region and network connectivity, highlighting a need to more closely examine appropriate usages for each treatment.

Differences in Brain Activity and Affected Regions between the Psychedelics. Functional imaging can isolate and characterize the unique effects of psilocybin and LSD on the brain. For example, despite their common agonist activity at 5-HT_{2A} receptors, the right amygdala and claustrum appear to undergo significant changes in connectivity following psilocybin administration, whereas with LSD the most affected regions are the caudate, bilateral amygdala, and thalamus.^{28,47,48} Though a 2013 rs-fMRI study found an increase in thalamic connectivity, a 2022 rs-fMRI study of 18 individuals using voxelwise component analysis instead found that psilocybin caused a decrease in thalamocortical connectivity in the visual and DMNs.^{39,54} Nonetheless, this thalamic network hypoconnectivity differs from LSD's effect, which shows increased connectivity throughout the thalamocortical pathway, implicating the cerebellum, insula, and lingual gyrus as well as sensory regions.^{46,48,55} The higher intensity of perceptual changes experienced following LSD administration in comparison with psilocybin coincides with this region-specific activation.

In addition to increased thalamic connectivity, LSD was shown in a 2017 study by Mueller et al⁵⁶ to cause a significant

decrease in activity of the left amygdala and right medial prefrontal cortex upon negative visual cues. Furthermore, a 2020 study by Bershad et al⁵⁷ of 20 individuals showed LSD increased connectivity from the amygdala to the right angular gyrus, middle frontal gyrus, and cerebellum. This opposes multiple psilocybin studies that show decreased connections to and from the right amygdala.^{28,30,31,57} Perhaps unique to DMT, a decrease in integrity of global connections within networks associated with language is observed, while 2 studies using LSD find increased FC between language networks and other areas of the brain.^{51,53,55} Thus, DMT may possess distinct effects that should be addressed in future studies.^{50,51,58} While these 3 hallucinogens possess similar downstream effects, they all retain specific activity-dependent modifying properties. Though functional neuroimaging permits in vivo observation of the brain activity likely underpinning subjective hallucinogenic experiences, it does not provide a tailored measure of the psychedelic compounds' serotonergic receptor and metabolic interactions, and thus prevents a more nuanced understanding of the neurobiology driving these changes.

PET Neuroimaging and Serotonergic Radiotracers

PET uses radioactive isotope tracers to measure metabolic changes and receptor binding alterations in the brain. PET thus serves as a molecular complement to the functional information derived from fMRI. To capture distinct, psychedelic-induced alterations at a neurometabolic and synaptic activity level in the context of imaging, the ROI needs to be considered alongside the selection of tracer. For example, psilocybin has been shown in murine models to increase dendritic spine attenuation and size in the frontal cortex; however, an open question is whether 5-HT_{2A} activation is required to induce the observed increase in neural plasticity.^{13,14} Thus, the use of radioligands with specific agonism or antagonism for certain serotonergic receptors can help dissect the neurobiological mechanisms and sequelae associated with psilocybin or LSD administration.

¹¹C Radioligands. ¹¹C radioligands, such as ¹¹C-MBL and ¹¹C-Cimbi36, agonize the 5-HT_{2A} receptor and can provide insight into psychedelic-driven receptor changes. Developed over the past 40 years, these ligands are particularly relevant for serotonergic psychedelic studies as they both show primary selectivity for 5-HT_{2A} receptors in the cerebellum and cerebral cortex, 2 ROIs of these drugs.^{59,60} Indeed, ¹¹C-MBL has been recommended over other carbon radioligands for serotonergic studies because of higher specificity for 5-HT_{2A} receptors; treatment with 5-HT_{2A} antagonist ketanserin blocks ¹¹C-MBL binding potential except at the cerebellum. However, this recommendation was in the context of current uses for general serotonergic imaging and not specific to studies using psychedelics.⁶¹ Another interesting finding was that the radiotracer ¹¹C-raclopride, a competitive D_{2/3} binding antagonist, displayed diminished binding potential following administration of psilocybin in the caudate and putamen in a 1999 study, suggesting that psilocybin may partially induce downstream release of endogenous dopamine release.⁶² Nonetheless, the binding strength of ¹¹C can function as an indirect marker of in vivo serotonin levels through the level of 5-

HT_{2A} receptor occupancy. Furthermore, ¹¹C-Cimbi36 showed greater sensitivity to 5-HT_{2A/2C} receptor level changes but is associated with a low signal-to-noise ratio, which when coupled with the short half-life of ¹¹C compounds, has somewhat limited its widespread adoption.^{63,64}

A 2019 study of 8 individuals by Madsen et al⁶⁵ using ¹¹C-Cimbi36 PET to assess psilocybin occupancy of the 5-HT_{2A} receptor was able to determine that high variability exists between each participant based on the dose-response curve. Higher occupancy of the neocortical serotonergic 5-HT_{2A} receptor and higher levels of psilocin plasma concentration levels corresponded to persisting behavioral effects.⁶⁵ This same data set was later reanalyzed in a 2022 study that looked at the binding capability of ¹¹C-Cimbi36 before drug administration and found a direct relationship to mindfulness, a measure of behavioral change that lasted up to 3 months later.⁶⁶ The lower binding capability in the right amygdala at baseline corresponded to higher levels of mindfulness 3 months after drug administration. Moreover, combining fMRI and PET can allow for a more complete image of individual baseline binding potential and subsequent functional outcomes; a 2022 study using both rs-fMRI and ¹¹C-Cimbi36 PET was able to correlate neocortical 5-HT_{2A} receptor binding at baseline with connectivity changes 3 months following psilocybin administration.²⁴ Furthermore, a 2023 DMT study combined fMRI with a 5-HT_{2A} receptor PET attenuation map and revealed a computationally verified relationship between 5-HT_{2A} receptor signaling and subsequent FC outcomes following DMT administration. Though various 5-HT receptors were assessed by using different carbon radioligands, ¹¹C-Cimbi36 was once again used to specifically focus on 5-HT_{2A} receptor activity. Thus, the observed downstream effects of 5-HT_{2A} receptor activation on within- and between-network connectivity in the brain emphasizes the role of combining fMRI and PET to gain a critical, personalized view of how a patient might potentially respond following the administration of serotonergic hallucinogens.⁵³ In addition to ¹¹C radioligands, ¹⁸F tracers have also been used in psilocybin studies to assess glucose uptake, synonymous with alterations in metabolic brain activity.

¹⁸F Radioligands. ¹⁸F-FDG-PET has emerged as a commonly used radiotracer to visualize general metabolic changes in resting-state networks because of its low reported incidence of signal interference secondary to neurovascular coupling and thus improved sensitivity and specificity.⁶⁷ FDG is a glucose analog used as a quantitative measure of glucose utilization in the brain; therefore, ¹⁸F-FDG serves as an indirect measure of brain metabolic activity. A 1997 ¹⁸F-FDG-PET study of 10 individuals found that psilocybin intake led to increased glucose uptake in fronto lateral and fronto medial regions, pointing to hypermetabolism in frontal regions of the brain.⁶⁸ In contrast, a 1999 study of 32 individuals revealed that psilocybin induced a similar increase in glucose metabolism, but only at the right frontotemporal region of the brain, particularly at the anterior cingulate cortex. Furthermore, a decrease in glucose metabolism was noted in the right thalamus in the same study.⁶⁹ Another PET ligand used to visualize serotonergic activity is the 5-HT_{2A} antagonist radioligand ¹⁸F-altanserin. This tracer is pertinent to psychedelic imaging studies for its ability

to assess 5HT_{2A} receptor binding potential. Unlike ¹¹C-Cimbi36, which has promiscuity for 5HT_{2C} receptors, ¹⁸F-altanserin has a higher specificity for 5HT_{2A} receptors.⁶⁴ A 2009 study found that psilocybin caused an overall decrease in total distribution volume of ¹⁸F-altanserin, most drastic in the insula, frontal, and anterior cingulate cortex, demonstrating selective region-specific activity in regions implicated by psilocybin.⁶⁰ Overall, PET radioligands enable sensitive and specific insights into neurometabolic and receptor-level activity changes in the brain, which optimizes the ability to study psychedelic mechanisms in a complementary manner to fMRI studies.

Limitations

A significant limitation of this review is its tailored nature; the selected published studies discussed herein only use fMRI or PET, and no other imaging technique, and only psilocybin, LSD, or DMT, and no other hallucinogens. Though many studies use similar data sets, the analyses performed are novel and provide additional insight into serotonergic psychedelic alternations in the brain. Further, the studies discussed had displayed an absence of demographic diversity, as most studies included only white individuals of European descent and limited sample sizes (all $n \leq 32$ unless combining multiple data sets), especially the PET studies. While this review placed focus on nonpsychiatric human subjects, the reported literature also reports significant inconsistencies in studies between hallucinogen-naïve and non-naïve individuals. It remains to be seen if these differences reflect true differences in neurobiology or if hallucinogen naïve and non-naïve individuals experience significantly different subject experiences that drives the observed results. Many of the included studies also lean on subjective and metaphysical notions.^{18,19} The intra-study interpretation of findings is thus confounded by an incomplete understanding of pharmacodynamics of serotonergic receptors, which highlights the need to study the long-term effects of psychedelic administration in the context of receptor internalization and (de)sensitization. Furthermore, the effect of receiving a sensationalized alternative treatment might increase the chances of conflated, positive experiences, but screening the participants carefully before inclusion seems to blunt this effect.⁷⁰ The fMRI studies included varied significantly in methods of drug administration and methodologic analysis, which may lead to unwanted variation despite using identical data sets. While many of the studies included in this review were based on 3 initial studies, it remains important to consider replicating previous data sets by using independent data, as recommended by McCulloch et al.⁷¹ Another smaller but notable limitation includes the surprising number of studies not reporting handedness of participants. Overall, this focused review is a novel and necessary contribution illustrating the effect of serotonergic psychedelics in nonpsychiatric populations and emphasizes the importance of combining PET and fMRI to obtain a comprehensive baseline of psychedelic neuroimaging in the human brain.

CONCLUSIONS

This review covered the use of rs-fMRI, task-based fMRI, and PET imaging, which has allowed for a global, integrated understanding of the CNS as it relates to the functional changes occurring

following serotonergic psychedelic therapy. The lacunas to accelerating mechanistic insight in the field of psychedelic biology can be addressed by employing a larger scale, with higher power, and by using multiparametric PET-fMRI technique for future psychedelic studies. This review suggests that combining PET and fMRI approaches will provide a comprehensive overview of the alterations seen in the psychedelic state and ultimately how these changes are associated with the observed treatment response. Ultimately, as the field begins to grow, it will be crucial to clarify and interpret the neurobiological effects of psychedelic therapies to increase insight into these specific mechanisms induced by psychedelics; this will hopefully complement current gaps of fMRI and result in a more personalized approach in the treatment of psychiatric illness.

Disclosure forms provided by the authors are available with the full text and PDF of this article at www.ajnr.org.




REFERENCES

1. Garcia-Romeu A, Davis AK, Erowid F, et al. **Cessation and reduction in alcohol consumption and misuse after psychedelic use.** *J Psychopharmacol* 2019;33:1088–101 CrossRef
2. Goodwin GM, Aaronson ST, Alvarez O, et al. **Single-dose psilocybin for a treatment-resistant episode of major depression.** *N Engl J Med* 2022;387:1637–48 CrossRef
3. Krediet E, Bostoen T, Brekkeema J, et al. **Reviewing the potential of psychedelics for the treatment of PTSD.** *Int J Neuropsychopharmacol* 2020;23:385–400 CrossRef
4. Schultes RE, Hofmann A. *Plants of the gods: their sacred, healing, and hallucinogenic powers.* New York: McGraw-Hill, 1992
5. Akers BP, Ruiz JF, Piper A, et al. **A prehistoric mural in Spain depicting neurotropic psilocybe mushrooms?** *Econ Bot* 2011;65:121–28 CrossRef
6. Bruhn JG, Smet PA, El-Seedi HR, et al. **Mescaline use for 5700 years.** *Lancet* 2002;359:1866 Medline
7. Brenan JP, Schultes RE, Hofmann A. **Plants of the gods: origins of hallucinogenic use.** *Kew Bull* 1980;35
8. Passie T, Seifert J, Schneider U, et al. **The pharmacology of psilocybin.** *Addict Biol* 2002;7:357–64 CrossRef Medline
9. Hofmann A. **How LSD originated.** *J Psychoactive Drugs* 1979;11
10. Holmstedt B, Lindgren JE, Plowman T, et al. **Indole alkaloids in Amazonian Myristicaceae: Field and laboratory research.** *Bot Mus Lealf Harv Univ* 1980;28
11. Saavedra JM, Axelrod J. **Psychotomimetic N-methylated tryptamines: formation in brain in vivo and in vitro.** *Science* 1972;175:1365–66 CrossRef Medline
12. Smigielski L, Kometer M, Scheidegger M, et al. **Characterization and prediction of acute and sustained response to psychedelic psilocybin in a mindfulness group retreat.** *Sci Rep* 2019;9:14914 CrossRef Medline
13. Kwan AC, Olson DE, Preller KH, et al. **The neural basis of psychedelic action.** *Nat Neurosci* 2022;25:1407–19 CrossRef Medline
14. Shao LX, Liao C, Gregg I, et al. **Psilocybin induces rapid and persistent growth of dendritic spines in frontal cortex in vivo.** *Neuron* 2021;109:2535–44.e4 CrossRef Medline
15. Hesselgrave N, Troppoli TA, Wulff AB, et al. **Harnessing psilocybin: antidepressant-like behavioral and synaptic actions of psilocybin are independent of 5-HT_{2R} activation in mice.** *Proc Natl Acad Sci U S A* 2021;118:e2022489118 CrossRef Medline
16. Strassman RJ. **Human psychopharmacology of N,N-dimethyltryptamine.** *Behav Brain Res* 1996;73:121–24 CrossRef Medline
17. Pilecki B, Luoma JB, Bathje GJ, et al. **Ethical and legal issues in psychedelic harm reduction and integration therapy. Background information on psychedelic therapy, harm reduction, and integration.** *Harm Reduct J* 2020;18:40 CrossRef Medline

18. Studerus E, Komater M, Hasler F, et al. **Acute, subacute and long-term subjective effects of psilocybin in healthy humans: a pooled analysis of experimental studies.** *J Psychopharmacol* 2011;25:1434–52 CrossRef
19. Madsen MK, Fisher PM, Stenbæk DS, et al. **A single psilocybin dose is associated with long-term increased mindfulness, preceded by a proportional change in neocortical 5-HT_{2A} receptor binding.** *Eur Neuropsychopharmacol* 2020;33:71–80 CrossRef Medline
20. Pochettino ML, Cortella AR, Ruiz M. **Hallucinogenic snuff from north-western Argentina: microscopical identification of *Anadenanthera colubrina* var. *cebil* (Fabaceae) in powdered archaeological material.** *Econ Bot* 1999;53:127–32 CrossRef
21. Page MJ, McKenzie JE, Bossuyt PM, et al. **The PRISMA 2020 statement: an updated guideline for reporting systematic reviews.** *BMJ* 2021;372:n71 CrossRef Medline
22. Portnow LH, Vaillancourt DE, Okun MS. **The history of cerebral PET scanning: from physiology to cutting-edge technology.** *Neurology* 2013;80:952–56 CrossRef Medline
23. Dale AM, Halgren E. **Spatiotemporal mapping of brain activity by integration of multiple imaging modalities.** *Curr Opin Neurobiol* 2001;11:202–08 CrossRef Medline
24. McCulloch DE, Madsen MK, Stenbæk DS, et al. **Lasting effects of a single psilocybin dose on resting-state functional connectivity in healthy individuals.** *J Psychopharmacol* 2022;36:74–84 CrossRef
25. Smigielski L, Scheidegger M, Komater M, et al. **Psilocybin-assisted mindfulness training modulates self-consciousness and brain default mode network connectivity with lasting effects.** *Neuroimage* 2019;196:207–15 CrossRef Medline
26. Tompson S, Chua HF, Kitayama S. **Connectivity between mPFC and PCC predicts post-choice attitude change: the self-referential processing hypothesis of choice justification.** *Hum Brain Mapp* 2016;37:3810–20 CrossRef Medline
27. Catlow BJ, Song S, Paredes DA, et al. **Effects of psilocybin on hippocampal neurogenesis and extinction of trace fear conditioning.** *Exp Brain Res* 2013;228:481–91 CrossRef Medline
28. Kraehenmann R, Preller KH, Scheidegger M, et al. **Psilocybin-induced decrease in amygdala reactivity correlates with enhanced positive mood in healthy volunteers.** *Biol Psychiatry* 2015;78:572–81 CrossRef Medline
29. Kraehenmann R, Schmidt A, Friston K, et al. **The mixed serotonin receptor agonist psilocybin reduces threat-induced modulation of amygdala connectivity.** *Neuroimage Clin* 2016;11:53–60
30. Grimm O, Kraehenmann R, Preller KH, et al. **Psilocybin modulates functional connectivity of the amygdala during emotional face discrimination.** *Eur Neuropsychopharmacol* 2018;28:691–700 CrossRef
31. Barrett FS, Doss MK, Sepeda ND, et al. **Emotions and brain function are altered up to one month after a single high dose of psilocybin.** *Sci Rep* 2020;10:2214 CrossRef Medline
32. Tagliazucchi E, Carhart-Harris R, Leech R, et al. **Enhanced repertoire of brain dynamical states during the psychedelic experience.** *Hum Brain Mapp* 2014;35:5442–56
33. Carhart-Harris RL, Erritzoe D, Williams T, et al. **Neural correlates of the psychedelic state as determined by fMRI studies with psilocybin.** *Proc Natl Acad Sci U S A* 2012;109:2138–43 CrossRef Medline
34. Roseman L, Leech R, Feilding A, et al. **The effects of psilocybin and MDMA on between-network resting state functional connectivity in healthy volunteers.** *Front Hum Neurosci* 2014;8:204 CrossRef Medline
35. Greicius MD, Flores BH, Menon V, et al. **Resting-state functional connectivity in major depression: abnormally increased contributions from subgenual cingulate cortex and thalamus.** *Biol Psychiatry* 2007;62:429–37 CrossRef Medline
36. Andrews-Hanna JR, Reidler JS, Sepulcre J, et al. **Functional-anatomic fractionation of the brain's default network.** *Neuron* 2010;65:550–62 CrossRef
37. Preller KH, Pokorny T, Hock A, et al. **Effects of serotonin 2A/1A receptor stimulation on social exclusion processing.** *Proc Natl Acad Sci U S A* 2016;113:5119–24 Medline
38. Lebedev AV, Lövdén M, Rosenthal G, et al. **Finding the self by losing the self: neural correlates of ego-dissolution under psilocybin.** *Hum Brain Mapp* 2015;36:3137–53 CrossRef Medline
39. Carhart-Harris RL, Leech R, Erritzoe D, et al. **Functional connectivity measures after psilocybin inform a novel hypothesis of early psychosis.** *Schizophr Bull* 2013;39:1343–51
40. Mason NL, Kuypers KP, Müller F, et al. **Me, myself, bye: regional alterations in glutamate and the experience of ego dissolution with psilocybin.** *Neuropsychopharmacology* 2020;45:2003–11 CrossRef Medline
41. Madsen MK, Stenbæk DS, Arvidsson A, et al. **Psilocybin-induced changes in brain network integrity and segregation correlate with plasma psilocin level and psychedelic experience.** *Eur Neuropsychopharmacol* 2021;50:121–32 CrossRef Medline
42. Preller KH, Duerler P, Burt JB, et al. **Psilocybin induces time-dependent changes in global functional connectivity.** *Biol Psychiatry* 2020;88:197–207
43. Barrett FS, Kimmel SR, Griffiths R, et al. **Psilocybin acutely alters the functional connectivity of the claustrum with brain networks that support perception, memory, and attention.** *Neuroimage* 2020;218:116980 CrossRef Medline
44. Carhart-Harris RL, Leech R, Hellyer PJ, et al. **The entropic brain: a theory of conscious states informed by neuroimaging research with psychedelic drugs.** *Front Hum Neurosci* 2014;8:20 CrossRef Medline
45. Felix M, Stefan B. **Acute effects of lysergic acid diethylamide (LSD) on resting brain function.** *Swiss Med Wkly* 2019;149:w20124
46. Müller F, Lenz C, Dolder P, et al. **Increased thalamic resting-state connectivity as a core driver of LSD-induced hallucinations.** *Acta Psychiatr Scand* 2017;136:648–57 CrossRef Medline
47. Tagliazucchi E, Roseman L, Kaelen M, et al. **Increased global functional connectivity correlates with LSD-induced ego dissolution.** *Curr Biol* 2016;26:1043–50 CrossRef
48. Preller KH, Burt JB, Ji JL, et al. **Changes in global and thalamic brain connectivity in LSD-induced altered states of consciousness are attributable to the 5-HT_{2A} receptor.** *Elife* 2018;7:e35082 CrossRef
49. Avram M, Müller F, Preller KH, et al. **Effective-connectivity of thalamocortical interactions following D-amphetamine, LSD, and MDMA administration.** *Biol Psychiatry Cogn Neurosci Neuroimaging* <https://doi.org/10.1016/J.BPSC.2023.07.010> CrossRef
50. Carhart-Harris RL, Muthukumaraswamy S, Roseman L, et al. **Neural correlates of the LSD experience revealed by multimodal neuroimaging.** *Proc Natl Acad Sci U S A* 2016;113:4853–58 Medline
51. Moujaes FF, Rieser NM, Phillips C, et al. **Comparing neural correlates of consciousness: from psychedelics to hypnosis and meditation.** *Biol Psychiatry Cogn Neurosci Neuroimaging* <https://doi.org/10.1016/J.BPSC.2023.07.003> CrossRef
52. Delli Pizzi S, Chiacchiaretta P, Sestieri C, et al. **Spatial correspondence of LSD-induced variations on brain functioning at rest with serotonin receptor expression.** *Biol Psychiatry Cogn Neurosci Neuroimaging* 2023;8:768–76 CrossRef Medline
53. Timmermann C, Roseman L, Haridas S, et al. **Human brain effects of DMT assessed via EEG-fMRI.** *Proc Natl Acad Sci U S A* 2023;120:e2218949120 CrossRef Medline
54. Gaddis A, Lidstone DE, Nebel MB, et al. **Psilocybin induces spatially constrained alterations in thalamic functional organization and connectivity.** *Neuroimage* 2022;274:120130 CrossRef Medline
55. Avram M, Müller F, Rogg H, et al. **Characterizing thalamocortical (dys)connectivity following D-amphetamine, LSD, and MDMA administration.** *Biol Psychiatry Cogn Neurosci Neuroimaging* 2022;7:885–94 CrossRef Medline
56. Mueller F, Lenz C, Dolder PC, et al. **Acute effects of LSD on amygdala activity during processing of fearful stimuli in healthy subjects.** *Transl Psychiatry* 2017;7:e1084 CrossRef Medline
57. Bershad AK, Preller KH, Lee R, et al. **Preliminary report on the effects of a low dose of LSD on resting-state amygdala functional connectivity.** *Biol Psychiatry Cogn Neurosci Neuroimaging* 2020;5:461–67 CrossRef Medline

58. Bedford P, Hauke DJ, Wang Z, et al. **The effect of lysergic acid diethylamide (LSD) on whole-brain functional and effective connectivity.** *Neuropsychopharmacology* 2023;48:1175–83 CrossRef Medline
59. Ettrup A, Svarer C, McMahon B, et al. **Serotonin 2A receptor agonist binding in the human brain with [11C]Cimbi-36: test–retest reproducibility and head-to-head comparison with the antagonist [18F]altanserin.** *Neuroimage* 2016;130:167–74 CrossRef Medline
60. Hasler F, Quednow BB, Treyer V, et al. **Role of prefrontal serotonin-2A receptors in self-experience during psilocybin induced altered states.** *Neuropsychobiology* 2009;59:S60
61. Cumming P, Scheidegger M, Dornbierer D, et al. **Molecular and functional imaging studies of psychedelic drug action in animals and humans.** *Molecules* 2021;26:2451 CrossRef
62. Vollenweider FX, Vontobel P, Hell D, et al. **5-HT modulation of dopamine release in basal ganglia in psilocybin-induced psychosis in man: a PET study with [11C]raclopride.** *Neuropsychopharmacology* 1999;20:424–33 CrossRef Medline
63. Barrett FS, Zhou Y, Carbonaro TM, et al. **Human cortical serotonin 2A receptor occupancy by psilocybin measured using [11C]MDL 100,907 dynamic PET and a resting-state fMRI-based brain parcellation.** *Front Neuroergonomics* 2022;2 CrossRef
64. Johansen A, Hansen HD, Svarer C, et al. **The importance of small polar radiometabolites in molecular neuroimaging: a PET study with ¹¹C Cimbi-36 labeled in two positions.** *J Cereb Blood Flow Metab* 2018;38:659–68 CrossRef Medline
65. Madsen MK, Fisher PM, Burmester D, et al. **Psychedelic effects of psilocybin correlate with serotonin 2A receptor occupancy and plasma psilocin levels.** *Neuropsychopharmacology* 2019;44:1328–34 CrossRef Medline
66. Søndergaard A, Madsen MK, Ozenne B, et al. **Lasting increases in trait mindfulness after psilocybin correlate positively with the mystical-type experience in healthy individuals.** *Front Psychol* 2022;13:948729 CrossRef Medline
67. Savio A, Fänger S, Tahmasian M, et al. **Resting-state networks as simultaneously measured with functional MRI and PET.** *J Nucl Med* 2017;58:1314–17 CrossRef
68. Vollenweider FX, Leenders KL, Scharfetter C, et al. **Positron emission tomography and fluorodeoxyglucose studies of metabolic hyperfrontality and psychopathology in the psilocybin model of psychosis.** *Neuropsychopharmacology* 1997;16:357–72 CrossRef Medline
69. Gouzoulis-Mayfrank E, Schreckenberger M, Sabri O, et al. **Neurometabolic effects of psilocybin, 3,4-methylenedioxyethylamphetamine (MDE) and D-methamphetamine in healthy volunteers: a double-blind, placebo-controlled PET study with [18F] FDG.** *Neuropsychopharmacology* 1999;20:565–81 CrossRef Medline
70. Aday JS, Heifets BD, Pratscher SD, et al. **Great expectations: recommendations for improving the methodological rigor of psychedelic clinical trials.** *Psychopharmacology (Berl)* 2022;239:1989–2010 CrossRef Medline
71. McCulloch DE, Knudsen GM, Barrett FS, et al. **Psychedelic resting-state neuroimaging: a review and perspective on balancing replication and novel analyses.** *Neurosci Biobehav Rev* 2022;138:104689 CrossRef Medline

Perspectives from the Inaugural “Spinal CSF Leak: Bridging the Gap” Conference: A Convergence of Clinical and Patient Expertise

 Andrew L. Callen, Samantha L. Pisani Petrucci, Peter Lennarson,  Marius Birlea,  Jennifer MacKenzie,  Andrea J. Buchanan, and the “Spinal CSF Leak: Bridging the Gap” Study Group



ABSTRACT

BACKGROUND AND PURPOSE: The inaugural “Spinal CSF Leak: Bridging the Gap” Conference was organized to address the complexities of diagnosing and treating spinal CSF leaks. This event aimed to converge the perspectives of clinicians, researchers, and patients with a patient-centered focus to explore the intricacies of spinal CSF leaks across 3 main domains: diagnosis, treatment, and aftercare.

MATERIALS AND METHODS: Physician and patient speakers were invited to discuss the varied clinical presentations and diagnostic challenges of spinal CSF leaks, which often lead to misdiagnosis or delayed treatment. Patient narratives were interwoven with discussions on advanced radiologic techniques and clinical assessments. Treatment-focused sessions highlighted patient experiences with various therapeutic options, including epidural blood patches, surgical interventions, and percutaneous and endovascular therapies. The intricacies of immediate and long-term postprocedural management were explored.

RESULTS: Key outcomes from the conference included the recognition of the need for increased access to specialized CSF leak care for patients and heightened awareness among health care providers, especially for atypical symptoms and presentations. Discussions underscored the variability in individual treatment responses and the necessity for personalized diagnostic and treatment algorithms. Postprocedural challenges such as managing incomplete symptom relief and rebound intracranial hypertension were also addressed, emphasizing the need for effective patient monitoring and follow-up care infrastructures.

CONCLUSIONS: The conference highlighted the need for adaptable diagnostic protocols, collaborative multidisciplinary care, and enhanced patient support. These elements are vital for improving the recognition, diagnosis, and management of spinal CSF leaks, thereby optimizing patient outcomes and quality of life. The event established a foundation for future advancements in spinal CSF leak management, advocating for a patient-centered model that harmonizes procedural expertise with an in-depth understanding of patient experiences.

ABBREVIATIONS: CTD = connective tissue disorders; CTM = CT myelography; CVF = CSF-venous fistula; DSM = digital subtraction myelography; PDPH = post-dural puncture headache; POTS = postural orthostatic tachycardia syndrome; RIH = rebound intracranial hypertension; SCSFL = spinal CSF leak

The inaugural “Spinal CSF Leak: Bridging the Gap” Conference, held on November 11, 2023, highlighted collective insights shared by a diverse cohort of clinicians, researchers and, crucially, patients. The goal of this conference was to foster a nuanced, patient-centered understanding of the diagnosis and treatment

of spinal CSF leak (SCSFL), a condition that has historically posed profound challenges to both patients and physicians.

SCSFL may be spontaneous, resulting in the syndrome of spontaneous intracranial hypotension, or may be caused by an intentional or unintentional dural puncture, producing acute or chronic post-dural puncture headache (PDPH). SCSFL frequently present a diagnostic conundrum due to ambiguous clinical presentations combined with a relative lack of recognition in the medical community. Many patients with SCSFL are initially misdiagnosed, leading to delays in care, inappropriate treatments, and degrading patient trust in the medical system.¹⁻³ This mismanagement is superimposed on a condition which, when left untreated, can cause immense disability and suffering.⁴


This conference was designed not only to feature physician experts in the field but to provide a platform for a diverse group of patients to synthesize their experiences in a didactic format and highlight their journey throughout SCSFL care. A variety of perspectives were presented, converging on a proposed framework

Received November 27, 2023; accepted after revision December 18.

From the Departments of Radiology (A.L.C., S.P.P.), Neuroradiology Section, Neurosurgery (P.L.), and Neurology (M.B.), University of Colorado Anschutz Medical Campus, Aurora, Colorado; and Spinal CSF Leak Foundation (J.M., A.B.), Spokane, Washington.

Financial support for this conference was provided by the Spinal CSF Leak Foundation and the University of Colorado Departments of Neuroradiology, Neurosurgery, and Neurology.

Please address correspondence to Andrew L. Callen MD, 12401 E 17th Ave, Aurora, CO 80045, Mail Stop L954; e-mail: andrew.callen@cuanschutz.edu; @AndrewCallenMD

 Indicates open access to non-subscribers at www.ajnr.org

<http://dx.doi.org/10.3174/ajnr.A8181>

Differential diagnoses in patients presenting with SCSFL

	Overlap with SCSFL	Key Differences from SCSFL
Chronic migraine	Headache as primary clinical presentation	<ul style="list-style-type: none">• Often evolves from less-frequent to more-frequent episodes• Less typically orthostatic• Often occur in the morning, rather than worsening throughout the day
Postconcussion headache	Both can be precipitated by trauma	<ul style="list-style-type: none">• Headache phenotype like migraine• Typically nonorthostatic• Associated cognitive issues
Postural orthostatic tachycardia syndrome	Orthostatic symptoms	<ul style="list-style-type: none">• Defined by changes in hemodynamic parameters on standing• If headache associated, more often migraine-like• Neck stiffness less common
Chiari I malformation	Cerebellar tonsillar ectopia may be present in both conditions	<ul style="list-style-type: none">• Brain MR imaging should not demonstrate downward herniation of posterior fossa structures, pituitary/venous engorgement, or pachymeningeal enhancement• Orthostatic headache less common

that balanced cutting-edge diagnostic and treatment techniques with a patient-centered approach. The conference was divided into 3 sessions: diagnosis, treatment, and aftercare.

MATERIALS AND METHODS

Content from lectures at the conference was reviewed and synthesized with current literature to summarize the major themes pertaining to SCSFL care. Patient lectures and video compilations were recorded and transcribed using a large language model (GPT-4) to convert patient narratives into written form. Recommendations were abstracted from the content of the conference and summarized by the authors.

Diagnosis

The Patient Perspective. The conference opened with a narrative shared by a patient detailing their decade-long struggle with undiagnosed symptoms of a SCSFL. At 11 years of age, the patient had a fall, which led to a diagnosis of postconcussion headaches, and at 15 years of age underwent corrective surgery for scoliosis. The patient developed worsening in orthostatic symptoms postoperatively, initially attributed to a postconcussion syndrome. It was not until a potential chronic surgical leak was identified by a subspecialist years later that the patient received epidural patching and symptom relief. This patient's journey highlights the potentially disabling delay in diagnosis commonly experienced by patients with SCSFL. This narrative emphasized the need for heightened awareness of SCSFL among health care providers for younger demographics, in whom the condition is often unexpected and the diagnosis challenging.

Another perspective was shared by a patient with a PhD and professional background in trauma therapy who had a CSF-venous fistula (CVF). Given this unique position, he shed light on the psychological challenges accompanying undiagnosed or misdiagnosed SCSFL, including the emotional toll and mental health implications of living with chronic, unexplained symptoms. Additionally, he suggested techniques for patients to process trauma associated with a SCSFL diagnosis and treatment to reclaim their health autonomy. This narrative advocated an enhanced, empathetic, and comprehensive approach by health care professionals to address the mental health aspects inherent in the patient journey of SCSFL. Specifically, it stressed the importance of the patient-provider relationship in SCSFL care,

extending beyond diagnostic and therapeutic procedures. This aspect is particularly important for procedural neuroradiologists, who often perform procedures in isolation and without a framework for continuity of care.

Clinical Challenges

The complexity of diagnosing SCSFL hinges on the wide spectrum of clinical presentations that often lead to misdiagnosis or delayed treatment (Table). The classic clinical presentation of SCSFL is characterized by an orthostatic headache. The headaches themselves can have nuanced features, which should be addressed via a thorough history. Patients also frequently describe acephalgic symptoms including fatigue, tinnitus, ear fullness, light sensitivity, cognitive dysfunction, and neck pain, and often experience worsening of symptoms during the day.⁵ Patients with acephalgic symptomatology may be particularly susceptible to misdiagnosis and inappropriately dismissed if a classic orthostatic headache is not described.

Patients with SCSFL are frequently misdiagnosed with migraine. Chronic migraine is characterized by headaches on >15 days per month for at least 3 months, with at least one-half of these days demonstrating unilateral throbbing pain, physical activity exacerbation, light and noise sensitivity, or nausea.⁶ Chronic migraine evolves across time with increased frequency of attacks, while SCSFL symptoms often begin suddenly. Cephalgia in SCSFL is typically orthostatic and worsens as the day progresses, while migraine attacks often occur in the morning. Patients may also be frequently misdiagnosed with postconcussion headaches, because some SCSFL leaks are precipitated by trauma.⁷ However, the postconcussion syndrome more commonly presents with migraine-like, nonorthostatic headaches and cognitive issues.⁸

Postural orthostatic tachycardia syndrome (POTS) is a condition predominantly affecting young women and is characterized by an abnormal heart rate increase on standing.⁶ Many patients with POTS also have headache; however, most POTS headaches are nonorthostatic and resemble migraine, while orthostatic headache and neck stiffness are more common in SCSFL.⁹

SCSFL can be radiographically misdiagnosed as Chiari I morphology due to potential presence of cerebellar tonsillar ectopia in both conditions. Scrutiny of the posterior fossa structures on brain MR imaging aids in the reliable differentiation of these 2 entities.^{2,10} While patients with both SCSFL and Chiari I can

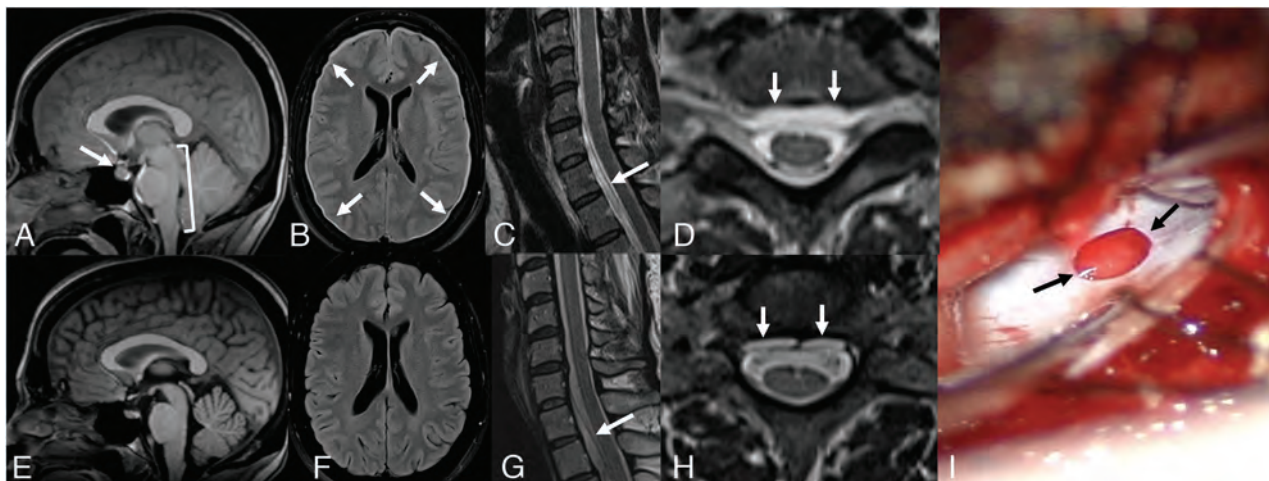


FIG 1. Normalization of MR imaging findings across time despite persistent spinal CSF leaks. A, Sagittal T1 noncontrast MR imaging in 2018 demonstrates sagging of posterior fossa structures (*bracket*), engorgement of the pituitary gland, and narrowed suprasellar distance (*arrow*). B, Axial FLAIR MR imaging in 2018 demonstrates a diffuse, thin subdural collection (*arrows*). Sagittal (C) and axial (D) T2 MR imaging of the cervical spine in 2018 shows a cervicothoracic ventral epidural fluid collection (*arrows*). The patient underwent a dorsal nontargeted epidural blood patch in 2018 with partial relief of symptoms. E, Sagittal T1 noncontrast MR imaging in 2023 demonstrates resolution of brain sag, pituitary engorgement, and narrowing of the suprasellar interval. F, Axial FLAIR MR imaging in 2023 with resolution of the subdural collection. Sagittal (G) and axial (H) T2 MR imaging of the cervical spine in 2023 shows persistence of the cervicothoracic ventral epidural fluid collection. I, Intraoperative photograph later in 2023, with a ventral dural defect identified at T2–T3 (*arrows*). After repair, the patient had substantial symptom improvement, with the Headache Impact Test score improving from 68 to 48 (Headache Impact Test: range, 36–78).

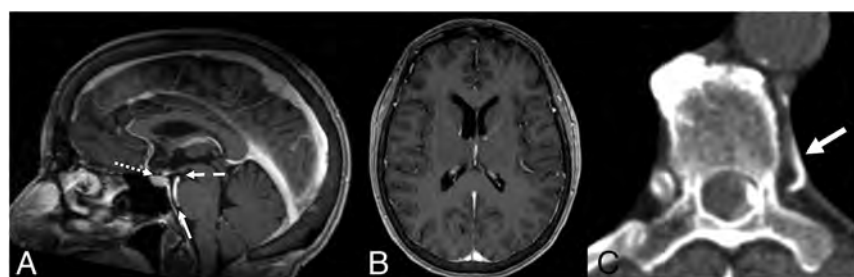


FIG 2. Brain MR imaging findings incorrectly reported as normal in a patient with spontaneous intracranial hypotension. A, Sagittal T1 postcontrast MR imaging demonstrates mild narrowing of the suprasellar (1 mm, *dotted arrow*), mamillopontine (4.8 mm, *dashed arrow*), and prepontine (3 mm, *solid arrow*) distances. B, No pachymeningeal thickening or subdural collection on axial T1 postcontrast MR imaging. C, Left-lateral decubitus dynamic CTM detected a CVF arising from the left T7–8 neural foramen (*arrow*).

present with occipital headaches and neck pain, patients with Chiari I do not commonly have orthostatic headaches but may experience lightheadedness or fainting.¹¹

Connective tissue disorders (CTD) are common in patients with SCSFL.¹² Patients with CTD often exhibit chronic, debilitating symptoms that are challenging to treat due to multifactorial etiologies. For instance, mast cell dysfunction has been linked to CTD, causing disordered immune/inflammatory responses.¹³ Patients may undergo evaluation for Ehler Danlos syndrome, small fiber neuropathy, and/or craniocervical instability, and pinpointing a specific diagnosis is often difficult. In designing diagnostic and treatment strategies for such patients, the interplay of these various disorders must be considered.

It is the synthesis of both clinical and radiographic clues that leads to diagnostic optimization for patients with SCSFL. Discussing patients in a formal, multidisciplinary conference incorporating

expertise from neurologists, neurosurgeons, and neuroradiologists can be critically important in this regard.¹⁴

Radiologic Challenges

In SCSFL, brain MR imaging classically demonstrates diffuse pachymeningeal enhancement, subdural collections, venous/pituitary engorgement, and/or sagging of the posterior fossa structures. However, a proportion of brain MR imaging studies will be interpreted as having normal findings in patients with proved SCSFL.¹⁵ Some patients experience normalization of brain MR imaging findings with time, despite

persistent symptoms and a localizable dural defect or CVF (Fig 1).¹⁶ It is, therefore, crucial to obtain all prior imaging for patients presenting with symptoms of SCSFL, particularly imaging available close to the onset of symptoms. Some patients may have their examinations incorrectly interpreted as having normal findings, particularly when these changes are subtle (Fig 2).¹⁷ Findings of others are truly normal even with careful scrutinization for subtle MR imaging findings. This outcome is particularly true of patients with PDPH, in whom findings of brain imaging are frequently normal, particularly in the chronic period despite known dural puncture and new headache symptoms.^{18,19}

The Bern Score is a probabilistic scoring system reflecting the likelihood of localizing a leak or CVF on myelography (Fig 3).^{20–22} It is derived from the sum of points ascribed to certain observations on brain MR imaging and can help radiologists avoid inappropriately characterizing an abnormal examination having

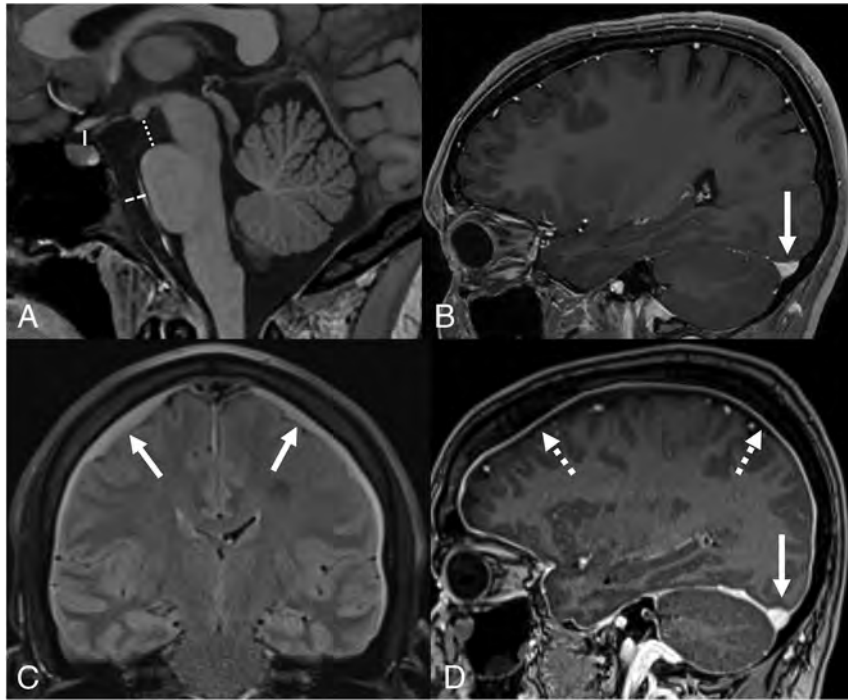


FIG 3. The Bern score. A, Sagittal T1 noncontrast MR imaging demonstrating the suprasellar interval (solid line, normal, >4 mm), mamillopontine interval (dotted line, normal, >6.5 mm), and prepontine interval (dashed line, normal, >5 mm). B, Sagittal T1 postcontrast MR imaging illustrates a normal flat appearance of the upward margin of the transverse sinus (arrow). C, Coronal FLAIR MR imaging with bilateral subdural fluid collections (arrows). D, Sagittal T1 postcontrast image demonstrates abnormal venous engorgement evidenced by an abnormal convex upward margin (solid arrow), as well as diffuse pachymeningeal enhancement (dotted arrows). The presence of a narrowed suprasellar interval, venous engorgement, or pachymeningeal enhancement are ascribed 2 points each, while a narrowed mamillopontine interval, prepontine interval, or the presence of subdural collections are ascribed 1 point each. A combined score of ≤ 2 equates to low probability, a score of 3 or 4 equates to moderate probability, and a score of ≥ 5 equates to high probability of localizing a CSF leak or venous fistula on subsequent myelography.²⁰

abnormal findings as having normal findings.¹⁷ However, a recent study by Houk et al²³ demonstrated that the Bern Score does not correlate with clinical headache severity. This finding challenges the hypothesis that symptoms in SCSFL are directly related to sagging/traction on meningeal layers and/or venous engorgement. Understanding the specific role of brain MR imaging findings and Bern Score applications and limitations is critical to appropriately triage patients with suspected SCSFL.

CVFs are not visible on conventional CT myelography (CTM) and thus have long evaded detection, with the first formal description published in 2014.³⁵ Dynamic lateral decubitus CT or fluoroscopic myelography (with or without digital subtraction, digital subtraction myelography [DSM]) producing densely layering contrast along the lateral thecal sac is key to localizing CVF.¹⁴ Provocative maneuvers such as resisted inspiration can also enhance fistula conspicuity.^{24,25} Whether DSM or CTM is performed for CVF localization depends on institutional resources and expertise. Newer CT technology, specifically photon-counting CT, has been shown to increase the sensitivity for small CVFs by using ultra-high-resolution imaging with 0.2-mm slices at lower radiation doses.²⁶

In the case of dural defects or ruptured meningeal diverticula, conventional, nondynamic CTM will confirm the presence of an

extradural collection but lacks the temporal resolution for precise leak localization. Furthermore, heavily T2-weighted, noncontrast 3D MR imaging of the spine is noninferior to conventional CTM for the detection of epidural fluid collections.^{27,28} Thus, conventional CTM is likely of limited utility in the work-up of suspected SCSFL. Additionally, CTM exposes patients to radiation and a dural puncture, risking the development of PDPH.

We recommend that patients with suspected SCSFL undergo contrast-enhanced brain MR imaging and heavily T2-weighted MR imaging of the entire spine before an invasive procedure. The Bern Score should be calculated to assess the potential yield of myelography, and spinal MR imaging should be scrutinized for the presence of any epidural fluid. This work-up strategy maximizes information for procedural planning and patient counseling.¹² In patients with a high clinical suspicion of SCSFL but a low Bern score and no spinal epidural fluid, a trial of empiric epidural blood patching is a useful treatment strategy, potentially providing symptom relief while minimizing the risk to the patient.²⁹

Treatment

The Patient Perspective. The experience of undergoing an epidural blood

patch was highlighted in a video montage of patient testimonials. These personal accounts detailed the effects of the procedure, ranging from marked relief to minimal or short-lived symptom improvement. Some patients described intense pain during the procedure, while others noted minimal discomfort. Patients expressed a range of emotions, from gratitude for the relief provided to frustration and disappointment in cases in which symptoms persisted or recurred. Their narratives underscored the complexity and variability of patient responses to this treatment, emphasizing the need for individualized care and the importance of patient-provider communication in managing expectations and outcomes of the procedure.

A family medicine physician who experienced an SCSFL shared her unique perspective as both a doctor and patient. In 2020, she developed a sudden-onset severe headache following a cough, which only improved on lying down, leading to suspicion of an SCSFL. Despite her medical background, she was unfamiliar with this condition and, like many patients, had to educate herself. She underwent epidural blood patching, which provided only partial relief. Communication with specialists led to a recommendation for surgery due to a suspected ventral dural defect. However, like many patients with SCSFL, she faced challenges obtaining definitive treatment, requiring approval for an out-of-

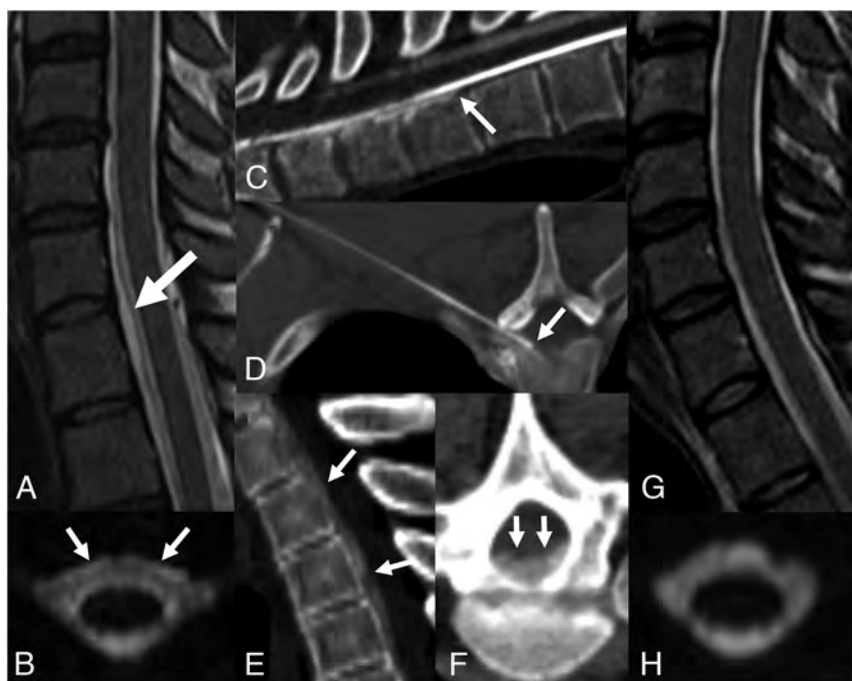


FIG 4. A 35-year-old man with spontaneous intracranial hypotension who underwent 2 prior nontargeted dorsal epidural blood patches. Sagittal (A) and axial (B) T2-weighted MR imaging sequences demonstrate a ventral epidural fluid collection (arrows). C, Prone dynamic CTM detected contrast extravasating from the subarachnoid into the ventral epidural space at T1-2, consistent with a ventral dural defect (arrow). D, Procedural image from a CT-guided epidural blood and fibrin patch using a 15-cm 22-ga spinal needle via a far-lateral transforaminal approach to target the ventral epidural space adjacent to the defect (arrow). Postinjection sagittal (E) and axial (F) images demonstrate spread of injected blood and fibrin glue along the ventral epidural space (arrows). Posttreatment sagittal T2 (G) and axial 3D T2 fat-saturated MR imaging (H) with resolution of the epidural fluid collection.

network referral and interstate travel for the procedure. She ultimately underwent surgical repair. The postoperative period was daunting, marked by the challenge of recovering away from her medical team. The surgery successfully alleviated her headaches; however, returning to work as a physician proved challenging due to persistent back pain, requiring an extended medical leave. More than 2 years postsurgery, she still experiences back pain, a condition she accepts as a trade-off for freedom from debilitating head pain. Her experience underscores the importance of having a support network while undergoing treatment and the reality of living with long-term effects of invasive medical interventions.

Percutaneous and Endovascular Therapies

Image-guided percutaneous treatments for SCSFL include image-guided injection of autologous blood and/or fibrin sealant into the epidural space, ideally targeted to the localized dural defect or CVF.³⁰ Patching can close the leak without surgical intervention, particularly when performed near symptom onset. However, as a leak persists into the chronic period, the likelihood that surgery will be required for definitive management increases.³¹ Thus, prompt recognition of an SCSFL is critical to maximize the success of percutaneous patching. Nontargeted epidural blood patching can be performed using a 2-level thoracolumbar interlaminar approach and ideally injecting at least

20 mL of autologous blood.^{32,33} Targeted patching is performed when a leak is localized and may be performed with fluoroscopy or CT guidance. When a ventral leak is identified, a far-lateral transforaminal approach may allow injection directly into the ventral epidural space (Fig 4).³⁴ Guidelines for post-patch management vary widely across institutions, especially regarding the duration of bed rest and activity restrictions. In most centers, patients are advised to lie flat for 24–72 hours postpatch and avoid bending, lifting, or twisting for 6 weeks. Because there is a relative lack of high-quality evidence supporting specific recommendations, guidance provided is often based on expert opinion and physiologic principles.

Initially described treatment for CVF included surgical ligation of the associated nerve root.³⁵ More recently, both transvenous embolization with liquid embolic agents and percutaneous occlusion with fibrin sealant have been described with success rates of >50%.^{36,37} At institutions equipped with such treatment modalities, an initial trial of either transvenous embolization or fibrin occlusion may be attempted before surgical ligation. If

these procedures fail to relieve the patient's symptoms, surgical intervention should be considered.

Surgical Treatment

Advancements in radiology, particularly DSM and dynamic CTM, have revolutionized the surgical approach to spinal CSF leaks, enabling a precise identification of the leak type and location and allowing minimally invasive approaches.³⁸ Such techniques can include a hemilaminectomy performed under microscopic visualization using tubular retractors placed through small incisions, thereby reducing postoperative pain.

Surgical strategies for repair of ventral dural defects have evolved with time. Rather than requiring an anterior approach with corpectomy and potential thoracotomy, ventral dural defects may be repaired using a transdural, posterior approach, improving patient outcomes and recovery time (Fig 5).^{39,40} Defects may be closed with direct suturing, collagen patches, or fat/muscle grafts.

Iatrogenic leaks can also require surgical intervention. Postdural puncture pseudomeningoceles, also known as arachnoid "blebs," have been reported to cause symptoms of SCSFL and can be repaired using minimally invasive surgical approaches.^{41,42} Treatment of a CVF can include ligation of the fistula alone versus transection of the involved nerve root. The postoperative length of the hospital stay can vary, influenced by the surgical approach and patient-specific factors such as rebound intracranial hypertension (RIH).

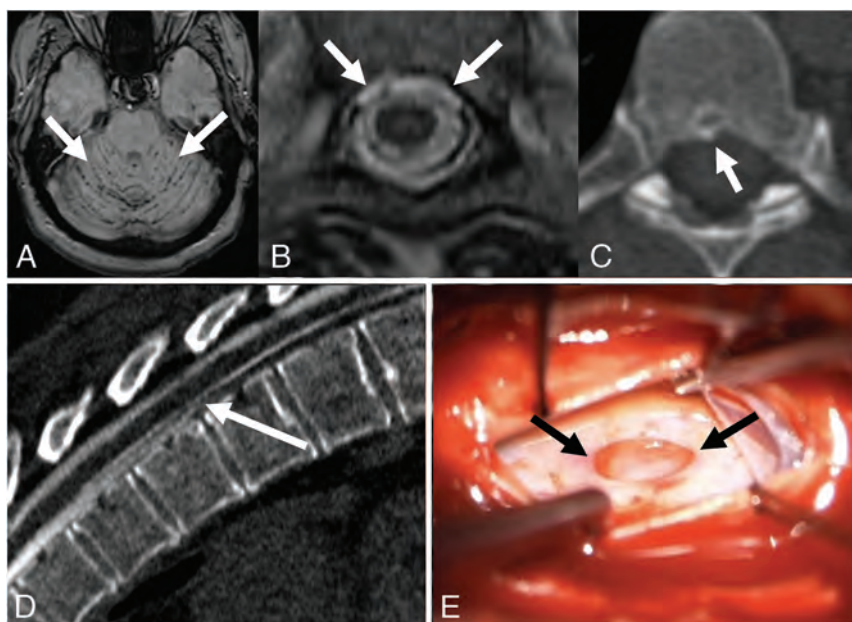


FIG 5. A 49-year-old man with a history of spontaneous intracranial hypotension, with persistent symptoms after 3 epidural blood patches. *A*, Axial SWI with hypointense signal along the cerebellar folia (arrows), consistent with superficial siderosis, a rare complication of chronic CSF leak. *B*, Axial T2-weighted MR imaging demonstrates a ventral epidural fluid collection (arrows). *C*, Axial noncontrast CT image shows a small osteophyte (arrows) along the ventral canal at T6–7. *D*, Prone dynamic CTM demonstrates extravasation of contrast from the subarachnoid space into the ventral epidural space at T6–7 (arrows), consistent with a ventral dural defect. *E*, Intraoperative photograph during repair of the ventral dural defect (arrows) at T6–7, accessed via hemilaminectomy, posterior durotomy, and lateral mobilization of the cord after dentate ligament resection.

A recent study identified substantial gaps in the evidence for the efficacy of epidural patching and surgery in the treatment of SCSFL.⁴³ Thus, there are opportunities for future research in this area, which could be supported by patient registries and multi-center collaborations.

Posttreatment

Patient Perspective: Recovery. A patient discussed her personal journey navigating the recovery process from a SCSFL. She shared her experience with a difficult-to-localize leak, and the many procedures were required before the leak was durably repaired. She described the challenge of undertaking recovery without locally available comprehensive care. She noted that for many patients who lived for years with SCSFL, recovery becomes an existential experience, questioning the meaning of healing and reckoning with a new reality that, while potentially characterized by meaningful clinical improvement, may look nothing like a prior normal life.

She reported that uncertainty is typical during the recovery process, even after successful treatment. Some techniques used to cope with her evolving posttreatment state included tracking symptoms, which helped her take a long view of ongoing severity or resolution, and using talk therapy to process the trauma of living with a SCSFL for so many years.

As noted in her talk, current quaternary referral programs are unable to provide sustained, holistic, comprehensive care to address not only diagnosis and treatment but the recovery process as well. She concluded with a call to action for those in the medical community to consider that although a leak may be

closed, it does not mean that the patient's symptoms have been fully addressed.

Patient Perspective When Treatments Fail: Living with a Leak

Another patient shared her experience with a chronic SCSFL in a presentation focused on acceptance and adaptation, highlighting practical tools and home modifications that have aided in managing daily life. Her journey began with a lumbar puncture performed with an 18-ga cutting needle, leading to a chronic PDPH that significantly impacted her daily activities. After undergoing several rounds of epidural patching, she experienced temporary relief before relapsing. She emphasized the challenges of living with an invisible illness, the emotional toll of acceptance, and the importance of therapy in coping with the condition. She described her fluctuating “uptime,” the duration she could spend upright, and how it shaped her living situation and reliance on family and friends.

She detailed various assistive devices and modifications in her home, including a spill-proof cup for drinking while

lying down, a tool for picking up items, comfortable pillows for sleep support, and accessible kitchen and bathroom equipment. She stressed the importance of creating a living environment tailored to the unique needs of individuals with SCSFL. This presentation offered a glimpse into the possibilities of independent living for those affected by long-term SCSFL, while simultaneously providing physicians a firsthand look at the modifications and adaptations required for daily living when available treatment options are inadequate.

RIH

Because treatment of SCSFLs can alter CSF homeostasis, RIH occurs in some cases. The symptoms of RIH include headaches different in character from the original SCSFL headache, often described as frontally located and worse when lying down rather than standing; patients may also experience symptoms of visual disturbances, nausea, and pulsatile tinnitus.⁴⁴ The morphology and caliber of the transverse venous sinuses, including unilateral hypoplasia and/or stenosis, have been linked to the development of RIH, suggesting a link between venous and CSF dynamics underpinning patient symptomatology.⁴⁵

The diagnosis of RIH involves clinical assessment and sometimes imaging studies to rule out other causes of increased intracranial pressure. Papilledema may or may not be present and can appear before symptoms occur. In some cases, patients may have had untreated idiopathic intracranial hypertension resulting in eventual dural dehiscence and subsequent SCSFL.⁴⁶ These patients can experience marked intracranial hypertension after leak repair.

Management can be challenging and typically focuses on symptom relief while allowing gradual CSF pressure homeostasis. Treatment options include medication to reduce production of CSF or relieve pain, and in severe cases, CSF diversion may be necessary. RIH can present acutely in the immediate posttreatment period or be delayed.⁴⁷ The course of RIH varies, with some patients experiencing a resolution of symptoms with time, while others may require ongoing management. It is important for clinicians to monitor patients closely after SCSFL treatment to identify and manage RIH promptly. Critically, a clinical follow-up infrastructure is needed to optimize symptomatic management for patients in the acute and chronic posttreatment period.

Final Patient Presentation: What Doctors Should Know

The concluding patient talk of the day was a montage of personal experiences and insights from individuals living with SCSFL, detailing struggles with a debilitating condition affecting their daily lives, ambitions, and relationships. The speakers discussed the isolating nature of SCSFL and the need for self-advocacy when pursuing treatment. Some patients expressed the disappointment of having normal imaging findings despite severe symptoms and the relief experienced when procedures confirmed a leak. Above all, they spoke to doctors directly, noting that patients suffer more when providers are unable or unwilling to listen to them and urging physicians to believe their patients.

DISCUSSION

While the understanding of optimal diagnostic strategies and treatments for SCSFL has rapidly increased in the past several years, these techniques are limited to a few institutions, leaving many patients underserved. Additionally, these advances are not stand-alone solutions. Patient experiences offer key clinical insights instrumental in refining diagnostic acumen, which is of particular value to the procedurally inclined neuroradiologist. Neuroradiologists are uniquely situated to advocate for the patient with SCSFL because they may be the first to suggest the condition on the basis of imaging and often have procedural skills required to localize and treat the leak. We advocate a patient-centered model, in which these skills are combined with a deeper, nuanced understanding of clinical presentations in the pre- and posttreatment period.

Discussions at the Bridging the Gap Conference illuminated several key topics for future focus. One such area is the need for a standardized-yet-flexible diagnostic protocol. Variability in clinical presentations and often-subtle radiographic findings necessitate a protocol adaptable to the nuances of individual cases. This process should integrate the latest radiologic techniques with thorough clinical assessment, incorporating patient history as a critical component in the diagnostic process. Specifically, key historical features including any prior intended or unintended dural puncture, how and when symptoms started, and the nature of the symptoms should be ascertained.

Another focal point of the conference was the need for collaborative, multidisciplinary care teams. Such teams, composed of neuroradiologists, neurologists, headache/pain specialists, neurosurgeons, and other health care professionals, are essential for providing comprehensive care that addresses all facets of SCSFL

diagnosis, treatment, and recovery. The value of this approach was evident through shared patient narratives in which multidisciplinary teams were often critical to achieving a correct diagnosis and effective treatment plan. Moreover, these teams can serve as a platform for ongoing education and awareness-building within the medical community, further improving the recognition and understanding of SCSFL.

The conference also highlighted the importance of patient support and advocacy. Patients' narratives and questions revealed common themes of physical, emotional, and psychological distress, often exacerbated by the struggle for diagnosis and effective treatment. This outcome underscores the need for health care providers to adopt a holistic approach, going beyond addressing physical symptoms in isolation. Providing emotional and psychological support, ensuring clear and empathetic communication, and fostering patient empowerment and education are key to improving the overall quality of life for individuals with SCSFL. Additionally, strengthening informed patient support networks and advocacy groups can provide crucial resources and a sense of community for those affected by this condition.

Attendees of the conference reported high levels of satisfaction with the content. A postconference survey was administered to patient attendees who were asked to rate their level of satisfaction with the content on a 5-point Likert Scale: 63% of responders reported being "very satisfied" with the content, while the remaining 36% reported being "satisfied." A CME evaluation form administered to physician attendees showed similar positive feedback, with 90.9% of physicians stating they would change the way they practice because of attending the conference.

The conference is planned to recur annually. A principal goal for the conference in the coming years includes the advocacy of patient-centered research through incorporation of a peer-reviewed scientific abstract-submission process. As the scope of the conference grows, we aim to incorporate additional institutions and more varied health care specialties/perspectives to increase both the breadth and depth of discussion surrounding optimal care of patients with SCSFL.

CONCLUSIONS

The Bridging the Gap Conference provided not only a comprehensive overview of the current state of SCSFL diagnosis and treatment but also set the stage for future advancements in this field. The ideal forward-focal points in SCSFL care include developing adaptable diagnostic protocols, fostering multidisciplinary care teams, and enhancing patient support and advocacy. These steps are essential for bridging the existing gaps in the understanding and management of spinal CSF leaks, ultimately leading to improved patient outcomes and quality of life.

APPENDIX







The "Spinal CSF Leak: Bridging the Gap" Study Group comprises: Nick Stevens, Deborah Friedman, John Reiman, Jessica Houk, Jill Rau, Ian R. Carroll, Wouter Schievink, Claudia Perez Sandhu, Terri Baker, Lalani Carlton Jones, Prem Subramanian, Ilene Ruhoy, Jodi Ettenberg, Danielle Wilhour.

REFERENCES

- Schievink WI, Maya MM, Moser F, et al. Frequency of spontaneous intracranial hypotension in the emergency department. *J Headache Pain* 2007;8:325–28 CrossRef Medline
- Schievink WI. Misdiagnosis of spontaneous intracranial hypotension. *Arch Neurol* 2003;60:1713–18 CrossRef Medline
- Schievink WI, Maya M, Prasad RS, et al. Spinal CSF-venous fistulas in morbidly and super obese patients with spontaneous intracranial hypotension. *AJNR Am J Neuroradiol* 2021;42:397–401 CrossRef Medline
- Liaw V, McCreary M, Friedman DI. Quality of life in patients with confirmed and suspected spinal CSF leaks. *Neurology* 2023;101:e2411–22 CrossRef Medline
- Amrhein TJ, McFatrigh M, Ehle K, et al. Patient experience of spontaneous intracranial hypotension (SIH): qualitative interviews for concept elicitation. *J Patient Rep Outcomes* 2023;7:82 CrossRef Medline
- Headache Classification Committee of the International Headache Society (IHS) The International Classification of Headache Disorders, 3rd edition. *Cephalalgia* 2018;38:1–211 CrossRef Medline
- Schievink WI, Louy C. Precipitating factors of spontaneous spinal CSF leaks and intracranial hypotension. *Neurology* 2007;69:700–02 CrossRef Medline
- Kjeldgaard D, Forchhammer H, Teasdale T, et al. Chronic post-traumatic headache after mild head injury: a descriptive study. *Cephalalgia* 2014;34:191–200 CrossRef Medline
- Graf N, Fernandes Santos AM, Ulrich CT, et al. Clinical symptoms and results of autonomic function testing overlap in spontaneous intracranial hypotension and postural tachycardia syndrome: a retrospective study. *Cephalalgia Reports* 2018;1:251581631877377 CrossRef
- Houk JL, Amrhein TJ, Gray L, et al. Differentiation of Chiari malformation type 1 and spontaneous intracranial hypotension using objective measurements of midbrain sagging. *J Neurosurg* 2021;136:1796–803. Oct 29. [Epub ahead of print] CrossRef Medline
- Straus D, Foster K, Zimmerman F, et al. Chiari drop attacks: surgical decompression and the role of tilt table testing. *Pediatr Neurosurg* 2009;45:384–89 CrossRef Medline
- Schievink WI, Gordon OK, Tourje J. Connective tissue disorders with spontaneous spinal cerebrospinal fluid leaks and intracranial hypotension: a prospective study. *Neurosurgery* 2004;54:65–70; discussion 70–71 CrossRef Medline
- Monaco A, Choi D, Uzun S, et al. Association of mast-cell-related conditions with hypermobile syndromes: a review of the literature. *Immunol Res* 2022;70:419–31 CrossRef Medline
- Callen AL, Timpone VM, Schwertner A, et al. Algorithmic multimodality approach to diagnosis and treatment of spinal CSF leak and venous fistula in patients with spontaneous intracranial hypotension. *AJNR Am J Roentgenol* 2022;219:292–301 CrossRef
- D'Antona L, Jaime Merchan MA, Vassiliou A, et al. Clinical presentation, investigation findings, and treatment outcomes of spontaneous intracranial hypotension syndrome: a systematic review and meta-analysis. *JAMA Neurol* 2021;78:329–37 CrossRef Medline
- Chen ST, Wu JW, Wang YF, et al. The time sequence of brain MRI findings in spontaneous intracranial hypotension. *Cephalalgia* 2022;42:12–19 CrossRef Medline
- Turner R, Zander D, Thaker AA, et al. Structured reporting for findings of spontaneous intracranial hypotension on brain MRI. *AJR Am J Roentgenol* 2023;221:282–83 CrossRef Medline
- Niraj G, Mushambi M, Gauthama P, et al; Accidental Dural Puncture Outcome Study Collaborative Group. Persistent headache and low back pain after accidental dural puncture in the obstetric population: a prospective, observational, multicentre cohort study. *Anaesthesia* 2021;76:1068–76 CrossRef Medline
- Gauthama P, Kelkar A, Basar SM, et al. Incidence of persistent headache at 18 months following accidental dural puncture in the obstetric population: a prospective service evaluation in 45 patients. *Headache* 2019;59:97–103 CrossRef Medline
- Dobrocky T, Grunder L, Breiding PS, et al. Assessing spinal cerebrospinal fluid leaks in spontaneous intracranial hypotension with a scoring system based on brain magnetic resonance imaging findings. *JAMA Neurol* 2019;76:580–87 CrossRef Medline
- Kim DK, Carr CM, Benson JC, et al. Diagnostic yield of lateral decubitus digital subtraction myelogram stratified by brain MRI findings. *Neurology* 2021;96:e1312–18 CrossRef Medline
- Callen A, Pattee J, Thaker AA, et al. Relationship of Bern score, spinal elastance, and opening pressure in patients with spontaneous intracranial hypotension. *Neurology* 2023;100:e2237–46 CrossRef Medline
- Houk JL, Morrison S, Peskoe S, et al. Validity of the Bern Score as a surrogate marker of clinical severity in patients with spontaneous intracranial hypotension. *AJNR Am J Neuroradiol* 2023;44:1096–100 CrossRef Medline
- Mark IT, Amans MR, Shah VN, et al. Resisted inspiration: a new technique to aid in the detection of CSF-venous fistulas. *AJNR Am J Neuroradiol* 2022;43:1544–47 CrossRef Medline
- Amrhein TJ, Gray L, Malinzak MD, et al. Respiratory phase affects the conspicuity of CSF-venous fistulas in spontaneous intracranial hypotension. *AJNR Am J Neuroradiol* 2020;41:1754–56 CrossRef Medline
- Madhavan AA, Cutsforth-Gregory JK, Brinjikji W, et al. Diagnostic performance of decubitus photon-counting detector CT myelography for the detection of CSF-venous fistulas. *AJNR Am J Neuroradiol* 2023;44:1445–50 CrossRef Medline
- Kim BR, Lee JW, Lee E, et al. Utility of heavily T2-weighted MR myelography as the first step in CSF leak detection and the planning of epidural blood patches. *J Clin Neurosci* 2020;77:110–15 CrossRef Medline
- Tay A-MS, Maya M, Moser FG, et al. Computed tomography vs heavily T2-weighted magnetic resonance myelography for the initial evaluation of patients with spontaneous intracranial hypotension. *JAMA Neurol* 2021;78:1275–76 CrossRef Medline
- Choi SY, Seong M, Kim EY, et al. Outcome of epidural blood patch for imaging-negative spontaneous intracranial hypotension. *Cephalalgia* 2023;43:3331024221140471 CrossRef Medline
- Shin HY. Recent update on epidural blood patch. *Anesth Pain Med (Seoul)* 2022;17:12–23 CrossRef Medline
- Schievink WI, Maya MM, Harris J, et al. Infratentorial superficial siderosis and spontaneous intracranial hypotension. *Ann Neurol* 2023;93:64–75 CrossRef Medline
- Patel R, Urits I, Orhurhu V, et al. A comprehensive update on the treatment and management of postdural puncture headache. *Curr Pain Headache Rep* 2020;24:24 CrossRef Medline
- Cheema S, Anderson J, Angus-Leppan H, et al. Multidisciplinary consensus guideline for the diagnosis and management of spontaneous intracranial hypotension. *J Neurol Neurosurg Psychiatry* 2023;94:835–43 CrossRef Medline
- Amrhein TJ, Befera NT, Gray L, et al. CT fluoroscopy-guided blood patching of ventral CSF leaks by direct needle placement in the ventral epidural space using a transforaminal approach. *AJNR Am J Neuroradiol* 2016;37:1951–56 CrossRef Medline
- Schievink WI, Moser FG, Maya MM. CSF-venous fistula in spontaneous intracranial hypotension. *Neurology* 2014;83:472–73 CrossRef Medline
- Callen AL, Jones LC, Timpone VM, et al. Factors predictive of treatment success in CT-guided fibrin occlusion of CSF-venous fistulas: a multicenter retrospective cross-sectional study. *AJNR Am J Neuroradiol* 2023;44:1332–38 CrossRef Medline
- Brinjikji W, Madhavan A, Garza I, et al. Clinical and imaging outcomes of 100 patients with cerebrospinal fluid-venous fistulas treated by transvenous embolization. *J Neurointerv Surg* 2023 Oct 28. [Epub ahead of print] CrossRef Medline

38. Beck J, Hubbe U, Klingler JH, et al. **Minimally invasive surgery for spinal cerebrospinal fluid leaks in spontaneous intracranial hypotension.** *J Neurosurg Spine* 2023;38:147–52 CrossRef Medline
39. Beck J, Raabe A, Schievink WI, et al. **Posterior approach and spinal cord release for 360° repair of dural defects in spontaneous intracranial hypotension.** *Neurosurgery* 2019;84:E345–51 CrossRef Medline
40. Häni L, Fung C, Jesse CM, et al. **Outcome after surgical treatment of cerebrospinal fluid leaks in spontaneous intracranial hypotension—a matter of time.** *J Neurol* 2022;269:1439–46 CrossRef Medline
41. Roytman M, Ulrich CT, Chazen JL. **Post-dural puncture pseudomeningocele (“arachnoid bleb”): an underrecognized etiology of spontaneous intracranial hypotension symptomatology.** *Clin Imaging* 2021;80:377–81 CrossRef Medline
42. Callen AL, Lennarson P, Carroll IR. **A causative role for remote dural puncture and resultant arachnoid bleb in new daily persistent headache: a case report.** *Headache* 2023;63:981–83 CrossRef Medline
43. Amrhein TJ, Williams JW Jr, Gray L, et al. **Efficacy of epidural blood patching or surgery in spontaneous intracranial hypotension: a systematic review and evidence map.** *AJNR Am J Neuroradiol* 2023;44:730–39 CrossRef Medline
44. Kranz PG, Amrhein TJ, Gray L. **Rebound intracranial hypertension: a complication of epidural blood patching for intracranial hypotension.** *AJNR Am J Neuroradiol* 2014;35:1237–40 CrossRef Medline
45. Schievink WI, Maya MM, Jean-Pierre S, et al. **Rebound high-pressure headache after treatment of spontaneous intracranial hypotension: MRV study.** *Neurol Clin Pract* 2019;9:93–100 CrossRef Medline
46. Sulioti G, Gray L, Amrhein TJ. **Popping the balloon: abrupt onset of a spinal CSF leak and spontaneous intracranial hypotension in idiopathic intracranial hypertension, a case report.** *Headache* 2022;62:208–11 CrossRef Medline
47. Jafari E, Karaminia M, Togha M. **Early and delayed rebound intracranial hypertension following epidural blood patch in a case of spontaneous intracranial hypotension.** *Case Rep Neurol Med* 2022;2022:5637276 CrossRef Medline

Epstein-Barr Virus–Associated Smooth-Muscle Tumor of the Brain

 Afra Alfalahi, Abdelsimar Il Omar,  Krystal Fox,  Julian Spears, Malika Sharma,  Aditya Bharatha,  David G. Munoz, and  Suradech Suthiphosuwana

ABSTRACT

SUMMARY: Epstein-Barr virus, a herpesvirus, has been associated with a variety of cancers, including Burkitt, Hodgkin, and non-Hodgkin lymphomas; posttransplant lymphoproliferative disorders; gastric carcinoma; and nasopharyngeal carcinoma, in both immunocompetent and immunocompromised individuals. Previous studies have established a connection between Epstein-Barr virus and the development of smooth-muscle tumors. Smooth-muscle tumors of the brain are very rare and are often misdiagnosed as meningiomas on imaging. To our knowledge, advanced imaging findings such as MR perfusion of smooth-muscle tumors of the brain have never been reported. We describe the radiologic and pathologic features of the Epstein-Barr virus–associated smooth-muscle tumors of the brain in a person with newly diagnosed advanced HIV.

ABBREVIATIONS: EBV = Epstein-Barr virus; EBV-SMT = Epstein-Barr virus–associated smooth-muscle tumor; rCBV = relative CBV; SMT = smooth-muscle tumor

A 35-year-old African-Caribbean man presented with a history of gait instability, confusion, and sensorial changes. Four weeks before the onset of the neurologic symptoms, he had presented to our hospital with a 3-week history of fevers, chills, sweats, and weight loss. He was diagnosed at that time with advanced HIV, with an initial CD4 count of 0 and HIV viral load of 410,000 copies/mL. He was started on antiretroviral therapy with bicittegravir/emtricitabine/tenofovir alafenamide (Biktarvy). When presenting with his new neurologic changes, he was found to be confused but able to obey commands with prodding, with bilateral dysmetria, worse on the right side. There were no other focal neurologic deficits.

Imaging

MR imaging demonstrated a solitary, rounded mass lesion located in the posterior medial aspect of the right posterior fossa. It had a broad dural base abutting the inferior surface of the right tentorium cerebelli without dural thickening or a dural tail sign.

The lesion measured up to 2.8 cm in maximum diameter. On pregadolinium T1WI, the lesion was predominantly isointense to the cerebellar cortex (Fig 1A). On T2WI and FLAIR, the lesion was predominantly hypointense to the cerebellar cortex (Fig 1B, -C). On postgadolinium T1WI, the lesion demonstrated solid, intense enhancement with minimal foci of necrosis peripherally (Fig 1F, -G). There was associated perilesional edema causing mild effacement of the fourth ventricle (Fig 1B, -C). There was no diffusion restriction on DWI (Fig 1D). A few small blooming foci were noted within the lesion seen on SWI (Fig 1E). On DSC MR perfusion-weighted imaging, the mass had low relative cerebral blood volume (rCBV) (Fig 1H).

Subsequent Clinical Course and Operative Report

Given the patient's history of HIV with a low CD4 count and high viral load, the clinical team was very concerned that the intracranial lesion might represent an atypical opportunistic infection, particularly CNS toxoplasmosis, or an HIV-related neoplasm, with CNS lymphoma being a specific concern, despite the imaging appearances not being typical for either condition. Consequently, the clinical team decided to start empiric treatment for CNS toxoplasmosis with pyrimethamine, leucovorin, and clindamycin, in the context of prior adverse drug reaction to trimethoprim-sulfamethoxazole (angioedema and rash). He also had extensive abdominal lymphadenopathy, prompting concern for atypical infection or HIV-related lymphoma with metastatic spread, and a lymph node biopsy was performed, diagnosing disseminated *Mycobacterium avium* complex. He was started on an appropriate therapy. Due to the lack of response of the intracranial lesion as

Received December 4, 2023; accepted after revision February 14, 2024.

From the Division of Diagnostic Neuroradiology (A.A., A.B., S.S.), Department of Medical Imaging, Division of Neurosurgery (A.I.O., K.F., J.S.), Department of Surgery, and Departments of Infectious Diseases (M.S.) and Laboratory Medicine (D.G.M.), St. Michael's Hospital-Unity Health Toronto, University of Toronto, Toronto, Ontario, Canada; Division of Diagnostic Neuroradiology (A.A.), Department of Medical Imaging, University Health Network, University of Toronto, Toronto, Ontario, Canada; and Division of Neurosurgery (A.I.O.), Department of Surgery, McMaster University, Hamilton, Ontario, Canada.

Please address correspondence to Suradech Suthiphosuwana, MD, FRCR, Department of Medical Imaging, St. Michael's Hospital-Unity Health Toronto, University of Toronto, 30 Bond St, Toronto, ON, M5B 1W8, Canada; e-mail: suradech.suthiphosuwana@unityhealth.to

<http://dx.doi.org/10.3174/ajnr.A8258>

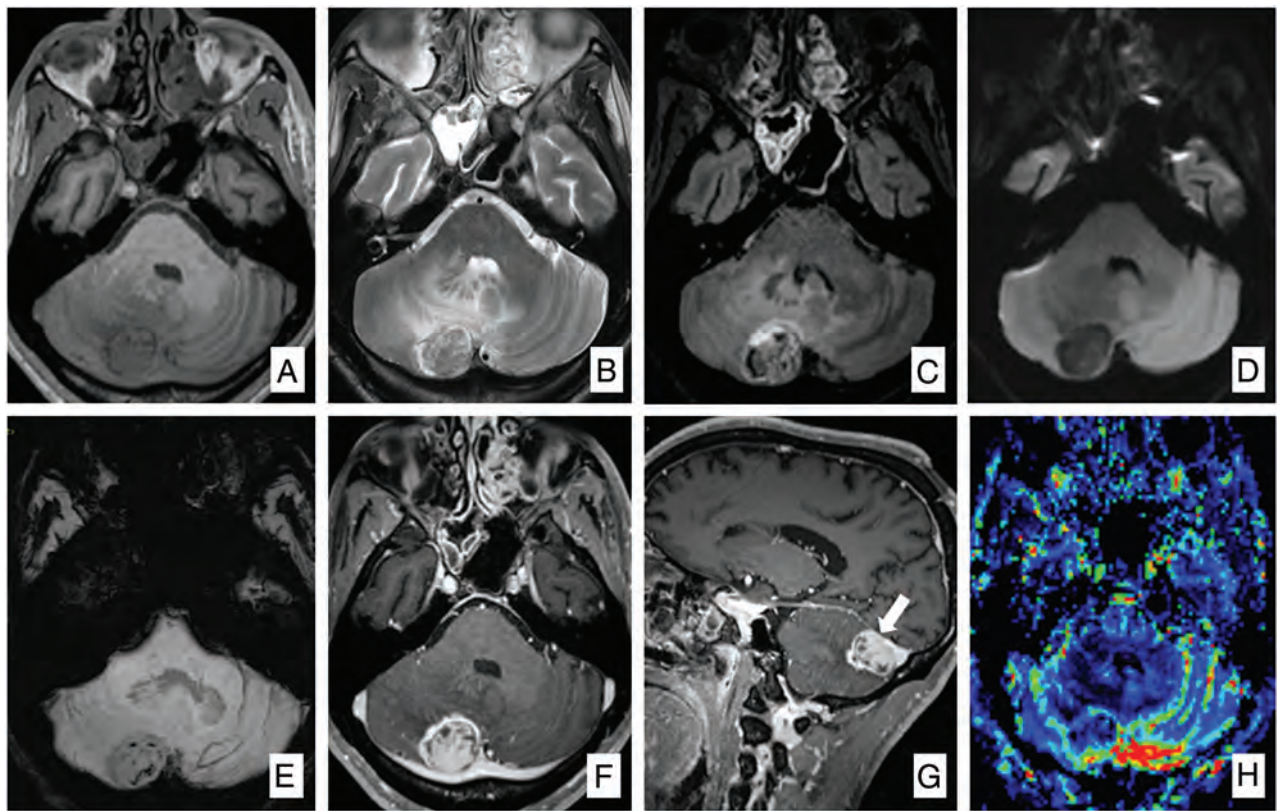


FIG 1. Tumor appearance on MR imaging. MR images show a right posterior fossa mass, which had isointense signal on pregadolinium T1WI (A) and hypointense signal on T2WI (B) and FLAIR (C) with perilesional edema (B and C). The mass does not show diffusion restriction on DWI (D). There are a few blooming foci within the tumor seen on SWI (E). The mass shows intense enhancement with multifocal, small, nonenhancing areas of necrosis on axial postgadolinium T1WI (F). Sagittal postgadolinium T1WI (G) demonstrates the tumor attached to the inferior surface of the right tentorium cerebelli (arrow). On DSC MR perfusion (H), the tumor had low rCBV.

determined on repeat imaging with empiric treatment at 2 weeks, surgical resection was performed. The goals of surgery were the following: a definitive tissue diagnosis, control of mass effect leading to improvement in symptoms, and possible oncologic control with a safe, maximal resection. He underwent suboccipital craniectomy and gross total resection of the tumor. Intraoperatively, we found that the lesion was extra-axial, intradural, and well-demarcated from the surrounding brain with a dural attachment to the tentorium. The tumor was tan-gray and firm and rubbery in consistency. He tolerated the surgery well and was discharged with his condition improved and complete resolution of his neurologic deficits. Subsequent MR imaging at the 1-year follow-up revealed no evidence of tumor recurrence.

Pathology

Histologic examination revealed a tumor made up of cells with spindle-shaped nuclei with blunted ends and wavy eosinophilic cytoplasm of uncertain limits (Fig 2B). Tumor cells were arranged in intersecting streams and whorls surrounding blood vessels, which often had thick, partially hyalinized walls (Fig 2A, -C). There were no tight whorls. The tumor attachment to the dura mater was demonstrated (Fig 2A). Areas of necrosis were scattered throughout, while mitotic activity was inconspicuous. Reticulin stains demonstrated wrapping of single cells, with no reticulin-free areas (Fig 2D). Immunohistochemistry showed positive expression of smooth-muscle actin (Fig 2E) and myosin (Fig 2F), with only a

subset of cells expressing desmin (Fig 2G). Scattered CD3-positive T lymphocytes were scattered throughout, with no CD20-positive B lymphocytes. The Ki-67 proliferation index was approximately 2%, high only in the lining of blood vessels (Fig 2H). Epstein-Barr virus (EBV)-encoded RNA in situ hybridization was intensely positive (Fig 2I). The tumor cells were negative for EMA, SOX-10, STAT6, and E-cadherin. Given these features, the definitive diagnosis was an EBV-associated smooth-muscle tumor (EBV-SMT). Meningioma was ruled out by the absence of tight whorls and expression of EMA and E-cadherin, as well as reticulin-free areas. Solitary fibrous tumor was excluded by the negative for STAT6.

DISCUSSION

EBV, a herpesvirus, has been linked to several types of tumors, including Hodgkin and non-Hodgkin lymphoma and nasopharyngeal carcinoma, in both immunocompetent and immunocompromised patients.¹⁻⁵ Several reports have found a link between EBV and the development of smooth-muscle tumors (SMTs), particularly in immunocompromised patients such as transplant recipients and people living with HIV, particularly those with low CD4 counts.^{2,5-7} It is believed that immune suppression predisposes patients to the development of SMTs.^{1,2,4,5,8-10}

EBV-SMTs have been variably labeled, ranging from “leiomyoma” to “smooth-muscle tumor of uncertain malignant potential”

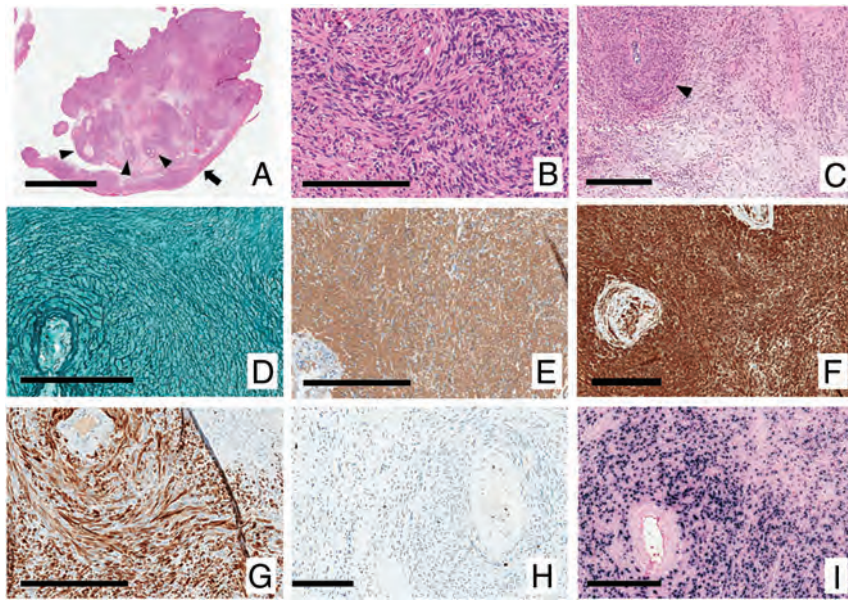


FIG 2. Histopathology. H&E-stained sections A, B, and C (magnification A, bar 4 mm; B, bar 200 μ m; and C, bar 300 μ m). A, The attachment to the dura mater is demonstrated at the lower right (arrow). B, Cells have spindle-shaped nuclei with blunted ends and wavy eosinophilic cytoplasm of uncertain limits and are arranged in intersecting streams and whorls. The tendency to surround blood vessels is seen in A and C (arrowheads). Reticulin stains demonstrate wrapping of single cells, with no reticulin-free areas (D, bar 200 μ m). Immunohistochemistry shows expression of smooth-muscle actin (E, bar 200 μ m) and myosin (F, bar 200 μ m) with only a subset of cells expressing desmin (G, bar 200 μ m). The Ki-67 proliferation index was approximately 2%; high only in the lining of blood vessels (H, bar 200 μ m). EBV-encoded RNA in situ hybridization was intensely positive (I, bar 200 μ m).

to "leiomyosarcoma."^{2,11,12} Approximately one-half of patients with EBV-SMT had multifocal lesions because the tumor can occur as multiple synchronous masses.^{2,3,5} Unlike conventional somatic SMTs, which tend to follow the distribution of smooth muscle throughout the body, EBV-SMTs exhibit an unusual predilection for atypical locations where there is little smooth muscle. The most common site of EBV-SMTs is the intracranial dura mater.^{2,4,5,7} Extracranial involvement has also been reported in various organs, including the spine, adrenal gland, lung, spleen, gallbladder, bone, bladder, nasopharynx, oropharynx, larynx, thyroid, and heart.^{2,4,5}

Although the exact origin of intracranial SMTs remains uncertain, EBV-associated SMTs exhibit distinct characteristics compared with conventional somatic SMTs. Intracranial EBV-SMTs appear closely associated with the walls of small blood vessels.^{2,5} The progenitor cell for EBV-SMT is believed to originate from an aberrant myogenous vascular smooth-muscle cell. It has been demonstrated that normal smooth-muscle cells express the CD21 receptor. In the case of EBV-SMT, EBV directly infects the smooth-muscle cells by binding to CD21, thereby facilitating and promoting replication within this cell. Another proposed pathogenic mechanism is the fusion of EBV-infected lymphocytes with smooth-muscle cells, which may play a critical role in disease development. Nevertheless, the mechanism of EBV-SMT clonal proliferation following EBV infection is still unknown.¹⁻⁵

Radiologically, EBV-SMTs are typically well-circumscribed extra-axial masses. These tumors typically demonstrate hypointense signal on T2-weighted imaging due to the T2-shortening effect of intramuscular actin, myosin, and collagen and densely packed cellular architecture relative to the surrounding brain

tissue.^{13,14} A few reports described the tumors as having a central hyperintense core due to central necrosis.^{6,7,15} They also tend to appear iso- to hypointense on T1-weighted imaging and usually show intense enhancement on postcontrast study. The frequency of necrosis or hemorrhage varies among case reports.^{6,7} The presence of peritumoral edema is also variable and is probably related to the aggressiveness of the tumor or associated infection. These tumors tend to be devoid of calcifications and do not demonstrate diffusion restriction.⁷ Although these tumors are primarily extra-axial in origin, they do not exhibit bone involvement or remodeling.^{2-4,16-18} To date, MR perfusion findings in EBV-SMT of the brain have never been reported.

The diagnosis of EBV-SMT of the brain on imaging can be challenging, because radiologic features often overlap with more common extra-axial brain tumors, particularly meningiomas.^{2,5,18,19} In our case, the tumor was located in the periphery of the posterior fossa, making the differentiation between intra- and

extra-axial locations radiologically challenging. The superficial location and broad dural-based abutment of the adjacent tentorial dura suggested an extra-axial origin of the lesion. The presence of low rCBV on DSC MR perfusion imaging allowed us to exclude more common posterior fossa tumors like meningiomas, hemangioblastoma, and hemangiopericytomas, which typically exhibit higher rCBV values. Additionally, the absence of diffusion restriction made CNS lymphoma, a common HIV-associated CNS neoplasm, less likely. Given the history of HIV infection with a low CD4 count, EBV-SMT of the brain was raised as a diagnostic possibility. There are several atypical opportunistic CNS infections that can present with intracranial masslike lesions, such as toxoplasmosis, cryptococcoma, tuberculoma, cytomegalovirus (CMV), and syphilitic gumma. An extra-axial location, lack of diffusion restriction, and no response to empiric treatment based on MR imaging findings made toxoplasmosis and other atypical opportunistic infections less likely. The negative results from microbiologic or serologic testing were reassuring.

DSC MR perfusion is an advanced MR imaging technique that can provide more information on the vascularity and angiogenesis degree of the tumor.^{20,21} MR perfusion measurements of rCBV have been shown to correlate with both conventional angiographic assessments of tumor vascular density and histologic measures of tumor neovascularization. However, increased tumor vascularity does not necessarily imply malignancy, especially for extra-axial tumors, such as meningiomas, hemangiopericytomas, and paragangliomas, which generally demonstrate high rCBV values.²⁰ In our patient with EBV-SMT, even though pathologically this tumor has a predilection for the smooth

muscles of the blood vessel walls, the tumor was not hypervascular and did not have marked neoangiogenesis based on our MR perfusion findings.

While MR perfusion is not routinely performed for assessing extra-axial intracranial masses, it has proved helpful in distinguishing less common extra-axial tumorlike lesions such as Rosai-Dorfman disease, Erdheim-Chester disease, and neurosarcomatosis, which typically display low rCBV values, from more common tumors like meningiomas, which are hypervascular and exhibit high rCBV values on conventional MR imaging.^{19,22-25} Adding MR perfusion could aid in distinguishing EBV-SMTs from meningiomas in patients with HIV presenting with atypical enhancing extra-axial masses.

There is limited literature available on nuclear scintigraphy and molecular imaging findings in EBV-SMTs. However, a few case reports have shown that [¹⁸F] FDG-PET/CT could be helpful in detecting multifocal synchronous EBV-SMTs in different organs and for assessing the treatment response.^{26,27} Recent studies have demonstrated that PET/CT imaging using radiolabeled somatostatin receptor ligands such as gallium 68 [⁶⁸Ga] DOTATOC or [⁶⁸Ga]-DOTATATE PET/CT may assist in distinguishing meningiomas from other extra-axial masses, including dural-based metastases, paragangliomas, schwannomas, and nontumor lesions.^{28,29} However, studies focusing on somatostatin receptor PET for differentiating meningiomas and EBV-SMTs have not been reported to date.

To our knowledge, there is no standardized therapy for intracranial or spinal EBV-SMTs. Surgical resection continues to be the primary treatment. In instances in which this is deemed feasible, a safe, maximal resection provides a definitive diagnosis, allows control of mass effect, and intuitively leads to improved oncologic control. Combining surgery with adjuvant radiation therapy or chemotherapy is an emerging therapeutic option that should be considered. Immune reconstitution is advised for all patients, given that the development of EBV-SMTs is strongly linked to an immunocompromised state.^{3-5,30}

Case Summary

- 1) EBV-SMTs constitute a very rare oncologic entity. They usually develop in the context of secondary immunodeficiency caused by HIV infection or immunosuppressive treatment after solid organ transplantation.
- 2) EBV-SMTs can manifest as solitary or multiple lesions. The most common site of these tumors is the intracranial dura mater, which usually mimics meningiomas on imaging.
- 3) EBV-SMTs typically show hypointense signal relative to the surrounding brain on T2WI due to the presence of smooth-muscle cells.
- 4) MR perfusion has been demonstrated to be helpful in distinguishing meningiomas from their mimics. In our patient with EBV-SMT, the tumor demonstrated low rCBV values on MR perfusion. This characteristic may be helpful in the differentiation from meningiomas, which typically present as hypervascular tumors and with elevated CBV values.
- 5) The primary treatment recommendation for EBV-SMTs is surgical resection, with or without combining adjunctive therapies, along with treatment of the underlying immunodeficiency.

Disclosure forms provided by the authors are available with the full text and PDF of this article at www.ajnr.org.

REFERENCES

1. Dekate J, Chetty R. **Epstein-Barr virus-associated smooth muscle tumor.** *Arch Pathol Lab Med* 2016;140:718–22 CrossRef Medline
2. Deyrup AT, Lee VK, Hill CE, et al. **Epstein-Barr virus-associated smooth muscle tumors are distinctive mesenchymal tumors reflecting multiple infection events.** *Am J Surg Pathol* 2006;30:75–82 CrossRef Medline
3. Issarachaikul R, Shuangshoti S, Suankratay C. **Epstein-Barr virus-associated smooth muscle tumors in AIDS patients: a largest case (series).** *Intern Med* 2014;53:2391–96 CrossRef Medline
4. Purgina B, Rao UN, Miettinen M, et al. **AIDS-related EBV-associated smooth muscle tumors: a review of 64 published cases.** *Pathol Res Int* 2011;2011:561548–10 CrossRef Medline
5. Willeke VM, Anderson MP, Mahadevan A, et al. **Epstein Barr virus associated smooth muscle tumors in the central nervous system: a case report and systematic review of the literature.** *J Neurooncol* 2020;147:247–60 CrossRef Medline
6. Bargiela A, Rey JL, Diaz JL, et al. **Meningeal leiomyoma in an adult with AIDS: CT and MRI with pathological correlation.** *Neuroradiology* 1999;41:696–98 CrossRef Medline
7. Soni N, Ora M, Singh R, et al. **Unpacking the CNS manifestations of Epstein-Barr virus: an imaging perspective.** *AJNR Am J Neuroradiol* 2023;44:1002–08 CrossRef Medline
8. Boudjemaa S, Boman F, Guignon V, et al. **Brain involvement in multicentric Epstein-Barr virus-associated smooth muscle tumours in a child after kidney transplantation.** *Virchows Arch* 2004;444:387–91 CrossRef Medline
9. Chiu YT, Lee JC, Cheng A, et al. **Epstein-Barr virus-associated smooth muscle tumor as the initial presentation of HIV infection: a case report.** *J Formos Med Assoc* 2018;117:82–84 CrossRef Medline
10. Lee ES, Locker J, Nalesnik M, et al. **The association of Epstein-Barr virus with smooth-muscle tumors occurring after organ transplantation.** *N Engl J Med* 1995;332:19–25 CrossRef Medline
11. Brown HG, Burger PC, Olivi A, et al. **Intracranial leiomyosarcoma in a patient with AIDS.** *Neuroradiology* 1999;41:35–39 CrossRef Medline
12. Mierau GW, Greffe BS, Weeks DA. **Primary leiomyosarcoma of brain in an adolescent with common variable immunodeficiency syndrome.** *Ultrastruct Pathol* 1997;21:301–05 CrossRef Medline
13. Bansal A, Goyal S, Goyal A, et al. **WHO classification of soft tissue tumours 2020: An update and simplified approach for radiologists.** *Eur J Radiol* 2021;143:109937 CrossRef Medline
14. Park SB. **Features of the hypointense solid lesions in the female pelvis on T2-weighted MRI: T2 hypointense solid lesions in female pelvis.** *J Magn Reson Imaging* 2014;39:493–503 CrossRef Medline
15. Lohan R, Bathla G, Gupta S, et al. **Epstein-Barr virus (EBV)-related smooth muscle tumors of central nervous system: a report of two cases and review of literature.** *Clin Imaging* 2013;37:564–68 CrossRef Medline
16. Barrett K, Tavakoli S, McGinity M, et al. **Intracranial Epstein-Barr virus-associated smooth muscle tumor with superimposed cryptococcal infection: a case report.** *Medicine (Baltimore)* 2022;101:e28806 CrossRef Medline
17. Gallien S, Zuber B, Polivka M, et al. **Multifocal Epstein-Barr virus-associated smooth muscle tumor in adults with AIDS: case report and review of the literature.** *Oncology* 2008;74:167–76 CrossRef Medline
18. Smith AB, Horkanyne-Szakaly I, Schroeder JW, et al. **From the radiologic pathology archives: mass lesions of the dura: beyond meningioma—radiologic-pathologic correlation.** *RadioGraphics* 2014;34:295–312 CrossRef Medline
19. Lyndon D, Lansley JA, Evanson J, et al. **Dural masses: meningiomas and their mimics.** *Insights Imaging* 2019;10:11 CrossRef Medline

20. Cha S. **Perfusion MR imaging: basic principles and clinical applications.** *Magn Reson Imaging Clin N Am* 2003;11:403–13 CrossRef Medline
21. Lacerda S, Law M. **Magnetic resonance perfusion and permeability imaging in brain tumors.** *Neuroimaging Clin N Am* 2009;19:527–57 CrossRef Medline
22. Idir I, Cuvinciuc V, Uro-Coste E, et al. **MR perfusion of intracranial Rosai-Dorfman disease mimicking meningioma.** *J Neuroradiol* 2011;38:133–34 CrossRef Medline
23. Nowosielski M, Galldiks N, Iglseder S, et al. **Diagnostic challenges in meningioma.** *Neuro Oncol* 2017;19:1588–98 CrossRef Medline
24. Sawlani V, Patel MD, Davies N, et al. **Multiparametric MRI: practical approach and pictorial review of a useful tool in the evaluation of brain tumours and tumour-like lesions.** *Insights Imaging* 2020; 11:84 CrossRef Medline
25. Zimny A, Sasiadek M. **Contribution of perfusion-weighted magnetic resonance imaging in the differentiation of meningiomas and other extra-axial tumors: case reports and literature review.** *J Neurooncol* 2011;103:777–83 CrossRef Medline
26. Liu Y, Chintalapati S, Dietz R, et al. **EBV-associated hepatic smooth muscle tumor of uncertain biologic behavior after heart transplantation in a pediatric patient: case report.** *J Gastrointest Oncol* 2017;8:E21–25 CrossRef Medline
27. Yuan H, Zeng B, He L, et al. **18F-FDG PET/CT imaging of multiple intrahepatic Epstein-Barr virus-associated smooth muscle tumors in a pediatric patient after heart transplantation.** *Hell J Nucl Med* 2022;25:320–22 CrossRef Medline
28. Galldiks N, Albert NL, Wollring M, et al. **Advances in PET imaging for meningioma patients.** *Neurooncol Adv* 2023;5:i84–93 CrossRef Medline
29. Hartmann K, Gillman JA, Lazor JW, et al. **68Ga-DOTATATE PET to characterize lesions in the neuroaxis.** *Clin Nucl Med* 2024;49:9–15 CrossRef Medline
30. Lau K, Hsu Y, Lin Y, et al. **Role of surgery in treating Epstein-Barr virus-associated smooth muscle tumor (EBV-SMT) with central nervous system invasion: a systemic review from 1997 to 2019.** *Cancer Med* 2021;10:1473–84 CrossRef Medline

Imaging Assessments and Clinical Significance of Brain Frailty in Moyamoya Disease

Liuxian Wang, Jinhao Lyu, Dongshan Han, Xiangbing Bian, Dekang Zhang, Hui Wang, Fangbin Hao, Lian Duan, Lin Ma, and Xin Lou



ABSTRACT

BACKGROUND AND PURPOSE: Imaging assessment of brain frailty in ischemic stroke has been extensively studied, while the correlation between brain frailty and Moyamoya disease remains obscure. This study aimed to investigate the imaging characteristics of brain frailty and its clinical applications in Moyamoya disease.

MATERIALS AND METHODS: This study included 60 patients with Moyamoya disease (107 hemispheres). All patients were divided into stroke and nonstroke groups based on clinical symptoms and imaging findings. The modified brain frailty score was adapted to consider 4 imaging signs: white matter hyperintensity, enlargement of perivascular space, old vascular lesions, and cerebral microbleed. The relative CBF of the MCA territory was quantified using pseudocontinuous arterial-spin labeling. Surgical outcome after revascularization surgery was defined by the Matsushima grade.

RESULTS: The relative CBF of the MCA territory decreased as the modified brain frailty score and periventricular white matter hyperintensity grades increased ($\rho = -0.22, P = .02$; $\rho = -0.27, P = .005$). Clinically, the modified brain frailty score could identify patients with Moyamoya disease with stroke (OR = 2.00, $P = .02$). Although the modified brain frailty score showed no predictive value for surgical outcome, basal ganglia enlargement of the perivascular space had a significant correlation with the postoperative Matsushima grade (OR = 1.29, $P = .03$).

CONCLUSIONS: The modified brain frailty score could reflect a cerebral perfusion deficit and clinical symptoms of Moyamoya disease, and its component basal ganglia enlargement of perivascular space may be a promising marker to predict surgical outcome and thus aid future clinical decision-making.

ABBREVIATIONS: CMB = cerebral microbleed; EDAS = encephaloduroarteriosynangiosis; EPVS = enlargement of the perivascular space; MMD = Moyamoya disease; PCA = posterior cerebral artery; pCASL = pseudocontinuous arterial-spin labeling; PVS = perivascular space; rCBF_{mca} = relative CBF of the MCA; WMH = white matter hyperintensity

Moyamoya disease (MMD) is an uncommon cerebrovascular disease characterized by progressive occlusion of the terminal portion of the ICA and its main branches within the circle of Willis.¹ Pathologically, MMD was also presumed to be related to disorders of the small vessels (perforating arterioles, capillaries, and probably venules) of the brain.^{2,3} Long-term impairment of both large arteries and small vessels could lead to chronic hypoperfusion, which would eventually cause brain parenchyma changes.

Received November 7, 2023; accepted after revision February 9, 2024.

From the Departments of Radiology (L.X.W., J.H.L., D.S.H., X.B.B., D.K.Z., H.W., L.M., X.L.) and Neurosurgery (F.B.H., L.D.), Chinese PLA General Hospital/Chinese PLA Medical School, Beijing, China.

This work was supported by the National Natural Science Foundation of China (No. 82327803, No. 81825012, No. 82151309 to X. Lou and No. 82271952 to J.H. Lyu).

Please address correspondence to Xin Lou, MD, Department of Radiology, Chinese PLA General Hospital/Chinese PLA Medical School, No. 28 Fuxing Rd, Haidian District, Beijing 100853, China; e-mail: louxin@301hospital.com.cn



Indicates article with online supplemental data.

<http://dx.doi.org/10.3174/ajnr.A8232>

Brain frailty was widely used in patients with stroke to reflect brain resilience or vulnerability.⁴ It could be conceptualized as the consequences associated with accumulation of multiple chronic damage.⁵ In most neuroimaging studies, brain frailty shares similar imaging features with cerebral small-vessel disease, including white matter hyperintensity (WMH), old vascular lesions or lacunes, brain atrophy, enlargement of the perivascular space (EPVS), and cerebral microbleed (CMB).^{6,7} These features were associated independently with a poor outcome of stroke and represent markers of brain frailty.⁸ However, the role of brain frailty in MMD remains largely unknown. In this study, we introduced a modified brain frailty score for MMD based on the research by Duan et al.⁷ The modified brain frailty score involved imaging assessments of WMH, old vascular lesions, EPVS, and CMB.

This study aimed to evaluate the imaging characteristics of brain frailty in MMD and further investigate the clinical implications of brain frailty and its component imaging findings.

SUMMARY SECTION

PREVIOUS LITERATURE: Brain frailty is a notion reflecting brain tissue vulnerability and decline of cerebral physiologic reserve following stressor events. Previous literature has proposed the utilization of neuroimaging markers to reflect brain frailty status, including white matter hyperintensity (WMH), enlargement of periventricular space (EPVS), vascular lesion, and cerebral micro-bleed. There is a growing focus on brain frailty in cerebrovascular disease. However, the evaluation of brain frailty and its clinical implications in Moyamoya disease remains unknown.

KEY FINDINGS: This study found that cerebral perfusion decreased as modified brain frailty score and periventricular WMH grades increased. Clinically, the modified brain frailty score could identify patients with Moyamoya disease with stroke. Basal ganglia EPVS presented significant correlation with postoperative Matsushima grade.

KNOWLEDGE ADVANCEMENT: The current study provided new knowledge regarding the overall estimation of brain frailty by using neuroimaging markers in Moyamoya disease. The modified brain frailty score could reflect the hemodynamic status, with its constituent, EPVS, exhibiting potential in predicting postoperative revascularization.

MATERIALS AND METHODS

Patient Characteristics

This observational study was approved by the institutional ethics committee and registered as a clinical trial (NCT03785171). Written informed consent was obtained from each patient or his or her legally authorized representative.

From September 2018 to June 2019, this cross-sectional, prospective study consecutively enrolled patients with MMD according to the Japanese guidelines published in 2012, excluding Moyamoya syndrome.⁹ All patients underwent MR imaging and were divided into stroke MMD (ischemic or hemorrhagic stroke confirmed by both clinical symptoms and imaging findings, including acute and chronic phases) and nonstroke MMD. In stroke MMD, the cerebral lesion found on imaging should be responsible for the clinical symptoms. Symptoms of nonstroke MMD were defined as episodic or nonspecific symptoms, such as TIA, headache, dizziness, and other symptoms without responsible structural lesions. The exclusion criteria were as follows: 1) patients 18 years of age or younger; 2) patients who previously underwent bypass surgery (direct or indirect revascularization); 3) hemispheres that showed a normal ICA and MCA without steno-occlusion; 4) patients with a history of systemic diseases such as terminal carcinoma and immune system diseases; and 5) poor imaging quality that prevented further imaging analysis.

Imaging Acquisition and Assessments

Imaging Acquisition. All patients were scanned on a 3T Discovery 750 MR scanner (GE Healthcare) with an 8-channel phased array head coil. Detailed MR imaging parameters were as follows: 1) FLAIR: TR = 6000 ms, TE = 160 ms, section thickness = 6 mm; 2) pseudocontinuous arterial-spin labeling (pCASL): TR = 4844 ms, TE = 10.5 ms, labeling duration = 1500 ms, postlabeling delay = 2000 ms, section thickness = 4 mm; 3) DWI: TR = 6800 ms, TE = 90 ms, $b=0$ and 1000 s/mm², section thickness = 5 mm; 4) TOF-MRA: TR = 34 ms, TE = minimum, section thickness = 1 mm; 5) T2-weighted imaging: TR = 5752 ms, TE = 93 ms, section thickness = 6 mm; 6) SWI: TR = 33.5 ms, TE = 37.9 ms, section thickness = 3 mm; 7) high-resolution T1-weighted structural imaging: TR = 6 ms, TE = 2.5 ms, section thickness = 1 mm.

DSA was performed after contrast injection in both ICAs, both external carotid arteries, and 1 or 2 vertebral arteries. Lateral and anterior-posterior views of each artery injection were collected.

Brain Frailty Assessment. Brain frailty was assessed by 2 radiologists with 5 years of experience in neuroimaging who were blinded to the clinical information. The Fazekas scale was used to score the severity of periventricular WMH (0, absence; 1, “caps” or pencil-thin lining; 2, smooth “halo”; 3, irregular hyperintensities extending into deep white matter and deep WMH (0, absence; 1, punctate foci; 2, beginning confluence of foci; 3, large confluent areas).¹⁰ The severity of basal ganglia EPVS was rated according to the study by Potter et al:¹¹ grade 0 (none), grade I (1–10), grade II (11–20), grade III (21–40), and grade IV (> 40). The presence of EPVS was carefully identified from lacunes.¹² Old vascular lesions were defined as ischemic or hemorrhagic lesions of the brain parenchyma, including lacunar infarction. CMB was rated on SWI as hypointense lesions. In this study, brain atrophy was not considered a component of brain frailty because it is not common in patients with MMD.

The modified brain frailty score was calculated as the sum of each point, ranging from 0 to 4.¹³ One point was given when ≥ 1 vascular lesion was present, 1 point was given when ≥ 1 CMB was present, 1 point was assigned when periventricular WMH was Fazekas 3 and/or deep WMH was Fazekas 2–3, and 1 point was assigned when moderate-to-severe EPVS (grades II–IV) was present in the basal ganglia.

Estimation of CBF. Quantitative estimation of CBF of the MCA territory was performed using the Clinical Toolbox (<https://www.nitrc.org/projects/clinicaltbx>) for Statistical Parametric Mapping (SPM12; <https://www.fil.ion.ucl.ac.uk/spm>) on a Matlab platform (R2020a; MathWorks). First, the CBF map of pCASL was generated using the FuncTool from AW 4.5 Workstation (GE Healthcare). Second, CBF maps were coregistered to original T1 images. Third, high-resolution T1 structural images were normalized to the Montreal Neurological Institute space using the Clinical Toolbox. This toolbox normalizes the high-resolution T1 images to Montreal Neurological Institute space with a combination of lesion maps, minimizing the influence of cerebral lesions. Each

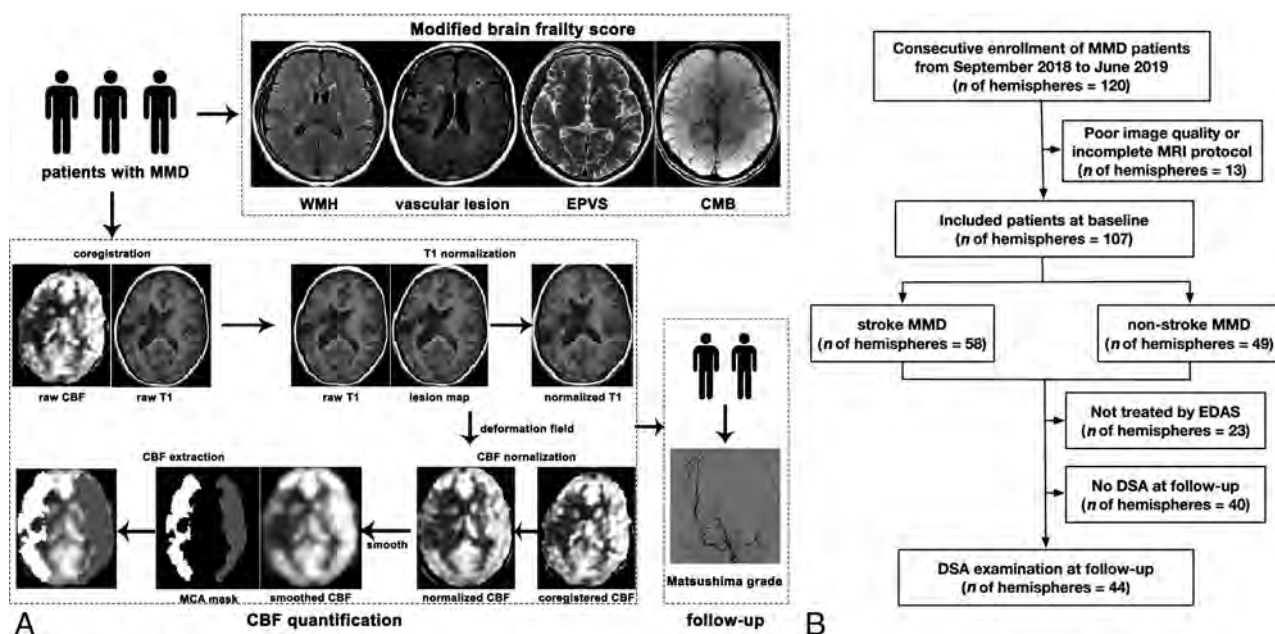


FIG 1. Flow diagram (A) and patient inclusion (B) in this study.

lesion map was manually delineated on original T1 images with FLAIR images as references. Fourth, the coregistered CBF maps were normalized to Montreal Neurological Institute space using the formerly generated deformation field for T1 images. Fifth, the normalized CBF maps were spatially smoothed by a 6-mm full width at half maximum Gaussian kernel. Sixth, a brain mask of the MCA territory was projected to the CBF maps, which has been described elsewhere.¹⁴

Eighteen hemispheres showed large, chronic infarctions exceeding the threshold of 15 mm for lacunes (10 lesions on the left hemisphere, 8 on the right). Those lesions were subtracted from the mask before calculating the mean CBF. We also calculated the mean lesion map showing the spatial distribution of those lesions. Seventh, a study-specified VOI in the ipsilateral cerebellum was used to reflect the relative decrease of CBF of MCA territory according to study by Calviere et al.¹⁵ Finally, the mean CBF of the MCA territory of each hemisphere and the cerebellum was extracted. The CBF of the MCA territory was defined as CBF_{mca} , while the CBF of the cerebellum was $CBF_{cerebellum}$. The adjusted ratio of the CBF of the MCA territory against the ipsilateral cerebellum was defined as relative CBF of the MCA ($rCBF_{mca}$).

Assessment of Matsushima Grade at Follow-Up. Fifty patients underwent encephaloduroarteriosynangiosis (EDAS) surgery. At least 3 months after surgery, postoperative revascularization of 27 patients (44 hemispheres) was graded using the Matsushima grade on DSA.¹⁶ Grade I indicates revascularization of less than one-third of the MCA distribution, grade II represents revascularization of one-third to two-thirds of the MCA distribution, and grade III indicates revascularization of more than two-thirds of the MCA distribution. Surgical outcome was defined as favorable (Matsushima grade III) and poor (Matsushima grade I–II).

Statistical Analysis

The test for agreement was calculated to assess interrater reliability. The Kolmogorov-Smirnov test was used to assess data normality. Two-sample *t* tests for continuous data and χ^2 tests or Fisher exact tests for categorical data were used for comparative analysis. The Spearman correlation analysis was used for correlational analysis. Ipsilateral posterior cerebral artery (PCA) involvement was considered a covariant because the leptomeningeal collateral from the PCA is a major source of blood supply in MMD.¹⁷ PCA involvement was defined as moderate-to-severe stenosis or occlusion. Logistic regression analysis was used to assess the modified brain frailty score and other variables (age, sex, PCA involvement, and vascular risk factors) in differentiating stroke from nonstroke MMD and to predict the postoperative Matsushima grade. Variables were selected in multivariate logistic regression analyses with a $P < .10$ threshold. $P < .05$ was considered statistically significant. All statistical analyses were performed using SPSS 26.0 (IBM).

RESULTS

Clinical and Imaging Characteristics

Sixty-seven patients with MMD were enrolled in this study, while 7 patients were excluded due to poor image quality or incomplete MR imaging sequences. As a result, 60 patients with MMD were finally analyzed, including 13 unilateral and 47 bilateral cases, for a total of 107 hemispheres. Of all patients who underwent EDAS surgery, 27 patients (44 hemispheres) underwent follow-up DSA assessment, with an average interval of 10.6 (SD, 4.8) months. The Online Supplemental Data provide a summary of included patients with MMD. Figure 1 shows the flow diagram of image-processing and patient enrollment in this study.

The interrater κ values for periventricular WMH, deep WMH, basal ganglia EPVS, vascular lesions, and CMB were 0.83, 0.83, 0.76, 0.92, and 0.80, respectively. Figure 2 presents a case of MMD.

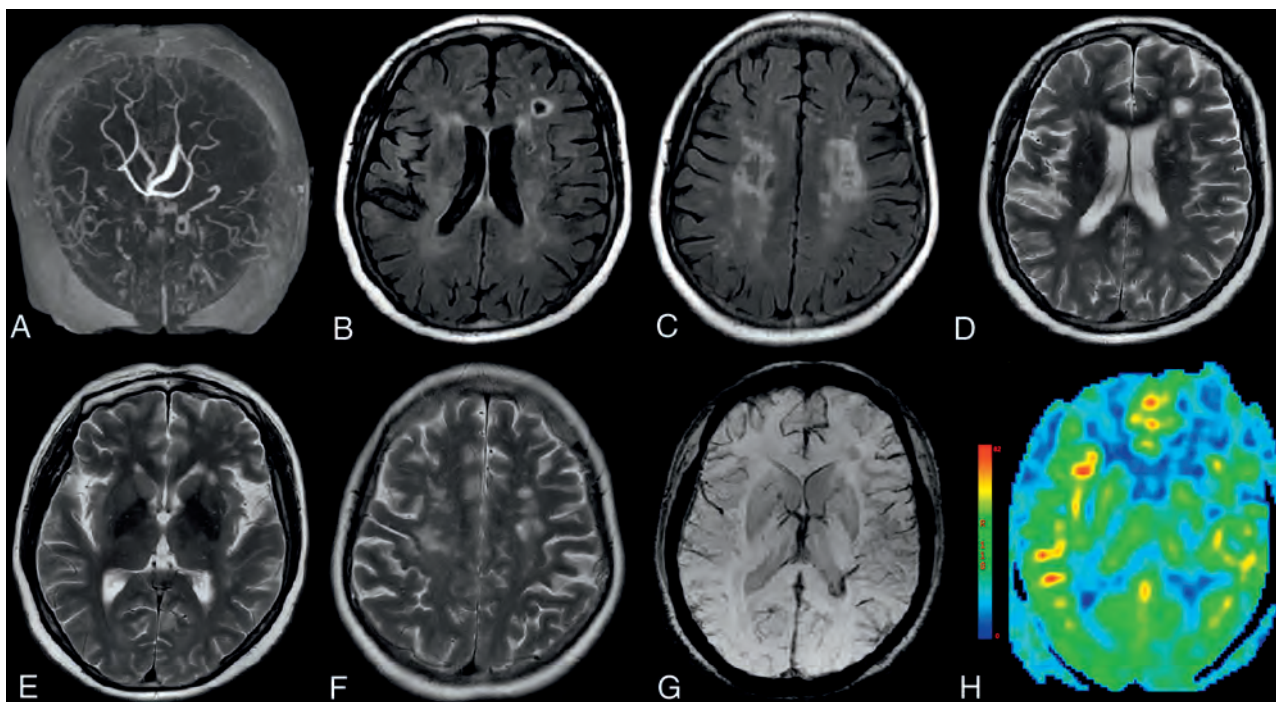


FIG 2. An illustrative case of a 46-year-old man with bilateral Moyamoya disease who presented with weakness of the right limb for 1 year. The modified brain frailty score was 2 for the left and 1 for the right hemisphere. MRA showed occlusion of the bilateral ICA (A). The periventricular and deep WMH was grade II for both sides on FLAIR images (B and C). Vascular lesions were found in the left frontal lobe on T2-weighted image (D). The EPVS in the basal ganglia was grade II for both sides on T2-weighted images (E and F). No microbleed was found on SWI (G). Both hemispheres showed perfusions deficits on CBF map (H).

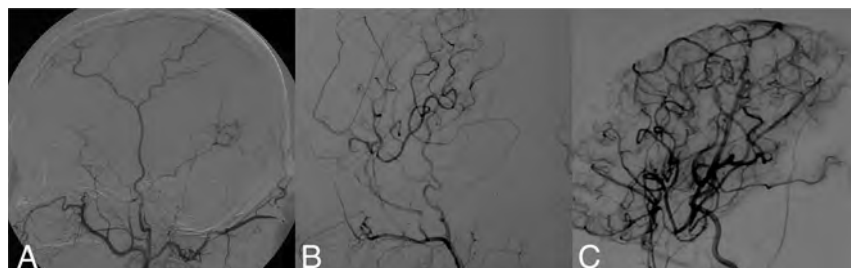


FIG 3. DSA of the Matsushima grade I (A), grade II (B), and grade III (C). Grade I indicates revascularization of less than one-third of the MCA distribution, grade II represents revascularization of one-third to two-thirds of the MCA distribution, and grade III indicates revascularization of more than two-thirds of the MCA distribution.

Figure 3 shows DSA images of postoperative Matsushima grades. The group-level lesion map shows that most large lesions were located at the frontotemporal and temporo-occipital watershed area (Fig 4). Between hemispheres with and without PCA involvement, the modified brain frailty score ($\chi^2 = 14.49$, $P = .006$), periventricular WMH ($\chi^2 = 15.18$, $P = .002$), and deep WMH ($\chi^2 = 18.38$, $P < .001$) showed significant differences, while the EPVS ($\chi^2 = 0.18$, $P = .91$), vascular lesions ($\chi^2 = 1.50$, $P = .22$), and CMB ($\chi^2 = 4.68$, $P = .06$) could not differentiate the 2 groups.

Correlations of the Modified Brain Frailty Score and Cerebral Perfusion

Results of correlations among the modified brain frailty score, WMH, and EPVS with cerebral perfusion are shown in Fig 5.

There were significant correlations between the modified brain frailty score ($\rho = -0.22$, $P = .02$) and periventricular WMH with $rCBF_{mca}$ ($\rho = -0.27$, $P = .005$). No significant differences were found between hemispheres with and without CMB ($t = 0.75$, $P = .46$), as well as vascular lesions ($t = 1.55$, $P = .12$).

Differentiation of Stroke from Nonstroke MMD

There were 58 (54%) hemispheres in the stroke MMD group and 49 (46%) hemispheres in the nonstroke MMD group.

The modified brain frailty score, sex, PCA involvement, and dyslipidemia met the threshold for multivariate logistic regression. Logistic regression analysis revealed that the modified brain frailty score and PCA involvement could differentiate stroke MMD from nonstroke MMD (OR = 2.00, $P = .02$; OR = 5.52, $P = .02$). The results are presented in Table 1. As for the separate features of brain frailty, periventricular WMH ($\chi^2 = 14.45$, $P = .002$), deep WMH ($\chi^2 = 8.27$, $P = .04$), and vascular lesions showed significant differences ($\chi^2 = 10.37$, $P = .001$) between the 2 groups. EPVS ($\chi^2 = 2.21$, $P = .33$) and CMB ($\chi^2 = 1.38$, $P = .24$) could not differentiate stroke and nonstroke MMD.

Subgroup Analysis in Stroke and Nonstroke MMD

To better understand whether the presence of brain parenchyma damage would affect the relationship between the modified brain

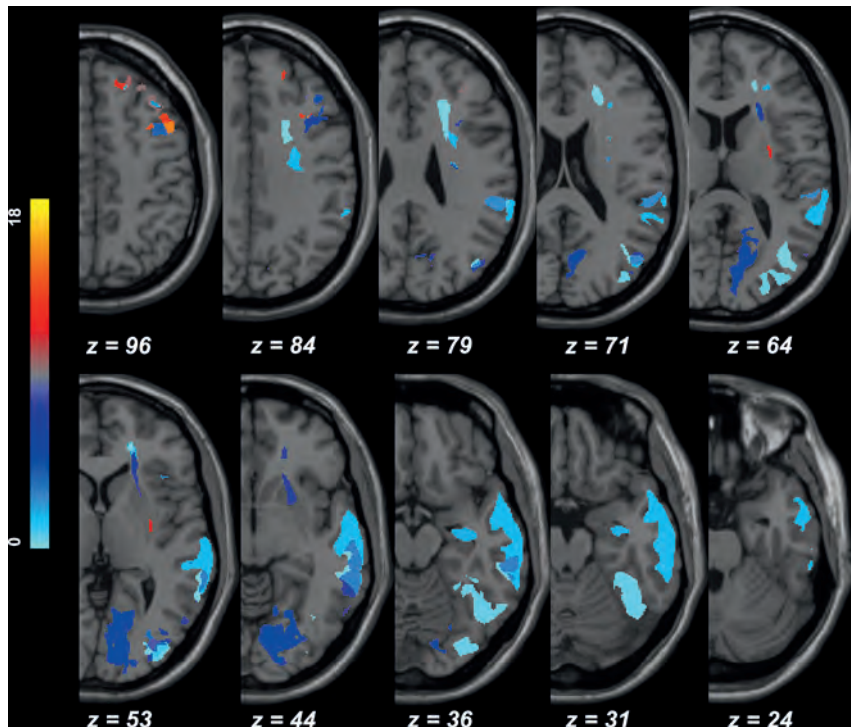


FIG 4. Lesion map ($n=18$). Most large lesions were located at the frontotemporal and temporo-occipital watershed areas. Z refers to the section location, and a voxel with a brighter color indicates a larger number of hemispheres involved that lesioned voxel.

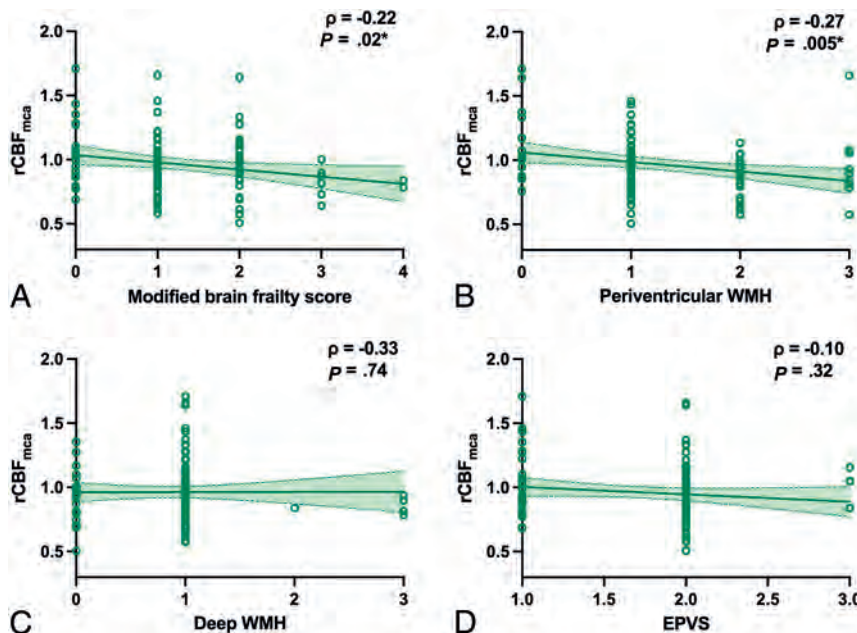


FIG 5. Scatterplots of the correlations between $rCBF_{mca}$ and the modified brain frailty score (A), periventricular WMH (B), deep WMH (C), and EPVS (D) ($n=107$).

frailty score and cerebral perfusion, we performed subgroup analysis in stroke and nonstroke MMD.

In stroke MMD, there was significant correlation between the modified brain frailty score with $rCBF_{mca}$ ($\rho = -0.28$, $P = .04$). No significant correlations were found between periventricular WMH ($\rho = -0.23$, $P = .09$), deep WMH ($\rho = -0.02$, $P = .91$),

and EPVS ($\rho = -0.11$, $P = .42$) with $rCBF_{mca}$. No significant differences were found between hemispheres with and without CMB ($t = 1.28$, $P = .20$), as well as vascular lesions ($t = 1.13$, $P = .26$).

In nonstroke MMD, there was significant correlation between the periventricular WMH with $rCBF_{mca}$ ($\rho = -0.29$, $P = .04$). No significant correlations were found among the modified brain frailty score ($\rho = -0.05$, $P = .74$), deep WMH ($\rho = -0.15$, $P = .31$), and EPVS ($\rho = -0.02$, $P = .89$) with $rCBF_{mca}$. No significant differences were found between hemispheres with and without CMB ($t = -0.86$, $P = .40$), as well as vascular lesions ($t = 0.43$, $P = .67$).

Prediction of Matsushima Grade

After EDAS surgery, 12 (27%) hemispheres showed favorable outcome (Matsushima grade III), and 32 (73%) showed poor outcome (Matsushima grades 0–II). The modified brain frailty score did not differ between the 2 groups ($\chi^2 = 1.36$, $P = .71$), similar to its component imaging findings of periventricular WMH, deep WMH, vascular lesions, and CMB ($\chi^2 = 5.74$, $P = .12$; Fisher $Z = 2.74$, $P = .25$; Fisher $Z = 1.45$, $P = .49$; Fisher $Z = 0.54$, $P = .47$). Nevertheless, basal ganglia EPVS showed a significant difference (Fisher $Z = 12.20$, $P = .001$). In addition, age, PCA involvement and a history of smoking also met the threshold for multivariate analysis. PCA involvement and basal ganglia EPVS could independently predict the postoperative Matsushima grade (OR = 0.56, $P = .01$; OR = 1.29, $P = .03$) (Table 2).

DISCUSSION

In this study, we found that patients with MMD with a higher modified brain frailty score showed lower cerebral perfusion. Moreover, the modified brain frailty score was higher in patients with MMD with stroke.

Although the frailty score showed no predictive value for postoperative revascularization, the basal ganglia EPVS was a promising indicator.

The correlation between the individual imaging components of brain frailty and perfusion in MMD has been reported by many studies. Sun et al¹⁸ found that lacunes, EPVS, and WMHs

Table 1: Differentiation of stroke MMD from nonstroke MMD (n = 107)

Variables	Univariate Analyses		Multivariate Logistic Regression	
	χ^2 or t	P	OR (95% CI)	P
Modified brain frailty score ^a	10.88	.03	2.00 (1.14–3.51)	.02
Age	–1.63	.11		
Sex ^a	3.27	.07	0.43 (0.17–1.05)	.63
Hypertension	1.01	.32		
Dyslipidemia ^a	2.79	.09	2.74 (0.88–8.55)	.08
Diabetes mellitus	0.02	.88		
History of smoking	2.35	.13		
PCA involvement ^a	10.52	.001	5.52 (1.03–1.36)	.02

^aP < .10 threshold for entry into multivariate logistic regression.

Table 2: Prediction of postoperative Matsushima grade (n = 44)

Variables	Univariate Analyses		Multivariate Logistic Regression	
	χ^2 or Fisher Z or t	P	OR (95% CI)	P
Basal ganglia EPVS ^a	12.20	.001	1.29 (1.02–1.63)	.03
Age ^a	1.97	.06	1.13 (0.99–1.28)	.06
Sex	1.73	.19		
Hypertension	1.49	.22		
Dyslipidemia	0.35	.56		
Diabetes mellitus	0.38	.54		
History of smoking ^a	4.24	.05	1.02 (0.99–1.06)	.13
PCA involvement ^a	4.30	.04	0.56 (0.37–0.86)	.01

^aP < .10 threshold for entry into multivariate logistic regression.

were associated with abnormal CBF in the cortex and basal ganglia. Komatsu et al¹⁹ found that WMH was reversible and CBF increased after revascularization surgery, indicating that the improvement in CBF was partially related to the improvement of the WMH. The current study found that the overall estimation of brain frailty could also reflect the hemodynamic status. However, the causal relationship between the frailty score and perfusion remained elusive, warranting further longitudinal studies. Furthermore, MR imaging perfusion techniques like pCASL or CTP are not available in some institutions, making the modified brain frailty score a useful indirect and practical marker of abnormal hemodynamics in MMD.

The relationship between imaging signs of brain frailty and CBF in atherosclerotic ischemic stroke has produced mixed results.^{20,21} One reason may be that stroke studies tend to include a large portion of elderly patients, who may have long-term coexisting metabolic abnormalities and lifestyle diversities that can influence the progression of brain frailty and the decline of cerebral perfusion. In contrast, patients with MMD usually present with symptoms at a younger age, with fewer confounding factors, making it an appropriate model for chronic hypoperfusion.

The decrease in cerebral perfusion was correlated with the increase of periventricular WMH grades, rather than deep WMH. A commonly accepted concept is that periventricular and deep WMH have different pathophysiologies, in that periventricular WMH is more relevant to perfusion abnormality, while deep WMH is more related to progressive demyelination.^{12,22,23} The association between cerebral perfusion and periventricular WMH was consistent with the established pathophysiology of MMD, which is characterized by a chronic perfusion deficit. Another possible explanation may be the anatomic location of periventricular WMH, which is primarily in the watershed region, making it

more sensitive to chronic hypoperfusion and subsequent damage.^{24,25}

Some patients with MMD could be asymptomatic and have nonspecific symptoms, such as headache or dizziness.⁹ Moreover, unlike ischemic or hemorrhagic strokes, many patients with MMD present with TIA with no apparent structural lesions.²⁶ The main difference between patients with stroke and those with TIA or nonspecific symptoms is cerebral structural damage. In this study, it was found that patients with MMD with stroke had higher modified brain frailty scores compared with those without stroke symptoms. This result may be attributed to the shared underlying mechanism of brain frailty and stroke, which is cerebral hypoperfusion.^{27,28} Chronic hypoperfusion can lead to the development of brain frailty, and a failure of blood supply can ultimately result in stroke onset. From the group-level lesion map, most large lesions are

located at the frontal, temporal, and occipital areas. Another evident feature of the lesion location was that large infarctions were mainly located in the cortical area compared with patients with conventional strokes due to arteriosclerosis diseases. This finding may, in part, be related to the selective vulnerability of the cortical gray matter to ischemia in patients with MMD, who may have experienced hypoperfusion since childhood.²⁹

In the subgroup analysis, we found that the modified brain frailty score was correlated with rCBF_{mca} in stroke MMD, while periventricular WMH was associated with rCBF_{mca} in nonstroke MMD. This result may suggest that extra attention should be paid to periventricular WMH before brain parenchyma damage occurs. In addition, the overall estimation of brain frailty may be more helpful to reflect perfusion status in patients with MMD, who have already had ischemic or hemorrhagic stroke. We assumed that the reason behind this finding was the overall impact of periventricular WMH, deep WMH, and vascular lesions on brain structural changes, not periventricular WMH itself.

Brain frailty and its several imaging features could not predict surgical outcomes. However, basal ganglia EPVS showed a marginally significant correlation with postoperative revascularization. The perivascular space (PVS) runs parallel to perforating vessels. Former literature suggested that the PVS forms a network to help clearance of waste products and exchange of various signaling molecules between the CSF and interstitial fluid.³⁰ Presumably, the enlargement of the PVS might impair the ability of this clearance pathway, which might damage the angiogenesis and arteriogenesis that take place in chronic ischemia. Similarly, abnormalities of EPVS could also affect angiogenesis after EDAS, leading to fewer newly formed transdural collaterals. However, the above hypothesis of EPVS still needs to be validated by future research that focuses on specific molecular mechanisms.

PCA involvement was also found to predict postoperative revascularization. The posterior circulation provides the main retrograde leptomeningeal collateral flow in MMD.^{31,32} In this study, we found that the modified brain frailty score, periventricular WMH, and deep WMH were different between hemispheres with and without PCA involvement. This finding may imply that compared with other frailty imaging features, WMH may be more sensitive to the blood supply insufficiency, mainly determined by the posterior circulation. Most interesting, results showed that patients with an intact PCA tend to have lower Matsushima grades. A possible explanation may be the change in the source of the blood supply after surgery. EDAS provides new blood supply from the external carotid artery system to compensate for the perfusion deficit of anterior circulation, which may conflict with preoperatively formed collaterals from the PCA. As a result, patients with well-established leptomeningeal collaterals before surgery might present with less favorable transdural revascularization on angiography. Further verification is needed through prospective studies with longer follow-ups.

Our study has several limitations. First, a drawback was the difficulty in adjusting arterial transit time using pCASL with a single post-labeling delay in MMD, in which slow collateral flows often occur. Perfusion studies of MMD could benefit from multi-delay arterial spin-labeling in the future. Second, the difference in the correlation between brain frailty and perfusion in ischemic and hemorrhagic MMD was not assessed due to a limited number of patients with hemorrhagic MMD. Third, because of the limited number of hemispheres with postoperatively evaluated Matsushima grades (44 hemispheres), future studies with larger sample sizes are needed to estimate the relationship between brain frailty and surgical outcomes. Fourth, former studies suggested that individual imaging markers of brain frailty reflect intracerebral arteriole distensibility.³³ Cerebrovascular reactivity may be a more sensitive measure of hemodynamic changes than CBF.

CONCLUSIONS

This study found a correlation between a higher modified brain frailty score with decreasing cerebral perfusion in MMD, suggesting the use of the modified brain frailty score as an indirect and comprehensive marker of hemodynamic abnormality. Additionally, patients with MMD with stroke symptoms showed more severe brain frailty. Finally, basal ganglia EPVS could be used to predict postoperative revascularization. The findings were considered credible to extend to other diseases with chronic cerebral hypoperfusion. Future studies should investigate the underlying mechanisms of brain frailty in MMD and validate the use of the modified brain frailty score in larger cohorts.

Disclosure forms provided by the authors are available with the full text and PDF of this article at www.ajnr.org.

REFERENCES

- Kuroda S, Houkin K. **Moyamoya disease: current concepts and future perspectives.** *Lancet Neurol* 2008;7:1056–66 CrossRef Medline
- Wardlaw JM, Smith C, Dichgans M. **Small vessel disease: mechanisms and clinical implications.** *Lancet Neurol* 2019;18:684–96 CrossRef Medline
- Shi Y, Thrippleton MJ, Makin SD, et al. **Cerebral blood flow in small vessel disease: a systematic review and meta-analysis.** *J Cereb Blood Flow Metab* 2016;36:1653–67 CrossRef Medline
- Evans NR, Todd OM, Minhas JS, et al. **Frailty and cerebrovascular disease: concepts and clinical implications for stroke medicine.** *Int J Stroke* 2022;17:251–59 CrossRef Medline
- Barnett K, Mercer SW, Norbury M, et al. **Epidemiology of multimorbidity and implications for health care, research, and medical education: a cross-sectional study.** *Lancet* 2012;380:37–43 CrossRef Medline
- Appleton JP, Woodhouse LJ, Adami A, et al; ENOS Investigators. **Imaging markers of small vessel disease and brain frailty, and outcomes in acute stroke.** *Neurology* 2020;94:e439–52 CrossRef Medline
- Duan Q, Lyu J, Cheng K, et al; MR-STARS Investigators. **MRI assessment of brain frailty and clinical outcome in patients with acute posterior perforating artery infarction.** *J Magn Reson Imaging* 2023;59:340–49 CrossRef Medline
- Bu N, Khlif MS, Lemmens R, et al. **Imaging markers of brain frailty and outcome in patients with acute ischemic stroke.** *Stroke* 2021;52:1004–11 CrossRef Medline
- Research Committee on the Pathology and Treatment of Spontaneous Occlusion of the Circle of Willis et al. **Guidelines for diagnosis and treatment of moyamoya disease (spontaneous occlusion of the circle of Willis).** *Neurol Med Chir (Tokyo)* 2012; 52:245–66 CrossRef
- Fazekas F, Chawluk JB, Alavi A, et al. **MR signal abnormalities at 1.5 T in Alzheimer's dementia and normal aging.** *AJR Am J Roentgenol* 1987;149:351–56 CrossRef Medline
- Potter GM, Chappell FM, Morris Z, et al. **Cerebral perivascular spaces visible on magnetic resonance imaging: development of a qualitative rating scale and its observer reliability.** *Cerebrovasc Dis* 2015;39:224–31 CrossRef Medline
- Wardlaw JM, Smith EE, Biessels GJ, et al; STRIVE v1. **Neuroimaging standards for research into small vessel disease and its contribution to ageing and neurodegeneration.** *Lancet Neurol* 2013;12:822–38 CrossRef Medline
- Staals J, Makin SD, Doubal FN, et al. **Stroke subtype, vascular risk factors, and total MRI brain small-vessel disease burden.** *Neurology* 2014;83:1228–34 CrossRef Medline
- Lyu J, Ma N, Liebeskind DS, et al. **Arterial spin-labeling magnetic resonance imaging estimation of antegrade and collateral flow in unilateral middle cerebral artery stenosis.** *Stroke* 2016;47:428–33 CrossRef Medline
- Calviere L, Catalaa I, Marlats F, et al. **Correlation between cognitive impairment and cerebral hemodynamic disturbances on perfusion magnetic resonance imaging in European adults with moyamoya disease: clinical article.** *J Neurosurg* 2010;113:753–59 CrossRef Medline
- Matsushima Y, Inaba Y. **The specificity of the collaterals to the brain through the study and surgical treatment of moyamoya disease.** *Stroke* 1986;17:117–22 CrossRef Medline
- Wang LX, Wang H, Hao FB, et al. **Ivy sign in Moyamoya disease: a comparative study of the FLAIR vascular hyperintensity sign against contrast-enhanced MRI.** *AJNR Am J Neuroradiol* 2021; 42:694–700 CrossRef Medline
- Sun H, Li W, Xia C, et al. **Magnetic resonance imaging markers of cerebral small vessel disease in adults with Moyamoya disease.** *Transl Stroke Res* 2021;13:533–42 CrossRef Medline
- Komatsu K, Mikami T, Noshiro S, et al. **Reversibility of white matter hyperintensity by revascularization surgery in Moyamoya disease.** *J Stroke Cerebrovasc Dis* 2016;25:1495–502 CrossRef Medline
- Shi Y, Thrippleton MJ, Blair GW, et al. **Small vessel disease is associated with altered cerebrovascular pulsatility but not resting cerebral blood flow.** *J Cereb Blood Flow Metab* 2020;40:85–99 CrossRef Medline
- Crane DE, Black SE, Ganda A, et al. **Gray matter blood flow and volume are reduced in association with white matter hyperintensity lesion burden: a cross-sectional MRI study.** *Front Aging Neurosci* 2015;7:131 CrossRef Medline

22. Gouw AA, Seewann A, van der Flier WM, et al. **Heterogeneity of small vessel disease: a systematic review of MRI and histopathology correlations.** *J Neurol Neurosurg Psychiatry* 2011;82:126–35 CrossRef Medline
23. Promjunyakul NO, Dodge HH, Lahna D, et al. **Baseline NAWM structural integrity and CBF predict periventricular WMH expansion over time.** *Neurology* 2018;90:e2119–26 CrossRef Medline
24. Thomas AJ, O'Brien JT, Barber R, et al. **A neuropathological study of periventricular white matter hyperintensities in major depression.** *J Affect Disord* 2003;76:49–54 CrossRef Medline
25. Moody DM, Brown WR, Challa VR, et al. **Cerebral microvascular alterations in aging, leukoaraiosis, and Alzheimer's disease.** *Ann N Y Acad Sci* 1997;826:103–16 CrossRef Medline
26. Zhu B, He L. **Transient ischemic attack after indirect revascularization surgery for pediatric patients with moyamoya disease: a retrospective study of intraoperative blood pressure.** *Anaesth Crit Care Pain Med* 2023;42:101168 CrossRef Medline
27. Wityk RJ, Hillis A, Beauchamp N, et al. **Perfusion-weighted magnetic resonance imaging in adult moyamoya syndrome: characteristic patterns and change after surgical intervention: case report.** *Neurosurgery* 2002;51:1499–505; discussion 1506 CrossRef Medline
28. Pu Y, Liu X, Wang Y, et al; CHANCE Investigators. **Higher early recurrence risk and potential benefit of dual antiplatelet therapy for minor stroke with watershed infarction: subgroup analysis of CHANCE.** *Eur J Neurol* 2020;27:800–08 CrossRef Medline
29. Cho HJ, Jung YH, Kim YD, et al. **The different infarct patterns between adulthood-onset and childhood-onset moyamoya disease.** *J Neurol Neurosurg Psychiatry* 2011;82:38–40 CrossRef Medline
30. Brown R, Benveniste H, Black SE, et al. **Understanding the role of the perivascular space in cerebral small vessel disease.** *Cardiovasc Res* 2018;114:1462–73 CrossRef Medline
31. Liu ZW, Han C, Wang H, et al. **Clinical characteristics and leptomeningeal collateral status in pediatric and adult patients with ischemic Moyamoya disease.** *CNS Neurosci Ther* 2020;26:14–20 CrossRef Medline
32. Yamada I, Murata Y, Umehara I, et al. **SPECT and MRI evaluations of the posterior circulation in Moyamoya disease.** *J Nucl Med* 1996;37:1613–17 Medline
33. Rocha M, Jovin TG. **Fast versus slow progressors of infarct growth in large vessel occlusion stroke: clinical and research implications.** *Stroke* 2017;48:2621–27 CrossRef Medline

A Comparison of CT Perfusion Output of RapidAI and Viz.ai Software in the Evaluation of Acute Ischemic Stroke

Saif Bushnaq, ^{1b} Ameer E. Hassan, Adam Delora, Ali Kerro, Anita Datta, ^{1b} Rime Ezzeldin, Zuhair Ali, Tunmi Anwoju, Layla Nejad, Rene Silva, Yazan Diya Abualnadi, Zorain Mustafa Khalil, and ^{1b} Mohamad Ezzeldin



ABSTRACT

BACKGROUND AND PURPOSE: Automated CTP postprocessing packages have been developed for managing acute ischemic stroke. These packages use image processing techniques to identify the ischemic core and penumbra. This study aimed to investigate the agreement of decision-making rules and output derived from RapidAI and Viz.ai software packages in early and late time windows and to identify predictors of inadequate quality CTP studies.

MATERIALS AND METHODS: One hundred twenty-nine patients with acute ischemic stroke who had CTP performed on presentation were analyzed by RapidAI and Viz.ai. Volumetric outputs were compared between packages by performing Spearman rank-order correlation and Wilcoxon signed-rank tests with subanalysis performed at early (<6 hours) and extended (>6 hours) time windows. The concordance of selecting patients on the basis of DAWN and DEFUSE 3 eligibility criteria was assessed using the McNemar test.

RESULTS: One hundred eight of 129 patients were found to have adequate-quality studies. Spearman rank-order correlation coefficients were calculated on time-to-maximum >6-second volume, time-to-maximum >10-second volume, CBF <30% volume, mismatch volume, and mismatch ratio between both software packages with correlation coefficients of 0.82, 0.65, 0.77, 0.78, 0.59, respectively. The Wilcoxon signed-rank test was also performed on time-to-maximum >6-second volume, time-to-maximum >10-second volume, CBF <30% volume, mismatch volume, and mismatch ratio with *P* values of .30, .016, <.001, .03, <.001, respectively. In a 1-sided test, CBF <30% was greater in Viz.ai (*P* < .001). Although this finding resulted in statistically significant differences, it did not cause clinically significant differences when applied to the DAWN and DEFUSE 3 criteria. A lower ejection fraction predicted an inadequate study in both software packages (*P* = .018; 95% CI, 0.01–0.113) and (*P* = .024; 95% CI, 0.008–0.109) for RapidAI and Viz.ai, respectively.

CONCLUSIONS: Penumbra and infarct core predictions between Rapid and Viz.ai correlated but were statistically different and resulted in equivalent triage using DAWN and DEFUSE3 criteria. Viz.ai predicted higher ischemic core volumes than RapidAI. Viz.ai predicted lower combined core and penumbra values than RapidAI at lower volumes and higher estimates than RapidAI at higher volumes. Clinicians should be cautious when using different software packages for clinical decision-making.

ABBREVIATIONS: AIS = acute ischemic stroke; EF = ejection fraction; EVT = endovascular treatment; LVO = large-vessel occlusion; LKW = last known well; Tmax = time-to-maximum peak

Large-vessel occlusion (LVO) strokes of the anterior circulation contribute disproportionately to stroke-related dependence

Received November 12, 2023; accepted after revision February 6, 2024.

From the Department of Neurology (S.B.), Texas Tech University Health Sciences Center, Lubbock, Texas; Department of Neurology (A.E.H.), Valley Baptist Medical Center Harlingen (L.N., R.S., Y.D.A., Z.M.K.), Harlingen, Texas; Department of Emergency Medicine (A. Delora, A. Datta), Clinical Sciences (Z.A., T.A.), and Neuroendovascular Surgery (M.E.), HCA Houston Healthcare Kingwood, Kingwood, Texas; Department of Neurology (A.K.), HCA Houston Healthcare Conroe, Conroe, Texas; Jordan University of Science and Technology (R.E.), Irbid, Jordan.

This research was supported (in whole or in part) by HCA Healthcare and/or an HCA Healthcare affiliated entity. The views expressed in this publication represent those of the author(s) and do not necessarily represent the official views of HCA Healthcare or any of its affiliated entities.

The HCA Healthcare has a minority equity stake in Viz.ai and also purchases products from the company for use in its facilities. Ameer Hassan is a consultant and a speaker for Viz.ai, which develops the Viz LVO algorithm that we tested, and

and mortality.¹ Mechanical thrombectomy is cost-effective and substantially reduces LVO stroke disability.^{2–4} Delayed reperfusion leads to worse outcomes. Therefore, accurate and timely LVO identification and endovascular team notification are critical to maximizing the benefit of proved reperfusion therapies.^{5,6} The use of advanced neuroimaging has been endorsed by the American Heart Association guidelines after the positive results of the

he is also involved in a study sponsored by Viz.ai called the LVO Synchronise Study, which looks at the impact of a Viz LVO implementation on patient timing and outcomes.

Please address correspondence to Mohamad Ezzeldin, MD, Hwy 59 N 405, Kingwood, TX 77339, United States; e-mail: mohamadezzeldin@hotmail.com; @EzzeldinMohamad



Indicates article with online supplemental data.

<http://dx.doi.org/10.3174/ajnr.A8196>

SUMMARY

PREVIOUS LITERATURE: Automated CTP postprocessing packages have emerged as valuable tools in managing acute ischemic stroke. Multiple software packages are currently available with different algorithms. Their ability to generate comprehensive perfusion maps aids clinicians in swiftly evaluating brain tissue viability, guiding timely interventions, and enhancing stroke care. Differences in volumetric outputs and triaging large-vessel occlusion using DAWN and DEFUSE 3 criteria between RapidAI and Viz.ai packages are limited. Herein, we aimed to compare these commonly available postprocessing packages.

KEY FINDINGS: RapidAI and Viz.ai postprocessing packages correlated well in predicting penumbra and infarct core volumes, resulting in equivalent large-vessel occlusion triage using DAWN and DEFUSE 3 criteria. However, Viz.ai predicted lower combined core and penumbra values than RapidAI at lower volumes and higher estimates than RapidAI at higher volumes.

KNOWLEDGE ADVANCEMENT: Both RapidAI and Viz.ai postprocessing packages resulted in equivalent large-vessel occlusion triage using DAWN and DEFUSE 3 criteria. Clinicians should be mindful of potential penumbra and infarct core variability between the packages, particularly in extreme volumes, as it may impact patient selection for mechanical thrombectomy.

Clinical Mismatch in the Triage of Wake Up and Late Presenting Strokes Undergoing Neurointervention with Trevo (DAWN) and Endovascular Therapy Following Imaging Evaluation for Ischemic Stroke 3 (DEFUSE 3) trials in well-selected patients beyond 6 hours of onset of ischemic stroke symptoms.⁷⁻⁹ These 2 trials were based on automated postprocessing results derived from the RapidAI software package (iSchemaView) to triage patients and have proved beneficial for patients with perfusion mismatch. Advances in image analysis software and artificial intelligence technology have facilitated the development of automated infarct core analysis and LVO detection.¹⁰⁻¹² The role of CTP is to differentiate between irreversibly infarcted (unsalvageable ischemic core) and potentially salvageable (penumbral) tissues. The brain is repeatedly scanned during the IV infusion of iodinated contrast media to create an attenuation-time curve. Perfusion measurements can then be calculated, such as relative CBV, relative CBF, MTT, and time to maximum peak (Tmax). These are then displayed on a brain map with color scales. Multiple software packages are currently available, and they differ in how the perfusion maps are calculated, possibly resulting in lesion volume variability.¹³ RapidAI uses a Fourier transform deconvolution algorithm.^{14,15} In our literature search, we did not find any reference to the implementation details of the Viz.ai algorithm (<https://www.viz.ai/>). In this study, we assess the outcomes of the 2 most commonly available commercial automated packages: RapidAI and Viz.ai. We also compared the difference between these two software packages in triaging patients for endovascular treatment (EVT) by DAWN or DEFUSE 3 criteria.

MATERIALS AND METHODS

Ethics Approval

Ethics approval HCA Houston Healthcare Kingwood Institutional Review Board has determined this retrospective research activity to be exempt or excluded from Institutional Review Board (IRB) oversight in accordance with current regulations and institutional policy. Our internal reference number for this determination is 2022-1055. There was no direct patient contact in performing this study. In addition, our patients sign a data usage form at registration related to data collection and utilization of their data for

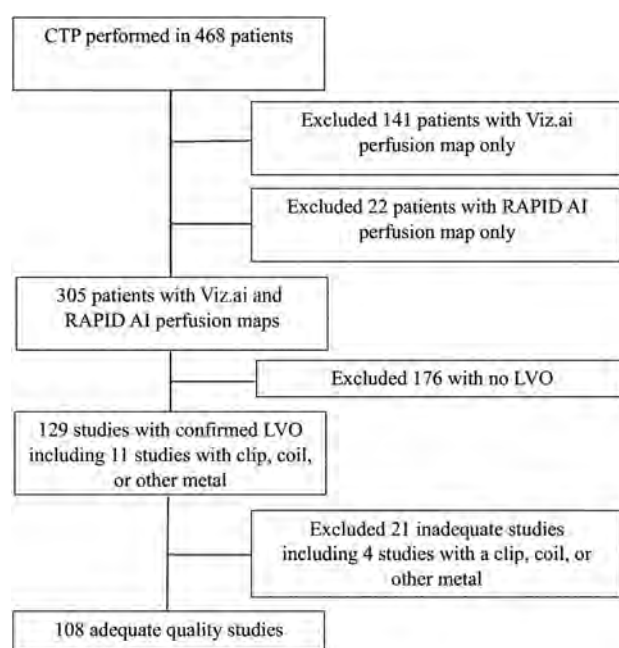


FIG 1. Flowchart for patients with LVO and adequate studies. This flow chart illustrates 468 patients with acute ischemic stroke who underwent a CTP study; 305 patients had concurrent RapidAI and Viz. ai perfusion maps available. Analysis was performed on 108 patients with LVO after excluding inadequate studies.

research. The research was overseen in our research protocol submitted for IRB review and research committee who holds monthly ethics reviews.

This was a multicenter retrospective study. We reviewed 1025 patients with acute ischemic stroke (AIS) admitted to 3 comprehensive stroke centers in Texas. We excluded patients who did not have both RapidAI and Viz.ai perfusion maps. We then excluded any patients without LVO, resulting in 129 patients from HCA Houston Healthcare Kingwood ($n = 60$, 46.51%), HCA Houston Healthcare Northwest ($n = 24$, 18.60%), and Valley Baptist Medical Center Harlingen ($n = 45$, 34.88%) between October 2020 and August 2023 (Fig 1). We analyzed clinical and radiologic data, including patient sex, age, ethnicity, vascular risk factors, NIHSS score, and intracranial

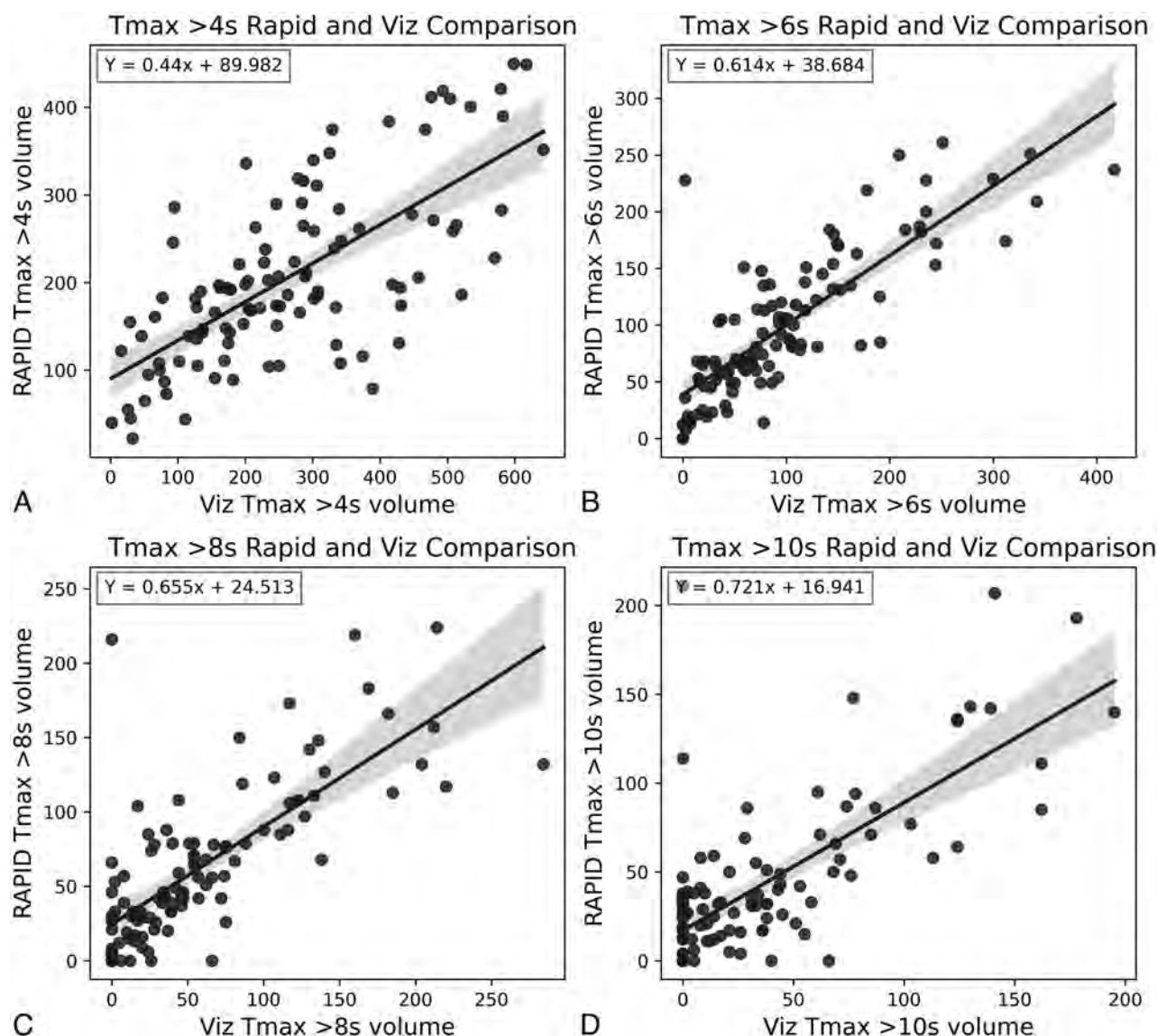


FIG 2. Tmax RapidAI and Viz.ai scatterplot of values with regression lines. This figure shows scatterplots and regression lines for Tmax >4 seconds (A), Tmax >6 seconds (B), Tmax >8 seconds (C), and Tmax >10 seconds (D). The regression equation is noted in the top left of each subplot.

atherosclerosis. We also collected CTP outcome maps. We included patients who met the following criteria: 1) CTP performed on arrival at the comprehensive stroke center within the early (<6 hours) or late (≥ 6 hours) window from the last known well (LKW), 2) 18 years of age or older, 3) NIHSS score ≥ 6 , and 4) AIS caused by intracranial large-artery occlusion.

The software packages used in these hospitals during the study period were RapidAI and Viz CTP (Version 1.11; Viz.ai). These software packages create threshold-based output for relative CBF, relative CBV, and time-to-maximum of the residue function Tmax. Preprocedural predicted infarct core volume was calculated on the basis of the relative CBF of <30% threshold, and hypoperfused tissue was calculated on the basis of Tmax of 6 seconds.¹⁶ We have compared the perfusion map results from RapidAI and Viz.ai and the agreement between both software packages at different time windows using the Spearman rank-order correlation coefficient and the Wilcoxon signed-rank test.

The magnitude of agreement was classified according to the following values: from 0.0 to 0.20 indicating poor agreement; 0.21 to 0.40 indicating fair agreement; 0.41 to 0.60 indicating moderate agreement; 0.61 to 0.80 indicating substantial agreement; and 0.81 to 1.0 indicating excellent agreement.¹⁷ Statistical analysis was performed using (Scipy Stats 1.9.1; <https://docs.scipy.org/doc/scipy-1.9.1/reference/stats.html>).¹⁸ The data supporting the findings of this study are available from the corresponding author on reasonable request.

RESULTS

A total of 129 patients were included in the analysis. Of 129 cases, 62 patients presented in the early time window. The NIHSS score on arrival was available in all patients (mean = 16). One hundred seventeen of 129 had a transthoracic echo with an ejection fraction (EF) documented. Nine patients had posterior circulation strokes.

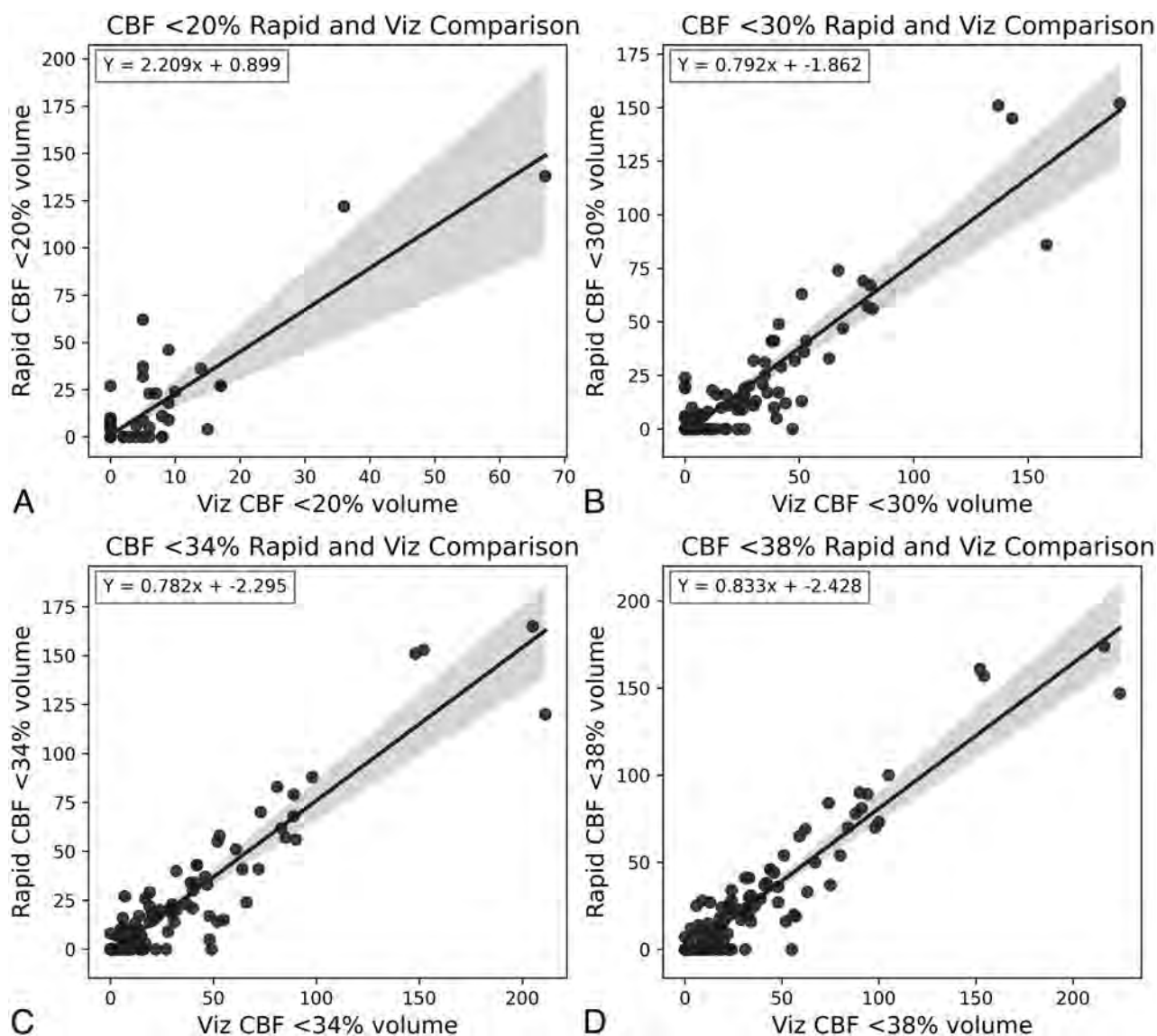


FIG 3. CBF RapidAI and Viz.ai scatterplot of values with regression lines. This figure shows scatterplots and regression lines for CBF <20% (A), CBF <30% (B), CBF <34% (C), and CBF <38% (D). The regression equation is noted in the top left of each subplot.

Summary statistics related to sex, race, age, comorbidities, smoking status, and features extracted from imaging are shown in the Online Supplemental Data. Viz.ai determined that 115 of the 129 studies were adequate for evaluation. RapidAI determined that 118 of the studies were adequate for evaluation. For the adequate studies, Spearman rank-order correlation coefficients were calculated for a Tmax of >6-second volume, Tmax >10-second volume, CBF <30% volume, mismatch volume, and mismatch ratio, and all were found to be concordant between both software packages of 0.82, 0.65, 0.77, 0.78, 0.59, respectively. The correlation coefficients at the extended time windows remained concordant at 0.88, 0.61, 0.7, 0.87, 0.80 for ≥6 hours and 0.74, 0.63, 0.83, 0.69, 0.78 for <6 hours, respectively (Online Supplemental Data). A 2-sided Wilcoxon signed-rank test was also performed on Tmax >6-second volume, Tmax >10-second volume, CBF <30% volume, mismatch volume, and mismatch ratio with *P* values of .306, .016, <.001, .03, and <.001. There was a statistically significant difference in CBF <30% volume at <6 hours (*P* < .001) and >6 hours

(*P* = .007) between RapidAI and Viz.ai. We also performed a subanalysis using the median as a cutoff and directional Wilcoxon signed-rank tests. This showed that Tmax >6-second Viz.ai predicted lower values than RapidAI at volumes lower than the median (Tmax >6-seconds < 78.5 mL, *P* < .001), but at high volumes, Viz.ai predicted higher values than RapidAI at volumes higher than the median (Tmax >6 seconds > 78.5 mL, *P* = .029). In contrast, for CBF <30%, Viz.ai predicted greater irreversible ischemic core volumes at volumes above CBF <30% < 9.5 mL, *P* = .002 and below the median (CBF <30% > 9.5 mL, *P* < .001).

Plots of the values and the lines of best fit are shown in Figs 2–5. We also ran a logistic regression on RapidAI and Viz.ai on whether the study was determined to be inadequate for analysis. The variance inflation factor was calculated for each variable to look for violations in the multicollinearity assumption of the logistic regression. Decreased EF predicted an inadequate study in Viz.ai (*P* = .024) and RapidAI (*P* = .018). Also, in Viz.ai, there were no intracranial hemorrhages in the data set to determine

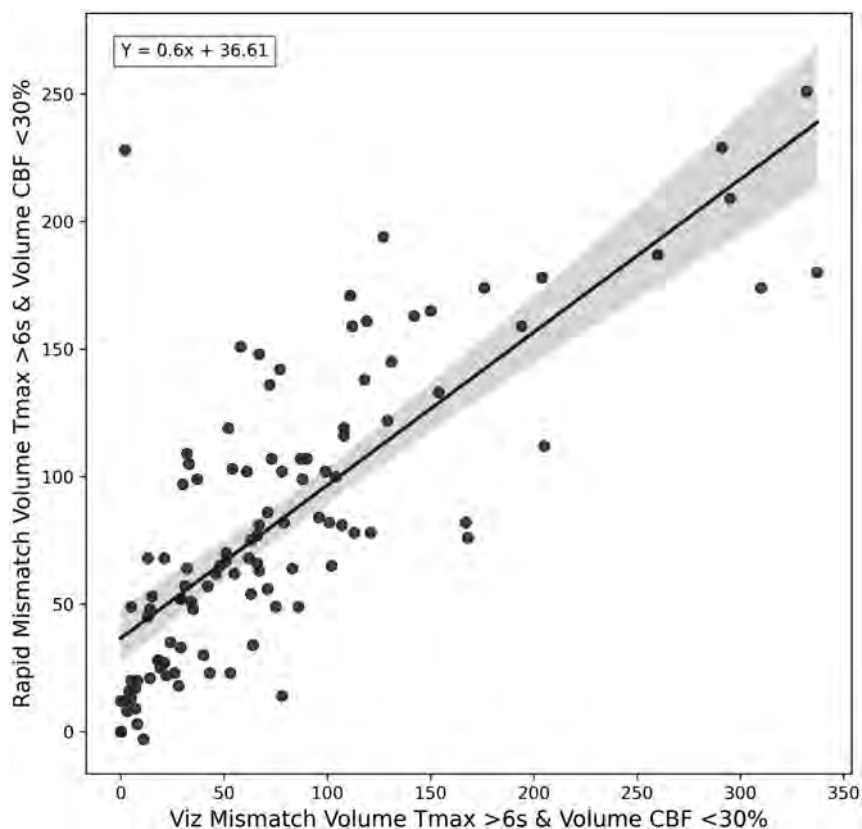


FIG 4. Mismatch volume comparison between RapidAI and Viz.ai. This figure shows a scatter plot and a regression equation between the mismatch volumes calculated from the CBF <30% and the Tmax <6 seconds. The regression equation is shown in the top left of the plot.

how that would impact study adequacy. There were 11 total studies with a clip, coil, or other metal, and 4 of these studies were marked as inadequate by Viz.ai, and none were marked as inadequate by RapidAI. Statistically, in Viz.ai, the presence of a clip, coil, or other metal predicted an inadequate study ($P = .042$). In contrast, in RapidAI, all studies with a clip, coil, or other metals were adequate (Table). We could not run a model with perfect separation, which was not included in the logistic regression with RapidAI. Additionally, we applied the DAWN and DEFUSE 3 criteria to the 35 eligible patients and performed a McNemar test on the confusion matrix. There was no significant statistical difference in triaging patients to thrombectomy intervention based on the DAWN and DEFUSE 3 eligibility criteria, as shown in Fig 6. Eligibility criteria are shown in the Online Supplemental Data. We have calculated the mean of the difference between the Tmax >6 seconds and CBF <30% volumes and found that the means of the absolute value of the differences were 32.36 and 9.5 mL, respectively. We partitioned the data because our clinicians reported a larger discrepancy between the software packages with larger infarct core and penumbra values. For Tmax >6 seconds, the mean absolute value of the difference was 16.81 (SD, 15.65) mL when volumes were less than the median of 78.5 and 38.40 (SD, 38.47) mL when the volumes were greater. For CBF <30%, the mean absolute difference was 1.8 (SD, 2.3) mL when volumes were less than the median of 9.5 and 15.07 (SD, 13.28) mL when the volumes were greater. Additionally, we calculated the mean (SD) of the absolute

difference between the volumes of Viz.ai and RapidAI. In patients in whom the LKW was ≥ 6 hours, the mean absolute difference of Tmax >6 seconds was 34.05 (SD, 35.08) mL and CBF <30% was 10.35 (SD, 11.37) mL. For patients with an LKW of <6 hours, the mean absolute difference of Tmax >6 seconds was 33.00 (SD, 40.06) mL and CBF <30% was 8.84 (SD, 12.79) mL.

DISCUSSION

CT perfusion imaging has become an important tool for triaging patients with AIS and determining the need for recanalization. Automated imaging analyses are increasingly used as selection tools for the EVT of LVO in the 6- to 24-hour time window. RapidAI software has been widely used in several large trials to estimate the volumes of ischemic core and perfusion lesions, with several guidelines relying on these trials.⁷⁻¹⁰ We compared RapidAI and Viz.ai software packages directly on the same image set to determine agreement with commonly used perfusion map parameters, predictors of poor quality CT perfusion studies, and differences between RapidAI and

Viz.ai on selecting patients with LVO stroke based on DAWN or DEFUSE 3 criteria.

RapidAI CTP and Viz.ai CTP software packages were highly correlated with correlation coefficients of 0.82 and 0.77, respectively, but produced statistically significantly different irreversibly ischemic cores ($P < .001$). This correlation remained significant in different time windows from LKW. The software packages were highly correlated at an early time window (<6 hours), with Tmax >6 seconds (correlation coefficient = 0.86) and CBF <30% (correlation coefficient = 0.71). There was also excellent correlation at an extended time window (≥ 6 hours) for Tmax >6 (correlation coefficient = 0.87) and substantial for CBF <30% (correlation coefficient = 0.87), but the estimates of the ischemic core were statistically significantly different by the Wilcoxon signed-rank matched pairs test. This finding shows that values can be correlated but are different. For Tmax >6 seconds, Viz.ai showed statistically significantly lower values than RapidAI at volumes lower than the median ($P < .001$). In contrast, at volumes of Tmax >6 seconds higher than the median of 78.5 mLs, Viz.ai predicted higher values than RapidAI ($P = .029$). We have also shown that Viz.ai consistently predicts higher irreversibly infarcted core (CBF <30%) than RapidAI.

The software differed by increased volumes at larger penumbra and core infarct values. The linear regression used to create the line of the Tmax >6-second plot had an intercept of 39 and a slope of 0.614. This finding indicates that RapidAI had larger predictions at lower volumes and Viz.ai had larger values at larger

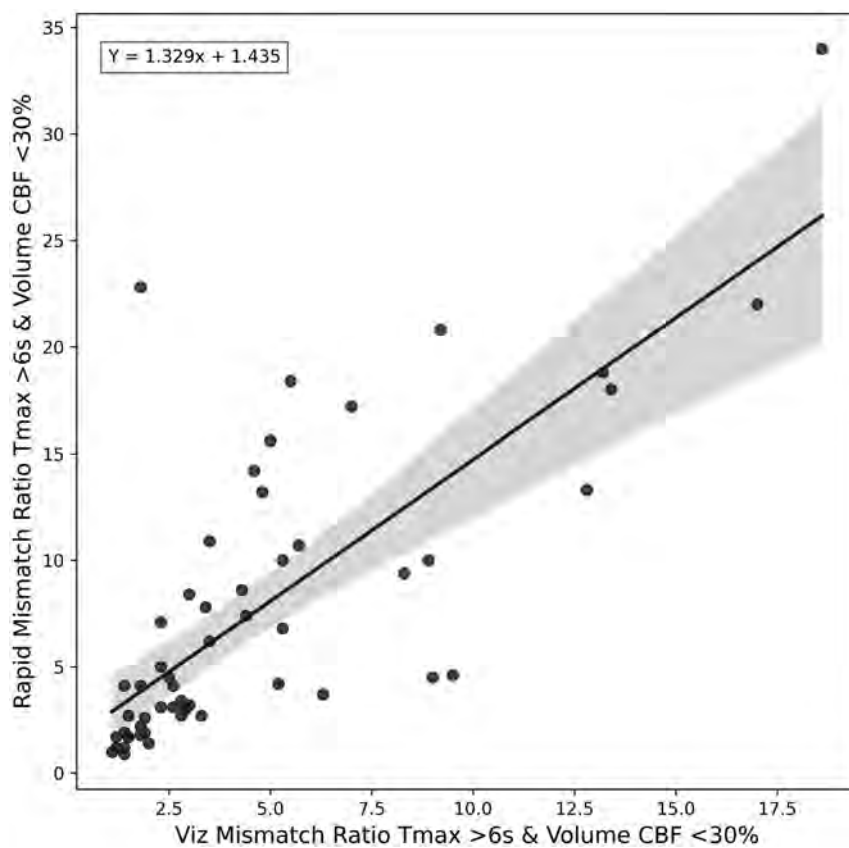


FIG 5. Mismatch ratio comparison between RapidAI and Viz.ai. This figure shows a scatterplot and a regression equation between the mismatch ratio calculated from the CBF <30% and the Tmax <6 seconds. The regression equation is shown in the top left of the plot. If either software produced a nan (not a number) or inf (infinity) value the point was removed from the plot.

Logistic regression study adequacy for RapidAI and viz.ai^a

Study	Coefficient	Standard Error	Z	P > z	[0.025	0.975]
Viz adequate study						
Age	−0.0179	0.021	−0.858	.391	−0.059	0.023
Sex	0.0418	0.634	0.066	.947	−1.2	1.284
Diabetes	−0.1406	0.628	−0.224	.823	−1.371	1.09
CHF	1.422	1.082	1.314	.189	−0.699	3.543
EF	0.0583	0.026	2.265	.024	0.008	0.109
Clip, coil, or other metal	−0.6559	0.816	−2.029	.042	−3.255	−0.057
NIHSS on arrival	−0.0187	0.034	−0.557	.577	−0.084	0.047
RapidAI adequate study						
Age	−0.019	0.021	−0.898	.369	−0.061	0.023
Sex	0.2462	0.662	0.372	.71	−1.052	1.544
Diabetes	−0.0579	0.652	−0.089	.929	−1.335	1.219
CHF	1.4731	1.089	1.353	.176	−0.661	3.607
EV	0.0615	0.026	2.357	.018	0.01	0.113
NIHSS on arrival	0.0368	0.034	1.088	.277	−0.03	0.103

Note:—CHF indicates congestive heart failure.

^a We performed a logistic regression to find predictors of adequate and inadequate studies. The table includes *P* values, confidence intervals, and coefficients for each predictor.

volumes, consistent with the subanalysis performed with the Wilcoxon signed-rank test. This prediction asymmetry suggests imperfections in the core and penumbra estimates from one or either software and merits additional investigations and potential optimization. In future studies, we will examine how this impacts the final infarct volumes on MR DWI sequences after

thrombectomy. Our study illustrates that in clinical practice, RapidAI and Viz.ai software produce statistically significantly different-but-highly correlated perfusion maps, and differences in volumes that are produced do not significantly change which patients are selected for thrombectomy on the basis of the predicted infarct core and penumbra volumes in the DAWN and DEFUSE 3 criteria. With the increase of large core infarct trials, the DAWN and DEFUSE 3 criteria are being used less in clinical practice, and the situations in which clinicians decide to use CTP are evolving.^{19,20} With CTP being applied in different clinical scenarios, it is incredibly important that physicians understand that using different software packages may produce different results that can impact their decisions.

A recently published study²¹ reviewed 242 patients with anterior circulation LVO and compared preprocedural prediction of final infarct volumes. The authors used RapidAI, Version 4.5.0, to analyze CTP maps on patient presentation. Then, Viz CTP, Version 1.3 (Viz.ai) automated software package was retrospectively applied to patients with ICA or MCA M1 occlusions. The median time from LKW to CTP time was 402 (interquartile range = 181–790) minutes. Similar to our findings, this study revealed that RapidAI and Viz.ai had an excellent correlation for Tmax >6 seconds (correlation coefficient = 0.81) and a substantial correlation for CBF <30% (correlation coefficient = 0.76), but the study did not look directly at differences in volumes. Our study is unique because RapidAI and Viz.ai were mostly run concurrently, with some images run after image collection to augment our sample size. Running the software packages concurrently provides a real-world comparison of the 2 software packages with their competing versions, can potentially reduce bias, and gives real-

world insight to hospitals looking to adopt these packages. Also, we included LVOs in the MCA M1, MCA M2, and ACA as well as the posterior circulation. We included patients in the ultra-early window presenting within 3 hours from the onset of symptoms and patients with unknown LKW. The median LKW to CTP time was 300 (interquartile range = 142.5–607.5) minutes.

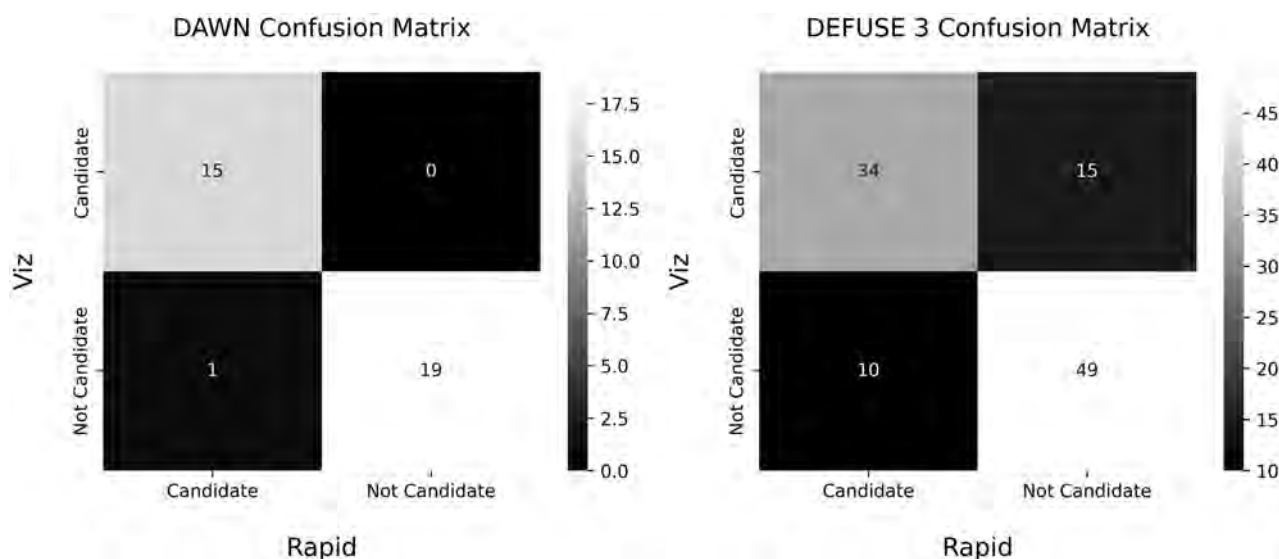


FIG 6. DAWN and DEFUSE 3 confusion matrices. This figure shows the DAWN and DEFUSE 3 confusion matrices for patients who had an ICA or proximal MCA occlusion. These matrices show whether a patient is a candidate for thrombectomy based on these criteria. A McNemar test was performed on these matrices that did not show a statistically significant marginal inhomogeneity of states.

Our Wilcoxon signed-rank tests showed that Viz.ai consistently predicts larger core infarcts better than RapidAI at all volumes and timeframes. Overestimation of the infarct core is well-described in the literature and is considered a critical pitfall of CTP in patients presenting in the early time window.²² Clinicians should be aware of this ghost infarct core (defined as initial core minus final infarct >10 mL) and exercise caution. We could not find a clear difference in predictions of the irreversibly ischemic core infarct when patients had CTP performed at <6 hours and at >6 hours by either software package.

The estimation of the ischemic core volume and tissue at risk (penumbra) is an important step in the evaluation and triaging of patients with LVO. In a subgroup of our cohort (35 patients of 129), we evaluated the performance of RapidAI and Viz.ai software packages in triaging patients with LVO based on DAWN and DEFUSE 3 selection criteria. Clinical and/or neuroimaging eligibility criteria included in DAWN and DEFUSE 3 were applied for individual patient triaging to determine the concordance of treatment decisions based on these 2 software packages. Specifically, mismatched profiles and mismatched volumes were calculated accordingly by using volumetric results. Then eligibility for mechanical thrombectomy was derived from each package for individual patients with AIS, and the agreement of patient triage was measured (represented on the confusion matrix). We performed a McNemar test on the confusion matrix and found that there was no significant difference between triage classification based on DAWN criteria ($P = 1.00$), which suggests that clinicians can use either software to triage patients with LVO for the extended time window. This finding is consistent with a recent study from the University of Cincinnati that analyzed 54 patients in whom the authors found no difference in the final decision to proceed with EVT by using either software when both DEFUSE 3 and DAWN criteria were considered.²³ Another recent study compared RapidAI and RealNow (<http://drbrain.net/product->

[nb_en.aspx](#)) software packages, and a diagnostic agreement based on DEFUSE 3 criteria was analyzed in a subgroup of patients. Concordance on the triaging agreement was found in 16/19 (84%) cases in subgroups with package-A-based infarct core volume of >70 mL and in 143/155 cases (92%) in the subgroup with infarct core volume <70 mL. A subgroup with a large ischemic core or core of <70 mL led to discordance in mismatched profiles, which affected patient selection for mechanical thrombectomy.²⁴

Finally, we evaluated the factors that contributed to inadequate interpretation by the software packages. In both RapidAI and Viz.ai, we found that a lower EF led to an inadequate study ($P = .018$; 95% CI, 0.01–0.113) and ($P = .024$; 95% CI, 0.008–0.109) for RapidAI and Viz.ai, respectively. To our knowledge, our study is the first to reveal this finding. A recent study evaluated CTA in 47 patients with LVO and found that a low EF was a predictor of incorrect identification of the LVO in both RapidAI and Viz.ai software packages.²⁵ A study that evaluated contrast curve truncation in CTP protocols found that reduced left ventricle EF and hypertension resulted in the truncation of CTP data and a lower-quality study.²⁶ In our study, there were no intracranial hemorrhages in the data set to determine how that would impact study adequacy. In the Viz.ai software, we found that the presence of a clip, coil, or other metal predicted an inadequate study ($P = .042$; 95% CI, –3.225 and –0.057), but the software only labeled 4/11 of the studies as inadequate. This result is likely because the software has a step during preprocessing that detects images with metal and removes those images. This explanation indicates that the software's metal-detection algorithm of the software could detect some of the metal. RapidAI has included the feature in a future version but this was not available to us at the time of this publication.

There are several limitations in our study. This is a retrospective study design with an inherent risk of bias. However, the data are from 3 high-volume comprehensive stroke

centers, and automated perfusion images were obtained during an overlap period on the same patient population using RapidAI and Viz.ai. Second, we did not collect data on the brands of CT scanners used to obtain the images. The CTP acquisition protocol (section thickness and collimator) information was not collected. Looking at final infarct volumes on MR DWI is outside the scope of this study, but in a future study, we will certainly make volume measurements of this MR DWI after thrombectomy and compare this volume with the CTP CBF <30% prediction of the irreversible ischemic core. Our goal was to determine whether there was a difference between the output of these 2 software packages to determine whether clinicians could use these data to make similar conclusions, and we have found that Viz.ai produces higher values than RapidAI. In a future study, we will compare CBF and the final infarct volume and look at how the CTP maps may predict poor thrombectomy outcomes.

CONCLUSIONS

Infarct core and penumbra predictions between Rapid and Viz.ai software were highly correlated but statistically different and resulted in equivalent patient triage based on DAWN and DEFUSE 3 eligibility criteria. Viz.ai produced consistently higher predictions of irreversible infarct core volumes than RapidAI. Viz.ai predicted lower combined core and penumbra values than RapidAI at lower volumes and predicted higher combined core and penumbra estimates than RapidAI at higher volumes. Users should be aware of these differences in triaging patients for mechanical thrombectomy, and further investigation should be performed into the accuracy of these two software packages.

Disclosure forms provided by the authors are available with the full text and PDF of this article at www.ajnr.org.

REFERENCES

- Malhotra K, Gornbein J, Saver JL. Ischemic strokes due to large-vessel occlusions contribute disproportionately to stroke-related dependence and death: a review. *Front Neurol* 2017;8:651 CrossRef Medline
- Kunz WG, Hunink MG, Almekhlafi MA, et al; HERMES Collaborators. Public health and cost consequences of time delays to thrombectomy for acute ischemic stroke. *Neurology* 2020;95:e2465–e2475 CrossRef Medline
- Goyal M, Menon BK, van Zwam WH, et al; HERMES Collaborators. Endovascular thrombectomy after large-vessel ischaemic stroke: a meta-analysis of individual patient data from five randomised trials. *Lancet* 2016;387:1723–31 CrossRef Medline
- Jovin TG, Nogueira RG, Lansberg MG, et al. Thrombectomy for anterior circulation stroke beyond 6 h from time last known well (AURORA): a systematic review and individual patient data meta-analysis. *Lancet* 2022;399:249–58 CrossRef Medline
- Saver JL. Time is brain-quantified. *Stroke* 2006;37:263–66 Jan CrossRef Medline
- Khatri P, Yeatts SD, Mazighi M, et al; IMS III Trialists. Time to angiographic reperfusion and clinical outcome after acute ischaemic stroke: an analysis of data from the Interventional Management of Stroke (IMS III) phase 3 trial. *Lancet Neurol* 2014;13:567–74 CrossRef Medline
- Nogueira RG, Jadhav AP, Haussen DC, et al; DAWN Trial Investigators. Thrombectomy 6 to 24 hours after stroke with a mismatch between deficit and infarct. *N Engl J Med* 2018;378:11–21 CrossRef Medline
- Albers GW, Marks MP, Kemp S, et al; DEFUSE 3 Investigators. Thrombectomy for stroke at 6 to 16 hours with selection by perfusion imaging. *N Engl J Med* 2018;378:708–18 CrossRef Medline
- Warner JJ, Harrington RA, Sacco RL, et al. Guidelines for the early management of patients with acute ischemic stroke: 2019 Update to the 2018 Guidelines for the Early Management of Acute Ischemic Stroke. *Stroke* 2019;50:3331–32 CrossRef Medline
- Hassan AE, Ringheanu VM, Rabah RR, et al. Early experience utilizing artificial intelligence shows significant reduction in transfer times and length of stay in a hub and spoke model. *Interv Neuroradiol* 2020;26:615–22 CrossRef Medline
- Shlobin NA, Baig AA, Waqas M, et al. Artificial intelligence for large-vessel occlusion stroke: a systematic review. *World Neurosurg* 2022;159:207–20.e1 CrossRef Medline
- Matsoukas S, Stein LK, Fifi JT. Artificial intelligence-assisted software significantly decreases all workflow metrics for large vessel occlusion transfer patients, within a large spoke and hub system. *Cerebrovasc Dis Extra* 2023;13:41–46 CrossRef Medline
- Christensen S, Lansberg MG. CT perfusion in acute stroke: Practical guidance for implementation in clinical practice. *J Cereb Blood Flow Metab* 2019;39:1664–68 CrossRef Medline
- Straka M, Albers GW, Bammer R. Real-time diffusion-perfusion mismatch analysis in acute stroke. *J Magn Reson Imaging* 2010;32:1024–37 CrossRef Medline
- Chung KJ, De Sarno D, Lee T-Y. Quantitative functional imaging with CT perfusion: technical considerations, kinetic modeling, and applications. *Front Phys* 2023;11:1246973 CrossRef
- Wing SC, Markus HS. Interpreting CT perfusion in stroke. *Pract Neurol* 2019;19:136–42 CrossRef Medline
- Akoglu H. User's guide to correlation coefficients. *Turk J Emerg Med* 2018;18:91–93 CrossRef Medline
- Virtanen P, Gommers R, Oliphant TE, et al; SciPy 1.0 Contributors. SciPy 1.0: fundamental algorithms for scientific computing in Python. *Nat Methods* 2020;17:261–72 CrossRef Medline
- Sarraj A, Hassan AE, Abraham MG, et al; SELECT2 Investigators. Trial of endovascular thrombectomy for large ischemic strokes. *N Engl J Med* 2023;388:1259–71 CrossRef Medline
- Yoshimura S, Sakai N, Yamagami H, et al. Endovascular therapy for acute stroke with a large ischemic region. *N Engl J Med* 2022;386:1303–13 CrossRef Medline
- Pisani L, Haussen DC, Mohammad M, et al. Comparison of CT perfusion software packages for thrombectomy eligibility. *Ann Neurol* 2023;94:848–55 CrossRef Medline
- Boned S, Padroni M, Rubiera M, et al. Admission CT perfusion may overestimate initial infarct core: the ghost infarct core concept. *J Neurointerv Surg* 2017;9:66–69 CrossRef Medline
- Stanton RJ, Wang LL, Smith MS, et al. Differences in automated perfusion software: do they matter clinically? *Stroke Vasc Interv Neurol*. 2022;2:e000424 CrossRef
- Zhou X, Nan Y, Ju J, et al. Comparison of two software packages for perfusion imaging: ischemic core and penumbra estimation and patient triage in acute ischemic stroke. *Cells* 2022;11:2547 CrossRef
- Delora A, Hadjialiakbari C, Percenti E, et al. Viz LVO versus Rapid LVO in detection of large vessel occlusion on CT angiography for acute stroke. *J Neurointerv Surg* 2023 Jun 24 [Epub ahead of print] CrossRef Medline
- Hartman JB, Moran S, Zhu C, et al. Use of CTA test dose to trigger a low cardiac output protocol improves acute stroke CTP data analyzed with RAPID Software. *AJNR Am J Neuroradiol* 2022;43:388–93 CrossRef Medline

CTP for the Screening of Vasospasm and Delayed Cerebral Ischemia in Aneurysmal SAH: A Systematic Review and Meta-analysis

 Amer Mitchell,  Vineet V. Gorolay,  Matthew Aitken,  Kate Hanneman,  Ya Ruth Huo,  Nathan Manning, Irene Tan, and  Michael V. Chan



ABSTRACT

BACKGROUND: Delayed cerebral ischemia and vasospasm are the most common causes of late morbidity following aneurysmal SAH, but their diagnosis remains challenging.

PURPOSE: This systematic review and meta-analysis investigated the diagnostic performance of CTP for detection of delayed cerebral ischemia and vasospasm in the setting of aneurysmal SAH.

DATA SOURCES: Studies evaluating the diagnostic performance of CTP in the setting of aneurysmal SAH were searched on the Cochrane Database of Systematic Reviews, Cochrane Central Register of Controlled Trials, Cochrane Clinical Answers, Cochrane Methodology Register, Ovid MEDLINE, EMBASE, American College of Physicians Journal Club, Database of Abstracts of Reviews of Effects, Health Technology Assessment, National Health Service Economic Evaluation Database, PubMed, and Google Scholar from their inception to September 2023.

STUDY SELECTION: Thirty studies were included, encompassing 1786 patients with aneurysmal SAH and 2302 CTP studies. Studies were included if they compared the diagnostic accuracy of CTP with a reference standard (clinical or radiologic delayed cerebral ischemia, angiographic spasm) for the detection of delayed cerebral ischemia or vasospasm in patients with aneurysmal SAH. The primary outcome was accuracy for the detection of delayed cerebral ischemia or vasospasm.

DATA ANALYSIS: Bivariate random effects models were used to pool outcomes for sensitivity, specificity, positive likelihood ratio, and negative likelihood ratio. Subgroup analyses for individual CTP parameters and early-versus-late study timing were performed. Bias and applicability were assessed using the modified QUADAS-2 tool.

DATA SYNTHESIS: For assessment of delayed cerebral ischemia, CTP demonstrated a pooled sensitivity of 82.1% (95% CI, 74.5%–87.8%), specificity of 79.6% (95% CI, 73.0%–84.9%), positive likelihood ratio of 4.01 (95% CI, 2.94–5.47), and negative likelihood ratio of 0.23 (95% CI, 0.12–0.33). For assessment of vasospasm, CTP showed a pooled sensitivity of 85.6% (95% CI, 74.2%–92.5%), specificity of 87.9% (95% CI, 79.2%–93.3%), positive likelihood ratio of 7.10 (95% CI, 3.87–13.04), and negative likelihood ratio of 0.16 (95% CI, 0.09–0.31).

LIMITATIONS: QUADAS-2 assessment identified 12 articles with low risk, 11 with moderate risk, and 7 with a high risk of bias.

CONCLUSIONS: For delayed cerebral ischemia, CTP had a sensitivity of >80%, specificity of >75%, and a low negative likelihood ratio of 0.23. CTP had better performance for the detection of vasospasm, with sensitivity and specificity of >85% and a low negative likelihood ratio of 0.16. Although the accuracy offers the potential for CTP to be used in limited clinical contexts, standardization of CTP techniques and high-quality randomized trials evaluating its impact are required.

ABBREVIATIONS: aSAH = aneurysmal SAH; DCI = delayed cerebral ischemia; LR = likelihood ratio; rCBF = relative CBF; rCBV = relative CBV; Tmax = time-to-maximum


SAH from ruptured intracranial aneurysms (aneurysmal SAHs [aSAHs]) accounts for 5% of all strokes, with 1 in 5 survivors

Received October 18, 2023; accepted after revision February 10, 2024.

From the Department of Radiology (A.M., Y.R.H., I.T., M.V.C.), Concord Repatriation and General Hospital, Sydney, Australia; Concord Hospital Clinical School (A.M., M.V.C.), The University of Sydney, Sydney, Australia; Department of Radiology (V.V.G.), University of California San Francisco, San Francisco, California; Department of Radiology (V.V.G.), Royal Prince Alfred Hospital, University of Sydney, Sydney, New South Wales, Australia; Department of Medical Imaging (M.A.), Gold Coast University Hospital, Queensland, Australia; Department of Medical Imaging (K.H.), University of Toronto, Joint Department of Medical Imaging, Toronto, Ontario, Canada; and Department of Neurointervention (N.M.), Liverpool Hospital, Sydney, Australia.

experiencing disability or cognitive impairment.^{1,2} In the era of early endovascular and surgical treatment of aneurysms, delayed cerebral ischemia (DCI) is the most common cause of late morbidity in these patients.²

Please address correspondence to Amer Mitchell, MD, Concord Repatriation General Hospital, Department of Radiology, 1 Hospital Rd, Concord, New South Wales 2139, Australia; e-mail: amer@nhs.net.au

 Indicates article with online supplemental data.
<http://dx.doi.org/10.3174/ajnr.A8249>

DCI is clinically defined as the development of focal neurologic impairment (including hemiparesis, aphasia, or neglect) or decreased consciousness of at least 2 points on the Glasgow Coma Scale. This should last >1 hour, is not apparent immediately after aneurysm occlusion, and is not attributable to other causes by means of clinical assessment, CT, or MR imaging investigation of the brain and appropriate laboratory studies.³ Cerebral infarction resulting from DCI is defined as the appearance of established hypodensity on CT or territorial ischemia on MR imaging within 6 weeks of SAH.³ It may commence as early as day 3 after aneurysm rupture, with the peak incidence at days 7–10.^{3,4} The diagnosis of DCI is challenging due to confounding factors, including impaired CSF transport, sedation, cerebral edema, coexistent cerebrovascular disease, or vascular stenosis due to treatment devices. Early recognition of DCI allows endovascular treatment before it leads to cortical infarction.^{5,6}

Cerebral arterial vasospasm, in contrast, is defined as focal or diffuse temporary narrowing of the vessel caliber due to contraction of the arterial wall smooth muscle as detected on, or inferred from, imaging studies (eg, DSA, transcranial Doppler, CT, or MR imaging) or as seen during surgical clipping.⁷ Vasospasm was long thought to be the sole cause of DCI, leading to an overlap in historical definitions. However, not all patients with angiographic vasospasm meet the clinical criteria for DCI, and most do not develop infarcts.^{4,8} Therefore, prevention of vasospasm does not necessarily reduce the incidence of DCI.^{4,8} Recent literature suggests that DCI has a multifactorial pathogenesis, including microvascular spasm, microthromboses, vascular dysregulation, breakdown of the blood-brain barrier, and cortical spreading depolarization.^{4,9} Vasospasm is now preferentially used to describe imaging findings, with “symptomatic vasospasm” now more accurately referred to as DCI when it meets the clinical criteria.³

There is wide practice variation with respect to surveillance for vasospasm, with institutions relying on a combination of serial clinical examination, transcranial Doppler ultrasonography, CTA, CTP, and DSA to predict and diagnose DCI and vasospasm. In particular, CTP has demonstrated promise in the early prediction and diagnosis of both vasospasm and DCI.^{8,10}

The purpose of this systematic review and meta-analysis was to pool diagnostic test accuracy metrics for CTP detection of DCI and vasospasm compared with the established reference standard definitions of clinical DCI or delayed infarct and DSA, respectively.

MATERIALS AND METHODS

Search Strategy and Information Sources

The search strategy was devised in accordance with the revised Preferred Reporting Items for Systematic Reviews and Meta-Analyses (PRISMA) 2020 statement and registered with PROSPERO (CRD42021288313; <https://www.crd.york.ac.uk/PROSPERO/>).^{11,12} Electronic searches were performed using the Cochrane Database of Systematic Reviews, Cochrane Central Register of Controlled Trials, Cochrane Clinical Answers, Cochrane Methodology Register, Ovid MEDLINE, EMBASE, American College of Physicians Journal Club, Database of Abstracts of Reviews of Effects, Health Technology Assessment, National Health Service Economic Evaluation Database, PubMed, and Google Scholar from their inception to September 2023.

Search terms included [“subarachnoid hemorrhage”] AND [“brain ischemia” OR “delayed cerebral ischemia” OR “vasospasm”] AND [“CT” OR “CT perfusion” or “perfusion imaging”] inclusive of relevant Medical Subject Headings terms or keywords, with US and UK spelling variations. Articles published between database inception to September 20, 2023, were included, without language restrictions. Following removal of duplicate studies, title and abstract screening was performed by 2 reviewers (V.V.G. and A.M.). Discrepancies were resolved by the senior investigators (M.V.C. and M.A.). Full texts were obtained, and their reference lists were reviewed to identify further relevant studies.

Selection Criteria

We included prospective and retrospective studies that published diagnostic test accuracy statistics regarding CTP performed at any time following aSAH. These encompassed studies for prediction (ie, performed within 72 hours of onset of aSAH or without deterioration) or for detection of DCI or vasospasm. Studies aiming to predict rather than detect DCI were included to capture a potential continuum between instigating factors (eg, microcirculatory dysfunction) and DCI. The reference standard for DCI was the clinical diagnosis of DCI or radiologic infarct, as per the established definition.³ For vasospasm, luminal narrowing on conventional (digital subtraction) angiography was the reference standard. When accuracy was reported by perfusion metrics, time, or on an ROI basis, these were extracted and considered for subanalysis. To avoid duplication of cohorts, we scrutinized studies with the risk of overlapping cohorts and included the most complete data set. We excluded studies with non-aSAH, <20 patients, or in which diagnostic test accuracy data were not extractable. Abstracts, case reports, case series, conference presentations, editorials, review articles, and prior systematic reviews and meta-analyses were also excluded. The search strategy and selection process are summarized graphically per the PRISMA guidelines.¹¹

Data Extraction and Critical Appraisal

All data were extracted from article texts, tables, and figures. Two investigators (V.V.G. and A.M.) independently extracted data including study design, patient demographics, study inclusion and exclusion criteria, cohort enrollment, CTP timing following ictus, CTP technique, reference standard, and diagnostic test accuracy data (true- and false-positives and -negatives, sensitivity, specificity, and positive and negative predictive values). When multiple diagnostic parameters were reported, we recorded all of these to facilitate subgroup analyses. Published data on transcranial Doppler for prediction of DCI was used as a comparator to define sensitivity and specificity of <70% as “low,” 70%–85% as “moderate,” and >85% as “high.”¹³

Discrepancies between the 2 reviewers were resolved by discussion and consensus, and the results were reviewed by the senior investigator (M.V.C.). To minimize the risk of bias due to missing results, we made an effort to contact all corresponding authors of potential articles in which data (such as 2 × 2 tables) were not available.¹⁴ The risk of bias in the included studies was assessed using the Quality Assessment of Diagnostic Accuracy of Studies (QUADAS-2; <https://www.bristol.ac.uk/population-health-sciences/projects/quadas/quadas-2/>) tool.¹⁵ Standardized

questions from the QUADAS-2 about patient selection, index test, reference standard, flow, and timing were performed by the 2 investigators (V.V.G. and A.M.). A conservative approach was used overall, with a “high” risk of bias used for any question within a domain rated “no” and “uncertain” if a question was not clearly answered.

Perfusion Parameters

Studies were not excluded on the basis of specific perfusion parameters used to demonstrate the marked heterogeneity in the assessment in the literature. Data included whether absolute or relative parameters were recorded, such as relative CBF (rCBF) and relative CBV (rCBV), in which case normalization of tissue perfusion was performed. In these cases, normalization was either to a contralateral ROI, or, more recently, such as in the case of RAPid processing of Perfusion and Diffusion (RAPID; iSchemaView) software, normalization was performed by dividing the CBF within a voxel by the median CBF of the patient’s normally perfused tissue.¹⁶ Most included articles used absolute threshold values, obtained by scaling using a venous outflow function. Qualitative analysis of CTP or nonconventional methods such as a derived circulation time were also included. The perfusion software, algorithm, and tracer-delay sensitivity have been collected in the Online Supplemental Data. Reported perfusion parameters have been summarized in the Online Supplemental Data. The synthesis of all perfusion parameters within this article represents the notable changes in CTP processing since inception, with the introduction of some parameters after the publication of several large included studies.

Statistical Analysis

Statistical analysis was performed using Meta-DiSc 2.0 (<https://bmcmmedresmethodol.biomedcentral.com/articles/10.1186/s12874-022-01788-2>), a Web-based application using the R-shiny software package (<https://shiny.posit.co/r/getstarted/shiny-basics/lesson1/index.html>).¹⁷ A 2-tailed *P* value < .05 was considered statistically significant. The Meta-DiSc 2.0 analysis used a bivariate random effects regression model via the glmer function of the lme4 package (<https://www.rdocumentation.org/packages/lme4/versions/1.1-35.3/topics/glmer>), allowing correlation between sensitivity and specificity.¹⁷ A minimum of 4 studies was required for pooling or subgroup analysis. A bivariate model was selected, and assessment of the relative sensitivity and specificity and their statistical significance was by means of the lmttest package (<https://cran.r-project.org/web/packages/lmttest/index.html>).¹⁷ Results were presented as summary sensitivities, specificities, likelihood ratios (LRs), and receiver operating characteristic area under the curve values with 95% CIs. Positive LR of 5–10 and >10 were considered moderate and strong diagnostic evidence, respectively. Similarly, negative LR of 0.1–0.2 and <0.1 were considered moderate and strong diagnostic evidence, respectively.¹⁸

RESULTS

A total of 1510 references were identified through 12 electronic database searches, of which 82 articles met criteria for full-text review. Manual search through reference lists did not yield additional relevant studies. After we applied the selection criteria, 30

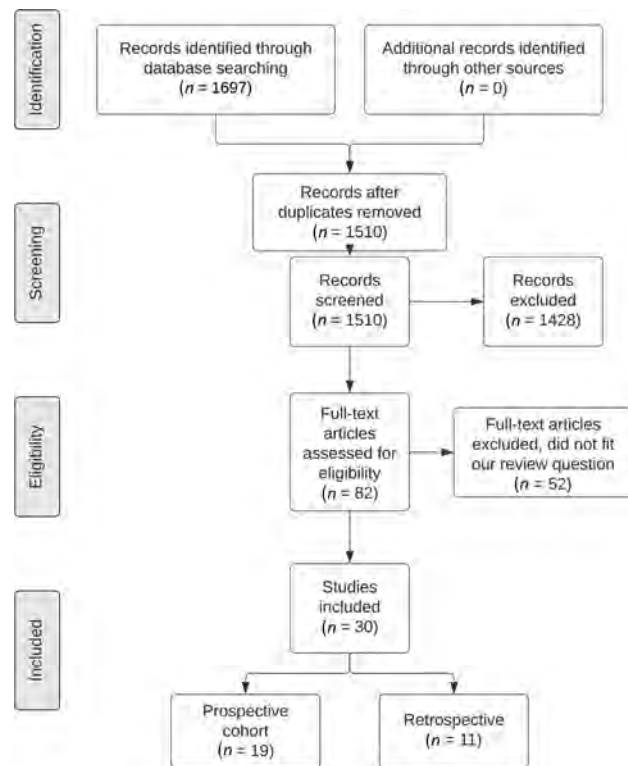


FIG 1. PRISMA flow chart.

studies were included in this meta-analysis with 19 assessing DCI, 8 assessing vasospasm, and 3 assessing both (Fig 1). Of the selected articles, 19 were prospective^{19–37} and 11 were retrospective (Online Supplemental Data).^{38–48} Twelve studies were primarily intended to predict DCI/vasospasm, 15 were primarily intended to detect the entities, and 3 were intended to do both (Online Supplemental Data). A total of 1786 patients were included, with an age range of 18–87 years, 66.5% of whom were women. A total of 2302 CTP studies were included. A summary of the included studies, patient baseline characteristics, and CTP techniques are presented in the Online Supplemental Data. For DCI subgroup analysis, data from 12 articles could be pooled for CBF, 7 for CBV, 12 for MTT, 8 for TTP, and 4 for time-to-maximum (Tmax). For vasospasm, CBF values were pooled from 5 studies.

Twenty-five studies used quantitative methods, and 5 studies used qualitative methods (Online Supplemental Data). When reported, most studies used tracer-delay-insensitive algorithms to generate CTP metrics, though many articles did not specify the algorithm or tracer-delay sensitivity of their methods (Online Supplemental Data). The prevalence of DCI, aneurysm location, and treatment modalities is summarized in the Online Supplemental Data.

Quality Assessment of Trials

Structured assessment of potential study bias using the QUADAS-2 tool is presented in the Online Supplemental Data. Twelve included studies were deemed to have a low risk of bias and had no applicability concerns. There were 11 studies deemed to have medium risk and 7 deemed to have a high risk of bias. The index test domain was most commonly deemed a high risk

of bias (Fig 2; 30%) when threshold values for CTP were not prospectively specified before interpretation. Failure to prospectively define the threshold criteria may overestimate the index test performance. Flow- and timing-related bias was considered high when DCI was diagnosed within too-short an interval (<48 hours) or when the reference standard was inconsistently applied. We considered articles at high risk of bias related to the reference standard if readers were not clearly blinded to the CTP outcome during determination of DCI or when infarct and DCI were determined during the same examination.

Diagnostic Assessment of DCI

The diagnostic accuracy of CTP for assessment of DCI was reported in 22 studies, with a pooled sensitivity of 82.1% (95% CI, 74.5%–87.8%), specificity of 79.6% (95% CI, 73.0%–84.9%), positive LR of 4.01 (95% CI, 2.94–5.47), and negative LR of 0.23 (95% CI, 0.12–0.33) (Table 1).

The most sensitive CTP parameter was TTP, reported in 7 studies with a pooled sensitivity of 82.2% (95% CI, 71.4%–89.5%) and specificity of 70.6% (95% CI, 59.2%–79.9%). The parameter with the highest positive LR was CBF, reported in 12 studies, with a positive LR of 4.62 (95% CI, 3.12–6.84). Pooled assessment of MTT was performed in 12 studies, showing a sensitivity of 80.7% (95% CI, 73.3%–86.5%) and specificity of 69.3% (95% CI, 61.4%–76.2%). Pooled assessment of Tmax revealed a sensitivity of 63.8% (95% CI, 52.5%–73.8%) and a specificity of 81.5% (95% CI, 72.5%–88.1%).

Subgroup Analysis for DCI

Subgroup analysis could be performed on 6 studies for the evaluation of the sensitivity between an MTT of 84.3% (95% CI,

76.9%–89.7%) and CBV of 70.6% (95% CI, 63.0%–77.2%) ($P = .009$) (Table 2).

However, specificity and the diagnostic OR in these studies were not statistically significant. Five studies included the timing of CTP performed, allowing accuracy data to be pooled with a 72-hour cutoff. This result showed a trend toward greater sensitivity at later timepoints, 84.5% (95% CI, 57.3%–95.7%) versus 55.8% (95% CI, 27.3%–80.8%), but it was not statistically significant ($P = .11$, Table 2).

Diagnostic Assessment of Vasospasm

The diagnostic accuracy of CTP for the assessment of vasospasm was performed in 11 studies, with a pooled sensitivity of 85.6% (95% CI, 74.2%–92.5%), specificity of 87.9% (95% CI, 79.2%–93.3%), a positive LR of 7.10 (95% CI, 3.87–13.04), and a negative LR of 0.16 (95% CI, 0.09–0.31) (Table 1). Pooled bivariate analysis could be performed on CBF only, which was reported in 5 studies with a sensitivity of 60.9% (95% CI, 45.0%–74.7%), specificity of 92.2% (95% CI, 80.7%–97.1%), a positive LR of 7.83 (95% CI, 3.06–20.06), and a negative LR of 0.42 (95% CI, 0.29–0.62).

DISCUSSION

This meta-analysis and systematic review demonstrates moderate sensitivity and specificity for DCI (82.1% and 79.6%, respectively) and vasospasm (85.6% and 87.9%). Furthermore, MTT was more sensitive than CBF for detecting DCI (84.3% versus 70.6%, $P = .009$). These results suggest that CTP may be useful as a non-invasive adjunct test for the diagnosis of DCI and vasospasm, but it may not be sufficiently accurate for use in isolation.

CTP Acquisition Technique, Parameters, and Postprocessing

There was heterogeneity of CTP techniques among the included studies, which limits comparability and may confound the assessment of optimal parameters for detecting DCI and vasospasm. Variability may be due to the model and generation of the CT scanner, contrast bolus and delivery, processing software, institutional optimization, and may be compounded by improvements

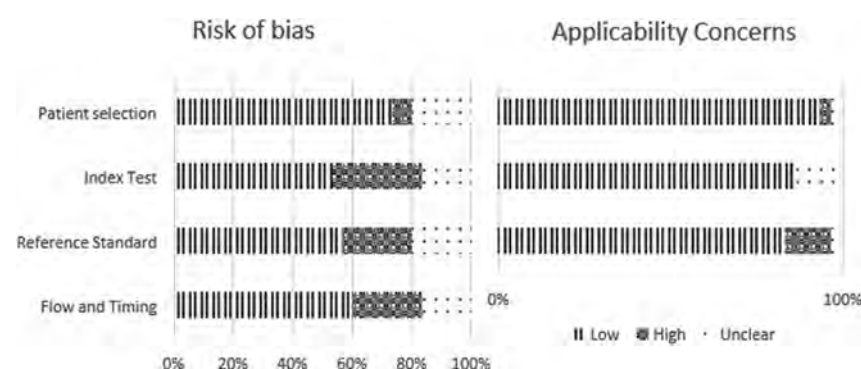


FIG 2. Risk of bias and applicability concerns by QUADAS-2 domain.

Table 1: Pooled analyses for CTP and subparameters for detection of vasospasm and delayed cerebral ischemia

	Studies	Pooled Sensitivity (%) (95% CI)	Pooled Specificity (%) (95% CI)	Positive LR	Negative LR	Diagnostic OR
Vasospasm						
CTP	11	85.6 (74.2–92.5)	87.9 (79.2–93.3)	7.10 (3.87–13.04)	0.16 (0.09–0.31)	43.41 (14.4–130.49)
CBF	5	60.9 (45.0–74.7)	92.2 (80.7–97.1)	7.83 (3.06–20.06)	0.42 (0.29–0.62)	18.47 (6.16–55.38)
DCI						
CTP	22	82.1 (74.5–87.8)	79.6 (73.0–84.9)	4.01 (2.94–5.47)	0.23 (0.12–0.33)	17.79 (9.66–32.76)
CBF	12	73.5 (62.0–82.4)	84.1 (77.1–89.3)	4.62 (3.12–6.84)	0.31 (0.32–0.47)	14.64 (7.58–28.25)
CBV	7	64.3 (50.6–75.9)	73.9 (60.1–84.1)	2.46 (1.72–3.52)	0.48 (0.37–0.64)	5.08 (3.16–8.17)
MTT	12	80.7 (73.3–86.5)	69.3 (61.4–76.2)	2.63 (2.04–3.39)	0.28 (0.20–0.40)	9.46 (5.49–16.29)
TTP	7	82.2 (71.4–89.5)	70.6 (59.2–79.9)	2.79 (1.91–4.09)	0.25 (0.15–0.43)	11.06 (4.85–25.20)
Tmax	4	63.8 (52.5–73.8)	81.5 (72.5–88.1)	3.45 (2.44–4.88)	0.44 (0.34–0.57)	7.77 (5.00–12.09)

Table 2: Pooled subgroup analysis and metaregression for CTP for detection of delayed cerebral ischemia

	Studies	Pooled Sensitivity (%) (95% CI)	Pooled Specificity (%) (95% CI)	Positive LR	Negative LR	Diagnostic OR
CTP <72 hr	5	55.8 (27.3–80.8)	93.7 (66.8–99.1)	8.81 (1.12–68.38)	0.47 (0.23–0.96)	18.0.66 (1.45–239.63)
CTP >72 hr	5	84.5 (57.3–95.7)	84.9 (48.0–97.2)	5.60 (1.14–27.60)	0.18 (0.05–0.65)	30.73 (2.50–378.08)
		<i>Relative sensitivity >72 hr vs <72 hr = 1.52 (95% CI, 0.85–2.68); P = .11; relative specificity >72 hr vs <72 hr = 0.91 (95% CI, 0.67–1.22); P = .47</i>				
MTT threshold	5	75.4 (61.6–85.4)	66.6 (51.3–79.0)	2.25 (1.33–3.81)	0.37 (0.20–0.69)	6.10 (1.98–18.78)
MTT qualitative	5	67.9 (56.9–85.9)	78.8 (69.2–85.9)	3.19 (2.09–4.89)	0.41 (0.29–0.57)	7.86 (3.92–15.76)
		<i>Relative sensitivity threshold vs qualitative = 1.14 (95% CI, 0.92–1.40); P = .24; relative specificity threshold vs qualitative = 0.82 (95% CI, 0.66–1.02); P = .10</i>				
CBF	7	74.1 (60.8–84.1)	87.4 (75.1–94.2)	5.91 (2.99–11.67)	0.30 (0.20–0.45)	19.96 (8.99–44.32)
CBV	7	64.3 (50.6–75.9)	73.9 (60.1–84.1)	2.45 (1.72–3.52)	0.48 (0.37–0.64)	5.08 (3.16–8.17)
		<i>Relative sensitivity CBV vs CBF = 0.88 (95% CI, 0.69–1.12); P = .30; relative specificity CBV vs CBF = 0.86 (95% CI, 0.70–1.05); P = .13</i>				
CBF	8	78.9 (72.7–84.0)	79.6 (64.7–89.3)	3.87 (2.11–7.10)	0.27 (0.19–0.36)	14.62 (6.38–33.49)
MTT	8	81.5 (73.5–87.5)	79.2 (69.9–86.2)	3.91 (2.68–5.71)	0.23 (0.16–0.34)	16.77 (9.31–30.22)
		<i>Relative sensitivity MTT vs CBF = 1.03 (95% CI, 0.93–1.14); P = .64; relative specificity MTT vs CBF = 1.02 (0.85–1.23); P = .85</i>				
CBV	6	70.6 (63.0–77.2)	68.5 (59.9–75.9)	2.24 (1.72–2.91)	0.43 (0.33–0.56)	5.21 (3.24–8.40)
MTT	6	84.3 (76.9–89.7)	74.4 (66.7–80.9)	3.30 (2.43–4.47)	0.21 (0.14–0.33)	15.64 (8.03–30.46)
		<i>Relative sensitivity MTT vs CBV = 1.182 (95% CI, 1.05–1.33); P = .009; relative specificity MTT vs CBV = 1.09 (95% CI, 0.94–1.25); P = .27</i>				

in CTP techniques since these have entered mainstream use for evaluation of ischemic stroke.⁴⁹

Z-axis spatial resolution is primarily dependent on the number of detectors in the multidetector CT array, which has progressively increased with newer scanner technology.⁵⁰ For example, the earliest studies included in our meta-analysis used 8-,⁴⁷ 16-,⁵¹ or 64-detector³⁶ CT scanners, with scan ranges between 20 and 40 mm, whereas the most recently included study used a 256-detector CT scanner with a scan range of 160 mm.³⁷ Thus, the volume of brain parenchyma interrogated has increased with newer scanners and may confound pooled results.

Acquisition times for CTP within the included studies ranged between 20 and 60 seconds, with temporal sampling intervals between 0.5 and 4.5 seconds. Shorter imaging times risk obtaining an incomplete concentration of tissue curve in patients with poor cardiac output, atrial fibrillation, and carotid stenoses,⁵⁰ whereas increasing temporal sampling intervals has been shown to overestimate rCBF, rCBV, and TTP and underestimate MTT in the context of ischemic stroke.⁵²

Comparison of commonly available software packages is known to demonstrate substantial variations in perfusion indices in the context of ischemic stroke.^{53,54} An in-depth review of these algorithms is beyond our scope but is well-described elsewhere.^{49,50} Tracer-delay sensitivity is thought to play an important role in accounting for such differences in vitro and in vivo.⁵³ Delay-sensitive models such as the maximum slope technique are reliant on accurate timing information and are prone to error when there is a delay or dispersion of the arterial input function. In contradistinction, delay-insensitive models such as block-circulant singular value decomposition are less susceptible to timing bolus delays.⁴⁹ At least 1 study found that both delay-sensitive and insensitive algorithms have similar performance for the detection of DCI in the setting of aSAH.⁵⁵ However, the reporting

of CT perfusion algorithms or time-delay sensitivity was very poor among included articles, limiting meaningful comparison between studies.

Delayed Cerebral Ischemia

Overall, CTP has a reasonable sensitivity for the diagnosis of DCI when pooling the best metric reported by individual studies. The most sensitive individual parameter for DCI was found to be a TTP at 82.2% (95% CI, 71.4%–89.5%), differing only slightly from MTT, demonstrating a sensitivity of 80.7% (95% CI, 73.3%–86.5%). The most specific parameter was found to be CBF.

TTP measures the time taken for contrast concentration to reach the maximum value within an ROI. It does not differentiate the cause a prolonged time and is influenced by any cause of delayed arrival of the injected contrast bolus. Causes of increased TTP include a poor bolus injection rate, poor cardiac output, and proximal (eg, proximal carotid) steno-occlusive disease. In the setting of medium vessel vasospasm in SAH, a prolonged TTP is expected due to the proximal delay of blood flow. While the underlying etiology of DCI remains uncertain, microvascular thrombosis at the capillary level may be a distal cause of prolonged TTP.

MTT, however, reflects the time taken for contrast to traverse the tissue capillary bed, and determination of MTT requires the use of delay-insensitive deconvolution. When delay-sensitive deconvolution is used, the MTT obtained is also affected by the delay in the arrival of contrast to the tissue voxel (ie, Tmax), explaining why early studies found MTT to be the optimal parameter in predicting penumbra.⁵⁶ If one assumes that DCI is a microvascular/capillary phenomenon rather than due to macrovascular spasm, MTT should be the most sensitive parameter. In the included articles, there is underreporting of the exact parameter calculation techniques, including the use of delay-insensitive deconvolution, possibly leading to a biased result. If delay-

sensitive techniques have been used but not reported, MTT no longer accurately represents capillary transit time. In contradistinction, TTP is far less susceptible to calculation technique-based variability. Possibly, the supremacy of TTP in the current study reflects the heterogeneity of the calculation technique rather than a true superiority.

While the meta-analysis suggests that CTP shows a promising sensitivity for DCI detection, one must consider the highly-selected patient cohort represented in the pooled studies.

Given the inherent risk of DCI and vasospasm among patients with aSAH, a sensitivity of 82.2% for TTP may not be high enough to meaningfully alter clinical practice. However, CTP could prove beneficial in scenarios in which clinical assessment is hindered, for example by sedation, electrolyte disturbances, or hydrocephalus. Despite the encouraging sensitivity, the low negative LR of 0.23 (95% CI, 0.12–0.33) for DCI necessitates cautious interpretation of negative results on CTP. A negative finding on CTP should not dissuade treatment if there is a strong index of suspicion for DCI on clinical grounds. Integrating clinical features, CT brain and angiogram findings, along with CTP results, could potentially enhance the overall diagnostic accuracy, but further research is warranted to definitively support this approach.

Tmax, defined as the time to the maximum of the tissue residue function after deconvolution, represents the delay between the arterial input function and the contrast arrival time in the tissue voxel. This delay is influenced by arterial stenosis or occlusion proximal to the voxel, including proximal arterial stenoses or occlusions, reduced cardiac output, and bolus dispersion. These may delay and broaden the arterial input function, leading to a prolonged Tmax. The deconvolution process does not completely account for all delays. The complexity of the effect of bolus dispersion on Tmax and the impact of the regularization process in deconvolution, which causes the Tmax to shift to later time points, are crucial considerations in interpreting Tmax values. Additionally, MTT also has a mild influence on Tmax.

Although Tmax has recently been recognized as the most sensitive predictor of tissue-at-risk for ischemic stroke,^{38,57} few articles have reported its utility in the context of aSAH. In DCI, the underlying pathophysiology is suspected to be at the capillary level and should therefore affect Tmax, which reflects macrovascular (arterial) transit, less so than MTT, which reflects microvascular transit. The parameter is, however, expected to be a marker for vasospasm, for which insufficient articles were identified to permit analysis.

Quantitative versus Semiquantitative Measures

There was heterogeneity in the methods of interpretation of CTP, particularly in defining DCI. Some studies rely on a subjective visual assessment by a neuroradiologist, while others use absolute threshold values. Another commonly used method is rCBF, which compares blood flow in a specific brain region with the blood flow in a normalized reference region, commonly the contralateral hemisphere. This method enables comparisons between different brain regions and individuals, in contrast to routine CBF, which provides only absolute blood flow in a specific brain region.

There is no consensus regarding which absolute CTP parameter or value should be used for the diagnosis of DCI. Varied

reporting methods limit pooling for meta-analysis so that standardization is needed—similar to the application of this technology in acute stroke. Of the studies included, 5 allowed direct subgroup analysis among threshold values.

Our results show that the threshold values had higher sensitivity and lower specificity than semiquantitative measures of MTT; however, the results were not statistically significant.

Timing of CTP

There was a wide range of reported timing of CTP following aSAH ictus. This is partly due to early studies examining its predictive value for DCI in the first 24 hours,⁵¹ before symptom onset, and subsequent studies assessing the diagnostic value, which is dependent on symptom onset rather than a specific time. A threshold of 72 hours was selected to facilitate pooling of at least 4 studies for comparison. Five studies that clearly defined results on the basis of CTP performed before and after 72 hours could be pooled, showing a trend toward greater sensitivity after 72 hours; however, the results were not statistically significant in the context of a small number of studies. The results suggest that CTP cannot be used confidently within 72 hours of presentation to detect DCI with a sensitivity from 4 studies of 59.9% (95% CI, 27.9%–85.3%). The timing of CTP in relation to vasospasm treatment was also not reported in any study and warrants attention in future studies. With the data available, the effect of endovascular treatment on perfusion parameters cannot be established.

Vasospasm

On the basis of our results, CTP is accurate for the diagnosis of vasospasm. Different methods for measuring CTP in vasospasm detection were used, with some studies measuring predefined ROIs and others assessing the whole brain on a quantitative or semiquantitative basis as with DCI. The pooled analysis demonstrated a higher sensitivity on a per-patient basis rather than at an ROI level.

Limitations

Our systematic review identified heterogeneity in the definitions and terms used for DCI and vasospasm throughout the literature. For example, many studies described the use of DSA as a reference standard for DCI. For purposes of meta-analysis, only articles that conformed to consensus DCI definitions proposed by Vergouwen et al³ were included, limiting the overall included number of patients. Additionally, the pooled studies were both prospective and retrospective, with varied inclusion criteria and definitions, increasing the risk of bias.

The impact of postadmission variables (such as poor cardiac output, infection, seizures, or method of aneurysm repair) on perfusion results was not specified in most patients. There were relatively small numbers in subgroup analysis, which also contributed to high heterogeneity.

While perfusion test parameters have been collected, correcting these parameters including contrast injection rate, contrast dose, and arterial input function, and ROI placement was not possible. This issue was partly due to the rapid change in CTP technology between the first and most recently included articles and partly due to a lack of standardization of CTP methods

across vendors. Specific factors have been detailed earlier in the Discussion, including variations in CTP acquisition hardware and z-axis resolution, acquisition time, software packages, and postprocessing algorithms, resulting in notable heterogeneity of included data sets. The lack of clarity regarding postprocessing software and deconvolution techniques, including the use of delay-sensitive processes, has limited the assessment of MTT in particular.

Finally, inclusion of studies in which CT perfusion was performed at <72 hours from ictus is likely to have skewed the results toward lower accuracy, due to these studies being aimed at predicting DCI rather than detecting it.

Directions for Future Research

As CTP technology advances, it offers the potential for the diagnosis of DCI and vasospasm in aneurysmal SAH. However, to ensure accurate systematic reviews, future studies should conform to the consensus definition of DCI³ and report 2 × 2 tables for each perfusion parameter with true-/false-positive values. The specific quantitative or qualitative thresholds used must be reported as well as postprocessing algorithm and tracer-delay sensitivity. A large study using MTT derived using a delay-insensitive deconvolution may provide greater accuracy for both early prediction of DCI and detection of DCI. Given the proved reliability of Tmax in ischemic stroke, it may emerge as a reliable marker of vasospasm; however, it is not necessarily expected to detect DCI.

Reporting the timing of CTP and its relation to endovascular vasospasm treatment is also crucial to better understand the effects of endovascular treatment on cerebral perfusion parameters. A study using standardized software is essential to ensure the comparability of CTP parameters.

CONCLUSIONS

The role of CTP in the diagnosis of both DCI and vasospasm remains limited as an adjunct to the overall clinical presentation. The data suggest that CTP has better performance for the detection of vasospasm than DCI. In subgroups of patients for whom the clinical assessment is unreliable or where transcranial Doppler is not available, CTP offers an alternative noninvasive test to guide or triage management. However, the data presented emphasize the need for standardized definitions, precise reporting of perfusion thresholds and outcomes, and standardized CTP parameters by vendors.


Disclosure forms provided by the authors are available with the full text and PDF of this article at www.ajnr.org.

REFERENCES

1. Etminan N, Chang H-S, Hackenberg K, et al. **Worldwide incidence of aneurysmal subarachnoid hemorrhage according to region, time period, blood pressure, and smoking prevalence in the population.** *JAMA Neurol* 2019;76:588–97 CrossRef Medline
2. Nieuwkamp DJ, Setz LE, Algra A, et al. **Changes in case fatality of aneurysmal subarachnoid haemorrhage over time, according to age, sex, and region: a meta-analysis.** *Lancet Neurol* 2009;8:635–42 CrossRef Medline
3. Vergouwen MD, Vermeulen M, van Gijn J, et al. **Definition of delayed cerebral ischemia after aneurysmal subarachnoid hemorrhage as an outcome event in clinical trials and observational studies: proposal of a multidisciplinary research group.** *Stroke* 2010;41:2391–95 CrossRef Medline
4. Ikram A, Javaid MA, Ortega-Gutierrez S, et al. **Delayed cerebral ischemia after subarachnoid hemorrhage.** *J Stroke Cerebrovasc Dis* 2021;30:106064 CrossRef Medline
5. Boulouis G, Labeyrie MA, Raymond J, et al. **Treatment of cerebral vasospasm following aneurysmal subarachnoid haemorrhage: a systematic review and meta-analysis.** *Eur Radiol* 2017;27:3333–42 CrossRef Medline
6. Saber H, Desai A, Palla M, et al. **Efficacy of cilostazol in prevention of delayed cerebral ischemia after aneurysmal subarachnoid hemorrhage: a meta-analysis.** *J Stroke Cerebrovasc Dis* 2018;27:2979–85 CrossRef Medline
7. Findlay JM, Nisar J, Darsaut T. **Cerebral vasospasm: a review.** *Can J Neurol Sci* 2016;43:15–32 CrossRef Medline
8. Rass V, Helbok R. **How to diagnose delayed cerebral ischaemia and symptomatic vasospasm and prevent cerebral infarction in patients with subarachnoid haemorrhage.** *Curr Opin Crit Care* 2021;27:103–14 CrossRef Medline
9. Viderman D, Tapinova K, Abdildin YG. **Mechanisms of cerebral vasospasm and cerebral ischaemia in subarachnoid haemorrhage.** *Clin Physiol Funct Imaging* 2023;43:1–9 CrossRef Medline
10. Francoeur CL, Mayer SA. **Management of delayed cerebral ischemia after subarachnoid hemorrhage.** *Crit Care* 2016;20:277 CrossRef Medline
11. Page MJ, McKenzie JE, Bossuyt PM, et al. **The PRISMA 2020 statement: an updated guideline for reporting systematic reviews.** *BMJ* 2021;372:n71 CrossRef Medline
12. Mitchell A, Gorolay V, Chan M. **Systematic review and meta-analysis of CT perfusion accuracy for the diagnosis of vasospasm and delayed cerebral ischaemia in patients with subarachnoid haemorrhage.** PROSPERO: National Institute of Health Care Research; 2021. https://www.crd.york.ac.uk/prosperto/display_record.php?RecordID=288313. Accessed September 1, 2023
13. Kumar G, Shahripour RB, Harrigan MR. **Vasospasm on transcranial Doppler is predictive of delayed cerebral ischemia in aneurysmal subarachnoid hemorrhage: a systematic review and meta-analysis.** *J Neurosurg* 2016;124:1257–64 CrossRef Medline
14. Page MJ, Higgins JPT, Sterne JAC. **Chapter 13: Assessing risk of bias due to missing results in a synthesis.** In: Higgins JPT, Thomas J, Chandler J, et al. (eds). *Cochrane Handbook for Systematic Reviews of Interventions*. version 6.4 (updated August 2023). Cochrane, 2023. Available from www.training.cochrane.org/handbook. Accessed August 1, 2023.
15. Greenberg ED, Gold R, Reichman M, et al. **Diagnostic accuracy of CT angiography and CT perfusion for cerebral vasospasm: a meta-analysis.** *AJNR Am J Neuroradiol* 2010;31:1853–60 CrossRef Medline
16. Amukotuwa S, Straka M, Aksoy D, et al. **Cerebral blood flow predicts the infarct core: new insights from contemporaneous diffusion and perfusion imaging.** *Stroke* 2019;50:2783–89 CrossRef Medline
17. Plana MN, Arevalo-Rodriguez I, Fernández-García S, et al. **Meta-DiSc 2.0: a Web application for meta-analysis of diagnostic test accuracy data.** *BMC Med Res Methodol* 2022;22:306 CrossRef Medline
18. Deeks JJ, Altman DG. **Diagnostic tests 4: likelihood ratios.** *BMJ* 2004;329:168–69 CrossRef Medline
19. Abdel-Tawab M, Hasan AA, Ahmed MA, et al. **Prognostic factors of delayed cerebral ischemia after subarachnoid hemorrhage including CT perfusion: a prospective cohort study.** *Egypt J Radiol Nucl Med* 2020;51 CrossRef
20. Malinova V, Tsogkas I, Behme D, et al. **Defining cutoff values for early prediction of delayed cerebral ischemia after subarachnoid hemorrhage by CT perfusion.** *Neurosurg Rev* 2020;43:581–87 CrossRef Medline
21. Shi D, Jin D, Cai W, et al. **Serial low-dose quantitative CT perfusion for the evaluation of delayed cerebral ischaemia following aneurysmal subarachnoid haemorrhage.** *Clin Radiol* 2020;75:131–39 CrossRef Medline

22. Dong L, Zhou Y, Wang M, et al. **Whole-brain CT perfusion on admission predicts delayed cerebral ischemia following aneurysmal subarachnoid hemorrhage.** *Eur J Radiol* 2019;116:165–73 CrossRef Medline
23. Murphy A, Lee TY, Marotta TR, et al. **Prospective multicenter study of changes in MTT after aneurysmal SAH and relationship to delayed cerebral ischemia in patients with good- and poor- grade admission status.** *AJNR Am J Neuroradiol* 2018;39:2027–33 CrossRef Medline
24. Sun H, Li W, Ma J, et al. **CT perfusion diagnoses delayed cerebral ischemia in the early stage of the time-window after aneurysmal subarachnoid hemorrhage.** *J Neuroradiol* 2017;44:313–18 CrossRef Medline
25. Rodriguez-Regent C, Hafsa M, Turc G, et al. **Early quantitative CT perfusion parameters variation for prediction of delayed cerebral ischemia following aneurysmal subarachnoid hemorrhage.** *Eur Radiol* 2016;26:2956–63 CrossRef Medline
26. Malinova V, Dolatowski K, Schramm P, et al. **Early whole-brain CT perfusion for detection of patients at risk for delayed cerebral ischemia after subarachnoid hemorrhage.** *J Neurosurg* 2016;125:128–36 CrossRef Medline
27. Westermaier T, Pham M, Stetter C, et al. **Value of transcranial Doppler, perfusion-CT and neurological evaluation to forecast secondary ischemia after aneurysmal SAH.** *Neurocrit Care* 2014;20:406–12 CrossRef Medline
28. Zhang H, Zhang B, Li S, et al. **Whole brain CT perfusion combined with CT angiography in patients with subarachnoid hemorrhage and cerebral vasospasm.** *Clin Neurol Neurosurg* 2013;115:2496–501 CrossRef Medline
29. Hickmann AK, Langner S, Kirsch M, et al. **The value of perfusion computed tomography in predicting clinically relevant vasospasm in patients with aneurysmal subarachnoid hemorrhage.** *Neurosurg Rev* 2013;36:267–78;discussion 278 CrossRef Medline
30. Lagares A, Cicuendez M, Ramos A, et al. **Acute perfusion changes after spontaneous SAH: a perfusion CT study.** *Acta Neurochir (Wien)* 2012;154:405–11;discussion 11–12 CrossRef Medline
31. Dankbaar JW, de Rooij NK, Rijdsdijk M, et al. **Diagnostic threshold values of cerebral perfusion measured with computed tomography for delayed cerebral ischemia after aneurysmal subarachnoid hemorrhage.** *Stroke* 2010;41:1927–32 CrossRef Medline
32. Wintermark M, Dillon WP, Smith WS, et al. **Visual grading system for vasospasm based on perfusion CT imaging: comparisons with conventional angiography and quantitative perfusion CT.** *Cerebrovasc Dis* 2008;26:163–70 CrossRef Medline
33. Pham M, Johnson A, Bartsch AJ, et al. **CT perfusion predicts secondary cerebral infarction after aneurysmal subarachnoid hemorrhage.** *Neurology* 2007;69:762–65 CrossRef Medline
34. Binaghi S, Colleoni ML, Maeder P, et al. **CT angiography and perfusion CT in cerebral vasospasm after subarachnoid hemorrhage.** *AJNR Am J Neuroradiol* 2007;28:750–58 Medline
35. van der Schaaf I, Wermer MJ, van der Graaf Y, et al. **CT after subarachnoid hemorrhage: relation of cerebral perfusion to delayed cerebral ischemia.** *Neurology* 2006;66:1533–38 CrossRef Medline
36. Sveri GE, Britz GW, Lewis DH, et al. **Dynamic perfusion computed tomography in the diagnosis of cerebral vasospasm.** *Neurosurgery* 2006;59:319–25;discussion 25 CrossRef Medline
37. Yang J, Han H, Chen Y, et al. **Application of quantitative computed tomographic perfusion in the prognostic assessment of patients with aneurysmal subarachnoid hemorrhage coexistent intracranial atherosclerotic stenosis.** *Brain Sciences* 2023;13:625 CrossRef Medline
38. Allen JW, Prater A, Kallas O, et al. **Diagnostic performance of computed tomography angiography and computed tomography perfusion tissue time-to-maximum in vasospasm following aneurysmal subarachnoid hemorrhage.** *J Am Heart Assoc* 2022;11:e023828 CrossRef Medline
39. Tanabe J, Nakahara I, Matsumoto S, et al. **Cortical blood flow insufficiency scores with computed tomography perfusion can predict outcomes in aneurysmal subarachnoid hemorrhage patients: a cohort study.** *Neurocrit Care* 2021;34:946–55 CrossRef Medline
40. Ditz C, Hartlieb M, Neumann A, et al. **Routine use of perfusion computed tomography for the detection of delayed cerebral ischemia in unconscious patients after aneurysmal subarachnoid hemorrhage.** *Acta Neurochir (Wien)* 2021;163:151–60 CrossRef Medline
41. Vulcu S, Wagner F, Santos AF, et al. **Repetitive computed tomography perfusion for detection of cerebral vasospasm-related hypoperfusion in aneurysmal subarachnoid hemorrhage.** *World Neurosurg* 2019;121:e739–46 CrossRef Medline
42. Neulen A, Pantel T, Dieter A, et al. **Volumetric analysis of intracranial vessels: a novel tool for evaluation of cerebral vasospasm.** *Int J Comput Assist Radiol Surg* 2019;14:157–67 CrossRef Medline
43. Duan Y, Xu H, Li R, et al. **Computed tomography perfusion deficits during the baseline period in aneurysmal subarachnoid hemorrhage are predictive of delayed cerebral ischemia.** *J Stroke Cerebrovasc Dis* 2017;26:162–68 CrossRef Medline
44. Othman AE, Afat S, Nikoubashman O, et al. **Volume perfusion CT imaging of cerebral vasospasm: diagnostic performance of different perfusion maps.** *Neuroradiology* 2016;58:787–92 CrossRef Medline
45. Lin CF, Hsu SP, Lin CJ, et al. **Prolonged cerebral circulation time is the best parameter for predicting vasospasm during initial CT perfusion in subarachnoid hemorrhagic patients.** *PLoS One* 2016;11:e0151772 CrossRef Medline
46. Killeen RP, Gupta A, Delaney H, et al. **Appropriate use of CT perfusion following aneurysmal subarachnoid hemorrhage: a Bayesian analysis approach.** *AJNR Am J Neuroradiol* 2014;35:459–65 CrossRef Medline
47. Wintermark M, Ko NU, Smith WS, et al. **Vasospasm after subarachnoid hemorrhage: utility of perfusion CT and CT angiography on diagnosis and management.** *AJNR Am J Neuroradiol* 2006;27:26–34 Medline
48. You F, Tang WJ, Zhang C, et al. **Whole-brain CT perfusion at admission and during delayed time-window detects the delayed cerebral ischemia in patients with aneurysmal subarachnoid hemorrhage.** *Curr Med Sci* 2023;43:409–16 CrossRef Medline
49. Heit JJ, Wintermark M. **Perfusion computed tomography for the evaluation of acute ischemic stroke: strengths and pitfalls.** *Stroke* 2016;47:1153–58 CrossRef Medline
50. Konstantas A, Goldmakher G, Lee TY, et al. **Theoretic basis and technical implementations of CT perfusion in acute ischemic stroke, Part 2: technical implementations.** *AJNR Am J Neuroradiol* 2009;30:885–92 CrossRef Medline
51. van der Schaaf I, Wermer MJ, van der Graaf Y, et al. **Prognostic value of cerebral perfusion-computed tomography in the acute stage after subarachnoid hemorrhage for the development of delayed cerebral ischemia.** *Stroke* 2006;37:409–13 CrossRef Medline
52. Wintermark M, Smith WS, Ko NU, et al. **Dynamic perfusion CT: optimizing the temporal resolution and contrast volume for calculation of perfusion CT parameters in stroke patients.** *AJNR Am J Neuroradiol* 2004;25:720–29
53. Kudo K, Sasaki M, Yamada K, et al. **Differences in CT perfusion maps generated by different commercial software: quantitative analysis by using identical source data of acute stroke patients.** *Radiology* 2010;254:200–09 CrossRef Medline
54. Koopman MS, Berkhemer OA, Geuskens RR, et al; MR CLEAN Trial Investigators. **Comparison of three commonly used CT perfusion software packages in patients with acute ischemic stroke.** *J Neurointerv Surg* 2019;11:1249–56 CrossRef Medline
55. Creemers CH, Dankbaar JW, Vergouwen MD, et al. **Different CT perfusion algorithms in the detection of delayed cerebral ischemia after aneurysmal subarachnoid hemorrhage.** *Neuroradiology* 2015;57:469–74 CrossRef Medline
56. Wintermark M, Flanders AE, Velthuis B, et al. **Perfusion-CT assessment of infarct core and penumbra: receiver operating characteristic curve analysis in 130 patients suspected of acute hemispheric stroke.** *Stroke* 2006;37:979–85 CrossRef Medline
57. Lansberg MG, Christensen S, Kemp S, et al; CT Perfusion to Predict Response to Recanalization in Ischemic Stroke Project (CRISP) Investigators. **Computed tomographic perfusion to predict response to recanalization in ischemic stroke.** *Ann Neurol* 2017;81:849–56 CrossRef Medline

Hypoperfusion Intensity Ratio Is Associated with Early Neurologic Deficit Severity and Deterioration after Mechanical Thrombectomy in Large-Vessel Occlusion Ischemic Stroke

Małgorzata M. Miller, Brian Wideman, Muhib Khan, and  Nils Henninger

ABSTRACT

BACKGROUND AND PURPOSE: The hypoperfusion intensity ratio is a surrogate marker for collateral status and a predictor of infarct growth, malignant cerebral edema, and hemorrhagic transformation. Its utility to predict a poor NIHSS score and early neurologic deterioration after mechanical thrombectomy for large vessel (LVO) versus distal and medium vessel occlusions (DMVO) has not been investigated. The objective of this study was to determine whether the higher hypoperfusion intensity ratio is associated with a worse NIHSS score at 24 hours post-mechanical thrombectomy and early neurologic deterioration in LVO versus DMVO acute ischemic stroke.

MATERIALS AND METHODS: This was a retrospective study of 231 patients with acute ischemic stroke with LVO or DMVO amenable for mechanical thrombectomy and available CTP for hypoperfusion intensity ratio assessment pre-mechanical thrombectomy. Clinical and imaging characteristics were abstracted from the medical records. The primary outcome was the NIHSS score at 24 hours post-mechanical thrombectomy. The secondary outcome was early neurologic deterioration, defined as a >4-point increase in the NIHSS score between the initial assessment and 24 hours post-mechanical thrombectomy. All analyses were first conducted in the entire cohort and then separately for the LVO versus DMVO groups.

RESULTS: The optimal hypoperfusion intensity ratio threshold to detect early neurologic deterioration was 0.54. A hypoperfusion intensity ratio ≥ 0.54 was more frequently present in LVO versus DMVO ($n = 37$ [77.1%] versus $n = 11$ [22.9%]; $P < .001$). On multivariable linear regression, the hypoperfusion intensity ratio ≥ 0.54 was independently associated with a worse NIHSS score at 24 hours post-mechanical thrombectomy in the entire cohort ($\beta = 0.163$; $P = .002$) and the LVO group ($\beta = 0.210$; $P = .005$), but not in the DMVO group. The early neurologic deterioration occurred in 26 (11.3%) subjects. On multivariable logistic regression, there was no association of the hypoperfusion intensity ratio ≥ 0.54 with early neurologic deterioration in the entire cohort. However, when analyzed separately, a hypoperfusion intensity ratio ≥ 0.54 significantly increased the odds of early neurologic deterioration in subjects with LVO (OR = 5.263; 95% CI, 1.170–23.674; $P = .030$) but not in the DMVO group.

CONCLUSIONS: The hypoperfusion intensity ratio ≥ 0.54 was independently associated with a worse 24-hour post-mechanical thrombectomy NIHSS score and early neurologic deterioration in LVO, but not in DMVO acute ischemic stroke. Pending confirmation in future, prospective studies assessing the hypoperfusion intensity ratio may help identify patients at risk of secondary decline to improve peri-thrombectomy care and clinical decision-making.

ABBREVIATIONS: AIS = acute ischemic stroke; DMVO = distal and medium vessel occlusion; END = early neurologic deterioration; ENI = early neurologic improvement; HIR = hypoperfusion intensity ratio; LA = leukoaraiosis; LKW = last known well; LVO = large vessel occlusion; MT = mechanical thrombectomy; PCA = posterior cerebral artery; rCBF = relative CBF; SBP = systolic blood pressure; Tmax = time-to-maximum

Early neurologic status after mechanical thrombectomy (MT) as assessed by the change in NIHSS score from baseline or the absolute NIHSS score at 24 hours post-MT has been shown as a strong predictor of the 90-day functional outcome.^{1,2} In

particular, early neurologic deterioration (END) is a feared complication after MT. Multiple clinical and procedural factors have been associated with END including age, NIHSS at presentation, the premorbid mRS score, pretreatment systolic blood

Received November 30, 2023; accepted after revision February 9, 2024.

From the Department of Neurosciences (M.M.M., B.W.), Corewell Health West, Grand Rapids, Michigan; College of Human Medicine (M.M.M.), Michigan State University, Grand Rapids, Michigan; Department of Neurology (M.K.), Mayo Clinic, Rochester, Minnesota; and Departments of Neurology (N.H.) and Psychiatry (N.H.), University of Massachusetts, Chan Medical School Worcester, Massachusetts.

Please address correspondence to Małgorzata M. Miller, MD, PhD, Department of Neurosciences, Corewell Health West, 25 Michigan Street NE, Suite 6100, Grand Rapids, MI 49503; e-mail: malgorzata.miller@corewellhealth.org
<http://dx.doi.org/10.3174/ajnr.A8234>

SUMMARY

PREVIOUS LITERATURE: CTP derived hypoperfusion intensity ratio (HIR) is an objective and easily available imaging biomarker of tissue microperfusion that has been shown to predict infarct growth, development of malignant edema, parenchymal hemorrhagic transformation, and long-term outcomes after mechanical thrombectomy for acute ischemic stroke. However, the utility of the HIR to predict early neurologic deterioration (END) and early neurologic status after mechanical thrombectomy for large vessel (LVO) versus distal and medium vessel occlusion (DMVO) has not been investigated.

KEY FINDINGS: The optimal HIR threshold to detect END was 0.54. $\text{HIR} \geq 0.54$ was independently associated with a worse NIHSS score at 24 hours post-mechanical thrombectomy and occurrence of END in LVO, but not in the DMVO group.

KNOWLEDGE ADVANCEMENT: HIR may expand its clinical utility to timely identify LVO population likely to develop severe neurologic deficits and those at risk for secondary neurologic deterioration. Further studies are needed to determine whether distinct CTP parameters should be used for outcome prediction and patient selection for endovascular treatment in DMVO.

pressure (SBP), the number of passes during MT, and achieved reperfusion status.³⁻⁵ In addition, imaging parameters such as a low baseline ASPECTS, occlusion site, and poor collateral circulation were found to be independent predictors of END.³

The hypoperfusion intensity ratio (HIR), which can be automatically derived in real-time from CTP imaging, has been recently described as a surrogate marker of collateral status.⁶ A high HIR, corresponding to poor collateral status, has been shown to predict greater infarct growth,⁷⁻¹⁰ development of malignant edema,¹¹ parenchymal hemorrhagic transformation,¹² and worse long-term outcomes.⁷ However, the utility of the HIR to predict a poor NIHSS and END after MT is uncertain. In addition, there is a paucity of data about whether the HIR is useful for predicting neurologic status after MT performed on both large vessel (LVO) versus distal and medium vessel occlusions (DMVO).

In this study, we sought to determine whether a higher HIR is associated with a worse NIHSS score at 24 hours post-MT as well as END (defined as a >4-point increase in the NIHSS score between the initial assessment and 24 hours after MT) in patients with LVO and DMVO. We hypothesized that a higher HIR is associated with a higher NIHSS score at 24 hours post-MT and a worse 90-day mRS score and is an independent predictor of END.

MATERIALS AND METHODS

Study Cohort

We retrospectively analyzed consecutive adult patients with acute ischemic stroke (AIS) who underwent MT at a comprehensive stroke center between January 2020 and December 2021. Patients were included if they had LVO or DMVO amenable to MT and available CTP imaging with HIR assessment before treatment. Our investigation was approved by Corewell Health West (formerly Spectrum Health) institutional review board, and a Health Insurance Portability and Accountability Act waiver of informed consent was granted. We adhered to the STrengthening the Reporting of OBservational studies in Epidemiology (STROBE) guidelines (www.strobe-statement.org).

Clinical Characteristics and Imaging Parameters

Patients' baseline characteristics, stroke presentation details including the last known well (LKW) time, initial NIHSS score,

SBP on arrival, and IV treatment with rtPA were abstracted from the medical records. Time from LKW to emergency department arrival was categorized as early (0–6 hours from LKW) versus late (>6 hours from LKW) presentation. ASPECTS and the presence of leukoaraiosis (LA) were assessed on the basis of the pretreatment NCCT. LA was defined as supratentorial WM hypoattenuation according to the STandards for ReportIng Vascular changes on nEuroimaging criteria.¹³ LA was graded on a 5-point scale using the scale of van Swieten et al¹⁴ and dichotomized (van Swieten scale 0–2 [absent-to-moderate] versus 3–4 [severe]). The site of the target vessel occlusion was determined on the basis of pretreatment CTA of the head and neck. LVO sites included the extracranial and/or intracranial ICA, MCA M1, and anterior cerebral artery A1 segment. We defined DMVO stroke as a stroke caused by an occlusion of the M2–4 segments of the MCA, A2–3 segments of the anterior cerebral artery, and P1–2 segments of the posterior cerebral artery (PCA). We included patients with PCA P1 occlusion consistent with the definition used in prior multicenter studies and ongoing clinical trials.¹⁵⁻¹⁸ Subjects with vertebral and basilar artery occlusions were excluded from the study, given the suboptimal assessment of the posterior fossa on CTP imaging.

We graded the collateral status on the basis of the score proposed by Tan et al.¹⁹ For the study, we dichotomized the collateral status into poor (grades 0–1) versus good collaterals (grades 2–3). All perfusion studies were automatically analyzed with RAPID software (iSchemaView). We assessed relative CBF (rCBF) and time-to-maximum (Tmax) maps including rCBF <30% (ischemic core), rCBF <38%, Tmax > 10 seconds, and Tmax >6 seconds. The HIR was automatically calculated as the ratio of Tmax >10 seconds/Tmax >6 seconds. NCCT, CTA, and CTP images were reviewed independently by experienced readers blinded to the clinical data. The degree of reperfusion was assessed by the TICI score and the number of passes abstracted as documented in the procedural notes. The stroke etiology was determined using the Trial of Org 10172 in Acute Stroke Treatment (TOAST) classification.²⁰

Outcome Measures

The primary study outcome was the absolute NIHSS score recorded at 24 hours post-MT. The secondary study outcome was the occurrence of END defined as a >4-point increase in

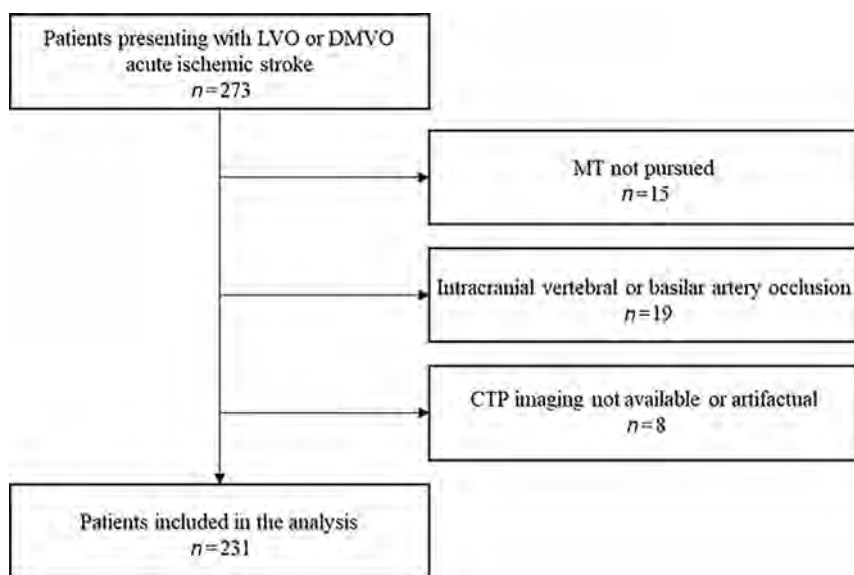


FIG 1. Flow chart of study design and patient selection.

the NIHSS score between the initial assessment and 24 hours after MT. Finally, we explored whether the HIR was associated with 90-day functional outcome. For the study, we dichotomized 90-day outcome into good (mRS 0–2) versus poor (mRS 3–6). All outcome measures were assessed in the entire cohort as well as separately for the LVO and DMVO groups. All NIHSS and mRS scores were assessed by staff certified in NIHSS and mRS.

Statistics

Unless otherwise stated, continuous variables are reported as medians (25th–75th percentile). Categorical variables are reported as proportions. Between-group comparisons for continuous and ordinal variables were made with the *t* test, Mann-Whitney *U* test, 1-way ANOVA, and Kruskal-Wallis 1-way ANOVA on ranks as appropriate. Categorical variables were compared using the χ^2 test or Fisher exact test as appropriate.

The optimal HIR threshold for predicting END was determined by maximizing the Youden index (sensitivity + specificity – 1). To determine whether the HIR threshold was independently associated with the 24-hour post-MT NIHSS score (dependent variable), we created multivariable linear regression models for the entire cohort, as well as separately for patients with LVO and DMVO. Similarly, we created separate multivariable logistic regression models to determine whether the HIR was independently associated with END and poor 90-day outcome (dependent variables) in the entire cohort or in patients with LVO and DMVO, respectively. All models were adjusted for age, sex, baseline NIHSS score, ASPECTS, rCBF < 38%, collateral status, LA severity, rtPA use, pre-MT SBP, time from LKW to presentation, TICI score, number of passes during MT, and stroke etiology. To avoid model overfitting, we sequentially removed variables (likelihood ratio) from the models at a significance level of 0.1. Collinearity diagnostics were performed (and their presence rejected) for all multivariable regression models. Model calibration was assessed by the Hosmer-Lemeshow test,

and model fit was determined by examining the –2 log-likelihood statistic and its associated χ^2 statistics.

Two-sided significance tests were used throughout, and unless stated otherwise, a 2-sided $P < .05$ was considered statistically significant. All statistical analyses were performed using SPSS Statistics, Version 24 (IBM).

RESULTS

Study Cohort

During the study period, 273 patients presented with AIS caused by an LVO or DMVO. We excluded 15 patients who did not undergo MT and 19 patients with occlusion of the intracranial vertebral or basilar artery. In addition, we excluded subjects with no or poor-quality CTP precluding HIR quantification ($n = 8$), leaving 231 patients for analysis

($n = 125$ LVO and $n = 106$ DMVO). Figure 1 depicts the patient flow chart. Data were complete for all variables.

Clinical and Imaging Characteristics

Baseline clinical and imaging characteristics of the entire cohort stratified according to HIR status are presented in Table 1. Among all included patients, the optimal HIR threshold to detect END was 0.54. An HIR ≥ 0.54 was present in 48 patients (20.8%), and it was more frequently observed in the LVO compared with DMVO group ($P < .001$). There was no difference in age, sex, LKW to presentation time, and the use of rtPA between HIR < 0.54 versus HIR ≥ 0.54 groups ($P > .05$, each). Patients with HIR ≥ 0.54 had worse baseline and 24-hour post-MT NIHSS scores ($P < .001$, each), lower ASPECTS ($P = .009$), worse collaterals ($P < .001$), larger ischemic core, rCBF < 38% ($P < .001$, each), mismatch ($P = .048$) and hypoperfusion volumes (defined either as Tmax > 6 seconds and Tmax > 10 seconds; $P < .001$, each). There was no difference in the TICI scores between HIR < 0.54 versus HIR ≥ 0.54 groups; however, in patients with HIR ≥ 0.54 , significantly more passes were required to achieve reperfusion during MT compared with patients with an HIR < 0.54 ($P = .030$).

Association of an HIR ≥ 0.54 with the NIHSS Score at 24 Hours after MT

In the entire cohort, an HIR ≥ 0.54 was independently associated with a worse NIHSS score at 24 hours post-MT after adjustment for pertinent confounders ($\beta = 0.163$, $P = .002$; Table 2). Results were similar when we restricted the analysis to subjects with LVO. An HIR ≥ 0.54 was independently associated with a worse NIHSS score at 24 hours post-MT ($\beta = 0.210$, $P = .005$; Table 2). However, HIR ≥ 0.54 was not associated with 24-hour post-MT NIHSS in the DMVO group (Table 2).

Association of an HIR ≥ 0.54 with END

END occurred in 26 (11.3%) subjects. Patients with END had lower initial NIHSS scores ($P = .005$; Table 3), were less frequently

Table 1: Patient characteristics of the entire cohort as stratified according to HIR status^a

	All Patients (n = 231)	HIR < 0.54 (n = 183)	HIR ≥ 0.54 (n = 48)	P Value
Characteristics				
Age (yr)	70 (58–78)	70 (59–79)	67 (56–75)	.323
Sex, female	119 (51.5)	96 (52.5)	23 (47.9)	.628
LKW to presentation 0–6 hr	141 (61)	111 (60.7)	30 (62.6)	.869
Initial NIHSS score	11 (5–18)	9 (4–16)	17 (11–21.5)	<.001
NIHSS score at 24 hr post-MT	8 (2–14)	6 (2–13)	13 (7.5–20)	<.001
Presence of END	26 (11.3)	20 (10.9)	6 (12.5)	.798
Use of rtPA	76 (32.9)	62 (33.9)	14 (29.2)	.607
ASPECTS	9 (8–10)	9 (8–10)	8 (7–9)	.009
Occlusion location				<.001
LVO	125 (54.1)	88 (48.1)	37 (77.1)	
DMVO	106 (45.9)	95 (51.9)	11 (22.9)	
LA grade 3–4	50 (21.6)	42 (23)	8 (16.7)	.433
Poor collateral grade (0–1)	86 (37.2)	52 (28.4)	34 (70.8)	<.001
Core volume (rCBF <30%, mL)	8 (0–23.5)	5 (0–13)	53 (22–76)	<.001
rCBF <38% (mL)	17 (6–40)	12 (5–24)	76 (44–106.5)	<.001
Tmax > 6 sec (mL)	87 (50–137.5)	71 (45.5–113)	147.5 (97.5–209.5)	<.001
Tmax > 10 sec (mL)	25 (9.5–53)	18 (6–35.5)	91.5 (62.5–131.5)	<.001
Mismatch volume (mL)	64 (40–112.5)	60 (39.5–102)	89.5 (46–122.5)	.048
Pre-MT SBP (mm Hg)	151.5 (137–170)	151 (135–170.5)	152 (141–163)	.802
TICI score				1.000
TICI 0–2a	24 (10.4)	19 (10.4)	5 (10.4)	
TICI 2b–3	207 (89.6)	164 (89.6)	43 (89.6)	
No. of passes	1 (1–2)	1 (1–2)	2 (1–3.5)	.030
Stroke etiology				.153
LAA	28 (12.1)	20 (10.9)	8 (16.7)	
Cardioembolic	96 (41.6)	74 (40.4)	22 (45.8)	
Cryptogenic	103 (44.6)	87 (47.5)	16 (33.3)	
Other determined	4 (1.7)	2 (1.1)	2 (4.2)	

Note:—LAA indicates large artery atherosclerosis.

^aData are No. (%) or median (25th–75th quartile).

Table 2: Multivariable linear regression models for factors associated with NIHSS score at 24 hours post-MT in the entire cohort, patients with LVOs, and DMVOs^a

	B	95% CI for B	β	P Value
All patients				
Initial NIHSS score	0.418	0.315–0.522	0.427	<.001
LA (grade 3–4)	2.685	0.716–4.654	0.138	.008
HIR ≥ 0.54	3.237	1.156–5.319	0.163	.002
Use of rtPA	−2.214	(−3.924)–(−0.505)	−0.129	.011
Pre-MT SBP	0.029	0.0001–0.058	0.101	.047
No. of passes	1.325	0.731–1.919	0.242	<.001
TICI score 2b–3	−2.803	−5.715–0.109	−0.103	.059
Stroke etiology (cryptogenic)	1.586	−0.019–3.1901	0.098	.053
LVOs				
Initial NIHSS score	0.373	0.226–0.520	0.366	<.001
HIR ≥ 0.54	3.968	1.194–6.742	0.210	.005
Use of rtPA	−3.802	(−6.428)–(−1.176)	−0.206	.005
Pre-MT SBP	0.045	0.003–0.087	0.154	.035
No. of passes	1.304	0.558–2.050	0.250	.001
Stroke etiology (cryptogenic)	2.430	0.022–4.837	0.140	.048
DMVOs				
LA (grade 3–4)	3.280	0.912–5.648	0.202	.007
No. of passes	1.088	0.181–1.995	0.181	.019
TICI score 2b–3	−5.978	(−9.64)–(−2.316)	−0.245	.002
Stroke etiology (LAA)	3.708	0.184–7.232	0.144	.039

Note:—LAA indicates large artery atherosclerosis.

^aModels are adjusted for age, sex, initial NIHSS score, ASPECTS, CTA collateral score, rCBF <38%, HIR, LA, rtPA use, pre-MT SBP, time from LKW to presentation, TICI score, number of passes during MT, and stroke etiology. We used $P < .1$ as a criterion for backward steps. All patients: Adjusted $R^2 = 0.452$, $F = 24.180$, $P < .001$. LVOs group: Adjusted $R^2 = 0.414$, $F = 15.262$, $P < .001$. DMVOs group: Adjusted $R^2 = 0.516$, $F = 22.994$, $P < .001$.

treated with rtPA ($P = .048$; Table 3), and had higher pre-MT SBP ($P = .010$; Table 3). In addition, subjects with END required higher number of passes ($P < .001$; Table 3) and achieved lower TICI scores ($P < .001$; Table 3). Pretreatment imaging parameters such as ASPECTS, core volume, rCBF <38%, CTA collateral score, HIR, or mismatch volume did not differ between patients with versus without END ($P > .05$; Table 3).

When we analyzed the entire cohort, we found no association of $HIR \geq 0.54$ with END after adjustment of pertinent clinical and imaging characteristics (Table 4). However, when we stratified our analyses, we found that an $HIR \geq 0.54$ significantly increased the odds of END in subjects with LVO ($OR = 5.263$; 95% CI, 1.170–23.674; $P = .030$; Table 4) but not in the DMVO group (Table 4).

Association of an $HIR \geq 0.54$ with 90-Day Functional Outcome

We found no association of $HIR \geq 0.54$ with poor 90-day functional outcome in the entire cohort ($OR = 0.667$; 95% CI, 0.231–1.927; $P = .455$). Results were similar when analyses were conducted separately for LVO ($OR = 0.898$; 95% CI 0.233–3.452; $P = .875$) and DMVO ($OR = 0.446$; 95% CI, 0.050–4.010; $P = .471$) groups.

DISCUSSION

The main finding of our study was that $HIR \geq 0.54$ assessed on initial CTP imaging was independently associated with a worse NIHSS score at 24 hours post-MT and END in patients with LVO, but not DMVO.

The 24-hour NIHSS score is a strong predictor of long-term outcomes after AIS,^{1,2} and it is impacted by multiple clinical factors such as the premorbid mRS score, admission blood glucose level, end-stage renal disease, the use of rtPA, time from groin puncture to recanalization, and the need for general anesthesia during MT.²¹ In our study, in the entire cohort as well as in the LVO subgroup, an $HIR \geq 0.54$ was independently associated with a worse 24-hour post-MT NIHSS score after

Table 3: Characteristics in patients with END versus without END^a

	All Patients (n = 231)	END Absent (n = 205)	END Present (n = 26)	P Value
Characteristics				
Age (yr)	70 (58–78)	69 (57–78)	73.5 (65–80)	.095
Sex, female	119 (51.5)	104 (50.7)	15 (57.7)	.538
LKW to presentation 0–6 hr	141 (61)	128 (62.4)	13 (50)	.286
Initial NIHSS score	11 (5–18)	12 (6–19)	6 (3–12)	.005
NIHSS score at 24 hr post-MT	8 (2–14)	6 (2–13)	18 (12–24)	<.001
Use of rtPA	76 (32.9)	72 (35.1)	4 (15.4)	.048
ASPECTS	9 (8–10)	9 (8–10)	9 (8–10)	.663
Occlusion location				.835
LVO	125 (54.1)	110 (53.7)	15 (57.7)	
DMVO	106 (45.9)	95 (46.3)	11 (42.3)	
LA grade 3–4	50 (21.6)	43 (21)	7 (26.9)	.613
CTA collateral score 0–1	86 (37.2)	172 (35.1)	14 (53.8)	.084
rCBF <38% (mL)	17 (6–40)	17 (6–45)	19 (6.5–32)	.836
Core volume (rCBF <30% mL)	8 (0–23.5)	8 (0–26)	6.5 (0–16)	.451
Tmax > 6 sec (mL)	87 (50–137.5)	89 (52–139)	66.5 (43–116)	.278
Tmax > 10 sec (mL)	25 (9–53)	28 (11–57)	18.5 (8–27)	.141
Mismatch volume (mL)	64 (40–112.5)	66 (40–113)	60.5 (35–103)	.479
HIR ≥ 0.54	48 (20.8)	42 (20.5)	6 (23.1)	.798
Pre-MT SBP (mm Hg)	151.5 (137–170)	151 (135–167)	167.5 (146–189)	.010
TICI score				<.001
TICI 0–2a	24 (10.4)	14 (6.8)	10 (38.5)	
TICI 2b–3	207 (89.6)	191 (93.2)	16 (61.5)	
No. of passes	1 (1–2)	1 (1–2)	2 (2–4)	<.001
Stroke etiology				.379
LAA	28 (12.1)	23 (11.2)	5 (19.2)	
Cardioembolic	96 (41.6)	88 (42.9)	8 (30.8)	
Cryptogenic	103 (44.6)	90 (43.9)	13 (50)	
Other determined	4 (1.7)	4 (2)	0 (0)	

Note:—LAA indicates large artery atherosclerosis.

^a Data are No. (%) or median (25th–75th quartile).

Table 4: Multivariable logistic regression models for factors associated with END in the entire cohort, patients with LVOs and DMVOs^a

	Adjusted OR	95% CI	P Value
All patients			
Age, per year	1.043	1.001–1.088	.044
Initial NIHSS score	0.842	0.771–0.919	<.001
ASPECTS	1.087	0.922–1.281	.320
HIR ≥ 0.54	3.100	0.838–11.598	.093
CTA collateral grade 0–1	3.013	1.058–8.582	.039
Pre-MT SBP (per mm Hg)	1.022	1.004–1.041	.018
TICI score 2b–3	0.096	0.028–0.328	<.001
LVOs			
Initial NIHSS score	0.836	0.751–0.932	.001
Pre-MT SBP (per mm Hg)	1.028	1.005–1.051	.016
Use of rtPA	5.195	0.606–44.535	.133
HIR ≥ 0.54	5.263	1.170–23.674	.030
DMVOs			
TICI 2b–3	0.020	0.003–0.124	<.001
Stroke etiology (LAA)	11.901	1.684–84.124	.013

Note:—LAA indicates large artery atherosclerosis.

^a Models are adjusted for age, sex, initial NIHSS score, ASPECTS, collateral status, rCBF <38%, HIR, LA, rtPA use, pre-MT SBP, time from LKW to presentation, TICI score, number of passes during MT and stroke etiology. We used $P < .1$ as a criterion for backward steps. All patients: Hosmer–Lemeshow goodness of fit $\chi^2 = 15.563$, $P = .049$; LVOs group: Hosmer–Lemeshow goodness of fit $\chi^2 = 6.235$, $P = .621$; DMVOs group: Hosmer–Lemeshow goodness of fit $\chi^2 = 0.002$, $P = .962$.

adjustment for pertinent confounders. It was previously shown that a high HIR correlates with poor collaterals;^{6,7} thus, it may distinguish fast from slow progressors^{10,22–24} and could be a useful imaging biomarker to predict the efficacy of MT.²⁵ Our result of $\text{HIR} \geq 0.54$ as predictor of the NIHSS score at 24 hours further

supports the notion that the HIR may reflect a promising, easy-to-assess, imaging biomarker to aid in decision-making in patients considered for MT. Our result is in line with prior studies that showed that a high HIR is an independent factor for increased final infarction volume,⁷ development of intraparenchymal hematoma,¹² and early malignant edema,¹¹ which are strongly correlated with a greater neurologic deficit severity as assessed by the NIHSS score.

Notably, in contrast to patients with LVO, we did not find an independent association of an $\text{HIR} \geq 0.54$ with the NIHSS score at 24 hours post-MT in the DMVO group. This finding is important because DMVOs are estimated to represent 25%–40% of all AISs,²⁶ and it is presently not well-established which patients with DMVO are likely to benefit from MT.²⁶ In our DMVO population, the number of passes during MT, reperfusion status, and severe LA were independently associated with the NIHSS score at 24 hours. This finding is consistent with those in previous reports indicating that procedural factors such as the number of passes and the degree of reperfusion may supersede the impact of the HIR on outcome in those with DMVO undergoing MT.^{27,28} As reported by Abdelrady et al,²⁸ complete reperfusion (mTICI score 2c–3) was the strongest predictor of the favorable outcome after MT for distal M2 and M3 occlusions. In addition, as shown by Ospel et al²⁹ in the subgroup analysis of the Endovascular Treatment for Small Core and Proximal Occlusion Ischemic Stroke (ESCAPE) trial, the rate of infarct progression differs on the basis of the site of the occlusion, with fast progressors being less frequent in those with more distal occlusions. Accordingly and consistent with previous reports,³⁰ we observed overall lower HIR values in the DMVO compared with the LVO group. In addition, a high HIR was associated with an increased rate of ischemic core progression in

DMVO,^{9,10} yet it did not correlate with clinical outcomes in this patient population. Distal occlusions may be better collateralized, and the area of tissue at risk is smaller in DMVO. Thus, smaller ischemic lesion volumes render reliable estimation of HIR in DMVO more challenging. Further studies are needed to

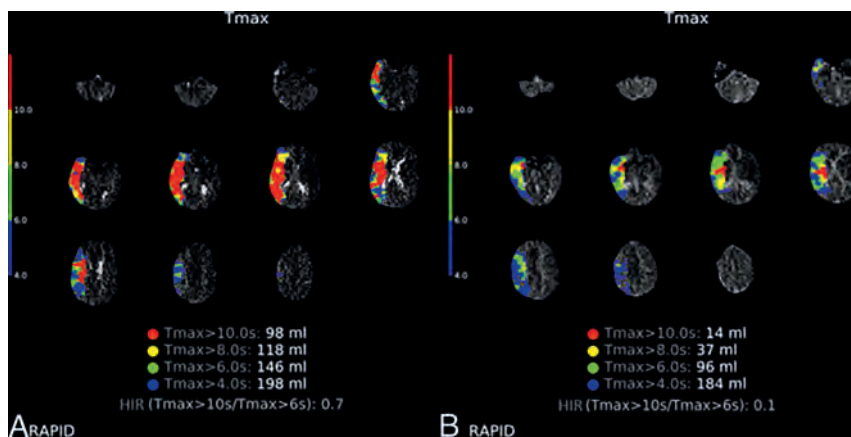


FIG 2. Representative imaging demonstrating HIR ≥ 0.54 (A) versus HIR < 0.54 (B) CTP profiles. A, Tmax maps illustrating HIR calculated at 0.7 by RAPID software in a 51-year-old patient who presented with an initial NIHSS score of 9, ASPECTS of 10, and right MCA M1 occlusion and underwent MT with TICI 3 reperfusion. The 24-hour post-MT NIHSS score worsened to 17, indicating the occurrence of END. B, Tmax maps illustrating HIR calculated at 0.1 by RAPID software in a 54-year-old patient who presented with an initial NIHSS score of 10, ASPECTS of 9, and right MCA M1 occlusion and underwent MT with TICI 2b reperfusion. The 24-hour post-MT NIHSS score improved to 4.

investigate whether different HIR thresholds should be used when assessing collateral circulation in LVO versus DMVO. Likewise, it would be interesting to know if patients with DMVO have distinct CTP parameters that should be used for short- and long-term outcome prediction as well patient selection for endovascular treatment.

The incidence of END in our population (11.26%) was comparable with those reported in large MT cohorts.^{3,4} In agreement with previous studies,³⁻⁵ we showed that older age, lower initial NIHSS score, worse collateral score, higher pretreatment SBP, and failed reperfusion status increased the odds of END in the entire cohort. Most important, we found that in the LVO subgroup, HIR ≥ 0.54 was independently associated with END. Using arterial spin-labeling MRA, Zhang et al³¹ showed that a high hypoperfusion volume ratio (an equivalent of HIR) is associated with END in AIS, yet the study predates the MT era. In a recent study, Faizy et al³² investigated the potential association of HIR with early neurologic improvement (ENI) and found that a favorable HIR was not associated with ENI. While the definitions for ENI and END differ, precluding direct translation between their and our results, they, nevertheless, highlighted the potential utility of using the HIR to identify patients both at increased risk of neurologic deterioration as well as a higher chance of recovery with recanalization therapy.

What is noteworthy, END comprises a variety of clinical conditions, including development of symptomatic intracranial hemorrhage and early malignant edema, both shown to correlate with a high HIR.^{11,12} Yet, most END causes are not clinically identifiable.³³ It has been hypothesized that unexplained END may relate to collateral failure and infarct growth beyond the initial penumbra tissue.³⁴ In the Endovascular Therapy Following Imaging Evaluation for Ischemic Stroke 3 (DEFUSE 3) cohort (Fig 2),³⁵ 34% of patients had infarcts larger than predicted despite successful reperfusion, and HIR in this group was significantly higher

compared with patients with final infarct volume within 25 mL of prediction. Conversely, smaller-than-predicted infarcts were observed in a substantial proportion of patients with partial and unsuccessful reperfusion (21% and 43%, respectively). Indirectly, this finding may suggest that collateral status can improve or fail with time. Thus, if our data are confirmed, assessment of the viability of hypoperfused tissue by the HIR may allow identification of patients in studies seeking to determine novel strategies to prevent early deterioration. For example, selecting patients with a high HIR for cerebral blood flow augmentation such as through maintaining higher blood pressure goals may delay collateral failure and impact early clinical outcomes in this patient population. Likewise, these patients may be ideal candidates for treatment with novel neuroprotective agents

aimed at improving collateral integrity and enhanced cerebral microperfusion.

A major advantage of using CTP for patient selection is that CTP is increasingly used as a part of the standard of care in AIS. HIR, which is an objective and easily available imaging biomarker of tissue microperfusion, may expand its clinical utility to timely identify the LVO population likely to develop severe neurologic deficits and those at risk of secondary neurologic deterioration. One may envision how novel artificial intelligence and machine learning tools could incorporate HIR metrics to further improve predicting neurologic outcomes and the best candidates for MT. Last, because strict clinical and imaging selection criteria for MT in patients with DMVO are not currently available, further studies are needed to determine whether distinct CTP parameters should be used for outcome prediction and patient selection for endovascular treatment in those with DMVO.

Consistent with prior observation,³⁶ we did not find an association between HIR and 90-day functional outcome. Nevertheless, other studies reported that the HIR can be a predictor of long-term functional outcome,^{7,11,12,24,37} which may, in part, be explained by differences in the baseline characteristics of patients included in our study. Additional research is warranted to determine whether alternative perfusion-based collateral indices (such as the perfusion collateral index) may outperform HIR.

Strengths of the study relate to the inclusion and characterization of many patients undergoing MT for both LVO and DMVO with available CTP imaging. Furthermore, we used the 24-hour NIHSS score as the primary outcome measure, which is thought to outperform changes in the NIHSS.¹ Limitations relate to the single-center design and retrospective nature of the study; thus, results should be considered hypothesis-generating. Most patients with DMVO had distal M2 and M3 occlusions, with relatively few patients having PCA P1 and P2 occlusions. Thus, it remains to be shown whether our results extend to patients with

non-MCA branch occlusions. In clinical practice, PCA occlusions are not uncommon targets for MT,³⁸ and the utility of CTP to predict outcomes in posterior circulation stroke has been reported previously.³⁹ Last, we did not assess the causes of END, such as hemorrhagic complications or the development of early malignant edema.

CONCLUSIONS

HIR is an easily accessible metric that may expand its clinical utility to timely identify the LVO population likely to develop severe neurologic deficits and those at risk of secondary neurologic deterioration. Pending confirmation in future, prospective studies assessing the HIR may further improve predicting neurologic outcomes and finding the best candidates for MT in LVO versus DMVO AIS.













Disclosure forms provided by the authors are available with the full text and PDF of this article at www.ajnr.org.

REFERENCES

- Mistry EA, Yeatts S, de Havenon A, et al. **Predicting 90-day outcome after thrombectomy: baseline-adjusted 24-hour NIHSS is more powerful than NIHSS score change.** *Stroke* 2021;52:2547–53 CrossRef Medline
- Knierp H, Meyer L, Bechstein M, et al; GSR-ET (German Stroke Registry—Endovascular Treatment). **How much of the thrombectomy related improvement in functional outcome is already apparent at 24 hours and at hospital discharge?** *Stroke* 2022;53:2828–37 CrossRef Medline
- Zhang M, Xing P, Tang J, et al; DIRECT-MT Investigators. **Predictors and outcome of early neurological deterioration after endovascular thrombectomy: a secondary analysis of the DIRECT-MT trial.** *J Neurointerv Surg* 2023;15:e9e16 CrossRef Medline
- Bhole R, Nouer SS, Tolley EA, et al; COMPASS Investigators. **Predictors of early neurologic deterioration (END) following stroke thrombectomy.** *J Neurointerv Surg* 2023;15:584–88 CrossRef Medline
- Giot JB, Richard S, Gariel F, et al; ETIS Investigators. **Predictors of unexplained early neurological deterioration after endovascular treatment for acute ischemic stroke.** *Stroke* 2020;51:2943–50 CrossRef Medline
- Guenego A, Fahed R, Albers GW, et al. **Hypoperfusion intensity ratio correlates with angiographic collaterals in acute ischaemic stroke with M1 occlusion.** *Eur J Neurol* 2020;27:864–70 CrossRef Medline
- Olivot JM, Mlynash M, Inoue M, et al; DEFUSE 2 Investigators. **Hypoperfusion intensity ratio predicts infarct progression and functional outcome in the DEFUSE 2 Cohort.** *Stroke* 2014;45:1018–23 CrossRef Medline
- Guenego A, Mlynash M, Christensen S, et al. **Hypoperfusion ratio predicts infarct growth during transfer for thrombectomy.** *Ann Neurol* 2018;84:616–20 CrossRef Medline
- Guenego A, Farouki Y, Mine B, et al. **Hypoperfusion intensity ratio predicts infarct growth after successful thrombectomy for distal medium vessel occlusion.** *Clin Neuroradiol* 2022;32:849–56 CrossRef Medline
- Nomani AZ, Kamtchum Tatuene J, Rempel JL, et al. **Association of CT-based hypoperfusion index with ischemic core enlargement in patients with medium and large vessel stroke.** *Neurology* 2021;97:e2079–87 CrossRef Medline
- Murray NM, Culbertson CJ, Wolman DN, et al. **Hypoperfusion intensity ratio predicts malignant edema and functional outcome in large-vessel occlusive stroke with poor revascularization.** *Neurocrit Care* 2021;35:79–86 CrossRef
- Winkelmeier L, Heit JJ, Adusumilli G, et al. **Hypoperfusion intensity ratio is correlated with the risk of parenchymal hematoma after endovascular stroke treatment.** *Stroke* 2023;54:135–43 CrossRef Medline
- Wardlaw JM, Smith EE, Biessels GJ, et al; STandards for Reporting Vascular changes on nEuroimaging (STRIVE v1). **Neuroimaging standards for research into small vessel disease and its contribution to ageing and neurodegeneration.** *Lancet Neurol* 2013;12:822–38 CrossRef Medline
- van Swieten JC, Hijdra A, Koudstaal PJ, et al. **Grading white matter lesions on CT and MRI: a simple scale.** *J Neurol Neurosurg Psychiatry* 1990;53:1080–83 CrossRef Medline
- Monteiro A, Makalanda HLD, Wareham J, et al. **Mechanical thrombectomy in medium vessel occlusions using the novel aspiration Q catheters: an international multicenter experience.** *J Neurointerv Surg* 2023 July 21. [Epub ahead of print] CrossRef Medline
- Schulze-Zachau V, Brehm A, Ntoulas N, et al. **Incidence and outcome of perforations during medium vessel occlusion compared with large vessel occlusion thrombectomy.** *J Neurointerv Surg* 2023 July 21. [Epub ahead of print] CrossRef Medline
- Pérez-García C, Moreu M, Rosati S, et al. **Mechanical thrombectomy in medium vessel occlusions: blind exchange with mini-pinning technique versus mini stent retriever alone.** *Stroke* 2020;51:3224–31 CrossRef Medline
- Radu RA, Gascou G, Machi P, et al. **Current and future trends in acute ischemic stroke treatment: direct-to-angiography suite, middle vessel occlusion, large core, and minor strokes.** *Eur J Radiol Open* 2023;11:100536 CrossRef Medline
- Tan JC, Dillon WP, Liu S, et al. **Systematic comparison of perfusion-CT and CT-angiography in acute stroke patients.** *Ann Neurol* 2007;61:533–43 CrossRef Medline
- Adams HP Jr, Bendixen BH, Kappelle LJ, et al. **Classification of subtype of acute ischemic stroke: definitions for use in a multicenter clinical trial. TOAST. Trial of Org 10172 in acute stroke treatment.** *Stroke* 1993;24:35–41 CrossRef Medline
- Weyland CS, Mokli Y, Vey JA, et al. **Predictors for failure of early neurological improvement after successful thrombectomy in the anterior circulation.** *Stroke* 2021;52:1291–98 CrossRef Medline
- Seners P, Scheldeman L, Christensen S, et al; Infarct-Growth Collaborators. **Determinants of infarct core growth during inter-hospital transfer for thrombectomy.** *Ann Neurol* 2023;93:1117–29 CrossRef Medline
- Mohammaden MH, Haussen DC, Pisani L, et al. **Characterizing fast and slow progressors in anterior circulation large vessel occlusion strokes.** *Interv Neuroradiol* 2023;29:379–85 CrossRef Medline
- Seners P, Yuen N, Olivot JM, et al; for Mismatch Prevalence. **Factors associated with fast early infarct growth in patients with acute ischemic stroke with a large vessel occlusion.** *Neurology* 2023;101:e2126–37 CrossRef Medline
- Guenego A, Marcellus DG, Martin BW, et al. **Hypoperfusion intensity ratio is correlated with patient eligibility for thrombectomy.** *Stroke* 2019;50:917–22 CrossRef Medline
- Saver JL, Chapot R, Agid R, et al; Distal Thrombectomy Summit Group. **Thrombectomy for distal, medium vessel occlusions: a consensus statement on present knowledge and promising directions.** *Stroke* 2020;51:2872–84 CrossRef Medline
- Farouki Y, Bonnet T, Mine B, et al. **First-pass effect predicts clinical outcome and infarct growth after thrombectomy for distal medium vessel occlusions.** *Neurosurgery* 2022;91:913–19 CrossRef Medline
- Abdelrady M, Derraz I, Dargazanli C, et al. **Complete recanalization predicts favorable outcome in patients with distal M2-M3 middle cerebral artery occlusions following endovascular thrombectomy.** *J Neuroradiol* 2023;50:230–36 CrossRef Medline
- Ospel JM, Hill MD, Kappelhof M, et al. **Which acute ischemic stroke patients are fast progressors? Results from the ESCAPE trial control arm.** *Stroke* 2021;52:1847–50 CrossRef Medline
- Faizy TD, Kabiri R, Christensen S, et al. **Distinct intra-arterial clot localization affects tissue-level collaterals and venous outflow profiles.** *Eur J Neurol* 2021;28:4109–16 CrossRef Medline

31. Zhang M, Zhu W, Ma Y, et al. **Early neurological deterioration and hypoperfusion volume ratio on arterial spin labeling in patients with acute ischemic stroke.** *J Stroke Cerebrovasc Dis* 2021;30:105885 CrossRef Medline
32. Faizy TD, Mlynash M, Kabiri R, et al. **Favourable arterial, tissue-level and venous collaterals correlate with early neurological improvement after successful thrombectomy treatment of acute ischaemic stroke.** *J Neurol Neurosurg Psychiatry* 2022 May 16. [Epub ahead of print] CrossRef Medline
33. Bourcier R, Goyal M, Muir KW, et al; HERMES Trialists Collaboration. **Risk factors of unexplained early neurological deterioration after treatment for ischemic stroke due to large vessel occlusion: a post hoc analysis of the HERMES study.** *J Neurointerv Surg* 2023;15:221–26 CrossRef Medline
34. Fu J, Zhou Y, Li Q, et al. **Perfusion changes of unexplained early neurological deterioration after reperfusion therapy.** *Transl Stroke Res* 2020;11:195–203 CrossRef Medline
35. Rao VL, Mlynash M, Christensen S, et al. **Collateral status contributes to differences between observed and predicted 24-h infarct volumes in DEFUSE 3.** *J Cereb Blood Flow Metab* 2020;40:1966–74 CrossRef Medline
36. Tsui B, Chen IE, Nour M, et al. **Perfusion collateral index versus hypoperfusion intensity ratio in assessment of collaterals in patients with acute ischemic stroke.** *AJNR Am J Neuroradiol* 2023;44:1249–55 CrossRef Medline
37. Yedavalli V, Koneru M, Hamam O, et al. **Pretreatment CTP collateral parameters predict good outcomes in successfully recanalized middle cerebral artery distal medium vessel occlusions.** *Clin Neuroradiol* 2023 Dec 28. [Epub ahead of print] CrossRef Medline
38. Nguyen TN, Qureshi MM, Strambo D, et al. **Endovascular versus medical management of posterior cerebral artery occlusion stroke: the PLATO study.** *Stroke* 2023;54:1708–17 CrossRef Medline
39. Pallesen LP, Lambrou D, Eskandari A, et al. **Perfusion computed tomography in posterior circulation stroke: predictors and prognostic implications of focal hypoperfusion.** *Eur J Neurol* 2018;25:725–31 CrossRef Medline

Association between CT Perfusion Parameters and Hemorrhagic Transformation after Endovascular Treatment in Acute Ischemic Stroke: Results from the ESCAPE-NA1 Trial

 Rosalie V. McDonough,  Nathaniel B. Rex,  Johanna M. Ospel,  Nima Kashani,  Leon A. Rinkel,  Arshia Sehgal,  Joachim C. Fladt, Ryan A. McTaggart, Raul Nogueira,  Bijoy Menon,  Andrew M. Demchuk,  Alexandre Poppe,  Michael D. Hill,  Mayank Goyal, on behalf of the ESCAPE-NA1 Investigators



ABSTRACT

BACKGROUND AND PURPOSE: Hemorrhagic transformation can occur as a complication of endovascular treatment for acute ischemic stroke. This study aimed to determine whether ischemia depth as measured by admission CTP metrics can predict the development of hemorrhagic transformation at 24 hours.

MATERIALS AND METHODS: Patients with baseline CTP and 24-hour follow-up imaging from the ESCAPE-NA1 trial were included. RAPID software was used to generate CTP volume maps for relative CBF, CBV, and time-to-maximum at different thresholds. Hemorrhage on 24-hour imaging was classified according to the Heidelberg system, and volumes were calculated. Univariable and multivariable regression analyses assessed the association between CTP lesion volumes and hemorrhage/hemorrhage subtypes.

RESULTS: Among 408 patients with baseline CTP, 142 (35%) had hemorrhagic transformation at 24-hour follow-up, with 89 (63%) classified as hemorrhagic infarction (HI1/HI2), and 53 (37%), as parenchymal hematoma (PH1/PH2). Patients with HI or PH had larger volumes of low relative CBF and CBV at each threshold compared with those without hemorrhage. After we adjusted for baseline and treatment variables, only increased relative CBF <30% lesion volume was associated with any hemorrhage (adjusted OR, 1.14; 95% CI, 1.02–1.27 per 10 mL), as well as parenchymal hematoma (adjusted OR, 1.23; 95% CI, 1.06–1.43 per 10 mL). No significant associations were observed for hemorrhagic infarction.

CONCLUSIONS: Larger “core” volumes of relative CBF <30% were associated with an increased risk of PH following endovascular treatment. This particular metric, in conjunction with other clinical and imaging variables, may, therefore, help estimate the risk of post-endovascular treatment hemorrhagic complications.

ABBREVIATIONS: AUC = area under the curve; eTICI = expanded TICI; EVT = endovascular treatment; HI = hemorrhagic infarction; IQR = interquartile range; PH = parenchymal hematoma; rCBF = relative CBF; sICH = symptomatic intracerebral hemorrhage; Tmax = time-to-maximum

Hemorrhagic transformation of ischemic stroke is common and part of the natural history. A large percentage of hemorrhagic transformations are asymptomatic, inconsequential to prognosis.^{1,2}

Received November 14, 2023; accepted after revision January 24, 2024.

From the Departments of Radiology (R.V.M., N.B.R., J.M.O., L.A.R., A.S., M.G.), and Clinical Neurosciences (B.M., A.M.D., M.D.H., M.G.), University of Calgary, Calgary, Alberta, Canada; Department of Diagnostic Imaging (N.B.R.), and Imaging (R.A.M.), Brown University, Providence, Rhode Island; Department of Neurosurgery (N.K.), University of Saskatchewan, Saskatchewan, Canada; Department of Neurology (L.A.R.), Amsterdam University Medical Centres, Amsterdam, the Netherlands; Department of Neurology and Stroke Center (J.C.F.), University Hospital Basel, Basel, Switzerland; Department of Neurology and Neurosurgery (R.N.), University of Pittsburgh School of Medicine, Pittsburgh, Pennsylvania; and Department of Neurosciences (A.P.), Centre Hospitalier de l'Université de Montréal, Montreal, Quebec, Canada.

Rosalie V. McDonough and Nathaniel B. Rex are co-first authors.

Please address correspondence to Rosalie McDonough, MD MSc, Department of Radiology, University of Calgary, Calgary, Alberta, Canada; e-mail: rosevmcd@gmail.com; @rosevmcd; @mayankGO; @johanna_ospel; @joachimfladt



Indicates article with online supplemental data.

<http://dx.doi.org/10.3174/ajnr.A8227>

They are associated with reperfusion therapy, thrombolysis, and endovascular treatment (EVT) and appear within 24 hours when these therapies are performed.³ Radiologically, hemorrhagic transformation can range in severity from small petechial hemorrhage without noticeable mass effect to larger, space-occupying parenchymal hematoma (PH).⁴ The presence of PH is unequivocally associated with worse outcomes and is symptomatic.^{5–7} PH occurs more commonly when there is a lack of early reperfusion.

Larger volumes of increasing ischemia depth as measured by the CTP parameters prolonged mean transit time, prolonged time-to-maximum (Tmax), and relative CBF (rCBF) may indicate impaired collateral circulation and an increased risk of hemorrhagic transformation.^{8–10} However, the current literature presents conflicting data on optimal CTP parameter thresholds for the prediction of hemorrhagic transformation, most studies being based on retrospective or observational analyses of small cohorts.¹¹

The aim of this study was to investigate the association between CTP-derived lesion volumes and the occurrence of hemorrhagic infarction (HI) or PH at 24 hours post-EVT using data from a randomized controlled trial.

MATERIALS AND METHODS

Patient Sample

Data are from the Safety and Efficacy of Nerinetide in Subjects Undergoing Endovascular Thrombectomy for Stroke (ESCAPE-NA1) trial, registered under clinicaltrials.gov with the identifier NCT02930018.¹² ESCAPE-NA1 was a double-blind, multicenter randomized controlled trial that aimed to evaluate the efficacy of nerinetide in patients with acute ischemic stroke who underwent EVT.

Patients were randomly assigned to receive either IV nerinetide or a placebo in addition to best medical management, including IV alteplase if deemed appropriate. The inclusion criteria for the parent trial were as follows: 1) 18 years of age or older with a large-vessel occlusion (intracranial ICA, MCA M1 or all M2 branches), 2) baseline NIHSS score of more than five, 3) time from the last seen well to randomization within 12 hours, 4) functional independence before the stroke, 5) moderate-to-good collateral circulation, and 6) ASPECTS of ≥ 4 . All patients underwent NCCT and single-phase or multiphase CTA at baseline.

For the current study, only patients who had baseline CTP imaging, performed as part of clinical routine at each respective site but not mandated by the trial, were included in the analysis. The participating sites obtained appropriate ethics and local regulatory approval, and informed consent was obtained from the participants, legally authorized representatives, or investigators, following the requirements of national laws or regulations, including 2-physician consent when necessary.

Imaging Analysis

All imaging data were evaluated by a central imaging core lab, which was blinded to treatment allocation and clinical outcomes. The baseline NCCT scan was used to assess the ASPECTS. Collateral circulation was evaluated on CTA and categorized as poor, moderate, or good. The location of the occlusion was reported as the terminal ICA, M1 segment of the MCA, or M2 segment of the MCA.

Perfusion source images were processed using RAPID processing of Perfusion and Diffusion (RAPID software, Version 5.2.2; iSchemaView) to generate rCBF, CBV, and Tmax volumes. Each volume was provided at specific standard thresholds. The output DICOM files were converted to NIfTI format by using `dcm2niix` (<http://www.github.com/rordenlab/dcm2niix>) and underwent automated segmentation using color-based thresholding in Python (Version 3.10). The segmentation volumes were extracted using 3D Slicer, Version 5.0.2 (<http://www.slicer.org>). These additional processing steps were performed to provide more detail regarding the affected brain regions at each threshold, allowing more precise segmentation/volume calculation. Key Python functions necessary for reproduction of feature extraction and processing are detailed on Github (https://github.com/naterex23/RAPID_Perfusion_Processing), and an additional Python source code is available on reasonable request.

Secondary CTP-based metrics, including the hypoperfusion intensity ratio, mismatch, and mismatch ratio, were calculated. The hypoperfusion intensity ratio represents the volume of Tmax >10 seconds divided by the volume of Tmax >6 seconds. The mismatch is calculated as the volume of Tmax >6 seconds minus the volume of rCBF $<30\%$, and the mismatch ratio is the volume of Tmax >6 seconds divided by the volume of rCBF $<30\%$.

The evaluation of the expanded TICI (eTICI) was performed on the final intracranial DSA run. The presence and volumes of any hemorrhagic transformation were determined as described by Ospel et al.⁷ Briefly, hemorrhagic transformation was assessed through visual inspection of the 24-hour follow-up imaging by an interventional neuroradiologist (M.G., with 24 years of experience) and a general radiologist (J.M.O., with 4 years of experience). Discrepancies were resolved by consensus. Hemorrhagic transformation was classified into 4 subtypes: HI types 1 and 2 and PH types 1 and 2, according to the Heidelberg criteria.⁴ Due to their infrequency, remote parenchymal hematomas ($n=3$) were included in the PH groups. For this analysis, HI-1 and HI-2 were combined, as were PH-1 and PH-2. Symptomatic intracerebral hemorrhage (sICH) was defined as any hemorrhage associated with clinical evidence of neurologic worsening, with the hemorrhage considered the main cause of the decline.¹³

Outcome Measures

The primary outcome was the presence of any intracranial hemorrhage at 24 hours. Secondary outcomes included the presence of HI1 or HI2 and the presence of PH1 or PH2. sICH was analyzed as a safety outcome.

Statistical Analysis

Baseline characteristics and treatment factors of the participants were described using descriptive statistics as appropriate to the type and distribution of the data. Comparisons were made between participants with and without any hemorrhage at follow-up imaging.

Unadjusted comparisons of CTP-derived lesion volumes at baseline between patients with and without outcomes of interest were made using nonparametric tests. Adjusted effect size estimates for associations of CTP-derived lesion volumes and outcomes were obtained using multivariable logistic regression. The multivariable regression models were adjusted for age, sex, baseline glucose level, NIHSS, ASPECTS, collateral score, alteplase administration, successful reperfusion (eTICI 2c/3), time to reperfusion, and procedural complications. Separate models were constructed for the RAPID-generated CTP parameters rCBF $<30\%$, Tmax >6 seconds, and CBV $<38\%$. These specific rCBF and Tmax thresholds were chosen because they represent the RAPID standard output for core and penumbra, respectively, while CBV $<38\%$ was chosen as a midrange indicator of ischemia depth.

Statistical analyses were performed using STATA 17 software (Stata Corp), and a level of $P < .05$ was considered statistically significant. No imputation was performed for minimal missing data. Finally, because this was an exploratory subgroup analysis, no formal power analysis was performed, and all results are considered exploratory.

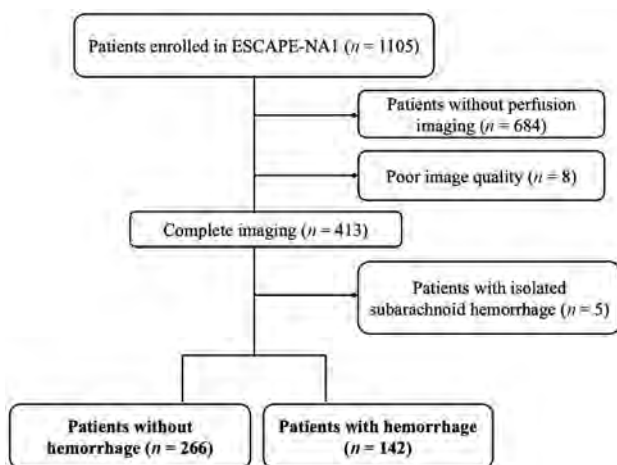


FIGURE. Flow chart of inclusion.

RESULTS

Patient Characteristics

Presence of Any Hemorrhage. Among the 1105 patients enrolled in the trial, baseline CTP source imaging was available for 421. Eight patients were excluded from the CTP analysis due to low scan quality, and 5 patients had isolated subarachnoid bleeds, resulting in a total of 408 patients included in the analysis (Figure). The median age of the patients was 70.1 years (interquartile range [IQR], 60.3–79.8 years), with 50% of them being women. Hemorrhage on follow-up imaging, observed in 142 patients (35%), was determined by segmented volumes from either CT (72 patients, 51%) or MR imaging (70 patients, 49%) at 24 hours. The Online Supplemental Data provide an overview of baseline clinical, imaging, treatment, and outcome variables for patients with and without hemorrhage, further stratified by the type of bleed (HI1/HI2 or PH1/PH2).

Patients with evidence of any intracranial hemorrhage on follow-up imaging ($n = 142$) had higher admission blood glucose levels (median, 7.1 mg/dL [IQR, 6.2–9.0 mmol/L] versus 6.6 mmol/L [IQR, 5.8–7.6 mmol/L]; respectively, $P < .001$), higher baseline NIHSS scores (median, 18 [IQR, 15–21] versus 17 [IQR, 12–20]; $P = .007$), lower baseline ASPECTS (median, 8 [IQR, 6–8] versus 8 [IQR, 7–9]; $P < .001$), and worse collateralization (15 of 141 participants [10.6%] versus 44 of 261 participants [16.7%] with good collateral vessels; $P = .022$). Regarding treatment, patients with evidence of any intracranial hemorrhage had longer onset-to-reperfusion times (median, 332.5 minutes [IQR, 214–550.5 minutes] versus 210 minutes [IQR, 158.5–297 minutes]; $P < .001$) and achieved successful recanalization less frequently (52 of 142 participants [36.6%] versus 131 of 263 participants [49.8%]; $P = .012$). There were no differences in alteplase administration observed (Online Supplemental Data).

Hemorrhage Subtypes. Within this cohort, most observed hemorrhages were classified as either HI1 (52 of 142, 36.6%) or HI2 (37, 26.0%). PH1 and PH2 accounted for 23.2% (33 of 142) and 14.1% (20 of 142), respectively. At 24 hours, sICH was present in 14 of 142 (9.9%) patients (Online Supplemental Data). When stratifying according to bleeding type, the significant differences

Table 1: Unadjusted associations between standard CTP parameters and the presence of any type of hemorrhage, HI1/HI2, and PH1/PH2, at follow-up^a

Variable	OR	LCL	UCL	P Value	AUC (95% CI)
Any hemorrhage					
rCBF <30%	1.17	1.09	1.26	<.001	0.64 (0.59–0.70)
Tmax > 6s	1.00	0.97	1.03	.787	0.52 (0.46–0.58)
CBV <38%	1.09	1.03	1.16	.003	0.61 (0.56–0.67)
HI1 and HI2					
rCBF <30%	1.18	1.09	1.28	<.001	0.65 (0.58–0.71)
Tmax > 6s	1.00	0.97	1.04	.747	0.52 (0.45–0.59)
CBV <38%	1.10	1.03	1.17	.004	0.61 (0.55–0.68)
PH1 and PH2					
rCBF <30%	1.15	1.04	1.28	.007	0.64 (0.56–0.72)
Tmax > 6s	1.00	0.97	1.04	.747	0.52 (0.44–0.60)
CBV <38%	1.08	0.99	1.17	.085	0.61 (0.54–0.69)

Note:—UCL indicates upper confidence limit; LCL, lower confidence limit.

^aFor CBF, CBV, Tmax, odds ratios are per 10 mL.

in baseline characteristics between cohorts with any hemorrhage versus none and patients with HI1/HI2 versus none remained, except for the rate of successful reperfusion, which was no longer significant in the latter (35 of 89 [39.3% versus 49.8%], respectively; $P = .110$) (Online Supplemental Data).

For patients with PH1/PH2, the baseline ASPECTS was lower (7.5 [IQR, 6–8] versus 8 [IQR, 7–9]; $P = .041$). In terms of procedural characteristics, patients with PH1/PH2 had lower rates of successful reperfusion (17 [32.1%] versus 131 [49.8%]; $P = .023$) and longer onset-to-reperfusion times (median, 394 minutes [IQR, 261–578 minutes] versus 311 minutes [IQR, 209–540 minutes]; $P < .001$) compared with those without any hemorrhage. Overall, few differences were observed between patients with and without sICH, with the former group generally having higher baseline systolic blood pressure (median, 157 mm Hg [IQR, 140–190 mm Hg] versus 144 mm Hg [IQR, 129–161 mm Hg]; $P = .027$) (Online Supplemental Data).

Perfusion-Based Characteristics

Presence of Any Hemorrhage. Significant differences in volume were observed at the rCBF <30% and CBV <38% thresholds between patients with any hemorrhage and those without at follow-up (Online Supplemental Data). In both cases, the hemorrhage group exhibited larger deficit volumes (rCBF <30%; median, 17.9 mL [IQR, 6.4–43.9 mL] versus rCBF <30%: 6.1 mL [IQR, 0.0–22.5 mL]; $P < .001$, and CBV <38%: median, 17.4 mL [IQR, 5.1–45.4 mL] versus CBV <38%: 6.9 mL [IQR, 0.0–32.7 mL]; $P < .001$, respectively). Although Tmax > 6-second volumes were numerically larger in the hemorrhage group, the difference was not significant (Online Supplemental Data).

Univariable regression analyses revealed significant associations between both rCBF <30% (OR, 1.17; 95% CI, 1.09–1.26; $P < .001$, area under the curve [AUC], 0.64) and CBV <38% (OR, 1.09; 95% CI, 1.03–1.16; $P = .003$, AUC, 0.61) thresholds and the presence of any hemorrhage at follow-up (Table 1). After adjusting for predefined variables, only the associations between rCBF <30% and hemorrhage at follow-up remained. Once again, no significant associations were found for Tmax > 6 seconds (Table 2).

Hemorrhage Subtypes. Both HI1/HI2 and PH1/PH2 groups differed with respect to rCBF <30% and CBV <38% compared with

Table 2: Adjusted associations between standard CTP parameters and the presence of any hemorrhage, HI1/HI2, and PH1/PH2, at follow-up^a

Variable	aOR	aLCL	aUCL	P Value	AUC (95% CI)
Any hemorrhage					
rCBF <30%	1.14	1.02	1.27	.017	0.78 (0.73–0.83)
Tmax > 6s	1.00	0.96	1.05	.912	0.77 (0.72–0.83)
CBV <38%	1.07	0.98	1.16	.122	0.78 (0.73–0.83)
HI1 and HI2					
rCBF <30%	1.11	0.99	1.26	.081	0.77 (0.70–0.84)
Tmax > 6s	1.00	0.94	1.05	.941	0.77 (0.70–0.83)
CBV <38%	1.05	0.96	1.14	.310	0.77 (0.70–0.84)
PH1 and PH2					
rCBF <30%	1.23	1.06	1.43	.007	0.81 (0.74–0.88)
Tmax > 6s	1.00	0.94	1.05	.941	0.77 (0.73–0.86)
CBV <38%	1.12	0.99	1.26	.063	0.81 (0.74–0.88)

Note:—aOR indicates adjusted OR; aLCL, adjusted upper confidence limit; aUCL, adjusted lower confidence limit.

^aFor CBF, CBV, Tmax, (adjusted) odds ratios are per 10 mL. Analyses were adjusted for age, sex, baseline glucose, NIHSS, ASPECTS, collateral score, alteplase, successful reperfusion (eTICI 2c/3), time to reperfusion, and procedural complications.

those without any hemorrhage (HI1/HI2: rCBF <30%; median, 15.5 mL [IQR: 5.9–47.7 mL] versus 6.1 mL [IQR: 0.0–22.5 mL]; $P < .001$; CBV <38%; 17.8 [IQR: 4.9–44.2] versus 6.9 [IQR: 0.0–32.7]; $P < .001$ and PH1/PH2: rCBF <30%; median, 19.9 mL [IQR, 6.9–32.8 mL] versus 6.1 mL [IQR, 0.0–22.5 mL]; $P = .001$; CBV <38%; 16.3 [IQR, 6.7–45.4] versus 6.9 [IQR, 0.0–32.7]; $P = .009$). Larger CBF <30% volumes were observed in the PH1/PH2 group compared with the HI1/HI2 group, while CBV <38% deficit volumes were generally larger in the HI1/HI2 cohort compared with the PH1/PH2 group (Online Supplemental Data). These differences, however, were not significant (data not shown). No differences in Tmax > 6 seconds were observed for HI1/HI2 or PH1/PH2 (Online Supplemental Data). None of the tested CTP metrics differed according to presence of sICH (Online Supplemental Data).

For HI1/HI2, univariable regression analyses demonstrated a significant relationship between the rCBF <30% (OR, 1.18; 95% CI, 1.09–1.28; $P < .001$, AUC, 0.65) and CBV <38% (OR, 1.10; 95% CI, 1.03–1.17; $P = .004$, AUC, 0.61) parameters, but not Tmax > 6 seconds (Table 1). After we adjusted for baseline, clinical, and procedural characteristics, however, neither relationship remained significant (Table 2).

When PH1/PH2 was taken as the dependent variable, univariable regression analysis revealed a significant relationship between rCBF <30% (OR, 1.15; 95% CI, 1.04–1.28; $P = .007$, AUC 0.64) (Table 1), which persisted following adjustment (Table 2). Neither univariable nor multivariable regression analyses showed significant associations between sICH and the CTP parameters (Online Supplemental Data).

No significant associations among any of the secondary CTP metrics, hypoperfusion-intensity ratio, mismatch, and mismatch ratio were observed (data not shown).

DISCUSSION

In the ESCAPE-NA1 trial, we found that higher volumes of rCBF <30% deficit (often operationally classified as “ischemic core”) were associated with the presence of any hemorrhage on

follow-up imaging. However, this relationship is very likely driven by the association with PH1/PH2 hemorrhage subtype on 24-hour follow-up imaging, because no significant relationships were observed between CTP parameters and HI1/HI2 or sICH.

There is substantial heterogeneity in the literature, with studies reporting associations with prolonged Tmax^{14,15} and low CBV values,^{16,17} while others emphasized associations of low rCBF.¹⁸ Meta-analyses conducted on this topic have been limited by variations in perfusion metrics, software programs, and study designs (eg, indication, technique, and timing of follow-up imaging for hemorrhage detection).^{11,19–21} Some have even identified a potential publication bias, suggesting an overestimation of the diagnostic performance of CTP for hemorrhage prediction.¹⁹

A few studies have specifically examined the associations of RAPID-generated CTP parameters. For instance, 1 study analyzed a cohort of 282 patients with (91 [32%]) and without (191 [68%]) hemorrhage at follow-up and found larger volumes of CTP parameters with hemorrhage.¹⁵ In this relatively small, single-center study, Tmax >6 was observed to be the strongest factor associated with hemorrhagic transformation. Another single-center study involving 392 patients undergoing EVT identified associations between ASPECTS and infarct core volume (defined by rCBF <30%), but the models were not adjusted for factors such as collaterals, blood pressure, or time to reperfusion, and the effect sizes were small.²²

While larger rCBF <30% volumes demonstrated an association with the presence of parenchymal hematoma, no significant correlation was observed between CTP metrics and sICH. This finding may, in part, be due to the relatively low incidence of sICH in this cohort (14/408, 3.4%). Indeed, the overall trend was toward larger volumes in the sICH group (rCBF <30%: 15.9 versus 10.2 mL; CBV <38%: 30.3 versus 11.6 mL) (Online Supplemental Data). Most interesting, there was a trend toward smaller volumes of Tmax > 6 seconds in the symptomatic hemorrhage group (119.2 versus 137.7 mL) (Online Supplemental Data), potentially highlighting the importance of decreased mismatch volume. Nevertheless, this discrepancy prompts consideration of factors beyond perfusion imaging that might contribute to symptomatic hemorrhage post-EVT.

A strength of this study lies in its relatively large sample size derived from a randomized controlled trial, which may also explain the somewhat discrepant results regarding Tmax between the current study and other studies. Furthermore, the use of the same software and standardized output for all perfusion images enhances the consistency and clinical relevance of the findings. While other promising perfusion-based metrics, such as the permeability surface-area product, have been identified for hemorrhage prediction, their widespread use in clinical practice remains limited.^{11,23,24}

Although certain baseline CTP parameters appear to be associated with hemorrhagic transformation at 24-hour follow-up, it is important to acknowledge that hemorrhage is a complex process influenced by multiple factors, many of which are not detectable through CTP imaging alone.

For instance, in addition to procedural factors such as treatment delays, complications, and reperfusion outcomes, previous studies have found associations of hemorrhagic transformation

and hyperglycemia, acute hypertension, blood pressure variability, and stroke severity.^{5,6,25} The current study confirmed these associations with regard to any type of parenchymal hemorrhage and HI1/HI2, emphasizing the likely stronger association of these non-CTP variables with hemorrhage at follow-up. No such associations being seen in patients with PH1/PH2 might be attributed to the smaller sample size of patients with PH1/PH2, resulting in underpowered analyses.

Additionally, there may be information loss during postprocessing.²⁶ By integrating clinical information with CTP, a more precise and individualized diagnostic framework for predicting hemorrhagic transformation could be achieved. However, larger studies are needed to further investigate these possibilities.

Limitations

Limitations of this study include those inherent to a randomized controlled trial, the heterogeneity introduced by batch-processing perfusion studies from different sites and machines, the reliance on the standard output parameters of RAPID without deeper analyses, and the use of both NCCT and MR imaging for assessing hemorrhagic transformation, all of which may have affected the precision of the estimates. Furthermore, without dual-energy CT, differentiating hemorrhage and contrast material staining on NCCT can be challenging. A study by Amans et al²⁷ demonstrated that brain parenchyma with contrast staining on CT after DSA in patients with acute ischemic stroke was likely to infarct and unlikely to hemorrhage, suggesting that most contrast staining did not progress to hemorrhage. Although contrast extravasation occurs during the breakdown of the BBB, which also leads to bleeding, the volumes may have been overestimated and our results should be interpreted with caution. Finally, the grouping of different subtypes (HI1, HI2, PH1, PH2) may mask nuanced relationships. This grouping decision was influenced by the limited number of patients in each subgroup. While primarily PHs have been shown to have an impact on clinical outcomes, this reduction in granularity remains a limitation, and further studies with larger subgroup sizes would be valuable for a more detailed analysis.

CONCLUSIONS

This study demonstrates that larger volumes of rCBF <30% deficit are associated with an increased risk of developing PH1/PH2. However, no significant associations were found for HI1/HI2 or sICH. These findings suggest that while CBF <30% may help estimate the risk of more severe types of intracranial hemorrhage following EVT for acute ischemic stroke, other imaging, clinical, and procedural factors are likely of greater value.

ACKNOWLEDGMENTS

We acknowledge the ESCAPE-NA1 sites and investigators.

Disclosure forms provided by the authors are available with the full text and PDF of this article at www.ajnr.org.

REFERENCES

1. Terruso V, D'Amelio M, Di Benedetto N, et al. **Frequency and determinants for hemorrhagic transformation of cerebral infarction.** *Neuroepidemiology* 2009;33:261–65 CrossRef Medline
2. Berger C, Fiorelli M, Steiner T, et al. **Hemorrhagic transformation of ischemic brain tissue.** *Stroke* 2001;32:1330–35 CrossRef Medline
3. **Intracerebral hemorrhage after intravenous t-PA therapy for ischemic stroke.** *Stroke* 1997;28:2109–18 CrossRef Medline
4. von Kummer R, Broderick JP, Campbell BC, et al. **The Heidelberg Bleeding Classification: classification of bleeding events after ischemic stroke and reperfusion therapy.** *Stroke* 2015;46:2981–86 CrossRef Medline
5. Boisseau W, Fahed R, Lapergue B, et al; ETIS Investigators. **Predictors of parenchymal hematoma after mechanical thrombectomy.** *Stroke* 2019;50:2364–70 CrossRef Medline
6. Kaesmacher J, Kaesmacher M, Maegerlein C, et al. **Hemorrhagic transformations after thrombectomy: risk factors and clinical relevance.** *Cerebrovasc Dis* 2017;43:294–304 CrossRef Medline
7. Ospel JM, Qiu W, Menon BK, et al; ESCAPE-NA1 Investigators. **Radiologic patterns of intracranial hemorrhage and clinical outcome after endovascular treatment in acute ischemic stroke: results from the ESCAPE-NA1 Trial.** *Radiology* 2021;300:402–09 CrossRef Medline
8. Shi F, Gong X, Liu C, et al. **Acute stroke: prognostic value of quantitative collateral assessment at perfusion CT.** *Radiology* 2019;290:760–68 CrossRef Medline
9. Lan L, Leng X, Ip V, et al. **Sustaining cerebral perfusion in intracranial atherosclerotic stenosis: the roles of antegrade residual flow and leptomeningeal collateral flow.** *J Cereb Blood Flow Metab* 2020;40:126–34 CrossRef Medline
10. Bang OY, Goyal M, Liebeskind DS. **Collateral circulation in ischemic stroke: assessment tools and therapeutic strategies.** *Stroke* 2015;46:3302–09 CrossRef Medline
11. Adebayo OD, Culpan G. **Diagnostic accuracy of computed tomography perfusion in the prediction of haemorrhagic transformation and patient outcome in acute ischaemic stroke: a systematic review and meta-analysis.** *Eur Stroke J* 2020;5:4–16 CrossRef Medline
12. Hill MD, Goyal M, Menon BK, et al; ESCAPE-NA1 Investigators. **Efficacy and safety of nerinetide for the treatment of acute ischaemic stroke (ESCAPE-NA1): a multicentre, double-blind, randomised controlled trial.** *Lancet* 2020;395:878–87 CrossRef Medline
13. Rao NM, Levine SR, Gornbein JA, et al. **Defining clinically relevant cerebral hemorrhage after thrombolytic therapy for stroke.** *Stroke* 2014;45:2728–33 CrossRef Medline
14. Yassi N, Parsons MW, Christensen S, et al. **Prediction of poststroke hemorrhagic transformation using computed tomography perfusion.** *Stroke* 2013;44:3039–43 CrossRef Medline
15. Elsaid N, Bigliardi G, Dell'Acqua ML, et al. **The role of automated computed topography perfusion in prediction of hemorrhagic transformation after acute ischemic stroke.** *Neuroradiol J* 2023;36:182–88 CrossRef Medline
16. Jain AR, Jain M, Kanthala AR, et al. **Association of CT perfusion parameters with hemorrhagic transformation in acute ischemic stroke.** *AJNR Am J Neuroradiol* 2013;34:1895–900 CrossRef Medline
17. Lin K, Zink WE, Tsiouris AJ, et al. **Risk assessment of hemorrhagic transformation of acute middle cerebral artery stroke using multimodal CT.** *J Neuroimaging* 2012;22:160–66 CrossRef Medline
18. Souza LC, Payabvash S, Wang Y, et al. **Admission CT perfusion is an independent predictor of hemorrhagic transformation in acute stroke with similar accuracy to DWI.** *Cerebrovasc Dis* 2012;33:8–15 CrossRef Medline
19. Suh CH, Jung SC, Cho SJ, et al. **Perfusion CT for prediction of hemorrhagic transformation in acute ischemic stroke: a systematic review and meta-analysis.** *Eur Radiol* 2019;29:4077–87 CrossRef Medline
20. Xu J, Dai F, Wang B, et al. **Predictive value of CT perfusion in hemorrhagic transformation after acute ischemic stroke: a systematic review and meta-analysis.** *Brain Sci* 2023;13:156 CrossRef Medline
21. Elsaid N, Mustafa W, Saied A. **Radiological predictors of hemorrhagic transformation after acute ischemic stroke: an**

- evidence-based analysis.** *Neuroradiol J* 2020;33:118–33 CrossRef Medline
22. Austein F, Fischer AC, Fiehler J, et al. **Value of perfusion CT in the prediction of intracerebral hemorrhage after endovascular treatment.** *Stroke Res Treat* 2021;2021:9933015 CrossRef Medline
23. Aviv RI, d'Esterre CD, Murphy BD, et al. **Hemorrhagic transformation of ischemic stroke: prediction with CT perfusion.** *Radiology* 2009;250:867–77 CrossRef Medline
24. Ande SR, Grynspan J, Aviv RI, et al. **Imaging for predicting hemorrhagic transformation of acute ischemic stroke: a narrative review.** *Can Assoc Radiol J* 2022;73:194–202 CrossRef Medline
25. Neuberger U, Kickingereder P, Schonenberger S, et al. **Risk factors of intracranial hemorrhage after mechanical thrombectomy of anterior circulation ischemic stroke.** *Neuroradiology* 2019;61:461–69 CrossRef Medline
26. Yu Y, Guo D, Lou M, et al. **Prediction of hemorrhagic transformation severity in acute stroke from source perfusion MRI.** *IEEE Trans Biomed Eng* 2018;65:2058–65 CrossRef Medline
27. Amans MR, Cooke DL, Vella M, et al. **Contrast staining on CT after DSA in ischemic stroke patients progresses to infarction and rarely hemorrhages.** *Interv Neuroradiol* 2014;20:106–15 CrossRef Medline

Comprehensive Analysis of Post-Pipeline Endothelialization and Remodeling

 Vera Sharashidze,  Eytan Raz,  Erez Nossek,  Svetlana Kvint,  Howard Riina, Caleb Rutledge,  Jacob Baranoski, Ayaz Khawaja,  Charlotte Chung, Peter Kim Nelson, and  Maksim Shapiro



ABSTRACT

BACKGROUND AND PURPOSE: Successful post-flow-diverter endoluminal reconstruction is widely believed to require endothelial overgrowth of the aneurysmal inflow zone. However, endothelialization/neointimal overgrowth is a complex process, over which we currently have very limited influence. Less emphasized is vascular remodeling of the target arterial segment, the dynamic response of the vessel to flow-diverter implantation. This process is distinct from flow modifications in covered branches. It appears that basic angiographic methods allow simple and useful observations. The purpose of this article was to quantitatively evaluate observable postimplantation changes in target vessels following deployment of Pipeline endoluminal constructs.

MATERIALS AND METHODS: One hundred consecutive adults with unruptured, previously untreated, nondissecting aneurysms treated with the Pipeline Embolization Device with Shield Technology and the availability of follow-up conventional angiography were studied with 2D DSA imaging. Target vessel size; Pipeline Embolization Device diameter; endothelial thickness; and various demographic, antiplatelet, and device-related parameters were recorded and analyzed.

RESULTS: The thickness of neointimal overgrowth (mean, 0.3 [SD, 0.1] mm; range, 0.1–0.7 mm) is inversely correlated with age and is independent of vessel size, smoking status, sex, and degree of platelet inhibition. The decrease in lumen diameter caused by neointimal overgrowth, however, appears counteracted by outward remodeling (dilation) of the target arterial segment. This leads to an increase in the diameter with a corresponding decrease in length (foreshortening) of the implanted Pipeline Embolization Device. This physiologic remodeling process affects optimally implanted devices and is not a consequence of stretching, device migration, vasospasm, and so forth. A direct, linear, statistically significant relationship exists between the degree of observed outward remodeling and the diameter of the implanted Pipeline Embolization Device relative to the target vessel. Overall, remodeled arterial diameters were reduced by 15% (SD, 10%) relative to baseline and followed a normal distribution. Clinically relevant stenosis was not observed.

CONCLUSIONS: Vessel healing involves both outward remodeling and neointimal overgrowth. Judicial oversizing could be useful in specific settings to counter the reduction in lumen diameter due to postimplant neointimal overgrowth; however, this oversizing needs to be balanced against the decrease in metal coverage accompanying the use of oversized devices. Similar analysis for other devices is essential.

ABBREVIATIONS: NIO = neointimal overgrowth; PED = Pipeline Embolization Device; PRU = VerifyNow P2Y12 reactivity; SW = Shapiro-Wilk

Flow diversion has revolutionized the treatment of intracranial aneurysms.^{1,2} In large part, the success of devices such as the Pipeline Embolization Device (PED; Medtronic) stems from the endoluminal reconstruction of the aneurysm neck and affected

vascular segment as opposed to strategies solely directed at the aneurysm sac. Multiple publications have addressed aspects of flow-diverter endothelialization or neointimal overgrowth (NIO) (the lining may be composed of multiple tissue types) believed, under most circumstances, to be responsible for the ultimate cure of targeted aneurysms.^{3,4} The complex relationship between alterations in intra-aneurysmal flow and NIO demands further consideration.^{5,6} Although potential avenues are being explored,⁷ our current influence on the NIO rate, extent, and long-term durability in the flow-diversion setting is limited. Antiplatelet therapy and surface modification reduce the probability of thrombus-related incidents, but these features may have little to do with NIO.⁸ Endothelial or intimal hyperplasia, terms used to describe a state

Received November 27, 2023; accepted after revision February 6, 2024.

From the Departments of Radiology (V.S., E.R., S.K., H.R., A.K., C.C., P.K.N., M.S.), Neurosurgery (V.S., E.R., E.N., H.R., C.R., J.B., P.K.N., M.S.), and Neurology (H.R., M.S.), NYU Grossman School of Medicine and Bellevue H+ Hospitals, New York, New York.

Please address correspondence to Maksim Shapiro, MD, NYU Medical Center, 550 First Avenue, 2nd floor, New York, New York 10016; e-mail: maksim.shapiro@nyumc.org; @neuroangio1



Indicates article with online supplemental data.

<http://dx.doi.org/10.3174/ajnr.A8228>

Baseline demographic characteristics and treatment results

Parameter	No.	SD
Age	54	14
Female sex	81	
Petrous	1	
Cavernous	6	
Paraophthalmic/paraclinoid	66	
PcomA	7	
Anterior choroidal	3	
MCA	3	
A1	1	
AcomA	7	
Pericallosal	2	
PICA	2	
Basilar	2	
Fusiform aneurysms, No.	3	
Smokers	27	
Discharge PRU, average	84	59
Aneurysm size, average (mm)	5	2
No. of PEDs, average	1.7	0.7
Follow-up length, average (mo)	9	3
No. complete occlusions	87	
Neointimal thickness, overall (mm)	0.3	0.1
Neointimal thickness, 1 PED construct ($n = 48$) (mm)	0.3	0.1
Neointimal thickness, 2 PED constructs ($n = 39$) (mm)	0.3	0.1
Neointimal thickness, 3+ PED constructs ($n = 13$) (mm)	0.3	0.1
Increase in PED diameter post-Rx (mm)	0.14	0.2
Percentage change in target vessel diameter, pre-/post-Rx	-15	10

Note:—PcomA indicates posterior communicating artery; AcomA, anterior communicating artery; Rx, treatment.

of excessive endothelialization for clinical or research purposes, lack clear biologic distinction from normal or desirable endothelialization. We have limited ability to curtail intimal hyperplasia pharmacologically, such as with drug-eluting balloons. However, even this technology is difficult to deploy in most intracranial locations where flow diverters are used. Apart from building flow-diverter constructs of presumably optimal metal coverage and possibly surface modification, we have no way of promoting desirable NIO at this point.^{4,9-11}

There is no meaningful definition of endothelial hyperplasia with respect to flow-diversion therapy; the 50% threshold for recordable stenosis in most trials is an arbitrary number, intentionally set below clinical significance in most settings.¹²⁻¹⁴ Most important, despite more than a decade of flow-diverter use, we lack objective benchmarks for normal or expected endothelial thickness/NIO, and their variability for any device presently on the market. While some instances of intimal hyperproliferation can be correlated with suboptimal deployment (malapposition and so forth), many occur without identified technical errors.¹⁵ Nearly all are asymptomatic, and a substantial portion improve spontaneously with conservative management.^{13,16}

Another important element of the vascular response to flow-diverter implantation is remodeling, defined as an adaptation in target vessel diameter, compliance, and likely other properties following implantation of a foreign body. The clinical and academic focus regarding remodeling has been concentrated on the fate of jailed branches and their collateral circulation. Deliberate, sometimes stepwise coverage of branches associated with target aneurysms can be used to drive development of the circle of Willis and other collaterals, strategically resulting in aneurysm occlusion with preservation of cerebral perfusion.¹⁷⁻²¹ However, this article addresses a different aspect of remodeling among the spectrum of

posttreatment changes in the target vessel, which is under-reported in the flow-diverter literature.

Simple morphologic data like NIO thickness, pre- and posttreatment diameter of the target artery, and flow-diverter diameter and length are readily available from conventional angiography. Although optical coherence tomography offers superior measurement and tissue-differentiation capabilities, it is not clinically available.²² Also known are various antiplatelets, device sizes, and demographic data that could influence healing. The purpose of this study was to analyze this information, in hopes of establishing parameters for a normal and desired healing response and determine if any of these can influence change in a favorable direction.

MATERIALS AND METHODS

In an institutional review board–approved retrospective cohort study setting, we collected data on 100 consecutive fusiform and saccular brain aneurysms treated

with single and multiple PEDs for which follow-up conventional angiography was available. Dissecting, previously ruptured, or treated aneurysms were excluded. All patients were premedicated with a dual antiplatelet regimen (aspirin, 81 mg daily, and clopidogrel, 75 mg daily). Preprocedural VerifyNow P2Y12 reactivity (PRU) was tested universally, and nonresponders were converted to ticagrelor (45–90 mg, twice daily, depending on sensitivity to the drug), with follow-up VerifyNow testing to ensure a response. Dual antiplatelet therapy was continued for at least 6 months posttreatment, followed by aspirin, 81 mg daily, or every other day monotherapy for varying periods depending on the clinical setting and preference of the treating physician.

Baseline demographics and derived values are shown in the Table. Specifically collected were discharge platelet reactivity values; device size and number; follow-up occlusion status; parent vessel diameter on initial 2D DSA and immediately preimplantation (to account for possible manipulation-related spasm), and immediately postimplantation; PED diameter immediately postimplantation, and PED and vessel diameter on follow-up 2D DSA obtained at least 5 months posttreatment. Five measurements of these parameters along the length of the treated segment were made for each metric and averaged, comparing averages pre- and posttreatment (Fig 1). Angiographic data were obtained on Artis Q and Icono biplane machines (Siemens). All length measurements were made on the Visage Client Pacs System (Version 7.1.18; PRO Medicus Limited). Measurements were correlated with those obtained directly from biplane units (both units undergo routine maintenance calibration) and with internal references (intermediate catheters) to ensure lack of systematic error. Two authors measured 10 cases together to establish a common measurement technique, with the remaining 90 cases measured by 1 of the 2

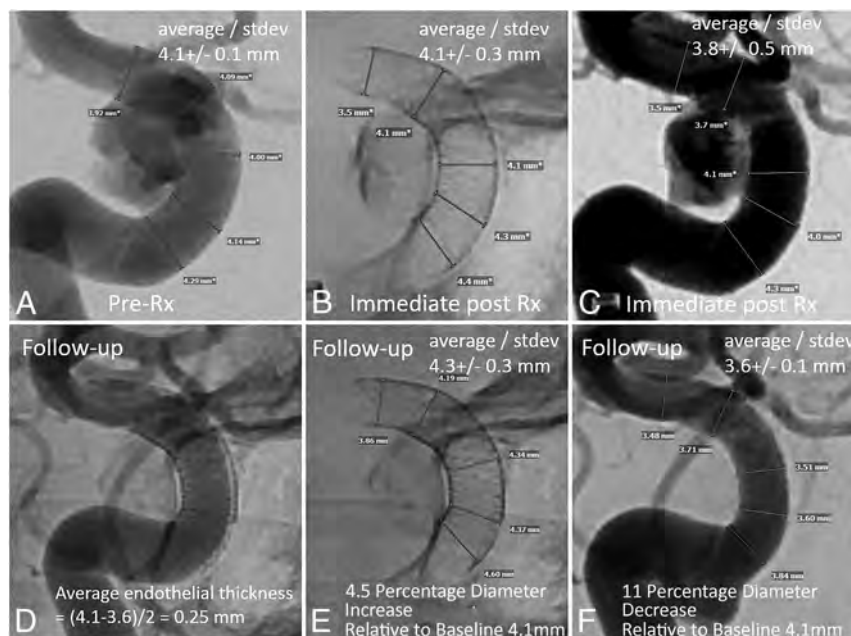


FIG 1. Example of target artery and PED diameter measurements before (A–C) and after (D–F) treatment. The immediate post-Rx DSA measurements (C) were not used for analysis. They are, however, indicative of the degree of procedure-related vasospasm. The PED is larger in diameter on follow-up (E) compared with immediately after implantation (B), despite a lack of vasospasm when C is compared with A. The expansion of PED in E compared with B is due to outward remodeling, which counteracts the endothelialization-driven decrease in follow-up vessel diameter (F). Rx indicates treatment.

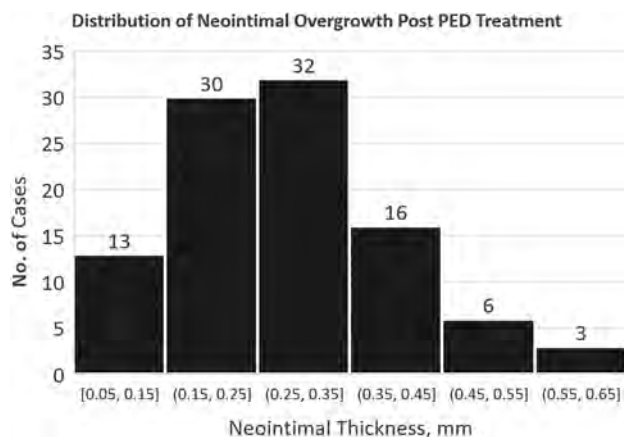


FIG 2. Distribution of NIO thickness on follow-up imaging. There is no statistical indication that subjects with greater NIO thickness represent a different population; there is no second peak. It is not clear if substantially larger samples would change this assessment.

authors, with the second author reviewing results for internal consistency. Conebeam CT was not used due to its unavailability for most follow-up angiograms performed in an awake setting.

Statistical Analysis

Demographic data were expressed as mean (SD) for continuous variables and percentage for categorical variables. Distributions of binned parameters were plotted as histograms, and relationships, as scatterplots. The more rigorous Shapiro-Wilk (SW) (compared with the less rigorous Kolomogorov-Smirnov) goodness-of-fit

test was used to assess deviation from normal distribution.²³ For the SW test, a P value $< .05$ rejects the hypothesis of normal distribution.

Pair-wise correlations were calculated as Pearson correlation coefficients using Excel (Microsoft); 95% confidence intervals were obtained using the Fisher transformation. Confidence intervals and SDs were reported, and a P value $< .05$ was considered statistically significant. Linear trendline and corresponding R^2 values were obtained for the Online Supplemental Data, and ordinary least squares regressions were performed using the same software.

RESULTS

Background demographic, device, aneurysm, target vessel, and PED information as well as key results are shown in the Table.

NIO thickness (0.3 [SD, 0.1] mm; 95% CI, 0.1–0.6 mm; range, 0.1–0.7 mm, Fig 2) is not distributed normally (SW test: $W = 0.972$, $P = .03$), ie, a skewed distribution with the tail to the right (thicker NIO lining).

NIO is independent of vessel diameter, smoking status, discharge PRU value, number of implanted devices, or aneurysm occlusion status. The corresponding correlation coefficients and 95% CIs are vessel diameter ($r = -0.02$, $P = .82$; 95% CI, -0.1771 – 0.2156), number of implanted devices ($r = -0.01$, $P = .89$; 95% CI, -0.18 – 0.20), PRU at discharge ($r = -0.01$, $P = .92$; 95% CI, -0.18 – 0.22), occlusion status ($r = -0.05$, $P = .63$; 95% CI, -0.19 – 0.22), sex ($r = 0.06$, $P = .59$; 95% CI, 0.16 – 0.23), and smoking ($r = -0.07$, $P = .48$; 95% CI, -0.15 – 0.24). The only significant correlation was with patient age ($r = -0.21$, $P = .04$; 95% CI, -0.381 to -0.004), implying an overall negative association between age and NIO (Online Supplemental Data).

The change in PED diameter on follow-up angiography, compared with immediate postimplantation, is shown in the Online Supplemental Data. Most PEDs expand in diameter (0.14 [SD, 0.2] mm) on follow-up (Fig 1). This expansion is not fully explained by faulty implantation (stretching or vasospasm) because most delayed PED average diameter is greater than the average diameter of the parent vessel before implantation, proving that at least some component of outward remodeling (vessel dilation) occurs posttreatment (Online Supplemental Data). The distribution is normal by the SW test ($W = 0.980$, $P = .12$).

Figure 3 shows a 15% average reduction in healed vessel caliber posttreatment, with an SD of 10%, and normal distribution (SW test: $W = 0.978$, $P = .09$). No instance of $>50\%$ narrowing was observed in our sample.

The ability of an artery to outwardly remodel is predicated on implantation of a device with the nominal diameter larger than that of the target artery, thus allowing subsequent expansion. To

quantitatively evaluate this situation, we defined oversizing as the difference between the diameter of the target vessel and that of the implanted PED or the smallest-diameter PED for multidevice constructs.

The relationship between oversizing and percentage change in artery diameter posttreatment is shown in Fig 4 for the overall data set and separately for single and double PED constructs, demonstrating nearly identical remodeling behavior. A similar relationship between percentage PED oversizing and percentage change in vessel diameter is shown in the Online Supplemental Data. There was not enough data for 3+ PED constructs for meaningful analysis.

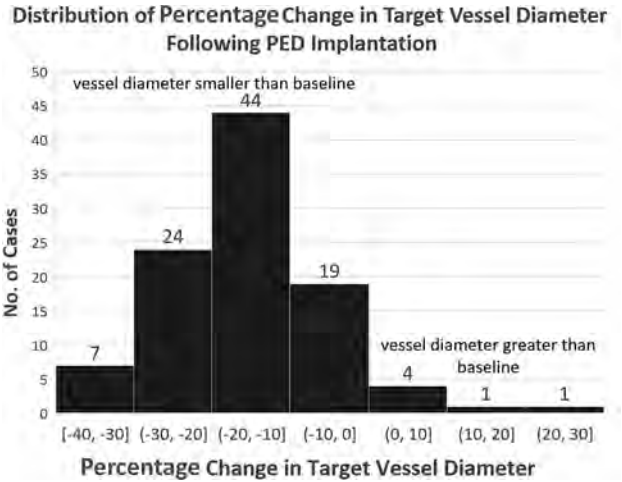


FIG 3. Distribution of percentage change in target artery diameter compared with the pretreatment baseline. Most vessels are smaller in diameter, while a few are larger. The final diameter is governed by opposing factors of endothelialization and outward remodeling.

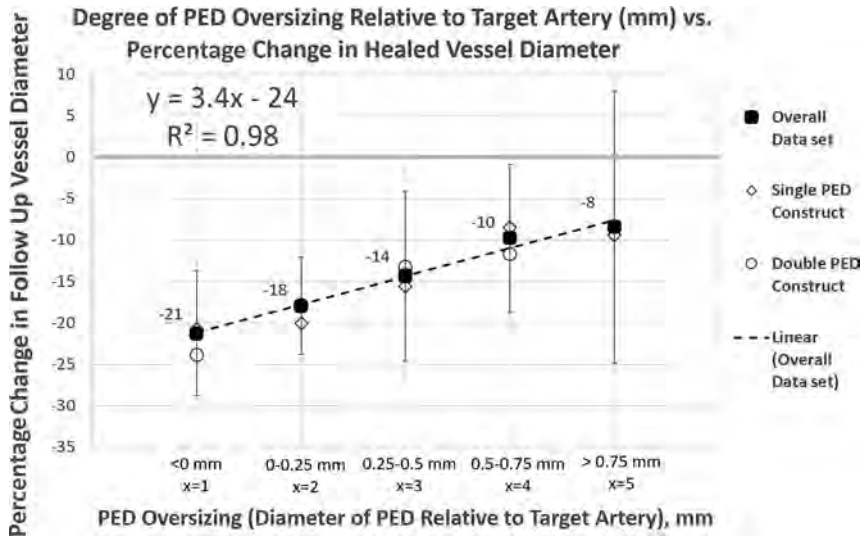


FIG 4. PED oversizing relative to target artery versus percentage change in target artery diameter on follow-up DSA. There is an extremely robust ($R^2 = 0.98$) linear relationship. Oversizing allows the vessel to expand (outward remodeling), thus mitigating an endothelialization-related decrease in vessel diameter. To what extent remodeling is influenced by device or construct radial force is unclear. The observation that single and double PED constructs behave similarly may suggest that radial force is not a major factor for PEDs in this range. However, possible differences may exist when baseline arterial diameter is considered by analyzing percentage PED oversize rather than absolute value (Online Supplemental Data). All findings are applicable to the PED only.

There is a strong, statistically significant linear relationship between PED oversizing and subsequent vessel diameter at follow-up angiography as shown by univariate ordinary least squares regression analysis. While the absolute luminal diameter of the posttreatment artery is most often reduced compared with the pretreatment diameter, greater oversizing is associated with a lesser degree of posttreatment vessel lumen reduction.

A 10% increase in PED diameter (oversizing) relative to vessel diameter is associated with a 3.1% relative increase in vessel size at follow-up ($P < .01$; 95% CI, 0.14–0.48) (Online Supplemental Data). In absolute lengths, oversizing the PED by 0.5 mm is associated with a 6% relative gain in vessel diameter ($P < .01$; 95% CI, 6.88–17.01), a potentially useful rule of thumb (Fig 4).

DISCUSSION

This study establishes a number of fundamental metrics and relationships pivotal to our understanding of healing after PED implantation. We quantitatively demonstrate that the treated arterial segment undergoes outward or positive remodeling (expansion, dilation) after PED treatment. This process, along with NIO, jointly determines the final vessel caliber. The concept of arterial remodeling is well-known in general vascular literature.²⁴ However, most studies are focused on atheromatous disease. The presumably nonatheromatous nature of most vessels affected by intracranial aneurysms, especially the saccular type, represents a unique group in which remodeling can be studied apparently independent of atherosclerosis.

There is a strong correlation between the size of the device and the degree of remodeling. We may directly influence the degree of outward remodeling by the choice of PED diameter relative to the target arterial segment. In contrast, the degree of NIO currently seems independent of modifiable factors such as device number, vessel caliber, extent of platelet inhibition, or smoking habits. Interest in the development of biologically active surface modifications aimed at influencing endothelialization is currently high.

We observed a reduction in average neointimal thickness with increasing age, a phenomenon not previously reported to our knowledge for nonatheromatous intracranial implants, though this has been documented for intracranial atherostenotic disease.²⁵

This observation suggests a possible muted (or less exuberant) biologic response with increasing age, highlighting the importance of gathering data for patients younger than 20 years of age (there were none in this sample).

The ability of the vessel to balance endothelialization with outward remodeling is remarkable and has significant practical implications. Opting for a device that is 0.5–0.75 mm larger than the target artery seems reasonable from a

remodeling perspective but may be associated with lower metallic coverage of the aneurysm neck.

Prior research indicates that oversizing decreases metal coverage/pore density, potentially diminishing treatment efficacy while promoting branch vessel patency.^{9,10,26} This issue is particularly relevant for larger-diameter PEDs, which inherently have less metal coverage. Ensuring optimal neck coverage (with multiple devices if necessary) and maximizing treatment efficacy should take precedence over outward remodeling potential in most cases.⁹

In smaller vessels, the interplay between NIO and remodeling may be more important. Because NIO thickness does not seem to depend on target vessel size, it proportionately narrows smaller vessels to a greater degree. This narrowing can be mitigated by judicious oversizing, especially because small-diameter PEDs offer higher degrees of metal coverage even when oversized.

Oversizing can also negatively impact conformability, the ability of a braided device to adjust to changes in parent vessel diameter and curvature or across wide necks or fusiform aneurysms. Our recommended judicious oversizing by 0.5–0.75 mm considers the balance between the positive effects of oversizing and its impact on metal coverage and device conformability.⁴

The use of multiple PEDs does not adversely affect NIO thickness or the degree of vessel remodeling, with the extent of outward remodeling appearing similar in double and single PED constructs (Fig 4 and Online Supplemental Data).

In striving for an objective definition of endothelial (or neointimal) hyperplasia, the primary consideration is a clinical event. However, these are often multifactorial, while reporting may be incomplete. From a statistical perspective, given the normal distribution of the posttreatment diameter change, 95% of follow-up diameters should fall within –35% and 5% of baseline, and 99.7%, within –45% and 15%. Thus, 50% stenosis should be an extremely rare occurrence; none were observed in our sample, though literature reports vary widely.^{1,27,28} Using a 45% reduction in vessel diameter as the threshold of hyperplasia appears to be a statistically valid approach.

Limitations

The findings are strictly limited to the PED (with Shield Technology; <https://shieldcctv.com/>). Differences among devices in terms of material (Drawn Filled Tubes, nitinol), treatment efficacy, elasticity, and posttreatment healing are likely. It is essential to gather comparable data for other devices.

This study does not address posttreatment vessel factors other than diameter, such as vessel compliance, elasticity, and pulsatility. Despite a relatively strong correlation between device oversizing and healed vessel diameter and a statistically significant inverse correlation between endothelial thickness and age, the individual variations are large. Therefore, case-specific device-size selection should be made with the overall clinical scenario and treatment goals in mind. A larger number of subjects would be needed to perform multivariate regression analyses to further investigate factors associated with NIO thickness.

The study included only patients with follow-up angiography, potentially missing cases of asymptomatic stenosis or occlusion in those lost to follow-up. Our institutional practice is to perform

at least 1 posttreatment catheter angiogram, and we are not aware of any symptomatic vessel occlusions during the study period.

Target vessel and aneurysm neck diameter is naturally variable, with a single average number being an oversimplification. Attention to specific parts of the construct, especially leading and trailing edges, may be needed.

The tissue overgrowing the PED is poorly defined and likely includes endothelium with a mix of subendothelial elements that we refer to collectively as neointima. Some amount of mural thrombus is also not possible to exclude. A more tissue-specific in vivo evaluation would require optical coherence tomography.²⁹

2D DSA measurements have limitations in precision. While absolute measurement errors are possible, relative errors in comparative DSA images are unlikely. We did not perform internal correlation to other uninvolved arteries, to control diameter change in all arteries between treatment and follow-up (due to differences in anesthesia for example). Another limitation of 2D DSA is an inability to accurately measure device length. The quantitative evaluation of delayed foreshortening remains unstudied.

Finally, this study did not focus on treatment efficacy. We believe that previously described factors rather than the degree of endothelialization influence occlusion status.³⁰

CONCLUSIONS

The vascular reactive process following PED implantation involves 2 key mechanisms: an endothelialization-related decrease in arterial diameter and outward remodeling (dilation) of the target arterial segment (surmised from the increase in implant diameter with time), mitigating against endothelialization-related narrowing. The extent of outward remodeling is directly influenced by the choice of PED diameter. This influence presents a clinical balancing act: Opting for a larger PED size (judicious oversizing) can enhance remodeling but leads to a reduction in metal coverage. Despite this trade-off, the PED demonstrates consistent effectiveness while preserving functional arterial diameter. Collection of similar data for other devices is essential.

Disclosure forms provided by the authors are available with the full text and PDF of this article at www.ajnr.org.

REFERENCES

1. Becske T, Kallmes DF, Saatci I, et al. **Pipeline for Uncoiled or Failed Aneurysms: results from a multicenter clinical trial.** *Radiology* 2013;267:858–68 CrossRef Medline
2. Becske T, Brinjikji W, Potts MB, et al. **Long-term clinical and angiographic outcomes following Pipeline embolization device treatment of complex internal carotid artery aneurysms: five-year results of the Pipeline for Uncoiled or Failed Aneurysms Trial.** *Neurosurgery* 2017;80:40–48 CrossRef Medline
3. Fiorella D, Lylyk P, Szikora I, et al. **Curative cerebrovascular reconstruction with the Pipeline embolization device: the emergence of definitive endovascular therapy for intracranial aneurysms.** *J Neurointerv Surg* 2009;1:56–65 CrossRef Medline
4. Shapiro M, Raz E, Becske T, et al. **Variable porosity of the Pipeline embolization device in straight and curved vessels: a guide for optimal deployment strategy.** *AJNR Am J Neuroradiol* 2014;35:727–33 CrossRef Medline
5. Ravindran K, Salem MM, Alturki AY, et al. **Endothelialization following flow diversion for intracranial aneurysms: a systematic review.** *AJNR Am J Neuroradiol* 2019;40:295–301 CrossRef Medline

6. Ravindran K, Casabella AM, Cebal J, et al. **Mechanism of action and biology of flow diverters in the treatment of intracranial aneurysms.** *Neurosurgery* 2020;86:S13–19 CrossRef Medline
7. Cortese J, Rasser C, Even G, et al. **CD31 mimetic coating enhances flow diverting stent integration into the arterial wall promoting aneurysm healing.** *Stroke* 2021;52:677–86 CrossRef Medline
8. Girdhar G, Andersen A, Pangerl E, et al. **Thrombogenicity assessment of Pipeline Flex, Pipeline Shield, and FRED flow diverters in an in vitro human blood physiological flow loop model.** *J Biomed Mater Res A* 2018;106:3195–202 CrossRef Medline
9. Shapiro M, Raz E, Becske T, et al. **Building multidevice Pipeline constructs of favorable metal coverage: a practical guide.** *AJNR Am J Neuroradiol* 2014;35:1556–61 CrossRef Medline
10. Makoyeva A, Bing F, Darsaut TE, et al. **The varying porosity of braided self-expanding stents and flow diverters: an experimental study.** *AJNR Am J Neuroradiol* 2013;34:596–602 CrossRef Medline
11. Aurboonyawat T, Blanc R, Schmidt P, et al. **An in vitro study of Silk stent morphology.** *Neuroradiology* 2011;53:659–67 CrossRef Medline
12. You W, Lv J, Li Z, et al. **The incidence and predictors of in-stent stenosis after Pipeline flow-diverter stenting for intracranial aneurysm treatment.** *Front Neurol* 2023;14:1140497 CrossRef Medline
13. Flores-Milan G, Pressman E, Peto I, et al. **Factors associated with in-stent stenosis after cerebral aneurysm embolization using a Pipeline Embolization Device.** *Interv Neuroradiol* 2022;28:731–36 CrossRef Medline
14. John S, Bain MD, Hui FK, et al. **Long-term follow-up of in-stent stenosis after Pipeline flow diversion treatment of intracranial aneurysms.** *Neurosurgery* 2016;78:862–67 CrossRef Medline
15. Wang T, Richard SA, Jiao H, et al. **Institutional experience of in-stent stenosis after Pipeline flow diverter implantation: a retrospective analysis of 6 isolated cases out of 118 patients.** *Medicine (Baltimore)* 2021;100:e25149 CrossRef Medline
16. Ravindran K, Salem MM, Enriquez-Marulanda A, et al. **Quantitative assessment of in-stent stenosis after Pipeline Embolization Device treatment of intracranial aneurysms: a single-institution series and systematic review.** *World Neurosurg* 2018;120:e1031–40 CrossRef Medline
17. Litao MS, Burkhardt JK, Tanweer O, et al. **Remodeling of the posterior cerebral artery P1-segment after Pipeline flow diverter treatment of posterior communicating artery aneurysms.** *Neurol Int* 2021;13:195–201 CrossRef Medline
18. Yavuz K, Geyik S, Saatci I, et al. **Endovascular treatment of middle cerebral artery aneurysms with flow modification with the use of the Pipeline Embolization Device.** *AJNR Am J Neuroradiol* 2014;35:529–35 CrossRef Medline
19. Diestro JD, Adeeb N, Dibas M, et al. **Flow diversion for middle cerebral artery aneurysms: an international cohort study.** *Neurosurgery* 2021;89:1112–21 CrossRef Medline
20. Pagiola I, Mihalea C, Caroff J, et al. **Flow diversion treatment of aneurysms of the complex region of the anterior communicating artery: which stent placement strategy should “I” use? A single center experience.** *J Neurointerv Surg* 2019;11:1118–22 CrossRef Medline
21. Sorenson TJ, Mendes Pereira V, Rangel Castilla L, et al. **Treatment of anterior cerebral artery and anterior communicating artery aneurysms with flow-diversion devices: a systematic review and meta-analysis.** *J Neurosurg Sci* 2020;64:200–05 CrossRef Medline
22. Guerrero BP, Pacheco CD, Saied A, et al. **First human evaluation of endothelial healing after a Pipeline Flex Embolization Device with Shield Technology implanted in posterior circulation using optical coherence tomography.** *Neurointervention* 2018;13:129–32 CrossRef Medline
23. Ghasemi A, Zahediasl S. **Normality tests for statistical analysis: a guide for non-statisticians.** *Int J Endocrinol Metab* 2012;10:486–89 CrossRef Medline
24. Ward MR, Pasterkamp G, Yeung AC, et al. **Arterial remodeling: mechanisms and clinical implications.** *Circulation* 2000;102:1186–91 CrossRef Medline
25. Turk AS, Levy EI, Albuquerque FC, et al. **Influence of patient age and stenosis location on Wingspan in-stent restenosis.** *AJNR Am J Neuroradiol* 2008;29:23–27 CrossRef Medline
26. Tong X, Han M, Wu Z, et al. **Effects of different stent size selection on Pipeline embolization device treatment of intracranial aneurysms.** *Ther Adv Neurol Disord* 2023;16:17562864231151475 CrossRef Medline
27. Chalouhi N, Polifka A, Daou B, et al. **In-Pipeline stenosis: incidence, predictors, and clinical outcomes.** *Neurosurgery* 2015;77:875–79; discussion 879 CrossRef Medline
28. Turhon M, Kang H, Liu J, et al. **In-stent stenosis after Pipeline Embolization Device in intracranial aneurysms: incidence, predictors, and clinical outcomes.** *Neurosurgery* 2022;91:943–51 CrossRef Medline
29. Monteiro A, Lopes DK, Aghaebrahim A, et al. **Optical coherence tomography for elucidation of flow-diversion phenomena: the concept of endothelialized mural thrombus behind reversible in-stent stenosis in flow-diverters.** *Interv Neuroradiol* 2021;27:774–80 CrossRef Medline
30. Shapiro M, Becske T, Nelson PK. **Learning from failure: persistence of aneurysms following Pipeline embolization.** *J Neurosurg* 2017;126:578–85 CrossRef Medline

Use of the Neuroform Atlas Stent or LVIS Jr Stent for Treatment of Unruptured Intracranial Aneurysms in Parent Arteries of <2 mm in Diameter: A Multicenter Experience

Tengfei Li, Shuailong Shi, Qingliang Chen, Chao Jiang, Wenxian Feng, Qi Tian, Shuhai Long, Zhuangzhuang Wei, Jie Yang, Ye Wang, Jianzhuang Ren, Xinwei Han, and Ji Ma



ABSTRACT

BACKGROUND AND PURPOSE: The Neuroform Atlas stent and the LVIS Jr stent are intracranial microstent systems for the treatment of wide-neck intracranial aneurysms. Hence, this study aimed to compare the efficacy and safety of the Neuroform Atlas stent and the LVIS Jr stent for the treatment of unruptured intracranial aneurysms in parent arteries of <2 mm in diameter.

MATERIALS AND METHODS: From March 2022 to April 2023, the clinical and imaging data of 135 patients with unruptured intracranial aneurysms treated with stent-assisted coiling using the Neuroform Atlas or LVIS Jr stent in parent arteries of <2 mm in diameter were retrospectively analyzed. Stent apposition was evaluated by high-resolution conebeam CT (HR-CBCT). Immediate aneurysm-embolization attenuation and occlusion at 6-month follow-up were evaluated using 2D DSA and the modified Raymond-Roy classification. Adverse events were recorded. Multivariate logistic regression analysis was undertaken to determine the independent factors affecting incomplete stent apposition.

RESULTS: One hundred thirty-five patients (135 aneurysms) underwent stent-assisted coiling (66 Neuroform Atlas stents and 69 LVIS Jr stents). Intraoperative HR-CBCT showed that 1 Neuroform Atlas stent and 11 LVIS Jr stents had incomplete stent apposition at the aneurysm neck ($P < .05$). Perioperative complications occurred in 3 cases (2.22%). These comprised 2 cases of neurologic complications (1 case of distal intracranial vascular embolism and 1 case of cerebral parenchymal hemorrhage) and 1 case of severe postprocedural gastrointestinal hemorrhage. DSA follow-up showed 3 cases of aneurysm recurrence in the LVIS Jr group. Multivariate regression analysis showed that a stent angle of $\geq 75^\circ$ (OR, 23.963; $P = .005$) or a parent artery diameter mismatch ratio of ≥ 1.25 (OR, 8.043; $P = .037$) were risk factors for incomplete stent apposition, especially for the LVIS Jr stent (OR, 20.297; $P = .015$).

CONCLUSIONS: The Neuroform Atlas stent and LVIS Jr stent are efficacious in the treatment of unruptured intracranial aneurysms in parent arteries of <2 mm in diameter. Apposition of the LVIS Jr stent was worse than in the Neuroform Atlas stent at the neck of some aneurysms.

ABBREVIATIONS: FD = flow diverter; HR-CBCT = high-resolution conebeam CT; IA = intracranial aneurysm; ISA = incomplete stent apposition; SAC = stent-assisted coiling

With the widespread application of flow diverters (FDs), stent-assisted coiling (SAC) appears to have been replaced in the treatment of intracranial aneurysms (IAs).^{1,2} Despite advances in FD treatment of bifurcation aneurysms, SAC continues to

be relevant.³⁻⁵ Traditional intracranial stents, such as the Solitaire AB (eV3), Enterprise (Codman & Shurtleff), and Neuroform EZ (Styker) can be difficult to implant smoothly for the following reasons: 1) tortuous parent arteries; 2) the large angle of the parent arteries at the aneurysm neck due to the large diameter (0.021 or 0.027 inches) of the microcatheter; and 3) poor compliance.^{6,7} Traditional stents are not suitable for the treatment of IAs in parent arteries of <2 mm in diameter because they have a thicker metal wall.⁸

Received November 14, 2023; accepted after revision February 11, 2024.

From the Department of Interventional Radiology (T.L., S.S., Q.T., S.L., Z.W., J.Y., Y.W., J.R., X.H., J.M.), The First Affiliated Hospital of Zhengzhou University, Zhengzhou, China; Interventional Institute of Zhengzhou University (T.L., S.S., Q.T., S.L., Z.W., J.Y., Y.W., J.R., X.H., J.M.), Zhengzhou, China; Department of Interventional Radiology (Q.C.), The Third People's Hospital of Henan Province, Zhengzhou, China; Department of Neurology (C.J.), The Fifth Affiliated Hospital of Zhengzhou University, Zhengzhou, China; and Department of Interventional Radiology (W.F.), Zhumadian Central Hospital, Zhumadian, China.

Tengfei Li and Shuailong Shi contributed equally to this article.

This work was supported by the National Natural Science Foundation of China (grant No. 81801806); Henan Provincial Science and Technology Research Project (grant No. KYDZ2020120441 and grant No. YXKC2022029).

Please address correspondence to Ji Ma, MD, Department of Interventional Radiology, The First Affiliated Hospital of Zhengzhou University, Jianshe Rd No. 1, Erqi district, Zhengzhou, Henan, China; e-mail: soulma@126.com



Indicates article with online supplemental data.

<http://dx.doi.org/10.3174/ajnr.A8238>

The laser cut Neuroform Atlas stent (Styker) and the braided LVIS Jr stent (MicroVention) are new-generation microembolization-assisted stents for IAs that can be released through smaller microcatheters (0.0165 or 0.017 inches). Multiple clinical studies have shown that these stents are more likely to be suitable for IAs in deep, tortuous parent arteries because of their good compliance and conformity.⁹⁻¹¹ However, comparative studies on the efficacy and safety of SAC using the Neuroform Atlas stent and LVIS Jr stent for IAs in parent arteries of <2 mm in diameter are scarce. Moreover, limited by the DSA performance and x-ray visualization of stent trabeculae, observation and evaluation of stent apposition are difficult.^{12,13}

In the present study, we compared the safety and efficacy of these 2 stent types to provide guidance on the SAC of unruptured IAs with parent arteries of <2 mm in diameter. Also, high-resolution conebeam CT (HR-CBCT) was used to evaluate the apposition of the Neuroform Atlas stent and LVIS Jr stent in parent arteries of <2 mm in diameter.

MATERIALS AND METHODS

Ethics

The protocol of this retrospective study was approved by the ethics committee (IRB: 2023KY0937) of Zhengzhou university and verified by the ethics department of each participating institution. The protocol complied with the 1964 Declaration of Helsinki and its later amendments or comparable ethical standards. The requirement to obtain informed consent from participants was waived because of the retrospective nature of this study.

Participants

Patients with unruptured IAs in a parent artery of <2 mm in diameter who were treated by SAC with the Neuroform Atlas stent or LVIS Jr stent at 4 centers from March 2022 to April 2023 were identified from the PACS of the hospitals. The inclusion criteria were the following: 1) unruptured IAs diagnosed by clinical evaluation and imaging examination (MRA, CTA, DSA) that were treated by SAC with the Neuroform Atlas stent or LVIS Jr stent; 2) the diameter of the parent artery of <2 mm; 3) intraoperative HR-CBCT of the stent-placement area; and 4) complete clinical follow-up data and DSA follow-up data at 6 months being available. The exclusion criteria were the following: 1) simultaneous use of FDs or multiple overlapping stents or combined with surgical clipping; 2) embolization with coils alone or with embolic material other than coils, such as Onyx (eV3); 3) the diameter of the parent artery of ≥ 2 mm; 4) blood blister-like aneurysms, pseudoaneurysms, or dissecting aneurysms caused by infection or trauma; 5) intraoperative HR-CBCT not undertaken; and 6) lack of 6-month DSA follow-up data or patient lost to follow-up.

Clinical and Imaging Data

All interventional procedures were undertaken on the Artis Zeego Endovascular Surgical Cath Lab (Siemens) and Allura Xper FD20 Cath/Angio System (Philips Healthcare) with HR-CBCT capability. Postprocessing of images was undertaken on the workstations of these 2 systems. All patients were subjected to pharmacogenetic testing for aspirin and clopidogrel. Patients who were sensitive to both drugs were given aspirin (100 mg/day)

and clopidogrel (75 mg/day) ≥ 5 days before surgery. Patients who were insensitive to one or both drugs could have an increased dose or be switched to ticagrelor (90 mg/day). All interventional procedures were undertaken by experienced senior neurointerventionalists with ≥ 10 years of experience and an annual volume of ≥ 300 cases.

During the procedure, the size and shape of the aneurysm and diameter of the parent artery were determined by global cerebral angiography and 3D reconstructed images. Then the type and size of the stent, the size of the bare coil, and the prerelease site of the stent were determined. We choose the Headway-17 microcatheter (MicroVention) to deliver the LVIS Jr stent or the SL-10 and XT-17 microcatheters (Styker) to deliver the Neuroform Atlas stent. The embolization microcatheter was selected with Echelon-10 straight, 45°, or 90° types (Medtronic) based on the morphology of the aneurysm and the relationship between the aneurysm neck and the parent artery. SAC was completed by pre-stent release or semi-stent release. The specific methods for implantation of the Neuroform Atlas stent and LVIS Jr stent and aneurysm embolization were similar to those described in the literature.¹⁴⁻¹⁶ The immediate attenuation of aneurysm embolization was evaluated, and the angles of stent placement were measured according to 2D DSA in the working position after the procedure.

The clinical and imaging data of enrolled patients were collected, including basic information (eg, sex, age, preoperative complications), parent artery characteristics (eg, mean diameter, diameter ratio), and aneurysm information (eg, location, shape, size). The mean diameter of the parent artery was defined as the average value of the 3 vessels in the aneurysm neck and beyond the neck, 5 mm at both ends. The diameter mismatch ratio of the parent artery was defined as the ratio of the larger vessel diameter to the narrower vessel diameter at the end of the aneurysm neck. The stent angles were defined as the angles formed by the extension lines at the 2 ends of the stent by selecting an appropriate angle to fully deploy the stent. The attenuation of aneurysm embolization was evaluated using the modified Raymond-Roy classification:¹⁷ I, complete obliteration; II, residual neck; IIIa, residual aneurysm with contrast within the coil interstices; and IIIb, residual aneurysm with contrast along the aneurysm wall.

Observation of Stent Apposition

All patients in this study underwent HR-CBCT of the area of stent placement after the procedure to observe whether the stent had been deployed completely and to detect local deformities or distortions. For patients who underwent intraoperative HR-CBCT with diluted contrast media, imaging information was used to reconstruct and observe stent apposition by reduction of metal artifacts at the postprocessing workstation. For patients who did not undergo intraoperative HR-CBCT with diluted contrast media, the HR-CBCT and 3D DSA data of the parent artery were imported into the postprocessing workstation. Then, images of the stent and parent artery were fused and reconstructed by technology for volume imaging and metal artifact reduction for the observation of stent apposition. The parameters and specific operating methods of HR-CBCT with diluted contrast media and

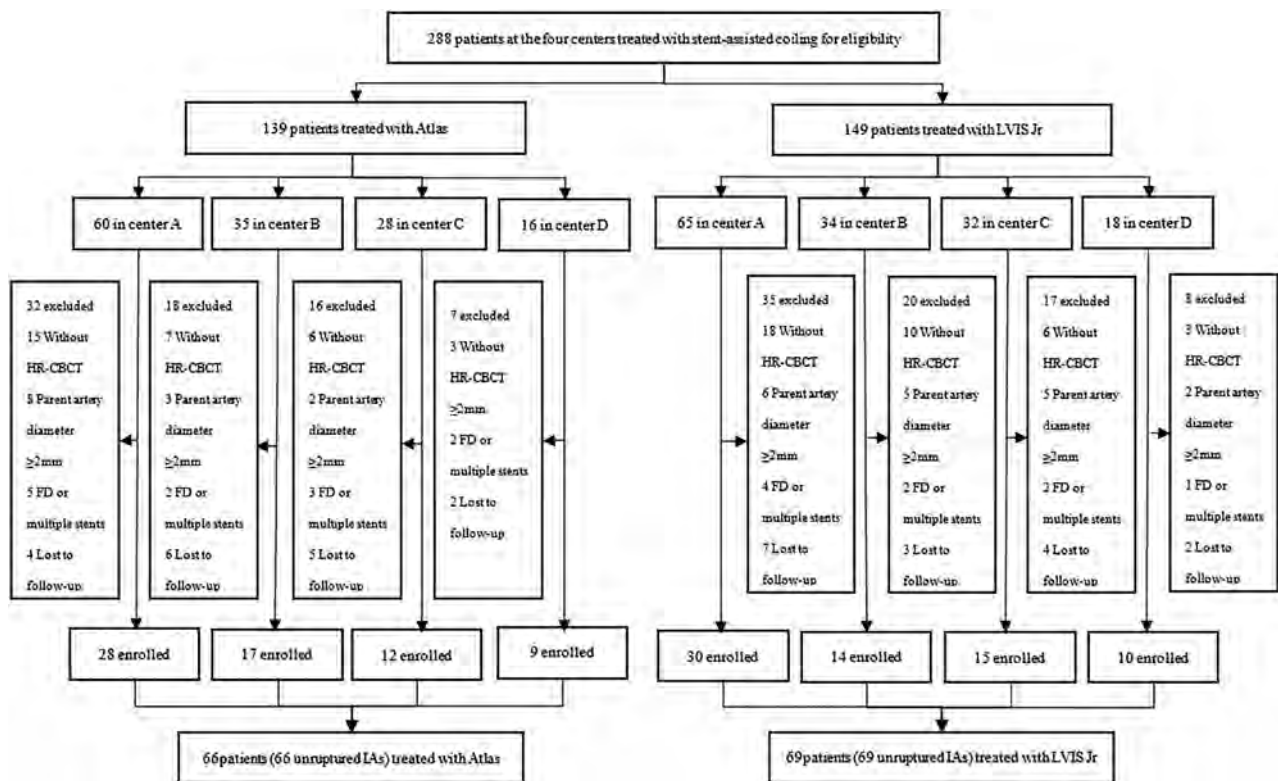


FIG 1. Flow chart of patient selection.

technology for volume reconstruction and metal-artifact reduction by imaging have been described.^{18–20}

Stent apposition was evaluated by 2 experienced neurointerventionalists independently. In case of a disagreement, stent apposition was evaluated by a third experienced neuroradiologist. With reference to the criteria of Li et al¹⁹ and Kato et al,²¹ incomplete stent apposition (ISA) was defined as the following: I, proximal or distal ISA; II, ISA at the greater or lesser curvature of the “crescent” or “saddle”; and III, incomplete deployment in long stent segments. Patients were divided into a complete apposition group and an incomplete apposition group. On the basis of the literature^{22,23} and clinical experience, univariate analysis was undertaken on the factors affecting ISA: aneurysm location, aneurysm size, diameter mismatch ratio of the parent artery, and stent angles. Factors with $P < .05$ were included in multivariate logistic regression analysis to determine the independent factors affecting ISA.

Complications and Follow-Up

Complications during the perioperative period and follow-up were recorded. Serious complications were defined as ischemic stroke caused by acute in-stent thrombosis or embolus dislodgement, parenchymal hemorrhage, or aneurysm rupture in the stent-placement area.

Postoperative follow-up in the outpatient department or over the telephone was undertaken regularly. The mRS score was used to evaluate the improvement of neurologic function at the final follow-up after SAC. Stent patency and the prevalence of complete occlusion of the aneurysm were observed at 6-month DSA follow-up. Aneurysm recurrence was defined as increased

visualization of the aneurysm body or neck under DSA, with or without coil compression.

Statistical Analyses

Statistical analyses were performed using SPSS 26.0 (IBM). Quantitative variables with a normal distribution are expressed as the mean (SD) and were compared between groups using the Student t test. Quantitative variables with a non-normal distribution are expressed as interquartile ranges and were compared between groups using the Mann-Whitney U test. Categorical variables are presented as numbers with percentages and were compared between groups using the χ^2 test or Fisher exact test. Univariate analysis was used to determine the predictors of ISA, and factors with $P < .05$ were included in the multivariate logistic regression analysis. $P < .05$ was considered significant.

RESULTS

Characteristics of the Study Cohort

From March 2022 to April 2023, we screened 288 patients. We excluded 153 patients (68 without HR-CBCT, 31 with a parent artery diameter of ≥ 2 mm, 21 with FDs or multiple stents, and 33 lost to follow-up). Eventually, 135 patients (with 135 unruptured IAs) met the inclusion criteria at the 4 centers (Fig 1). They were divided into the Neuroform Atlas group ($n = 66$) and the LVIS Jr group ($n = 69$) depending on the stent type. Among these 135 patients, there were 66 men (48.89%) and 69 women (51.11%), with an average age of 58.78 (SD, 9.60) years. The average size of aneurysms was 4.81 (SD, 1.38) mm. The most common locations of aneurysms were the anterior communicating artery (60/135, 44.44%) and the M1 bifurcation

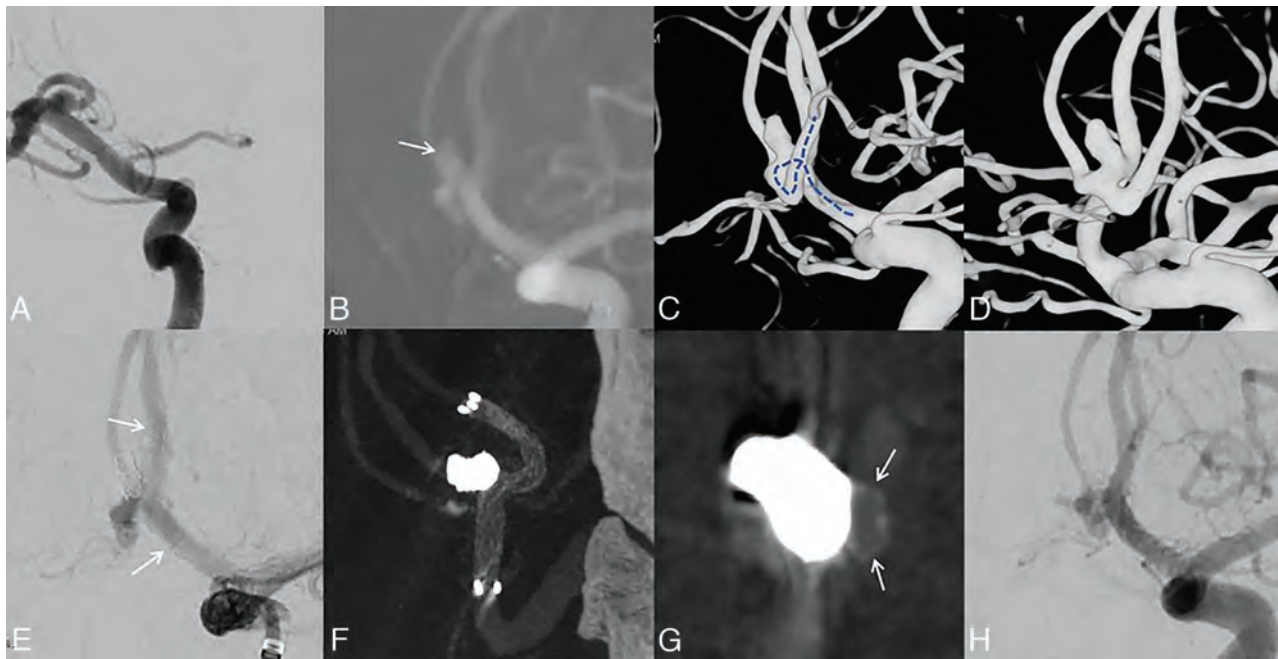


FIG 2. Use of the Neuroform Atlas stent in SAC for the treatment of an unruptured anterior communicating artery aneurysm. A, 2D DSA of the right ICA shows the right A1 artery to be slender and the anterior communicating artery to be open. B, 2D DSA of the left ICA shows an aneurysm of the anterior communicating artery of 2.2×4.5 mm. The anterior communicating artery sends out a median callosal artery and the bilateral A2 arteries together to form a triploid anterior cerebral artery (aneurysm is shown by a white arrow). C and D, 3D DSA shows the position between the 3 A2 arteries and the aneurysms (blue dashed line denotes the stent-placement area, the parent artery diameter is 1.91 mm, and the diameter mismatch ratio is 1.09). E, SAC using a Neuroform Atlas stent (3.0×24 mm) was performed, and the occlusion attenuation of the aneurysm was Raymond-Roy class I (white arrows indicate the ends of the stent). F and G, HR-CBCT with diluted contrast media shows complete stent apposition and satisfactory protection of the coils at the aneurysm neck (the stent wire at the aneurysm neck is indicated by white arrows). H, DSA follow-up at 6 months shows the stent patency and well-healed aneurysm (Raymond-Roy class I).

(36/135, 26.67%). The morphology of aneurysms was mainly saccular (111/135, 82.22%). There were no significant differences in sex, age, aneurysm size, or parent artery characteristics between the 2 groups (all $P > .05$), but the Neuroform Atlas stent was used more widely than the LVIS Jr stent at the M1 bifurcation ($P = .036$) (Online Supplemental Data).

Outcomes of Interventional Therapy

Implantation of the Neuroform Atlas stent or LVIS Jr stent was successful in all patients. Neuroform Atlas stents were 3 mm in diameter, and 15 mm (20 cases), 21 mm (39 cases), or 24 mm (7 cases) in length. LVIS Jr stents were 2.5 mm in diameter, and 13 mm (8 cases), 17 mm (16 cases), or 23 mm (45 cases) in length. The coils used in this study were all bare coils, and the average number ranged from 2 to 14. 2D DSA images revealed no significant difference in the results for immediate aneurysm occlusion between the 2 groups ($P > .05$) (Online Supplemental Data and Figs 2 and 3).

Complications and Follow-Up Outcomes

During the perioperative period (within 30 days after SAC), 2 neurologic complications (1 distal vascular embolism and 1 cerebral parenchymal hemorrhage) and 1 non-neurologic complication (manifested as severe gastrointestinal bleeding) were observed. One patient with an aneurysm in an anterior communicating artery had an embolic A2 occlusion of the left anterior cerebral artery after implantation of the Neuroform Atlas stent. After evaluation, the occipital branch of the left MCA was fully

compensated without special treatment. The other patient with an aneurysm in the M1 bifurcation had a cerebral parenchymal hemorrhage in the non-stent-implantation area 13 hours after implantation of the LVIS Jr stent, and the hemorrhage did not increase after discontinuation of dual antiplatelet therapy. One non-neurologic complication manifested as severe hemorrhage in the upper gastrointestinal tract 4 hours after implantation of the Neuroform Atlas stent. The hemorrhage stopped after emergency embolization of the left gastric artery and right gastroepiploic artery combined with acid-suppression drugs. The mRS scores of the 3 patients before hospital discharge were 0, 1, and 0, respectively. No serious complications (eg, aneurysm rupture, stent migration, coil escape) occurred in the remaining patients during the perioperative period.

All patients were followed up by telephone or examination in the outpatient department. The mean duration of follow-up was 9.44 (SD, 2.27) months. At the final follow-up, residual neurologic symptoms (mRS score = 3–5) or death did not occur in any patient. DSA follow-up at 6 months showed 3 cases of aneurysm recurrence in the LVIS Jr group, and the prevalence of complete occlusion of aneurysms was significantly lower than that in the Neuroform Atlas group (84.1%, 58/69 versus 95.5%, 63/66) ($P = .030$). However, there was no significant difference in the prevalence of in-stent stenosis (2.9%, 2/69 versus 0%, 0/66; $P = .497$). Three patients with recurrent aneurysms and their families refused further treatment, so we conducted only regular follow-up (Online Supplemental Data).

Stent Apposition

Intraoperative HR-CBCT showed that 11 LVIS Jr stents had incomplete apposition at the neck, whereas only 1 Neuroform Atlas stent had incomplete apposition. Patients were divided into the complete-apposition group ($n = 123$) and the incomplete-apposition group ($n = 12$). There were no significant differences in sex, age, preoperative complications, or other clinical data between the 2 groups (all $P > .05$). Univariate analysis showed

that aneurysm size, diameter mismatch ratio of the parent artery, stenosis of the parent artery, stent angles, and stent type affected stent apposition (all $P < .05$) (Online Supplemental Data). The facts stated above were included in multivariate logistic regression analysis, after which the stent angles, diameter mismatch ratio of the parent artery, and stent type were found to be independent factors affecting stent apposition. Stent angles of $\geq 75^\circ$ or diameter mismatch ratio of the parent artery of ≥ 1.25

were risk factors for ISA, and apposition of the LVIS Jr stent was worse than that of the Neuroform Atlas stent (Tables 1 and 2).

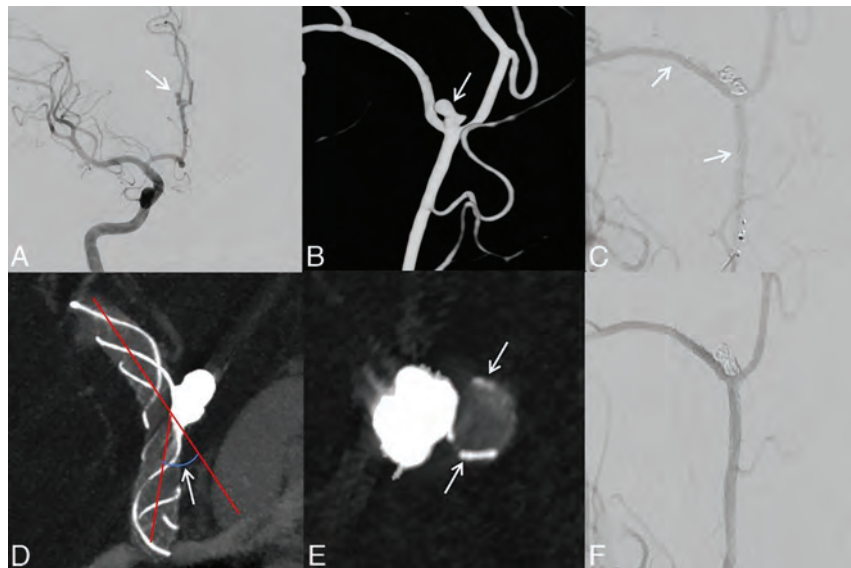


FIG 3. Use of the LVIS Jr stent in SAC for the treatment of an unruptured A2-segment aneurysm. A and B, 2D DSA and 3D DSA of the right ICA show an A2-segment aneurysm of the right anterior cerebral artery, with an irregular shape and a size of 1.5×2.7 mm. The parent artery diameter is 1.79 mm, and the diameter mismatch ratio is 1.15 (aneurysm is shown by a white arrow). C, SAC using a LVIS Jr stent (2.5×13 mm) was performed, and the aneurysm occlusion attenuation was Raymond-Roy class I (white arrows indicate the ends of the stent). D, HR-CBCT with diluted contrast media shows that the stent was completely deployed and stent angles were 43.34° (the stent angles are indicated by a white arrow). E, HR-CBCT shows complete stent apposition at the aneurysm neck and the coils protected satisfactorily (stent wire at the aneurysm neck is indicated by white arrows). F, DSA follow-up at 6 months shows stent patency, and the aneurysm has healed well (Raymond-Roy class I).

Table 1: Included variables and assignment in multivariable regression analysis of incomplete stent apposition^a

Variable	Name	Assign
Aneurysm dome	X1	Quantitative variable
Aneurysm neck	X2	Quantitative variable
Parent artery diameter mismatch ratio	X3	$<1.25 = 0^a$, $\geq 1.25 = 1$
Parent artery stenosis	X4	No = 0^a , yes = 1
Stent type	X5	Atlas = 0^a , LVIS Jr = 1
Stent angles	X6	$<75^\circ = 0^a$, $\geq 75^\circ = 1$

^a A value of zero was assigned as the reference group.

Table 2: Multivariable logistic analysis of the factors associated with incomplete stent apposition of unruptured intracranial aneurysms treated with Neuroform Atlas or LVIS Jr stents

Variable	OR	95% CI	P Value
Aneurysm dome	1.122	0.655~1.922	.675
Aneurysm neck	1.683	0.936~3.027	.082
Parent artery diameter mismatch ratio	8.043	1.137~56.895	.037
Parent artery stenosis	1.794	0.310~10.369	.514
Stent type	20.297	1.794~229.636	.015
Stent angles	23.963	2.602~220.693	.005

DISCUSSION

We showed that the Neuroform Atlas stent and LVIS Jr stent had good clinical outcomes and radiographic follow-up results, and a low recurrence rate in the SAC of unruptured IAs in parent arteries of <2 mm in diameter. It has been reported that the rate of immediate complete occlusion of IAs in SAC using the LVIS Jr stent varied from 42% to 91%,^{12,24,25} and for the Neuroform Atlas stent, it varied from 48% to 97%.^{13,14,26,27} Those data are basically consistent with the results of immediate aneurysm occlusion in our study: 84.8% for the Neuroform Atlas and 73.9% for the LVIS Jr. In the present study, although the stent was placed in a parent artery diameter of <2 mm, the rate of immediate aneurysm occlusion remained satisfactory, and there was no significant difference between the 2 groups. On the one hand, this scenario results from improvement of the stent design, such as the metal coverage of the Neuroform Atlas stent at only 6%–12%. Due to its hybrid design with distal open and proximal closed cells, the Neuroform Atlas stent can adhere closely to the lesser curvature of the vessel and has good perforation performance in tortuous parent arteries. The LVIS Jr stent has high metal coverage (15%–18%), and the small stent mesh (diameter <1.5 mm) can prevent escape of the coil during SAC of small IAs to improve the chances of complete occlusion and cure of the aneurysm.

On the other hand, due to rational application of the advantages and characteristics of different stents, such as through the semi-release method of the stent and the “vault” technique, part of the stent at the aneurysm neck can be

herniated into the aneurysm cavity, and a wide-neck aneurysm can be changed into a relatively narrow-neck aneurysm. Therefore, the Neuroform Atlas stent can be used for SAC in small IAs and coils do not escape easily, especially for wide-neck aneurysms at vascular bifurcations (eg, M1 bifurcation, basilar artery tip). This phenomenon aligns with the fact that the Neuroform Atlas stent is used more widely in M1 bifurcated aneurysms than the LVIS Jr stent used in our study.

Studies^{9,25,28,29} have reported that the Neuroform Atlas stent and LVIS Jr stent had a prevalence of neurologic perioperative complications of 3.4%–13.6% and 4.9%–19.0%, with ischemic complications of about 1.7%–6.2% and 4.1%–14.0% and bleeding complications of about 0%–3.0% and 2.4%–5.2%, respectively. In the present study, bleeding complications were documented in 2 patients (cerebral parenchymal hemorrhage in the non-stent-implantation area and hemorrhage in an ulcer after stent implantation), but the causes were not related directly to stent implantation. Traditional Neuroform EZ and LVIS stents are not suitable for small parent arteries due to the large diameter of the microcatheter and poor compliance. Also, the prevalence of postoperative ischemic complications (eg, acute in-stent thrombosis and in-stent stenosis) was higher, possibly related to the incomplete apposition of metal stents with a thick wall in small parent arteries. In the present study, although the Neuroform Atlas stent or LVIS Jr stent was implanted into a parent artery of <2 mm in diameter, the prevalence of ischemic complications was not increased significantly (only 1 instance of embolic detachment) and serious events (eg, acute in-stent thrombosis) did not occur. This observation may have been related to the Neuroform Atlas stent and LVIS Jr stent having a relatively thin wall, which aids in easy deployment and complete apposition in the small parent artery.

DSA follow-up at 6 months showed that the prevalence of complete occlusion of aneurysms in the Neuroform Atlas group was significantly higher than that in the LVIS Jr group and that 3 patients (4.3%) had aneurysm recurrence in the LVIS Jr group. This finding is consistent with reports of a prevalence of recurrence of 3.8%–8.3% after SAC using the LVIS Jr stent.^{9,12} Intraoperative HR-CBCT showed significant ISA at the aneurysm neck in 11 patients treated with a LVIS Jr stent, but in only 1 patient treated with the Neuroform Atlas stent. Multiple studies have shown that ISA is closely associated with delayed occlusion and recurrence of aneurysms, in-stent thrombosis, and delayed endothelialization.^{30,31} For example, Li et al³² reported that ISA using FDs prolonged the time to endothelialization significantly and caused delayed occlusion of the aneurysm. Use of the lantern method during implantation of the LVIS Jr stent can protect from the escape of coils at the aneurysm neck, but a braided metal stent may cause local stress changes during pushing and pulling, which may lead to ISA.^{22,33}

Continuous blood flow into the aneurysm cavity through the gap of the ISA at the aneurysm neck also causes delayed occlusion or recurrence of the aneurysm. This phenomenon may have been the main reason for the lower rate of long-term occlusion and the higher recurrence rate of partial LVIS Jr stents with incomplete apposition. We showed that a stent angle of $\geq 75^\circ$ or a diameter mismatch ratio of the parent artery of ≥ 1.25 were independent

risk factors for ISA and that the LVIS Jr stent was more prone to ISA than the Neuroform Atlas stent. These data are in accordance with the results of study by Monteiro et al.²⁵ They reported that the Neuroform Atlas stent was more suitable for aneurysms in the parent artery with a larger curvature or different diameters than the LVIS Jr stent. This observation suggests that the apposition achieved by the LVIS Jr stent should be highly focused on if the parent artery is too angulated or has a larger diameter mismatch ratio at the aneurysm neck.

Our study had several limitations. First, this was a retrospective study with a small sample size, and its conclusions must be verified in additional large-sample, multicenter, prospective, randomized controlled studies. Second, there were selection biases for stents and coils. Third, despite use of a method to reduce metal artifacts, stent apposition at the neck of some aneurysms was affected by the metal artifact of the coil, which may have affected our results. Fourth, the follow-up period was short, and long-term DSA results after SAC were not observed. Fifth, the operator-assessed imaging, patient selection, and variability (including operation procedures, operator experience, and stent preference) among different institutions may have influenced the study results. Sixth, the limited visibility of the nitinol wires may be a potential limitation in the assessment of stent wall apposition.

CONCLUSIONS

The Neuroform Atlas stent and LVIS Jr stent had good efficacy and a low prevalence of complications in SAC of unruptured IAs in parent arteries of <2 mm in diameter. Apposition of the LVIS Jr stent was worse than that of the Neuroform Atlas stent at the neck of some aneurysms.

Disclosure forms provided by the authors are available with the full text and PDF of this article at www.ajnr.org.

REFERENCES

- Sciacca S, Bassiouny A, Mansoor N, et al. **Early outcomes of the Pipeline Vantage flow diverter: a multicentre study.** *Clin Neuroradiol* 2023;33:887–96 CrossRef Medline
- Stahl J, Marsh LM, Thormann M, et al. **Assessment of the flow-diverter efficacy for intracranial aneurysm treatment considering pre- and post-interventional hemodynamics.** *Comput Biol Med* 2023;156:106720 CrossRef Medline
- Hanel RA, Cortez GM, Jankowitz BT, et al; ATLAS Investigators. **Anterior circulation location-specific results for stent-assisted coiling: carotid versus distal aneurysms: 1-year outcomes from the Neuroform Atlas stent pivotal trial.** *J Neurointerv Surg* 2023 Nov 8 [Epub ahead of print] CrossRef Medline
- Oishi H, Fujii T, Yatomi K, et al. **Stent-assisted coil embolization of unruptured middle cerebral artery aneurysms using LVIS Jr stents.** *J Clin Neurosci* 2020;80:87–91 CrossRef Medline
- Zhang X, Wang R, Ding Y, et al. **Embolization of unruptured wide-necked aneurysms at the MCA bifurcation using the Neuroform Atlas stent-assisted coiling: a two-center retrospective study.** *Front Neurol* 2023;14:1199390 CrossRef Medline
- Daou BJ, Palmateer G, Linzey JR, et al. **Stent-assisted coiling of cerebral aneurysms: head-to-head comparison between the Neuroform Atlas and EZ stents.** *Interv Neuroradiol* 2021;27:353–61 CrossRef Medline

7. Iwakami T, Fujii N, Son J. **Comparison of the physical characteristics of support stents for cerebral aneurysm embolization.** *J Neuroendovasc Ther* 2021;15:778–86 CrossRef Medline
8. Kim YN, Choi JW, Lim YC, et al. **Usefulness of silent MRA for evaluation of aneurysm after stent-assisted coil embolization.** *Korean J Radiol* 2022;23:246–55 CrossRef Medline
9. Gross BA, Ares WJ, Ducruet AF, et al. **A clinical comparison of Atlas and LVIS Jr stent-assisted aneurysm coiling.** *J Neurointerv Surg* 2019;11:171–74 CrossRef Medline
10. Jankowitz BT, Jadhav AP, Gross B, et al. **Pivotal trial of the Neuroform Atlas stent for treatment of posterior circulation aneurysms: one-year outcomes.** *J Neurointerv Surg* 2022;14:143–48 CrossRef Medline
11. Zaidat OO, Hanel RA, Sauvageau EA, et al; ATLAS Investigators. **Pivotal trial of the Neuroform Atlas stent for treatment of anterior circulation aneurysms: one-year outcomes.** *Stroke* 2020;51:2087–94 CrossRef Medline
12. Kim J, Han HJ, Lee W, et al. **Safety and efficacy of stent-assisted coiling of unruptured intracranial aneurysms using low-profile stents in small parent arteries.** *AJNR Am J Neuroradiol* 2021;42:1621–26 CrossRef Medline
13. Ozaki T, Fujinaka T, Kidani T, et al. **Coil embolization of unruptured cerebral aneurysms using stents in small arteries less than 2 mm in diameter.** *Neurosurgery* 2022;90:538–46 CrossRef Medline
14. Dong L, Chen X, Wang J, et al. **Neuroform Atlas stent-assisted coiling of tiny wide-necked intracranial aneurysms.** *Front Neurol* 2022;13:1020785 CrossRef Medline
15. Foo M, Maingard J, Hall J, et al. **Endovascular treatment of intracranial aneurysms using the novel low profile visualized intraluminal support EVO stent: multicenter early feasibility experience.** *Neurointervention* 2021;16:122–31 CrossRef Medline
16. Hanel RA, Yoon N, Sauvageau E, et al. **Neuroform Atlas stent for treatment of middle cerebral artery aneurysms: 1-year outcomes from Neuroform Atlas stent pivotal trial.** *Neurosurgery* 2021;89:102–08 CrossRef Medline
17. Ten Brinck MFM, de Vries J, Bartels R, et al. **Neuroform Atlas stent-assisted coiling: preliminary results.** *Neurosurgery* 2019;84:179–89 CrossRef Medline
18. Kotsugi M, Nakagawa I, Konishi K, et al. **Three-dimensional reconstruction imaging by C-arm computed tomography accurately visualizes in-stent neointimal formation in patients with stent-assisted coil embolization.** *Front Neurol* 2023;14:1131061 CrossRef Medline
19. Li TF, Ma J, Han XW, et al. **Application of high-resolution C-arm CT combined with streak metal artifact removal technology for the stent-assisted embolization of intracranial aneurysms.** *AJNR Am J Neuroradiol* 2019;40:1752–58 CrossRef Medline
20. Li TF, Shi CC, Ma J, et al. **Clinical study of high-resolution C-arm CT in mechanical recanalization and stent implantation for chronic cerebral artery occlusion.** *Neurol India* 2022;70:694–98 CrossRef Medline
21. Kato N, Yuki I, Ishibashi T, et al. **Visualization of stent apposition after stent-assisted coiling of intracranial aneurysms using high-resolution 3D fusion images acquired by C-arm CT.** *J Neurointerv Surg* 2020;12:192–96 CrossRef Medline
22. Kwon MY, Ko YS, Kwon SM, et al. **Evaluation of stent apposition in the Lvis blue stent-assisted coiling of distal internal carotid artery aneurysms: correlation with clinical and angiographic outcomes.** *J Korean Neurosurg Soc* 2022;65:801–15 CrossRef Medline
23. Wu D, Lai N, Zhao X, et al. **Enterprise 2 stent-assisted embolization of paraclinoid aneurysms: a single-center preliminary study.** *Clin Interv Aging* 2022;17:1833–40 CrossRef Medline
24. Martinez-Galdamez M, Orlov K, Kadziolka K, et al. **Safety and efficacy of intracranial aneurysm embolization using the “combined remodeling technique:” low-profile stents delivered through double lumen balloons—a multicenter experience.** *Neuroradiology* 2019;61:1067–72 CrossRef Medline
25. Monteiro A, Cortez GM, Aghaebrahim A, et al. **Low-Profile Visualized Intraluminal Support Jr braided stent versus Atlas self-expandable stent for treatment of intracranial aneurysms: a single-center experience.** *Neurosurgery* 2021;88:E170–78 CrossRef Medline
26. Dong L, Wang J, Chen X, et al. **Stent-assisted coiling using the Neuroform Atlas stent for treatment of aneurysms that recur after coil embolization.** *Front Neurol* 2022;13:967942 CrossRef Medline
27. Sweid A, Herial N, Sajja K, et al. **Early multicenter experience with the Neuroform Atlas stent: feasibility, safety, and efficacy.** *Neurosurgery* 2020;87:E321–35 CrossRef Medline
28. Choo YS, Kim EJ, Sung SM, et al. **Additional rescue stenting with Neuroform Atlas stents during stent-assisted coiling of saccular aneurysms.** *Clin Neurol Neurosurg* 2023;230:107777 CrossRef Medline
29. Liu C, Guo K, Wu X, et al. **Utility of Low-Profile Visualized Intraluminal Support (LVIS) stent for treatment of acutely ruptured bifurcation aneurysms: a single-center study.** *Front Neurol* 2023;14:1050369 CrossRef Medline
30. Ando H, Nakano Y, Sawada H, et al. **Diagnostic performance of high-resolution intravascular ultrasound for abnormal post-stent findings after stent implantation: a comparison study between high-resolution intravascular ultrasound and optical coherence tomography.** *Circ J* 2021;85:883–90 CrossRef Medline
31. Wang N, Lu Y, Feng L, et al. **Identifying risk factors for in-stent restenosis in symptomatic intracranial atherosclerotic stenosis: a systematic review and meta-analysis.** *Front Neurol* 2023;14:1170110 CrossRef Medline
32. Li J, Gong W, Li D, et al. **Evaluation of the apposition in unruptured aneurysms treated with flow diverters by optical coherence tomography: preliminary clinical experience.** *Front Neurol* 2022;13:1029699 CrossRef Medline
33. Zhang H, Gao X, Liang H, et al. **Incomplete stent apposition of Low-Profile Visualized Intraluminal Support stents in the treatment of cerebral aneurysms.** *J Neurointerv Surg* 2020;12:591–97 CrossRef Medline

Predictors of Aneurysm Obliteration in Patients Treated with the WEB Device: Results of a Multicenter Retrospective Study

 Panagiotis Mastorakos,  Kareem El Naamani,  Nimer Adeeb, Mathews Lan, James Castiglione,  Omaditya Khanna, Ritam Ghosh,  Jose Danilo Bengzon Diestro,  Mahmoud Dibas, Rachel M. McLellan,  Oktay Algin,  Sherief Ghozy,  Nicole M. Cancelliere, Assala Aslan, Hugo H. Cuellar-Saenz,  Sovann V. Lay,  Adrien Guenego, Leonardo Renieri, Joseph Carnevale,  Guillaume Saliou,  Eimad Shotar,  Kevin Premat,  Markus Möhlenbruch, Michael Kral,  Justin E. Vranic,  Charlotte Chung,  Mohamed M. Salem,  Ivan Lylyk,  Paul M. Foreman,  Jay A. Vachhani, Hamza Shaikh, Vedran Župančić, Muhammad U. Hafeez, Joshua Catapano, Muhammad Waqas, Vincent M. Tutino, Mohamed K. Ibrahim, Marwa A. Mohammed, James D. Rabinov, Yifan Ren, Clemens M. Schirmer, Mariangela Piano, Maria Bres Bullrich, Michael Mayich, Anna L. Kühn, Caterina Michelozzi, Stéphanie Elens, Robert M. Starke, Ameer E. Hassan, Mark Ogilvie, Anh Nguyen, Jesse Jones, Waleed Brinjikji, Marios Psychogios, Christian Ulfert, Julian Spears, Brian T. Jankowitz, Jan-Karl Burkhardt, Ricardo A. Domingo, Thien Huynh, Rabih G. Tawk, Boris Lubicz, Marie T. Nawka, Pietro Panni, Ajit S. Puri, Guglielmo Pero, Erez Nossek, Eytan Raz, Monika Killer-Oberpfalzer, M. Ozgur Ozates, Giyas Ayberk, Robert W. Regenhart, Christoph J. Griessenauer, Hamed Asadi, Adnan Siddiqui, Andrew F. Ducruet, Felipe C. Albuquerque, Nirav J. Patel, Christopher J. Stapleton, Peter Kan, Vladimir Kalousek, Pedro Lylyk, Srikanth Boddu, Jared Knopman, Mohammad A. Aziz-Sultan, Frédéric Clarençon, Nicola Limbucci, Mario Zanaty, Juan Carlos Martinez-Gutierrez, Sunil Sheth, Gary Spiegel, Rawad Abbas, Abdelaziz Amlay, Stavropoula I. Tjoumakaris, Michael R. Gooch, Nabeel A. Herial, Robert H. Rosenwasser, Hekmat Zarzour, Richard F. Schmidt, Vitor Mendes Pereira, Aman B. Patel, Pascal M. Jabbour, and Adam A. Dmytriw

ABSTRACT

BACKGROUND AND PURPOSE: Despite the numerous studies evaluating the occlusion rates of aneurysms following WEB embolization, there are limited studies identifying predictors of occlusion. Our purpose was to identify predictors of aneurysm occlusion and the need for retreatment.

MATERIALS AND METHODS: This is a review of a prospectively maintained database across 30 academic institutions. We included patients with previously untreated cerebral aneurysms embolized using the WEB who had available intraprocedural data and long-term follow-up.

RESULTS: We studied 763 patients with a mean age of 59.9 (SD, 11.7) years. Complete aneurysm occlusion was observed in 212/726 (29.2%) cases, and contrast stasis was observed in 485/537 (90.3%) of nonoccluded aneurysms. At the final follow-up, complete occlusion was achieved in 497/763 (65.1%) patients, and retreatment was required for 56/763 (7.3%) patients. On multivariable analysis, history of smoking, maximal aneurysm diameter, and the presence of an aneurysm wall branch were negative predictors of complete occlusion (OR, 0.5, 0.8, and 0.4, respectively). Maximal aneurysm diameter, the presence of an aneurysm wall branch, posterior circulation location, and male sex increase the chances of retreatment (OR, 1.2, 3.8, 3.0, and 2.3 respectively). Intraprocedural occlusion resulted in a 3-fold increase in the long-term occlusion rate and a 5-fold decrease in the retreatment rate ($P < .001$), offering a specificity of 87% and a positive predictive value of 85% for long-term occlusion.

CONCLUSIONS: Intraprocedural occlusion can be used to predict the chance of long-term aneurysm occlusion and the need for retreatment after embolization with a WEB device. Smoking, aneurysm size, and the presence of an aneurysm wall branch are associated with decreased chances of successful treatment.

ABBREVIATION: ROC = receiver operating characteristic

Intrasaccular flow disruption has become a viable option for the treatment of technically challenging wide-neck bifurcation

aneurysms. The Woven EndoBridge (WEB; MicroVention) device provides a stable construct that sits at and above the neck of

Received July 18, 2023; accepted after revision November 21.

From the Department of Neurosurgery (P.M., K.E.N., M.L., J. Castiglione, O.K., R.G., M.Z., R.A., A. Amlay, S.I.T., M.R.G., N.A.H., R.H.R., H.Z., R.F.S., P.M.J.), Thomas Jefferson University, Philadelphia, Pennsylvania; Department of Neurosurgery and Neurointerventional Surgery (N.A., M.D., A. Aslan, H.H.C.-S.), Louisiana State University, Shreveport, Louisiana; Division of Diagnostic and Therapeutic

Neuroradiology, Department of Radiology, St. Michael's Hospital (J.D.B.D., N.M.C., J.S., V.M.P., A.A.D.), University of Toronto, Toronto, Ontario, Canada; Neuroendovascular Program (R.M.M., J.E.V., J.D.R., N.J.P., C.J.S., M.A.A.-S., A.B.P., A.A.D.), Massachusetts General Hospital and Brigham and Women's Hospital, Harvard University, Boston, Massachusetts; Department of Radiology (O.A., M.O.O., G.A.), City Hospital, Bilkent, Medical Faculty of Yildirim Beyazit University, Ankara, Turkey; Departments of Radiology and Neurosurgery (S.G.), Mayo Clinic, Rochester, Minnesota; Service de

the aneurysm. Several prospective and retrospective studies have demonstrated its efficacy and safety compared with other treatment modalities.¹⁻⁴ Also, studies have evaluated the long-term durability of the WEB device. Complete occlusion and adequate (with neck remnant) occlusion occurred in 53%–74% and 79%–94% of cases at initial follow-up, respectively, and 6.5%–16% of aneurysms underwent retreatment.⁵⁻⁸ Additionally, long-term follow-up studies have demonstrated that complete occlusion and adequate occlusion occur in 51%–72% and 74%–100% of cases.⁵⁻¹⁰

Despite the numerous studies evaluating the occlusion rates of aneurysms following WEB embolization, there are limited studies identifying predictors of occlusion.⁵⁻¹⁰ Previous studies have demonstrated that rupture status, smaller neck size, and posterior circulation are associated with incomplete occlusion on follow-up.¹⁰ In addition to aneurysm morphology and patient demographics, it is vital to identify intraoperative indicators of aneurysm occlusion. Compared with the immediate posttreatment angiogram, 60%–90% of WEB-treated aneurysms continue to further occlude on short-term follow-up, while 3%–5% worsen.^{2,4} Similar to other endovascular technologies such as coiling and intraluminal flow diversion, it is important to better identify preoperative and intraoperative predictors of aneurysm occlusion following WEB deployment to guide future case selection, intra-procedural decision-making, and postoperative management strategies.

Here, we analyze an international multicenter cohort of patients treated with the WEB device to identify predictors of aneurysm occlusion at follow-up and retreatment. We mainly identify medical history, aneurysm characteristics, and intraprocedural findings that predict outcomes.

MATERIALS AND METHODS

Study Criteria

Data were obtained from a prospectively maintained multicenter database including adult patients (18 years of age or older) with ruptured and unruptured intracranial aneurysms treated with the

WEB device at 30 academic institutions in North and South America, Europe, and Australia. The institutional review board approval was obtained from the primary institution, and individualized approval was obtained from each site. We included patients with cerebral bifurcation aneurysms treated with the WEB device and available follow-up on digital DSA, MRA, or CTA, or documented retreatment. Exclusion criteria included the use of adjunctive modalities of treatment and previously treated aneurysms.

Data Collection


Patient charts were reviewed to determine patient characteristics, including age, sex, smoking status, preprocedural antithrombotic use, and aneurysm rupture status. Procedural duration time to last follow-up and imaging technique at last follow-up were also determined by chart review. Interpretation of imaging was completed by the treatment team, who reported anatomic location, dimensions, the presence of a daughter sac and a vessel branch arising from aneurysm wall, the degree of occlusion (interprocedurally and at last follow-up), intraprocedural contrast stasis, and complete occlusion at last follow-up. The need for retreatment was determined by the treatment team, and retreatment was documented.

The intraoperative degree of occlusion was divided into complete occlusion (100%), near-complete occlusion (>90%), and aneurysm residual (<90%). This was calculated on the basis of the optimal aneurysm projection and the area of contrast opacification pre- and post-device deployment. Occlusion at final follow-up was evaluated on the basis of the WEB Intra saccular Therapy (WEB-IT) trial angiographic scale, including complete occlusion, near-complete occlusion with a residual neck, and residual aneurysm. Adequate occlusion was defined as complete or near-complete occlusion with a residual neck.² At final follow-up, the treatment team also reported the presence of complete occlusion. If patients had additional treatment, final follow-up occlusion rates were based on the patient's reported imaging follow-up available before retreatment. Stasis was assessed on

Neuroradiologie Diagnostique et Thérapeutique (S.V.L.), Centre Hospitalier de Toulouse, Hôpital Purpan, Toulouse, France; Service de Neuroradiologie Interventionnelle (A.G., S.E., B.T.J., B.L.), Hôpital Universitaire Erasme, Bruxelles, Belgique; Interventistica Neurovascolare (L.R., N.L.), Ospedale Careggi di Firenze, Florence, Italy; Neurosurgery and Interventional Neuroradiology, Weill Cornell School of Medicine (J. Carnevale, R.W.R., S.B., J.K.), NY Presbyterian Hospital, New York, New York; Service de Radiodiagnostic et Radiologie Interventionnelle (G. Salou), Centre Hospitalier Vaudois de Lausanne, Lausanne, Switzerland; Department de Neuroradiologie (E.S., K.P., F.C.), Hôpital Pitié-Salpêtrière, Université Sorbonne, Paris, France; Sektion Vaskuläre und Interventionelle Neuroradiologie (M. Möhlenbruch, C.U.), Universitätsklinikum Heidelberg, Heidelberg, Germany; Department of Neurology/Institute of Neurointervention (M.K., M.K.-O., C.J.G.), Christian Doppler University Hospital and Institute of Neurointervention, Paracelsus Medical University, Salzburg, Austria; Departments of Radiology and Neurosurgery (C.C., E.N., E.R., H.A.), NYU Langone Health Center, New York, New York; Department of Neurosurgery (M.M.S., B.T. Jankowitz, J.-K.B.), University of Pennsylvania Medical Center, Philadelphia, Pennsylvania; Equipo de Neurocirugía Endovascular y Radiología Intervencionista (I.L., P.L.), Clínica La Sagrada Familia, Buenos Aires, Argentina; Neurosurgery Department (P.M.F., J.A.V.), Orlando Health Neuroscience and Rehabilitation Institute, Orlando, Florida; Departments of Radiology and Neurosurgery (H.S.), Cooper University Health Care, Cooper Medical School of Rowan University, Camden, New Jersey; Subdivision of Interventional Neuroradiology, Department of Radiology (V.Ž.), Clinical Hospital Center Sisters of Mercy, Zagreb, Croatia; Department of Neurosurgery (M.U.H., P.K., V.K.), UTMB and Baylor School of Medicine, Houston, Texas; Department of Neurosurgery (J. Catapano, A.F.D., F.C.A.), Barrow Neurological Institute, Phoenix, Arizona; Department of Neurosurgery (M.W., V.M.T., A.S.), State University of New York at Buffalo, Buffalo, New York; Departments of Radiology and Neurosurgery

(M.K.I., M.A.M., W.B.), Mayo Clinic, Rochester, Minnesota; Interventional Radiology and Neurointerventional Services, Department of Radiology (Y.R., R.G.T.), Austin Health, Melbourne, Victoria, Australia; Department of Neurosurgery and Radiology (C.M.S.), Geisinger Hospital, Danville, Pennsylvania; Interventistica Neurovascolare (M. Piano, P.P., G.P.), Ospedale Niguarda Cà Granda, Milano, Italy; Neurointerventional Program, Departments of Medical Imaging and Clinical Neurological Sciences (M.B.B., M. Mayich), London Health Sciences Centre, Western University, London, Ontario, Canada; Department of Neurointerventional Radiology (A.L.K., A.S.P.), UMass Memorial Hospital, Worcester, Massachusetts; Interventistica Neurovascolare (C.M.), Ospedale San Raffaele Milano, Milano, Italy; Department of Neurosurgery (R.M.S.), University of Miami, Miami, Florida; Department of Neuroscience (A.E.H.), Valley Baptist Neuroscience Institute, Harlingen, Texas; Departments of Neurosurgery and Radiology (M.O., J.J.), University of Alabama at Birmingham, Birmingham, Alabama; Department of Diagnostic and Interventional Neuroradiology (A.N., M. Psychogios), University Hospital Basel, Basel, Switzerland; Departments of Radiology & Neurosurgery (R.A.D., T.H.), Mayo Clinic, Jacksonville, Florida; Department of Diagnostic and Interventional Neuroradiology (M.T.N.), University Medical Center Hamburg-Eppendorf, Hamburg, Germany; and Department of Neurology (J.C.M.-G., S.S., G. Spiegel), UTHealth McGovern Medical School, Houston, Texas.

Please address correspondence to Adam A. Dmytriw, MD, MPH, MSc, Neuroendovascular Program Massachusetts General Hospital, Harvard Medical School, 55 Fruit St, Boston, MA 02114; e-mail: admytriw@mgh.harvard.edu; @panos_mast; @kareemnaamanim; @adamdmytriw

 Indicates article with online supplemental data.
<http://dx.doi.org/10.3174/ajnr.A8324>

the basis of contrast persistence within the aneurysm at the capillary phase and was only assessed in patients with noncomplete intraoperative occlusion.

Statistical Analysis

Data are presented as mean (SD) for numeric variables and as a frequency and percentage for categoric variables. Univariate logistic regression analysis was used to test covariates predictive of complete aneurysm occlusion at the most recent follow-up. Interaction and confounding were assessed through stratification and linear regression analysis. Factors predictive in univariate analysis ($P < .15$) were entered into a multivariate logistic regression analysis. However, because different measures of aneurysm size are highly correlated both physiologically and statistically, only the aneurysm maximum diameter was entered into the multivariate analysis. Logistic regression results are represented as ORs and 95% confidence intervals with the associated P value. A similar analysis was used to test covariates predictive of the need for retreatment. Categoric variables were compared using the χ^2 test with a Bonferroni correction for multiple-comparison adjustment. Intraoperative complete occlusion was evaluated as a predictor of complete occlusion and the need for retreatment using the receiver operating characteristic (ROC) curve. P values $\leq .05$ were considered statistically significant except for application of the Bonferroni correction for multiple-comparison adjustment as indicated. Statistical analysis was performed with SPSS Software 29.0.0.0 (IBM) and GraphPad Prism (GraphPad Software).

RESULTS

Baseline Characteristics

The study cohort comprised 763 patients who were predominantly women ($n = 510$, 66.8%), with a mean age of 59.9 (SD, 11.7) years. Of them, 210 (31.2%) patients were current smokers, 193 (28.7%) were former smokers, and 270 (40.1%) were non-smokers. On admission, 327 (46.6%) patients were not being treated with antithrombotic agents, 91 (12.1%) were on a single agent, and 283 (40.4%) were on 2 agents. With respect to aneurysm characteristics, 230 (30.1%) were ruptured on admission, 639 (83.7%) were bifurcation aneurysms, 215 (30.1%) were accompanied by a daughter sac, and 78 (10.4%) had a vessel arising from the aneurysm wall. The mean aneurysm neck was 4.0 (SD, 1.4) mm, the mean maximal diameter was 6.9 (SD, 2.4) mm, the mean aneurysm height was 6.1 (SD, 2.3) mm, and the mean aneurysm width was 5.8 (SD, 2.1) mm. Patient demographics and aneurysm characteristics are summarized in Table 1.

Procedure and Follow-Up

The mean duration of the procedures was 88.0 (SD, 47.9) minutes. Immediately after WEB deployment, 212 (29.2%) patients achieved complete intraprocedural occlusion, 185 (25.5%) achieved $>90\%$ intraprocedural occlusion, and 328 (45.2%) achieved $<90\%$ intraprocedural occlusion. Contrast stasis was observed in 485 (90.3%) cases. The mean duration to final follow-up was 17.7 (SD, 20.3) months, with a minimum follow-up of 3 months and a maximum follow-up of 115 months, and the following imaging modalities were used to evaluate aneurysm obliteration: 206 (27.3%) on DSA, 376 (49.9%) on MRA, 131

Table 1: Patient demographics and aneurysm characteristics

	No. (%), Mean (SD)
Total No. of patients	763
Sex (female)	510 (66.8)
Mean age (yr)	59.9 (SD, 11.7)
Smoking status ^a	
Current	210 (31.2)
Former	193 (28.7)
Nonsmoker	270 (40.1)
Ruptured aneurysm	230 (30.1)
Aneurysm location	
AcomA	223 (29.2)
Basilar tip	123 (16.1)
ACA	56 (7.3)
ICA	15 (2.0)
MCA	206 (27.0)
PcomA	54 (7.1)
PICA	14 (1.8)
ICA terminus	60 (7.9)
SCA	5 (0.7)
VA	6 (0.8)
PCA	1 (0.1)
Mean aneurysm neck (mm) ^b	4.0 (SD, 1.4)
Mean maximal diameter (mm)	6.9 (SD, 2.4)
Mean aneurysm height (mm) ^c	6.1 (SD, 2.3)
Mean aneurysm width (mm) ^d	5.8 (SD, 2.1)
Bifurcation aneurysms	639 (83.7)
Daughter sac ^e	215 (30.1)
Vessel from aneurysm wall ^f	78 (10.4)
Preprocedural AP/AC ^g	
None	327 (46.6)
Single agent	91 (12.1)
Two agents	283 (40.4)

Data missing for a = 90, b = 66, c = 10, d = 4, e = 351, f = 49, g = 10, h = 62.

Note:—AcomA indicates anterior communicating artery; PcomA, posterior communicating artery; ACA, anterior cerebral artery; SCA, superior cerebellar artery; VA, vertebral artery; PCA, posterior cerebral artery; AP/AC, antiplatelets/anticoagulants.

(17.4%) on CTA, 9 (1.2%) on MRA/DSA, 5 (0.7%) on CTA/DSA, and 27 (3.6%) on CTA/MRA. At the final follow-up, 695 patients had the degree of aneurysm occlusion recorded and had not undergone retreatment. Of those, complete occlusion was achieved in 497 (71.5%) patients; near-complete occlusion with a neck remnant, in 139 (20%) patients; and aneurysm residual, in 59 (8.5%) patients. Of all the patients, complete aneurysm obliteration was observed in 497 (65.1%) patients on the most recent available follow-up, while 56 (7.3%) patients required retreatment. The procedural characteristics, follow-up, and outcomes are summarized in Table 2.

Predictors of Aneurysm Occlusion

Univariate and multivariate analyses were performed to identify independent predictors of complete obliteration at final follow-up (Online Supplemental Data).

On univariate analysis, factors associated with a decreased chance of complete obliteration at final follow-up were being a former smoker (OR, 0.6; 95% CI, 0.370–0.845; $P = .006$), neck diameter (OR, 0.7; 95% CI, 0.646–0.815; $P < .001$), maximal diameter (OR, 0.8; 95% CI, 0.745–0.850; $P < .001$), aneurysm width (OR, 0.8; 95% CI, 0.745–0.864; $P < .001$), aneurysm height (OR, 0.8; 95% CI, 0.742–0.854; $P < .001$), the presence of a daughter sac (OR, 0.7; 95% CI, 0.505–0.983; $P = .039$), and the presence of

a wall branch (OR, 0.4; 95% CI, 0.278–0.725; $P = .001$). In addition, intraprocedural complete occlusion at the time of treatment increased the chance of follow-up aneurysm occlusion by 3.6-fold compared with <90% occlusion (OR, 3.6; 95% CI, 2.285–5.534; $P < .001$). On multivariate analysis, independent factors negatively correlated with complete aneurysm occlusion at the last follow-up were former smoking (OR, 0.5; 95% CI, 0.311–0.82; $P = .005$) maximal aneurysm diameter (OR, 0.8; 95% CI, 0.743–0.873; $P < .001$) and the presence of an aneurysm wall branch (OR, 0.4). Intraprocedural complete occlusion increased the chance of complete occlusion at last follow-up by 3-fold (OR, 3.0; 95% CI, 1.8–4.9; $P < .001$).

Predictors of Retreatment

Univariate and multivariate analysis were performed to identify independent predictors of retreatment (Online Supplemental Data).

Factors associated with retreatment at final follow-up were younger age (OR, 0.96; 95% CI, 0.944–0.986; $P = .001$), male sex (OR, 2.1; 95% CI, 1.234–3.687; $P = .007$), ruptured status (OR, 2.0; 95% CI, 1.124–3.414; $P = .018$), posterior circulation location (OR, 1; 95% CI, 1.038–3.449; $P = .037$), neck diameter (OR, 1.2; 95% CI, 0.965–1.385, $P < .001$), maximal diameter (OR, 1.2; 95% CI, 1.120–1.357; $P < .001$), aneurysm width (OR, 1.3; 95% CI, 1.123–1.405; $P < .001$), and aneurysm height (OR, 1.3; 95% CI, 1.152–1.418; $P < .001$). Intraprocedural complete occlusion at

the time of treatment decreased the chance of retreatment 5-fold compared with <90% occlusion (OR, 0.2; 95% CI, 0.058–0.476; $P < .001$). On multivariate analysis, independent predictors of retreatment were male sex (OR, 2.3; 95% CI, 1.119–4.707; $P = .023$), posterior circulation location (OR, 3.0; 95% CI, 1.367–6.476; $P = .006$), maximal aneurysm diameter (OR, 1.2; 95% CI, 1.068–1.362; $P < .001$), and the presence of a wall branch (OR, 3.8; 95% CI, 1.577–9.175; $P = .002$). Intraprocedural complete occlusion decreased the chance of retreatment 5-fold compared with <90% occlusion (OR, 0.2; 95% CI, 0.06–0.582; $P = .003$).

Intraoperative Predictors of Outcomes

We further focused on understanding how intraoperative radiographic findings at the time of treatment predict occlusion at last follow-up and ultimate retreatment. The χ^2 with a Bonferroni correction for multiple comparison adjustment demonstrated that intraoperative complete occlusion at the time of treatment leads to an 85% rate of obliteration at last follow-up and a 98.1% rate of not requiring additional treatment. In contrast, 90%–99% occlusion and <90% occlusion lead to 51.4% and 61.3% rates of occlusion at last follow-up, respectively, as well as 90.3% and 89.6% rates of no additional treatment, respectively (Table 3).

We proceeded to evaluate the intraoperative evidence of 100% occlusion as a test for predicting occlusion at last follow-up. This evaluation provided 0.874 specificity with only 0.373 sensitivity and a positive predictive value of 0.85 (Pearson χ^2 P value and ROC curve P value < .001). Similarly, we evaluated intraoperative 100% occlusion as a predictor of no need for additional treatment. This step provided 0.929 specificity with only 0.31 sensitivity and a positive predictive value of 0.981 (Pearson χ^2 P value < .001 and ROC curve P value = .003; Table 4).

Predictors of Intraoperative Complete Occlusion. Univariate and multivariate analyses were performed to identify independent predictors of intraoperative complete obliteration (Online Supplemental Data). On univariate analysis, factors associated with a decreased chance of complete obliteration intraoperatively were neck diameter (OR, 0.7; 95% CI, 0.629–0.844; $P < .001$), aneurysm width (OR, 0.9; 95% CI, 0.850–0.998; $P = .045$), and bifurcation aneurysm (OR, 0.5; 95% CI, 0.336–0.77; $P < .001$). On multivariate analysis, aneurysm neck diameter was negatively correlated with complete intraoperative aneurysm occlusion (OR, 0.6; 95% CI, 0.573–0.817; $P < .001$).

DISCUSSION

The WEB device has been added to our armamentarium for the treatment of wide-neck bifurcation aneurysms.^{1–4} Given that an

Table 2: Occlusion rates of treated aneurysms intraoperatively and at most recent follow-up

	No. (%), Mean (SD)
Mean duration of procedure (min) ^a	88.0 (47.9)
Immediate occlusion ^b	
100%	212 (29.2)
>90%	185 (25.5)
<90%	328 (45.2)
Contrast stasis in nonoccluded aneurysms ^c	485 (90.3)
Mean duration to last follow-up (mo)	17.7 (20.3)
Technique of last follow-up ^d	
DSA	206 (27.3)
MRA	376 (49.9)
CTA	131 (17.4)
MRA/DSA	9 (1.2)
CTA/DSA	5 (0.7)
MRA/CTA	27 (3.6)
Occlusion at last follow-up ^e	
Complete	497 (71.5)
Near-complete occlusion	139 (20)
Aneurysm residual	59 (8.5)
Complete occlusion	497 (65.1)
Retreatment	56 (7.3)

Note:—Data missing for a = 113, b = 37, c = 68, d = 9, e = 68.

Table 3: Intraoperative degree of occlusion and stasis as predictors of long-term outcomes

	Imaging Findings			Management		
	Obliteration	Residual/Recurrence	P Value	Treatment	No. Treatment	P Value
Intraoperative 100% occlusion	175 (85%) ^a	31 (15%) ^a	<.001 ^a	4 (1.9%) ^a	207 (98.1%) ^a	<.001 ^a
90%–99% occlusion	94 (51.4%)	89 (48.6%)		18 (9.7%)	167 (90.3%)	
<90% occlusion	200 (61.3%)	126 (38.7%)		34 (10.4%)	193 (89.6%)	
Contrast stasis	284 (59.2%)	196 (40.8%)	.259	48 (9.9%)	436 (90.1%)	.606
No stasis	26 (51%)	25 (49%)		4 (7.7%)	48 (92.3%)	

^a Significant.

Table 4: Test parameters of intraoperative complete occlusion as a predictor of long-term obliteration and no additional treatment

Obliteration at Last Follow-Up	P Value	No Retreatment	P Value
Sensitivity	.373	Sensitivity	.310
Specificity	.874	Specificity	.929
Positive predictive value	.850	Positive predictive value	.981
Negative predictive value	.422	Negative predictive value	.102
Positive likelihood ratio	2.961	Positive likelihood ratio	4.345
Pearson χ^2 P value	<.001 ^a	Pearson χ^2 P value	<.001 ^a
ROC curve P value	<.001 ^a	ROC curve P value	.003 ^a

^aSignificant.

adequate occlusion rate is 80% and treatment failure occurs in 5% of cases, it is important to describe factors that are associated with treatment failure.¹⁰ Herein, we identified that aneurysm characteristics, including anatomic location, size and wall branch vessel, and smoking status affect the probability of long-term occlusion and retreatment. We also report that intraoperative occlusion at the time of treatment predicts outcomes. These findings can inform patient selection for treatment with the WEB device and help determine postprocedural expectations and observation regimen.

We identified that immediate intraoperative occlusion predicts an 85% chance of complete occlusion at the last follow-up and a 98.1% rate of not requiring retreatment. This finding indicates a 3-fold increase in the occlusion rate compared with aneurysms with <90% intraoperative occlusion. However, intraoperative near-complete occlusion and the presence of contrast stasis were not predictive of the outcomes at last follow-up. Initial studies on the efficacy of WEB embolization indicated that most aneurysms continue to occlude compared with immediate intraoperative findings. However, 5% will worsen at short-term imaging, and 11.5% will further recanalize at long-term follow-up.² Goertz et al⁵ reported that incomplete intraoperative occlusion was associated with incomplete occlusion at short-term follow-up (<12 months). Here, we confirm that this correlation persists at last follow-up.¹¹ Near-complete occlusion with a neck remnant did not correlate with long-term occlusion or recurrence rate. This finding differs from the improved rate of occlusion observed when Raymond-Roy II is achieved during coil embolization.¹² Additionally, similar to intraluminal flow diversion, while contrast stasis is often considered a desirable intraprocedural finding, it does not appear predictive of long-term outcome.¹³

In our cohort, occlusion at the last follow-up was achieved in 71.5% of cases, and adequate occlusion, in 91.5% of cases, with retreatment required in 7.3% of cases. These results are consistent with findings in previous literature.⁵⁻¹⁰ Long-term occlusion rates appeared to decrease and the probability of retreatment increased as aneurysm size parameters increased. These include maximum aneurysm diameter, height, width, and neck dimension. Goertz et al⁵ demonstrated that the midterm (<12 months) occlusion rate negatively correlates with aneurysm diameter and height, while they only associated aneurysm neck with long-term occlusion rates. Similarly, Fujimoto et al⁹ reported that their retreatment group had significantly larger aneurysm sizes. Of note, Zhang et al¹⁰ reported that an aneurysm neck of 4–10 mm may be optimal for WEB treatment. Aneurysm size has been correlated with a decreased chance of occlusion after treatment with other

endovascular modalities as well.^{14,15}

Like previous studies, in our cohort, aneurysms in the posterior circulation had a lower chance of complete occlusion and were more likely to require retreatment.^{10,16}

Compared with coiling, the WEB device has a predetermined shape and relies on flow disruption to achieve embolization. Aneurysm characteristics such as irregular shape and the pres-

ence of an aneurysm wall branch vessel can affect WEB placement and flow diversion, respectively, and impede aneurysm occlusion. The presence of a wall branch was identified as a risk factor for nonobliteration and retreatment. While this factor has not been identified before, the presence of an aneurysm wall branch tends to promote persistent flow through the aneurysm. This phenomenon has also been observed with intraluminal flow diverters.¹⁷ Additionally, a daughter sac was associated with decreased rate of complete occlusion. While further studies are needed to explain this phenomenon, the presence of a daughter sac likely makes optimal WEB sizing more challenging.⁹

In accordance with previous analysis, we confirm here that ruptured and unruptured aneurysms have the same occlusion rates,¹⁸ and we demonstrated a 2-fold increase in the retreatment rate only on univariate analysis. The literature on the occlusion rate of ruptured aneurysms is variable, with some studies suggesting a decreased occlusion rate for these aneurysms,^{5,10} while others found that ruptured status does not affect the occlusion rate.^{11,18} Most important, Diestro et al¹⁸ previously reported no evidence of rerupture following WEB embolization of ruptured aneurysms, and the occlusion rate was decreased by only 20%. Ruptured aneurysm status represents a well-known risk factor for recanalization after coiling.¹⁹

Intraprocedural complete occlusion being a strong predictor of long-term outcomes independent of patient and aneurysm characteristics suggests that proceduralists should aim to achieve immediate occlusion. This finding also suggests that the degree of occlusion should be considered postdeployment but before detachment of the WEB device to determine whether positioning and sizing are adequate. Complete occlusion of the aneurysm post-WEB deployment can provide confidence that this aneurysm has a good chance of remaining occluded and not requiring retreatment. Most interesting, immediate occlusion in our data was only inversely correlated with aneurysm neck size and no other patient or aneurysm parameters. This result may be attributed to the WEB device apposition in the neck driving the initial flow disruption leading to immediate occlusion.

Limitations

This study is limited by its retrospective design; however, to our knowledge, this is the largest retrospective study assessing predictors of prognosis after WEB aneurysm treatment. The mean duration to last follow-up was also 17.7 months, with a range from 3 to 115 months, and longer follow-up is certainly needed to clarify outcomes of patients with residual aneurysm filling after WEB device placement. Additionally, follow-up was completed with a

variety of modalities including DSA, CTA, or MRA. On the basis of a recent analysis by El Naamani et al,²⁰ there is no difference in the positive predictive value among these imaging modalities when predicting recurrence rates. Rating intraprocedural occlusion and aneurysm contrast stasis can be subjective and may be inaccurate. Additionally, assessment of occlusion at angiographic follow-up was self-adjudicated. The gradual introduction of automatic segmentation and rating of occlusion will improve the accuracy of these studies.

CONCLUSIONS

This retrospective study allows analysis of factors associated with aneurysm occlusion or retreatment following intrasaccular flow disruption. Specifically, we were able to determine which intraoperative imaging factors physicians can rely on to predict the postoperative course. Additionally, we confirm the established rate of aneurysm occlusion following WEB embolization and the correlation with aneurysm size and anatomic location. We also note how aneurysm architecture (wall branch or presence of a daughter sac) can affect the flow-diverting properties of the WEB device. This analysis will provide information to improve patient selection and guide postoperative management.

Disclosure forms provided by the authors are available with the full text and PDF of this article at www.ajnr.org.

REFERENCES

- Naamani KE, Chen CJ, Abbas R, et al. **Woven EndoBridge versus stent-assisted coil embolization of cerebral bifurcation aneurysms.** *J Neurosurg* 2022;137:1786–93 Medline
- Arthur AS, Molyneux A, Coon AL, et al; WEB-IT Study Investigators. **The safety and effectiveness of the Woven EndoBridge (WEB) system for the treatment of wide-necked bifurcation aneurysms: final 12-month results of the pivotal WEB Intrasaccular Therapy (WEB-IT) study.** *J Neurointerv Surg* 2019;11:924–30 CrossRef Medline
- Fiorella D, Molyneux A, Coon A, et al; WEB-IT Study Investigators. **Demographic, procedural and 30-day safety results from the WEB Intra-saccular Therapy Study (WEB-IT).** *J Neurointerv Surg* 2017;9:1191–96 CrossRef Medline
- Pierot L, Moret J, Barreau X, et al. **Safety and efficacy of aneurysm treatment with WEB in the cumulative population of three prospective, multicenter series.** *J Neurointerv Surg* 2018;10:553–59 CrossRef Medline
- Goertz L, Liebig T, Siebert E, et al. **Long-term clinical and angiographic outcome of the Woven EndoBridge (WEB) for endovascular treatment of intracranial aneurysms.** *Sci Rep* 2022;12:11467 CrossRef Medline
- Mine B, Goutte A, Brisbois D, et al. **Endovascular treatment of intracranial aneurysms with the Woven EndoBridge device: mid-term and long-term results.** *J Neurointerv Surg* 2018;10:127–32 CrossRef Medline
- Monteiro A, Lazar AL, Waqas M, et al. **Treatment of ruptured intracranial aneurysms with the Woven EndoBridge device: a systematic review.** *J Neurointerv Surg* 2022;14:366–70 CrossRef Medline
- Pierot L, Szikora I, Barreau X, et al. **Aneurysm treatment with WEB in the cumulative population of two prospective, multicenter series: 3-year follow-up.** *J Neurointerv Surg* 2021;13:363–68 CrossRef Medline
- Fujimoto M, Lylyk I, Bleise C, et al. **Long-term outcomes of the WEB device for treatment of wide-neck bifurcation aneurysms.** *AJNR Am J Neuroradiol* 2020;41:1031–36 CrossRef Medline
- Zhang SM, Liu LX, Ren PW, et al. **Effectiveness, safety and risk factors of Woven EndoBridge device in the treatment of wide-neck intracranial aneurysms: systematic review and meta-analysis.** *World Neurosurg* 2020;136:e1–23 PMC|CrossRef Medline
- Kabbasch C, Goertz L, Siebert E, et al. **Factors that determine aneurysm occlusion after embolization with the Woven EndoBridge (WEB).** *J Neurointerv Surg* 2019;11:503–10 CrossRef Medline
- Greve T, Sukopp M, Wostrack M, et al. **Initial Raymond-Roy occlusion classification but not packing density defines risk for recurrence after aneurysm coiling.** *Clin Neuroradiol* 2021;31:391–99 CrossRef Medline
- Vakharia K, Waqas M, Munich SA, et al. **Is contrast stasis after Pipeline Embolization Device deployment associated with higher aneurysm occlusion rates?** *World Neurosurg* 2020;133:e434–42 CrossRef Medline
- Pierot L, Cognard C, Anxionnat R, et al; CLARITY Investigators. **Endovascular treatment of ruptured intracranial aneurysms: factors affecting midterm quality anatomic results: analysis in a prospective, multicenter series of patients (CLARITY).** *AJNR Am J Neuroradiol* 2012;33:1475–80 CrossRef Medline
- Pierot L, Barbe C, Thierry A, et al. **Patient and aneurysm factors associated with aneurysm recanalization after coiling.** *J Neurointerv Surg* 2022;14:1096–101 CrossRef Medline
- Adeeb N, Dibas M, Diestro JD, et al. **Comparing treatment outcomes of various intracranial bifurcation aneurysms locations using the Woven EndoBridge (WEB) device.** *J Neurointerv Surg* 2023;15:558–65 CrossRef Medline
- Bender MT, Colby GP, Lin LM, et al. **Predictors of cerebral aneurysm persistence and occlusion after flow diversion: a single-institution series of 445 cases with angiographic follow-up.** *J Neurosurg* 2018;130:259–67 CrossRef Medline
- Diestro JD, Dibas M, Adeeb N, et al. **Intrasaccular flow disruption for ruptured aneurysms: an international multicenter study.** *J Neurointerv Surg* 2022;15:844–50 CrossRef Medline
- Raymond J, Guilbert F, Weill A, et al. **Long-term angiographic recurrences after selective endovascular treatment of aneurysms with detachable coils.** *Stroke* 2003;34:1398–403 CrossRef Medline
- El Naamani K, Mastorakos P, Adeeb N, et al; WorldWideWEB Consortium. **Long-term follow-up of cerebral aneurysms completely occluded at 6 months after intervention with the Woven EndoBridge (WEB) device: a retrospective multicenter observational study.** *Transl Stroke Res* 2023;15:591–98 CrossRef Medline

Reduced Diffusivity along Perivascular Spaces on MR Imaging Associated with Younger Age of First Use and Cognitive Impairment in Recreational Marijuana Users

Christina Andica, Koji Kamagata, Kaito Takabayashi, Zaimire Mahemuti, Akifumi Hagiwara, and Shigeki Aoki



ABSTRACT

BACKGROUND AND PURPOSE: The impairment of the glymphatic system, a perivascular network crucial for brain waste clearance, has been linked to cognitive impairment, potentially attributed to the accumulation of brain waste. Although marijuana use has been associated with poorer cognitive performance, particularly in adolescents, its influence on the glymphatic system remains unexplored. This study evaluated the influence of the age of first marijuana use and the total number of lifetime uses on the glymphatic system, measured using the index of DTI along the perivascular space (DTI-ALPS). Furthermore, we explored the correlation between glymphatic clearance and cognitive performance among marijuana users.

MATERIALS AND METHODS: In this study, 125 individuals who reported using marijuana at least once in their lifetime (43 men; mean age, 28.60 [SD, 3.84] years) and 125 individuals with zero lifetime cannabis use (nonusers; 44 men; mean age, 28.82 [SD, 3.56] years) were assessed. ALPS indices of all study participants were calculated using 3T diffusion MR imaging data ($b = 1000$ s/mm²).

RESULTS: After we adjusted for age, sex, education years, Pittsburgh Sleep Quality Index, alcohol use, tobacco use, and intracranial volume, our analysis using a univariate General Linear Model revealed no significant difference in the ALPS index among nonusers and marijuana users with different ages of first use or various frequencies of lifetime usage. However, in marijuana users, multiple linear regression analyses showed associations between a lower ALPS index and earlier age of first marijuana use (standardized β , -0.20 ; $P = .041$), lower accuracy in the working memory 0-back task (standardized β , 0.20 ; $P = .042$), and fewer correct responses in the Fluid Intelligence Test (standardized β , 0.19 ; $P = .045$).

CONCLUSIONS: This study shows the potential use of DTI-ALPS as a noninvasive indirect indicator of the glymphatic clearance in young adults. Our findings show novel adverse effects of younger age at first use of marijuana on the glymphatic system function, which is associated with impaired working memory and fluid intelligence. Gaining insight into the alterations in glymphatic function following marijuana use could initiate novel strategies to reduce the risk of cognitive impairment.

ABBREVIATIONS: ALPS = along the perivascular space; CBI = type-1 cannabinoid; FA = fractional anisotropy; HCP = Human Connectome Project; ICV = intracranial volume; ISF = interstitial fluid; MLR = multiple linear regression; PSQI = Pittsburgh Sleep Quality Index; SE = standard error; SSAGA = Semi-Structured Assessment for the Genetics of Alcoholism; VIF = variance inflation factor

Marijuana is currently the most extensively used psychoactive substance globally, partly due to shifts in legal and societal attitudes toward its use.¹ In 2020, approximately 209 million individuals 15–64 years of age reported past-year marijuana use.² The past-year prevalence of marijuana use is higher among

adolescents compared with adults.² Marijuana use during the crucial neurodevelopment period of adolescence may lead to alterations in brain structure and function.^{3,4} Consequently, regular marijuana use during adolescence is correlated with a higher risk of adverse outcomes, including cognitive impairment and mood disorders (ie, anxiety and depression).^{5,6} A recent systematic literature review on diffusion MR imaging studies involving marijuana users reported a notable lower WM integrity, particularly in the superior longitudinal fasciculus and corpus callosum.⁷

Received November 21, 2023; accepted after revision February 20, 2024.

From the Department of Radiology (C.A., K.K., K.T., Z.M., A.H., S.A.), Juntendo University Graduate School of Medicine, Tokyo, Japan; and Faculty of Health Data Science (C.A., S.A.), Juntendo University, Chiba, Japan.

This study was supported by the Juntendo Research Branding Project, the Project for Training Experts in Statistical Sciences; the Japan Society for the Promotion of Science Grants-in-Aid for Scientific Research (KAKENHI; grant Nos. 23H02865 and 23K14927), a Grant-in-Aid for Special Research in Subsidies for ordinary expenses of private schools from The Promotion and Mutual Aid Corporation for Private Schools of Japan, and the Brain/MINDS Beyond program of the Japan Agency for Medical Research and Development (grant Nos. JP18dm0307004 and JP19dm0307101), and Agency for Medical Research and Development (grant No. JP21wm0425006).

Please address correspondence to Christina Andica, MD, PhD, Department of Radiology, Juntendo University Graduate School of Medicine, 2-1-1 Hongo, Bunkyo-ku, Tokyo 113-8421; e-mail: christina@juntendo.ac.jp

Indicates open access to non-subscribers at www.ajnr.org

Indicates article with online supplemental data.

<http://dx.doi.org/10.3174/ajnr.A8215>

SUMMARY

PREVIOUS LITERATURE: Alterations of the glymphatic system, a perivascular network essential for clearing brain waste, has been linked with cognitive impairment, possibly because of waste accumulation. Concurrently, marijuana use has shown associations with poorer cognitive performance, particularly in adolescents; however, its impact on the glymphatic system has not yet been investigated.

KEY FINDINGS: In marijuana users, multiple linear regression analyses showed significant associations between a lower ALPS index and earlier age of first marijuana use, lower accuracy in the working memory 0-back task, and fewer correct responses in the Fluid Intelligence Test.

KNOWLEDGE ADVANCEMENT: Our findings indicated that in young adults, dysfunction in glymphatic clearance, as measured by the ALPS index correlated with an earlier initiation of marijuana use. Furthermore, the glymphatic dysfunction in marijuana users is associated with deficits in working memory and fluid intelligence.

Studies suggest a close association between glymphatic system dysfunction and cognitive impairment, as well as mood disorders.^{6,8,9} The glymphatic, or glia-lymphatic system, has gained recent recognition as a brain waste clearance mechanism.¹⁰ According to the glymphatic hypothesis, the pulsation of the arterial walls propels CSF through aquaporin-4 channels in astrocytic endfeet, along perivascular spaces, and into the brain parenchyma. This influx of CSF into the parenchyma subsequently facilitates the movement of interstitial fluid (ISF) and metabolic waste toward the perivenous spaces surrounding the deep veins.¹¹ Impairment of the glymphatic clearance system has a direct effect on brain waste accumulation, contributing to cognitive decline.^{12,13} The glymphatic system has also been shown to play a role in maintaining WM integrity.¹⁴ Therefore, alterations in glymphatic clearance could potentially impact the health of the WM structure.

MR imaging using intrathecal contrast agents, such as gadolinium-based contrast agents, allows the evaluation of the glymphatic system in humans.¹⁵ However, this method is relatively invasive, and gadolinium accumulation in the brain has raised concerns,¹⁶ limiting its clinical application. A more recent approach, DTI along the perivascular space (DTI-ALPS), based on diffusion MR imaging, has emerged as a promising noninvasive method for studying the human glymphatic system.^{17,18} The DTI-ALPS method yields the ALPS index, representing the ratio of diffusivity along the perivascular space surrounding the deep medullary vein at the level of the lateral ventricle body to the diffusivity in a direction perpendicular to the major fiber tracts.^{17,18} At the level of the lateral ventricle body, the medullary veins run perpendicular to the ventricular wall, paralleling the direction of the perivascular space, whereas the medullary arteries and veins, as vessels of the brain parenchyma, accompany the perivascular space, which is a principal drainage pathway of the glymphatic system. Meanwhile, the projection fibers run in the cranial-caudal direction, and the association fibers run in the anterior-posterior direction. Thus, in this region, the perivascular space is perpendicular to both the association and projection fibers.¹⁸ Although the ALPS index is a noninvasive, indirect measure of the human glymphatic system, a previous study has showed a strong correlation with the glymphatic clearance function, as assessed through glymphatic MR imaging following intrathecal gadolinium administration, the current criterion standard evaluation of the human glymphatic system,¹⁹ validating the use of the ALPS index.

Reductions in the ALPS index have been noted in older adults at risk of dementia and in individuals with Alzheimer disease.^{9,18,20} This observation implies that the decrease in the ALPS index could be attributed to the accumulation of amyloid- β , potentially due to a deficiency in glymphatic clearance.^{9,18,20} ALPS index studies have mainly been conducted on older adult cohorts; however, recently, studies have applied the ALPS index to younger age groups. For example, a lower ALPS index has been observed in patients with juvenile myoclonic epilepsy (age range, 12–46 years)²¹ and in patients with acute lymphoblastic leukemia (age range, 4–16 years).²²

Alterations of the glymphatic system, a perivascular network essential for clearing brain waste, has been linked to cognitive impairment, possibly because of waste accumulation. Concurrently, marijuana use has shown associations with poorer cognitive performance, particularly in adolescents; however, its impact on the glymphatic system has not yet been investigated. We hypothesized that marijuana use could influence the glymphatic system and is correlated with cognitive decline. Our study using the ALPS index explored the influence of the age of first marijuana use and the number of lifetime uses on the glymphatic system. Furthermore, we evaluated the association between the ALPS index and cognitive performance in recreational marijuana users from the Washington University–University of Minnesota (WU-Minn) Human Connectome Project (HCP) consortium.²³ Gaining a deeper understanding of the alterations of glymphatic clearance following marijuana use could initiate strategies to reduce the risk of cognitive decline.

MATERIALS AND METHODS

Study Participants

The data analyzed in this study were obtained from the S1200 data set of the WU-Minn HCP consortium (https://www.humanconnectome.org/storage/app/media/documentation/s1200/HCP_S1200_Release_Reference_Manual.pdf).²³ The inclusion criteria of study participants (Fig 1) are provided in the Online Supplemental Data.

Marijuana Use

Following previous studies,^{1,24–28} we used “lifetime use” to categorize the study participants as nonusers (individuals with zero

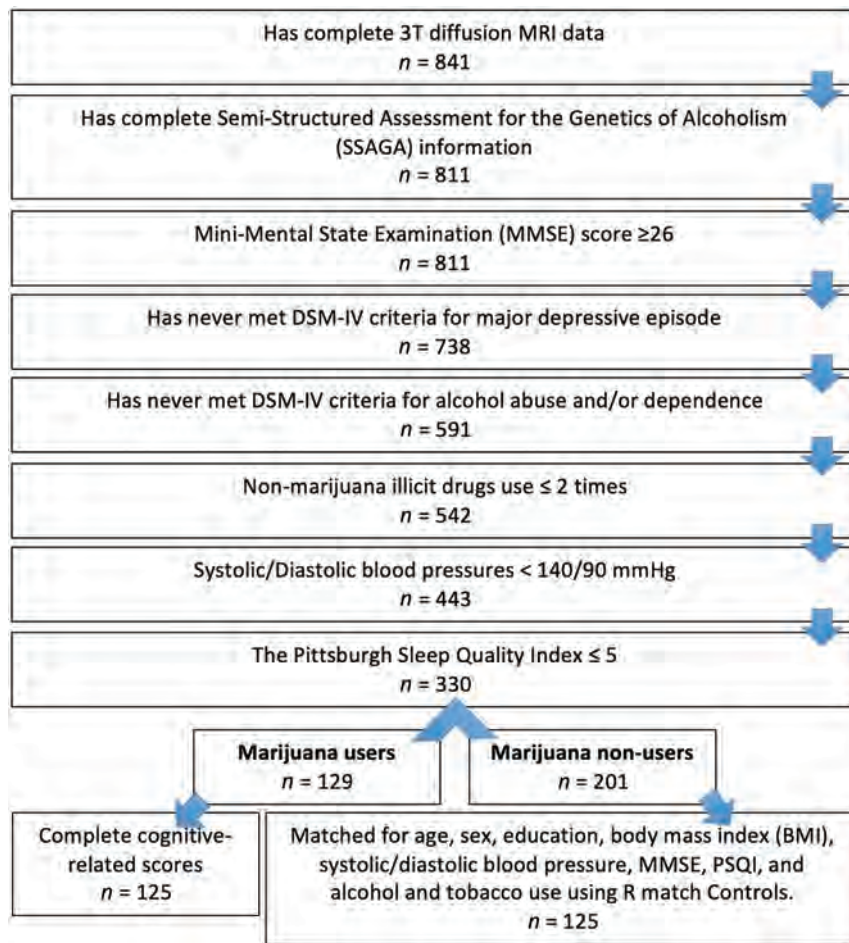


FIG 1. Flow chart of inclusion and exclusion criteria, along with the count of individuals meeting the criteria and included in the study population. MMSE indicates the Mini-Mental State Examination; DSM-IV, Diagnostic and Statistical Manual of Mental Disorders, 4th edition.

lifetime cannabis use) and users (those who reported using marijuana at least once in their lifetime). Marijuana use was assessed using self-report measures obtained through the Semi-Structured Assessment for the Genetics of Alcoholism (SSAGA). The number of times used was categorized as follows: 0 (never used), 1 (1–5 uses), 2 (6–10 uses), 3 (11–100 uses), 4 (101–999 uses), or 5 (≥ 1000 uses). The SSAGA categorized the age of first use as the following: 1 (14 years of age or younger), 2 (15 – 17 years of age), 3 (18 – 20 years of age), 4 (21 years of age or older), or 5 (never used). In this study, the age of first use was reverse-scored (0 [never used], 1 [21 years of age or older], 2 [15 – 17 years of age], 3 [18 – 20 years of age], 4 [14 years of age or younger]), yielding higher scores to indicate an earlier age of first use, aligning with the frequency of use measure.

Tobacco and Alcohol Use

The criteria of tobacco and alcohol use are provided in the Online Supplemental Data.

Imaging Data Acquisition and Preprocessing

Imaging data were acquired using a HCP-customized 3T Connectome Magnetom Skyra magnet (Siemens).²⁹ DWIs downloaded from the HCP portal underwent a minimal preprocessing pipeline.³⁰ To calculate the ALPS index, we obtained the DWIs

with 2 b-values, 0 and 1000 s/mm², extracted from the preprocessed data set. Further details of DWIs are provided in the Online Supplemental Data.

Calculation of the ALPS Index

The ALPS index was calculated using a validated semiautomated pipeline.³¹ The fractional anisotropy (FA) map of all individuals was initially registered into the FMRIB58_FA standard space (https://fsl.fmrib.ox.ac.uk/fsl/fslwiki/FMRIB58_FA) using both linear and nonlinear transformations. For ROI placement, 1 subject with the smallest degree of warping was selected. Using this subject's color-coded FA map, we placed spherical ROIs measuring 5 mm in diameter in the projection and association areas at the level of the bilateral lateral ventricle body (Fig 2). The resulting ROIs were then registered to the same FA template, and the position of the ROIs was visually confirmed for each participant. If necessary, a manual correction was performed by slightly adjusting the ROIs.

In the projection fibers area, the main fibers run along the z-axis direction, while the x-axis and y-axis are perpendicular to the main fibers. Moreover, in the association fibers area, the main fibers run in the direction of the y-axis, and the x-axis and z-axis are perpendicular

to the main fibers. Therefore, the ALPS index was derived from the ratio of the average values of the x-axis diffusivity in the projection fibers area (D_{xxproj}) and the x-axis diffusivity in the association fibers area ($D_{xxassoc}$) to the average values of the y-axis diffusivity in the projection fibers area (D_{yyproj}) and the z-axis diffusivity in the association fibers area ($D_{zzassoc}$), as shown below:

$$ALPS\ index = \frac{(\text{mean } [D_{xxproj}, D_{xxassoc}])}{(\text{mean } [D_{yyproj}, D_{zzassoc}])}.$$

The average values of left and right ALPS indices were evaluated. An ALPS index closest to 1 reflects minimal diffusion along the perivascular space, whereas a larger ratio indicates larger water diffusivity along the perivascular space.¹⁸

Furthermore, we extracted FA values, which serve as an index of WM integrity in the association and projection fibers, using identical ROIs. Subsequently, the statistical analyses incorporated the average FA values of both the left and right projection and association fibers.

Intracranial Volume Measurements

The intracranial volume (ICV) was obtained for each study participant and was used as a covariate in the statistical analyses. The

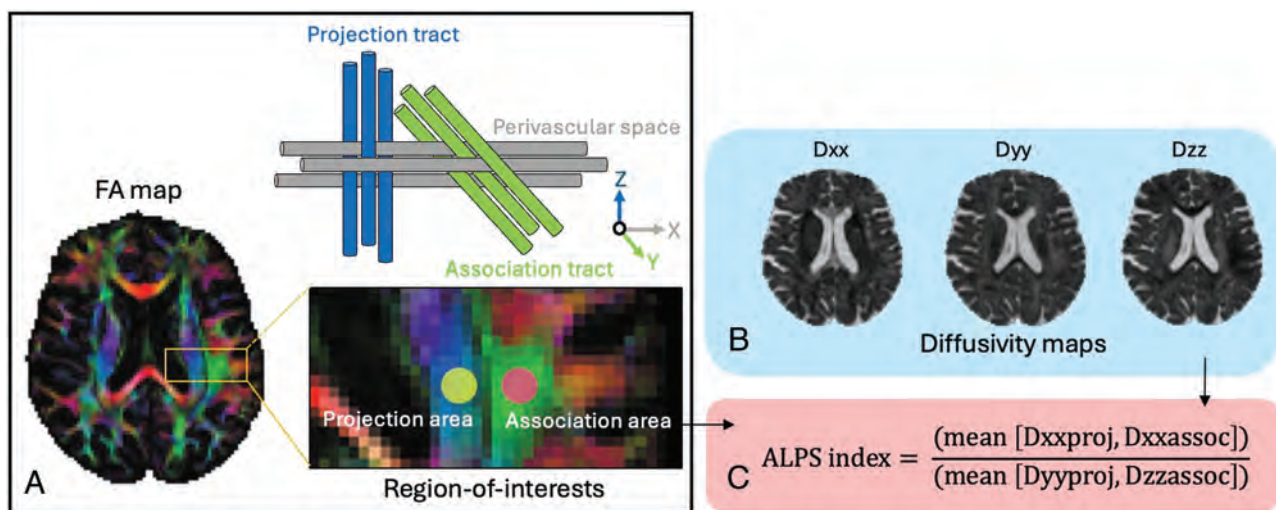


FIG 2. Calculation of the DTI index along the perivascular space (ALPS index). **A**, Color-coded FA map shows the distribution of projection fibers (blue, z-axis) and association fibers (green, y-axis) at the lateral ventricle level of the body. Spherical ROIs measuring 5 mm in diameter were positioned in projection and association areas. The perivascular space runs perpendicular to the projection and association tracts. **B**, Diffusivity maps in the x-axis (Dxx), y-axis (Dyy), and z-axis (Dzz). **C**, The ALPS index was derived from the ratio of the mean x-axis diffusivity in the projection area (Dxxproj) and x-axis diffusivity in the association area (Dxxassoc) to the mean of y-axis diffusivity in the projection area (Dyyproj) and z-axis diffusivity in the association area (Dzzassoc).

details of ICV measurements are provided in the Online Supplemental Data.

Statistical Analysis

Statistical analyses were conducted with SPSS Statistics Version 27 for Macintosh (IBM). The normality of the data was assessed using the Kolmogorov-Smirnov test. Demographic and clinical data of nonusers and users were analyzed using independent samples *t* tests for normally distributed continuous data or the Mann-Whitney *U* tests for non-normally distributed continuous data. For categorical variables, the χ^2 test was used. In all analyses, statistical significance was set at *P* (2-tailed) < .05.

The ALPS index was compared among nonusers and marijuana users with different ages of first use (nonuser group versus user group 1 [14 years of age or younger] versus group 2 [15–17 years of age] versus group 3 [18–20 years of age] versus group 4 [21 years of age or older]) or those with various frequencies of lifetime usage (nonuser group versus user group 1 [1–5 uses] versus group 2 [6–10 uses] versus group 3 [11–100 uses] versus group 4 [101–999 uses] versus group 5 [≥ 1000 uses]) using a univariate General Linear Model with a Bonferroni correction to adjust for multiple group comparisons. This analysis controlled for age, sex, years of education, tobacco use, alcohol use, the Pittsburgh Sleep Quality Index (PSQI) score, and the ICV (model 1). Marijuana use has been associated with loss of WM integrity, including in the association and projection fibers.⁷ Therefore, the average FA values, an index of WM integrity,³² measured in the ROIs of the association and projection fibers were included as control variables in the evaluation of the ALPS index, in addition to the covariates in model 1 (model 2).

Multiple linear regression (MLR) analysis was used to model the associations between the ALPS index (dependent variable) and the age of first marijuana use or number of lifetime uses. MLR analysis was also conducted to identify associations between

the ALPS index and cognitive assessment scores. The multicollinearity of predictor variables was addressed by assessing variance inflation factor (VIF) values, with VIF values ≤ 5 indicating the absence of multicollinearity.³³ Furthermore, we performed partial correlation tests to assess relationships between the ALPS index and variables, including the age of first marijuana use, lifetime use count, and cognition scores. In linear regression and partial correlation analyses, the same covariates as those included in the between-group comparison analyses (models 1 and 2) were used.

Additionally, we compared the average FA values measured in the ROIs of the association and projection fibers between nonusers and users with different ages of first use or those with various lifetime usage frequencies using a univariate General Linear Model, while controlling for age, sex, years of education, tobacco use, alcohol use, PSQI score, and ICV. Moreover, we performed partial correlation analysis to examine the association between the ALPS index and ICV across all subjects, while controlling for age, sex, years of education, tobacco use, alcohol use, and the PSQI scores as covariates.

RESULTS

Study Participants' Demographics, Clinical Characteristics, and Substance Use

In this study, we analyzed 250 subjects with an age range of 22–37 years, including 125 marijuana recreational users (43 men and 82 women; mean age, 28.60 [SD, 3.84] years) and 125 nonusers (44 men and 81 women; mean age, 28.82 [SD, 3.56] years). The demographic and clinical characteristics of participants are summarized in the Online Supplemental Data.

No differences were observed between nonusers and marijuana users in age, sex, years of education, body mass index, systolic and diastolic blood pressures, as well as the Mini-Mental State Examination scores. Marijuana users had significantly

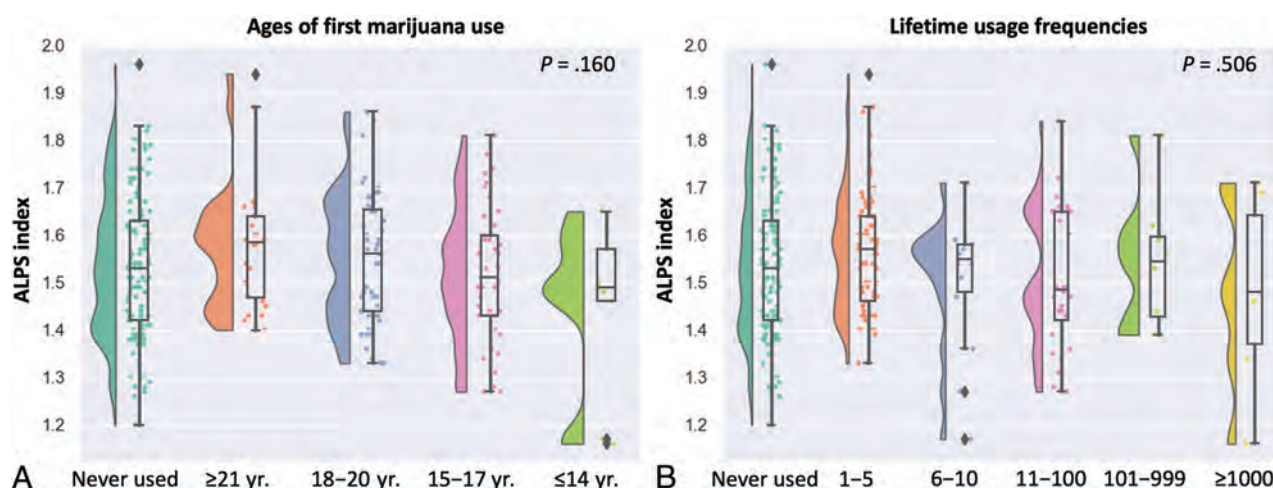


FIG 3. Raincloud plots of ALPS indices (A) among nonusers (individuals with zero lifetime cannabis use) and users (those who reported using marijuana at least once in their lifetime) with different ages of first use and (B) among nonusers and users with various lifetime usage frequencies. The *P* values correspond to a univariate General Linear Model after controlling for age, sex, years of education, tobacco use, alcohol use, PSQI score, and intracranial volume.

higher PSQI scores ($P = .022$) and significantly higher ($P < .001$) alcohol and tobacco usage. Additionally, marijuana users had significantly lower ICV compared with nonusers ($P = .033$).

Marijuana users had significantly lower correct responses ($P = .010$) and reaction times ($P = .011$) in the Fluid Intelligence Test compared with nonusers. No significant differences were observed in other cognitive test scores (Online Supplemental Data).

The Evaluation of ALPS Index

Between-Group Differences in ALPS Index. We found no significant differences in the ALPS index among nonusers and marijuana users with different ages of first use (model 1 [$P = .16$], model 2 [$P = .15$]; Fig 3A). Furthermore, we also observed no significant differences in the ALPS index among nonusers and marijuana users with various lifetime usage frequencies (model 1 [$P = .506$], model 2 [$P = .488$]; Fig 3B).

Associations between the Age of First Marijuana Use or the Number of Uses in a Lifetime and the ALPS Index in Marijuana Users. We observed that a lower ALPS index was associated with younger ages at first marijuana use in both linear regression (model 1: standardized β , -0.20 [standard error, SE: 0.016]; $P = .041$; VIF = 1.22; model 2 [standardized β , -0.20 ; SE: 0.016]; $P = .037$; VIF = 1.23) and partial correlation (model 1 [$r = -0.19$; $P = .041$], model 2 [$r = -0.19$; $P = .037$]) analyses. However, no significant association was found between the ALPS index and the number of marijuana uses in both the linear regression (model 1 [standardized β , -0.090 ; SE: 0.011]; $P = .36$; VIF = 1.25; model 2 [standardized β , -0.088 ; SE: 0.011]; $P = .37$; VIF = 1.25) and partial correlation (model 1 [$r = -0.086$; $P = .36$], model 2 [$r = -0.084$; $P = .37$]) analyses.

Associations between Cognitive Performance and the ALPS Index in Marijuana Users. A lower ALPS index was significantly associated with lower accuracy in the working memory 0-back task in MLR (model 1 [standardized β , 0.20; SE: 0.001]; $P = .042$;

VIF = 1.27; model 2 [standardized β , 0.22; SE: 0.001]; $P = .030$; VIF = 1.32) and partial correlation (model 1 [$r = 0.19$; $P = .041$], model 2 [$r = 0.20$; $P = .030$]) analyses. Additionally, a lower ALPS index was associated with fewer correct responses in the Fluid Intelligence Test in MLR (model 1 [standardized β , 0.19; SE: 0.003]; $P = .045$; VIF = 1.16; model 2 [standardized β , 0.21; SE: 0.003]; $P = .031$; VIF = 1.20) and partial correlation (model 1 [$r = 0.19$; $P = .040$]; model 2 [$r = 0.21$; $P = .031$]) analyses. These findings suggest subtle-but-substantial effects of marijuana use on working memory and fluid intelligence.

Additional Analyses

Between-Group Differences in FA. We found no significant differences in FA values among nonusers and marijuana users with different ages of first use ($P = .866$) or those with various lifetime usage frequencies ($P = .742$).

Association between the ALPS Index and ICV. No significant association was observed between the ALPS index and ICV ($r = -0.11$; $P = .257$).

DISCUSSION

The present study has expanded the potential applications of diffusion MR imaging-based measures, including the ALPS index, as noninvasive, indirect indicators of the glymphatic system in young adults. Our results provide evidence of the adverse effects of younger age at first use of marijuana on the glymphatic system function, as indexed by the ALPS index. Furthermore, associations were observed between a lower ALPS index and impaired working memory and fluid intelligence in marijuana users.

Our findings suggest that an earlier age of first marijuana use is linked to potential impairment of the glymphatic system, indicated by a lower ALPS index. A lower ALPS index appears to signify reduced water diffusivity within the perivenous spaces, possibly due to compromised glymphatic clearance flow, specifically, a reduction in CSF-ISF drainage toward the perivenous

space.¹⁸ However, group comparison revealed no significant differences in the ALPS index among nonusers and marijuana users with different ages of first marijuana use or those with various lifetime usage frequencies. This observation could imply that the marijuana use in our study sample might not be severe enough to yield noticeable effects. Our findings align with a prior study assessing HCP data, indicating that an earlier onset of marijuana use was associated with lower WM coherence.¹ They found no significant differences in WM between marijuana users and nonusers, similar to our results.¹ Furthermore, these negative findings may be because of the imbalanced number of subjects in user subgroups, particularly the limited number of younger age first-time marijuana users and those with a higher frequency of lifetime use, possibly reducing the statistical power. Future studies should aim to include a larger and more balanced number of subjects in each user subgroup.

The early initiation of substance use has been observed to impact the developing adolescent brain, including the endocannabinoid system.³⁴ $\Delta 9$ -tetrahydrocannabinol, the primary psychoactive component of cannabis, acts as an agonist of the type 1 cannabinoid (CB1) receptor.³⁵ CB1 receptors are expressed in astrocytes, and mounting evidence suggests that persistent activation of mouse astroglial CB1 receptors associated with mitochondria disrupts glucose metabolism and lactate production in the brain. Consequently, this disturbance leads to changes in neuronal activity and impaired cognitive function.³⁶ Astrocytes play a crucial role in the glymphatic system by creating perivascular spaces with their vascular endfeet around the cerebral vasculature.³⁷ Thus, it is possible that marijuana use disrupts glymphatic flow by affecting astrocyte function, warranting further investigation.

The use of cannabis, especially at an early age and with frequent usage, has been associated with an increased risk of cognitive impairment.^{38,39} Consistent with a previous study,⁴⁰ marijuana users in our cohort exhibited significantly lower Fluid Intelligence Test scores compared with nonusers, indicating a reduced ability to think logically and solve problems in novel, unfamiliar situations. We also observed a correlation between a lower ALPS index and a decrease in the number of correct responses in the Fluid Intelligence Test. Furthermore, despite no difference between marijuana users and nonusers, we identified a correlation between a lower ALPS index and a decrease in accuracy on the working memory test. Early investigations of working memory in marijuana users have indicated that acute cannabis use is associated with impairment in holding, manipulating, and remembering information.⁴¹ A study comparing groups based on amyloid- β status found a more significant decline in fluid intelligence among those in the amyloid- β -positive group compared with the amyloid- β -negative group.⁴² However, this study involved older adults. On the basis of our findings, further research should evaluate amyloid- β deposition in young adults, particularly in marijuana users. $\Delta 9$ -tetrahydrocannabinol has been suggested as the primary contributor to working memory deficits linked to the duration of cannabis use.⁴¹ Taken together, our findings suggest that cognitive impairment related to marijuana use might be linked to reduced clearance of brain waste products (eg, amyloid- β) due to glymphatic system

dysfunction, potentially associated with the activation of CB1 receptors.

Our findings revealed a significant difference in ICV between marijuana users and nonusers, with marijuana users having lower ICV values. Most interesting, prior studies have consistently reported no significant differences in ICV between individuals who use marijuana and those who do not.^{43,44} Consequently, we assumed that the observed lower ICV values among marijuana users may be attributed to individual variation. To account for the potential influence of ICV on the evaluation of the ALPS index, we incorporated ICV as a covariate in all statistical analyses. Furthermore, we assessed the correlation between ICV and the ALPS index and found no significant results. However, a previous study suggested that marijuana use during adolescence is linked to reduced cortical thickness, particularly in the prefrontal regions.²⁸ In our future research, we will explore the correlation between the ALPS index and regional cortical thickness to gain further insight.

The present study has some limitations. First, it is a cross-sectional study. To assess changes in the marijuana-related ALPS index, future studies should use longitudinal data from larger population samples with a balanced representation of marijuana usage levels. Second, the study did not use MR imaging-based tracers, considered the current criterion standard for assessing glymphatic function in humans.¹⁷ However, the ALPS index showed a high correlation with glymphatic clearance function, as determined through glymphatic MR imaging following intrathecal administration of gadolinium.¹⁴ Third, the ALPS index does not solely assess the diffusivity of the perivenous space surrounding the deep medullary vein; it is also influenced by the adjacent WM microstructure within the ROI. As a result, the interpretation of the ALPS index requires careful consideration and warrants additional investigation. However, the significant associations between the ALPS index and younger ages at first marijuana use or cognitive performance were maintained even after including FA as a covariate in model 2. Furthermore, we did not observe significant changes in FA between nonusers and users with different ages of first use or various levels of lifetime usage. These findings suggest that the ALPS index measurements in marijuana users identified in this study were primarily attributed to changes in water diffusivity in the perivenous space and were less likely affected by alterations in WM integrity. However, considering that marijuana users have shown reduced WM integrity and given the known role of the glymphatic system in maintaining this integrity, further research is warranted to explore the potential link between the integrity of individual WM tracts and glymphatic clearance in marijuana users. Finally, this study focused only on the ALPS index; however, there are some alternative methods for evaluating the human glymphatic system, each with its own advantages and disadvantages, as recently nicely summarized by Kamagata et al.¹⁷

CONCLUSIONS

Our findings show that a lower ALPS index value was correlated with an earlier age of first marijuana use. The lower ALPS index observed in recreational marijuana users may indicate a potential

link between marijuana use and glymphatic function impairment. This study suggests associations between glymphatic dysfunction in marijuana users and deficits in working memory and fluid intelligence. However, no significant differences in the ALPS index were observed among nonusers and marijuana users with different ages of first marijuana use or those with various lifetime usage frequencies. The lack of significant findings might be because of the nature of marijuana use in our study sample, which may not have been severe enough, and the imbalanced number of subjects in user subgroups. Future studies should aim to include subjects with heavier use and a more balanced number of subjects in each user subgroup. Finally, it is important to exercise caution when interpreting the results due to the limitations of this study.

Disclosure forms provided by the authors are available with the full text and PDF of this article at www.ajnr.org.

REFERENCES

- Orr JM, Paschall CJ, Banich MT. **Recreational marijuana use impacts white matter integrity and subcortical (but not cortical) morphometry.** *Neuroimage Clin* 2016;12:47–56 CrossRef Medline
- United Nations Office on Drugs. **World Drug Report 2022.** <https://www.unodc.org/unodc/data-and-analysis/world-drug-report-2022.html>. Accessed May 3, 2023
- Blest-Hopley G, Colizzi M, Giampietro V, et al. **Is the adolescent brain at greater vulnerability to the effects of cannabis? A narrative review of the evidence.** *Front Psychiatry* 2020;11:859 CrossRef Medline
- Jacobus J, Tapert SF. **Effects of cannabis on the adolescent brain.** *Curr Pharm Des* 2014;20:2186–93 CrossRef Medline
- Volkow ND, Baler RD, Compton WM, et al. **Adverse health effects of marijuana use.** *N Engl J Med* 2014;370:2219–27 CrossRef Medline
- Zhang D, Li X, Li B. **Glymphatic system dysfunction in central nervous system diseases and mood disorders.** *Front Aging Neurosci* 2022;14:873697 CrossRef Medline
- Robinson EA, Gleeson J, Arun AH, et al. **Measuring white matter microstructure in 1,457 cannabis users and 1,441 controls: a systematic review of diffusion-weighted MRI studies.** *Front Neuroimaging* 2023;2:1129587 CrossRef Medline
- Andica C, Kamagata K, Takabayashi K, et al. **Neuroimaging findings related to lymphatic system alterations in older adults with metabolic syndrome.** *Neurobiol Dis* 2023;177:105990 CrossRef Medline
- Kamagata K, Andica C, Takabayashi K, et al; Alzheimer's Disease Neuroimaging Initiative. **Association of MRI indices of lymphatic system with amyloid deposition and cognition in mild cognitive impairment and Alzheimer disease.** *Neurology* 2022;99:e2648–60 CrossRef Medline
- Liff JJ, Wang M, Liao Y, et al. **A paravascular pathway facilitates CSF flow through the brain parenchyma and the clearance of interstitial solutes, including amyloid beta.** *Sci Transl Med* 2012;4:147ra111 CrossRef Medline
- Mestre H, Mori Y, Nedergaard M. **The brain's lymphatic system: current controversies.** *Trends Neurosci* 2020;43:458–66 CrossRef Medline
- Kress BT, Liff JJ, Xia M, et al. **Impairment of paravascular clearance pathways in the aging brain.** *Ann Neurol* 2014;76:845–61 CrossRef Medline
- Xia M, Yang L, Sun G, et al. **Mechanism of depression as a risk factor in the development of Alzheimer's disease: the function of AQP4 and the lymphatic system.** *Psychopharmacology (Berl)* 2017;234:365–79 CrossRef Medline
- Sabayan B, Westendorp RG. **Neurovascular-lymphatic dysfunction and white matter lesions.** *Geroscience* 2021;43:1635–42 CrossRef Medline
- Iliff JJ, Lee H, Yu M, et al. **Brain-wide pathway for waste clearance captured by contrast-enhanced MRI.** *J Clin Invest* 2013;123:1299–309 CrossRef Medline
- Kanda T, Ishii K, Kawaguchi H, et al. **High signal intensity in the dentate nucleus and globus pallidus on unenhanced T1-weighted MR images: relationship with increasing cumulative dose of a gadolinium-based contrast material.** *Radiology* 2014;270:834–41 CrossRef Medline
- Kamagata K, Saito Y, Andica C, et al. **Noninvasive magnetic resonance imaging measures of lymphatic system activity.** *J Magn Reson Imaging* 2024;59:1476–93 CrossRef Medline
- Taoka T, Masutani Y, Kawai H, et al. **Evaluation of lymphatic system activity with the diffusion MR technique: diffusion tensor image analysis along the perivascular space (DTI-ALPS) in Alzheimer's disease cases.** *Jpn J Radiol* 2017;35:172–78 CrossRef Medline
- Zhang W, Zhou Y, Wang J, et al. **Glymphatic clearance function in patients with cerebral small vessel disease.** *Neuroimage* 2021;238:118257 CrossRef Medline
- Steward CE, Venkatraman VK, Lui E, et al. **Assessment of the DTI-ALPS parameter along the perivascular space in older adults at risk of dementia.** *J Neuroimaging* 2021;31:569–78 CrossRef Medline
- Lee HJ, Lee DA, Shin KJ, et al. **Glymphatic system dysfunction in patients with juvenile myoclonic epilepsy.** *J Neurol* 2022;269:2133–39 CrossRef Medline
- Lin LP, Su S, Hou W, et al. **Glymphatic system dysfunction in pediatric acute lymphoblastic leukemia without clinically diagnosed central nervous system infiltration: a novel DTI-ALPS method.** *Eur Radiol* 2023;33:3726–34 CrossRef Medline
- Van Essen DC, Smith SM, Barch DM, et al; WU-Minn HCP Consortium. **The WU-Minn Human Connectome Project: an overview.** *Neuroimage* 2013;80:62–79 CrossRef Medline
- Allen JP, Danoff JS, Costello MA, et al. **Lifetime marijuana use and epigenetic age acceleration: a 17-year prospective examination.** *Drug Alcohol Depend* 2022;233:109363 CrossRef Medline
- Andersson F, Sundin E, Magnusson C, et al. **Prevalence of cannabis use among young adults in Sweden comparing randomized response technique with a traditional survey.** *Addiction* 2023;118:1801–10 CrossRef Medline
- Auer R, Vittinghoff E, Yaffe K, et al. **Association between lifetime marijuana use and cognitive function in middle age: the Coronary Artery Risk Development in Young Adults (CARDIA) study.** *JAMA Intern Med* 2016;176:352–61 CrossRef Medline
- Wise J. **Long term marijuana use is linked to impaired verbal memory.** *BMJ* 2016;352:i619 CrossRef Medline
- Albaugh MD, Ottino-Gonzalez J, Sidwell A, et al; IMAGEN Consortium. **Association of cannabis use during adolescence with neurodevelopment.** *JAMA Psychiatry* 2021;78:1–11 CrossRef Medline
- Van Essen DC, Ugurbil K, Auerbach E, et al; WU-Minn HCP Consortium. **The Human Connectome Project: a data acquisition perspective.** *Neuroimage* 2012;62:2222–31 CrossRef Medline
- Glasser MF, Sotiropoulos SN, Wilson JA, et al; WU-Minn HCP Consortium. **The minimal preprocessing pipelines for the Human Connectome Project.** *Neuroimage* 2013;80:105–24 CrossRef Medline
- Taoka T, Ito R, Nakamichi R, et al. **Reproducibility of diffusion tensor image analysis along the perivascular space (DTI-ALPS) for evaluating interstitial fluid diffusivity and lymphatic function: CHanges in Alps index on Multiple conditiON acquisition eXperiment (CHAMONIX) study.** *Jpn J Radiol* 2022;40:147–58 CrossRef Medline
- Andica C, Kamagata K, Hatano T, et al. **MR biomarkers of degenerative brain disorders derived from diffusion imaging.** *J Magn Reson Imaging* 2020;52:1620–36 CrossRef Medline
- Kim JH. **Multicollinearity and misleading statistical results.** *Korean J Anesthesiol* 2019;72:558–69 CrossRef Medline
- Renard J, Krebs MO, Le Pen G, et al. **Long-term consequences of adolescent cannabinoid exposure in adult psychopathology.** *Front Neurosci* 2014;8:361 CrossRef Medline

35. Hodges EL, Ashpole NM. **Aging circadian rhythms and cannabinoids.** *Neurobiol Aging* 2019;79:110–18 CrossRef Medline
36. Jimenez-Blasco D, Busquets-Garcia A, Hebert-Chatelain E, et al. **Glucose metabolism links astroglial mitochondria to cannabinoid effects.** *Nature* 2020;583:603–08 CrossRef Medline
37. Mogensen FL, Delle C, Nedergaard M. **The glymphatic system (en)during inflammation.** *Int J Mol Sci* 2021;22:7491 CrossRef Medline
38. Morin JG, Afzali MH, Bourque J, et al. **A population-based analysis of the relationship between substance use and adolescent cognitive development.** *Am J Psychiatry* 2019;176:98–106 CrossRef Medline
39. Volkow ND, Swanson JM, Evins AE, et al. **Effects of cannabis use on human behavior, including cognition, motivation, and psychosis: a review.** *JAMA Psychiatry* 2016;73:292–97 CrossRef Medline
40. Petker T, Owens MM, Amlung MT, et al. **Cannabis involvement and neuropsychological performance: findings from the Human Connectome Project.** *J Psychiatry Neurosci* 2019;44:414–22 CrossRef Medline
41. Morie KP, Potenza MN. **A mini-review of relationships between cannabis use and neural foundations of reward processing, inhibitory control and working memory.** *Front Psychiatry* 2021;12:657371 CrossRef Medline
42. Harrington KD, Dang C, Lim YY, et al. **The effect of preclinical Alzheimer's disease on age-related changes in intelligence in cognitively normal older adults.** *Intelligence* 2018;70:22–29 CrossRef
43. Gilman JM, Kuster JK, Lee S, et al. **Cannabis use is quantitatively associated with nucleus accumbens and amygdala abnormalities in young adult recreational users.** *J Neurosci* 2014;34:5529–38 CrossRef Medline
44. Weiland BJ, Thayer RE, Depue BE, et al. **Daily marijuana use is not associated with brain morphometric measures in adolescents or adults.** *J Neurosci* 2015;35:1505–12 CrossRef Medline

The Differentiation between Progressive Disease and Treatment-Induced Effects with Perfusion-Weighted Arterial Spin-Labeling in High-Grade Gliomas

Christina Maria Flies, Tom Jan Snijders, Beverly Iendra De Leeuw, Emiel Alexander van Maren, Bart Jean Pieter Kersten, Joost Jacobus Cornelis Verhoeff, Filip Yves Francine De Vos, Pierre Alain Robe, Jeroen Hendrikse, and Jan Willem Dankbaar



ABSTRACT

BACKGROUND AND PURPOSE: Treatment-induced effects are difficult to differentiate from progressive disease in radiologically progressing diffuse gliomas after treatment. This retrospective, single-center cohort study investigated the diagnostic value of arterial spin-labeling perfusion in differentiating progressive disease from treatment-induced effects in irradiated patients with a high-grade glioma.

MATERIALS AND METHODS: Adults with a high-grade glioma diagnosed between January 1, 2012, and December 31, 2018, with a new or increasing contrast-enhancing lesion after radiotherapy with or without chemotherapy and arterial spin-labeling were consecutively included. Arterial spin-labeling is part of the routine follow-up examinations of patients with a high-grade glioma. The outcomes of progressive disease or treatment-induced effects were defined after histologic or >6 weeks radiologic follow-up. Two neuroradiologists graded the arterial spin-labeling visually as negative (hypointense to gray matter) or positive (iso-/hyperintense). Additionally, the arterial spin-labeling signal intensity in the enhancing lesion was compared quantitatively with that in the contralateral normal brain. Diagnostic test properties and the Cohen κ inter- and intrarater reliability were determined. We present data according to the time after radiation therapy.

RESULTS: We included 141 patients with 173 lesions (median age, 63 years). Ninety-four (54%) lesions showed treatment-induced effects, and 79 (46%), progressive disease. For visual analysis, the ORs of an arterial spin-labeling positive for progressive disease in the group with progression within 3, between 3 and 6, and after 6 months after radiation therapy were 0.65 (95% CI, 0.28–1.51; $P = .319$), 3.5 (95% CI, 0.69–17.89; $P = .132$), and 6.8 (95% CI, 1.48–32; $P = .014$). The areas under the curve were 0.456, 0.652, and 0.719. In quantitative analysis, the areas under the curve were 0.520, 0.588, and 0.587 in these groups. Inter- and intrarater reliability coefficients were 0.67 and 0.62.

CONCLUSIONS: Arterial spin-labeling performed poorly in differentiating progressive disease from treatment-induced effects in high-grade gliomas within 6 months after radiation therapy, with fair performance after this period. Arterial spin-labeling may need to be combined with other imaging features and clinical information for better performance.

ABBREVIATIONS: ASL = arterial spin-labeling; AUC = area under the curve; HGG = high-grade glioma; PD = progressive disease; PPV = positive predictive value; RT = radiotherapy; TIE = treatment-induced effects; WHO = World Health Organization

High-grade gliomas (HGG) are the most common type of primary, malignant brain tumors and are subdivided into World Health Organization (WHO) grades 3 and 4.¹ Molecularly,

this group consists of isocitrate dehydrogenase (*IDH*)-mutated astrocytomas, 1p/19q-codeleted oligodendrogliomas, and the most lethal, *IDH* wild-type glioblastomas.

After treatment, almost all patients develop a new or increasing contrast-enhancing lesion during follow-up with MR imaging. Such a lesion originates from either true progressive disease (PD), from treatment-induced effects (TIE), or a mix of both. TIE consist of posttreatment alterations of tumor cells and healthy brain tissue, including pseudoprogression and radionecrosis.

Early TIE within 3 months after completion of radiation therapy with or without chemotherapy are common and notoriously difficult to discern from true PD.^{2,3} From 3 to 6 months postradiotherapy, early-delayed TIE are still common,⁴ whereas progression after 6 months may consist of “late radionecrosis,” but it is more likely to be PD.

Received December 6, 2023; accepted after revision February 5, 2024.

From the Department of Neurology and Neurosurgery (C.M.F., T.J.S., B.J.P.K., P.A.R.), UMC Utrecht Brain Center, University Medical Center Utrecht, Utrecht, the Netherlands; Departments of Radiology (E.A.v.M., J.H., J.W.D.), Radiation Oncology (J.J.C.V.), and Medical Oncology (F.Y.F.D.V.), University Medical Center Utrecht, Utrecht, the Netherlands; and Faculty of Medicine (B.J.P.K.), Utrecht University, Utrecht, the Netherlands.

This work was supported by a donation from the Stopphersenkanker.nu Foundation to T.J.S and F.Y.F.D.V. and the Foundation Vrienden UMC Utrecht.

Please address correspondence to Tom Jan Snijders, MD, University Medical Center Utrecht, Heidelberglaan 100, 3584 CX, Utrecht, the Netherlands; e-mail: T.J.Snijders@umcutrecht.nl; @UMCUtrecht; @UMCU_Intl

Indicates article with online supplemental data.

<http://dx.doi.org/10.3174/ajnr.A8336>

PD and TIE often have similar appearances on conventional MR imaging. However, the diagnosis of PD or TIE determines the further course of treatment because PD generally implies a decision to discontinue ongoing therapy and/or start the next-line therapy.

Gradually, perfusion MR imaging became part of routine clinical follow-up in patients with a HGG and is used most commonly as a tool to discriminate high-grade from low-grade tumors, or PD from TIE. Arterial spin-labeling (ASL) is a perfusion technique with no need for an IV contrast agent. Magnetized (labeled) water molecules in arterial blood serve as an endogenous tracer and are followed along the capillaries into the tissue. The images are obtained by subtracting the labeled from the nonlabeled control images.⁵

In previous retrospective and prospective studies that investigated ASL for the differentiation of PD and TIE, areas under the receiver operating curve (AUC) between 0.875 and 0.967, sensitivities of 53.9%–100%, and specificities of 50%–100% have been reported in small series (21–69 patients) with mainly HGG.^{6–14} Most of these authors manually placed an ROI within the contrast-enhancing lesion on ASL and used a contralateral ROI for normalization to calculate a relative CBF.^{7,8,10,13,15,16} To reproduce these findings in a larger sample, with specific attention to the diagnostic value at different time points postradiation, we present a retrospective cohort study of patients with a HGG and a new or increasing contrast-enhancing lesion after radiotherapy with or without chemotherapy. Our main hypothesis stated that a positive/high ASL perfusion signal forms a reliable diagnostic marker of PD.

MATERIALS AND METHODS

Patients had previously given written informed consent for the use of MR images for response evaluation in the context of another study, which was approved by the Medical Ethical/Biobank Committee of the University Medical Center Utrecht (protocol No.16–342/16–229).

For this single-center, retrospective cohort study, all consecutive adults diagnosed with a diffuse glioma by surgery between January 1, 2012, and December 31, 2018, who developed a new or increasing contrast-enhancing lesion on T1 MR imaging with contrast agent (progression MR imaging) after treatment with RT with an available ASL (index test) from the same date or shortly after and a reference test, were eligible for inclusion. Patients who received bevacizumab previous to or during ASL were excluded.

A new or increasing contrast-enhancing lesion was defined as an increase on T1 MR imaging with contrast agent that was described in the radiology reports. Small lesions, defined as smaller than the 7-mm ASL voxel thickness, were excluded.

The reference test consisted of radiologic follow-up of at least 6 weeks or preferably histologic follow-up. Radiologic PD was defined as further progression during a minimum of 6 weeks follow-up after an initial increase and at least 1 follow-up MR imaging described in the radiology reports and confirmed by the multidisciplinary meeting. Radiologic TIE were defined as stable/regressive contrast-enhancing lesions without a change in treatment during a minimum of 6 weeks and at least 1 follow-up MR imaging, according to the modified Response Assessment

in Neuro-Oncology (RANO; <https://ascopubs.org/doi/abs/10.1200/JCO.23.01059>) criteria.¹⁷ Histologic PD was defined as any proliferating tumor, and histologic TIE, as pure TIE with no proliferation and ≤ 1 mitosis per high-power-field. Mixed lesions (with TIE and proliferating tumor) were treated as PD. All lesions up to a maximum of 5 per patient were reviewed individually.

Histopathologic diagnoses were interpreted according to the WHO 2007 or 2016 criteria, depending on the year of the first resection. We updated all the diagnoses to a WHO 2016 interpretation for better comparisons.

A junior researcher (B.I.d.L.), blinded to the ASL results, extracted the clinical data and the reference standard from the electronic patient files. Clinical data included sex, age at the time of ASL, tumor type, and type of surgery and treatment. A subtotal resection was defined as residual enhancement on the postoperative MR imaging.

Time-to-progression was defined as the time from the end of RT to the progression MR imaging and was converted into 3 categories: within 3, between 3 and 6, and after 6 months after RT. All analyses were performed separately for these time-based categories to reflect clinical practice.

Duration of follow-up was defined as the time from the ASL to the reference standard.

Imaging Parameters

Pseudocontinuous ASL perfusion MR imaging was performed on a 3T MR imaging scanner (Ingenia, Ingenia CX, Achieva; Philips Healthcare) with the following sequence parameters: TR/TE, 4000/16 ms; flip angle, 90°; field of view, 240 × 240 × 119 mm (right/left, anterior/posterior, foot/head); section thickness, 7 mm; in-plane voxel, size, 3 × 3 × 7 mm; number of slices in the acquisition, 17; water-fat shift (pixel)/bandwidth (Hz), 8.254/52.6; postlabeling delays, 1525 ms; readout type, 2DEPI; background suppression pulses on; label duration, 1650 ms; and total scan time, around 3 minutes 20 seconds. The parameters for the 3D T1-weighted imaging included TR/TE, 5.3/2.4 ms; flip angle, 10°; field of view, 230 × 230 × 160 mm (right/left, anterior/posterior, foot/head); and gap, –0.5 mm.

Analysis of the Index Test

The qualitative analysis was based on the method of a previous publication:¹⁸ Two neuroradiologists (J.W.D. with 11 years of experience, E.A.v.M. with 2 years of experience), blinded to the outcome and clinical data, visually graded the randomly ordered ASL images as the following: 0, hypointensity; 1, isointensity; and 2, hyperintensity, compared with cortical normal-appearing gray matter on the perfusion-weighted maps. Subsequently, the ASL results were dichotomized as positive (grades 1–2) or negative (grade 0). As a sensitivity analysis, we repeated the calculations with grade 2 scans classified as positive, and grade 0, as negative, after omitting the grade 1 scans.

The first observer (J.W.D.) evaluated all ASL images, and we used these results for our main analysis. The second observer (E.A.v.M.) evaluated a subset for an interrater reliability analysis. After 12 weeks to avoid any recall, the first observer re-evaluated a subset for an intrarater reliability analysis. The sample size for the interrater analysis was calculated with the sample size

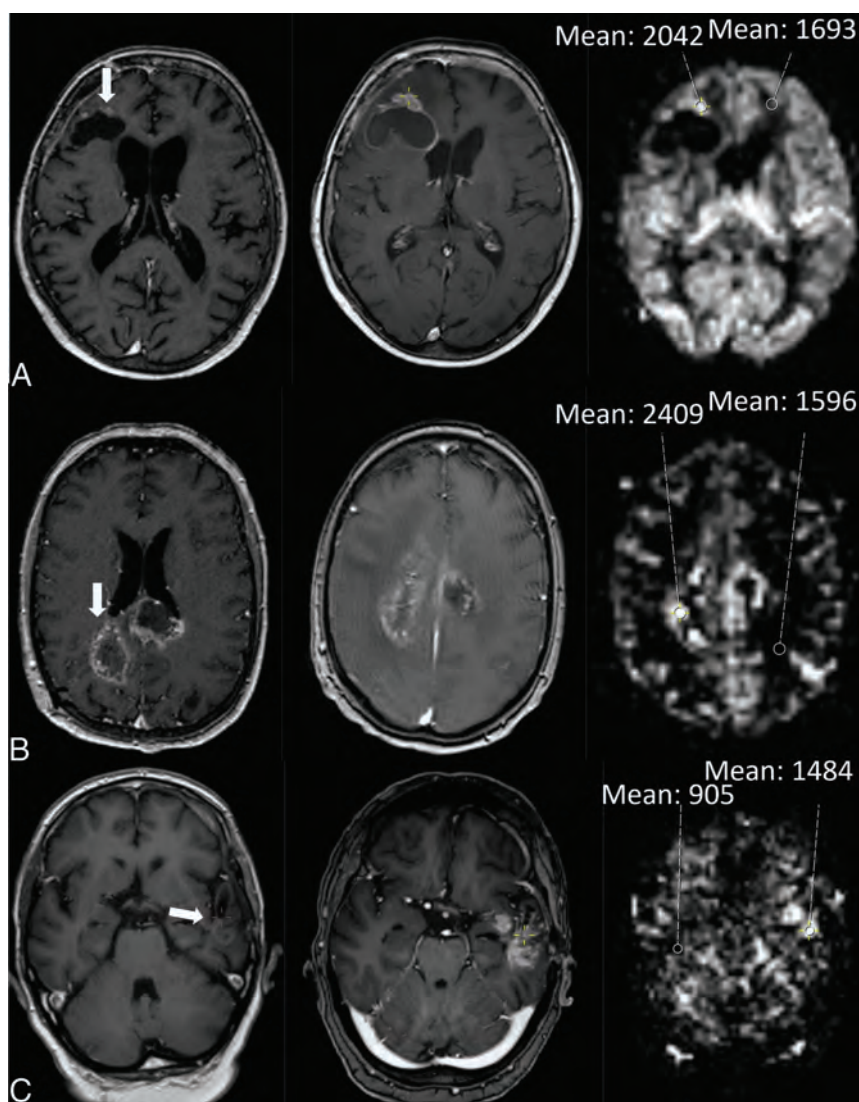


FIG 1. Illustration of an assessment of PD in each timeframe: within 3, 3–6, and after 6 months after RT. The quantitative cutoffs for maximum sensitivity and specificity for PD were respectively 2.2, 1.3, and 1.3. *A*, A 75-year-old woman with an *IDH* wild-type glioblastoma was treated with RT. The axial T1 MR imaging with contrast agent on the left shows contrast enhancement (CE) around the surgical cavity (arrow). Two months later (middle), the CE has grown. On the corresponding ASL image on the right, the ASL was visually rated as hyperperfusion, and the mean signal intensity of an ROI in the tumor was compared with the contralateral white matter. *B*, A 55-year-old man with an *IDH* wild-type glioblastoma was treated with temozolomide-based chemoradiation. The axial T1 MR imaging with contrast agent on the left shows subependymal CE (arrow). After 3.5 months (middle), the CE has grown. On the corresponding ASL image on the right, the ASL was visually rated as hyperperfusion. *C*, A 64-year-old man with an *IDH* wild-type glioblastoma was treated with temozolomide-based chemoradiation. The axial T1 MR image with contrast agent on the left shows CE around the surgical cavity (arrow). After 9.4 months (middle), the CE has grown. On the corresponding ASL image on the right, the ASL was visually rated as hyperperfusion.

estimator N2.cohen.kappa in R statistical and computing software (<http://www.r-project.org/>) with the following values: probability of either score = 0.3; 0.3; 0.4, true $\kappa = 0.7$ based on previous literature,^{18–20} null hypothesis = 0.4, two-sided $\alpha = .05$, and power = 0.8. We approximately doubled the required sample size of 45 to 88 (package irr, R, Version 4.0.3 [October 10, 2020; <https://www.npckd.org/p/r/4.0.3>]). The 88 patients (108 lesions) were chosen at random.

Another junior researcher (B.J.P.K.), blinded to the clinical data, the outcome, and the qualitative ASL results, performed the quantitative analysis. On the basis of the previous literature, we used a crosshair cursor on the T1 MR imaging with contrast agent and drew an ROI of 29 mm² in the contrast-enhancing lesion in the region showing the highest perfusion signal on ASL by number (not by CBF). The signal-intensity value of the tumor was then divided by the intensity value of a reference ROI in the contralateral white matter. Forty-four lesions (one-quarter of 173) were reviewed by an experienced neuroradiologist (J.W.D.) for consistency. A clinical researcher (C.M.F.) performed the data entry, cleaning, and analysis. An illustration of PD and TIE in each timeframe (within 3, from 3 to 6, and after 6 months after RT) is shown in Figs 1 and 2.

Statistical Analysis

For the qualitative image analysis, an OR with a 95% CI and *P* value was calculated. The diagnostic value was estimated with an AUC, sensitivity, specificity, and positive (PPV) and negative predictive value. The outcome set of the quantitative image analysis consisted of an AUC and the determination of a signal-intensity cutoff value on the ROC curve maximizing sensitivity and specificity. Furthermore, we calculated an OR with a 95% CI and *P* value after categorization of the signal-intensity values based on the cutoff value.

We performed our main analyses separately for each timeframe: progression before 3, between 3 and 6, and after 6 months after RT. We further performed exploratory analyses in the following subgroups: patients with a glioblastoma treated with temozolomide-based chemoradiation and a histologic reference standard. SPSS, Version 26.0.0.1 (2019;

IBM) and MedCalc for Windows, Version 20.019 (2021, MedCalc Software) were used for the calculations.

The funding organizations did not take part in the study design, execution, analysis, or manuscript writing.

RESULTS

In total, 799 patients were reviewed, and 179, with 266 lesions met the inclusion criteria. Finally, 173 lesions from 141 patients

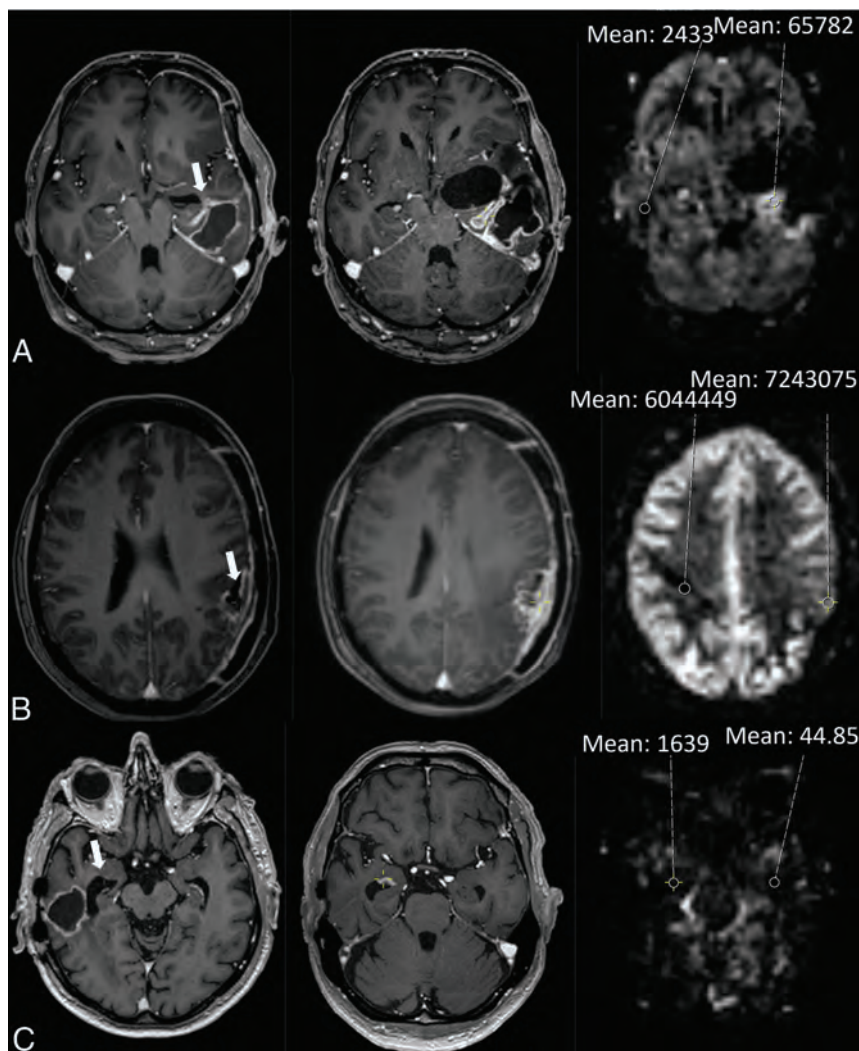


FIG 2. Illustration of an assessment of treatment-induced effects in each timeframe: within 3, 3–6, and after 6 months after RT. **A,** A 42-year-old man with an *IDH* wild-type glioblastoma was treated with temozolomide-based chemoradiation. The axial T1 MR image with contrast agent on the left shows contrast enhancement (CE) around the surgical cavity (arrow). After 2.5 months (middle), the CE has grown. On the corresponding ASL image on the right, the ASL was visually rated as hyperperfusion, and the mean signal intensity of an ROI in the tumor was compared with that of the contralateral white matter. **B,** A 46-year-old woman with an *IDH* wild-type glioblastoma was treated with temozolomide-based chemoradiation. The axial T1 MR image with contrast agent on the left shows CE around the surgical cavity (arrow). After 3.2 months (middle), the CE has grown. On the corresponding ASL image on the right, the ASL was visually rated as hypoperfusion. **C,** A 79-year-old man with an *IDH* wild-type glioblastoma was treated with temozolomide-based chemoradiation. The axial T1 MR image with contrast agent on the left shows subependymal CE (arrow). After 16.1 months (middle), the CE has grown. On the corresponding ASL image on the right, the ASL was visually rated as isoperfusion.

were included in the study. Figure 3 depicts the flow chart of patient inclusion. Most patients were men (118, 68.2%) and had a glioblastoma *IDH* wild-type (151, 87.3%); the median age was 63 years (interquartile range, 55–69 years). Treatment consisted mostly of a subtotal resection (128, 74%) and temozolomide-based chemoradiation (133, 76.9%). Baseline characteristics are shown in the Online Supplemental Data. The median time to progression was 1.1 month after RT (interquartile range, 0.7–4.5 months). After follow-up, 94 lesions (54%) were diagnosed as

TIE, and 79 (46%), as PD. The reference standard was based on histology in 46 lesions (26.6%).

The median follow-up time was 17.7 weeks (range, 1.14–195.1 weeks). Nineteen patients were followed for <6 weeks, of whom 18 had a histologic reference standard. One patient had his last follow-up MR imaging showing TIE after 5.3 weeks, and he died 3 weeks later from another disease.

Early-versus-Late Progression

For the qualitative image analysis of a positive ASL for PD in the group of patients with progression within 3 months after RT ($n = 110$), the OR was 0.65 (95% CI, 0.28–1.51; $P = .319$) with 38.0% PPV and an AUC of 0.456 (95% CI, 0.35–0.57). Between 3 and 6 months after RT ($n = 26$), the OR was 3.5 (95% CI, 0.69–17.89; $P = .132$) with a PPV of 58.3% and an AUC of 0.652 (95% CI, 0.43–0.87).

After six months after RT ($n = 37$), the OR was 6.8 (95% CI, 1.48–32; $P = .014$) with a PPV of 83.3% and an AUC of 0.719 (95% CI, 0.55–0.89). The results of the sensitivity analysis were consistent.

The Online Supplemental Data present the detailed qualitative and quantitative results.

The quantitative analysis revealed AUCs of 0.520, 0.588, and 0.587 in the groups of progression within 3, from 3 to 6, and after 6 months after RT, respectively. The optimal cutoff values were 2.241, 1.302, and 1.278. These cutoffs were found at 51.1%, 90.9%, and 78.3% sensitivity and 53.9%, 40%, and 50% specificity. The application of the cutoffs in these groups generated ORs of 1.2 (95% CI, 0.57–2.61; $P = .609$), 6.7 (95% CI, 0.67–66.5; $P = .106$), and 3.6 (95% CI, 0.85–15.2; $P = .082$), respectively.

Subgroups

In the subgroup of patients with a glioblastoma treated with temozolomide-based chemoradiation, the OR was near 1, the confidence interval included 1, the P value was large, and the AUC was low.

In the group with a histologic reference standard ($n = 46$), the final diagnosis was TIE in 14, PD in 7, and mixed histology in 25, classified as PD. The re-resection was total or subtotal in 38 and a biopsy in 8. Patients with positive ASL findings had 3 times the odds of PD compared with patients with negative ASL findings (95% CI, 0.9–12.0; $P = .07$). The AUC was 0.638 (95% CI, 0.46–0.81), and the PPV, 77%. Assessments of mixed lesions

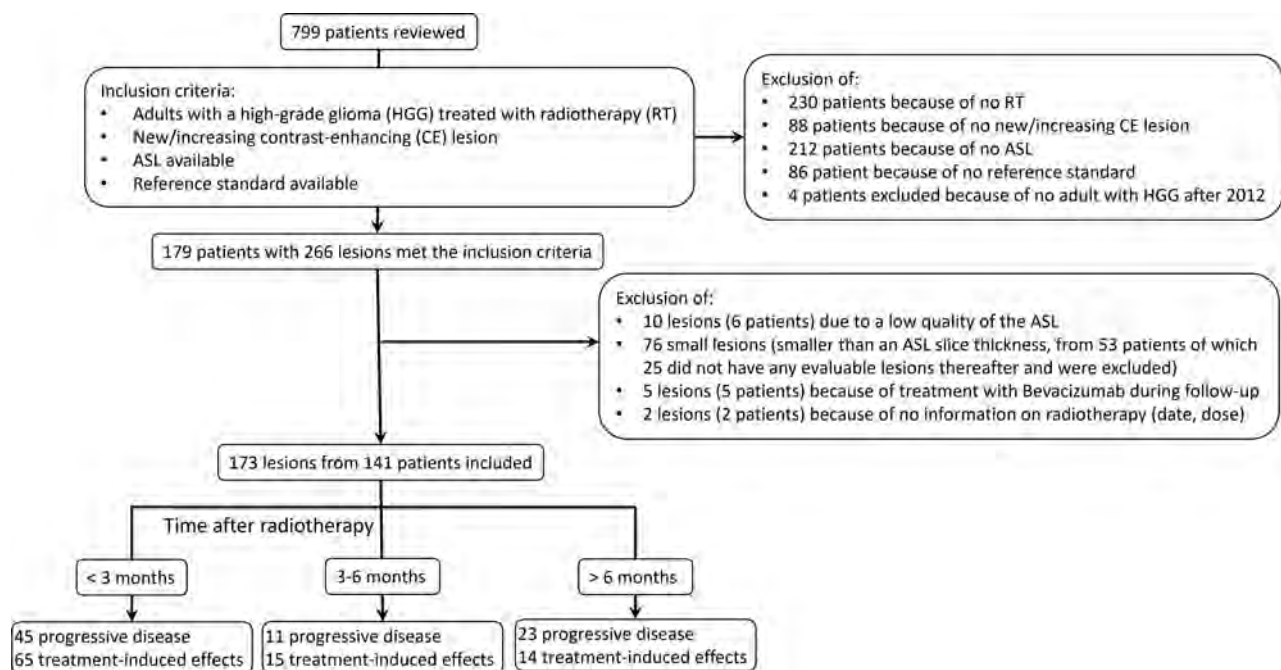


FIG 3. Flow chart of patient inclusion.

after biopsy and total resection are illustrated in the Online Supplemental Data.

We performed a post hoc analysis of patients with progression before and after 6 months post-RT for each reference standard (radiologic/histologic). In the late timeframe, the diagnostic accuracy was higher with a histologic reference ($n = 22$) compared with a radiologic reference ($n = 15$) but was comparable with the results of the whole-group analysis ($AUC = 0.760$, Online Supplemental Data).

The findings of quantitative analysis of the subgroups were consistent.

Reliability

Intrarater and interrater reliability analysis revealed κ values of 0.62 and 0.67, respectively, which represent a substantial agreement.²¹ No notable changes in the median signal-intensity ratio or interquartile range were found during the review of 44 lesions by a neuroradiologist (1.8, 1.2–10 versus 2.0, 1.3–10).

The median time between the progression MR imaging and the ASL imaging session was 2 days (interquartile range, 0–50 days). The results did not change significantly after omitting all lesions with >3 weeks between the progression MR imaging and the ASL ($n = 73$).

DISCUSSION

In this retrospective cohort study of 173 lesions, our main objective was to assess the diagnostic value of ASL perfusion MR imaging in differentiating PD from TIE in irradiated HGG. The ASL images were rated qualitatively and quantitatively and showed a limited diagnostic value with both methods. The PPVs of the qualitative (visual) image analysis were low for progression within 6 months and high for progression after 6 months after RT. The diagnostic performance was similar in our quantitative

image analysis, with high sensitivities and low specificities for progression after 3 months after RT.

In comparison with previous literature, the diagnostic accuracy of ASL was lower in our study. Two earlier retrospective studies, one with 62 patients with a glioblastoma and another with 30 patients with grade 2–4 gliomas, used a 3-point scale for a qualitative analysis and found a significant OR of 4.73, and AUC of 0.774, sensitivity of 79.4% and 88%, and specificity of 64.3% and 89%.^{9,12} However, 1 study included only patients with progression within 4 weeks post-RT,⁹ and the other was limited to patients after proton beam RT with progression after 6 months or later post-RT and only 1 ASL-slice.¹²

Three prospective and 7 retrospective studies (or with an unknown study design), including 21–69 patients with low-grade gliomas and HGG after standard-of-care RT or chemoradiation, performed quantitative analysis. An ROI in the tumor was compared with contralateral brain to calculate either a CBF,^{7,8,10,11,13–16} or tumor blood flow.⁶ In 1 study, intensity values were analysed.¹² The reference region was mostly described as normal brain.^{7,8,11,12} Others specifically used the contralateral white matter¹⁶ or the cerebellum.¹⁴ AUCs in these studies were ≥ 0.848 .^{6–8,10,11,14} Cutoff values of 1.02–2.18 generated 53.9%–100% sensitivity and 50%–92.9% specificity.^{7,8,10,12–14} In a recently published meta-analysis including most of these studies, the relative CBF in tumor recurrence differed significantly from the one in treatment effect.²²

We included new or increasing contrast-enhancing lesions from all time points after RT, possibly negatively influencing our findings. In our study, 110 of 173 lesions (64%) progressed within 3 months after the end of RT, and 59% of these were diagnosed as TIE. The specificity of a positive ASL finding in this group with the qualitative method was only 24.6%. A high incidence of inflammatory, apoptotic pseudoprogression in the first months

after RT may have led to many false-positives in comparison with more uniform radionecrosis with vascular changes in the later period, especially beyond 6 months post-RT. The better diagnostic performance in our explorative subgroup analysis with late progression supports this hypothesis, suggesting that a positive ASL beyond 6 months after RT is associated with PD, but a negative signal in this timeframe is still difficult to interpret. These findings on “beyond 6 months postradiation” need to be replicated in an independent cohort. The specificity in the previously mentioned smaller study with 62 progressive lesions before 3 months after RT including 45% TIE was 64.3%.⁹ Two other studies included only patients with late MR imaging changes.^{6,12}

Another explanation for our moderate diagnostic value may be a high number of mixed lesions (with PD as well as TIE). We considered the progressive component within a mixed lesion as most important because this component determines the patient's prognosis. Consequently, we regarded mixed lesions as PD. Thus, we ignored the TIE component of the mixed lesion, even though this component is likely to be represented in parts of the lesion on the ASL images. The outcome was retrieved by a different person than the one who retrieved the ASL (test); therefore, this inherent misclassification of the outcome was probably nondifferential. Nondifferential misclassification of the criterion standard can lead to an underestimation of the observed diagnostic value. In previous research, a higher percentage of tumor correlated with a higher CBF,¹⁵ but others reported no change of ASL sensitivity or specificity after omitting mixed lesions.¹²

The interrater reliability coefficient was similar or inferior compared with previous studies (0.65, 0.813, 0.67; Fleiss κ).¹⁸⁻²⁰ The imperfect inter- and intrarater reliability coefficient could also have negatively influenced the diagnostic performance. The consistent results of the interrater and intrarater reliability largely exclude a difference in rating between the 2 observers. A possible source of this nonrobustness in the ASL reading is the sensitivity to artifacts due to patient movement, hemorrhage, and flow effects.⁵ Furthermore, the low spatial resolution and the lack of standard protocols for the quantitative evaluation constitute limitations of the ASL method in general.

The large, representative sample gathered during 6 years constituted the main strength of our study and contributes to the generalizability of our findings. The exclusion of recurrent low-grade gliomas and patients treated with bevacizumab further homogenized our sample. We applied qualitative (visual) as well as quantitative analyses of the ASL images, and both results were consistent. Last, the second, independent, read of the ASL images blinded to the clinical data provided important information on the test characteristics of ASL imaging.

Limitations of our study were the retrospective and single-center design. Also, we did not register the patients' dexamethasone doses. Dexamethasone is used as a treatment of the symptoms of TIE and can influence the MR imaging appearance of the lesion. However, our design reflects clinical practice, in which dexamethasone use is common in patients with symptomatic edema. Additionally, 73% of patients lacked a histologic reference standard. Nevertheless, the risk of sampling error, the interrater variability between pathologists, the molecular evolution of the tumor after treatment, and the impossibility of performing high-

risk brain surgery in every patient hamper the applicability of histology as the criterion standard.²³⁻²⁵ Last, we considered only a single-time point ASL in this study, which does not correlate with clinical practice. Generally, radiologists have access to other sequences, previous MR images (sometimes including previous ASL images), and clinical information as well. All previously reported studies compared the ASL with another technique, mostly DSC perfusion MR imaging.^{7-10,12-14,16} In 3 studies, the raters had access to conventional MR imaging.^{8,9,15} In 1 study, the researchers reported a comparison with previous MR imaging examinations.¹⁵

Future prospective studies should include a larger sample size to account for the inevitable, nondifferential misclassification of the criterion standard, to study the value of longitudinal ASL imaging instead of the current single-time point index test, and to combine ASL with other modalities, both from conventional imaging⁴ and advanced methods. The group with *IDH*-mutated HGG ($n = 6$) also deserves more in-depth studying. Our analyses suggest that ASL is less suitable for diagnosis in early progression within 3–6 months after radiation therapy. For the early progressive lesions, other imaging modalities should be considered. The diagnostic value of different imaging methods may be increased with the application of machine learning/radiomics in image analysis.²⁶

CONCLUSIONS

We found a poor diagnostic value of ASL in differentiating progressive disease and TIE in irradiated high-grade gliomas with radiologic progression within 6 months after radiation therapy. In radiologic progression after 6 months, the diagnostic value was better. Our study gives valuable feedback for the application of ASL in clinical practice. Clinicians should be aware of the possibility of a high percentage of false-positives (52% of all positives in our qualitative assessment), especially in the early phase after RT.






Disclosure forms provided by the authors are available with the full text and PDF of this article at www.ajnr.org.

REFERENCES

1. Louis DN, Perry A, Wesseling P, et al. **The 2021 WHO Classification of Tumors of the Central Nervous System: a summary.** *Neuro Oncol* 2021;23:1231–51 CrossRef Medline
2. Taal W, Brandsma D, de Bruin HG, et al. **Incidence of early pseudoprogression in a cohort of malignant glioma patients treated with chemoradiation with temozolomide.** *Cancer* 2008;113:405–10 CrossRef Medline
3. Brandes AA, Tosoni A, Spagnoli F, et al. **Disease progression or pseudoprogression after concomitant radiochemotherapy treatment: pitfalls in neurooncology.** *Neuro Oncol* 2008;10:361–67 CrossRef Medline
4. Flies CM, van Leuken KH, Ten Voorde M, et al. **Conventional MRI criteria to differentiate progressive disease from treatment-induced effects in high-grade (WHO grade 3–4) gliomas.** *Neurology* 2022;99:e77–88 CrossRef Medline
5. Grade M, Hernandez Tamames JA, Pizzini FB, et al. **A neuroradiologist's guide to arterial spin labeling MRI in clinical practice.** *Neuroradiology* 2015;57:1181–202 CrossRef Medline
6. Razek A, El-Serougy L, Abdelsalam M, et al. **Differentiation of residual/recurrent gliomas from postradiation necrosis with arterial**

- spin labeling and diffusion tensor magnetic resonance imaging-derived metrics. *Neuroradiology* 2018;60:169–77 CrossRef Medline
7. Manning P, Daghighi S, Rajaratnam MK, et al. Differentiation of progressive disease from pseudoprogression using 3D pCASL and DSC perfusion MRI in patients with glioblastoma. *J Neurooncol* 2020;147:681–90 CrossRef Medline
8. Jovanovic M, Radenkovic S, Stosic-Opincal T, et al. Differentiation between progression and pseudoprogression by arterial spin labeling MRI in patients with glioblastoma multiforme. *J BUON* 2017;22:1061–67 Medline
9. Choi YJ, Kim HS, Jahng GH, et al. Pseudoprogression in patients with glioblastoma: added value of arterial spin labeling to dynamic susceptibility contrast perfusion MR imaging. *Acta Radiol* 2013;54:448–54 CrossRef Medline
10. Xu Q, Liu Q, Ge H, et al. Tumor recurrence versus treatment effects in glioma: a comparative study of three dimensional pseudo-continuous arterial spin labeling and dynamic susceptibility contrast imaging. *Medicine (Baltimore)* 2017;96:e9332 CrossRef Medline
11. Pellerin A, Khalife M, Sanson M, et al. Simultaneously acquired PET and ASL imaging biomarkers may be helpful in differentiating progression from pseudo-progression in treated gliomas. *Eur Radiol* 2021;31:7395–405 CrossRef Medline
12. Ozsunar Y, Mullins ME, Kwong K, et al. Glioma recurrence versus radiation necrosis? A pilot comparison of arterial spin-labeled, dynamic susceptibility contrast enhanced MRI, and FDG-PET imaging. *Acad Radiol* 2010;17:282–90 CrossRef Medline
13. Seeger A, Braun C, Skardelly M, et al. Comparison of three different MR perfusion techniques and MR spectroscopy for multiparametric assessment in distinguishing recurrent high-grade gliomas from stable disease. *Acad Radiol* 2013;20:1557–65 CrossRef Medline
14. Wang YL, Chen S, Xiao HF, et al. Differentiation between radiation-induced brain injury and glioma recurrence using 3D pCASL and dynamic susceptibility contrast-enhanced perfusion-weighted imaging. *Radiother Oncol* 2018;129:68–74 CrossRef Medline
15. Nyberg E, Honce J, Kleinschmidt-DeMasters BK, et al. Arterial spin labeling: Pathologically proven superiority over conventional MRI for detection of high-grade glioma progression after treatment. *Neuroradiol J* 2016;29:377–83 CrossRef Medline
16. Ye J, Bhagat SK, Li H, et al. Differentiation between recurrent gliomas and radiation necrosis using arterial spin-labeling perfusion imaging. *Exp Ther Med* 2016;11:2432–36 CrossRef Medline
17. Ellingson BM, Wen PY, Cloughesy TF. Modified criteria for radiographic response assessment in glioblastoma clinical trials. *Neurotherapeutics* 2017;14:307–20 CrossRef Medline
18. Flies CM, Snijders TJ, Van Seeters T, et al. Perfusion imaging with arterial spin-labeling (ASL)-MRI predicts malignant progression in lowgrade (WHO grade II) gliomas. *Neuroradiology* 2021;63:2023–33 CrossRef Medline
19. Wang N, Xie SY, Liu HM, et al. Arterial spin-labeling for glioma grade discrimination: correlations with IDH1 genotype and 1p/19q status. *Transl Oncol* 2019;12:749–56 CrossRef Medline
20. Bert RJ, Colantoni W, Ney DE, et al. Comparison of arterial spin labeling and dynamic susceptibility contrast-enhanced MR perfusion in differentiating tumor recurrence from treatment-related changes. *Int J Radiol Imaging Technol* 2017;3:022 CrossRef
21. Sim J, Wright CC. The kappa statistic in reliability studies: use, interpretation, and sample size requirements. *Phys Ther* 2005;85:257–68 CrossRef Medline
22. Liu Y, Chen G, Tang H, et al. Systematic review and meta-analysis of arterial spin-labeling imaging to distinguish between glioma recurrence and post-treatment radiation effect. *Ann Palliat Med* 2021;10:12488–97 CrossRef Medline
23. van den Bent MJ. Interobserver variation of the histopathological diagnosis in clinical trials on glioma: a clinician's perspective. *Acta Neuropathol* 2010;120:297–304 CrossRef Medline
24. Wen P, van den Bent M, Youssef G, et al. RANO 2.0: update to the Response Assessment in Neuro-Oncology criteria for high- and low-grade gliomas in adults. *J Clin Oncol* 2023;41:5186–99 CrossRef Medline
25. Draaisma K, Chatzipli A, Taphoorn M, et al. Molecular evolution of IDH wild-type glioblastomas treated with standard of care affects survival and design of precision medicine trials: a report from the EORTC 1542 Study. *J Clin Oncol* 2020;38:81–99 CrossRef Medline
26. Kocher M, Ruge MI, Galdiks N, et al. Applications of radiomics and machine learning for radiotherapy of malignant brain tumors. *Strahlenther Onkol* 2020;196:856–67 CrossRef Medline

Differentiating Low-Grade from High-Grade Intracranial Ependymomas: Comparison of Dynamic Contrast-Enhanced MRI and Diffusion-Weighted Imaging

 Julio Arevalo-Perez,  Elena Yllera-Contreras,  Kyung K. Peck, Vaios Hatzoglou,  Onur Yildirim, Marc K. Rosenblum, and  Andrei I. Holodny

ABSTRACT

BACKGROUND AND PURPOSE: The aim of this study was to determine the diagnostic value of fractional plasma volume derived from dynamic contrast-enhanced perfusion MR imaging versus ADC, obtained from DWI in differentiating between grade 2 (low-grade) and grade 3 (high-grade) intracranial ependymomas.

MATERIALS AND METHODS: A hospital database was created for the period from January 2013 through June 2022, including patients with histologically-proved ependymoma diagnosis with available dynamic contrast-enhanced MR imaging. Both dynamic contrast-enhanced perfusion and DWI were performed on each patient using 1.5T and 3T scanners. Fractional plasma volume maps and ADC maps were calculated. ROIs were defined by a senior neuroradiologist manually by including the enhancing tumor on every section and conforming a VOI to obtain the maximum value of fractional plasma volume ($V_{p_{max}}$) and the minimum value of ADC (ADC_{min}). A Mann-Whitney U test at a significance level of corrected $P = .01$ was used to evaluate the differences. Additionally, receiver operating characteristic curve analysis was applied to assess the sensitivity and specificity of $V_{p_{max}}$ and ADC_{min} values.

RESULTS: A total of 20 patients with ependymomas (10 grade 2 tumors and 10 grade 3 tumors) were included. $V_{p_{max}}$ values for grade 3 ependymomas were significantly higher ($P < .002$) than those for grade 2. ADC_{min} values were overall lower in high-grade lesions. However, no statistically significant differences were found ($P = .12114$).

CONCLUSIONS: As a dynamic contrast-enhanced perfusion MR imaging metric, fractional plasma volume can be used as an indicator to differentiate grade 2 and grade 3 ependymomas. Dynamic contrast-enhanced perfusion MR imaging plays an important role with high diagnostic value in differentiating low- and high-grade ependymoma.

ABBREVIATIONS: ADC_{min} = minimum ADC; AIF = arterial input function; AUC = area under the curve; DCE = dynamic contrast-enhanced; rCBV = relative CBV; ROC = receiver operating characteristic; VEGF = vascular endothelial growth factor; $V_{p_{max}}$ = maximum plasma volume; V_p = fractional plasma volume; WHO = World Health Organization

Intracranial ependymomas are a heterogeneous group of glial cell tumors of the CNS that arise from the ependymal lining of the ventricles, cerebral hemispheres, and central canal of the spinal cord. Intracranial ependymomas are uncommon primary neoplasms, accounting for 2.5% of all intracranial gliomas and 7% of primary CNS malignancies diagnosed annually.¹ They

account for 1%–3% of brain tumors in adults and 5%–12% in children.^{1,2}

Categorization of these tumors is essential because their treatment and prognosis vary. In 2016, the World Health Organization (WHO) classified ependymomas as low-grade (grade 2) and anaplastic ependymomas as high-grade (grade 3).^{2,3} Surgery is the primary treatment in both pediatric and adult populations. In patients with low-grade tumors, close surveillance can be sufficient, provided there has been complete resection. In contrast, patients with high-grade ependymoma need postoperative radiation therapy after gross total resection.^{3–6} Additionally, high-grade ependymomas have a poorer prognosis. Five-year overall survival and 2-year progression-free survival rates are 30% and 20%, respectively, compared with 100% and 77.8% for their low-grade counterparts.³ Consequently, preoperative classification of ependymomas is crucial for tailored management and risk stratification. Unfortunately, imaging findings on conventional MR imaging and

Received December 19, 2023; accepted after revision February 7, 2024.

From the Departments of Radiology (J.A.-P., E.Y.-C., V.H., O.Y., A.I.H.), Medical Physics (K.K.P.), and Pathology (M.K.R.), Memorial Sloan Kettering Cancer Center, New York, New York.

Drs Julio Arevalo-Perez and Elena Yllera-Contreras contributed equally to the work as coauthors.

This work was supported by the National Institutes of Health: NIH-NCI P30 CA008748 (Vickers, PI).

Please address correspondence to Julio Arevalo-Perez, MD, PhD., Memorial Sloan Kettering Cancer Center, Department of Radiology, 1275 York Ave, New York, NY, 10065-6007; e-mail: arevalj@mskcc.org

<http://dx.doi.org/10.3174/ajnr.A8226>

SUMMARY SECTION

PREVIOUS LITERATURE: Previous literature has shown that ADC values are different between high-grade and low-grade ependymomas, supporting the use of ADC as an objective and noninvasive marker for presurgical differentiation of low-grade and high-grade ependymomas. Other authors have also shown that perfusion marker relative CBV derived from DSC MR imaging was higher in high-grade ependymomas than those of low-grade tumors. These advanced techniques have also been compared showing lower relative ADC_{min} and higher relative CBV_{max} values among patients with high-grade ependymomas than with low-grade ependymomas. Based on the above findings we seek to compare DCE and ADC.

KEY FINDINGS: Vp_{max}, a surrogate marker of vascularization derived for DCE MR imaging, showed significant differences between ependymoma grades. ADC_{min} values differed also between high-grade and low-grade ependymomas but no statistically significant differences were found, implying that Vp_{max} is a better discriminator of ependymoma grade.

KNOWLEDGE ADVANCEMENT: Because Vp_{max}, derived from DCE MR imaging, less susceptible to artifacts than DSC, is superior to ADC_{min} in the classification of ependymomas according to grades, the inclusion of fractional plasma volume (Vp) perfusion maps in the standard MR imaging of primary brain tumors could represent an improved added diagnostic value and help in treatment guidance.

clinical manifestations often overlap, making presurgical classification difficult to achieve.⁷

Conventional MR imaging is a noninvasive imaging technique that supports the diagnosis, surgical planning, clinical management, and assessment of the treatment response of brain tumors. Despite its utility, conventional MR imaging provides little information concerning the physiologic behavior of a tumor.⁸ In fact, it is complicated to differentiate low- and high-grade ependymomas solely on the basis of the enhancement pattern or morphologic features that conventional MR imaging provides. Advanced MR imaging techniques, such as MR imaging perfusion and DWI, have proved helpful for the assessment of tumor neovascularity and cellularity, as well as in grading tumors.^{9,10} Recently, a few attempts have been made to classify ependymomas from an imaging standpoint, including a comparison of DSC and ADC.^{3,7}

The objective of our study was to compare the differences of maximum plasma volume (Vp_{max}) derived from dynamic contrast-enhanced (DCE) MR imaging and minimum ADC (ADC_{min}) in differentiating grade 2 and 3 ependymomas. We hypothesized that Vp_{max}, derived from T1-weighted DCE-MR imaging perfusion, would outperform ADC_{min} in discriminating ependymoma grades.

MATERIALS AND METHODS

Patients, Imaging Protocol, and Statistical Analysis

This retrospective study was performed after local institutional review board approval, including a waiver of informed consent. A hospital database was created for the period from January 2013 through June 2022, including patients with a histologically-proved ependymoma diagnosis with available DCE-MR imaging.

MR Imaging Acquisition

MR imaging sequences were acquired via 1.5T (Optima 450W; GE Healthcare) and 3T (Signa Premier 750W; GE Healthcare) and a standard 8-channel head coil. A bolus of gadolinium-diethylenetriaminepentaacetic acid, Gadobutrol (Gadavist; Bayer), was administered via a power injector at 0.1 mmol/kg body weight and a rate of 2–3 mL/s via a venous catheter (18–21 ga). Kinetic enhancement of the tissue was obtained both during and after

injection of gadolinium-diethylenetriaminepentaacetic acid by using a 3D T1-weighted fast echo-spoiled gradient-echo sequence (TR = 4–5 ms; TE = 1–2 ms; section thickness = 5 mm; flip angle = 25°;^{11,12} FOV = 32 cm; temporal resolution = 5–6 seconds) and consisted of 32 images in the axial plane.

Matching contrast T1-weighted (TR/TE = 600/8 ms; thickness = 4.5 mm) and T2-weighted (TR/TE = 4000/102 ms; thickness = 4.5 mm) spin-echo images were obtained. The kinetic enhancement of tissue before, during, and after injection of gadolinium-diethylenetriaminepentaacetic acid was obtained by using a 3D T1-weighted fast-spoiled gradient-echo sequence (TR, 4–5 ms; TE, 1–2 ms; section thickness, 3 mm; flip angle, 25°; FOV, 24 cm; matrix, 128 × 128; temporal resolution, 5–6 seconds) and consisted of 10–12 images in the axial plane. Ten phases for preinjection time delay and 30 phases for postinjection were obtained. DCE matching post-T1-weighted images were additionally acquired after DCE-MR imaging.

DWI was performed in the axial plane using a spin-echo EPI sequence with the following parameters: TR/TE = 8000/104.2 ms; diffusion gradient encoding in 3 orthogonal directions; $b = 1000$ s/mm²; FOV = 240 mm; matrix size = 128 × 128 pixels; section thickness = 5 mm; section gap = 1 mm; and number of averages = 2. DWI scans were obtained before DCE-MR imaging. The ADC values were calculated as follows: $ADC = [\ln(S/S_0)]/b$, wherein S is the signal intensity of the ROI obtained through 3 orthogonally oriented DWIs or diffusion trace images, S_0 is the signal intensity of the ROI acquired through reference T2-weighted images, and b is the gradient b factor with a value of 1000 s/mm². ADC maps were calculated on a pixel-by-pixel basis.

Image Analysis

We processed and analyzed DCE-MR perfusion imaging data using NordicICE (Version 4.2.0; NordicNeuroLab). Preprocessing steps included background noise removal, spatial and temporal smoothing, and detection of the arterial input function (AIF) from the MCA. AIF was individually computed, and AIF curves with a rapid increase in signal enhancement and sharp peak followed by minimal temporal noises were selected. We applied the extended Tofts 2-compartment pharmacokinetic model, which assumes that the contrast agent is either in the interstitial space

or in the intravascular compartment, to calculate the DCE-MR perfusion imaging parameter fractional plasma volume (V_p).¹³ A senior neuroradiologist with 15 years of experience manually delineated ROIs by including the enhancing tumor on every section and conforming a VOI, with careful consideration to exclude large vessels on each T1-weighted DCE-MR perfusion image. FuncTool software (AW5.2; GE Healthcare) was used for ADC map postprocessing. Because previous studies have found that maximal perfusion values and minimum ADC values are most accurate for tumor grading,^{9,14-19} the volumes were then transferred to V_p maps to obtain the maximum plasma volume value ($V_{p_{max}}$) and to ADC maps to obtain the ADC_{min} . A ratio of tumor to normal brain parenchyma was obtained in both parameters for normalization purposes by placing ROIs in healthy-appearing white/gray matter of the contralateral hemisphere over normal brain parenchyma.

Statistical Analysis

A Mann-Whitney U test at a significance level of corrected $P < .01$ was applied to evaluate ADC and DCE MR imaging differences across tumor grades. Additionally, receiver operating characteristic (ROC) curve analysis was used to assess the sensitivity and specificity of $V_{p_{max}}$ and ADC_{min} values. SPSS statistical software (SPSS Statistics for Windows, Version 27.0; IBM) was used to perform the ROC curve analysis.

RESULTS

Patient Population

Twenty patients (age range, 6–72 years; interquartile range, 41.75 years; mean, 35.2 [SD, 21.67] years) with the diagnosis of ependymoma and DCE-MR imaging perfusion scans were identified. They were classified according to tumor grade: 10 low-grade ependymomas (grade 2) (8 males [80%] and 2 females [20%]) and 10 high-grade ependymomas (grade 3) (6 females and 4 males [50%]). The Table and Fig 1 show examples of histopathologic findings for low-grade (A) and high-grade (B)

ependymoma. Figure 2 shows examples of T1-weighted post-contrast, plasma volume, and ADC maps of low- and high-grade ependymomas.

Quantitative Perfusion Analysis

Normalized $V_{p_{max}}$ values for high-grade (grade 3) ependymomas were significantly higher ($P = .00018$) than those for low-grade ependymomas (grade 2). A boxplot of normalized V_p and ADC between low- and high-grade ependymomas is shown in Fig 3. In high-grade ependymomas, the mean normalized $V_{p_{max}}$ was 14.95 (SD, 6.91). In the low-grade group, the mean normalized $V_{p_{max}}$ was 2.01 (SD, 0.76). Normalized ADC_{min} values were overall lower in high-grade lesions (mean, 0.76 [SD, 0.25]) compared with low-grade lesions (mean, 0.88 [SD, 0.078]). However, no statistically significant differences were found ($P = .14156$).

ROC Analysis

The ROC curve analysis was applied to evaluate the diagnostic value of the normalized $V_{p_{max}}$ and ADC_{min} values to differentiate high- and low-grade ependymomas. On the basis of the ROC analysis, normalized $V_{p_{max}}$ shows a sensitivity of 100% and specificity of 100% to differentiate high- and low-grade ependymomas (Fig 4). The area under the curve (AUC) for $V_{p_{max}}$ was the highest (AUC = 1), indicating a better classification ability in differentiating low- and high-grade ependymomas, compared with ADC_{min} (AUC = 0.29; asymptotic 95% CI, 0.05–0.53).

DISCUSSION

Our study demonstrated that $V_{p_{max}}$ was a superior discriminator over ADC_{min} between low- and high-grade ependymomas. Notably, the parameter $V_{p_{max}}$, a surrogate marker of vascularization, showed statistically significant differences, while ADC_{min} values showed no statistically significant differences despite variance between grades.

Perfusion imaging has been widely used in recent years to classify brain tumors.^{8,20} Extensive documentation can be found

Demographic data, location of tumor, field strength of scanner, and normalized $V_{p_{max}}$ and ADC_{min} values

Histopathology	Age	Location	Sex	Field Strength	rVP _{max}	rADC _{min}
Low-grade ependymoma	21	Posterior Fossa	M	3T	2.57	0.8
Low-grade ependymoma	72	Supratentorial	M	3T	0.95	1.02
Low-grade ependymoma	51	Posterior Fossa	F	3T	1.09	0.91
Low-grade ependymoma	70	Posterior Fossa	M	3T	1.8	0.9
Low-grade ependymoma	20	Posterior Fossa	M	3T	1.53	0.73
Low-grade ependymoma	57	Posterior Fossa	M	3T	2.75	0.85
Low-grade ependymoma	36	Posterior Fossa	M	3T	1.41	0.89
Low-grade ependymoma	58	Posterior Fossa	M	1.5T	2.98	0.93
Low-grade ependymoma	9	Supratentorial	F	3T	2.12	0.92
Low-grade ependymoma	13	Posterior Fossa	M	3T	2.93	0.85
Anaplastic ependymoma	16	Posterior Fossa	M	1.5T	16.29	0.73
Anaplastic ependymoma	14	Posterior Fossa	M	3T	21.56	0.79
Anaplastic ependymoma	59	Supratentorial	M	1.5T	5.43	0.29
Anaplastic ependymoma	29	Supratentorial	F	3T	23.19	0.53
Anaplastic ependymoma	32	Supratentorial	F	3T	11.11	0.9
Anaplastic ependymoma	58	Supratentorial	M	1.5T	7.07	1.15
Anaplastic ependymoma	6	Posterior Fossa	F	3T	21.9	0.99
Anaplastic ependymoma	42	Supratentorial	F	1.5T	22.5	0.83
Anaplastic ependymoma	10	Posterior Fossa	F	3T	10.04	0.51
Anaplastic ependymoma	31	Posterior Fossa	F	3T	10.4	0.83

Note:—rVP_{max} indicates relative maximum plasma volume, rADC_{min}, relative ADC_{min}.

in the literature about the correlation between perfusion imaging with conventional angiography of vascular density and histologic analysis of microvascular density, as well as the expression of vascular endothelial growth factor (VEGF).^{21–26}

High-grade ependymomas are aggressive and express more VEGF. Consequently, they are more proliferating with more

vascular invasion, which leads to insufficient tumor blood supply. Therefore, necrosis is more frequently seen in high-grade ependymomas than in low-grade ependymomas.²⁷ The assessment of ependymomas using perfusion imaging has been minimal. To our knowledge, only 1 prior study has attempted to classify ependymomas exclusively by using perfusion imaging. Xing et al³

used DSC-perfusion, an advanced MR imaging technique that uses relative CBV (rCBV) to evaluate the vascularity of brain tumors indirectly. Their study comprised 15 patients (11 with high-grade ependymoma and 4 with low-grade ependymoma) who underwent DSC perfusion. This was, to date, the largest reported cohort. In this cohort, the relative CBV_{max} values of high-grade ependymomas were higher than those of low-grade tumors, probably due to vascular proliferation in high-grade lesions. However, the cohort's low-grade ependymoma sample comprised a small

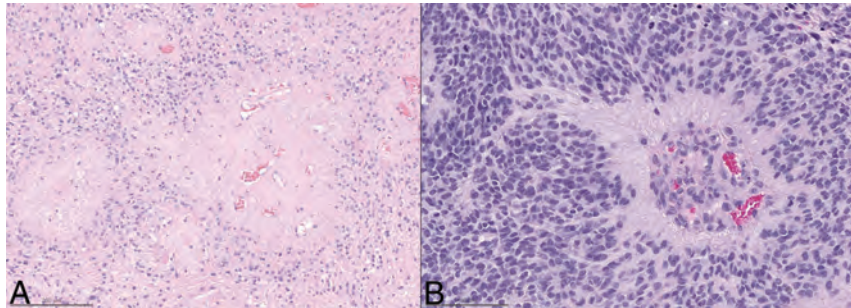


FIG 1. Histopathologic features of low-grade (A) and high-grade (B) ependymomas. A, Modestly cellular low-grade ependymoma, with broad perivascular pseudorosettes, devoid of mitotic activity. B, Densely cellular high-grade ependymoma, with a narrower perivascular pseudorosette, microvascular proliferation, and mitotic activity.

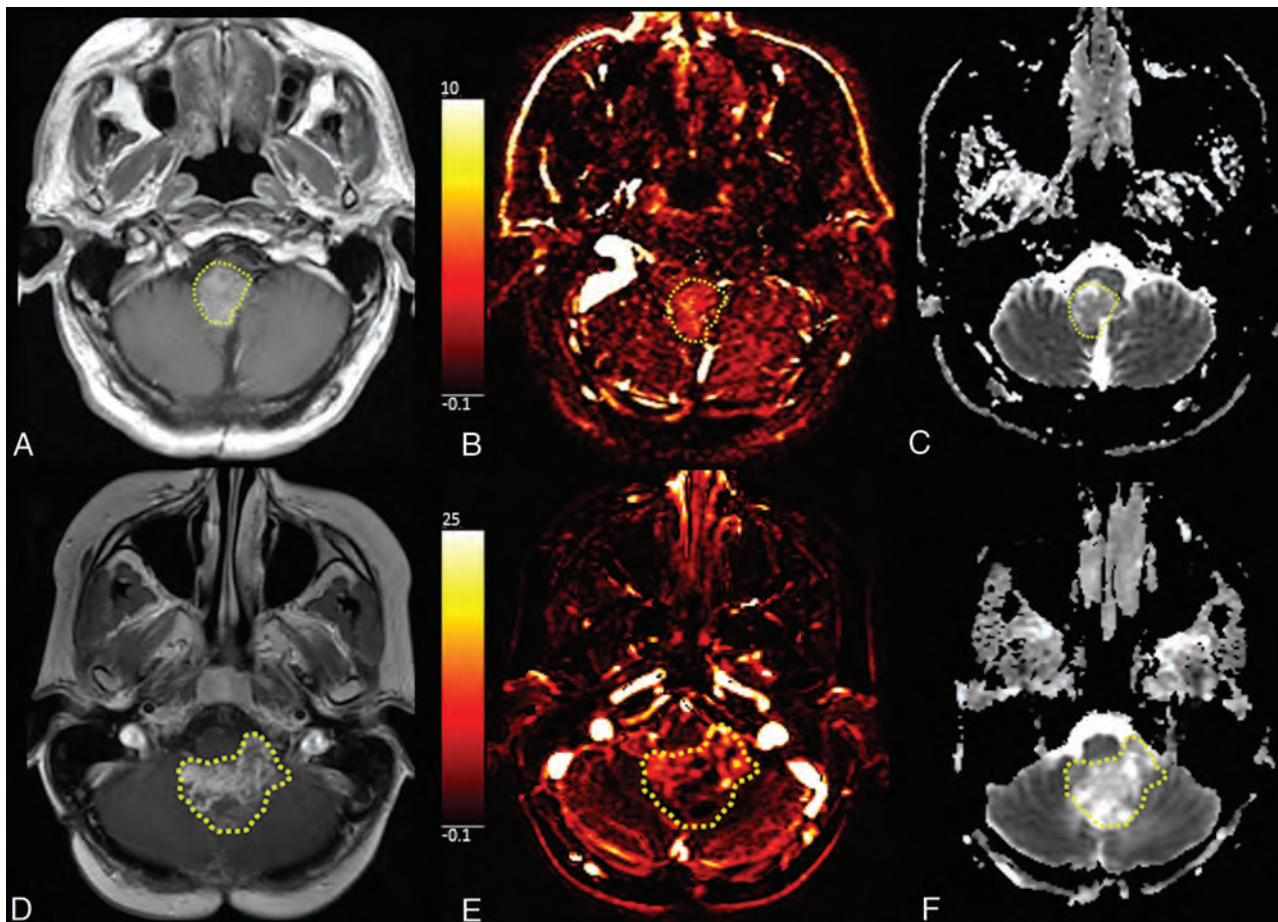


FIG 2. Examples of low-grade ependymomas (A, B, and C). A, T1-weighted postcontrast axial image demonstrates an enhancing mass in the inferior fourth ventricle and along the lower pons and dorsal medulla. B, Vp perfusion map shows mild elevation of Vp, 5.43. C, ADC map shows mildly elevated ADC values (579 mm²/s). Examples of high-grade ependymomas (D, E, and F). D, T1-weighted postcontrast axial image shows a heterogeneously enhancing partially cystic mass centered within the fourth ventricle with mass effect. E, Vp map shows areas of cystic changes and necrosis but also foci of elevated Vp (19.39), suggesting high vascularity. F, ADC map shows overall increased values with scattered areas of low ADC (514 mm²/s). The highlighted areas show the enhancing tumor in the inferior fourth ventricle; low-grade ependymoma, images A, B and C and high-grade ependymoma, images D, E and F.

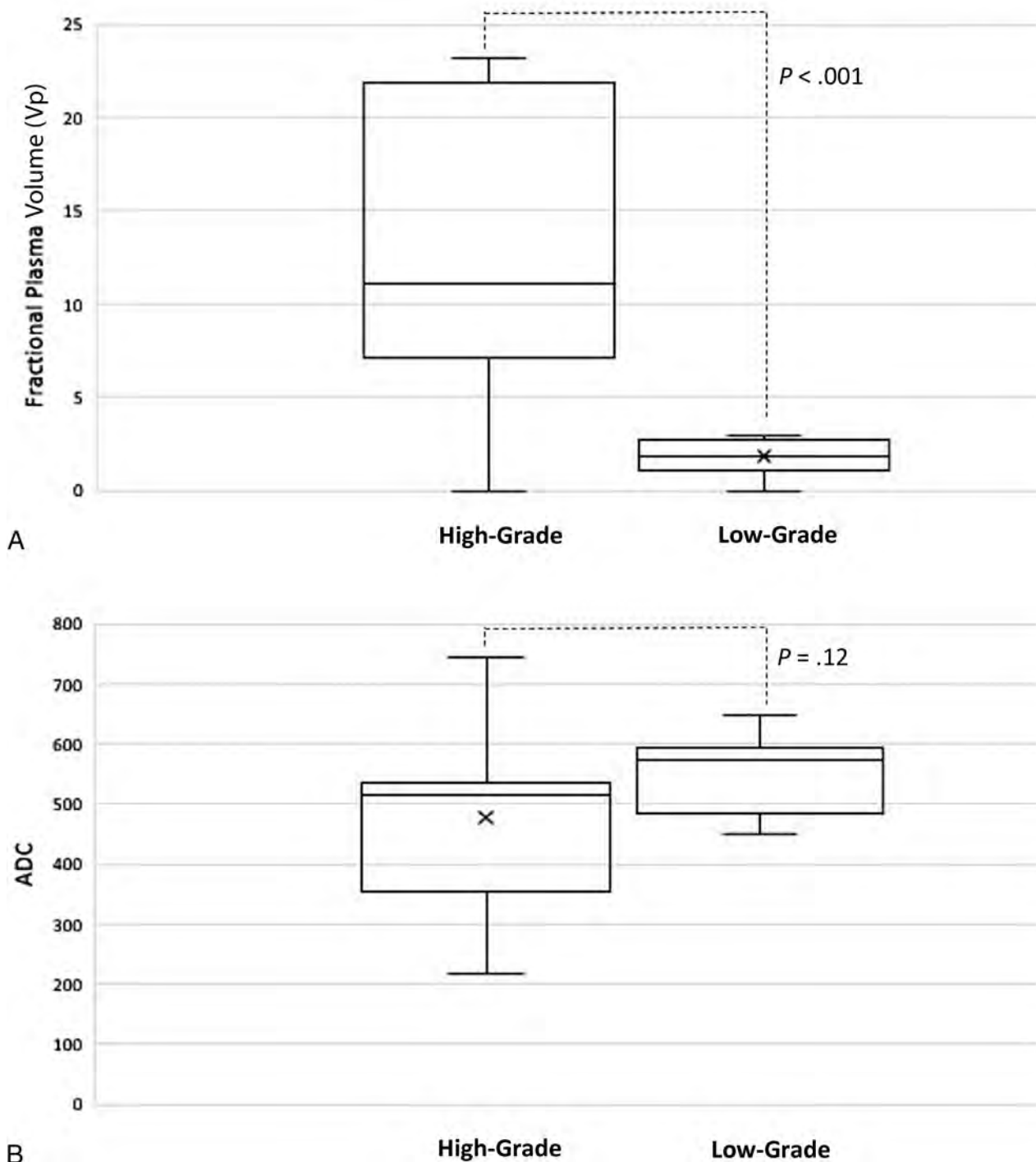


FIG 3. Boxplot of normalized Vp and ADC between low-grade and high-grade ependymomas.

number of patients, and their conclusions should consequently be interpreted cautiously.³ Additionally, it is known that rCBV values obtained from DSC are a semiquantitative measurement, which can be influenced by several postprocessing phases, including a correction technique, to address contrast extravasation and the choice of normal contralateral white matter.^{28,29} DSC perfusion imaging is also exquisitely sensitive to susceptibility artifacts. It can easily be affected by calcification, hemorrhage, and bone and has a potentially biased measurement

due to T1 effects from extravascular contrast leakage in tumor vasculature.³⁰

In our study, we used DCE-MR imaging, a T1-weighted perfusion method that is less sensitive to susceptibility artifacts than DSC in estimating absolute CBV. We used Vp, a pharmacokinetic parameter derived from DCE-MR imaging that is similar to the physiologic meaning of rCBV calculated from DSC. However, Hacklander et al³¹ demonstrated that Vp was superior to rCBV for quantitative estimation of CBV because

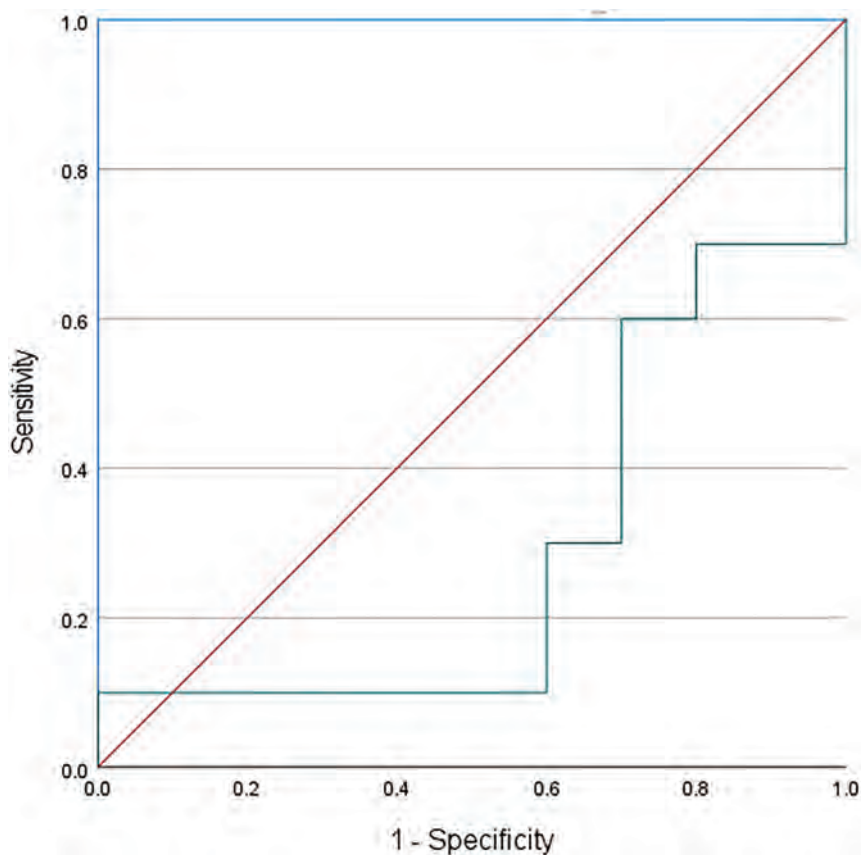


FIG 4. ROC curve of Vp (blue) and ADC (green) values to differentiate low- and high-grade of ependymoma (reference line: red).

it is based on T1-weighted perfusion and is less prone to artifacts. Our patient cohort comprised 20 histologically confirmed cases and had a well-balanced ratio of high-grade-to-low-grade tumors (10:10). Also, ROC curve analysis showed that $V_{p_{max}}$ has a sensitivity and specificity of 100%. We realize, however, that MR imaging characteristics are very rarely if ever 100% sensitive and specific. Our, perhaps overly optimistic, results are probably due to the small sample size.

DWI is a functional MR imaging technique that measures the random motion of water molecules within a tissue volume. ADC maps, derived from DWI, show the reduction of the mobility of water molecules due to high cellularity or cellular swelling. In the context of tumor characterization, a decrease in ADC values suggests higher cellularity and, therefore, a higher tumor grade.⁹ This principle has been used in the literature to characterize different tumors, but only 1 study has addressed the classification of ependymomas by using ADC.⁷ In their study, Xianwang et al⁷ found that ADC_{mean} values of adult intracranial ependymomas were higher than those of high-grade ependymomas, supporting the use of ADC as an objective and noninvasive marker for presurgical differentiation of low- and high-grade ependymomas. They analyzed 20 low-grade and 15 high-grade ependymomas, all with histologic confirmation. Additionally, they provided the Ki-67 proliferation index of each patient's tumor tissue.

Xing et al³ compared conventional MR imaging, DWI, and DSC-PWI to show lower relative ADC_{min} and higher relative

CBV_{max} values among patients with high-grade extraventricular ependymomas than those with low-grade ependymomas. This finding may be attributable to the high proportion of cellularity and vascular proliferation in high-grade ependymomas. Prior studies have shown that analysis of entire tumor volume, including possibly cystic and necrotic areas, could influence ADC measurements by increasing the ADC values.^{9,32} Necrosis and cystic changes are more frequently found in high-grade tumors, which could represent a confounding factor when attempting tumor classification via ADC_{mean} alone. Instead, we used ADC_{min} , which showed that high-grade ependymomas had lower ADC values than in the low-grade group. However, no statistically significant differences were found, possibly explained by the smaller sample size.

One of the main limitations of our study was its small sample size (20 patients with histologically-proved ependymomas). Many patients are referred to our highly specialized oncologic care center for a second opinion in therapeutic management after the initial resection of their tumor at another institution. It

is, therefore, challenging for us to find unresected, treatment-naïve primary brain tumors. Our study span intersected with the release of the updated WHO classification in 2021; therefore, all tumors were classified according to the WHO classifications of 2007 and 2016, considering only histologic features. Consequently, the absence of a correlation between patient immunohistochemical characteristics is an additional limitation, which could offer supplementary insight into prognostic, genetic, and predictive information. Finally, the manual method by which tumor volumes were extracted and calculated could represent another limitation. However, we tried to mitigate the reproducibility bias by having a single trained operator perform all VOIs.

CONCLUSIONS

DCE perfusion MR imaging and plasma volume parameters in particular perform better than ADC in noninvasive differentiation of grade 2 and grade 3 ependymomas. Including DCE perfusion maps in the standard MR imaging of primary brain tumors can help to improve diagnostic value and treatment guidance.

Disclosure forms provided by the authors are available with the full text and PDF of this article at www.ajnr.org.

REFERENCES

1. Lombardi G, Della Puppa A, Pizzi M, et al. **An overview of intracranial ependymomas in adults.** *Cancers (Basel)* 2021;13:6128 CrossRef Medline

2. Louis DN, Perry A, Reifenberger G, et al. **The 2016 World Health Organization Classification of Tumors of the Central Nervous System: a summary.** *Acta Neuropathol* 2016;131:803–20 CrossRef Medline
3. Xing Z, Zhou X, Xiao Z, et al. **Comparison of conventional, diffusion, and perfusion MRI between low-grade and anaplastic extraventricular ependymoma.** *AJR Am J Roentgenol* 2020;215:978–84 CrossRef Medline
4. Shuangshoti S, Rushing EJ, Mena H, et al. **Supratentorial extraventricular ependymal neoplasms: a clinicopathologic study of 32 patients.** *Cancer* 2005;103:2598–605 CrossRef Medline
5. Sun S, Wang J, Zhu M, et al. **Clinical, radiological, and histological features and treatment outcomes of supratentorial extraventricular ependymoma: 14 cases from a single center.** *J Neurosurg* 2018;128:1396–402 CrossRef Medline
6. Oya N, Shibamoto Y, Nagata Y, et al. **Postoperative radiotherapy for intracranial ependymoma: analysis of prognostic factors and patterns of failure.** *J Neurooncol* 2002;56:87–94 CrossRef Medline
7. Xianwang L, Lei H, Hong L, et al. **Apparent diffusion coefficient to evaluate adult intracranial ependymomas: relationship to Ki-67 proliferation index.** *J Neuroimaging* 2021;31:132–36 CrossRef Medline
8. Gupta PK, Saini J, Sahoo P, et al. **Role of dynamic contrast-enhanced perfusion magnetic resonance imaging in grading of pediatric brain tumors on 3T.** *Pediatr Neurosurg* 2017;52:298–305 CrossRef Medline
9. Arevalo-Perez J, Peck KK, Young RJ, et al. **Dynamic contrast-enhanced perfusion MRI and diffusion-weighted imaging in grading of gliomas.** *J Neuroimaging* 2015;25:792–98 CrossRef Medline
10. Vajapeyam S, Brown D, Johnston PR, et al. **Multiparametric analysis of permeability and ADC histogram metrics for classification of pediatric brain tumors by tumor grade.** *AJNR Am J Neuroradiol* 2018;39:552–57 CrossRef Medline
11. Nam JG, Kang KM, Choi SH, et al. **Comparison between the prebolus T1 measurement and the fixed T1 value in dynamic contrast-enhanced MR imaging for the differentiation of true progression from pseudoprogression in glioblastoma treated with concurrent radiation therapy and temozolomide chemotherapy.** *AJNR Am J Neuroradiol* 2017;38:2243–50 CrossRef Medline
12. Conte GM, Altabella L, Castellano A, et al. **Comparison of T1 mapping and fixed T1 method for dynamic contrast-enhanced MRI perfusion in brain gliomas.** *Eur Radiol* 2019;29:3467–79 CrossRef Medline
13. Tofts PS, Brix G, Buckley DL, et al. **Estimating kinetic parameters from dynamic contrast-enhanced T(1)-weighted MRI of a diffusible tracer: standardized quantities and symbols.** *J Magn Reson Imaging* 1999;10:223–32 CrossRef Medline
14. Hilario A, Ramos A, Perez-Nunez A, et al. **The added value of apparent diffusion coefficient to cerebral blood volume in the preoperative grading of diffuse gliomas.** *AJNR Am J Neuroradiol* 2012;33:701–07 CrossRef Medline
15. Santarosa C, Castellano A, Conte GM, et al. **Dynamic contrast-enhanced and dynamic susceptibility contrast perfusion MR imaging for glioma grading: preliminary comparison of vessel compartment and permeability parameters using hotspot and histogram analysis.** *Eur J Radiology* 2016;85:1147–56 CrossRef Medline
16. Calli C, Kitis O, Yuntun N, et al. **Perfusion and diffusion MR imaging in enhancing malignant cerebral tumors.** *Eur J Radiol* 2006;58:394–403 CrossRef Medline
17. Kono K, Inoue Y, Nakayama K, et al. **The role of diffusion-weighted imaging in patients with brain tumors.** *AJNR Am J Neuroradiol* 2001;22:1081–88 Medline
18. Lee EJ, Lee SK, Agid R, et al. **Preoperative grading of presumptive low-grade astrocytomas on MR imaging: diagnostic value of minimum apparent diffusion coefficient.** *AJNR Am J Neuroradiol* 2008;29:1872–77 CrossRef Medline
19. Kim HS, Kim SY. **A prospective study on the added value of pulsed arterial spin-labeling and apparent diffusion coefficients in the grading of gliomas.** *AJNR Am J Neuroradiol* 2007;28:1693–99 CrossRef Medline
20. Vajapeyam S, Stamoulis C, Ricci K, et al. **Automated processing of dynamic contrast-enhanced MRI: correlation of advanced pharmacokinetic metrics with tumor grade in pediatric brain tumors.** *AJNR Am J Neuroradiol* 2017;38:170–75 CrossRef Medline
21. Cha S, Johnson G, Wadghiri YZ, et al. **Dynamic, contrast-enhanced perfusion MRI in mouse gliomas: correlation with histopathology.** *Magn Reson Med* 2003;49:848–55 CrossRef Medline
22. Maia AC, Jr., Malheiros SM, da Rocha AJ, et al. **MR cerebral blood volume maps correlated with vascular endothelial growth factor expression and tumor grade in nonenhancing gliomas.** *AJNR Am J Neuroradiol* 2005;26:777–83 Medline
23. Aronen HJ, Gazit IE, Louis DN, et al. **Cerebral blood volume maps of gliomas: comparison with tumor grade and histologic findings.** *Radiology* 1994;191:41–51 CrossRef Medline
24. Aronen HJ, Pardo FS, Kennedy DN, et al. **High microvascular blood volume is associated with high glucose uptake and tumor angiogenesis in human gliomas.** *Clin Cancer Res* 2000;6:2189–200 Medline
25. Sugahara T, Korogi Y, Kochi M, et al. **Correlation of MR imaging-determined cerebral blood volume maps with histologic and angiographic determination of vascularity of gliomas.** *AJR Am J Roentgenol* 1998;171:1479–86 CrossRef Medline
26. Arevalo-Perez J, Kebede AA, Peck KK, et al. **Dynamic contrast-enhanced MRI in low-grade versus anaplastic oligodendrogliomas.** *J Neuroimaging* 2016;26:366–71 CrossRef Medline
27. Wu J, Armstrong TS, Gilbert MR. **Biology and management of ependymomas.** *Neuro Oncol* 2016;18:902–13 CrossRef Medline
28. Ellingson BM, Zaw T, Cloughesy TF, et al. **Comparison between intensity normalization techniques for dynamic susceptibility contrast (DSC)-MRI estimates of cerebral blood volume (CBV) in human gliomas.** *J Magn Reson Imaging* 2012;35:1472–77 CrossRef Medline
29. Boxerman JL, Schmainda KM, Weisskoff RM. **Relative cerebral blood volume maps corrected for contrast agent extravasation significantly correlate with glioma tumor grade, whereas uncorrected maps do not.** *AJNR Am J Neuroradiol* 2006;27:859–67 Medline
30. Boxerman JL, Prah DE, Paulson ES, et al. **The role of preload and leakage correction in gadolinium-based cerebral blood volume estimation determined by comparison with MION as a criterion standard.** *AJNR Am J Neuroradiol* 2012;33:1081–87 CrossRef Medline
31. Hacklander T, Reichenbach JR, Modder U. **Comparison of cerebral blood volume measurements using the T1 and T2* methods in normal human brains and brain tumors.** *J Comput Assist Tomogr* 1997;21:857–66 CrossRef Medline
32. Lee J, Choi SH, Kim JH, et al. **Glioma grading using apparent diffusion coefficient map: application of histogram analysis based on automatic segmentation.** *NMR Biomed* 2014;27:1046–52 CrossRef Medline

Territory-Related Functional Connectivity Changes Associated with Verbal Memory Decline in Patients with Unilateral Asymptomatic Internal Carotid Stenosis

Jyun-Ru Chen,  Chun-Jen Lin, Feng-Chi Chang,  I-Hui Lee, and Chia-Feng Lu

ABSTRACT

BACKGROUND AND PURPOSE: Verbal memory decline is a common complaint of patients with severe asymptomatic stenosis of the internal carotid artery (aICS). Previous publications explored the associations between verbal memory decline and altered functional connectivity (FC) after aICS. Patients with severe aICS may show reduced perfusion in the ipsilateral territory and redistribution of cerebral blood flow to compensate for the deficient regions, including expansion of the posterior and contralateral ICA territories via the circle of Willis. However, aICS-related FC changes in anterior and posterior territories and the impact of the sides of stenosis were less explored. This study aims to investigate the altered FC in anterior and posterior circulation territories of patients with left or right unilateral aICS and its association with verbal memory decline.

MATERIALS AND METHODS: We enrolled 15 healthy controls (HCs), 22 patients with left aICS (aICS_L), and 33 patients with right aICS (aICS_R) to receive fMRI, Mini-Mental State Examination (MMSE), the Digit Span Test (DST), and the 12-item Chinese version of Verbal Learning Tests. We selected brain regions associated with verbal memory within anterior and posterior circulation territories. Territory-related FC alterations and verbal memory decline were identified by comparing the aICS_L and aICS_R groups with HC groups ($P < .05$, corrected for multiple comparisons), respectively. Furthermore, the association between altered FC and verbal memory decline was tested with the Pearson correlation analysis.

RESULTS: Compared with HCs, patients with aICS_L or aICS_R had significant impairment in delayed recall of verbal memory. Decline in delayed recall of verbal memory was significantly associated with altered FC between the right cerebellum and right middle temporal pole in the posterior circulation territory ($r = 0.40$, $P = .03$) in the aICS_R group and was significantly associated with altered FC between the right superior medial frontal gyrus and left lingual gyrus in the anterior circulation territory ($r = 0.56$, $P = .01$) in the aICS_L group.

CONCLUSIONS: Patients with aICS_L and aICS_R showed different patterns of FC alterations in both anterior and posterior circulation territories, which suggests that the side of aICS influences the compensatory mechanism for decline in delayed recall of verbal memory.

ABBREVIATIONS: AAL = Automatic Anatomical Labeling Atlas; aICS = asymptomatic internal carotid artery stenosis; aICS_L = left-side asymptomatic internal carotid artery stenosis; aICS_R = right-side asymptomatic internal carotid artery stenosis; BOLD = blood oxygen level-dependent; DST = Digit Span Test; FC = functional connectivity; FDR = false discovery rate; HC = healthy control; MMSE = Mini-Mental State Examination; rs-fMRI = resting-state fMRI; SPM12 = Statistical Parametric Mapping 12; VCID = vascular contributions to cognitive impairment and dementia

A symptomatic internal carotid artery stenosis (aICS) is defined as the presence of ICA stenosis without a history of ischemic

events.¹ With advances in contemporary medical management, the estimated occurrence rate of ipsilateral acute ischemic stroke in patients with aICS has dropped to 4.7% over 5 years.² However, verbal memory decline is one of the major cognitive complications for patients with aICS.³⁻⁷

Patients with severe aICS may show reduced perfusion in the ipsilateral territory and redistribution of cerebral blood flow to

Received December 6, 2023; accepted after revision February 12, 2024.

From the Department of Biomedical Imaging and Radiological Sciences (J.-R.C., C.-F.L.), School of Medicine (C.-J.L., F.-C.C., I.-H.L.) and Institute of Brain Science (I.-H.L.), National Yang Ming Chiao Tung University, Taipei, Taiwan; and Neurological Institute (C.-J.L., I.-H.L.), Department of Radiology (F.-C.C.), Taipei Veterans General Hospital, Taipei, Taiwan.

Jyun-Ru Chen and Chun-Jen Lin contributed equally to this article.

This work was funded by the National Science and Technology Council (NSTC 112-2314-B-A49-060, 112-2314-B-075-037), Veterans General Hospitals and University System of Taiwan Joint Research Program (VGHUST113-G1-2-3), and the Taipei Veterans General Hospital (V112B-010). The funding bodies played no part in the study design, data collection, analysis, interpretation, or manuscript preparation.

Please address correspondence to Chia-Feng Lu, Department of Biomedical Imaging and Radiological Sciences, National Yang Ming Chiao Tung University, Taipei, Taiwan, No. 155, Sec. 2, Linong St, Beitou District, Taipei 11221, Taiwan; e-mail: alvin4016@nycu.edu.tw

<http://dx.doi.org/10.3174/ajnr.A8248>

SUMMARY

PREVIOUS LITERATURE: Previous literature has reported the verbal memory decline in asymptomatic internal carotid artery stenosis (aICS). However, the functional connectivity (FC) alterations and associated compensatory mechanisms induced by the brain hypoperfusion in the unilateral hemisphere were less explored. In this study, we aim to investigate the impact of 2 key factors, including the circulation territories (anterior and posterior circulations) and the laterality of aICS (left and right hemisphere), on the FC alterations and verbal memory decline. The difference of compensatory mechanisms between left aICS (aICS_L) and right aICS (aICS_R) groups was investigated.

KEY FINDINGS: Decline in delayed recall of verbal memory was significantly associated with alterations of FC within the posterior circulation territory in the aICS_R group and was significantly associated with alterations of FC within the anterior circulation territory in the aICS_L group.

KNOWLEDGE ADVANCEMENT: The differences in compensatory mechanisms reflecting on FC alterations between the aICS_L and aICS_R groups may be associated with the lateralization of verbal memory (ie, left hemisphere–dominant). We provided neuroimaging evidence suggesting the influences of the side in which aICS occurs on the decline in delayed recall of verbal memory.

compensate for the deficient regions, including expansion of the posterior and contralateral ICA territories via the circle of Willis.^{8–10} Previous studies have reported an association between brain perfusion and functional connectivity (FC),¹¹ which is further correlated with verbal memory function.¹² He et al¹³ reported an association between FC disruption in left aICS and impairment of short-term memory. However, further investigation is needed to determine the FC alterations and verbal memory impairment of patients with aICS.

Performing verbal memory tasks can activate the superior medial frontal gyrus, middle temporal pole, lingual gyrus, cerebellum VIII, and vermis VIII.^{14–16} The superior medial frontal gyrus, which is involved in attention, is in charge of memory storage;¹⁷ the middle temporal pole and lingual gyrus, which process visual stimuli and text, are responsible for memory encoding;^{18,19} cerebellum VIII and vermis VIII are involved in the process of memory manipulating.²⁰ Previous resting-state functional MR imaging (rs-fMRI) studies have proposed activation alterations in these regions after aICS.^{14,15} Accordingly, studying the alterations in FC among these regions may provide potential biomarkers for verbal memory decline after aICS.

Language is one of the main components of verbal memory.²¹ Functional brain areas in the language network are mainly in the left hemisphere,²² and the left superior temporal gyrus is one of the key areas for verbal memory.^{23,24} Reduced perfusion in the left or right hemisphere may therefore lead to different degrees of verbal memory decline. However, the impact of the side of aICS on verbal memory decline is still unclear. Furthermore, FC in homologous brain regions could be altered by acute hypoxia. Guo et al²⁵ reported increased FC in the contralesional temporal gyrus and inferior frontal gyrus in patients with poststroke aphasia. However, the functional alterations due to left and right unilateral aICS have received less attention.

Considering the lateralization of brain functions, we hypothesized that stenosis in the left and right ICA may cause verbal memory decline and FC alterations with different compensatory mechanisms. This study aimed to evaluate verbal memory impairment and identify FC alterations in anterior and posterior circulation territories in patients with left or right unilateral aICS.

MATERIALS AND METHODS

Participants

We prospectively enrolled 22 patients with asymptomatic stenosis in the left ICA (aICS_L), 33 patients with asymptomatic stenosis in the right ICA (aICS_R), and 15 age- and sex-matched healthy controls (HCs). The inclusion criteria were as follows: 1) diagnosed with severe aICS (defined as stenosis of lumen diameter greater than 50%), 2) had T1-weighted images and functional MR images, and 3) had MR images free from old infarcts or other structural lesions. The exclusion criteria were as follows: 1) history of transient ischemic attack or ischemic stroke, 2) functional disability (modified Rankin Scale score >2), 3) clinical diagnosis of dementia according to *Diagnostic and Statistical Manual of Mental Disorders, Fifth Edition*, or 4) other major neurologic and psychological disorder (such as Parkinsonism, depression, generalized anxiety disorder) or malignancy. Neuropsychological tests, including the 12-item Chinese version of immediate and delayed recall of Verbal Learning Tests, were used to evaluate working verbal memory and short-term verbal memory performance, respectively.²⁶ In the 12-item Chinese Version Verbal Learning Test, participants were asked to memorize 12 items. First, a neuropsychologist read the 12 items 4 times. The participant then had 5 recall trials 30 seconds later. The sum of item numbers recalled in each trial was indicated as immediate recall performance. Afterward, the participant was requested to recall the items once again 10 minutes later, the sum of which was used to determine the score of delayed recall. The comprehensive cognitive function of each case was assessed by using Mini-Mental State Examination (MMSE). The Digit Span Tests (DST), including forward and reverse tests, were employed to evaluate attentional capacity and working memory, especially for number sequences. This study was approved by the Institutional Review Board of the Taipei Veterans General Hospital (VGHIRB No. 2012–01–016AC; 2015–11–006C; 2020–02–017A). All the participants provided written informed consent before participating in this study.

MR Imaging Acquisition

MR imaging data, including 3D T1WI data, 3D FLAIR data, and blood oxygen level–dependent (BOLD) fMRI data, were collected

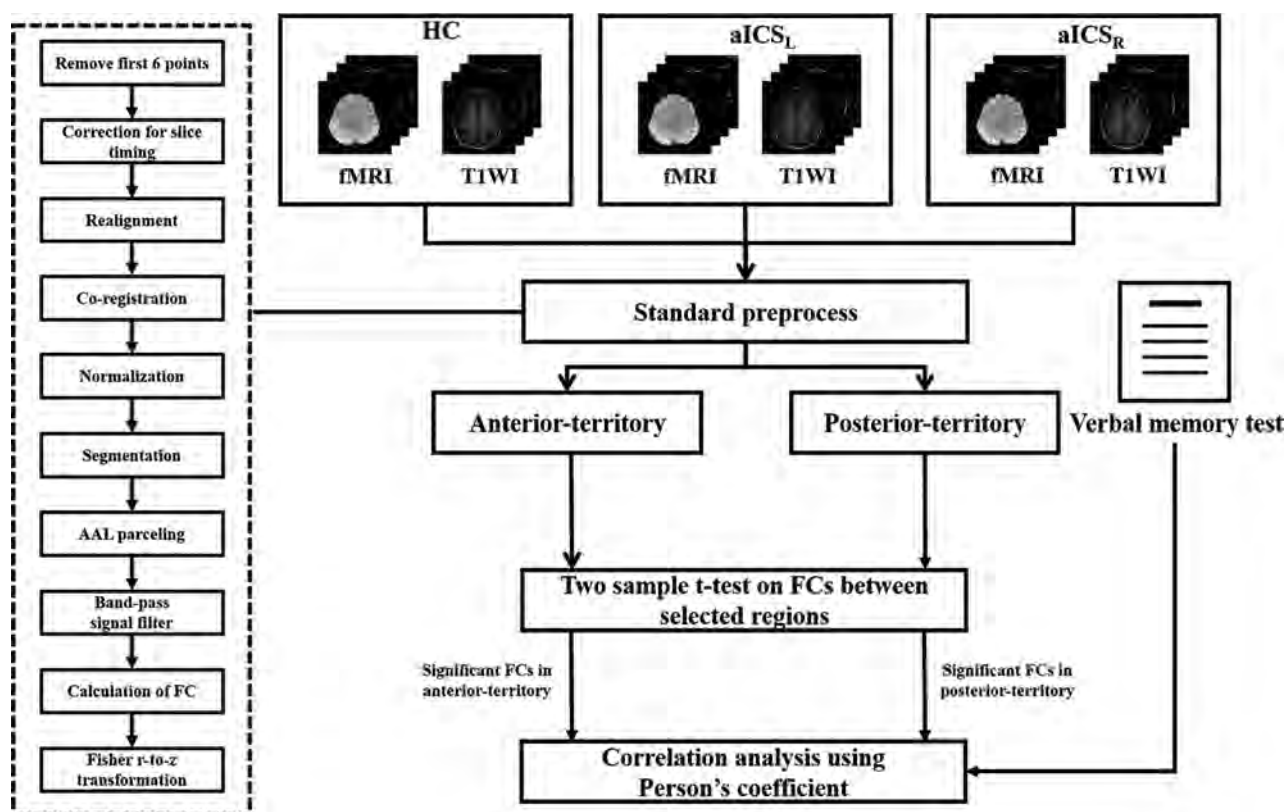


FIG 1. Flow chart for the study.

by using a 3T Discovery 750 MR scanner (GE Healthcare). The 3D T1WI data were acquired by using a axial MRI 3D brain volume (BRAVO) sequence (TR/TE: 12.2/5.2 ms, flip angle: 12°, voxel size: $1 \times 1 \times 1 \text{ mm}^3$, and field of view: $256 \times 256 \text{ mm}^2$). Rs-fMRI data were acquired by using the gradient-echo echo-planar imaging sequence (TR/TE: 3000/30 ms, flip angle: 90°, thickness: 3 mm, field of view: $222 \times 222 \text{ mm}^2$, and 124 repetitions). During BOLD fMRI scanning, the participants were instructed to remain relaxed and awake and keep their eyes open. The 3D FLAIR images were acquired with TR of 9000 ms, TE of 143.9 ms, flip angle of 110°, voxel size of $0.5 \times 0.5 \times 0.5 \text{ mm}^3$, and field of view of $256 \times 256 \text{ mm}^2$. This study adopted the Fazekas scores to evaluate white matter hyperintensities on FLAIR images.²⁷

Image Preprocessing

The fMRI data were processed following the standard procedure by using Statistical Parametric Mapping 12 (SPM12).²⁸ After removing the first six time points, we performed corrections for slice timing, realignment, coregistration of T1WI to BOLD images, spatial normalization, and spatial smoothing with an 8-mm full width at half maximum Gaussian kernel and regressed out the confounding effects of motion parameters and signals from white matter and CSF. In this study, all the participants showed minor head motion during the fMRI examination and were all included in the subsequent analyses.

Analysis of FC Associated with Verbal Memory

In this study, the targeted regions, including the superior medial frontal gyrus, lingual gyrus, middle temporal pole, cerebellum

VIII, and vermis VIII, were parceled based on the Automatic Anatomical Labeling atlas.²⁹ The average BOLD signals of these targeted regions were bandpass-filtered with the frequency band of 0.01–0.1 Hz. The FC was estimated by calculating the Pearson correlation coefficients between each pair of targeted regions in the anterior and posterior circulation territories, followed by Fisher r-to-z transformation (Fig 1). The 4×4 FC matrix among 4 areas, including the bilateral superior medial frontal and lingual gyri, was used to measure the FC within the anterior circulation. The 5×5 FC matrix among 5 areas, including vermis 8, the bilateral middle temporal pole, and cerebellum VIII, was used to assess FC in areas in the posterior circulation territory (Fig 2).

Furthermore, because the language network is one of the main components of verbal memory, we also calculated the 6×6 FC matrix among primary language regions, including Broca, Geschwind, and Wernicke areas and corresponding regions in the bilateral hemispheres.

Statistical Analyses

To investigate the altered FC within the anterior circulation territory, posterior circulation territory, and language matrices induced by stenosis in the left and right ICA, 2-sample *t* tests were used to compare the FC among the aICS_L, aICS_R, and HC groups ($P < .05$, with false discovery rate [FDR] correction for multiple comparisons). The statistical power was estimated for the clinical features, altered FCs, and association between the clinical features and FCs found to significantly differ after aICS.

Partial correlation analysis ($P < .05$) was applied to evaluate the associations between immediate and delayed recall of verbal

memory and altered FC in the anterior and posterior circulation territories induced by aICSL and aICSR. To regress out the effects of age and sex, these 2 characteristics were assigned as confounding factors during the test for partial correlation between verbal memory and altered FC.

RESULTS

Demographic Characteristics and Neuropsychological Data

Age, sex, degree of stenosis, and handedness did not significantly differ among the 3 groups. The aICSL group showed significantly reduced MMSE scores compared with the HCs ($P = .002$ with a statistical power of 0.94) and aICSR ($P = .01$ with a statistical power of 0.76) groups. The aICSL group showed a significantly poor level of reverse DST scores compared with the HCs group ($P = .01$ with a statistical power of 0.77). In the comparison of verbal memory scores, the aICSL group presented significant

deficits in immediate recall of verbal memory compared with the HC group. In addition, both the aICSL and aICSR groups showed significantly lower scores on the verbal memory delayed recall test than the HC group. No significant difference in verbal memory function between the aICSL and aICSR groups was found (Table 1). In addition, we confirmed no significant difference in distribution of Fazekas scores among HC, aICSL, and aICSR groups (Table 2).

Comparisons of FC among the aICSL, aICSR, and HC Groups

In the anterior circulation territory FC matrix, significantly higher FC between right superior medial frontal gyrus and left lingual gyrus (aICSL = 0.34 ± 0.15 , HC = 0.20 ± 0.15 , corrected $P = .05$ with a statistical power of 0.78), as well as right lingual gyrus (aICSL = 0.34 ± 0.18 , HC = 0.19 ± 0.15 , corrected $P = .04$ with a statistical power of 0.79), were observed in patients with

aICSL than in HCs (Figure 3A). The comparison between the aICSR and HC groups showed no significant findings. In the posterior circulation territory FC matrix, significantly higher FC between right cerebellum VIII and the right middle temporal pole (aICSR = 0.24 ± 0.17 , HC = 0.11 ± 0.06 , corrected $P = .05$ with a statistical power of 0.90) as well as the right cerebellum VIII and vermis VIII (aICSR = 0.62 ± 0.24 , HC = 0.41 ± 0.19 , corrected $P = .04$ with a statistical power of 0.86), were observed in patients with aICSR than in HCs (Figure 3B). The comparison between the aICSL and HC groups showed no significant findings. In the comparison of FC between the aICSL and aICSR groups, no significant difference was observed in either the anterior or posterior circulation territory. Regarding the language network, no significant differences in FC were identified by comparing the aICSL or aICSR group with the HC group (Table 3).

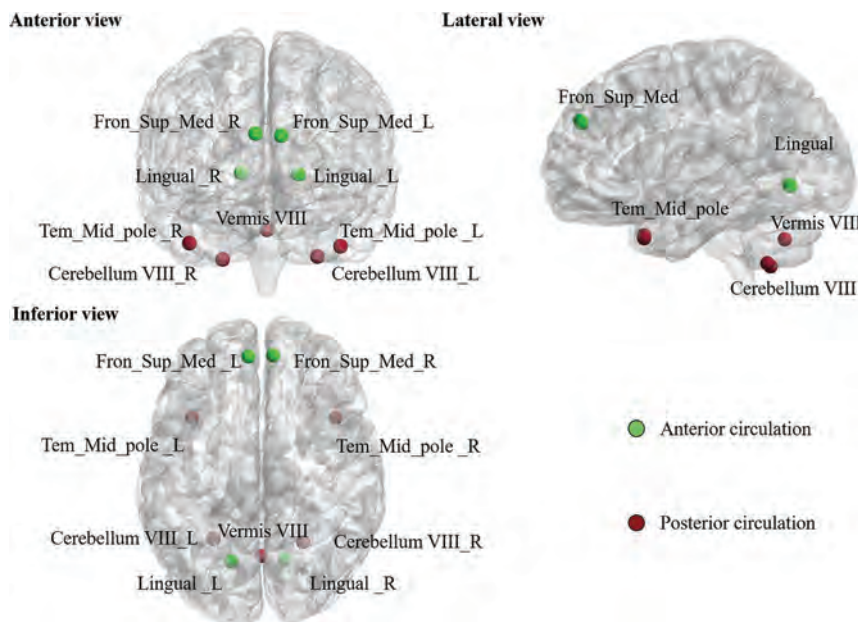


FIG 2. The 9 brain regions were parceled based on the automated anatomical labeling atlas with 116 areas (AAL 116) and highlighted in the following analyses. The green nodes indicate brain regions in the anterior circulation territory; the wine-colored nodes indicate brain regions in the posterior circulation territory.

Table 1: Demographic characteristics and neuropsychological scores of the study cohort

	HC (n = 15)	aICS (n = 55)		P Values (Power)		
		aICSL (n = 22)	aICSR (n = 33)	aICSL vs HC	aICSR vs HC	aICSL vs aICSR
Age	70.67 ± 3.09	64.50 ± 11.68	68.82 ± 9.03	.06	.45	.13
Sex (M:F)	8:7	16:6	25:8	.23	.06	.85
Stenosis (%)	—	80.22 ± 12.68	78.91 ± 12.75	—	—	.71
Handedness (L/R)	0/15	0/22	2/31	1	.33	.24
Mini-Mental State Examination	29.33 ± 0.82	27.32 ± 2.21	28.67 ± 1.31	.002 ^b (0.94)	.08	.01 ^b (0.76)
Digit Span Test						
Forward	8.40 ± 0.74	7.95 ± 1.50	8.21 ± 0.99	.29	.52	.45
Reverse	5.73 ± 1.03	4.45 ± 1.65	5.03 ± 1.67	.01 ^a (0.77)	.14	.21
Verbal Learning Test						
Immediate recall	53.93 ± 8.37	45.95 ± 12.43	49.64 ± 8.37	.04 ^a (0.81)	.15	.23
Delayed recall	10.93 ± 1.44	8.14 ± 3.44	9.48 ± 2.00	.01 ^b (0.92)	.02 ^a (0.87)	.07

^aP < .05.

^bP < .01.

Table 2: The distribution of the severity of white matter hyperintensities for aICSL and aICSR groups. The total Fazekas score is the summation of scores for periventricular white matter and deep white matter

		HC (n = 15)	aICSL (n = 22)	aICSR (n = 33)	P Value		
					aICSL vs HC	aICSR vs HC	aICSL vs aICSR
Fazekas score for periventricular white matter					.501	.586	.637
	0	1 (6.7%)	3 (13.6%)	4 (12.1%)			
	1	11 (73.3%)	9 (50.0%)	19 (60.6%)			
	2	3 (20.0%)	6 (31.8%)	6 (18.2%)			
	3	0 (0.0%)	1 (4.5%)	3 (9.1%)			
Fazekas score for deep white matter					.705	.693	.693
	0	3 (20.0%)	3 (13.6%)	6 (18.2%)			
	1	10 (66.7%)	10 (59.1%)	20 (60.6%)			
	2	2 (13.3%)	5 (22.7%)	3 (12.1%)			
	3	0 (0.0%)	1 (4.5%)	3 (9.1%)			
Total Fazekas score					.413	.801	.157
	0	1 (6.7%)	3 (13.6%)	1 (3.0%)			
	1	2 (13.3%)	0 (0.0%)	8 (24.2%)			
	2	8 (53.3%)	8 (45.5%)	14 (42.4%)			
	3	3 (20.0%)	3 (18.2%)	3 (12.1%)			
	4	1 (6.7%)	4 (18.2%)	3 (9.1%)			
	5	0 (0.0%)	0 (0.0%)	1 (3.0%)			
	6	0 (0.0%)	1 (4.5%)	2 (6.1%)			

Note:—T2 FLAIR images are not available in 10 HCs, 3 aICSL and 1 aICSR patients. The Fazekas scores for those cases were assessed with diffusion tensor imaging.

Correlation between FC and Delayed Recall of Verbal Memory

We observed negative correlations between FC and delayed recall of verbal memory, indicating that stronger FC is associated with a lower level of delayed recall of verbal memory. In the anterior circulation territory, the FC between the right superior medial frontal gyrus and left lingual gyrus showed a significant negative correlation with delayed recall of verbal memory in the aICSL group ($r = -0.559$, $P = .01$ with a statistical power of 0.99). In the posterior circulation territory, the FC between the right middle temporal pole and right cerebellum VIII showed a significant negative correlation with delayed recall of verbal memory in the aICSR group ($r = -0.395$, $P = .03$ with a statistical power of 0.99) (Fig 4).

DISCUSSION

In the current study, patients with either left or right aICS were observed to have lower delayed recall of verbal memory than the HC group. Although the laterality of aICS was not associated with the severity of decline in delayed recall of verbal memory, the stenosis side (in the left and right ICA) influences different FC changes in the anterior and posterior circulation territories compared with HCs. Correlation analyses indicated different functional compensations for decline in delayed recall of verbal memory after left or right unilateral aICS.

MMSE assesses comprehensive cognitive functions, including orientation, delayed recall, working memory, language, and visuoconstruction.³⁰ DST is one of the most commonly used measures of attentional capacity, immediate verbal recall, and working memory, especially for memorization of number

sequences.³¹ In this study, the aICSL group showed significantly reduced MMSE scores compared with HC and aICSR groups. The aICSL group also showed significantly poor levels of reverse DST compared with HC group. In general, multiple cognitive functions exhibited lateralization (left-hemisphere dominance), including language, memory, and logic processing.³² Accordingly, reduced perfusion from the left internal carotid artery may cause a significant influence on the cognitive functions assessed by the MMSE tests and reverse DST. However, the MMSE and reverse DST scores in the aICSL group showed no significant correlations with FC between selected brain regions.

The white matter hyperintensities in T2 FLAIR images indicated an increased risk of cerebrovascular events, stroke, and dementia and can be further employed to predict cognitive impairment.³³ In this study, we found no significant difference in the distribution of Fazekas scores among HC, aICSL,

and aICSR groups. Accordingly, the confounding effect of white matter hyperintensities on the comparisons among 3 groups is controlled in this study.

Recent evidence has shown that cerebrovascular disease is a major contributor to later-life dementia, accounting for up to 20% of cases of dementia.³⁴ Therefore, research of vascular contributions to cognitive impairment and dementia (VCID) is growing. The proposed underlying mechanisms of VCID include cerebral autoregulatory dysfunction, endothelial impairment, and neurovascular uncoupling.³⁵ Normal brain function depends on adequate blood flow supplied by cervico-cerebral blood vessels via competent neurovascular coupling.³⁶ Severe stenosis of carotid arteries leads to impairment of cerebral perfusion. Cerebral autoregulation triggered by decreased cerebral blood perfusion modulates the distribution of blood flow.^{37,38} The altered perfusion from the ipsilateral ICA and contralateral vertebral artery compensates for cerebral perfusion in the affected regions to maintain cognitive function. A cohort study enrolling 19 patients with asymptomatic carotid stenosis and 24 healthy controls showed aICS-induced alteration of regional activation in compensatory regions, including the superior medial frontal gyrus, middle temporal pole, lingual gyrus, and cerebellum.³⁹ The reported FC among compensatory regions in that study is considered to be related to the modulations in language, attention, visual, and memory networks.⁴⁰ The superior medial frontal gyrus is involved in attention,¹⁷ while the lingual gyrus handles the processing of visual stimuli, especially letters.⁴¹ The middle temporal pole and cerebellum VIII participate in memory encoding.⁴² The current study showed that patients with aICS with enhanced FC among compensatory regions exhibit poor delayed

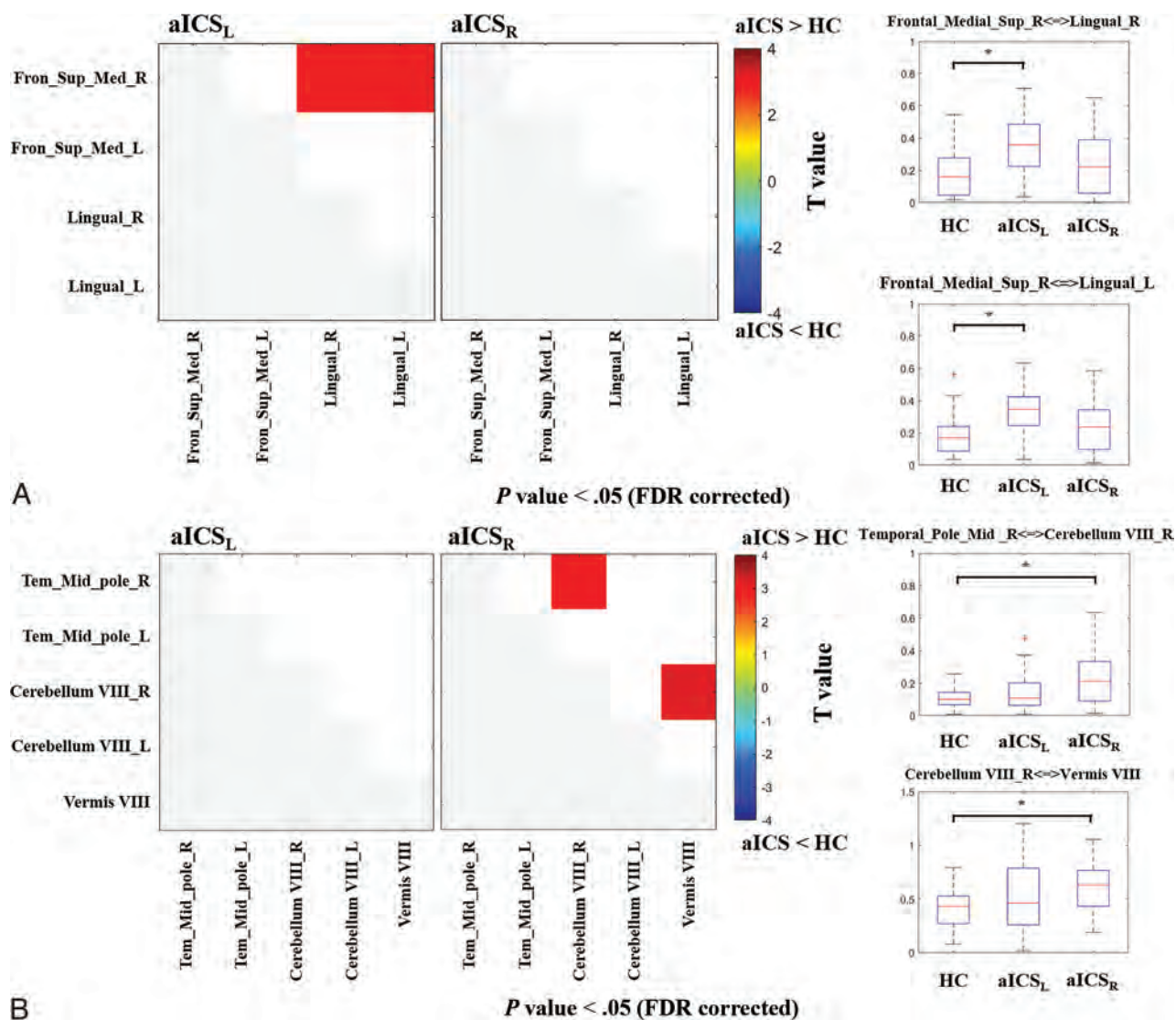


FIG 3. The t maps from the comparisons of FC among the aICS_L, aICS_R, and HC groups. A, The matrices show the comparison between the aICS and HC groups in regions in the anterior territory. The boxplot presents the distribution of altered FC in the anterior circulation territory. B, The matrices show the comparison between the aICS and HC groups in regions in the posterior territory. The boxplot presents the distribution of altered FC in the posterior circulation territory. Red or blue nodes indicate that patients with stenosis in the right internal carotid artery show a significant increase or reduction in FC, respectively. Fron_Sup_Med: superior medial frontal gyrus, Tem_Mid_pole: middle temporal pole, R: right, and L: left. **P* value < .05 (FDR corrected).

Table 3: List of primary language regions with altered FC. The first 3 columns show the distribution of FC in the HC, aICS_L, and aICS_R groups. The fourth and fifth columns list FDR-corrected *P* values of comparison between the HC and aICS_L groups and between the HC and aICS_R groups, respectively

	HC	aICS _L	aICS _R	aICS _L vs HC	aICS _R vs HC
Homopotic					
Broca_L-Broca_R	0.22 ± 0.16	0.18 ± 0.13	0.22 ± 0.17	.73	.99
Geschwind_L-Geschwind_R	0.89 ± 0.25	0.95 ± 0.32	0.85 ± 0.33	.73	.93
Wernicke_L-Wernicke_R	1.21 ± 0.29	0.98 ± 0.36	1.04 ± 0.32	.60	.71
Left hemisphere					
Broca-Geschwind	0.21 ± 0.15	0.23 ± 0.16	0.21 ± 0.20	.73	.99
Broca-Wernicke	0.22 ± 0.14	0.19 ± 0.14	0.26 ± 0.22	.73	.99
Geschwind-Wernicke	0.18 ± 0.15	0.29 ± 0.33	0.22 ± 0.19	.73	.93
Right hemisphere					
Broca-Geschwind	0.15 ± 0.11	0.18 ± 0.13	0.20 ± 0.20	.73	.75
Broca-Wernicke	0.57 ± 0.39	0.61 ± 0.28	0.48 ± 0.25	.73	.75
Wernicke-Geschwind	0.18 ± 0.12	0.20 ± 0.14	0.26 ± 0.23	.53	.75

Note:—FDR-corrected *P* value. L: left, R: right.

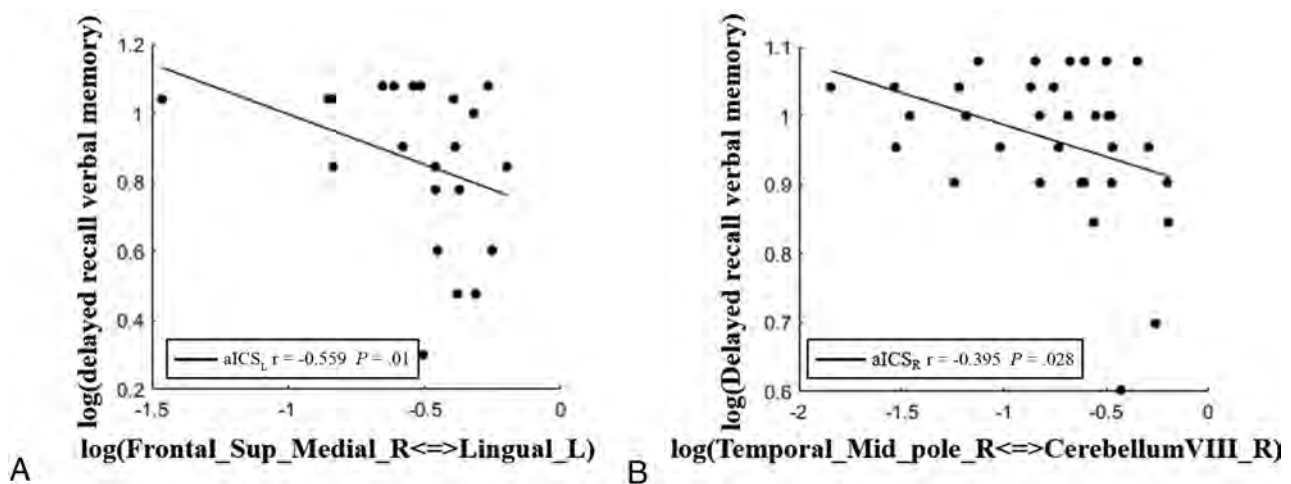


FIG 4. Scatterplots showing correlations between the delayed recall of verbal memory and altered FC in the anterior and posterior vascular territories after aICS_L and aICS_R. The dots represent the strength of the altered FC and delayed recall of verbal memory for patients. The fitted lines are also displayed in the scatterplots. A, In the anterior circulation territory FC matrix, the FC between the right superior medial frontal gyrus and left lingual gyrus was significantly correlated with delayed recall of verbal memory after aICS_L. B, In the posterior circulation territory FC matrix, the FC between the right middle temporal pole and cerebellum VIII was significantly correlated with delayed recall of verbal memory after aICS_R.

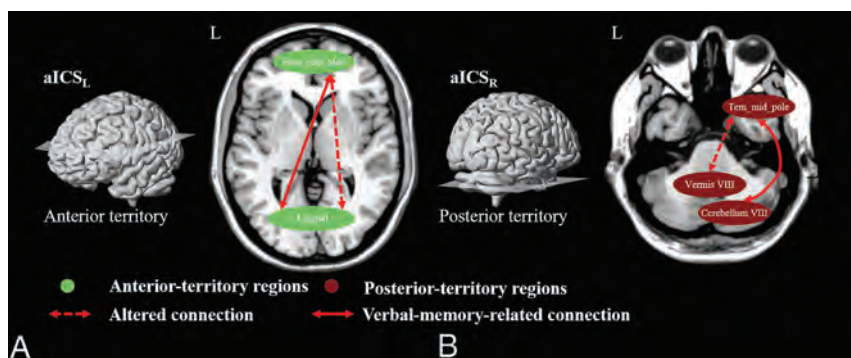


FIG 5. Diagram summarizing the underlying compensatory mechanism (neuroplasticity) after aICS_L and aICS_R. A, Anterior circulation territory compensation for verbal memory recall after aICS_L. B, Patients with aICS_R showed posterior circulation territory compensation for recall verbal memory. The green nodes indicate brain regions in the anterior circulation territory; the wine-colored nodes represent brain regions in the posterior circulation territory. The dashed double arrows indicate altered FC after aICS. The altered connections related to verbal memory recall are presented with double arrows.

recall of verbal memory, which may indicate that altered FC leads to inefficient delayed recall of verbal memory function. However, the negative correlation suggests that enhanced FC among compensatory regions indicates the severity of delayed recall of verbal memory decline following left or right aICS.

The effects of the laterality of aICS on structural and functional connections were less explored.^{12,39,43-46} We observed the aICS_L and aICS_R groups showed different patterns of association between verbal memory decline and altered FC in the anterior and posterior circulation territories, respectively (Fig 5). In this study, we suggest that the side of aICS may involve different compensatory mechanisms associated with the decline in delayed recall of verbal memory. In the patients with aICS_L, we found that the compensation was presented by significantly increased FC related to the right superior medial frontal gyrus in the anterior circulation territory (Figure 3A). However, in patients with

aICS_R, we found different compensation presented by significantly increased FC related to the right cerebellum VIII in the posterior circulation territory (Figure 3B). We speculated that the differences in compensatory mechanisms between the aICS_L and aICS_R groups may be related the lateralization of verbal memory (ie, left-hemisphere dominance).³² While the cerebral perfusion in the left hemisphere (dominant regions of verbal memory) was reduced in the aICS_L group, the primary auxiliary FC related to the contralateral superior medial frontal gyrus was increased as a response (Fig 5). He et al¹³ also observed the cross-hemispheric FC in the patients with unilateral left aICS.

Contrarily, while the perfusion in the right hemisphere (auxiliary regions of verbal memory) was reduced in the aICS_R group, the secondary auxiliary FC related to the ipsilateral cerebellum VIII was increased instead (Fig 5). Carlson et al⁴⁷ reported that patients with severe perfusion reduction in the right hemisphere, such as caused by ischemic stroke, showed significant FC differences in the ipsilateral posterior circulation territory.

A decline in verbal memory is one of the common complaints of patients with aICS. A previous review reported no evidence that the degree of stenosis was predictive of verbal memory decline.⁵ To evaluate the severity of verbal memory decline in the present study, patients with aICS completed a well-developed and well-validated Chinese version of the Verbal Learning Test.⁴⁸ However, the period of rs-fMRI acquisition was approximately 20 minutes, which is shorter than the duration of a Verbal Learning Test. This study employed fMRI-based FC analysis to

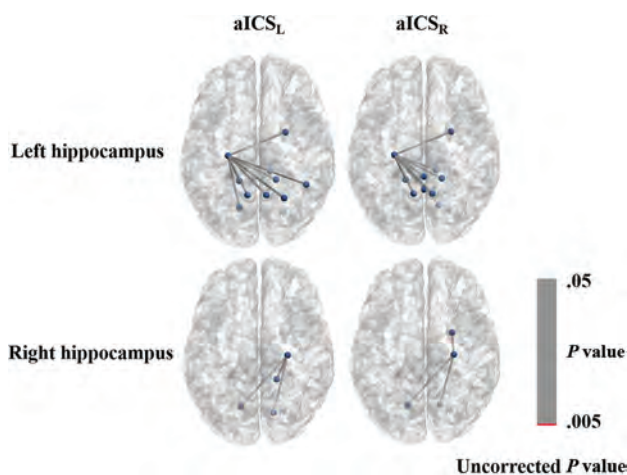


FIG 6. Graph displaying the FC of the left or right hippocampus gyrus with uncorrected P values less than .05. The connections with P values less than .005 are shown in red; those connections with P values between .005 and .05 are shown in gray.

extract quantitative image biomarkers for evaluating functional remodeling following a disease.

This study employed the pretreatment fMRI data to separately explore the association between the altered FC and decline in delayed recall of verbal memory in the aICSL and aICSR groups. We aimed to unravel the influence of the aICS side on the verbal memory decline and investigate corresponding compensatory mechanisms. However, comparing FC changes between pretreatment and posttreatment fMRI for the aICSL and aICSR groups may provide new insights into the therapeutic effect of revascularization. Most previous studies performed the investigation by pooling the aICSL and aICSR groups,^{49,50} which may cause a mixing effect to prevent the identification of significant FC alterations. Previous literature has reported the inconsistent recovery of FC and verbal memory after the revascularization. Wang et al⁴⁹ have reported the significant decreased activation in cerebellar regions in a group of 5 patients with aICSL and 11 with aICSR after the treatment. Quandt et al⁵⁰ have suggested a more significant increase in FC within the contralateral hemisphere in a group of 8 patients with aICSL and 4 with aICSR after the treatment. These inconsistent findings may indicate the influences of aICS side on recovery of FC after the revascularization. Accordingly, the therapeutic effect and recovery mechanism associated with the side of aICS after the revascularization are worthy of further investigation.

Several limitations of the current study are described as follows: First, no hippocampus-related imaging biomarkers for decline in delayed recall of verbal memory were observed (Fig 6). The hippocampal region is mainly perfused by branches of the posterior cerebral artery, which was not significantly affected after aICS.^{51,52} Our study indicated that functional compensation for decline in delayed recall of verbal memory after aICS may be associated with other brain areas, including frontal, temporal, and cerebellar regions. Second, although patients with insufficient blood perfusion in the left hemisphere may exhibit severe decline in delayed recall of verbal memory,⁵³ the small sample size of this study may have impeded detection of significant differences in

delayed recall of verbal memory decline between the aICSL and aICSR groups. We matched the variables, including age, sex, degree of stenosis, and handedness among the 3 groups. The statistical power in FC analysis achieved statistical power between 0.78 and 0.90, suggesting that our results are reliable even with a small sample size. However, further study with a larger sample size is required to consolidate the identified association between FC alteration and verbal memory decline.

CONCLUSIONS

This study suggested that the side of aICS may influence the FC alterations in both the anterior and posterior circulation territories. Stenosis in the left or right ICA was associated with different compensatory mechanisms for the decline in delayed recall of verbal memory.








Disclosure forms provided by the authors are available with the full text and PDF of this article at www.ajnr.org.

REFERENCES

- Krist AH, Davidson KW, Mangione CM, et al. **Screening for asymptomatic carotid artery stenosis: US preventive services task force recommendation statement.** *JAMA* 2021;325:476–81 CrossRef Medline
- Chang RW, Tucker L-Y, Rothenberg KA, et al. **Incidence of ischemic stroke in patients with asymptomatic severe carotid stenosis without surgical intervention.** *JAMA* 2022;327:1974–82 CrossRef Medline
- Jackson DC, Sandoval-Garcia C, Rocque BG, et al. **Cognitive deficits in symptomatic and asymptomatic carotid endarterectomy surgical candidates.** *Arch Clin Neuropsychol* 2016;31:1–7 CrossRef Medline
- Lin C-J, Tu P-C, Chern C-M, et al. **Connectivity features for identifying cognitive impairment in presymptomatic carotid stenosis.** *PLoS One* 2014;9:e85441 CrossRef Medline
- Paraskevas KI, Faggioli G, Ancetti S, et al. **Editor's choice - asymptomatic carotid stenosis and cognitive impairment: a systematic review.** *Eur J Vasc Endovasc Surg* 2021;61:888–99 CrossRef Medline
- Kim JE, Lee BR, Chun JE, et al. **Cognitive dysfunction in 16 patients with carotid stenosis: detailed neuropsychological findings.** *J Clin Neurol* 2007;3:9–17 CrossRef Medline
- Cheng H-L, Lin C-J, Soong B-W, et al. **Impairments in cognitive function and brain connectivity in severe asymptomatic carotid stenosis.** *Stroke* 2012;43:2567–73 CrossRef Medline
- Khan AA, Patel J, Desikan S, et al. **Asymptomatic carotid artery stenosis is associated with cerebral hypoperfusion.** *J Vasc Surg* 2021;73:1611–21.e2 CrossRef Medline
- Chen Y-F, Tang S-C, Wu W-C, et al. **Alterations of cerebral perfusion in asymptomatic internal carotid artery steno-occlusive disease.** *Sci Rep* 2017;7:1841 CrossRef Medline
- Sheth SA, Liebeskind DS. **Imaging evaluation of collaterals in the brain: physiology and clinical translation.** *Curr Radiology Rep* 2014;2:29 CrossRef Medline
- Liang X, Zou Q, He Y, et al. **Coupling of functional connectivity and regional cerebral blood flow reveals a physiological basis for network hubs of the human brain.** *Proc Natl Acad Sci U S A* 2013;110:1929–34 CrossRef Medline
- Dall'Acqua P, et al. **Functional and structural network recovery after mild traumatic brain injury: a 1-year longitudinal study.** *Front Hum Neurosci* 2017;11:280.
- He S, Duan R, Liu Z, et al. **Altered functional connectivity is related to impaired cognition in left unilateral asymptomatic carotid artery stenosis patients.** *BMC Neurol* 2021;21:350 CrossRef Medline
- Maguire EA, Mummery CJ, Buchel C. **Patterns of hippocampal-cortical interaction dissociate temporal lobe memory subsystems.** *Hippocampus* 2000;10:475–82 CrossRef Medline

15. Chen SH, Desmond JE. **Temporal dynamics of cerebro-cerebellar network recruitment during a cognitive task.** *Neuropsychologia* 2005;43:1227–37 CrossRef Medline
16. Ding H, Qin W, Jiang T, et al. **Volumetric variation in subregions of the cerebellum correlates with working memory performance.** *Neurosci Lett* 2012;508:47–51 CrossRef Medline
17. Kozasa EH, Sato JR, Lacerda SS, et al. **Meditation training increases brain efficiency in an attention task.** *Neuroimage* 2012;59:745–49 CrossRef Medline
18. Nyberg L, Eriksson J. **Working memory: maintenance, updating, and the realization of intentions.** *Cold Spring Harb Perspect Biol* 2015;8:a021816 CrossRef Medline
19. Herlin B, Navarro V, Dupont S. **The temporal pole: from anatomy to function-A literature appraisal.** *J Chem Neuroanat* 2021;113:101925 CrossRef Medline
20. Luis EO, Arrondo G, Vidorreta M, et al. **Successful working memory processes and cerebellum in an elderly sample: a neuropsychological and fMRI study.** *PLoS One* 2015;10:e0131536 CrossRef Medline
21. Ojemann GA. **The neurobiology of language and verbal memory: observations from awake neurosurgery.** *Int J Psychophysiol* 2003;48:141–46 CrossRef Medline
22. Knecht S, Deppe M, Dräger B, et al. **Language lateralization in healthy right-handers.** *Brain* 2000;123 (Pt 1):74–81 CrossRef Medline
23. Binder JR, Frost JA, Hammeke TA, et al. **Human brain language areas identified by functional magnetic resonance imaging.** *J Neurosci* 1997;17:353–62 CrossRef Medline
24. Leunen D, Caroff X, Chmura S, et al. **Verbal and spatial learning after temporal lobe excisions in children: an adaptation of the Grober and Buschke procedure.** *Epilepsy Behav* 2009;16:534–38 CrossRef Medline
25. Guo J, Yang M, Biswal BB, et al. **Abnormal functional connectivity density in post-stroke aphasia.** *Brain Topogr* 2019;32:271–82 CrossRef Medline
26. Chang CC, Kramer JH, Lin KN, et al. **Validating the Chinese version of the verbal learning test for screening Alzheimer's disease.** *J Int Neuropsychol Soc* 2010;16:244–51 CrossRef Medline
27. Fazekas F, Chawluk JB, Alavi A, et al. **MR signal abnormalities at 1.5 T in Alzheimer's dementia and normal aging.** *AJR Am J Roentgenol* 1987;149:351–56 CrossRef Medline
28. Yan C-G, Wang X-D, Zuo X-N, et al. **DPABI: data processing & analysis for (resting-state) brain imaging.** *Neuroinformatics* 2016;14:339–51 CrossRef Medline
29. Tzourio-Mazoyer N, Landeau B, Papathanassiou D, et al. **Automated anatomical labeling of activations in SPM using a macroscopic anatomical parcellation of the MNI MRI single-subject brain.** *NeuroImage* 2002;15:273–89 CrossRef Medline
30. Folstein MF, Paul SEF, McHugh R, et al. *Mini-Mental State Examination: MMSE User's Guide.* Psychology Assessment Resources; 2000:12.
31. Ostrosky-Solis F, Lozano A. **Digit Span: Effect of education and culture.** *Int J Psychol* 2006;41:333–41 CrossRef
32. Coleman S, Zenhausen R. **Processing speed, laterality patterns, and memory encoding as a function of hemispheric dominance.** *Bull Psychon Soc* 1979;14:357–60 CrossRef
33. Stéphanie D, Markus HS. **The clinical importance of white matter hyperintensities on brain magnetic resonance imaging: systematic review and meta-analysis.** *BMJ* 2010;341:c3666 CrossRef Medline
34. Knopman DS. **Cerebrovascular disease and dementia.** *Br J Radiology* 2007;80 Spec No 2:S121–7 CrossRef Medline
35. Toth P, Tarantini S, Csizsar A, et al. **Functional vascular contributions to cognitive impairment and dementia: mechanisms and consequences of cerebral autoregulatory dysfunction, endothelial impairment, and neurovascular uncoupling in aging.** *Am J Physiol Heart Circ Physiol* 2017;312:H1–H20 CrossRef Medline
36. Phillips AA, Chan FH, Zheng MMZ, et al. **Neurovascular coupling in humans: physiology, methodological advances and clinical implications.** *J Cereb Blood Flow Metab* 2016;36:647–64 CrossRef Medline
37. Paulson OB, Strandgaard S, Edvinsson L. **Cerebral autoregulation.** *Cerebrovasc Brain Metab Rev* 1990;2:161–92
38. Shekhar S, et al. **Cerebral autoregulation in hypertension and ischemic stroke: a mini review.** *J Pharm Sci Exp Pharmacol* 2017;2017:21–27
39. Wang T, Xiao F, Wu G, et al. **Impairments in brain perfusion, metabolites, functional connectivity, and cognition in severe asymptomatic carotid stenosis patients: an integrated MRI study.** *Neural Plast* 2017;2017:1–7 CrossRef
40. Tatsumi IF, Watanabe M. **Verbal Memory.** In: *Encyclopedia of Neuroscience.* Binder MD, Hirokawa N, Windhorst U, eds. Springer-Verlag Berlin Heidelberg; 2009:4176–78 CrossRef
41. Mechelli A, Humphreys GW, Mayall K, et al. **Differential effects of word length and visual contrast in the fusiform and lingual gyri during reading.** *Proc Biol Sci* 2000;267:1909–13 CrossRef Medline
42. Cui D, Zhang L, Zheng F, et al. **Volumetric reduction of cerebellar lobules associated with memory decline across the adult lifespan.** *Quant Imaging Med Surg* 2020;10:148–59 CrossRef Medline
43. Gao L, Wang T, Qian T, et al. **Severe asymptomatic carotid stenosis is associated with robust reductions in homotopic functional connectivity.** *Neuroimage Clin* 2019;24:102101 CrossRef Medline
44. He S, Liu Z, Xu Z, et al. **Brain functional network in chronic asymptomatic carotid artery stenosis and occlusion: changes and compensation.** *Neural Plast* 2020;2020:9345602.
45. Herweh C, Attigah N, Nagel S, et al. **Quantitative high-field diffusion tensor imaging of cerebral white matter in asymptomatic high-grade internal carotid artery stenosis.** *Eur Neurol* 2012;67:246–51 CrossRef Medline
46. Liu X, Xu D, Zhong X, et al. **Altered callosal morphology and connectivity in asymptomatic carotid stenosis.** *J Magn Reson Imaging* 2023;59:998–1007 CrossRef Medline
47. Carlson HL, Sugden C, Brooks BL, et al. **Functional connectivity of language networks after perinatal stroke.** *Neuroimage Clin* 2019;23:101861 CrossRef Medline
48. Birn RM, Molloy EK, Patriat R, et al. **The effect of scan length on the reliability of resting-state fMRI connectivity estimates.** *Neuroimage* 2013;83:550–58 CrossRef Medline
49. Wang T, Sun D, Liu Y, et al. **The impact of carotid artery stenting on cerebral perfusion, functional connectivity, and cognition in severe asymptomatic carotid stenosis patients.** *Front Neurol* 2017;8:403 CrossRef Medline
50. Quandt F, Fischer F, Schröder J, et al. **Normalization of reduced functional connectivity after revascularization of asymptomatic carotid stenosis.** *J Cereb Blood Flow Metab* 2019;40:1838–48 CrossRef Medline
51. Goetzen B, Sztamska E. **Comparative anatomy of the arterial vascularization of the hippocampus in man and in experimental animals (cat, rabbit and sheep).** *Neuropatol Pol* 1992;30:173–84
52. Bannerman DM, Rawlins JNP, McHugh SB, et al. **Regional dissociations within the hippocampus-memory and anxiety.** *Neurosci Biobehav Rev* 2004;28:273–83 CrossRef Medline
53. Andrews G, Halford GS, Shum DHK, et al. **Verbal learning and memory following stroke.** *Brain Inj* 2014;28:442–47 CrossRef Medline

MR Imaging Features of Critical Spinal Demyelinating Lesions Associated with Progressive Motor Impairment

 B. Mark Keegan,  Steven A. Messina,  Dennis Hanson,  David Holmes, Jon Camp, Elia Sechi, Shreya Nayak,  Benan Barakat, Rowaid Ahmad, Jay Mandrekar, W. Scott Harmsen,  Orhun Kantarci, Brian G. Weinshenker, and  Eoin P. Flanagan



ABSTRACT

BACKGROUND AND PURPOSE: Progressive MS is typically heralded by a myelopathic pattern of asymmetric progressive motor weakness. Focal individual “critical” demyelinating spinal cord lesions anatomically associated with progressive motor impairment may be a compelling explanation for this clinical presentation as described in progressive solitary sclerosis (single CNS demyelinating lesion), progressive demyelination with highly restricted MR imaging lesion burden (2–5 total CNS demyelinating lesions; progressive paucisclerotic MS), and progressive, exclusively unilateral hemi- or monoparetic MS (>5 CNS demyelinating progressive unilateral hemi- or monoparetic MS [PUHMS] lesions). Critical demyelinating lesions appear strikingly similar across these cohorts, and we describe their specific spinal cord MR imaging characteristics.

MATERIALS AND METHODS: We performed a retrospective, observational MR imaging study comparing spinal cord critical demyelinating lesions anatomically associated with progressive motor impairment with any additional “noncritical” (not anatomically associated with progressive motor impairment) spinal cord demyelinating lesions. All spinal cord MR images (302 cervical and 91 thoracic) were reviewed by an experienced neuroradiologist with final radiologic assessment on the most recent MR imaging. Anatomic association with clinical progressive motor impairment was confirmed independently by MS subspecialists.

RESULTS: Ninety-one individuals (PUHMS, 37 [41%], progressive paucisclerosis 35 [38%], progressive solitary sclerosis 19 [21%]) with 91 critical and 98 noncritical spinal cord MR imaging demyelinating lesions were evaluated. MR imaging characteristics that favored critical spinal cord demyelinating lesions over noncritical lesions included moderate-to-severe, focal, lesion-associated spinal cord atrophy: 41/91 (45%) versus 0/98 (0%) (OR, 161.91; 9.43 to >999.9); lateral column axial location (OR, 10.43; 3.88–28.07); central region (OR, 3.23; 1.78–5.88); ventral column (OR, 2.98; 1.55–5.72); and larger lesion size of the axial width (OR, 2.01; 1.49–2.72), transverse axial size (OR, 1.66; 1.36–2.01), or lesion area (OR, 1.14; 1.08–1.2). Multiple regression analysis revealed focal atrophy and lateral axial location as having the strongest association with critical demyelinating lesions.

CONCLUSIONS: Focal, lesion-associated atrophy, lateral column axial location, and larger lesion size are spinal cord MR imaging characteristics of critical demyelinating lesions. The presence of critical demyelinating lesions should be sought as these features may be associated with the development of progressive motor impairment in MS.

ABBREVIATIONS: PUHMS = progressive unilateral hemi- or monoparetic MS; PPS = progressive paucisclerosis; PSS = progressive solitary sclerosis

Insidiously progressive, asymmetric, myelopathic upper motor neuron weakness is the hallmark of and among the most debilitating features in individuals with progressive demyelinating disease such as progressive MS.¹ The direct association between

specific, individual, focal demyelinating lesions (the most common radiologic and pathologic feature of MS) with progressive motor impairment has been less clear. Prior studies examining progressive MS development have mainly focused on brain parenchymal changes, including whole-brain atrophy, gray matter atrophy, cortical demyelinating lesions, and slowly expanding brain lesions,^{2–6} but there remains a “clinical-radiologic paradox,”⁷ whereby the presence and number of MR imaging brain lesions do not reliably predict the development of progressive MS.

Received December 19, 2023; accepted after revision February 19, 2024.

From the Department of Neurology (B.M.K., E.S., S.N., B.B., R.A., J.M., O.K., B.G.W., E.P.F.), Center for Multiple Sclerosis and Autoimmune Neurology, Department of Radiology (S.A.M.), Biomedical Imaging Resource (D. Hanson, D. Holmes, J.C.), and Quantitative Health Services (J.M., W.S.H.), Mayo Clinic, Rochester, Minnesota; Università degli Studi di Sassari (E.S.), Sassari, Italy; St. Elizabeth Dearborn Hospital (S.N.), Lawrenceburg, Indiana; Mercy St. Vincent Medical Center (B.B.), Toledo, Ohio; University of Texas Medical Branch (R.A.), Galveston, Texas; and Department of Neurology (B.G.W.), University of Virginia Health, Charlottesville, Virginia.

This work was funded by the Mayo Clinic Center for Individualized Medicine and Applebaum Family Fund Philanthropy.

Please address correspondence to B. Mark Keegan, MD, FRCP(C), Multiple Sclerosis and Autoimmune Neurology, Mayo Clinic College of Medicine, Mayo Clinic, 200 First St SW, Rochester, MN 55905; e-mail: keegan.bmark@mayo.edu

<http://dx.doi.org/10.3174/ajnr.A8304>

SUMMARY SECTION

PREVIOUS LITERATURE: Progressive myelopathic motor impairment is the hallmark feature of progressive multiple sclerosis (MS). Brain involvement such as whole brain atrophy, cortical demyelinating lesions, and slowly expanding brain lesions partially explain progressive MS. Spinal cord atrophy is associated with progression, but there remains an incomplete understanding of how specific focal demyelinating lesions may contribute to progressive MS. Some selected patient cohorts have specific focal “critical” demyelinating lesions anatomically associated with motor progression even with very few additional demyelinating lesions. MR imaging characteristics of “critical” demyelinating lesions are undefined and could provide clinical usefulness in assessing progressive MS.

KEY FINDINGS: “Critical” demyelinating spinal cord lesions anatomically and clinically associated with progressive motor impairment have MR imaging features of focal spinal cord atrophy, lateral axial location, and are larger in size.

KNOWLEDGE ADVANCEMENT: MR imaging assessment of the characteristic features of “critical” demyelinating lesions may be useful in correlating clinical features of progressive motor impairment of progressive MS. “Critical” demyelinating lesions may be important prognostic features in the development of progressive MS.

Spinal cord atrophy is present in those with primary and secondary-progressive MS more commonly than in those remaining without progressive disease (“benign” MS). The association with individual focal demyelinating lesions and progressive MS is less certain.⁸ Spinal cord atrophy is found due to both white and gray matter involvement and distinguishes individuals with this condition from healthy controls. MS spinal cord pathology shows focal demyelinating and decreased axonal density compared with healthy controls.⁹

The progressive and asymmetric myelopathic pattern could be better explained anatomically by multifocal demyelinating lesions within the spinal cord. Recently, we termed a “critical” demyelinating lesion as that in which an anatomic association was apparent between a specific focal demyelinating plaque and progressive upper motor neuron weakness or spasticity.¹⁰ “Critical demyelinating lesions” are a suggested term used at our MS center to describe a lesion that is anatomically associated with the progressive motor impairment seen clinically, and if the patient did not have that lesion, he or she would be almost without impairment. Such critical demyelinating lesions were described in those with only a single CNS demyelinating lesion (progressive solitary sclerosis [PSS]),¹¹ those with a highly restricted (2–5 total MR imaging lesions) demyelinating disease (progressive paucisclerosis [PPS]),¹² and those with unlimited CNS demyelinating lesion burden (>5 CNS lesions) but with exclusively unilateral progressive motor impairment (progressive unilateral hemi- or monoparetic MS [PUHMS]).¹³ While a critical demyelinating lesion may be located within the cervicomedullary junction/brainstem¹⁴ or cerebral white matter parenchyma, the most common location is within the spinal cord.^{11,13,14} Clinical features of progressive motor impairment and MR imaging features of a critical demyelinating lesion appear to be strikingly similar in PSS, PPS, and PUHMS. The aim of this study was to assess the MR imaging characteristics of critical demyelinating spinal cord lesions in these cohorts and compare them with additionally found noncritical spinal cord MR imaging lesions.

MATERIALS AND METHODS

Patient Ascertainment

A retrospective, comparative study of our clinic population assessing individuals with progressive motor impairment for >1

year due to a spinal cord critical demyelinating lesion reviewed data from January 1, 1996, to December 31, 2020 (Fig 1). Patients provided written informed consent according to the Declaration of Helsinki for the use of their de-identified information for research purposes. The study was approved by Mayo Clinic institutional review board (IRB 09–7045).

We included individuals with progressive upper motor neuron impairment for >1 year, consistent with PSS (MR imaging burden of a single lesion), PPS (defined as a total CNS MR imaging burden of between 2 and 5 demyelinating lesions), or PUHMS (defined as exclusively unilateral, hemi- or monoparetic motor impairment with >5 total CNS MR imaging demyelinating lesions), and clinical and MR imaging available and of adequate quality.

This was a retrospective study, identified on retrospective review of records following appropriate assessment into the 3 cohorts described. Participants were collected from prior publications ($n = 78$)^{11–13} and subsequent enrollment ($n = 13$). We attempted to enroll all qualifying patients, but we could have missed additional, otherwise-qualified patients. MS-trained neurologists assessed progressive motor impairment by both a consistent clinical history of progressive upper motor neuron weakness characteristics of MS and, when possible, by repeat clinical examination.

Exclusion criteria were PSS, PPS, and PUHMS, when the critical demyelinating lesion was not in the spinal cord (ie, brain or brainstem corticospinal tract lesion) and there were nondefinitive progressive motor impairment and identifiable alternative etiologies of progressive motor impairment. Alternative etiologies for progressive motor impairment apart from CNS demyelinating disease were determined, including compressive, infectious, inherited, nutritional, neoplastic or vascular disease or other immune-mediated demyelinating diseases such as aquaporin-4 immunoglobulin G seropositive neuromyelitis optica spectrum disorder or myelin oligodendrocyte glycoprotein antibody-associated disease. Neuromyelitis optica spectrum disorder and myelin oligodendrocyte glycoprotein antibody-associated disease were excluded by the clinical presentation, neuroimaging findings, and, when available, serologic assessment specific to these immune demyelinating

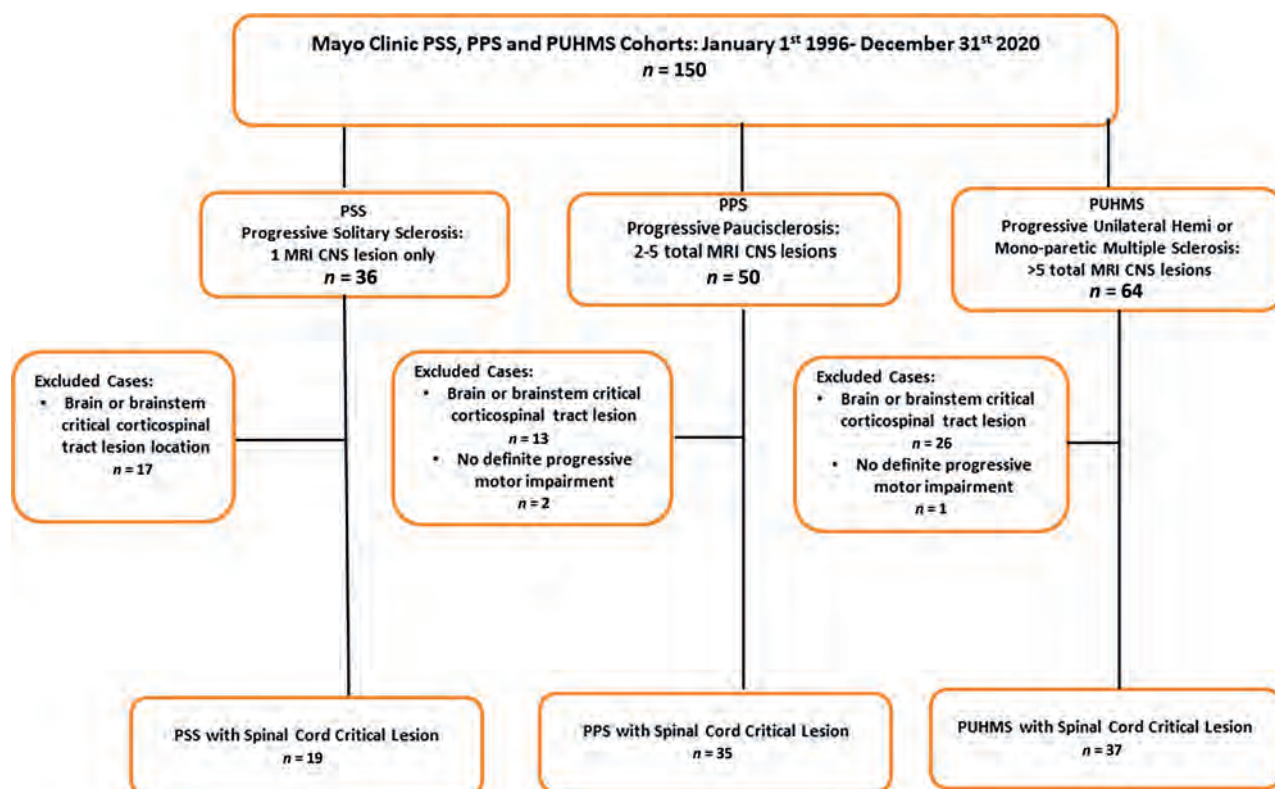


FIG 1. Patient ascertainment algorithm.

diseases. Peripheral nervous system involvement contributing to progressive motor impairment was evaluated by neurologic examination by neurologists and, when indicated, with nerve conduction studies and electromyography.

Clinical Evaluation. All participants except one were evaluated by our MS subspecialty neurologists. The remaining person declined face-to-face evaluation, and clinical evaluation was documented at an outside facility and by MR images retrieved electronically for review.

Data recorded included participant sex, age at CNS demyelinating disease symptom onset, demyelinating disease clinical course (relapse onset before progressive motor impairment, “secondary-progressive,” or progressive motor impairment from onset “primary-progressive”), and CSF findings including white blood cell count, protein, glucose, neural autoantibodies, and cytology when available. CSF abnormalities consistent with demyelinating disease were defined as either or all of ≥ 2 unique CSF abnormal oligoclonal bands (compared with serum oligoclonal bands) or immunoglobulin G (index of >0.85 or CSF κ free light chain of >0.1000 mg/dL).

MR Imaging Evaluation

Spinal Cord MR imaging Acquisition. For imaging performed at our institution, spinal cord MR imaging consisted of sagittal T1- and T2-weighted, frequently sagittal T1- and T2-weighted STIR, axial T2-weighted, sagittal postgadolinium T1-weighted and, in some, axial postgadolinium T1-weighted imaging. Brain MR imaging included T1- and T2-weighted, T2-weighted FLAIR, and postgadolinium T1-weighted sequences. The demyelinating

protocol at our institution for a spinal cord section thickness is set to 3 mm for sagittal and 4 mm for axial images, and brain MR imaging currently has a section thickness of 1 mm for T2 FLAIR and T1-weighted (pre- and postcontrast) images. Most MR imaging examinations were performed at 3T: cervical spine: GE Healthcare: sagittal T1 FLAIR (FOV = 220; matrix = 320×224 ; TR = 2800 ms; TE = 28 ms), sagittal T2 (FOV = 220; matrix = 384×256 ; TR = 3000–6000 ms; TE = 105 ms), sagittal STIR (FOV = 220; matrix = 352×224 ; TR = 2600 ms; TE = 42 ms; TI = 143 ms), and axial T2 (FOV = 200; matrix = 320×256 ; TR = 3000–6000 ms; TE = 105 ms). Siemens: sagittal T1 (FOV = 220; matrix = 320×224 ; TR = 600 ms; TE = 9 ms), sagittal T2 (FOV = 220; matrix = 384×269 ; TR = 3000–6000 ms; TE = 94 ms), sagittal STIR (FOV = 220; matrix = 256×218 ; TR = 3000–6000 ms; TE = 52 ms; TI = 145 ms), and axial T2 (FOV = 140; matrix = 320×240 ; TR = 3000–6000 ms; TE = 99 ms). Thoracic spine: GE Healthcare: sagittal T1 FLAIR (FOV = 300; matrix = 384×56 ; TR = 2800 ms; TE = 24 ms), sagittal T2 (FOV = 300; matrix = 488×288 ; TR = 3000–6000 ms; TE = 102 ms), sagittal STIR (FOV = 300; matrix = 352×288 ; TR = 3248 ms; TE = 42 ms; TI = 143 ms), and axial T2 (FOV = 200; matrix = 384×256 ; TR = 3000–6000 ms; TE = 102 ms). Siemens: sagittal T1 (FOV = 320; matrix = 384×288 ; TR = 600 ms; TE = 7.2 ms), sagittal T2 (FOV = 320; matrix = 448×336 ; TR = 3000–6000 ms; TE = 94 ms), sagittal STIR (FOV = 320; matrix = 320×256 ; TR = 2600–6000 ms; TE = 42 ms; TI = 145 ms), and axial T2 (FOV = 200; matrix = 320×256 ; TR = 3000–6000 ms; TE = 91 ms).

Spinal cord MR imaging from outside institutions, at a minimum, consisted of sagittal T1- and T2-weighted and axial

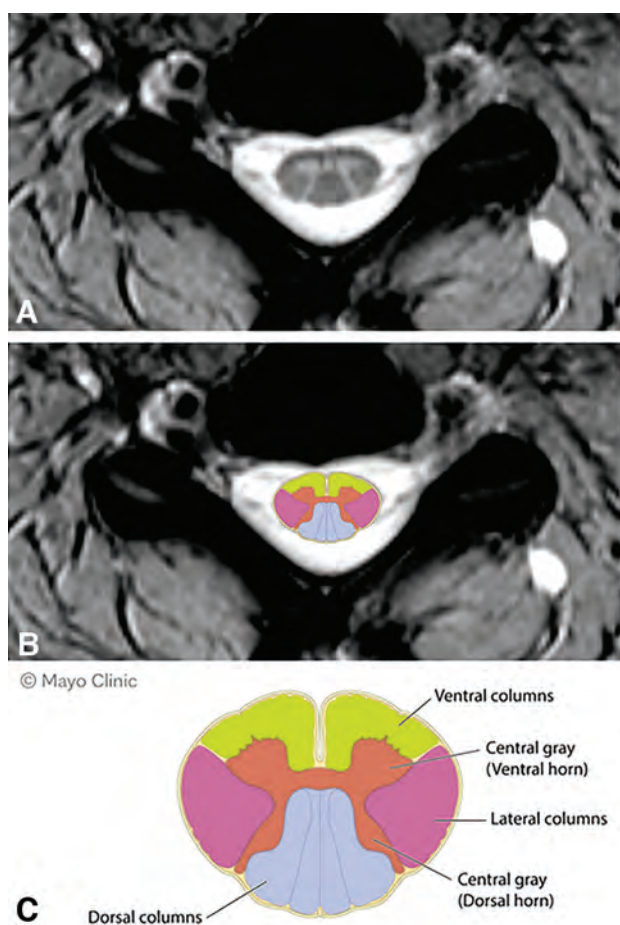


FIG 2. Axial spinal cord columns. A, Axial T2 spinal cord imaging. B, Superimposed schematic of axial columns on axial MR image. C, Schematic diagram of axial columns of spinal cord.

T2-weighted sequences. Brain MR imaging from outside institutions required a minimum of T1- and T2-weighted and T2-weighted FLAIR sequences.

Spinal Cord MR Imaging Lesion Evaluation/Spinal Cord Tool. All spinal cord MR images in each participant were reviewed in a blinded fashion from the neurologic evaluation by an experienced, board-certified neuroradiologist to identify all unequivocal spinal cord demyelinating lesions and their location (Fig 2). Assessments were made manually and then entered into an interactive case report form tool similar to others developed previously.¹⁵ Because individuals with PSS have only 1 demyelinating lesion, additional spinal cord lesions were seen in those with PPS and PUHMS. The categoric definition of MR imaging assessment was defined before data collection. Data acquired for each critical and noncritical lesion included sagittal assessment of the corresponding vertebral body location, laterality (left versus right), axial assessment of specific spinal cord column involvement (ventral, dorsal, central, lateral, and combinations of each when >1 column was affected [Fig 2]), and lesion size (the number of vertebrae involved and width, height, and area of each detected lesion in each image were drawn and measured by the neuroradiologist).

The spinal cord interactive tool was developed by our Biomedical Imaging Resource to manage the cohort images and allow a generally unencumbered examination of the images while forcing decisions of lesion presence and count or absence in specific regions of the brain scans and providing tools to fully characterize the lesions detected in the thoracic and cervical scans. The width, height, and area of each detected lesion in each image was measured, along with the number of vertebrae involved and the ROI saved with sufficient detail to allow additional review/auditing of the acquired data as well as the ability to retrieve all lesion samples for future training of an artificial intelligence model to detect lesions.

Critical Lesion versus Noncritical Lesion Assessment

Neurologists with expertise in MS independently reviewed all available clinical data regarding assessment of progressive motor impairment due to demyelinating disease. Prior experience from assessment of such lesions in earlier studies identified a lesion anatomically associated with progressive motor impairment. For example, a person with progressive face-sparing, left hemiparesis could be classified as having a critical spinal cord lesion only if there was a cervical spinal cord lesion involving the left hemi-spinal cord and no additional demyelinating lesions along the corticospinal tracts of the cerebrum, brainstem, or cervicomedullary junction. To be classified as critical, the demyelinating lesion must account for all involved limbs. However, a person with progressive left monoparesis of the lower extremity would qualify if either a cervical or thoracic spinal cord lesion of the left hemi-spinal cord were present.¹³ A contralateral hemi-spinal cord lesion would not be included because it would not explain the progressive clinical findings. When uncertainty arose as to the classification of critical demyelinating lesions, consensus was reached by the evaluating coauthors (B.M.K., S.A.M., E.P.F.).

Focal Spinal Cord Atrophy

Focal spinal cord atrophy was gauged initially by visual inspection. With no reliable, objective, and validated methods to assess focal spinal cord atrophy formally, a visually highly compelling and robust atrophy was sought. The presence of atrophy was dichotomized as “present” only when judged to be unequivocally moderate or severe (ie, at least 20% loss of spinal cord with area of T2 signal abnormality compared with the unaffected hemicord at that level) and judged to be “absent” when only mild or no atrophy was observed. In equivocal circumstances, consensus was reached by the evaluating coauthors.

Statistical Analysis

Age was summarized using median, range, and SD, while PSS, PPS, and PUHMS were summarized using count and percentage. Logistic regression was used to examine the relationship between critical and noncritical lesions and multiple biologic variables. Multiple logistic regression and the Firth option were used to assess multiple biologic variables including atrophy. Analysis was performed using SAS, Version 9.4 (SAS Institute).

Data Availability

Anonymized data used for this study are available.

RESULTS

Demographics and Clinical Presentation

Participant demographics and clinical presentations are detailed in Table 1. Most participants were women and of white ethnicity. The most common clinical courses were progression from onset (primary-progressive) and PUHMS.

Neuroimaging

Formal assessment was performed on 302 cervical and 91 thoracic spinal cord MR images. Ninety-one critical demyelinating lesions were identified and compared with 88 noncritical lesions assessed (Table 2). The critical demyelinating lesion was in the cervical spinal cord, associated with corresponding ipsilateral hemiparesis or monoparesis in 74 patients, and in the thoracic spinal cord associated with corresponding ipsilateral monoparesis in 17 patients. Critical demyelinating lesions were more commonly observed in the upper cervical spinal cord (C1–4; $n = 52$) and lower cervical spinal cord (C5–7; $n = 22$) than in the upper thoracic spinal cord (T1–5; $n = 12$) or lower thoracic cord (T6–12; $n = 5$). Sixty-three noncritical cervical spinal cord lesions were evaluated in 39 individuals, and 25 noncritical thoracic spinal cord lesions were evaluated in 24 individuals.

Table 1: Clinical characteristics of 91 individuals with critical demyelinating lesions

Clinical Characteristics	
Demographics	
Female sex (No.) (%)	51 (56%)
White ethnicity (No.) (%)	88 (97%)
Median age at first symptom (range) (yr)	50 (28–65)
Median age at last MR imaging (range) (yr)	58 (36–80)
Median age at progression (range) (yr)	52 (30–73)
Clinical course (No.) (%)	
Progression from onset (primary-progressive)	56/91 (62%)
Relapse onset (secondary-progressive)	25/91 (28%)
Clinical cohort (No.) (%)	
PUHMS	37 (41%)
PPS	35 (38%)
PSS	19 (21%)

Moderate-to-Severe Focal Lesional Atrophy

All spinal cord lesions with moderate-to-severe focal lesional atrophy were critical demyelinating lesions, and no noncritical demyelinating lesions had moderate-to-severe focal lesion atrophy (OR, 161.907; 95% CI, 9.433 to >999.999; $P = .0005$). Of the critical demyelinating lesions, 41/91 (45.1%) had moderate-to-severe focal lesional atrophy (Table 2 and Figs 3 and 4).

Axial Column Lesion Location

On univariate analysis, critical demyelinating lesions were most commonly identified as involving the lateral axial region of the spinal cord (OR, 10.43; 95% CI, 3.88–28.07; $P < .0001$), the central axial region (OR, 3.23; 95% CI, 1.78–5.88; $P = .0001$), and the ventral axial region (OR, 2.98; 95% CI, 1.55–5.72; $P = .001$). Lesions were less likely to be critical when they involved the dorsal axial regions of the spinal cord (OR, 0.45; 95% CI, 0.24–0.86; $P = .0145$; Table 2 and Figs 3 and 4).

Critical demyelinating lesions were more likely to involve >1 tract (Table 2). There was an increased association with critical demyelinating lesions, especially when the lateral column plus additional columns were involved (lateral only: OR, 5.01; 95% CI, 1.71–14.64; $P = .0033$); lateral column and any additional column lateral + other: OR, 17.27; 95% CI, 6.12–48.70; $P < .0001$).

Central and ventral lesions may be critical if the lateral column is also involved (Table 2). When lesions involved solely the central region, they were rarely critical. Critical lesions were more common in those with either ventral or central lesion and lateral lesion involvement versus those with central or ventral or dorsal with no lateral lesion involvement (OR, 8.60; 95% CI, 2.81–33.00; $P < .001$). No critical lesion solely involved the ventral column but always involved the lateral column as well.

Larger lesion size is associated with critical lesion status, including the area of the lesion (median, 14 versus 7.6 mm; OR, 1.14; 95% CI, 1.08–1.20; $P = < .0001$; C-statistic per 1 mm = 0.75; 95% CI, 0.68–0.81), axial anterior-posterior width

Table 2: MR imaging characteristics in 91 critical and 88 noncritical spinal cord demyelinating lesions

	Critical Spinal Cord Demyelinating Lesion ($n = 91$)	Noncritical Spinal Cord Demyelinating Lesion ($n = 88$)	OR 95% CI	P Value
Sagittal location (No.) (%)				
Cervical	74 (81)	63 (64)		
Thoracic	17 (19)	25 (26)		
Moderate/severe atrophy (No.) (%)	41 (45)	0 (0%)	161.91 (9.43 to >999.9)	.0005
Axial column location (No.) (%)				
Lateral	86 (95)	61 (62)	10.43 (3.88–28.07)	<.0001
Central	62 (68)	39 (40)	3.23 (1.78–5.88)	.0001
Ventral	38 (42)	19 (19)	2.98 (1.55–5.72)	.001
Dorsal	21 (23)	39 (40)	0.45 (0.24–0.86)	.0145
Axial column lateral involvement				<.0001
Lateral with additional columns	63 (69)	34 (35)		
Lateral only	23 (25)	27 (28)		
No lateral involved	5 (6)	37 (38)		
Median lesion size (mm)				
Axial A/P width	4.1	3.3	2.01 (1.49–2.72)	<.0001
Transverse axial (mm ³)	5.2	3.5	1.66 (1.36–2.01)	<.0001
Area lesion	14.0	7.6	1.14 (1.08–1.2)	<.0001

Note:—A/P indicates anterior-posterior.

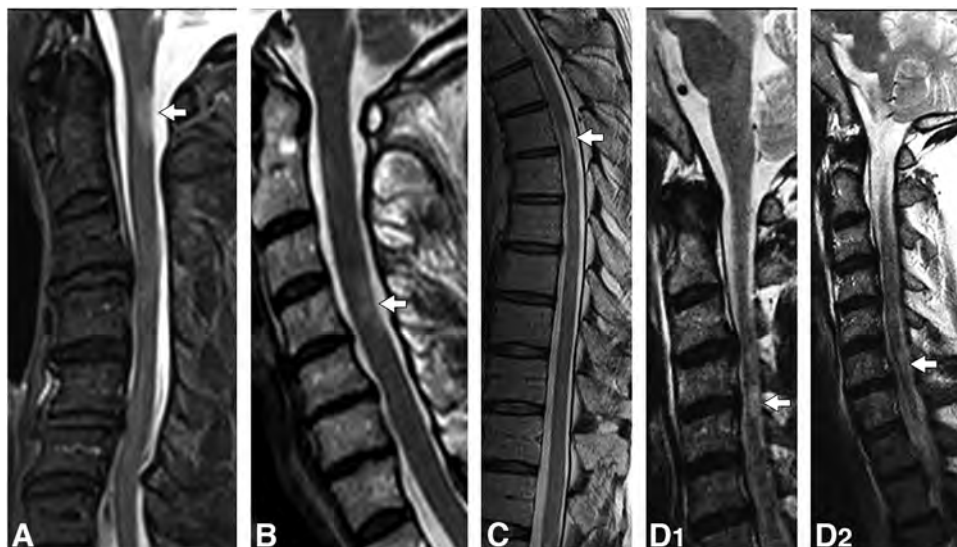


FIG 3. Examples of critical T2-hyperintense demyelinating lesions on sagittal T2-weighted images. Imaging composite of sagittal T2-weighted images in patients with critical lesions with corresponding axial images. A right C1 T2-hyperintense lesion with focal atrophy (A, arrow). A left C4 T2-hyperintense lesion with focal atrophy (B, arrow). A right-sided upper thoracic spine; T2-hyperintense lesion with focal atrophy (C, arrow). A left-sided C4-C5 T2-hyperintense lesion with focal atrophy (D₁, arrow). An additional noncritical lesion is noted at the C6 level (D₂, arrow).

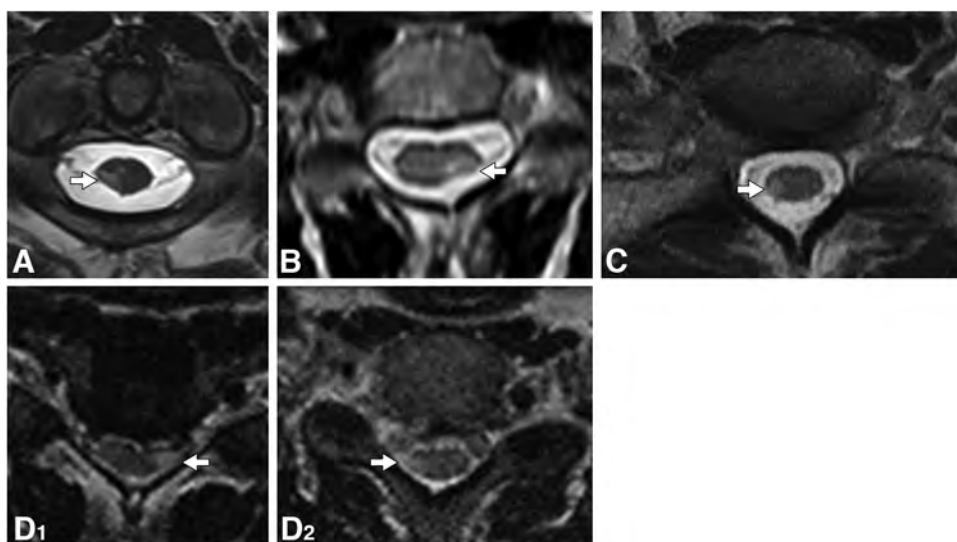


FIG 4. Examples of critical T2-hyperintense demyelinating lesions on axial T2-weighted images. Imaging composite of axial T2-weighted images in patients with critical lesions, corresponding to sagittal images and clinical details. The corresponding axial images reveal a T2-hyperintense lesion in the right lateral column with focal atrophy (A, arrow), a T2-hyperintense lesion in the left lateral column with focal atrophy (B, arrow), a T2-hyperintense lesion in the right lateral column with focal atrophy (C, arrow), a T2-hyperintense lesion in the left lateral column with focal atrophy (D₁, arrow), and a T2-hyperintense lesion in the right lateral column without focal atrophy (D₂, arrow).

(4.1 versus 3.3 mm; OR, 2.01; 95% CI, 1.49–2.72; $P = <.0001$), and the transverse axial diameter of the lesion (median, 5.2 versus 3.5 mm; OR, 1.66; 95% CI, 1.36–2.01; $P = <.0001$; C-statistic per 1 mm = 0.71; 95% CI, 0.64–0.78; Table 2). The association with lesion size remained even though such lesions were often atrophic, making them smaller. This association between larger lesion size and the critical nature of the lesion is especially pronounced if considered in the absence of moderate-to-severe atrophy, which reduces the lesion size.

Multiple Regression Analysis

A multiple regression analysis demonstrated that the factors independently associated with a critical demyelinating lesion were the presence of moderate-to-severe atrophy (OR, 78.216; 95% CI, 4.267 to >999.999; $P = .0026$) and axial location involving the lateral column of the spinal cord, lateral column only versus no lateral column involvement (OR, 4.998; 95% CI, 1.572–15.888; $P = .0064$), and lateral column with additional column involvement versus no lateral column involvement (OR, 7.069; 95% CI,

2.292–21.800; $P = .0007$). Lesion size was not associated with critical demyelinating lesion documentation following multiple regression analysis (lesion area: OR, 1.061; 95% CI, 0.993–1.134; $P = .0806$).

DISCUSSION

Critical spinal cord demyelinating lesions associated with progressive motor impairment have MR imaging characteristics of moderate-to-severe focal lesion–associated spinal cord atrophy and are most commonly in the lateral column, both when restricted to 1 column and when combined with additional spinal cord column involvement. Central and ventral column distributions were also associated with critical demyelinating lesions in univariate analysis but only when also associated with lateral column involvement. Dorsal column lesions were inversely associated with progressive motor impairment. Critical demyelinating lesions were larger than noncritical lesions, with a particularly strong association noted when focally atrophic lesions were excluded.

Critical demyelinating lesions capture the eloquent territory and anatomic plausibility of association with progressive motor impairment due to demyelinating disease, and these results emphasize the importance of axial spinal cord imaging for column localization and focal atrophy assessment. Most descending motor corticospinal tracts are located within the lateral columns. The ventral spinal cord column contains the ventral motor corticospinal tracts (10%), possibly explaining its association but to a lesser degree, with progressive motor impairment. The dorsal columns contain predominantly ascending vibratory and joint position sense, so they may be expected to contribute to ambulatory impairment with sensory ataxia but would not be expected to contribute to progressive motor weakness.

The importance of spinal cord MR imaging assessment in progressive demyelinating disease is increasingly recognized. The presence of spinal cord lesions is associated with both the future development of relapsing MS and progressive MS in radiologically isolated syndrome.¹⁶ In individuals with clinically isolated syndromes of demyelination, spinal cord lesions are associated with development of progressive MS and increased disability.^{17,18} Spinal cord volume loss is associated with progressive MS at its earliest stages.^{19–22} Spinal cord atrophy, including cervical enlargement volume loss, is an active area of MS spinal cord imaging research.^{23,24} Increased spinal cord demyelinating lesion load is found to be higher in primary- and secondary-progressive than in relapsing-remitting MS, and the upper cervical cord lesion load and cord atrophy are independently correlated with disability and progressive MS.²⁵ Furthermore, the number of focal spinal cord lesions within the lateral column and gray matter is independently associated with disability in MS.²⁶ Demyelinating lesion location along the corticospinal tracts in the lateral funiculus of the spinal cord and entire CNS is associated with progressive MS and disability.^{27,28} Central spinal cord involvement was more frequent in primary-progressive MS than in relapsing-remitting MS, and lateral and central cord involvement correlated with disability on the Expanded Disability Status Scale.²⁸

The importance of MR imaging lesion location in differing phenotypes of progressive MS and disability is recognized as well. A demyelinating lesion located within the posterior fossa (cerebellum, brainstem) increases both the likelihood of a diagnosis of relapsing-remitting MS and of disability accumulation²⁹ in individuals with clinically isolated syndrome. However, in another study, early spinal cord lesions were more associated with disability progression than infratentorial lesions across time in MS,³⁰ highlighting the crucial importance of MR imaging assessment of the spinal cord in evaluating and prognosticating progressive MS. One strength of the study is the collection of human annotation data, which can serve as the basis for developing new algorithms to detect and characterize spinal cord demyelinating lesions, as well as possibly predicting progression or guiding interventions. Modern artificial intelligence has proved to be a viable pathway to clinical care in MS;³¹ however, the veracity of these approaches depends on the quality of the data used in training the model.

There are several limitations to this study. This is a retrospective, single, tertiary care center study. MR images were obtained as part of routine clinical care across many years on scans of variable quality. Despite this limitation, the critical lesions were reliably identified and assessed, indicating a strong likelihood of generalizability of the findings across typical clinical care in many centers assessing progressive demyelinating disease. Furthermore, this finding encourages improvement in spinal cord MR imaging assessment and techniques.³² Individuals in this study were highly selected as having progressive motor impairment associated with individual critical lesions, and a circular argument may be made that a lesion is deemed critical if it corresponds to the clinical presentation. A few individuals in the progressive solitary sclerosis cohort did not meet current diagnostic criteria for primary-progressive MS because they had fewer demyelinating lesions than required. However, critical lesions are strikingly similar in each group; they are highly characteristic of progressive MS in many aspects (age at progression,³³ CSF biomarkers³⁴). Ideally, a cohort of unselected patients with MS with additional, blindly assessed spinal cord scans would allow a clearer assessment of spinal cord demyelinating lesions associated and unassociated with motor progression. While we found focal atrophy and axial lateral column location to be important, additional pathologic factors such as severity of the axonal loss versus demyelination predominance and the degree of remyelination may be involved, and neuropathologic spinal cord tissue examination is lacking in these presented individuals.

Findings consistent with this study have been reported in a variety of demyelinating disease subtypes, including radiologically isolated syndrome, clinically isolated syndromes of demyelination, and MS cohorts. Additionally, in a population-based study, our group found that those with longstanding MS (>25 years' disease duration) who do not have such critical demyelinating lesions are more likely to remain with relapsing-remitting MS rather than developing progressive MS.¹⁰ Future investigations of such critical demyelinating lesions will assess how often they occur in unselected individuals with MS, when the critical lesions become radiologically evident, and how they evolve on MR imaging in association with the clinical presentation of progressive, anatomically consistent motor impairment. Optimal

current and future spinal cord imaging techniques to identify critical demyelinating lesions and better understand their underlying pathophysiology will be important.

CONCLUSIONS

Critical demyelinating lesions in these cohorts with progressive motor impairment are associated with MR imaging spinal cord characteristics of moderate-to-severe focal atrophy, lateral spinal column location, and large lesion size. Critical spinal cord demyelinating lesions may represent a compelling prognostic and therapeutic target of demyelinating conditions such as progressive MS.

ACKNOWLEDGMENTS

The authors greatly appreciate Ms Lea Dacy and Mr Jon Harrington for administrative assistance.

Disclosure forms provided by the authors are available with the full text and PDF of this article at www.ajnr.org.

REFERENCES

- Reich DS, Lucchinetti CF, Calabresi PA. **Multiple sclerosis.** *N Engl J Med* 2018;378:169–80 CrossRef Medline
- Mahajan KR, Nakamura K, Cohen JA, et al. **Intrinsic and extrinsic mechanisms of thalamic pathology in multiple sclerosis.** *Ann Neurol* 2020;88:81–92 CrossRef Medline
- Ontaneda D, Raza PC, Mahajan KR, et al; North American Imaging in Multiple Sclerosis Cooperative (NAIMS). **Deep grey matter injury in multiple sclerosis: a NAIMS consensus statement.** *Brain* 2021;144:1974–84 CrossRef Medline
- Popescu BF, Lucchinetti CF. **Meningeal and cortical grey matter pathology in multiple sclerosis.** *BMC Neurol* 2012;12:11 CrossRef Medline
- Preziosa P, Pagani E, Meani A, et al. **Slowly expanding lesions predict 9-year multiple sclerosis disease progression.** *Neurol Neuroimmunol Neuroinflamm* 2022;9:1139 CrossRef Medline
- Rocca MA, Battaglini M, Benedict RH, et al. **Brain MRI atrophy quantification in MS: From methods to clinical application.** *Neurology* 2017;88:403–13 CrossRef Medline
- Barkhof F. **The clinico-radiological paradox in multiple sclerosis revisited.** *Curr Opin Neurol* 2002;15:239–45 CrossRef Medline
- Bonek R, Orlicka K, Maciejek Z. **Demyelinating lesions in the cervical cord in multiple sclerosis 10 years after onset of the disease: correlation between MRI parameters and clinical course.** *Neurol Neurochir Pol* 2007;41:229–33 Medline
- Petrova N, Carassiti D, Altmann DR, et al. **Axonal loss in the multiple sclerosis spinal cord revisited.** *Brain Pathol* 2018;28:334–48 CrossRef Medline
- Sechi E, Messina S, Keegan BM, et al. **Critical spinal cord lesions associate with secondary progressive motor impairment in long-standing MS: a population-based case-control study.** *Mult Scler* 2021;27:667–73 CrossRef Medline
- Keegan BM, Kaufmann TJ, Weinshenker BG, et al. **Progressive solitary sclerosis: gradual motor impairment from a single CNS demyelinating lesion.** *Neurology* 2016;87:1713–19 CrossRef Medline
- Keegan BM, Kaufmann TJ, Weinshenker BG, et al. **Progressive motor impairment from a critically located lesion in highly restricted CNS-demyelinating disease.** *Mult Scler* 2018;24:1445–52 CrossRef Medline
- Sechi E, Keegan BM, Kaufmann TJ, et al. **Unilateral motor progression in MS: association with a critical corticospinal tract lesion.** *Neurology* 2019;93:e628–34 CrossRef Medline
- Jackson-Tarlton CS, Flanagan EP, Messina SA, et al. **Progressive motor impairment from “critical” demyelinating lesions of the cervicomedullary junction.** *Mult Scler* 2022;29:74–80 CrossRef Medline
- Long Z, Hanson DP, Mullan BP, et al. **Analysis of brain SPECT images coregistered with MRI in patients with epilepsy: comparison of three methods.** *J Neuroimaging* 2018;28:307–12 CrossRef Medline
- Kantarci OH, Lebrun C, Siva A, et al. **Primary progressive multiple sclerosis evolving from radiologically isolated syndrome.** *Ann Neurol* 2016;79:288–94 CrossRef Medline
- Arrambide G, Rovira A, Sastre-Garriga J, et al. **Spinal cord lesions: a modest contributor to diagnosis in clinically isolated syndromes but a relevant prognostic factor.** *Mult Scler* 2018;24:301–12 CrossRef Medline
- Brownlee WJ, Altmann DR, Prados F, et al. **Early imaging predictors of long-term outcomes in relapse-onset multiple sclerosis.** *Brain* 2019;142:2276–87 CrossRef Medline
- Bischof A, Papinutto N, Keshavan A, et al; University of California, San Francisco MS-EPIC Team. **Spinal cord atrophy predicts progressive disease in relapsing multiple sclerosis.** *Ann Neurol* 2022;91:268–81 CrossRef Medline
- Rocca MA, Valsasina P, Meani A, et al; MAGNIMS Study Group. **Clinically relevant cranio-caudal patterns of cervical cord atrophy evolution in MS.** *Neurology* 2019;93:e1852–66 CrossRef Medline
- Tsagkas C, Magon S, Gaetano L, et al. **Spinal cord volume loss: a marker of disease progression in multiple sclerosis.** *Neurology* 2018;91:e349–58 CrossRef Medline
- Zeydan B, Gu X, Atkinson EJ, et al. **Cervical spinal cord atrophy: an early marker of progressive MS onset.** *Neurol Neuroimmunol Neuroinflamm* 2018;5:e435 CrossRef Medline
- Bussas M, El Hussein M, Harabacz L, et al. **Multiple sclerosis lesions and atrophy in the spinal cord: distribution across vertebral levels and correlation with disability.** *Neuroimage Clin* 2022;34:103006 CrossRef Medline
- Rocca MA, Preziosa P, Filippi M. **What role should spinal cord MRI take in the future of multiple sclerosis surveillance?** *Expert Rev Neurother* 2020;20:783–97 CrossRef Medline
- Kearney H, Altmann DR, Samson RS, et al. **Cervical cord lesion load is associated with disability independently from atrophy in MS.** *Neurology* 2015;84:367–73 CrossRef Medline
- Kearney H, Miszkil KA, Yiannakas MC, et al. **Grey matter involvement by focal cervical spinal cord lesions is associated with progressive multiple sclerosis.** *Mult Scler* 2016;22:910–20 CrossRef Medline
- Eden D, Gros C, Badji A, et al. **Spatial distribution of multiple sclerosis lesions in the cervical spinal cord.** *Brain* 2019;142:633–46 CrossRef Medline
- Kerbrat A, Gros C, Badji A, et al. **Multiple sclerosis lesions in motor tracts from brain to cervical cord: spatial distribution and correlation with disability.** *Brain* 2020;143:2089–105 CrossRef Medline
- Tintore M, Rovira A, Arrambide G, et al. **Brainstem lesions in clinically isolated syndromes.** *Neurology* 2010;75:1933–38 CrossRef Medline
- Dekker I, Sombekke MH, Balk LJ, et al. **Infratentorial and spinal cord lesions: cumulative predictors of long-term disability?** *Mult Scler* 2020;26:1381–91 CrossRef Medline
- Hindsholm AM, Cramer SP, Simonsen HJ, et al. **Assessment of artificial intelligence automatic multiple sclerosis lesion delineation tool for clinical use.** *Clin Neuroradiol* 2022;32:643–53 CrossRef Medline
- Krieger S. **On cave paintings and shallow waters—the case for advancing spinal cord imaging in multiple sclerosis.** *JAMA Neurol* 2022;79:9–10 CrossRef Medline
- Kassa RM, Sechi E, Flanagan EP, et al. **Onset of progressive motor impairment in patients with critical central nervous system demyelinating lesions.** *Mult Scler* 2021;27:895–902 CrossRef Medline
- Barakat B, Messina S, Nayak S, et al. **Cerebrospinal fluid evaluation in patients with progressive motor impairment due to critical central nervous system demyelinating lesions.** *Mult Scler J Exp Transl Clin* 2022;8:20552173211052159 CrossRef Medline

Lateral Spinal CSF Leaks in Patients with Spontaneous Intracranial Hypotension: Radiologic-Anatomic Study of Different Variants

Wouter I. Schievink, Marcel M. Maya, Angelique Sao-Mai S. Tay, Rachelle B. Taché, Ravi S. Prasad, Vikram Wadhwa, and Miriam Nuño



ABSTRACT

BACKGROUND AND PURPOSE: Spinal CSF leaks cause spontaneous intracranial hypotension. Several types of leaks have been identified, and one of these types is the lateral dural tear. Performing myelography with the patient in the decubitus position allows precise characterization of these leaks. The purpose of the current study was to describe the different variants of spontaneous lateral CSF leaks.

MATERIALS AND METHODS: This retrospective cohort study included a consecutive group of patients with spontaneous intracranial hypotension and lateral CSF leaks who underwent digital subtraction myelography in the decubitus position and underwent surgery to repair the CSF leak between July 2018 and June 2023.

RESULTS: The mean age of the 53 patients (37 women and 16 men) was 35.5 years. Three different variants of lateral CSF leak could be identified. Forty-nine patients (92.5%) had a lateral dural tear associated with the nerve root sleeve. The dural tear was at the axilla of the nerve root sleeve in 36 patients (67.9%) and at the shoulder in 13 patients (24.5%). Four patients (7.5%) had a lateral dural tear at the level of the pedicle that was not associated with the nerve root sleeve. Findings on digital subtraction myelography were concordant with intraoperative findings in all patients. An extradural CSF collection was seen in all patients with a lateral dural tear associated with the nerve root sleeve but in only 2 of the 4 patients with the pedicular variant of a lateral dural tear.

CONCLUSIONS: We identified 3 variants of spontaneous lateral dural tears. Most lateral dural tears are associated with extradural CSF collections and arise from either the axilla (67.9%) or the shoulder (24.5%) of the nerve root sleeve. Lateral dural tears at the level of the pedicle (7.5%) not associated with the nerve root sleeve are uncommon and may require specialized imaging for their detection.

ABBREVIATIONS: DSM = digital subtraction myelography; SIH = spontaneous intracranial hypotension

Spontaneous intracranial hypotension (SIH) is an increasingly recognized disorder with an incidence of about 4 per 100,000 per year.^{1,2} In addition to the prototypical symptom of orthostatic headache, a wide variety of other clinical manifestations have been reported.³ In most patients, a spontaneous leak of CSF at the level of the spine is responsible for SIH.³ With the advent of specialized spinal imaging techniques, such as digital subtraction myelography (DSM) or dynamic CT myelography, it has become

possible to identify different types of spinal CSF leaks.⁴ Type 1 CSF leaks are those caused by spontaneous dural tears that occur on the ventral (type 1a) or posterolateral (type 1b) aspect of the thecal sac.⁴ Type 2 CSF leaks are associated with simple (type 2a) or complex (type 2b [dural ectasia]) meningeal diverticula. Type 3 CSF leaks are CSF-venous fistulas. Type 4 CSF leaks are of indeterminate origin.

Performing myelography with the patient in the lateral decubitus position has allowed precise characterization of lateral dural tears, and we now report the different variants of lateral CSF leaks that we have been able to identify since performing DSM with the patient in the lateral decubitus position.

MATERIALS AND METHODS

This retrospective cohort study was approved by our Medical Center's institutional review board.

Since January 2001, all patients with SIH evaluated by us in person at Cedars-Sinai Medical Center in Los Angeles, California,

Received December 12, 2023; accepted after revision February 15, 2024.

From the Departments of Neurosurgery (W.I.S., M.M.M., A.S.-M., S.T., R.B.T., R.S.P., V.W.) and Imaging (M.M.M., R.S.P., V.W.), Cedars-Sinai Medical Center, Los Angeles, California; and Department of Public Health Sciences (M.N.), University of California, Davis, California.

Please address correspondence to Wouter I. Schievink, MD, Department of Neurosurgery, Cedars-Sinai Medical Center, 127 South San Vicente Boulevard, Los Angeles, CA 90048; e-mail: schievinkw@cshs.org; @WouterSchievink



Indicates article with online supplemental data.

<http://dx.doi.org/10.3174/ajnr.A8261>

SUMMARY

PREVIOUS LITERATURE: Spontaneous intracranial hypotension can cause debilitating headaches and various other more or less serious neurologic symptoms. The underlying cause is almost always a CSF leak at the level of the spine and several types of CSF leak have been identified. The lateral dural tear is a well-known type of spinal CSF leak causing spontaneous intracranial hypotension, but this type has not been studied in detail.

KEY FINDINGS: Digital subtraction myelography and intra-operative observations in 53 patients distinguished 3 variants of lateral CSF leak, the shoulder and axillary variants associated with the nerve root sleeve and the uncommon pedicular variant not associated with the nerve root sleeve. Extensive extradural CSF collections were present in the great majority of patients but no extradural CSF could be identified on conventional spine imaging in one-half of the patients with the pedicular type of lateral CSF leak.

KNOWLEDGE ADVANCEMENT: Three distinct variants of lateral dural tears can be identified as the cause of spontaneous intracranial hypotension.

have been enrolled prospectively in a registry. Patients evaluated remotely with the use of telehealth were not included. Using this registry, we reviewed the medical records, radiographic studies, and intraoperative findings of a consecutive series of patients with SIH and lateral spontaneous spinal CSF leaks who underwent DSM in the lateral decubitus position and underwent surgery to repair the CSF leak during the 5-year period between July 2018 and June 2023. The diagnosis of SIH was based on the criteria of the International Classification of Headache Disorders, third edition, with minor modifications.^{3,5} These criteria require objective evidence of SIH, consisting of brain MR imaging showing the stigmata of SIH (ie, pachymeningeal enhancement, brain sagging, or subdural fluid collections), spinal imaging showing a CSF leak (ie, the presence of extradural CSF or a CSF-venous fistula), or low CSF opening pressure (ie, <6.0-mL CSF). The modification consists of also including patients who do not have headaches but whose symptoms are best explained by SIH.

Our imaging protocol consisted of brain MR imaging and heavily T2-weighted MR myelography.⁶ DSM was used to accurately localize the exact site of the CSF leak if heavily T2-weighted MR myelography was inconclusive. In all patients, the DSM technique as described by Hoxworth et al⁷ was used with some minor modifications.⁸ Briefly, DSM was performed with the patient under general endotracheal anesthesia with deep paralysis and suspended respiration for maximal detail and temporal resolution. Patients were positioned in the lateral decubitus position in a biplane angiography suite, with tilt table capability. Pillows or foam padding was placed to optimize cervicothoracic alignment. Under fluoroscopic guidance, a 22-ga needle was placed midline usually at the L2–3 level, being careful to avoid tenting and subdural injection. Then, the accurate needle position was confirmed with an injection of 0.5 mL of contrast (Omnipaque, 240 mg/mL or 300 mg/mL; GE Healthcare). Patients were then further positioned on the basis of the area of interest, with table tilting to achieve contrast flow to the cervicothoracic spine. Finally, 12 mL of contrast was injected manually, 1 mL per second with suspended respiration for 60–75 seconds, while acquiring biplane subtraction images at 1–2 frames per second. Post-DSM CT was performed within 90 minutes of intrathecal contrast injection. We used multidetector CT units capable of helical scanning with

a pitch of 0.51, kV(peak) of 120, milliampere-second, 200–440, depending on the patient's size. Imaging output consisted of axial 0.625-mm-thick slices with the same intervals, reconstructed to 2.5-mm-thick axial, sagittal, and coronal reformatted images.

Statistical Analysis

The study presents continuous variables with means and SDs, and categorical variables, as absolute numbers and percentages. We compared demographic characteristics by type of leak using the Mann-Whitney *U* test for continuous variables. χ^2 and Fisher exact tests were used for comparisons involving categorical variables. Given the limited sample size, we opted for nonparametric tests. We acknowledge that while opting for nonparametric tests to address distributional concerns in small sample sizes, there remains inherent limitations in the statistical power of these tests to detect a true association. All statistical analyses were performed using SAS, Version 9.4 (SAS Institute).

RESULTS

Study Population

During the study period, 65 patients underwent surgery for a spontaneous lateral spinal CSF leak. Twelve patients were excluded from the analysis because they did not undergo a preoperative DSM in the lateral decubitus position: Five patients had undergone DSM in the prone position, showing the level of the CSF leak, 4 patients had undergone surgery elsewhere but had a persistent CSF leak and the level of the CSF leak had been adequately identified, 2 patients underwent surgery on the basis of heavily T2-weighted MR myelography showing the level of the CSF leak, and 1 patient refused DSM, but conventional CT myelography had identified the approximate level of the CSF leak.

The mean age of the 53 study patients (37 women and 16 men) at the onset of SIH symptoms was 35.5 years (Table 1). Five patients had 2 lateral CSF leaks, and 48 patients had a single lateral CSF leak for a total of 58 lateral CSF leaks.

Classification of Lateral CSF Leak Variants

Three different variants of lateral CSF leak could be identified (Fig 1). Of the 53 patients, 49 patients (92.5%) had a lateral dural tear associated with the nerve root sleeve. The dural tear was at

Table 1: Cohort demographics and clinical characteristics (N = 53)

Variables	No. (%)
Age at onset of symptoms (yr)	
Mean (SD)	35.5 (10.8)
Range	12–76
Sex	
Male	16 (30.2)
Female	37 (69.8)
Symptom duration (mo)	
Mean (SD)	35.8 (49.7)
Range	0–205
CSF leak type	
Axilla of nerve root sleeve	36 (67.9)
Pedicle	4 (7.6)
Shoulder of nerve root sleeve	13 (24.5)
CSF leak side ^a	
Left	27 (46.6)
Right	31 (53.4)
CSF leak level ^a	
Cervical	3 (5.7)
Thoracic 4–6	4 (7.8)
Thoracic 7–9	13 (24.5)
Thoracic 10–12	31 (58.5)
Lumbar	2 (3.8)

^a From a total of 58 CSF leak sites.

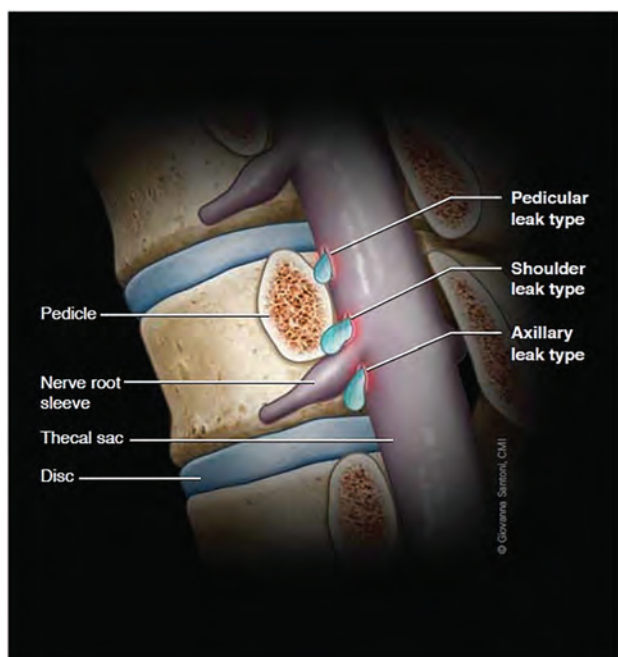


FIG 1. Illustration depicting the 3 variants of spontaneous lateral spinal CSF leaks. We found spontaneous lateral CSF leaks to be associated with the axilla of the nerve root sleeve in about two-thirds of patients and associated with the shoulder of the nerve root sleeve in about one-fourth of patients. Uncommonly (7.5%), the lateral dural tear was found at the level of the pedicle and was not associated with the nerve root sleeve.

the axilla (Fig 2 and Online Supplemental Data), caudal to the nerve root sleeve in 36 patients (67.9%) or at the shoulder (Fig 3 and Online Supplemental Data), cranial to the nerve root sleeve in 13 patients (24.5%). Four patients (7.6%) had a lateral dural tear at the level of the pedicle that was not associated with the

nerve root sleeve (Fig 4). Findings on DSM were concordant with intraoperative findings in all patients.

Patients with a lateral dural tear at the shoulder of the nerve root were younger (mean age, 28.9 years) than those with a lateral dural tear at the axilla of the nerve root (mean age, 38.1 years) or at the level of the pedicle (mean age, 32.8 years) ($P = .029$), but there were no differences in sex or symptom duration (Table 2).

An extradural CSF collection was present on heavily T2-weighted MR myelography as well as post-DSM CT in all 49 patients with a lateral CSF leak associated with the nerve root sleeve (Online Supplemental Data). The extradural CSF collection was extensive, extending over 3–21 spinal levels in 45 patients but confined to a single spinal level in 4 patients. In 2 of these 4 patients with a confined extradural CSF collection, prior imaging had shown an extensive extradural CSF collection indicating considerable-but-incomplete improvement of the CSF leak. Among the 4 patients with the pedicular variant of a lateral CSF leak, an extensive extradural CSF collection was present in 1 patient, a small confined extradural CSF collection could be identified on heavily T2-weighted MR myelography but not on post-DSM CT in 1 patient, while neither heavily T2-weighted MR myelography nor post-DSM CT could demonstrate an extradural CSF collection in 2 patients (Fig 4 and Online Supplemental Data). Dynamic CT myelography with the patient in the lateral decubitus position was not performed in any of these patients.

The extradural CSF collection was symmetric and nonlateralizing in 14 patients (27.5%), bilateral but asymmetric lateralizing to the side of the lateral CSF leak in 24 patients (47.1%), and unilateral in 13 patients (25.5%).

Five patients (9.4%) had 2 lateral CSF leaks, and 48 patients (90.6%) had a single lateral CSF leak, for a total of 58 lateral CSF leaks. Multiple lateral CSF leaks were identified in 3 (23.1%) of the 13 patients with a CSF leak at the shoulder of the nerve root sleeve, in 2 (5.6%) of the 36 patients with a CSF leak at the axilla of the nerve root sleeve, and in none of the patients with a pedicular type lateral CSF leak ($P = .128$). The variant of a lateral CSF leak was the same in each of these 5 patients, ie, 3 patients had 2 lateral CSF leaks at the shoulder of the nerve root sleeve and 2 patients had 2 lateral CSF leaks at the axilla of the nerve root sleeve.

Most lateral CSF leaks (58.6%) in this study were found in the lower thoracic spine (Table 1). We found no evidence of a calcified lesion associated with a lateral dural tear in any patient.

We found the coexistence of a spontaneous lateral CSF leak and a CSF-venous fistula in one (7.7%) of the 13 patients with a lateral CSF leak at the shoulder of the nerve root sleeve and in 2 (5.6%) of the 36 patients with a lateral CSF leak at the axilla of the nerve root sleeve (Online Supplemental Data).

Surgical Repair

At surgery, a lateral dural tear could be identified in all patients, and the dural tear was repaired with sutures (7-0 Gore-Tex; W. L. Gore & Associates) and/or a muscle graft in 3 (5.2%) and with titanium aneurysm clips (Yasargil; B. Braun) in 55 (94.8%) of the 58 lateral CSF leaks.

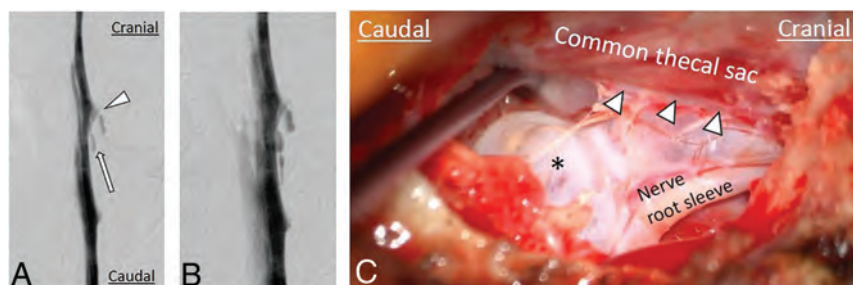


FIG 2. Imaging and intraoperative findings of spontaneous lateral spinal CSF leaks arising from the axilla of the nerve root sleeve. DSMs (A and B) show a lateral CSF leak (arrow) arising caudal to the nerve root sleeve (arrowhead). C, Intraoperative photograph shows a lateral dural tear (arrowheads) caudal to the take-off of the nerve root sleeve with arachnoid (asterisk) protruding through the dural tear.

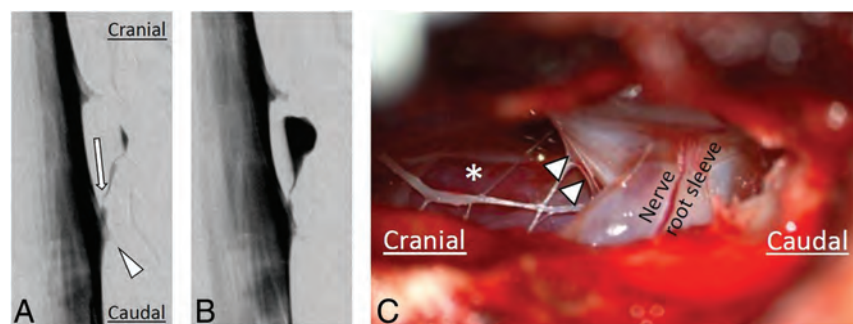


FIG 3. Imaging and intraoperative findings of spontaneous lateral spinal CSF leaks arising from the shoulder of the nerve root sleeve. DSMs (A and B) show a lateral CSF leak (arrow) arising cranial to the nerve root sleeve (arrowhead). C, Intraoperative photograph shows a lateral dural tear (arrowheads) cranial to the take-off of the nerve root sleeve after the arachnoid membrane has been resected, leaving a clear view of the extended extradural space (asterisk).

Postoperative Imaging

Postoperative imaging with heavily T2-weighted MR myelography or high-resolution spine MRI was performed in all patients and showed complete resolution of the extradural CSF collection in 55 (98.2%) of the 56 CSF leaks that had been associated with an extradural CSF collection (Online Supplemental Data). Of the 2 patients with the pedicular variant of a lateral CSF leak that was not associated with an extradural CSF collection, SIH symptoms and brain MRI stigmata of SIH resolved postoperatively in one patient, and postoperative DSM was performed in the other patient, showing resolution of the lateral CSF leak (Online Supplemental Data).

DISCUSSION

In this study, we identified 3 different variants of spontaneous lateral spinal CSF leaks. Most CSF leaks are associated with the nerve root sleeve, and these can be divided into 2 variants, those at the axilla, caudal to, or at the shoulder, cranial to the nerve root sleeve. No significant differences were found in sex distribution or the duration of symptoms between these 2 variants, but the same variant being observed among all patients with multiple lateral CSF leaks and the significant age difference suggest that these may be 2 distinct types of lateral CSF leaks.

The variant we observed at the level of the pedicle that was unrelated to the nerve root sleeve has, to our knowledge, not

been described previously. We have only been aware of this variant since 2022, and it is possible that previously, we have failed to identify this particular variant of lateral CSF leak on DSM. Of the 4 patients we have encountered so far, an extensive extradural CSF collection was present in only 1 patient. In the other 3 patients, the appearance of the lateral leak was subtle but clearly visible on DSM, while a small amount of extradural CSF was visible on heavily T2-weighted MR myelography in only 1 of these 3 patients, and no extradural CSF was visible on post-DSM CT in any of these 3 patients. Thus, in addition to the CSF-venous fistula,⁹⁻¹¹ the pedicular variant of a lateral CSF leak may be the second type of CSF leak that may require specialized imaging such as DSM or dynamic CT myelography. DSM has excellent spatial resolution of only 300 μm (0.3 mm). None of our patients were investigated with primary lateral dynamic CT myelography.

We found the extradural CSF collection associated with the lateral dural tears to be lateralizing in about three-fourths of patients, facilitating the choice of positioning of the patient for DSM (left or right side down). We did not observe a clear sidedness to the

location of the lateral dural tear that could help decide positioning of those patients with symmetric nonlateralizing extradural CSF collections.

Identifying the different variants of lateral CSF leaks may have some practical implications for both directed percutaneous procedures, ie, blood or fibrin glue patching, as well as for a more tailored surgical approach to the lateral CSF leak, especially with the more recently developed minimally invasive tubular approaches.^{12,13} Targeted percutaneous fibrin glue and/or blood patch procedures are based on traditional nerve block and epidural injection techniques, which were developed with the goals of minimal risk of nerve injury, intrathecal puncture, or vascular injections. A traditional subpedicular “safe triangle” approach targets the anterior superior aspect of the neuroforamen.¹⁴ The safety of the safe triangle approach has been questioned recently due to the location of the radicular or radiculomedullary artery in the anterior-superior quadrant of the neuroforamen.

An alternative approach targets the Kambin triangle, a region described in the context of accessing intervertebral discs for surgery.^{15,16} The Kambin triangle describes an area overlying the posterolateral disc that is bounded by the inferior vertebral body at its base, the exiting spinal nerve root at the hypotenuse, and the traversing nerve root or dura at the vertical leg.^{15,16} The relative location of lateral tears has significant implications on

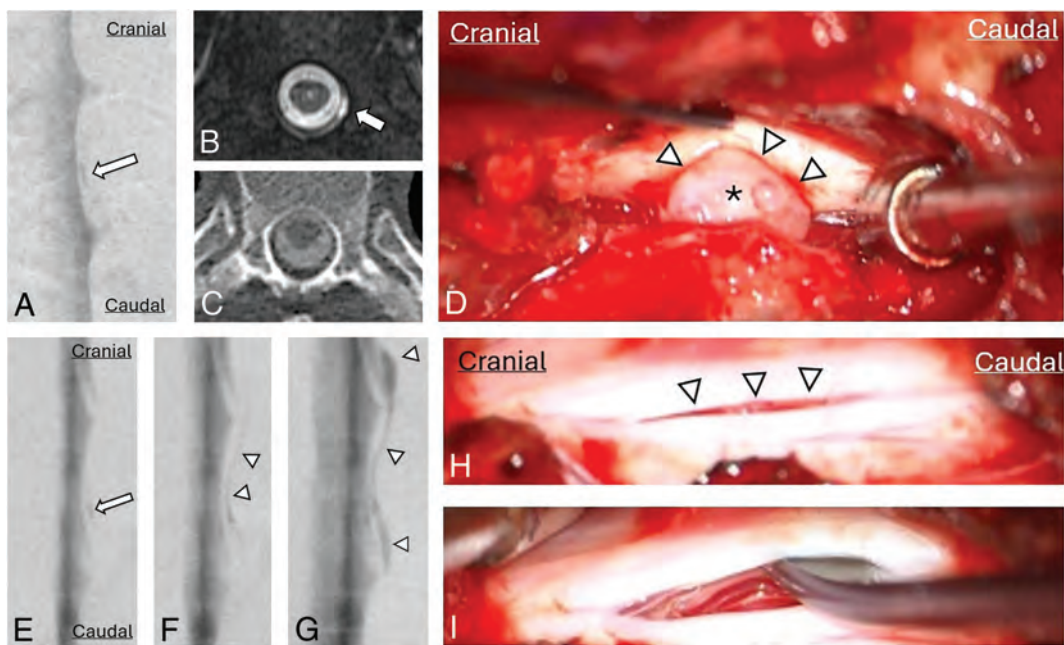


FIG 4. Imaging and intraoperative findings of spontaneous lateral spinal CSF leaks arising at the level of the pedicle. DSM (A) shows a small, defined lateral extradural CSF collection (arrow) at the level of the pedicle, not associated with the nerve root sleeve. Axial T2-weighted MRI (B) shows a corresponding small extradural CSF collection (arrow) that was not visible on post-DSM CT (C). The intrathecal contrast on the post-DSM CT is faint, possibly limiting the sensitivity of leak detection. Intraoperative photograph (D) shows a lateral dural tear (arrowheads) with arachnoid billowing out (asterisk) through the dural defect. DSMs (E–G) show a lateral dural tear (arrow) at the level of the pedicle, not associated with the nerve root sleeve, resulting in an extensive CSF leak, with CSF spreading in both cranial and caudal directions (arrowheads). Intraoperative photographs (H and I) show a linear dural tear (arrowheads) without arachnoid protruding through the dural tear. The underlying spinal cord is visible after spreading the dural tear (H).

Table 2: Characteristics per leak type

Variables	CSF Leak Type			P Value
	Axilla 36 (67.9%)	Pedicle 4 (7.6%)	Shoulder 13 (24.5%)	
Age at onset of symptoms (yr)				.0295
Mean (SD)	38.1 (10.2)	32.8 (12.8)	28.9 (9.3)	
Minimum-maximum	20–76	14–43	12–43	
Sex				
Male	11 (30.6)	1 (25.0)	4 (30.8)	1.0000
Female	25 (69.4)	3 (75.0)	9 (69.2)	
Symptom duration (mo)				.7359
Mean (SD)	34.8 (48.4)	47.8 (45.7)	35.2 (57.7)	
Range	1–205	0–106	0–195	

the optimal choice that combines efficacy with minimal neurovascular injury risk. The safe triangle approach may be more effective with the shoulder variant of the lateral tear and not suitable for the axillary or pedicular variants.

In this study, we were able to confirm the presence of a lateral dural tear in all patients in accordance with the findings on DSM. In the past, we have classified many of these patients as having leaking spinal meningeal diverticula.⁴ However, the lateral dural tear is the primary pathology with the arachnoid billowing out through the dural tear, giving the appearance of a leaking meningeal diverticulum, while the actual site of CSF leakage often occurs around the arachnoid diverticulum at the edges of the lateral dural tear.

After achieving good success with identifying CSF-venous fistulas with DSM performed with the patient in the lateral

decubitus position since April 2018,¹⁷ we have been performing DSM in the lateral decubitus position for suspected lateral CSF leaks since July 2018. Other investigators have also reported their positive experience with myelographic techniques in the lateral decubitus position for the identification of lateral CSF leaks.^{18–24} Prior studies have generally not mentioned the exact anatomic site of the lateral CSF leak except for 1 study showing 4 of 4 lateral CSF leaks occurring at the level of the axilla of the nerve root sleeve¹⁹ and other reports noting that lateral CSF leaks typically occur at the shoulder²⁵ or axilla²⁶ of the nerve root sleeve.

CONCLUSIONS

Using DSM in the lateral decubitus position, we identified 3 variants of lateral dural tears among patients with SIH. Most lateral dural tears are associated with extensive extradural CSF collections and arise from either the axilla or the shoulder of the nerve root sleeve. Lateral dural tears located at the level of the pedicle that are not associated with the nerve root sleeve are uncommon and may require specialized imaging for their detection.

Disclosure forms provided by the authors are available with the full text and PDF of this article at www.ajnr.org.

REFERENCES

- Schievink WI, Maya MM, Moser FG, et al. **Incidence of spontaneous intracranial hypotension in a community: Beverly Hills, California, 2006–2020.** *Cephalalgia* 2022;42:312–16 CrossRef Medline
- Pradeep A, Madhavan AA, Brinjikji W, et al. **Incidence of spontaneous intracranial hypotension in Olmsted County, Minnesota: 2019–2021.** *Interv Neuroradiol* 2023 Mar 22 [Epub ahead of print] CrossRef Medline
- Schievink WI. **Spontaneous intracranial hypotension.** *N Engl J Med* 2021;385:2173–78 CrossRef Medline
- Schievink WI, Maya MM, Jean-Pierre S, et al. **A classification system of spontaneous spinal CSF leaks.** *Neurology* 2016;87:673–79 CrossRef Medline
- Headache Classification Committee of the International Headache Society: the International Classification of Headache Disorders, 3rd ed. *Cephalalgia* 2018;38:1–211 CrossRef Medline
- Tay ASS, Maya M, Moser FG, et al. **Computed tomography vs heavily T2-weighted magnetic resonance myelography for the initial evaluation of patients with spontaneous intracranial hypotension.** *JAMA Neurol* 2021;78:1275–76 CrossRef Medline
- Hoxworth JM, Patel AC, Bosch EP, et al. **Localization of a rapid CSF leak with digital subtraction myelography.** *AJNR Am J Neuroradiol* 2009;30:516–19 CrossRef Medline
- Galvan J, Maya MM, Prasad RS, et al. **Spinal CSF leak localization with digital subtraction myelography: tips, tricks, and pitfalls.** *Radiol Clin North Am* 2024;62:321–32 CrossRef Medline
- Schievink WI, Moser FG, Maya MM. **CSF-venous fistula in spontaneous intracranial hypotension.** *Neurology* 2014;83:472–73 CrossRef Medline
- Kranz PG, Amrhein TJ, Gray L, et al. **CSF venous fistulas in spontaneous intracranial hypotension: imaging characteristics on dynamic and CT myelography.** *AJR Am J Roentgenol* 2017;209:1360–66 CrossRef Medline
- Dobrocky T, Nicholson P, Häni L, et al. **Spontaneous intracranial hypotension: searching for the CSF leak.** *Lancet Neurol* 2022;21:369–80 CrossRef Medline
- Lohkamp LN, Marathe N, Nicholson P, et al. **Minimally invasive surgery for spinal cerebrospinal fluid-venous fistula ligation: patient series.** *J Neurosurg Case Lessons* 2022;3:CASE21730 CrossRef Medline
- Beck J, Hubbe U, Klingler JH, et al. **Minimally invasive surgery for spinal cerebrospinal fluid leaks in spontaneous intracranial hypotension.** *J Neurosurg Spine* 2022;38:147–52 CrossRef Medline
- Gil HY, Jeong S, Cho H, et al. **Kambin's triangle approach versus traditional safe triangle approach for percutaneous transforaminal epidural adhesiolysis using an inflatable balloon catheter: a pilot study.** *J Clin Med* 2019;8:1996 CrossRef Medline
- Kambin P, Sampson S. **Posterolateral percutaneous suction-excision of herniated lumbar intervertebral discs: report of interim results.** *Clin Orthop Relat Res* 1986;207:37–43 Medline
- Fanous AA, Tumialán LM, Wang MY. **Kambin's triangle: definition and new classification schema.** *J Neurosurg Spine* 2020;32:390–98 CrossRef Medline
- Schievink WI, Maya MM, Moser FG, et al. **Lateral decubitus digital subtraction myelography to identify spinal CSF-venous fistulas in spontaneous intracranial hypotension.** *J Neurosurg Spine* 2019;31:902–05 CrossRef Medline
- Chu E, McAuliffe W. **Use of flat panel DynaCT myelography to locate the site of CSF leak.** *J Med Imaging Radiat Oncol* 2013;57:455–59 CrossRef Medline
- Dobrocky T, Mosimann PJ, Zibold F, et al. **Cryptogenic cerebrospinal fluid leaks in spontaneous intracranial hypotension: role of dynamic CT myelography.** *Radiology* 2018;289:766–72 CrossRef Medline
- Farb RI, Nicholson PJ, Peng PW, et al. **Spontaneous intracranial hypotension: a systematic imaging approach for CSF leak localization and management based on MRI and digital subtraction myelography.** *AJNR Am J Neuroradiol* 2019;40:745–53 Medline
- Kranz PG, Gray L, Malinzak MD, et al. **Spontaneous intracranial hypotension: pathogenesis, diagnosis, and treatment.** *Neuroimaging Clin N Am* 2019;29:581–94 CrossRef Medline
- Madhavan AA, Verdoorn JT, Shlapak DP, et al. **Lateral decubitus dynamic CT myelography for fast cerebrospinal fluid leak localization.** *Neuroradiology* 2022;64:1897–1903 CrossRef Medline
- Mamlouk MD, Shen PY, Dahlin BC. **Modified dynamic CT myelography for type 1 and 2 CSF leaks: a procedural approach.** *AJNR Am J Neuroradiol* 2023;44:341–46 CrossRef Medline
- Lützen N, Demerath T, Volz F, et al. **Conebeam CT as an additional tool in digital subtraction myelography for the detection of spinal lateral dural tears.** *AJNR Am J Neuroradiol* 2023;44:745–47 CrossRef Medline
- Luetzen N, Dovi-Akue P, Fung C, et al. **Spontaneous intracranial hypotension: diagnostic and therapeutic workup.** *Neuroradiology* 2021;63:1765–72 CrossRef Medline
- Häni L, Fung C, El Rahal A, et al. **Distinct pattern of membrane formation with spinal cerebrospinal fluid leaks in spontaneous intracranial hypotension.** *Oper Neurosurg (Hagerstown)* 2024;26:71–77 CrossRef Medline

The Spatial Relationship between Spinal Osteoarthritis and CSF Venous Fistulas in Patients with Spontaneous Intracranial Hypotension

Emma M.Z. Sechrist, Samantha L. Pisani Petrucci, Nadya Andonov, Peter Lennarson, and  Andrew L. Callen

ABSTRACT

BACKGROUND AND PURPOSE: CSF venous fistula leads to spontaneous intracranial hypotension. The exact mechanisms underlying the development of CSF venous fistula remain unclear. Some researchers have postulated that underlying chronic intracranial hypertension may lead to damage to spinal arachnoid granulations, given that many patients with CSF venous fistulas have an elevated body mass index (BMI). However, individuals with higher BMIs are also more prone to spinal degenerative disease, and individuals with CSF venous fistulas also tend to be older. CSF venous fistula tends to occur in the lower thoracic spine, the most frequent location of thoracic degenerative changes. The current study aimed to examine whether CSF venous fistulas are more likely to occur at spinal levels with degenerative changes.

MATERIALS AND METHODS: Forty-four consecutive patients with CSF venous fistulas localized on dynamic CT myelography were included in analyses. Whole-spine CT was scrutinized for the presence of degenerative changes at each spinal level. The proportion of levels positive for CSF venous fistula containing any degenerative findings was compared to levels without CSF venous fistula using the Fisher exact test. The Pearson correlation coefficient was calculated to explore the association between the burden of degenerative disease and BMI and age and between BMI and opening pressure.

RESULTS: Forty-four patients with 49 total CSF venous fistulas were analyzed (5 patients had 2 CSF venous fistulas). Mean patient age was 62.3 (SD, 9.5) years. Forty-seven CSF venous fistulas were located in the thoracic spine; 1, in the cervical spine; and 1, in the lumbar spine. Within the thoracic spine, 39/49 (79.6%) fistulas were located between levels T7–8 and T12–L1. Forty-four of 49 (89.8%) CSF venous fistulas had degenerative changes at the same level. The levels without CSF venous fistulas demonstrated degenerative changes at 694/1007 (68.9%) total levels. CSF venous fistulas were significantly more likely to be present at spinal levels with associated degenerative changes (OR = 4.03; 95% CI, 1.58–10.27; $P = .001$). Age demonstrated a positive correlation with the overall burden of degenerative disease (correlation coefficient: 0.573, $P < .001$), whereas BMI did not (correlation coefficient: 0.076, $P = .625$). There was a statistically significant positive correlation between BMI and opening pressure (correlation coefficient: 0.321, $P = .03$).

CONCLUSIONS: Results suggest a potential association between spinal degenerative disease and development of CSF venous fistula.

ABBREVIATIONS: BMI = body mass index; CVF = CSF venous fistula; DCTM = dynamic CT myelography; SIH = spontaneous intracranial hypotension

CSF venous fistula (CVF) is increasingly recognized as a major cause of spontaneous intracranial hypotension (SIH), comprising a substantial number of SIH cases evaluated at quaternary referral centers.¹ While it is well-understood that CVF causes abnormal egress of CSF through the paraspinal veins and/or the epidural venous plexus, the exact pathogenesis of this phenomenon is unclear.

Prior studies have demonstrated that CVFs tend to occur in older individuals with an increased body mass index (BMI).^{2,3} This finding has led previous authors to hypothesize that CVFs may result from pre-existing chronic intracranial hypertension causing damage to the spinal arachnoid granulations and dysregulation of physiologic CSF egress from the spinal subarachnoid space.⁴ However, overweight/obese and older individuals are also more prone to spinal degenerative disease.^{5,6} CVFs have repeatedly been shown to occur mostly in the thoracic spine, which may be explained, in part, by a predominance of arachnoid villi.⁷ More specifically, prior studies indicate a predilection of CVF for the lower thoracic spine, with most CVFs clustered between T7 and T12.^{2,8} Interestingly, this finding coincides with the distribution of osteoarthritis in the thoracic spine, which tends to occur

Received January 12, 2024; accepted after revision February 13.

From the Department of Radiology (E.M.Z.S., S.L.P.P., N.A., A.L.C.) and Neurosurgery (P.L.), University of Colorado School of Medicine Anschutz Medical Campus, Aurora, Colorado.

Please address correspondence to Andrew L. Callen, MD, 12401 E 17th Ave, Aurora, CO 80045, Mail Stop L954; e-mail: andrew.callen@cuanschutz.edu; @AndrewCallenMD

<https://dx.doi.org/10.3174/ajnr.A8247>

in the lower thoracic levels with a reported prevalence ranging from 68% to 75%.⁹⁻¹² In this study, we hypothesized that there may be a spatial relationship between CVF incidence and the presence of spinal degenerative changes at a given spinal level.

MATERIALS AND METHODS

This was a retrospective, cross-sectional cohort study evaluating 44 consecutive patients who had CVFs localized on dynamic CT myelography (DCTM) at the University of Colorado Anschutz Medical Campus between February 1, 2021, and December 6, 2023. Approval from the institutional review board was obtained, and written informed consent was waived. Whole-spine CT obtained during dynamic CT myelography (DCTM) was scrutinized by a neuroradiology fellow and a board-certified subspecialty-trained neuroradiologist by consensus for the presence of

spinal osteoarthritis at each of 24 spinal levels (C1–C2 through L5–S1). The presence of osteoarthritis was treated as a binary variable and not characterized on the basis of severity or laterality. Osteoarthritis was considered to be present if there was any disc pathology (bulge, protrusion, extrusion, or vacuum phenomenon), osteophytosis, and/or facet arthrosis; these specific types of degenerative findings were recorded for each level. Disagreements on the presence or absence of degenerative changes were resolved by consensus. The proportion of CVF levels containing any degenerative findings was compared with non-CVF levels using the Fisher exact test. The Pearson correlation coefficient was calculated to explore associations between the burden of degenerative disease and BMI and age and between BMI and opening pressure.

RESULTS

Forty-four total patients with 49 total CVFs were analyzed (5 patients had 2 CVFs). The mean patient age was 62.3 (SD, 9.5) years; 18/44 (40.9%) were men, and 26/44 (59.1%) were women. The mean BMI was 28.0 (SD, 4.4) (Table). Forty-seven CVFs were located in the thoracic spine; 1, in the cervical spine; and 1, in the lumbar spine. Within the thoracic spine, 39/49 (79.6%) fistulas were between the levels of T7–T8 and T12–L1, with 1/47 at T1–T2, 1/47 at T4–T5, 6/47 at T6–T7, 7/47 at T7–8, 5/47 at T8–T9, 8/47 at T9–T10, 9/47 at T10–T11, 6/47 at T11–T12 and 4/47 at T12–L1.

Forty-four of 49 (89.8%) CVFs had degenerative osteoarthritis changes present at the same level. The levels without CVFs had degenerative changes at 694/1007 (68.9%) total levels. CVFs were more significantly likely to be present at a level with spinal degenerative changes (OR = 4.03; 95% CI, 1.58–10.27; *P* = .001). The relationship and distribution of CVFs and spinal degenerative changes are illustrated in Fig 1.

In levels with degenerative disease and a CVF, there was disc degeneration at 29/44 (65.9%) levels, osteophyte formation at 43/44 (97.7%) levels, and facet arthrosis at 31/44 (70.5%) levels. Figure 2 demonstrates osteoarthritis findings at CVF levels.

Patient, CVF, and spinal osteoarthritis characteristics	
	Overall (n = 44)
Total fistulas	49
Age	
Mean (SD)	62.3 (9.5)
BMI	
Mean (SD)	28.0 (4.4)
Sex	
Female	26/44 (59.1%)
Male	18/44 (40.9%)
Fistula location	
Cervical	1/49 (2.0%)
Thoracic (T1–T2 through T6–T7)	8/49 (16.3%)
Thoracic (T7–T8 through T12–L1)	39/49 (79.6%)
Lumbar	1/49 (2.0%)
Osteoarthritis	
Nonfistula levels	694/1007 (68.9%)
Fistula levels	44/49 (89.8%)
Disc disease	29/44 (65.9%)
Osteophytes	43/44 (97.7%)
Facet arthrosis	31/44 (70.5%)

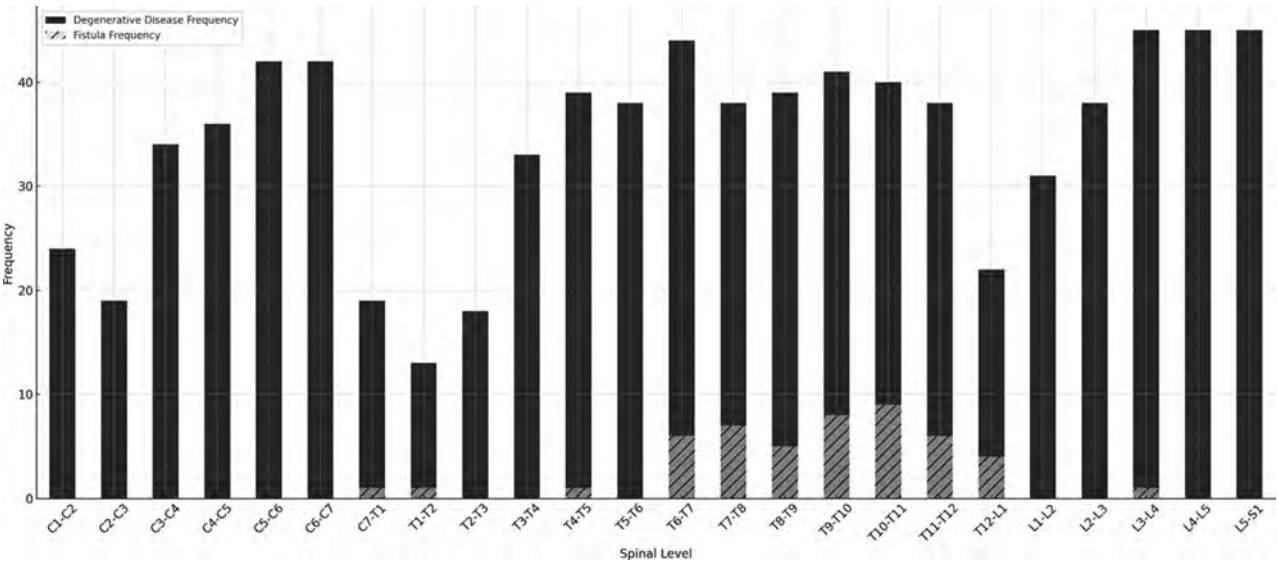


FIG 1. Distribution of spinal degenerative disease and CVFs.



FIG 2. Three patients with osteoarthritis at the level of their CVFs. *Upper row, A* 66-year-old woman with intracranial hypotension and a right T7–T8 CVF. *A*, Midline sagittal CT image from dynamic myelography demonstrates anterior endplate osteophytes clustered from T4–T5 through T9–T10 (*dashed arrows*) and disc protrusions at T6–

Age demonstrated a moderate yet-statistically significant positive correlation with the overall burden of degenerative disease (correlation coefficient: 0.573, $P < .001$), whereas BMI did not (correlation coefficient: 0.076, $P = .625$).

Opening pressures were recorded for all 44 patients. The opening mean (SD) pressure was 13.0 (4.7) cm H₂O. The median value was 12.0 cm H₂O. Two of 44 patients had an opening pressure of < 6.0 cm H₂O.¹³ One patient had an opening pressure of > 20 cm H₂O (26 cm H₂O). BMI demonstrated a moderate-yet-statistically significant positive correlation with opening pressure (correlation coefficient: 0.321, $P = .03$).

DISCUSSION

In this retrospective cohort study of 44 consecutive patients with CVFs, most CVFs were present in the thoracic spine between T7–T8 and T12–L1, overlapping with the thoracic levels most prone to osteoarthritis.¹⁴ Moreover, degenerative disease was statistically significantly more likely to be present at levels with CVF compared with non-CVF levels; 89.8% of CVFs in our cohort had degenerative changes at the same level, compared with 68.9% of non-CVF levels.

Several studies have observed that most thoracic osteoarthritis occurs in the lower thoracic levels.^{14,15} This distribution can be explained, in part, by anatomic differences in the lower thoracic spine, resulting in increased motion. The ribs arising from the T7 vertebral body are the most inferior that individually fuse to the sternum. The eighth through 10th ribs indirectly articulate with the sternum through a collective costal cartilage, which articulates with the seventh costal cartilage, and the 11th and 12th ribs do not articulate with the sternum at all. This articulation permits increased flexibility, motion, and less weight-bearing ability in the lower spine, resulting in a higher likelihood of developing degenerative disease.¹⁴

In addition to both being caused by and resulting in increased biomechanical stress, spinal osteoarthritis and specifically osteophyte formation (the most prevalent osteoarthritic finding in our cohort) have been linked to an inflammatory milieu within the joint environment. Transforming growth factor β , bone morphogenic proteins, and insulin-like growth factor 1 play significant roles in osteophyte formation.¹⁶ The nerve root, where CVFs tend to occur, straddles the environments of both the disc space and facet joints and is thus susceptible to both the mechanical and inflammatory stresses induced by spinal osteoarthritis. Given that most spinal levels with osteoarthritis in our cohort demonstrated osteophyte formation, a potential link among osteophytosis, inflammation, and

T7, T7–T8, and T8–T9. *B*, Paramidline sagittal CT image from dynamic myelography demonstrates a CVF arising from the right T7–T8 neural foramen (*solid arrows*). *Middle row, A* 61-year-old man with intracranial hypotension and a left T11–T12 CVF. *C*, Oblique coronal MIP CT image from dynamic myelography demonstrates a CVF arising from a meningeal diverticulum at T11–T12 on the left (*arrow*). *D*, Axial image from DCTM demonstrates left T11–T12 facet arthrosis (*dashed arrow*) and a corresponding CVF (*solid arrow*). *Lower row, A* 61-year-old man with intracranial hypotension and a right T10–T11 CVF. *E*, Axial CT image from dynamic myelography demonstrates a disc bulge and endplate osteophytes (*dashed arrows*) and a CVF (*solid arrow*) at the T10–T11 level. *F*, Sagittal paramidline CT image demonstrates disc bulging with lateral endplate osteophytes at T10–T11 (*dashed arrow*) and an adjacent CVF (*solid arrow*).

CVF pathogenesis should be the target of future study. Finally, patients with SIH may report thoracic radicular symptoms, the etiology of which is unclear.¹⁷ Future work should continue to explore these associations and potential relationships.

If spinal osteoarthritis is linked to CVF formation, it begs the question why CVFs do not occur more frequently in the cervical or lumbar spine, which exhibit degenerative disease at much higher rates than the thoracic spine.¹⁵ This discrepancy may be, in part, explained by the normal anatomic distribution of spinal arachnoid villi, the points of physiologic egress of CSF from the spinal subarachnoid space. Thus, CVF development may require a biomechanical or inflammatory insult at or near the nerve roots where physiologic CSF resorption occurs. Prior work examining the distribution of spinal arachnoid villi in postmortem specimens has had varied results: Kido et al⁷ reported a predilection for the thoracic spine, which parallels CVF distribution; however, Tubbs et al¹⁸ noted a predilection of spinal arachnoid villi in the lumbar spine. Thus, it is unclear whether the distribution of spinal arachnoid villi alone explains the distribution of CVF. CVF potentially arising in the lower lumbar spine presents a particularly interesting paradigm, because DCTM commonly interrogates spinal levels cephalad to the puncture level, raising the question of whether CVFs caudal to the lumbar puncture site are missed with any significant frequency.

Prior authors have hypothesized that underlying intracranial hypertension and subsequent damage to the spinal arachnoid villi may predispose patients to CVF development. While 1 patient (2.2%) in our cohort had an opening pressure of >20 cm H₂O, only 2/44 (4.5%) patients had an opening pressure of <6 cm H₂O, a finding that has been replicated in prior literature.¹⁹ Thus, it could be the case that before CVF development, these patients had higher CSF pressures, and the CVF acted as a release valve so that opening pressures were within the normal range at the time of their DCTM. This possibility warrants further investigation, and a multifactorial model for CVF pathogenesis should be considered.

This study is limited by its retrospective design, single-institution experience, and modest sample size. The lack of a control group further limits the potential generalizability of these findings. Furthermore, we emphasize the critical difference between correlation and causation, particularly in explaining the observed overlap in the distribution of thoracic osteoarthritis and CVF. Thus, we recommend interpretation of the findings of this study with caution. We encourage other centers to investigate the replicability of these findings in their patient cohorts. In addition to providing potential insight into the pathogenesis of CVF, an association of CVF with degenerative changes may aid in cases where there is high suspicion of underlying CVF but DCTM findings are indeterminate.

CONCLUSIONS

This analysis of 44 consecutive patients with CVFs suggests a spatial relationship between spinal osteoarthritis and the incidence of CVF. Future work should continue to assess the factors influencing CVF pathogenesis.

Disclosure forms provided by the authors are available with the full text and PDF of this article at www.ajnr.org.

REFERENCES

1. Mamlouk MD, Shen PY, Dahlin BC. Headache response after CT-guided fibrin glue occlusion of CSF-venous fistulas. *Headache* 2022;62:1007–18 CrossRef Medline
2. Mamlouk MD, Shen PY, Jun P, et al. Spontaneous spinal CSF leaks stratified by age, body mass index, and spinal level. *AJNR Am J Neuroradiol* 2022;43:1068–72 CrossRef Medline
3. Callen AL, Jones LC, Timponi VM, et al. Factors predictive of treatment success in CT-guided fibrin occlusion of CSF-venous fistulas: a multicenter retrospective cross-sectional study. *AJNR Am J Neuroradiol* 2023;44:1332–38 CrossRef Medline
4. Schievink WI, Maya M, Prasad RS, et al. Spinal CSF-venous fistulas in morbidly and super obese patients with spontaneous intracranial hypotension. *AJNR Am J Neuroradiol* 2021;42:397–401 CrossRef Medline
5. Kalichman L, Guermazi A, Li L, et al. Association between age, sex, BMI and CT-evaluated spinal degeneration features. *J Back Musculoskelet Rehabil* 2009;22:189–95 CrossRef Medline
6. Su CA, Kusin DJ, Li SQ, et al. The association between body mass index and the prevalence, severity, and frequency of low back pain: data from the Osteoarthritis Initiative. *Spine (Phila Pa 1976)* 2018;43:848–52 CrossRef Medline
7. Kido DK, Gomez DG, Pavese AM Jr, et al. Human spinal arachnoid villi and granulations. *Neuroradiology* 1976;11:221–28 CrossRef Medline
8. Kim DK, Carr CM, Benson JC, et al. Diagnostic yield of lateral decubitus digital subtraction myelogram stratified by brain MRI findings. *Neurology* 2021;96:e1312–18 CrossRef Medline
9. Rätsep T, Minajeva A, Asser T. Relationship between neovascularization and degenerative changes in herniated lumbar intervertebral discs. *Eur Spine J* 2013;22:2474–80 CrossRef Medline
10. Molinos M, Almeida CR, Caldeira J, et al. Inflammation in intervertebral disc degeneration and regeneration. *J R Soc Interface* 2015;12:20141191 CrossRef Medline
11. Han S, Jang IT. Prevalence and distribution of incidental thoracic disc herniation, and thoracic hypertrophied ligamentum flavum in patients with back or leg pain: a magnetic resonance imaging-based cross-sectional study. *World Neurosurg* 2018;120:e517–24 CrossRef Medline
12. Pfirrmann CW, Resnick D. Schmorl nodes of the thoracic and lumbar spine: radiographic-pathologic study of prevalence, characterization, and correlation with degenerative changes of 1,650 spinal levels in 100 cadavers. *Radiology* 2001;219:368–74 CrossRef Medline
13. Headache classification committee of the International Headache Society (IHS) the International Classification of Headache Disorders, 3rd edition *Cephalalgia* 2018;38:1–211 CrossRef Medline
14. Sarsılmaz A, Yencilek E, Özelçi Ü, et al. The incidence and most common levels of thoracic degenerative disc pathologies. *Turk J Phys Med Rehabil* 2018;64:155–61 CrossRef Medline
15. McInerney J, Ball PA. The pathophysiology of thoracic disc disease. *Neurosurg Focus* 2000;9:e1 CrossRef Medline
16. van der Kraan PM, van den Berg WB. Osteophytes: relevance and biology. *Osteoarthritis Cartilage* 2007;15:237–44 CrossRef Medline
17. Son BC, Ha SW, Lee SH, et al. The relief of unilateral painful thoracic radiculopathy without headache from remote spontaneous spinal cerebrospinal fluid leak. *Pain Res Manag* 2016;2016:4798465 CrossRef Medline
18. Tubbs RS, Hanssuta A, Stetler W, et al. Human spinal arachnoid villi revisited: immunohistological study and review of the literature. *J Neurosurg Spine* 2007;7:328–31 CrossRef Medline
19. Callen A, Pattee J, Thaker AA, et al. Relationship of Bern score, spinal elastance, and opening pressure in patients with spontaneous intracranial hypotension. *Neurology* 2023;100:e2237–46 CrossRef Medline

Improved Cerebral Glymphatic Flow after Transvenous Embolization of CSF-Venous Fistula

 Derrek Schartz, Alan Finkelstein, Jianhui Zhong,  Waleed Brinjikji, and Matthew T. Bender



ABSTRACT

SUMMARY: Spontaneous intracranial hypotension is characterized by symptoms of low intracranial CSF volume due to various mechanisms of CSF leakage. One such mechanism is a CSF-venous fistula, treatable with transvenous embolization resulting in substantial radiographic and clinical improvement. However, the exact mechanisms underlying these improvements, including the potential involvement of the glymphatic system, remain unclear. To noninvasively assess glymphatic clearance in spontaneous intracranial hypotension, we used an advanced MR imaging technique called the DTI along the perivascular spaces in 3 patients with CSF-venous fistula before and after embolization. All 3 patients with spontaneous intracranial hypotension initially had low glymphatic flow, which improved postembolization. Two patients with symptomatic improvement exhibited a more substantial increase in glymphatic flow compared with a patient with minimal improvement. These findings suggest a possible link between cerebral glymphatics in spontaneous intracranial hypotension pathophysiology and symptomatic improvement, warranting larger studies to explore the role of the glymphatic system in spontaneous intracranial hypotension.

ABBREVIATIONS: CSFVF = CSF-venous fistula; DTI-ALPS = DTI analysis along the perivascular space; FA = fractional anisotropy; SIH = spontaneous intracranial hypotension

Spontaneous intracranial hypotension (SIH) is an orthostatic headache syndrome caused by several possible mechanisms of CSF leakage with resultant low intracranial CSF volume.¹⁻³ CSF-venous fistula (CSFVF) has recently been identified as an important cause of SIH. Likewise, treatment of CSFVF with transvenous embolization has emerged as a robust treatment strategy with substantial radiographic and clinical improvement.⁴⁻⁶ However, while symptomatic improvement may presumably be attributed to improved CSF dynamics and normalized intracranial CSF volume, questions remain regarding the impact of SIH on cerebral blood flow and metabolism, including cerebral glymphatic clearance. Broadly, the glymphatic system is a cerebral metabolic waste-removal/drainage system involving CSF diffusion along the perivascular space.⁷ Given that SIH often results from abnormal CSF drainage via a CSFVF, it is conceivable that SIH may also be related to impaired glymphatic outflow. Prior

studies have noninvasively quantified cerebral glymphatic clearance in several CNS diseases by leveraging the DTI analysis along the perivascular space (DTI-ALPS), an advanced MR imaging technique.⁸⁻¹⁰ However, no studies have evaluated glymphatic clearance in patients with SIH or investigated how it might change following transvenous embolization of the culprit CSFVF. Here, we report 3 patients with SIH with impaired cerebral glymphatic flow, which improved following transvenous embolization of the CSFVF.

MATERIALS AND METHODS

From the 7 patients with CSFVF who were treated with transvenous embolization at our tertiary care institution at the University of Rochester Medical Center, 3 patients had sufficient pre-/post-embolization MR imaging required to evaluate their cerebral glymphatic outflow using the DTI-ALPS technique. Abbreviated details regarding the DWI sequence processing are described below. Additionally, clinical and radiographic parameters were collected, including the pre-/postembolization Bern Score.¹¹ At 3-month follow-up, postembolization brain MR imaging was acquired along with clinical assessment of symptomatic change.

Glymphatic DWI Analysis

The DTI-ALPS technique measures the diffusivity along the perivascular space of the medullary veins, the primary drainage

Received January 8, 2024; accepted after revision February 6.

From the Departments of Imaging Sciences (D.S. A.F., J.Z.) and Neurosurgery (M.T.B.), University of Rochester Medical Center, Rochester, New York; and Department of Radiology (W.B.), Mayo Clinic, Rochester, Minnesota.

Funding was provided by the Department of Imaging Sciences, University of Rochester Medical Center via the Fischer Fund Grant.

Please address correspondence to Derrek Schartz, MD, Department of Imaging Sciences, University of Rochester Medical Center, 601 Elmwood Ave, Rochester, NY 14642; e-mail: derrek_schartz@urmc.rochester.edu; @D_SchartzMD



Indicates article with online supplemental data.

<http://dx.doi.org/10.3174/ajnr.A8229>

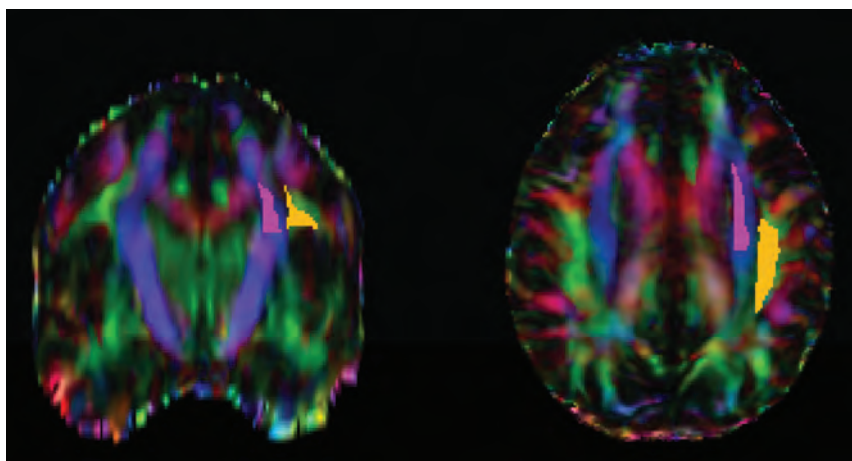


FIG 1. Sample of ROI determination using the atlas-based ALPS index. The projection (superior and posterior corona radiata, magenta ROI) and association (superior longitudinal fasciculus, yellow ROI) fibers were defined by the labels of the ICBM DTI-81 Atlas.

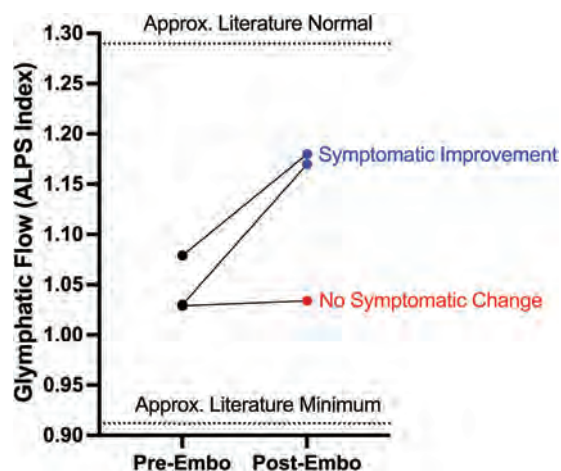


FIG 2. Change in cerebral glymphatic clearance in patients with SIH after transvenous embolization of a CSFVF. Embo indicates embolization; Approx., approximate.

pathway of the glymphatic system, and has been previously validated and robustly described in prior studies.^{8–10} The DWI data were corrected for eddy current-induced distortion using EDDY_CORRECT in FSL (<https://fsl.fmrib.ox.ac.uk/fsl/fslwiki/eddy>). Susceptibility-induced distortion was corrected using INVERSION, consisting of inverse contrast normalization of T1WI data and diffeomorphic coregistration using symmetric normalization in Advanced Normalization Tools (ANTs; <http://stnava.github.io/ANTs/>).¹² Diffusivity maps along the x-axis (Dxx), y-axis (Dyy), and z-axis (Dzz) were computed in addition to fractional anisotropy (FA), mean diffusivity, axial diffusivity, and radial diffusivity using DIPY (<https://docs.dipy.org/stable/index.html>). FA maps were coregistered to the FA map template FMRIB58 atlas using ANTs. The FA registration matrix was used to warp all other DTI maps to standard space. Modified JHU ICBM (https://www.researchgate.net/figure/Johns-Hopkins-University-ICBM-DTI-81-White-Matter-Labeled-Atlas-regions-of-interest-on_fig1_349013706) WM labels were used for the projection (superior corona radiata) and association fibers (superior longitudinal fasciculus)

in the periventricular area. An example of an atlas-based ROI determination can be seen in Fig 1. The ALPS index, which is used as a measure of glymphatic clearance, was then computed using these labels, defined by

$$ALPS\ index = \frac{mean(Dxx_{proj}, Dxx_{assoc})}{mean(Dyy_{proj}, Dzz_{assoc})}.$$

For purposes of reference and scale, a literature normal ALPS index is approximately 1.29, and a literature minimum value can be as low as 0.93.¹⁰

RESULTS

Three patients with SIH due to CSFVF were identified with sufficient MR imaging for analysis before and after transvenous embolization. Two patients were women, and one was a man; the average age was 65 years. The average preoperative Bern Score on MR imaging was 6.7. Each of the 3 patients had a lower than (literature) normal ALPS index suggestive of impaired glymphatic flow at baseline (Fig 2). All 3 patients had right-sided thoracic CSFVFs on digital subtraction myelography, which were subsequently embolized with Onyx (Medtronic) (example can be seen in Fig 3). Two patients (patients 1 and 2) had substantial clinical improvement of their symptoms (defined as >75% improvement) after embolization and a decrease in the Bern Score on imaging (Online Supplemental Data). Likewise, patients 1 and 2 had improvement in their glymphatic clearance after embolization on 3-month follow-up (Online Supplemental Data, Fig 2). Patient 3 had only slight improvement in glymphatic clearance (ALPS index, 1.029–1.034), with mild improvement in the Bern Score and no notable change in his clinical symptoms (Online Supplemental Data).

DISCUSSION

It is entirely unknown whether glymphatic clearance is altered in patients with SIH due to CSFVF and if/how it may contribute to symptomatology or pathophysiology. In this brief report, all 3 patients demonstrated impaired baseline glymphatic clearance (ALPS Index, 1.029–1.078) compared with a literature normal reference value (ALPS Index, ~1.29).¹⁰ If a minimum literature ALPS Index value is considered to be approximately 0.93, this suggests that patients with CSFVF may have <50% of baseline glymphatic outflow compared with healthy patients. Additionally, in all 3 patients, CSFVF embolization at least partially recovered glymphatic function, suggesting that the observed low ALPS values might be attributed to the CSFVF.

Although the mechanism underlying the presented observation is unknown, it has been previously shown that abnormal intracranial pressure alters CSF clearance pathways, suggesting a possible connection between intracranial pressure homeostasis and cerebral glymphatic flow.¹³ Likewise, it is also possible that glymphatic function may be pressure-dependent, in which a decrease in outflow might parallel the decreased CSF volume.

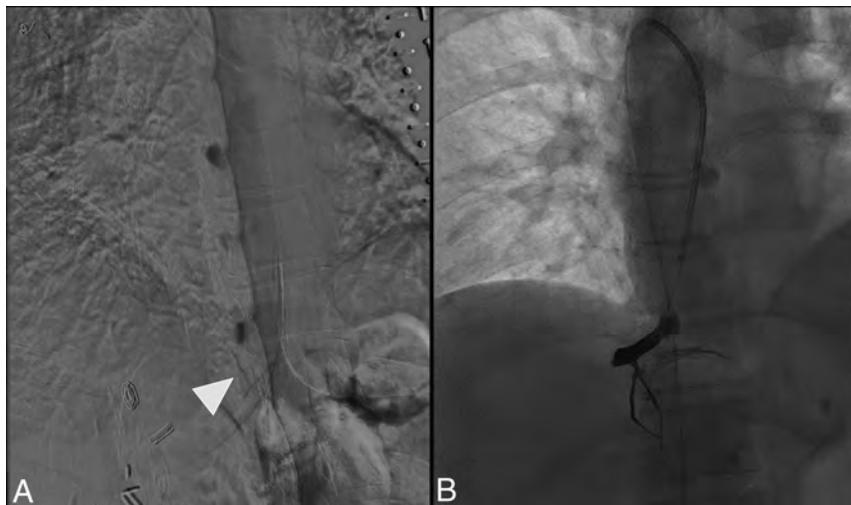


FIG 3. A, Patient 1 is a representative example of CSFVF (white arrowhead) on digital subtraction myelography located on the right at the level of T10. B, Onyx cast within the foraminal vein, intercistal vein, and adjacent venous plexus following transvenous embolization.

Additionally, we hypothesize that general brain sagging due to low intracranial CSF volume may structurally distort the cerebral venoglymphatic system and could result in the observed impaired flow. Furthermore, venous sinus engorgement, a common neuroimaging finding in SIH, could possibly compress and compromise the adjacent cerebral perivascular lymphatics. Last, low CSF intracranial volume could conceivably alter the homeostasis of the cerebral interstitial space, which may compromise cerebral interstitial compliance and the glymphatic system.¹⁴

While purely theoretical, one potential implication of this study is that it could explain some CSFVF symptoms that are not as well-explained by gross structural abnormalities such as brain sag. In general, it is accepted that brain sag with resultant traction of pain-sensitive fibers or trigeminal nerve ganglia is the possible reason for headaches. However, other common SIH symptoms and complications including drowsiness, brain fog, and frontotemporal dementia are not as well-explained by brain sag. Given that impaired glymphatic flow has been implicated as the final common pathway for dementia, it is possible that this may be a mechanism for some of the harder-to-localize symptoms of SIH due to CSFVF.⁷

In addition to possibly implicating the glymphatic system in SIH due to CSFVF, the DTI-ALPS method could be used for diagnostic purposes. It is feasible that the extent of impaired glymphatic flow could function as a quantitative neuroimaging marker for patients with CSFVF and may theoretically be combined with the Bern Score to aid in the diagnosis. However, impaired glymphatic flow is nonspecific to SIH and can be seen in other conditions, which may limit this possibility.^{9,10} Regardless, given the diagnostic challenge of SIH and CSFVF, a low ALPS index obtained noninvasively from a brain MR imaging could serve as an additional data point for further work-up, including a diagnostic myelogram. Similarly, while not previously investigated, the ALPS index could also assist in the diagnosis and management in patients with a low Bern Score, which could be explored in future studies.

While the DTI-ALPS method is noninvasive and can be completed retrospectively, additional techniques have been described to image the glymphatic system. For example, following IV or intrathecal administration of gadolinium-based contrast, MR cisternography can be used to track CSF transport and measure glymphatic clearance along the paravascular routes.¹⁵ Meningeal lymphatic vessels can also be directly imaged via FLAIR MR imaging following contrast administration, when the rate of meningeal lymphatic efflux reflects the rate of paravascular/glymphatic outflow.¹⁵ Additional advanced MR imaging techniques include intravoxel incoherent motion and chemical exchange saturation transfer to measure cerebral interstitial fluid transport.¹⁵ These methods, among others,

could also be used to study the glymphatic system in patients with SIH.

While the obvious limitation of this study is the modest sample size of 3 patients and absence of age-matched controls, in all instances, glymphatic flow increased following transvenous embolization. Most interesting, we also observed that in the 2 patients with symptomatic improvement, the postembolization glymphatic flow increase was notably higher than the minimal increase in patient 3, who demonstrated a mild radiographic improvement and no appreciable symptomatic improvement (Online Supplemental Data, Fig 2). This finding could suggest that the extent of glymphatic clearance rescue may at least partially reflect/explain the substantial radiographic and clinical improvement that is often observed with transvenous embolization.⁴⁻⁶ Alternatively, normalized intracranial volume after CSFVF embolization may structurally restore the venoglymphatic system, resulting in at least partially normalized glymphatic flow. Nonetheless, a change in glymphatic clearance could conceivably function as a quantitative marker of treatment success based on our modest $n = 3$. An additional limitation is that we only included patients with SIH with an identified CSFVF. It is possible that SIH due to other mechanisms (ventral tear and so forth) may not have impaired glymphatic clearance as suggested here. Future studies researching the glymphatic system in SIH should investigate CSF leaks of different etiologies and with appropriate controls.

CONCLUSIONS

The glymphatic flow in patients with SIH due to a CSFVF can be quantitatively measured with the DTI-ALPS method. This small series suggests that patients with SIH have impaired glymphatic clearance of unclear etiology and mechanism and that transvenous embolization could restore glymphatic flow. Although this series does not function as proof, this report does open a new line of inquiry in SIH. Additional studies are required to validate the presented findings and to clarify the role that the glymphatic system might play in SIH.

REFERENCES

- Cheema S, Anderson J, Angus-Leppan H, et al. **Multidisciplinary consensus guideline for the diagnosis and management of spontaneous intracranial hypotension.** *J Neurol Neurosurg Psychiatry* 2023;94:835–43 CrossRef Medline
- Schartz D, Ellens N, Ismail R, et al. **Prevalence of SLEC-negative spontaneous intracranial hypotension in patients with spinal nerve root sleeve diverticula on MRI.** *Neuroradiol J* 2023;36:736–39 CrossRef Medline
- Kranz PG, Gray L, Malinzak MD, et al. **Spontaneous intracranial hypotension: pathogenesis, diagnosis, and treatment.** *Neuroimaging Clin N Am* 2019;29:581–94 CrossRef Medline
- Brinjikji W, Madhavan A, Garza I, et al. **Clinical and imaging outcomes of 100 patients with cerebrospinal fluid-venous fistulas treated by transvenous embolization.** *J Neurointerv Surg* 2023 Oct 28. [Epub ahead of print] CrossRef Medline
- Brinjikji W, Savastano LE, Atkinson JL, et al. **A novel endovascular therapy for CSF hypotension secondary to CSF-venous fistulas.** *AJNR Am J Neuroradiol* 2021;42:882–87 CrossRef Medline
- Ellens NR, Schartz D, Ismail R, et al. **Efficacy of transvenous embolization of CSF-venous fistula in spontaneous intracranial hypotension: case-series.** *Interv Neuroradiol* 2023 Dec 21 [Epub ahead of print] CrossRef Medline
- Nedergaard M, Goldman SA. **Glymphatic failure as a final common pathway to dementia.** *Science* 2020;370:50–56 CrossRef Medline
- Taoka T, Masutani Y, Kawai H, et al. **Evaluation of glymphatic system activity with the diffusion MR technique: diffusion tensor image analysis along the perivascular space (DTI-ALPS) in Alzheimer's disease cases.** *Jpn J Radiol* 2017;35:172–78 CrossRef Medline
- Taoka T, Ito R, Nakamichi R, et al. **Reproducibility of diffusion tensor image analysis along the perivascular space (DTI-ALPS) for evaluating interstitial fluid diffusivity and glymphatic function: CHanges in Alps index on Multiple conditiON acqUisition eXperiment (CHAMONIX) study.** *Jpn J Radiol* 2022;40:147–58 CrossRef Medline
- Schartz D, Finkelstein A, Hoang N, et al. **Diffusion-weighted imaging reveals impaired glymphatic clearance in idiopathic intracranial hypertension.** *AJNR Am J Neuroradiol* 2024;45:149–54 CrossRef Medline
- Dobrocky T, Grunder L, Breiding PS, et al. **Assessing spinal cerebrospinal fluid leaks in spontaneous intracranial hypotension with a scoring system based on brain magnetic resonance imaging findings.** *JAMA Neurol* 2019;76:580–87 CrossRef Medline
- Bhushan C, Haldar JP, Choi S, et al. **Co-registration and distortion correction of diffusion and anatomical images based on inverse contrast normalization.** *Neuroimage* 2015;115:269–80 CrossRef Medline
- Vinje V, Eklund A, Mardal KA, et al. **Intracranial pressure elevation alters CSF clearance pathways.** *Fluids Barriers CNS* 2020;29–29 CrossRef Medline
- Iliff JJ, Thrane AS, Nedergaard M. **The glymphatic system and brain interstitial fluid homeostasis.** In: Caplan LR, Biller J, Zhang JH, eds. *Primer on Cerebrovascular Diseases*. 2nd ed. Academic Press, 2017:17–25
- Klostranec JM, Vucevic D, Bhatia KD, et al. **Current concepts in intracranial interstitial fluid transport and the glymphatic system, Part II: imaging techniques and clinical applications.** *Radiology* 2021;301:516–32 CrossRef Medline

Comparison of a Whole-Brain Contrast-Enhanced 3D TSE T1WI versus Orbits Contrast-Enhanced 2D Coronal T1WI at 3T MRI for the Detection of Optic Nerve Enhancement in Patients with Acute Loss of Visual Acuity

David Prillard, Frédérique Charbonneau, Pierre Clavel, Catherine Vignal-Clermont, Romain Deschamps, Marine Boudot de la Motte, Jessica Guillaume, Julien Savatovsky, and Augustin Lecler



ABSTRACT

BACKGROUND AND PURPOSE: MR imaging is the technique of choice for patients presenting with acute loss of visual acuity with no obvious ophthalmologic cause. The goal of our study was to compare orbits contrast-enhanced 2D coronal T1WI with a whole-brain contrast-enhanced 3D (WBCE-3D) TSE T1WI at 3T for the detection of optic nerve enhancement.

MATERIALS AND METHODS: This institutional review board–approved retrospective single-center study included patients presenting with acute loss of vision who underwent 3T MR imaging from November 2014 to February 2020. Two radiologists, blinded to all data, individually assessed the presence of enhancement of the optic nerve on orbits contrast-enhanced 2D T1WI and WBCE-3D T1WI separately and in random order. A McNemar test and a Cohen κ method were used for comparing the 2 MR imaging sequences.

RESULTS: One thousand twenty-three patients (638 women and 385 men; mean age, 42 [SD, 18.3] years) were included. There was a strong concordance between WBCE-3D T1WI and orbits contrast-enhanced 2D T1WI when detecting enhancement of the optic nerve: $\kappa = 0.87$ (95% CI, 0.84–0.90). WBCE-3D T1WI was significantly more likely to detect canicular enhancement compared with orbits contrast-enhanced 2D T1WI: 178/1023 (17.4%) versus 138/1023 (13.5%) ($P < .001$) and 108/1023 (10.6%) versus 90/1023 (8.8%) ($P = .04$), respectively. The WBCE-3D T1WI sequence detected 27/1023 (3%) instances of optic disc enhancement versus 0/1023 (0%) on orbits contrast-enhanced 2D T1WI. There were significantly fewer severe artifacts on WBCE-3D T1WI compared with orbits contrast-enhanced 2D T1WI: 68/1023 (6.6%) versus 101/1023 (9.8%) ($P < .001$). The median reader-reported confidence was significantly higher with coronal T1WI compared with 3D TSE T1WI: 5 (95% CI, 4–5) versus 3 (95% CI, 1–4; $P < .001$).

CONCLUSIONS: Our study showed that there was a strong concordance between WBCE-3D T1WI and orbits contrast-enhanced 2D T1WI when detecting enhancement of the optic nerve in patients with acute loss of visual acuity with no obvious ophthalmologic cause. WBCE-3D T1WI demonstrated higher sensitivity and specificity in diagnosing optic neuritis, particularly in cases involving the canicular segments.

ABBREVIATIONS: ON = optic neuritis; OCE-2D = orbits contrast-enhanced 2D; WBCE-3D = whole-brain contrast-enhanced 3D

Optic neuritis (ON) is an inflammatory disease of the CNS affecting the optic nerve, clinically characterized by acute vision loss associated with orbital pain and dyschromatopsia.^{1,2} ON can be isolated or associated with various diseases such as MS or neuromyelitis optica spectrum disorder.^{3,4} It is important

to diagnose it correctly and accurately to adapt both management and treatment.⁵

Brain imaging is recommended by the international guidelines when diagnosing ON to assess any associated brain lesion related to previously mentioned etiologies.⁶ MR imaging is the criterion standard to diagnose ON for patients presenting with a loss of visual acuity. Conventional protocol includes fat-suppressed coronal T2WI and contrast-enhanced fat-suppressed coronal T1WI sequences covering the optic nerve along with FLAIR-weighted and contrast-enhanced T1WI covering the brain.⁷ Typical MR imaging features of acute ON consist of a high signal intensity of the optic nerve on T2WI sequences and enhancement, which is routinely evaluated on contrast-enhanced coronal T1WI sequences.⁸

Received March 19, 2023; accepted after revision February 7, 2024.

From the Departments of Neuroradiology (D.P., F.C., P.C., J.S., A.L.), Ophthalmology (C.V.-C.), Neurology (R.D., M.B.d.l.M.), and Clinical Research (J.G.), A. Rothschild Foundation Hospital, Paris, France.

Please address correspondence to David Prillard, MD, Department of Neuroradiology, A. Rothschild Foundation Hospital, 25 rue Manin, 75019 Paris, France; e-mail: alecler@for.paris



Indicates article with online supplemental data.

<http://dx.doi.org/10.3174/ajnr.A8233>

Table 1: Detailed MR imaging acquisition parameters of OCE-2D coronal T1WI and WBCE-3D TSE T1WI

MR Imaging Sequence	OCE-2D T1WI	WBCE-3D T1WI
Sequence type	TSE	TSE
Acquisition mode	2D	3D
Acquisition plane	Coronal	Sagittal
TR (ms)	400	500
TE (ms)	12	26
Section thickness (mm)	3	1
Gap	No	No
No. of excitations	1	1
Echo-train length	1	20
Flip angle	90°	90°
Bandwidth (Hz)	218	288
Matrix	232 × 224	252 × 252 × 400
Field of view (mm)	140 × 140	252 × 252 × 200
Acquired voxel size (mm)	0.6 × 0.6 × 3	1 × 1 × 1
Reconstructed voxel size (mm)	0.16 × 0.16 × 3	0.49 × 0.49 × 0.50
Acquisition time (min)	04:22	03:37

However, evaluating the optic nerve using 2D sequences can be challenging due to its oblique and nonlinear course along its pathway. Additionally, certain segments, such as the intracanalicular segment, can be particularly challenging due to the orientation of the optic canal and the presence of artifacts, including magnetic susceptibility artifacts, due to its proximity of the sinuses.

Recent studies evaluated the diagnostic performance of new MR imaging sequences, such as double inversion recovery or 3D TSE black-blood T1WI, to increase the detection of signal abnormalities and enhancement of the optic nerve.^{9,10} Contrast-enhanced 3D TSE T1WI has the advantage of covering both the brain and the orbits. It might be accurate to detect enhancement of the optic nerve in patients with a suspected diagnosis of ON.

Therefore, the purpose of our study was to compare a whole-brain contrast-enhanced 3D (WBCE-3D) TSE T1WI versus orbits contrast-enhanced 2D (OCE-2D) coronal T1WI at 3T to detect optic nerve enhancement in patients with acute loss of vision with no obvious ophthalmologic cause.

MATERIALS AND METHODS

Study Design

This retrospective single-center study was conducted in a tertiary referral center specializing in ophthalmologic disorders. It was approved by an independent institutional review board and adhered to the tenets of the Declaration of Helsinki (CE_20200204_2_ALR, NCT04793087). Signed informed consent was waived by the institutional review board. This study follows the Standards for Reporting of Diagnostic Accuracy Studies guidelines.¹¹

Participants

We included all patients presenting to our center with acute loss of visual acuity who underwent MR imaging from November 2014 to February 2020. Inclusion criteria were the following: 1) older than 18 years of age; 2) acute loss of vision with no obvious ophthalmologic cause; and 3) completion of brain and orbital MR imaging. Exclusion criteria were an incomplete MR imaging examination defined by the absence of either contrast-enhanced T1WI or WBCE-3D T1WI and detection of an orbital or brain

abnormality explaining the vision loss, such as tumors involving the optic nerve or its sheaths or the optic pathways. One thousand twenty-three participants were ultimately included for analysis.

The selection of participants is shown in the Online Supplemental Data.

MR Imaging Protocol

All MR images were acquired with a 3T MR imaging scanner (Ingenia Elition; Philips Healthcare) using a 32-channel array head coil.

The brain MR imaging protocol was standardized in our institution, including fat-suppressed WBCE-3D T1WI covering the whole brain and fat-sup-

pressed OCE-2D T1WI covering the whole length of the optic nerve as well as the optic chiasm, as recommended by the Magnetic Resonance Imaging in Multiple Sclerosis international consensus group.⁷ IV gadobutrol (Gadovist; Bayer) was administered at a concentration of 0.1 mmol/kg. Contrast-enhanced sequences were acquired >5 minutes after injection to obtain satisfactory postdelay contrast of structures.

Detailed acquisition parameters are shown in Table 1.

MR Imaging Analysis

WBCE-3D T1WI and OCE-2D T1WI were anonymized into 2 distinct imaging data sets. Two radiologists, 1 junior radiologist (D.P.) and 1 senior neuroradiologist (F.C.) with 6 months and 15 years of experience, respectively, blinded to all data, individually read both imaging data sets in a random order to avoid establish recognition patterns. A second reading was performed 4 weeks later to evaluate intrareader agreement. Four weeks later, a consensus reading session was performed with a third senior neuroradiologist, also blinded to all data, who was specialized in ophthalmologic imaging with 10 years of experience (A.L.). This last reading was considered the reference standard for statistical analysis. All reading sessions were on a dedicated workstation with the Carestream software (Onex).

The readers assessed the following characteristics of participants' MR images:

- The primary judgment criterion was the presence of enhancement of the optic nerve or the optic chiasm, with the normal-appearing white matter serving as a reference
- Secondary judgment criteria were the following:
- The side of the enhancement
- The location of the enhancement of the optic nerve, defined as intraorbital, canalicular, or cisterna
- The presence of enhancement of the optic disc, considered distinct from the intraorbital segment
- The presence of artifacts defined as follows: no artifacts, moderate artifacts not preventing the interpretation of the scan, and severe artifacts preventing any accurate interpretation of the scan

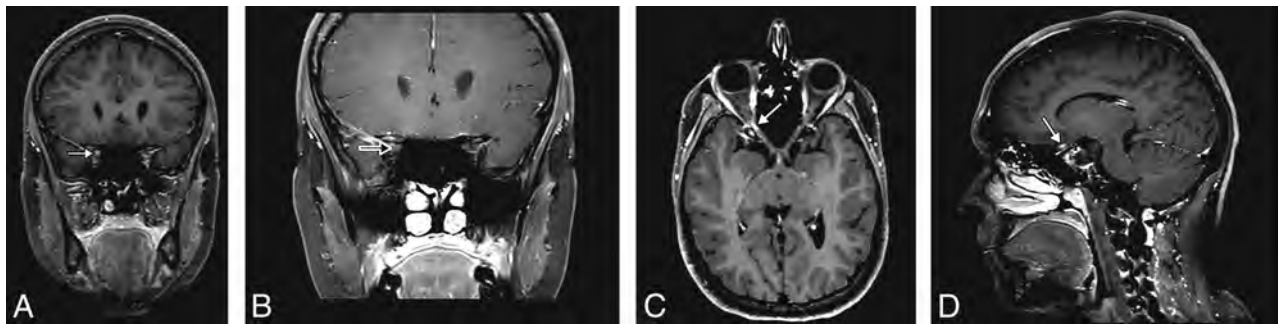


FIG 1. A 21-year-old woman presenting with acute vision loss and orbital pain of the right eye. WBCE-3D TSE TIWI reformatted in the coronal plane (A) shows enhancement of the intraorbital segment of the right optic nerve at the orbital apex (*white arrow*), whereas no optic nerve enhancement was detected on OCE-2D coronal TIWI (*black arrow*) (B). The WBCE-3D TIWI sequence reformatted in the axial (C) and sagittal (D) planes confirming and precisely localizing the enhancement of the optic nerve.

Table 2: Comparison of WBCE-3D TSE TIWI and OCE-2D coronal TIWI

	OCE-2D TIWI (n = 1023) (%)	WBCE-3D TIWI (n = 1023) (%)	P Value
Optic nerve enhancement	205/1023 (20)	245/1023 (24)	<.001 ^a
Localization of the enhancement			
Bilateral	14/1023 (1.4)	23/1023 (2.2)	.05
Intraorbital	138/1023 (13.5)	151/1023 (14.8)	<.4
Canalicular	90/1023 (8.8)	108/1023 (10.6)	.04 ^a
Cisternal	38/1023 (3.7)	27/1023 (2.6)	.09
Optic chiasm	9/1023 (0.9)	10/1023 (1.0)	>.9
Optic disc	0/1023 (0.0)	27/1023 (2.6)	NA
Artifacts			
None	562/1023 (55.0)	853/1023 (83.4)	P < .001 ^a
Moderate	360/1023 (35.2)	102/1023 (10.0)	
Severe	101/1023 (9.8)	68/1023 (6.6)	
Reader-reported confidence			
1	36/1023 (3.5)	314/1023 (30.7)	P < .001 ^a
2	28/1023 (2.7)	194/1023 (19.0)	
3	99/1023 (9.7)	236/1023 (23.1)	
4	269/1023 (26.3)	188/1023 (18.4)	
5	591/1023 (57.8)	91/1023 (8.9)	

Note:— NA indicates not applicable.

^aStatistically significant difference.

- The reader-reported confidence when detecting optic nerve or optic chiasm enhancement, measured on a 5-point scale was follows: 1 corresponded to very low confidence; 2, to low; 3, to moderate; 4, to high; and 5, to very high confidence.

Statistical Analysis. Quantitative variables were presented as mean (SD) and median (interquartile range); and categorical variables, as percentages. A McNemar test and the Cohen κ method were used for comparing the 2 MR imaging sequences.

A Wilcoxon signed-rank test was used to compare the reader-reported confidence and the presence of artifacts. All tests were 2-tailed.

Inter- and intraobserver agreement for the MR imaging reading was assessed using a weighted Cohen κ method for ordinal variables and the Cohen κ method for binary variables with a 95% confidence interval and were interpreted as follows: <0.20, none; 0.21–0.39, minimal; 0.40–0.59, weak; 0.60–0.79, moderate; 0.80–0.90, strong; and >0.9, almost perfect.

Data were analyzed by using R software (Version 4.0.3; <http://www.r-project.org/>).¹²

RESULTS

Demographics

One thousand two hundred twenty patients presented to our center with an acute loss of vision from November 2014 to February 2020. One hundred fifty-six (13%) patients were excluded due to the absence of either OCE-2D T1WI or WBCE-3D T1WI. Forty-one (3%) patients were excluded due to the presence of a tumor involving the optic nerve or its sheaths or the optic pathways on imaging (31 meningiomas, 6 pituitary macroadenomas, 2 optic nerve gliomas, 1 craniopharyngioma, and 1 occipital glioblastoma).

One thousand twenty-three patients were ultimately included in the study (638 women and 385 men; mean age, 42 [SD, 18.3] years) (Online Supplemental Data). Three hundred one of 1023

(29%) patients had a final diagnosis of acute ON.

Concordance of WBCE-3D TIWI and OCE-2D TIWI Sequences When Detecting Optic Nerve Enhancement

There was a strong concordance between WBCE-3D T1WI and OCE-2D T1WI when detecting enhancement of the optic nerve: $\kappa = 0.87$ (95% CI, 0.84–0.90).

WBCE-3D T1WI was significantly more likely to detect canalicular enhancement compared with OCE-2D T1WI: 108/1023 (10.6%) versus 90/1023 (8.8%) ($P = .04$), respectively (Fig 1). WBCE-3D T1WI detected 27/1023 (3%) optic disc enhancements versus 0/1023 (0%) on OCE-2D T1WI.

Three patients had optic nerve enhancement that was observable on the OCE-2D T1WI sequence but not on the WBCE-3D T1WI sequence.

Detailed results are shown in Table 2.

Diagnostic Performance of WBCE-3D TIWI and OCE-2D TIWI Sequences When Detecting ON

Two hundred thirty-five of 301 (78%) patients with a final diagnosis of ON had contrast enhancement of the optic nerve on

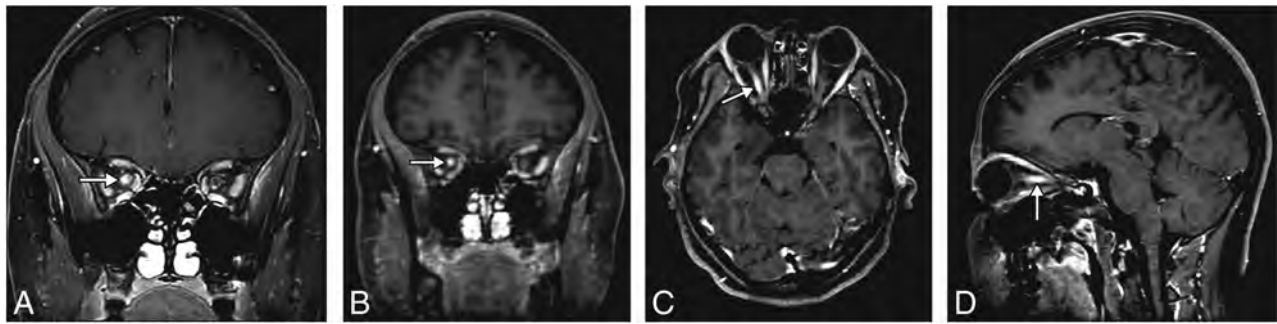


FIG 2. A 27-year-old woman presenting with acute vision loss and orbital pain of the right eye. OCE-2D coronal T1WI (A) shows enhancement of the intraorbital segment of the right optic nerve (arrow), also seen on the WBCE-3D TSE T1WI reformatted in the coronal (B), axial (C), and sagittal (D) planes.

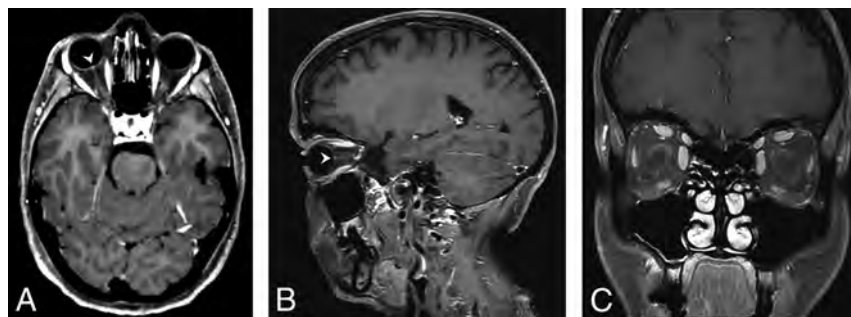


FIG 3. A 53-year-old woman presenting with acute vision loss of the right eye. WBCE-3D TSE T1WI reformatted in the axial plane (A) shows enhancement of the right optic disc (arrowhead). The WBCE-3D T1WI sequence reformatted in the sagittal plane (B), confirming the enhancement. No enhancement was detected on OCE-2D coronal T1WI (C).

WBCE-3D T1WI versus 205/301 (68%) on OCE-2D T1WI (Fig 2).

The sensitivity, specificity, positive predictive value, and negative predictive value of WBCE-3D T1WI and OCE-2D T1WI when diagnosing ON were 0.78 versus 0.68, 0.97 versus 0.92, 0.92 versus 0.77, and 0.91 versus 0.87, respectively (Fig 3).

Presence of Artifacts

There were significantly fewer severe artifacts on WBCE-3D T1WI compared with OCE-2D T1WI: 68/1023 (6.6%) versus 101/1023 (9.8%) ($P < .001$).

Reader-Reported Confidence

Median reader-reported confidence was significantly higher with OCE-2D T1WI compared with WBCE-3D T1WI: 5 (95% CI, 4–5) versus 3 (95% CI, 1–4) ($P < .001$).

Detailed results are shown in Table 2.

Interobserver and Intraobserver Agreement

The interobserver agreement when detecting optic nerve enhancement was strong on OCE-2D T1WI versus moderate on WBCE-3D T1WI: $\kappa = 0.80$ (95% CI, 0.75–0.85) versus 0.65 (95% CI, 0.60–0.71). The intraobserver agreement when detecting optic nerve enhancement was moderate on OCE-2D T1WI and almost perfect on WBCE-3D T1WI: $\kappa = 0.75$ (95% CI, 0.70–0.80) and $\kappa = 1$ (95% CI, 1–1).

Detailed inter- and intraobserver agreement is reported in Table 3.

DISCUSSION

Our study showed a strong concordance between 3D WBCE-3D TSE T1WI and OCE-2D coronal T1WI when detecting enhancement of the optic nerve in patients with acute loss of visual acuity with no obvious ophthalmologic cause. WBCE-3D T1WI showed fewer severe artifacts compared with OCE-2D T1WI and could detect optic disc enhancement.

To the best of our knowledge, our study is the largest one comparing the diagnostic concordance of these 2 sequences in clinical practice.

We showed that WBCE-3D T1WI had a higher detection rate when detecting optic nerve enhancement in its canicular segments. Our study is in concordance with existing literature, especially with the study of Riederer et al⁹ comparing a 3D T1WI black-blood sequence with a 3D T1WI MPRAGE sequence. In that study, 70% of the patients diagnosed with ON had optic nerve enhancement, with a sensitivity of 70% and specificity of 90% for detecting optic nerve contrast enhancement. Canicular segments are considered difficult to assess using coronal T1WI because of the orientation of the optic canal, the reduced contrast between the optic nerve and the surrounding hypointense bones, and the presence of artifacts due to the proximity of the sinuses. The higher detection rate of WBCE-3D T1WI might be due to the ability of multiplanar reconstructions used in 3D sequences, improving both detection and localization of the enhancement. 3D reformatting is known to increase accuracy by overcoming the partial volume effect compared with 2D sequences.¹³ The increase might also be due to the presence of fewer artifacts, which were significantly lower using the WBCE-3D T1WI compared with OCE-2D T1WI. This result is in line with the better clarity of the optic nerve and the higher visual enhancement of the optic nerve with 3D Cube T1WI (GE Healthcare) compared with 2D T1WI as reported by a recent study comparing these 2 sequences when diagnosing contrast-enhancing lesions of the optic nerve.¹⁴

WBCE-3D T1WI has several advantages over OCE-2D T1WI. It allows analysis of the whole brain to detect white matter lesions

Table 3: Inter- and intraobserver agreement for a WBCE-3D TSE T1WI and OCE-2D coronal T1WI when detecting optic nerve or optic chiasm enhancement

	Interobserver		Intraobserver	
	OCE-2D T1WI κ (95% CI)	WBCE-3D T1WI κ (95% CI)	OCE-2D T1WI κ (95% CI)	WBCE-3D T1WI κ (95% CI)
Optic nerve enhancement	0.80 (0.75–0.85)	0.65 (0.60–0.71)	0.75 (0.70–0.80)	1 (1–1)
Localization of the enhancement				
Bilateral	0.90 (0.78–1)	0.53 (0.34–0.71)	0.75 (0.58–0.92)	1 (1–1)
Intraorbital segment	0.76 (0.70–0.82)	0.63 (0.57–0.70)	0.81 (0.76–0.87)	0.81 (0.76–0.87)
Canalicular segment	0.64 (0.56–0.73)	0.72 (0.65–0.79)	0.71 (0.64–0.79)	0.68 (0.58–0.75)
Cisternal segment	0.58 (0.45–0.72)	0.54 (0.37–0.72)	0.49 (0.34–0.65)	0.81 (0.76–0.87)
Optic chiasm	0.44 (0.15–0.73)	0.73 (0.51–0.96)	0.33 (0.04–0.61)	1 (1–1)

with excellent diagnostic performance.¹⁵ It can analyze the optic disc and thus detect optic disc enhancement, which is not feasible with OCE-2D T1WI. In our study, 27 patients had enhancement of the optic disc on WBCE-3D T1WI, which could not be assessed on OCE-2D T1WI. Fat saturation slightly reduces the SNR of the WBCE-3D T1WI. However, fat saturation prevents certain folding artifacts, especially those of fat in the cerebral parenchyma, particularly in patients who have slight movement. This is our routine sequence for analyzing cerebral parenchyma after contrast injection.

Most interesting, self-reported confidence was significantly higher with OCE-2D T1WI compared with WBCE-3D T1WI. Better confidence might be explained by the radiologist's habit of looking for optic nerve enhancement on dedicated OCE-2D T1WI rather than on WBCE-3D T1WI in routine clinical practice.

Despite the strong concordance between WBCE-3D T1WI and OCE-2D T1WI, our study advocates the use of both sequences when performing MR imaging in patients with a suspected diagnosis of ON instead of replacing OCE-2D T1WI with WBCE-3D T1WI, because both sequences have strengths and weaknesses. A combination of both sequences might increase the detection rate of optic nerve enhancement and the confidence of readers, especially in cases of artifacts, such as susceptibility or motion artifacts involving only 1 sequence.

Our findings emphasize the importance for radiologists to look for optic nerve enhancement on a WBCE-3D T1WI sequence during the diagnosis or follow-up of patients with inflammatory brain lesions, in order to diagnose asymptomatic ON, which is reported to occur in up to 50% of patients with MS.¹⁶ Because there are no official guidelines regarding the recommended MR imaging protocol for diagnosing ON among patients presenting with acute loss of vision, we suggest performing both WBCE-3D T1WI and OCE-2D T1WI in patients with a suspected diagnosis or during follow-up of ON.

Our study has several limitations: First, this is a retrospective study from a single center. Second, readers could not be blinded to the type of sequences they were reading because of their easily recognizable visual features, possibly leading to a certain bias. The randomized pattern of reading we used avoided radiologists' reading images obtained from the same patient at the same time. Third, our analysis was based only on WBCE-3D T1WI and OCE-2D T1WI. Readers did not have access to other sequences such as coronal T2WI and 3D FLAIR imaging, which have excellent performance for detecting ON, or DWI, proving useful to

detect anterior ischemic optic neuropathy.^{17,18} Our routine MR imaging protocol does not include axial contrast-enhanced 2D T1 fat-suppressed sequences, performed in many centers to assess the optic nerve. This practice may have reduced the diagnostic performance of 2D compared with 3D, considering the ability of readers to reformat the 3D sequence in all planes, not just the coronal plane. Fourth, all our images were acquired exclusively on 3T MR imaging scanners, which may not be representative of the most common MR imaging equipment worldwide and may prevent the generalizability of our results, but this equipment has proved to be more sensitive in detecting optic nerve enhancement compared with 1.5T MR imaging.¹⁹ Moreover, the WBCE-3D T1WI we used had a relatively high resolution and optimal fat suppression, which might not be achievable in all centers.

Finally, WBCE-3D T1WI and OCE-2D T1WI sequences were always performed in the same order, with different contrast-enhanced delays, possibly affecting the enhancement of the optic nerve, because the sensitivity of contrast-enhanced images increases with the delay after administration of a gadolinium-based contrast agent.^{20,21}

CONCLUSIONS

Our study showed that there was a strong concordance between contrast-enhanced 3D (WBCE-3D) TSE T1WI and OCE-2D coronal T1WI when detecting enhancement of the optic nerve in patients with acute loss of visual acuity with no obvious ophthalmologic cause. WBCE-3D T1WI showed fewer severe artifacts compared with OCE-2D T1WI and could detect optic disc enhancement. WBCE-3D T1WI demonstrated higher sensitivity and specificity in diagnosing ON, particularly in cases involving the canalicular segments.

Disclosure forms provided by the authors are available with the full text and PDF of this article at www.ajnr.org.

REFERENCES

- Petzold A, Wattjes MP, Costello F, et al. **The investigation of acute optic neuritis: a review and proposed protocol.** *Nat Rev Neurol* 2014;10:447–58 CrossRef Medline
- Petzold A, Fraser CL, Abegg M, et al. **Diagnosis and classification of optic neuritis.** *Lancet Neurol* 2022;21:1120–34 CrossRef Medline
- Dutra BG, da Rocha AJ, Nunes RH, et al. **Neuromyelitis optica spectrum disorders: spectrum of MR imaging findings and their differential diagnosis.** *Radiographics* 2018;38:169–93 CrossRef Medline

4. Marques IB, Matias F, Silva ED, et al. **Risk of multiple sclerosis after optic neuritis in patients with normal baseline brain MRI.** *J Clin Neurosci* 2014;21:583–86 CrossRef Medline
5. Wilhelm H, Schabet M. **The diagnosis and treatment of optic neuritis.** *Dtsch Arztebl Int* 2015;112:616–25; quiz 626 CrossRef Medline
6. Thompson AJ, Banwell BL, Barkhof F, et al. **Diagnosis of multiple sclerosis: 2017 revisions of the McDonald criteria.** *Lancet Neurol* 2018;17:162–73 CrossRef Medline
7. Filippi M, Rocca MA, Ciccarelli O, et al; MAGNIMS Study Group. **MRI criteria for the diagnosis of multiple sclerosis: MAGNIMS consensus guidelines.** *Lancet Neurol* 2016;15:292–303 CrossRef Medline
8. Winter A, Chwalisz B. **MRI characteristics of NMO, MOG and MS related optic neuritis.** *Semin Ophthalmol* 2020;35:333–42 CrossRef Medline
9. Riederer I, Sollmann N, Mühlau M, et al. **Gadolinium-enhanced 3D T1-weighted black-blood MR imaging for the detection of acute optic neuritis.** *AJNR Am J Neuroradiol* 2020;41:2333–38 CrossRef Medline
10. Hodel J, Outteryck O, Bocher AL, et al. **Comparison of 3D double inversion recovery and 2D STIR FLAIR MR sequences for the imaging of optic neuritis: pilot study.** *Eur Radiol* 2014;24:3069–75 CrossRef Medline
11. Bossuyt PM, Reitsma JB, Bruns DE, et al; STARD Group. **STARD 2015: an updated list of essential items for reporting diagnostic accuracy studies.** *BMJ* 2015;351:h5527 CrossRef Medline
12. Benchoufi M, Matzner-Lober E, Molinari N, et al. **Interobserver agreement issues in radiology.** *Diagn Interv Imaging* 2020;101:639–41 CrossRef Medline
13. Poillon G, Collin A, Benhamou Y, et al. **Increased diagnostic accuracy of giant cell arteritis using three-dimensional fat-saturated contrast-enhanced vessel-wall magnetic resonance imaging at 3 T.** *Eur Radiol* 2020;30:1866–75 CrossRef Medline
14. Yang R, Qu B, Liu WV, et al. **Detection of acute optic neuritis using contrast-enhanced 3-dimensional Cube T1-weighted imaging: a preliminary study.** *Comb Chem High Throughput Screen* 2023;26:1480–87 CrossRef Medline
15. Sommer NN, Saam T, Coppenrath E, et al. **Multiple sclerosis: improved detection of active cerebral lesions with 3-dimensional T1 black-blood magnetic resonance imaging compared with conventional 3-dimensional T1 GRE imaging.** *Invest Radiol* 2018;53:13–19 CrossRef Medline
16. Davion JB, Lopes R, Drumez É, et al. **Asymptomatic optic nerve lesions: an underestimated cause of silent retinal atrophy in MS.** *Neurology* 2020;94:e2468–78 CrossRef Medline
17. Healy GM, Redmond CE, Gaughan M, et al. **The accuracy of standard multiple sclerosis MRI brain sequences for the diagnosis of optic neuropathy.** *Mult Scler Relat Disord* 2020;38:101521 CrossRef Medline
18. Mournet S, Sené T, Charbonneau F, et al. **Early diffusion-weighted MRI at 3 Tesla detects ischemic changes of the optic nerve in anterior ischemic optic neuropathy.** *Eur Radiol* 2022;32:3588–96 CrossRef Medline
19. Hur M, Madhavan AA, Hodge DO, et al. **Comparison of 1.5 Tesla and 3.0 Tesla magnetic resonance imaging in the evaluation of acute demyelinating optic neuritis.** *J Neuroophthalmol* 2022;42:297–302 CrossRef Medline
20. Piechotta PL, Bonekamp D, Sill M, et al. **Increased delay between gadolinium chelate administration and T1-weighted magnetic resonance imaging acquisition increases contrast-enhancing tumor volumes and T1 intensities in brain tumor patients.** *Invest Radiol* 2018;53:223–28 CrossRef Medline
21. Kushnirsky M, Nguyen V, Katz JS, et al. **Time-delayed contrast-enhanced MRI improves detection of brain metastases and apparent treatment volumes.** *J Neurosurg* 2016;124:489–95 CrossRef Medline

7T MRI for Cushing Disease: A Single-Institution Experience and Literature Review

 Ian T. Mark,  Kirk Welker, Dana Erickson,  Derek R. Johnson,  Girish Bathla,  Steven Messina,  Paul J. Farnsworth, and  Jamie Van Gompel



ABSTRACT

BACKGROUND AND PURPOSE: Cushing disease is typically caused by a pituitary adenoma that frequently is small and challenging to detect on conventional MR imaging. High-field-strength 7T MR imaging can leverage increased SNR and contrast-to-noise ratios compared with lower-field-strength MR imaging to help identify small pituitary lesions. We aimed to describe our institutional experience with 7T MR imaging in patients with Cushing disease and perform a review of the literature.

MATERIALS AND METHODS: We performed a retrospective analysis of 7T MR imaging findings in patients with pathology-proved Cushing disease from a single institution, followed by a review of the literature on 7T MR imaging for Cushing disease.

RESULTS: Our institutional experience identified Cushing adenomas in 10/13 (76.9%) patients on 7T; however, only 5/13 (38.5%) lesions were discrete. Overall, the imaging protocols used were heterogeneous in terms of contrast dose as well as type of post-contrast T1-weighted sequences (dynamic, 2D versus 3D, and type of 3D sequence). From our institutional data, specific postgadolinium T1-weighted sequences were helpful in identifying a surgical lesion as follows: dynamic contrast-enhanced, 2/7 (28.6%); 2D FSE, 4/8 (50%); 3D sampling perfection with application-optimized contrasts by using different flip angle evolution (SPACE), 5/6 (83.3%); and 3D MPRAGE, 8/11 (72.7%). The literature review identified Cushing adenomas in 31/33 (93.9%) patients on 7T.

CONCLUSIONS: 7T MR imaging for pituitary lesion localization in Cushing disease is a new technique with imaging protocols that vary widely. Further comparative research is needed to identify the optimal imaging technique as well as assess the benefit of 7T over lower-field-strength MR imaging.

ABBREVIATIONS: DCE = dynamic contrast-enhanced; SPACE = sampling perfection with application-optimized contrasts by using different flip angle evolution; VIBE = volumetric interpolated brain examination

Adrenocorticotrophic hormone–producing pituitary adenomas causing Cushing disease are often small and difficult to detect with MR imaging.^{1,2} Cushing disease can manifest as hypertension, diabetes mellitus, obesity, hypercoagulability, osteoporosis, mood disorders, and a plethora of other symptoms and is associated with increased mortality.^{3,4} Successful pituitary surgery with selective adenoma resection and subsequent biochemical

remission has been associated with imaging-defined lesion localization.⁵ Given the gravity of this medical condition, optimizing MR imaging protocols to help identify small pituitary lesions is imperative for improving patient outcomes.^{1,6}

Prior work has shown the benefit of 3T MR imaging over lower-field-strength 1.5T MR imaging in the detection of pituitary adenomas.^{7–9} Increasing the magnetic field strength can provide the benefit of improved SNR and contrast-to-noise ratios.¹⁰ Clinical ultra-high-field 7T MR imaging first became FDA-approved in the United States in 2017.¹¹ Several articles have described the use of 7T MR imaging to evaluate the pituitary gland but in small numbers, given the overall lack of availability of 7T MR imaging scanners. Some of these previous articles from other institutions have reported 100% sensitivity for identifying a pituitary adenoma in Cushing disease, while anecdotally, our experience has not been as rewarding. Herein, we present our institutional experience imaging patients with Cushing disease using ultra-high-field 7T MR imaging to add to the limited body of current literature on this topic, and we also performed a review of the literature on 7T pituitary MR imaging in Cushing

Received December 13, 2023; accepted after revision February 13, 2024.

From the Departments of Radiology (I.T.M., K.W., D.R.J., G.B., S.M., P.J.F.), Endocrinology (D.E.), and Neurosurgery (J.V.G.), Mayo Clinic, Rochester, Minnesota.

All authors contributed to all categories established by the International Committee of Medical Journal Editors including the following: conception and design, or acquisition of data, or analysis and interpretation of data, drafting the article or revising it critically for important intellectual content, final approval of the version to be published, and agreement to be accountable for all aspects of the work in ensuring that questions related to the accuracy or integrity of any part of the work are appropriately investigated and resolved.

Please address correspondence to Ian Mark, MD, 200 1st Street SW, Rochester, MN 55905; e-mail: Mark.ian@mayo.edu; @iantmark



Indicates article with online supplemental data.

<http://dx.doi.org/10.3174/ajnr.A8209>

SUMMARY

PREVIOUS LITERATURE: Prior reports have described high sensitivity of 7T MRI for the detection of corticotroph pituitary adenoma in Cushing disease, but in small numbers. The existing literature describes heterogeneous imaging protocols that vary in terms of contrast dose, use of dynamic contrast-enhanced imaging, and 2D versus 3D postcontrast imaging.

KEY FINDINGS: Our 7T institutional data identified pituitary lesions in 10/13 patients with Cushing disease, and one-half of these lesions were ill-defined and not discrete. By describing pituitary adenomas as discrete vs non-discrete, we believe the current study reflects routine practice and therefore is pertinent to clinical neuroradiology.

KNOWLEDGE ADVANCEMENT: We summarize the current state of 7T pituitary imaging in Cushing disease based on a literature review and our institutional experience. The heterogeneity among imaging protocols calls for further evaluation with multi-center involvement to determine the ideal imaging protocol.

disease to provide an overview of the heterogeneous nature of current 7T pituitary imaging techniques and areas for possible improvement.

MATERIALS AND METHODS

Institutional Case Series

Following institutional review board approval, we retrospectively reviewed clinical pituitary images on a 7T Magnetom Terra scanner (Siemens) from our department. Using an internal database to access cases of pathology-proved Cushing disease, we reviewed patients from 2018 to 2022 who had dedicated 7T MR imaging of the pituitary gland. Images on 7T and lower-field-strength comparison studies were independently reviewed by 2 board-certified neuroradiologists who attempted to detect a pituitary microadenoma. Detected adenomas were categorized as discrete or nondiscrete, the former having distinct margins. Lesions were identified not only by having different enhancement relative to the native pituitary gland but by T2 signal intensity relative to the native pituitary gland as well. Discrepancies were resolved with a consensus read. We recorded the following 7T MR imaging protocol details: postcontrast pulse sequence, section thickness (millimeters), and dose of IV gadolinium. All pulse sequences were FDA-approved. For all enrolled patients' scans, a determination was made as to whether a pituitary adenoma could be visualized. If an adenoma was visible, its laterality and size were recorded along with a determination of the pulse sequence that best demonstrated the lesion. A 1Tx/32Rx Head Coil (Nova Medical) and gadobutrol (Gadavist [Bayer Schering] 1 mol/mL) was used for all 7T images. Comparison with lower-field-strength (1.5T or 3T) imaging was

also reviewed in the same fashion on a different day with the readers blinded to the 7T results. Basic patient demographic information, including age and sex, were tabulated.

Literature Review

A comprehensive search of several databases from January 1, 2012, to July 19, 2023, in any language, was conducted. The databases included Ovid MEDLINE and Epub Ahead of Print, In-Process & Other Non-Indexed Citations and Daily, Ovid EMBASE, Ovid Cochrane Central Register of Controlled Trials, Ovid Cochrane Database of Systematic Reviews, and Scopus. The search strategy (Online Supplemental Data) was designed and conducted by an experienced librarian with input from the principal investigator of the study. Controlled vocabulary supplemented with keywords was used to search for 7T MR imaging detection of Cushing disease. For each study, we extracted the following information: first author, year of publication, comparison MR imaging field strength, surgical pathology results, number of pathology-proved lesions that were identified on 7T MR imaging, any use of 7T dynamic contrast-enhanced (DCE) postcontrast imaging, 7T postcontrast T1-weighted sequence used, and IV gadolinium dose. Descriptive statistics were used to compare different 7T imaging protocols.

RESULTS

Institutional Case Series

Thirteen patients with Cushing disease who underwent 7T MR imaging and transsphenoidal surgical resection were included in our study. Six (46.2%) were male. The mean age was 38.6 years (range, 12–66 years). Eleven patients had lower-field-strength comparison MR imaging, and a surgical lesion was visualized in 5/8 (62.5%) patients on 3T and 1/3 (33.3%) on 1.5T. Of the 13 patients with pathology-proved corticotroph adenomas included in the study, 7T MR imaging was able to identify a pituitary lesion that corresponded, including in laterality, with a pathology-proved adenoma in 10 (76.9%) patients (Fig 1). Only 5/13 (38.5%) had discrete lesions on 7T MR imaging, while 5/13 (38.5%) had nondiscrete

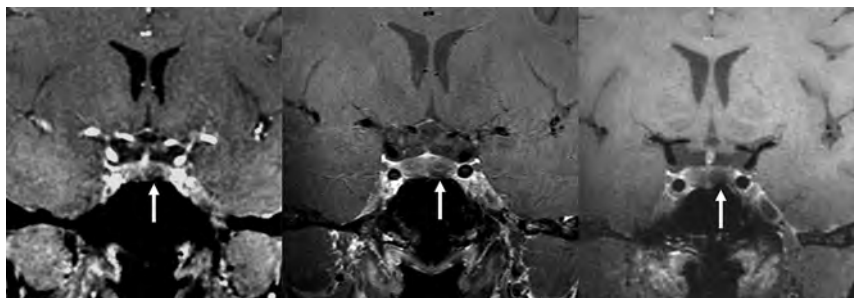


FIG 1. Three different types of 7T postcontrast T1-weighted imaging in a patient with a left-sided pituitary adenoma (arrows): (left to right) DCE, 2D TSE, and 3D SPACE with 1.5-, 1.5-, and 0.7-mm slice thickness, respectively.

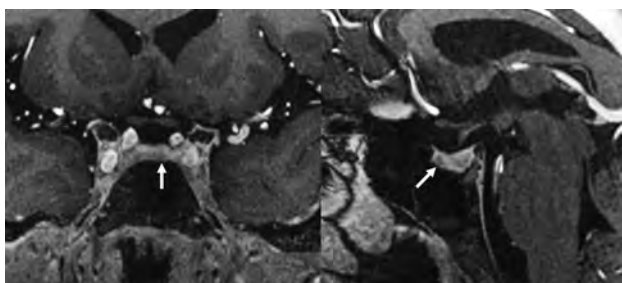


FIG 2. An example of 7T MR imaging showing a nondiscrete lesion (arrows) in the left paramidline pituitary gland on postcontrast MPAGE T1-weighted imaging at 0.33 mm that was a pathology-confirmed Cushing adenoma.

lesions (Fig 2). All identified lesions were hypoenhancing relative to the pituitary gland. Four lesions were identified on T2-weighted imaging with 3 lesions showing hyperintense signal and 1 lesion with hypointense signal. Consensus reads were required in three 7T studies that were agreed to be nondiscrete and one 3T study that was agreed to be nondiscrete as well.

Contrast doses were fixed (5 mL, 1 mmol/mL of Gadavist) for protocols including DCE and were weight-based (0.1 mL/kg, 1 mmol/mL of Gadavist) when DCE was not performed. Our contrast-enhanced imaging protocol was heterogeneous. The initial 3 patients, shortly after the FDA approval of 7T MR imaging, were imaged initially on lower-field-strength magnets, then transferred to 7T, on which only delayed postcontrast imaging was acquired (30–70 minutes after contrast injection). Even with the atypically long delay in imaging on 7T after contrast, we were able to see pituitary lesions in 2 patients.

Postcontrast T1-weighted imaging 7T sequences were also heterogeneous: 7 (53.8%) had DCE, 9 (69.2%) had 2D T1-weighted imaging, 7 (53.8%) had 3D T1-weighted sampling perfection with application optimized contrast by using different flip angle evolution (SPACE sequence; Siemens), and 12 (92.3%) had 3D T1-weighted MPAGE. One patient had nondiagnostic motion-degraded 2D imaging, 3D SPACE, and 3D MPAGE. Of note, 5 of our patients who were imaged with 7T had already undergone a prior partial pituitary resection and underwent further imaging before a second resection.

Literature Review Patients

The literature review identified 33 patients with Cushing disease using 7T MR imaging (Fig 3). The patients in the study of de Rotte et al,¹² in 2014, were included in the 2016 article by the same authors,¹³ and, therefore, were only counted once for this review. Overall, 7T MR imaging identified pathology-confirmed pituitary lesions in 31/33 (93.9%) patients. There was a large amount of variance between each MR imaging protocol, not only between each article but even within the same study at a single institution. Only 2 studies used 3D postcontrast T1-weighted imaging sequences, with the remainder using 2D sequences. One prior study used DCE imaging. The gadolinium doses also varied between weight-based and fixed-dose.

The first work on 7T pituitary MR imaging (Philips Healthcare) was performed by de Rotte et al,¹² in 2014. They scanned 10 healthy volunteers and 5 patients with suspected Cushing disease. The latter

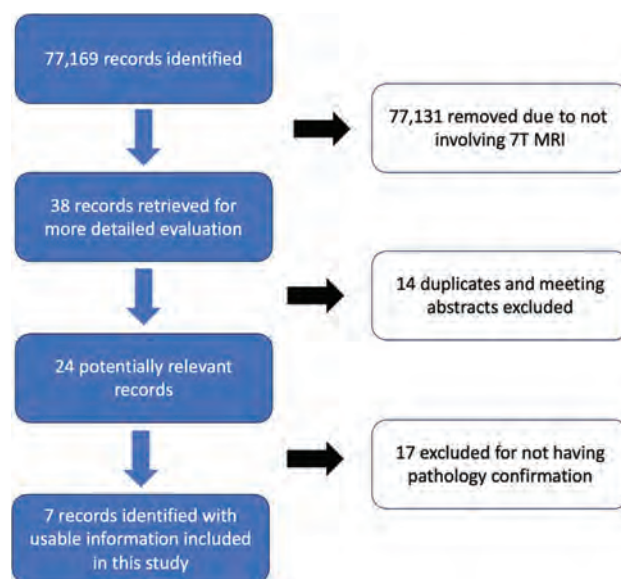


FIG 3. Flow chart of the search and selection of studies.

patient group was included as part of a larger population that was published 2 years later.¹³ In total, they evaluated 16 patients with clinically and biochemically confirmed Cushing disease whose initial 1.5T MR imaging report was negative for Cushing disease or inconclusive for adenoma detection. This work had dynamic postcontrast imaging at 1.5T, but not at 7T. Pituitary lesions were identified at 7T in 13 of the 16 patients with biochemically proved Cushing disease. Only 13 of their patients underwent surgical resection. Of those, 4 patients had incomplete operative details and the laterality of the positive pathology was not known. Of the 9 patients with pathology-proved adenomas, all were identified on 7T MR imaging. Most interesting, in their study, the adenomas were hyperenhancing relative to the pituitary gland on 7T. This authorship laid the groundwork for 7T pituitary imaging while acknowledging the limitations of a long acquisition time (10 minutes 40 seconds), incomplete surgical reports to confirm the MR imaging findings in several patients, and lack of 7T DCE sequences.

Law et al¹⁴ added to this work with a case report of a patient with Cushing disease who had prior negative 1.5T and 3T MR imaging findings, and detected a microadenoma on 7T imaging. This protocol used postcontrast 3D MPAGE but did not have DCE imaging.

Later, from the same institution as Law et al,¹⁴ Patel et al¹⁵ scanned 8 patients with pathology-confirmed Cushing disease on a Magnetom Terra 7T system (Siemens). They performed 3 types of postcontrast T1-weighted imaging but did not have dynamic postcontrast imaging in their protocol. Their 7T MR imaging studies identified lesions in all 8 patients. Seven (88%) were shown to be corticotroph adenomas, and 1 patient had Crooke hyaline change with endocrinologic remission after surgery. 3D SPACE imaging detected a lesion in all 8 patients who were included. MPAGE postcontrast imaging was performed in 5 patients, and a lesion was detected in 4 patients. 2D TSE postcontrast T1-weighted imaging detected a lesion in 3/4 patients.

More recently, Eisenhut et al¹⁶ scanned 18 patients for suspected microadenomas with 3T and 7T MR imaging. Their 7T protocol used a 2D FLASH sequence. This was the first article to include dynamic postcontrast imaging. The authors did not use 3D thin-section, submillimeter, postcontrast imaging as was the case with prior studies. Of the 18 patients, 16 had pathology-proven adenomas; 13 of whom were patients with Cushing disease. 7T identified the lesion in 12/13 (92.3%) patients. All were seen on the T1 coronal postcontrast sequences, and 13/15 (86.7) of all microadenomas (including non-Cushing) were seen on the DCE sequences. 7T also detected 3 lesions that were not seen at 3T.

Feng et al¹⁷ reported on the surgical resection technique for a single patient with MR imaging negative for Cushing disease. Their patient underwent 3T and 7T MR imaging. Findings of both were negative; however, imaging details were not provided.

Eisenhut et al¹⁸ described their 7T MR imaging experience with pituitary macroadenomas to evaluate cavernous sinus invasion. They did not have DCE or 3D postcontrast T1-weighted imaging; however, they found the 7T image quality to be improved over 1.5/3T. One patient had Cushing disease, and the authors were able to identify the lesion on 7T. They also found improved ability to detect cavernous sinus invasion on 7T.

DISCUSSION

In the current study, we have described our institutional experience with 7T MR imaging for pituitary lesion localization in patients with Cushing disease. Additionally, we performed a literature review of the use of 7T MR imaging in Cushing disease. Exploring accurate and reliable imaging techniques is critical because lower-field-strength MR imaging can miss up to 50% of adenomas in Cushing disease.^{1,2} We highlight the effectiveness of using 7T over lower-field-strength MR imaging to evaluate pituitary lesions in patients with Cushing disease as well as the need for further improvement and standardization in clinical 7T MR imaging of the sella.

Both the literature review and our single-center experience demonstrate the extreme heterogeneity in pituitary MR imaging protocols. This finding is not unexpected given the recent FDA approval of clinical 7T MR imaging and the lack of consensus on optimal imaging protocols. Pituitary adenomas in Cushing disease are frequently microadenomas, which pose a substantial challenge for detection due to their small size—often only a few millimeters in diameter.¹⁹ The improved sensitivity of 3T MR imaging over 1.5T for the detection of microadenomas has previously been established.¹⁹ Therefore, many have hoped that a further increase in the magnetic field strength of MR imaging would continue to improve detection of these miniscule tumors. In our institutional patients, while we identified pathology-confirmed lesions in 10/13 (76.9%) patients, one-half of the lesions on contrast-enhanced 7T MR imaging were nondiscrete and quite subtle. Our work is the first 7T article to describe pituitary adenomas as discrete versus nondiscrete, reflecting routine practice in the reading room and is, therefore, relevant to clinical neuroradiology. Within this context, it remains unclear how the varying technical aspects of 7T pituitary imaging protocols impact this sensitivity.

DCE

Only 1 article in our literature review used DCE postcontrast imaging at 7T.¹⁶ The authors found a pathology-confirmed pituitary lesion in 12/13 patients; however, this was surpassed by their 2D FLASH postcontrast sequence that identified a pituitary lesion in all 13 patients. Prior studies on lower-field-strength MR imaging have found DCE to be superior to delayed postcontrast imaging in detecting microadenomas.¹⁹⁻²¹ Our institutional cohort provided the second report of using DCE at 7T for patients with Cushing disease. The DCE sequences in our institution were low-yield, identifying a lesion in only 2/7 (28.6%) patients. However, in 1 of the 2 successful cases, DCE was the only sequence that was able to identify a pituitary lesion because the other pulse sequences were limited by motion artifacts. This result is due to the decreased acquisition time of DCE as a potential additional benefit over other conventional sequences because the latter may be more prone to motion degradation in certain patients. In the earlier articles listed in the literature review,^{12,13} the nondynamic 7T sequences required >10 minutes to acquire. DCE performed at 7T can repeatedly image the pituitary gland at 15- to 25-second intervals, similar to lower field strengths. It is, therefore, substantially less motion-sensitive than other pituitary pulse sequences.

Nondynamic, T1-Weighted Postcontrast Sequences

The studies in our literature review used a variety of postcontrast T1-weighted images, which reflects the overall lack of evidence regarding their comparative effectiveness. Work evaluating multiple 3D postcontrast T1-weighted sequences in brain tumors found that SPACE and volumetric interpolated brain examination (VIBE) sequences obtained higher contrast rating, contrast-to-noise ratio, and visual conspicuity ratings over MPRAGE in both gliomas and metastases.²² Specific to pituitary imaging, prior work has advocated the use of volume isotropic TSE acquisition (or VISTA),²³ while others have shown the benefit of VIBE.²⁴ Patel et al¹⁵ had similar success with different postgadolinium 3D T1-weighted pulse sequences: 88% sensitivity with SPACE and 80% with MPRAGE. In our institutional data with a small sample size, we found more success with MPRAGE over SPACE in patients in whom both sequences were used. Overall, there is a lack of data to provide strong evidence to support any specific postgadolinium T1 sequence.

Additionally, our literature review revealed heterogeneity between the use of 3D versus 2D postcontrast imaging. 3D has the benefit of providing multiplanar reformats. Also, it typically provides increased spatial resolution when assessed by voxel-size metrics compared with 2D techniques. The latter would seem to be most beneficial in Cushing disease because small adenomas <4 mm are challenging to detect with MR imaging.¹⁹ Wang et al²⁵ found that 3D SPACE imaging outperformed 2D imaging in defining pituitary lesions at 3T. Additional 3D sequences, including VIBE/echo-spoiled gradient echo, have been found to detect Cushing microadenomas at a higher rate than 2D spin-echo T1-weighted postcontrast images.²⁶ At 7T field strength, Eisenhut et al¹⁶ had the largest collection of cases and good success (92.3% sensitivity) with 2D postcontrast imaging with 1.5-mm section thickness. In our institutional data, we had 8 patients with both 2D and 3D postcontrast imaging (Fig 4). In 2 patients, we saw lesions on

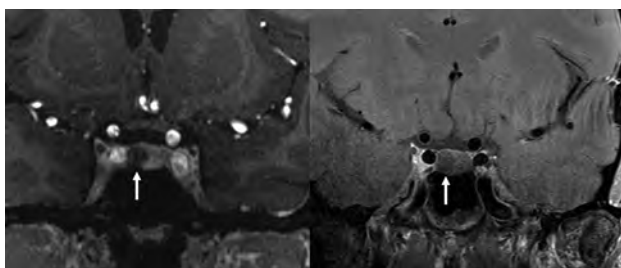


FIG 4. 7T postcontrast T1-weighted imaging in a patient with a right-sided pituitary adenoma (arrows). The left image is a 3D MPRAGE sequence, while the right image is a 2D TSE sequence. The MPRAGE image demonstrates greater contrast between the normally enhancing pituitary gland compared with the hypoenhancing adenoma.

3D imaging that were not seen on 2D. On the other hand, we did not have any patients in whom lesions were seen only on 2D.

Additional Sequences

Neither our institutional patient experience nor prior studies have described the use of postcontrast T2-weighted FLAIR imaging or CISS sequences, both of which have been described as being useful at lower field strengths.^{24,27} CISS is a volumetric imaging technique that has been more frequently used to outline the subarachnoid spaces in the posterior fossa. Similarly, T2-weighted FLAIR imaging has some T1-weighted properties as well. In fact, it is very sensitive to low concentrations of gadolinium contrast, and has been predominantly used to identify leptomeningeal disease.²⁸ More recently, contrast-enhanced 3D STIR FLAIR imaging was found to have increased pituitary adenoma conspicuity compared with 2D T1-weighted sequences.²⁹ This study was performed at 3T, but a similar technique has not been described at 7T.

Gadolinium Dose

The ideal gadolinium dose for pituitary MR imaging is unknown. There are 2 standard approaches to IV contrast dosing: fixed versus weight-based. Our literature review included studies with both types of dosing. When weight-based dosing is used, standard brain MR imaging is performed with 0.1 mmol/kg of gadolinium contrast. In 2006, Bartynski et al³⁰ used half-dose (0.05 mmol/kg), normal-dose (0.1 mmol/kg), and double-dose (0.2 mmol/kg) IV gadolinium-based contrast on a 1.5T scanner. The calculated contrast ratio between lesions and the pituitary gland were the same at each dose, but the absolute signal difference was largest at the double-dose, suggesting a theoretic benefit. Four years later, Portocarrero-Ortiz et al³¹ found that half-dose weight-based contrast increased the detection of adrenocorticotrophic hormone-secreting pituitary adenomas in patients with Cushing disease. Prior work has shown that higher field strength MR imaging increases the effectiveness of gadolinium contrast agents, with higher lesion enhancement at 7T MR imaging using a half-dose of contrast compared with a full dose of contrast on 3T; however, this research was evaluating primary brain tumors and metastases rather than pituitary adenomas.³²

Our article has several limitations. First, our literature review and institutional data have small patient numbers. This is due to clinical 7T MR imaging only recently receiving regulatory clearance in the United States and the European Union in 2017 as well

as the low incidence of Cushing disease. Additionally, one of the studies¹³ reported 7T MR imaging results in 16 patients but had incomplete or absent pathology confirmation in 7 patients. One of the other studies¹⁴ was a single case report of a case with findings positive on 7T. Therefore, the composite sensitivity of 41/46 (89.1%) across studies should be interpreted with caution, acknowledging the limitations of the individual studies. Our study should not be interpreted as measuring the true sensitivity of 7T, as oftentimes MR imaging negative cases do not go to surgery and therefore were not included in the literature.

Given the 7T MR imaging protocol heterogeneity between and within institutions, larger numbers of patients must be studied to determine the 7T pituitary protocol with the best sensitivity and specificity. This issue could be potentially addressed with standardization of imaging protocols, larger samples sizes, and multisite collaboration. Second, as already discussed, several sequences (such as postcontrast FLAIR and CISS) that have been described as beneficial in the lower-field-strength pituitary imaging literature were not performed in any of the 7T imaging cohorts reviewed in this article. Our institutional experience has found that sphenoid sinus pneumatization limits the usefulness overall on 7T. We are in the early stages of clinical implementation of 7T imaging. 7T MR imaging cannot yet be determined to be entirely superior to 3T MR imaging in the detection of pituitary microadenomas. Rather, it should be viewed as a valuable tool that is yet to be perfected.

In addition to clarifying the role of DCE, 2D-versus-3D post-contrast imaging and IV contrast dose, future areas to further improve 7T pituitary imaging may include the addition of novel pulse sequences. Artificial intelligence-based reconstruction algorithms and hardware improvements such as increased scanner gradient performance and parallel transmit techniques may help through a combination of higher resolution, better lesion-to-background contrast, shorter acquisition times, and reduction in skull base artifacts.¹¹ Further refinement of 7T pituitary imaging could also lead to detecting more incidental pituitary findings and, may therefore, be most beneficial in pathologies such as Cushing disease, in which surgical resection is imminent and lesion identification will directly impact patient care.

CONCLUSIONS

7T MR imaging for pituitary lesion localization in Cushing disease is a new technique with only small case series having been published and little consensus among imaging protocols for optimal evaluation of pituitary tumors. Accurate preoperative assessment of pituitary lesions in Cushing disease is paramount to successful patient outcomes. Further comparative research, possibly through multisite collaboration, is needed to identify the optimal imaging technique as well as to assess the benefit of 7T over lower-field-strength MR imaging.


Disclosure forms provided by the authors are available with the full text and PDF of this article at www.ajnr.org.

REFERENCES

1. Castle-Kirsbaum M, Amukotuwa S, Fuller P, et al. **MRI for Cushing disease: a systematic review.** *AJNR Am J Neuroradiol* 2023;44:311–16 CrossRef Medline

2. Bashari WA, Gillett D, MacFarlane J, et al. **Modern imaging in Cushing's disease.** *Pituitary* 2022;25:709–12 CrossRef Medline
3. Lonser RR, Nieman L, Oldfield EH. **Cushing's disease: pathobiology, diagnosis, and management.** *J Neurosurg* 2017;126:404–17 CrossRef Medline
4. Ntali G, Asimakopoulou A, Siamatras T, et al. **Mortality in Cushing's syndrome: systematic analysis of a large series with prolonged follow-up.** *Eur J Endocrinol* 2013;169:715–23 CrossRef Medline
5. Lonser RR, Wind JJ, Nieman LK, et al. **Outcome of surgical treatment of 200 children with Cushing's disease.** *J Clin Endocrinol Metab* 2013;98:892–901 CrossRef Medline
6. Newell-Price J, Bertagna X, Grossman AB, et al. **Cushing's syndrome.** *Lancet* 2006;367:1605–17 CrossRef Medline
7. Pinker K, Ba-Ssalamah A, Wolfsberger S, et al. **The value of high-field MRI (3T) in the assessment of sellar lesions.** *Eur J Radiol* 2005;54:327–34 CrossRef Medline
8. Stobo DB, Lindsay RS, Connell JM, et al. **Initial experience of 3 Tesla versus conventional field strength magnetic resonance imaging of small functioning pituitary tumours.** *Clin Endocrinol (Oxf)* 2011;75:673–77 CrossRef Medline
9. Kim LJ, Lekovic GP, White WL, et al. **Preliminary experience with 3-Tesla MRI and Cushing's disease.** *Skull Base* 2007;17:273–77 CrossRef Medline
10. Trattig S, Springer E, Bogner W, et al. **Key clinical benefits of neuroimaging at 7T.** *Neuroimage* 2018;168:477–89 CrossRef Medline
11. Burkett BJ, Fagan AJ, Felmlee JP, et al. **Clinical 7-T MRI for neuroradiology: strengths, weaknesses, and ongoing challenges.** *Neuroradiology* 2021;63:167–77 CrossRef Medline
12. de Rotte AAJ, van der Kolk AG, Rutgers D, et al. **Feasibility of high-resolution pituitary MRI at 7.0 Tesla.** *Eur Radiol* 2014;24:2005–11 CrossRef Medline
13. de Rotte AA, Groenewegen A, Rutgers DR, et al. **High-resolution pituitary gland MRI at 7.0 Tesla: a clinical evaluation in Cushing's disease.** *Eur Radiol* 2016;26:271–77 CrossRef Medline
14. Law M, Wang R, Liu CJ, et al. **Value of pituitary gland MRI at 7 T in Cushing's disease and relationship to inferior petrosal sinus sampling: case report.** *J Neurosurg* 2018 Mar 1. [Epub ahead of print] CrossRef Medline
15. Patel V, Liu CJ, Shiroishi MS, et al. **Ultra-high field magnetic resonance imaging for localization of corticotropin-secreting pituitary adenomas.** *Neuroradiology* 2020;62:1051–54 CrossRef Medline
16. Eisenhut F, Schlaffer SM, Hock S, et al. **Ultra-high-field 7 T magnetic resonance imaging including dynamic and static contrast-enhanced T1-weighted imaging improves detection of secreting pituitary microadenomas.** *Invest Radiol* 2022;57:567–74 CrossRef Medline
17. Feng JJ, Cheok SK, Chartrain AG, et al. **Endoscopic endonasal approach for MRI negative Cushing's microadenoma.** *Neurosurg Focus Video* 2023;9:V5 CrossRef Medline
18. Eisenhut F, Schmidt MA, Buchfelder M, et al. **Improved detection of cavernous sinus invasion of pituitary macroadenomas with ultra-high-field 7 T MRI.** *Life (Basel)* 2022;13:49 CrossRef Medline
19. Bonneville JF, Potorac I, Petrossians P, et al. **Pituitary MRI in Cushing's disease: an update.** *J Neuroendocrinol* 2022;34:e13123 CrossRef Medline
20. Tabarin A, Laurent F, Catargi B, et al. **Comparative evaluation of conventional and dynamic magnetic resonance imaging of the pituitary gland for the diagnosis of Cushing's disease.** *Clin Endocrinol (Oxf)* 1998;49:293–300 CrossRef Medline
21. Kucharczyk W, Bishop JE, Plewes DB, et al. **Detection of pituitary microadenomas: comparison of dynamic keyhole fast spin-echo, unenhanced, and conventional contrast-enhanced MR imaging.** *AJR Am J Roentgenol* 1994;163:671–79 CrossRef Medline
22. Danieli L, Riccitelli GC, Distefano D, et al. **Brain tumor-enhancement visualization and morphometric assessment: a comparison of MPRAGE, SPACE, and VIBE MRI techniques.** *AJNR Am J Neuroradiol* 2019;40:1140–48 CrossRef Medline
23. Guo R, Wu Y, Guo G, et al. **Application of contrast-enhanced 3-dimensional T2-weighted volume isotropic turbo spin echo acquisition sequence in the diagnosis of prolactin-secreting pituitary microadenomas.** *J Comput Assist Tomogr* 2022;46:116–23 CrossRef Medline
24. Lang M, Habboub G, Moon D, et al. **Comparison of constructive interference in steady-state and T1-weighted MRI sequence at detecting pituitary adenomas in Cushing's disease patients.** *J Neurol Surg B Skull Base* 2018;79:593–98 CrossRef Medline
25. Wang J, Wu Y, Yao Z, et al. **Assessment of pituitary micro-lesions using 3D sampling perfection with application-optimized contrasts using different flip-angle evolutions.** *Neuroradiology* 2014; 56:1047–53 CrossRef Medline
26. Grober Y, Grober H, Wintermark M, et al. **Comparison of MRI techniques for detecting microadenomas in Cushing's disease.** *J Neurosurg* 2018;128:1051–57 CrossRef Medline
27. Chatain GP, Patronas N, Smirniotopoulos JG, et al. **Potential utility of FLAIR in MRI-negative Cushing's disease.** *J Neurosurg* 2018; 129:620–28 CrossRef Medline
28. Fukuoka H, Hirai T, Okuda T, et al. **Comparison of the added value of contrast-enhanced 3D fluid-attenuated inversion recovery and magnetization-prepared rapid acquisition of gradient echo sequences in relation to conventional postcontrast T1-weighted images for the evaluation of leptomeningeal diseases at 3T.** *AJNR Am J Neuroradiol* 2010;31:868–73 CrossRef Medline
29. Osawa I, Nagawa K, Hara Y, et al. **Utility of contrast-enhanced 3D STIR FLAIR imaging for evaluating pituitary adenomas at 3 Tesla.** *Eur J Radiol Open* 2023;11:100500 CrossRef Medline
30. Bartynski WS, Boardman JF, Grahovac SZ. **The effect of MR contrast medium dose on pituitary gland enhancement, microlesion enhancement and pituitary gland-to-lesion contrast conspicuity.** *Neuroradiology* 2006;48:449–59 CrossRef Medline
31. Portocarrero-Ortiz L, Bonifacio-Delgadillo D, Sotomayor-González A, et al. **A modified protocol using half-dose gadolinium in dynamic 3-Tesla magnetic resonance imaging for detection of ACTH-secreting pituitary tumors.** *Pituitary* 2010;13:230–35 CrossRef Medline
32. Noebauer-Huhmann IM, Szomolanyi P, Kronnerwetter C, et al. **Brain tumours at 7T MRI compared to 3T-contrast effect after half and full standard contrast agent dose: initial results.** *Eur Radiol* 2015;25:106–12 CrossRef Medline
33. Liu Z, Zhang X, Wang Z, et al. **High positive predictive value of the combined pituitary dynamic enhanced MRI and high-dose dexamethasone suppression tests in the diagnosis of Cushing's disease bypassing bilateral inferior petrosal sinus sampling.** *Sci Rep* 2020;10:14694 CrossRef Medline

MR Imaging Findings in Anti-Leucine-Rich Glioma Inactivated Protein 1 Encephalitis: A Systematic Review and Meta-analysis

 Francisco C. Almeida, Ana I. Pereira, Catarina Mendes-Pinto, Joana Lopes, João Moura, José Maria Sousa, Gonalo Videira,  Raquel Samoes, and  Tiago Gil Oliveira



ABSTRACT

BACKGROUND: Antibodies against leucine-rich glioma inactivated protein 1 (LGI1) constitute a common form of autoimmune encephalitis. On MR imaging, it may show T2 FLAIR hyperintensities of the medial temporal lobe (T2 FLAIR-MTL), involve the basal ganglia, or be unremarkable.

PURPOSE: We performed a systematic review and meta-analysis to obtain prevalence estimates of abnormal findings on MR imaging in anti-LGI1 encephalitis. A human brain map of the *LGI1* microarray gene expression was derived from the Allen Human Brain Atlas.

DATA SOURCES: PubMed and Web of Science were searched with the terms “LGI1” and “encephalitis” from inception to April 7, 2022.

STUDY SELECTION: Thirty-one research publications, encompassing case series and retrospective cohort and case-control studies, with >10 patients with anti-LGI1 encephalitis and MR imaging data were included.

DATA ANALYSIS: Pooled prevalence estimates were calculated using Freeman-Tukey double-arcsine transformation. Meta-analysis used DerSimonian and Laird random effects models.

DATA SYNTHESIS: Of 1318 patients in 30 studies, T2 FLAIR-MTL hyperintensities were present in 54% (95% CI, 0.48–0.60; $I^2 = 76\%$). Of 394 patients in 13 studies, 27% showed bilateral (95% CI, 0.19–0.36; $I^2 = 71\%$) and 24% unilateral T2 FLAIR-MTL abnormalities (95% CI, 0.17–0.32; $I^2 = 61\%$). Of 612 patients in 15 studies, basal ganglia abnormalities were present in 10% (95% CI, 0.06–0.15; $I^2 = 67\%$). *LGI1* expression was highest in the amygdala, hippocampus, and caudate nucleus.

LIMITATIONS: Only part of the spectrum of MR imaging abnormalities in anti-LGI1 encephalitis could be included in a meta-analysis. MR imaging findings were not the main outcomes in most studies, limiting available information. I^2 values ranged from 62% to 76%, representing moderate-to-large heterogeneity.

CONCLUSIONS: T2 FLAIR-MTL hyperintensities were present in around one-half of patients with anti-LGI1. The prevalence of unilateral and bilateral presentations was similar, suggesting unilaterality should raise the suspicion of this disease in the appropriate clinical context. Around 10% of patients showed basal ganglia abnormalities, indicating that special attention should be given to this region. *LGI1* regional expression coincided with the most frequently reported abnormal findings on MR imaging. Regional specificity might be partially determined by expression levels of the target protein.

ABBREVIATIONS: ADAM = a disintegrin and metalloprotease domain; AIE = autoimmune encephalitis; AMPA = α -amino-3-hydroxy-5-methyl-4-isoxazole-propionic acid; BG = basal ganglia; CASPR2 = contactin-associated protein-like 2; EEG = electroencephalogram; FBDS = faciobrachial dystonic seizures; LGI1 = leucine-rich glioma inactivated protein 1; MTL = medial temporal lobe

Antibodies against leucine-rich glioma inactivated protein 1 (LGI1) characterize the second most common form of


autoimmune encephalitis (AIE).¹ These antibodies were first described in 2010 and were previously clustered within voltage-gated potassium channel antibodies, which included contactin-associated protein-like 2 (CASPR2) along with LGI1.² The LGI1

Received November 14, 2023; accepted after revision February 14, 2024.

From the Departments of Neuroradiology (F.C.A., A.I.P., C.M.-P.) and Neurology (J.L., J.M., G.V., R.S.), Centro Hospitalar Universit rio de Santo Ant nio, Porto, Portugal; Life and Health Science Research Institute (F.C.A., T.G.O.), School of Medicine, University of Minho, Braga, Portugal; Life and Health Sciences Research Institute/3B's-PT Government Associate Laboratory (F.C.A., T.G.O.), Braga/Guimar es, Portugal; Department of Neuroradiology (J.M.S.), Centro Hospitalar Universit rio de S o Jo o, Porto, Portugal; Unit for Multidisciplinary Research in Biomedicine (R.S.), Instituto de Ci ncias Biom dicas de Abel Salazar da Universidade do Porto, Porto, Portugal; and Department of Neuroradiology (T.G.O.), Hospital de Braga, Braga, Portugal.

Raquel Samoes and Tiago Gil Oliveira contributed equally to this work.

Please address correspondence to Francisco C. Almeida, MD, Neuroradiology Department, Largo do Prof. Abel Salazar, 4099-001 Porto, Portugal; e-mail: franciscoalmeida.neuroradiologia@chporto.min-saude.pt

 Indicates article with online supplemental data.
<http://dx.doi.org/10.3174/ajnr.A8256>

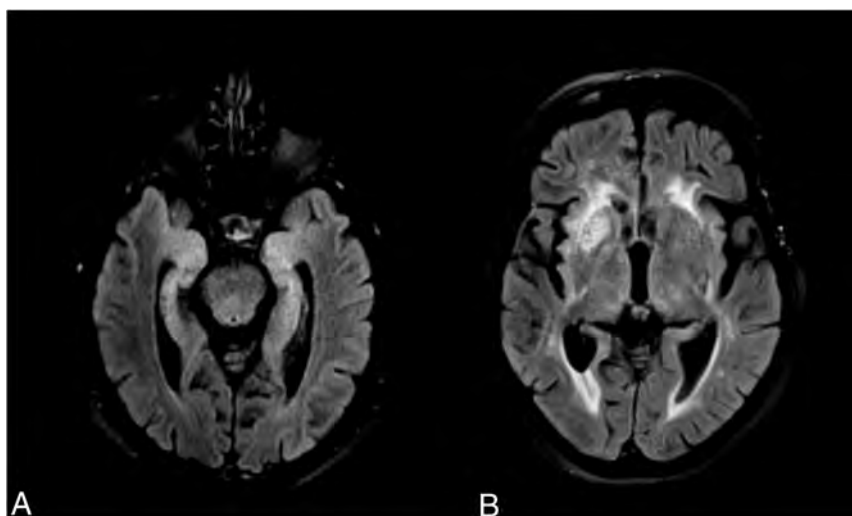


FIG 1. Illustrative examples of signal abnormalities in 2 cases of confirmed anti-LGI1 encephalitis, one with medial temporal lobe T2-FLAIR hyperintensities (A) and another with right BG T2-FLAIR hyperintensity (B).

protein is widely expressed in the CNS and particularly in neurons, where it forms a trans-synaptic protein complex that regulates ion channel and synaptic activity.^{3,4}

This disease typically presents with subacute cognitive impairment and epilepsy, but faciobrachial dystonic seizures (FBDS) are the most distinctive clinical feature. Although presenting across a wide variety of ages, it is thought to be most common in those older than 60 years of age.³ The clinical presentation thus leads to a vast differential diagnosis, in which clinical suspicion plays an important role.^{5,6} MR imaging is relevant in supporting the diagnosis of AIE and excluding alternative diagnoses. Characteristically, it involves medial temporal lobe (MTL) hyperintensities on T2 FLAIR sequences, which represent a criterion for a definite diagnosis of AIE when observed bilaterally (Fig 1A).^{7,8} This laterality issue is because in the absence of antibody confirmation, unilateral hippocampal/MTL abnormalities have a wider radiologic differential diagnosis.^{7,9} The main diagnostic considerations in this imaging presentation include seizure-related MR imaging abnormalities;¹⁰ viral encephalitis, particularly herpes simplex virus 1 and 2 and human herpesvirus 6;¹¹ neurosyphilis;¹² Whipple disease,¹³ temporal lobe glioma,¹⁴ and acute posterior circulation ischemic infarction.¹⁵

However, not all cases of anti-LGI1 encephalitis present with MTL abnormalities at the time of MR imaging. MR imaging can also be unremarkable or show basal ganglia (BG) involvement (Fig 1B).¹⁶ Moreover, given the relatively recent description of the wide range of antibodies causing AIE, MR imaging findings are not yet thoroughly described for each antibody group.^{8,17} It is, therefore, important to provide prevalence estimates of MR imaging abnormalities in the literature for each type of antibody-mediated encephalitis. Indeed, given the wide clinical and brain imaging differential diagnoses involved in these cases, detailing the prevalence of specific patterns of abnormal findings on MR imaging for each encephalitis might aid the radiologist in providing a narrower differential while waiting for laboratory results.

Furthermore, abnormalities on MR imaging are likely reflective of pathophysiologic mechanisms. Characterizing the topography of the most frequently reported abnormalities may shed light on the underlying causative pathology. Although most studies have focused on *LGI1* expression in rodent models derived from immunohistochemistry or patient-derived antibodies,^{3,4} a human brain map of the *LGI1* gene might reveal why selective brain areas are impacted in this disease.

In this study, we performed a systematic review and meta-analysis of the proportion of MTL and BG MR imaging signal abnormalities in LGI1 encephalitis. Moreover, we used the publicly accessible Allen Human Brain Atlas (<https://human.brain-map.org>) to derive a *LGI1* gene expression map

of the human brain, which can provide potential hints as to why LGI1 encephalitis preferentially affects certain brain regions.

MATERIALS AND METHODS

This systematic review and meta-analysis was conducted in accordance with the PRISMA guidelines.¹⁸

Search Strategy and Selection Criteria

We searched PubMed and the Web of Science from inception to April 7, 2022, using the search terms “LGI1” and “encephalitis.” PubMed had 511 publications and the Web of Science had 646 publications. Bibliographic sources from selected articles were also used to assess research publications for eligibility. Original research articles, including case series, retrospective or prospective cohort studies, and case-control studies were considered for selection. Case reports, systematic reviews, meta-analyses, review articles, and other nonoriginal research publications were excluded during screening. Only studies conducted with human participants and published in English were considered. The number of each article type found during screening is provided in the Online Supplemental Data.

Inclusion and Exclusion Criteria

Research publications were eligible if they included a clinical population of LGI1 encephalitis and reported >10 cases, when revealed in the abstract. The clinical definition of LGI1 encephalitis was then confirmed on inspection of the publications to comply with definite autoimmune encephalitis, requiring detection of anti-LGI1 antibodies on CSF and/or serum.⁷ Exclusion criteria after retrieval were the following: the study did not present MR imaging data, did not clearly specify the MR imaging abnormalities/brain location/MR imaging sequence used, did not use T2-FLAIR sequences or used other types of MR imaging data not widely used in clinical practice, had ≤10 patients with LGI1 encephalitis, did not separate LGI1 from CASPR2 encephalitis or from other autoantibodies; and the data were previously

published in other research publications, there was no accessibility of the full text, or the article had low manuscript quality.

Data Extraction

Two authors independently screened titles and abstracts and assessed the full text for eligibility (F.C.A., A.I.P.). Discrepancies were solved after discussion between the 2 authors. Clinical data (J.L., J.M.), electroencephalogram (EEG) data (G.V., F.C.A.), and neuroimaging data (F.C.A., C.M.-P.) were extracted independently by 2 authors. When necessary, discrepancies were solved by a third party (clinical: R.S.; neuroimaging: T.G.O.). The quality of the studies was assessed independently by 2 authors (F.C.A. and A.I.P.) on the basis of a previously published tool for prevalence studies.¹⁹ This tool consists of 10 items consisting of 4 external validity and 6 internal validity items, the sum score of which provides a summary assessment of the risk of bias.

Data Analysis

Pooled prevalence estimates of neuroimaging findings were calculated using Freeman-Tukey double-arcsine transformation. Meta-analysis was conducted using DerSimonian and Laird random-effects models. Heterogeneity was calculated using I^2 statistics, and the Cochran Q test was used to assess statistical significance. The metaprop package in R (<https://www.rdocumentation.org/packages/meta/versions/6.2-1/topics/metaprop>) was used for this analysis.

Metaregression analysis was conducted to assess modifiers of prevalence. Clinical symptoms and CSF antibody positivity were used in univariate models to assess the effects on the prevalence of both T2 MTL hyperintensities and BG signal abnormalities (T2 hyperintensities and T1 hypo- and hyperintensities). Studies with missing data on modifier variables were excluded. R^2 was used to assess the proportion of the heterogeneity explained by the modifier, the P value of the Quantitative Methods statistics was used for statistical significance, and I^2 , for residual heterogeneity left unexplained. The Meta package in R was used for this analysis (<https://cran.r-project.org/web/packages/meta/index.html>).

Publication bias was assessed with visual inspection of funnel plots and assessed for statistical significance using the Egger weighted linear regression test. The meta package in R was used for this analysis.

LGII Gene Brain-Expression Map

Regional microarray expression data were obtained from 6 post-mortem brains (1 woman; age range, 24.0–57.0 years; mean age, 42.50 [SD, 13.38] years) provided by the Allen Human Brain Atlas.²⁰ Data were processed with the abagen toolbox (version 0.1.3; <https://github.com/rmarkello/abagen>) using an 83-region volumetric atlas in Montreal Neurological Institute space. First, microarray probes were reannotated using data provided by Arnatkeviciute et al.²¹ Probes not matched to a valid Entrez ID were discarded. Next, probes were filtered on the basis of their expression intensity relative to background noise²² so that probes with intensity less than the background in $\geq 50\%$ of samples across donors were discarded, yielding 31,569 probes. When multiple probes indexed the expression of the same gene, we selected and used the probe with the most consistent pattern of regional

variation across donors (ie, differential stability²³). Here, regions correspond to the structural designations provided in the ontology from the Allen Human Brain Atlas. The Montreal Neurological Institute coordinates of tissue samples were updated to those generated via nonlinear registration using the Advanced Normalization Tools (ANTs; <http://stnava.github.io/ANTs/>). Samples were assigned to brain regions in the provided atlas if their Montreal Neurological Institute coordinates were within 2 mm of a given parcel.

To reduce the potential for misassignment, sample-to-region matching was constrained by hemisphere and gross structural divisions (ie, cortex, subcortex/brainstem, and cerebellum, such that for example, a sample in the left cortex could only be assigned to an atlas parcel in the left cortex²¹). All tissue samples not assigned to a brain region in the provided atlas were discarded. Intersubject variation was addressed by normalizing tissue sample expression values across genes using a robust sigmoid function.²⁴ Normalized expression values were then rescaled to the unit interval. Gene expression values were then normalized across tissue samples using an identical procedure. Samples assigned to the same brain region were averaged separately for each donor and then across donors, yielding a regional expression matrix with 83 rows corresponding to brain regions and 15,633 columns corresponding to the retained genes. Normalized gene expression values were then plotted in a brain map using the ggseg R package (<https://cran.r-project.org/web/packages/ggseg/index.html>)²⁵ with a Desikan-Killiany atlas.

Data Availability

Data used in this meta-analysis will be provided at request.

RESULTS

Study and Clinical Characteristics

In this study, we included 31 research publications (Fig 2).^{5,16,26–54} Two studies reported partially on the same patients but focused on different neuroimaging findings.^{16,50} For summary statistics regarding each of the clinical and neuroimaging findings, we excluded the publication with fewer patients. In total, the sample was composed of 1409 patients with anti-LGI1 encephalitis. The mean quality-assessment score of the research publications was 3, indicating overall good quality (Online Supplemental Data).

Most of the studies were retrospective and based on clinical cohorts, with some studies drawing their sample from EEG or PET cohorts. Case definition was mostly based on criteria for definite AIE,⁷ with 3 studies basing their definition on FBDS and LGII antibody positivity.^{16,43,49}

Table 1 reports summary statistics for the whole study population. The mean age was 61.4 years, and 64% of patients were men. Seventy-eight percent of the patients presented with cognitive impairment (1095 of 1409). For FBDS, 27 studies presented data, totaling 1252 patients, among whom 639 (51%) had FBDS at any point in time. Twenty-eight studies reported seizures other than FBDS, totaling 1368 patients, of whom 989 (72%) were affected. Twenty-four studies, encompassing 1146 patients included data on hyponatremia, among whom 512 (45%) patients presented with low serum sodium. Consciousness impairment was evaluated in 12 studies with 574 patients and was present in

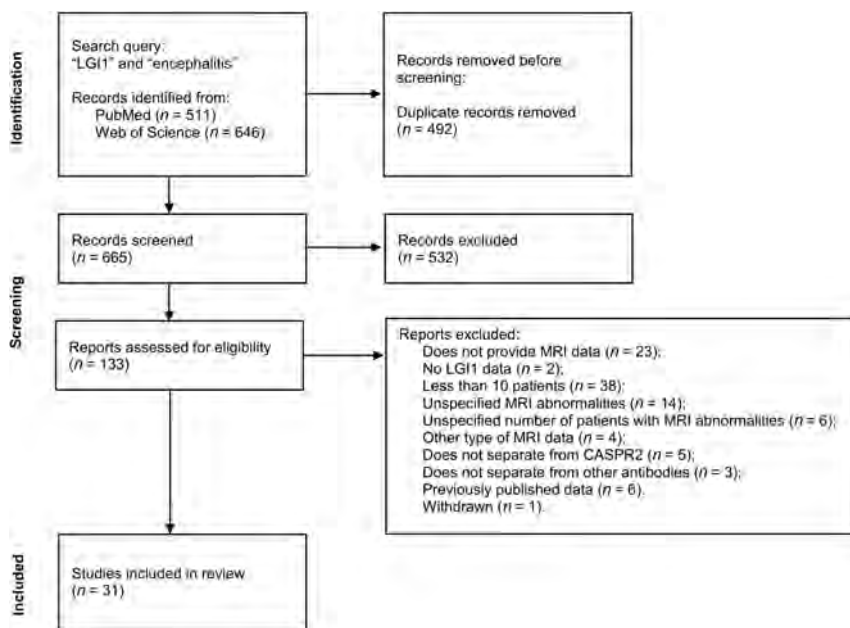


FIG 2. Study selection flow chart.¹⁸ PubMed and Web of Science were searched for the terms “LGII” and “encephalitis.” Of 665 records screened, 133 were assessed for eligibility, resulting in 31 included publications.

Table 1: Summary statistics for the whole study population

	Studies (No.)	Total Subjects (No.)	Summary Statistic
Mean age (yr)	30	1409	61.4
Male sex (No.) (%)	30	1409	895 (64%)
Cognitive impairment (No.) (%)	30	1409	1095 (78%)
FBDS (No.) (%)	27	1252	639 (51%)
Other seizures (No.) (%)	28	1368	989 (72%)
Psychiatric symptoms (No.) (%)	25	1203	612 (51%)
Hallucinations (No.) (%)	9	493	80 (16%)
Hyponatremia (No.) (%)	24	1146	512 (45%)
Sleep disorder (No.) (%)	21	1166	417 (36%)
Consciousness impairment (No.) (%)	12	574	180 (31%)
Autonomic dysfunction (No.) (%)	15	812	155 (19%)
Abnormal EEG findings (No.) (%)	19	698	508 (73%)
CSF antibody positivity (No.) (%)	14	713	457 (64%)

180 (31%). Autonomic dysfunction was present in 155 patients of 812 (19%) in 15 studies. Sleep disorder was present in 417 patients of 1166 (36%) in the 21 studies that reported data on this symptom. Of 1203 patients, 612 in 25 studies presented with psychiatric symptoms (51%). Hallucinations were present in 80 of 493 patients (16%) in 9 studies. Personality changes and psychosis (unspecified) were among other symptoms reported in the included literature. In 14 studies with 713 patients, CSF antibody positivity was found in 457 (64%). In 19 studies with data on EEG, 508 of 698 patients (73%) presented with abnormal findings.

Neuroimaging Findings

Of the whole sample of 1409 patients, 1318 had reported data on MR imaging. Thirty studies reported data on T2 or T2 FLAIR-MTL hyperintensities. Meta-analysis of the proportion of patients with T2 FLAIR-MTL revealed that this finding was present in 54% of patients (Fig 3; 95% CI, 0.48–0.60; $I^2 = 76\%$). Thirteen

studies reported T2 FLAIR-MTL laterality with a total of 394 patients. Meta-analysis revealed 27% with bilateral T2-MTL findings (Fig 4A; 95% CI, 0.19–0.36; $I^2 = 71\%$) and 24% with unilateral abnormalities (Fig 4B; 95% CI, 0.17–0.32; $I^2 = 61\%$) of the whole population (ie, with and without T2-MTL abnormalities).

Fifteen studies encompassing 612 patients reported data on BG MR imaging signal abnormalities, which included T2 hyperintensities and T1 hypo- and hyperintensities. Altogether, meta-analysis of proportions revealed these signal abnormalities to be present in 10% of patients (Fig 5; 95% CI, 0.06–0.15; $I^2 = 67\%$).

Inspection of funnel plots and linear regression testing for funnel asymmetry did not reveal a significant potential for publication bias (Online Supplemental Data).

Although not reported frequently enough to undergo meta-analysis, studies showed anti-LGII encephalitis with other regional and MR abnormalities.^{26–38,40,41,43,45–48,51,54} Amygdala, insula, and other neocortical T2-FLAIR hyperintensities were found in around 10%, 8%, and 18% of patients, respectively (Table 2). Two patients presented with cortical diffusion restriction (2%). Leptomeningeal gadolinium enhancement was described in 3 patients (5%). MTL swelling was reported in 18 patients (15%), and atrophy, in 55 patients (16%), whereas gadolinium enhancement was found in 5 patients (3%). In the studies with available

longitudinal follow-up, 46% of patients of 154 in 6 studies developed atrophy or mesial temporal sclerosis. BG atrophy was reported in 3 patients (3%). Neocortical and cerebellum gadolinium enhancement was described in 1 patient each in 1 study.²⁷ Diffusion restriction in the basal ganglia was reported in 1 study.¹⁶

Given the high heterogeneity found in the meta-analysis of these neuroimaging findings, we performed meta-regression analysis for T2-MTL and BG signal abnormalities with clinical predictors (Online Supplemental Data). We did not find any statistically significant modifiers of the proportion of MR imaging signal abnormalities.

LGII Gene Expression Map of the Human Brain

To assess whether the *LGII* gene is differentially expressed in the selective regions affected on MR imaging, we next used publicly available data from the Allen Human Brain Atlas to create a

Medial Temporal Lobe T2-FLAIR Hyperintensities

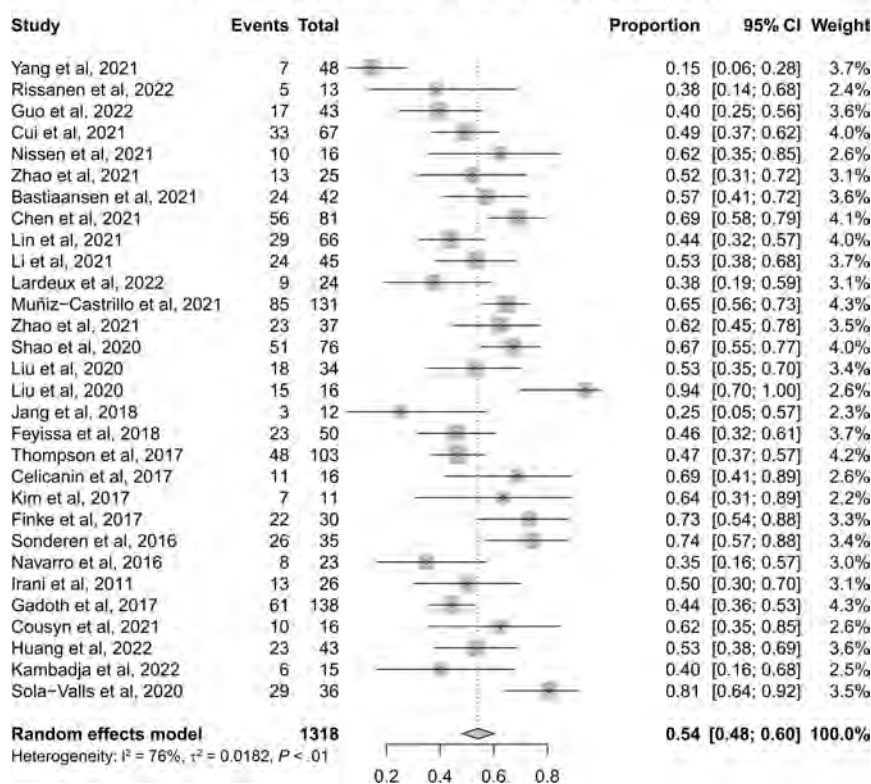


FIG 3. Forest plot showing the prevalence of T2 FLAIR-MTL hyperintensities. Of 1318 patients in 30 studies, 54% presented with this signal abnormality.

gene-expression brain map. We found that *LGII* is expressed widely across the cortex but is particularly predominant in subcortical regions, namely, the amygdala, hippocampus, and caudate nucleus (Fig 6A,-B; and Online Supplemental Data).

DISCUSSION

In this systematic review and meta-analysis, we focused on neuroimaging findings of anti-LGI1 encephalitis. We included 31 studies and 1409 patients. Our studied population had a mean age of 61.4 years and a mild predominance of male patients (64%). The most frequently reported symptoms were cognitive impairment, seizures other than FBDS, followed by FBDS and psychiatric symptoms. These clinical and demographic characteristics are in agreement with those in previous studies.⁵⁵

We found that 54% of patients presented with T2-FLAIR hyperintensities of the MTL (Fig 3). This finding reinforces the idea that a negative MR imaging in anti-LGI1 encephalitis is frequent. In a subgroup analysis, unilateral and bilateral presentations were similar, with a prevalence of 24% and 27%, respectively (Fig 4A, -B). This finding suggests that in the appropriate clinical context, the presence of unilateral MTL abnormalities on MR imaging should raise the possibility of AIE, namely anti-LGI1 encephalitis, and may aid in therapeutic decisions while awaiting antibody confirmation. A common imaging differential diagnosis for T2 FLAIR-MTL hyperintensities frequently associated with volume expansion includes other autoimmune/paraneoplastic

encephalitis cases, among which the neuronal-surface antigen group includes NMDAR,⁵⁶ CASPR2,^{57,58} GABA-B,^{59,60} Neurexin-3a,⁶¹ AMPAR,^{62,63} mGluR5,⁶⁴ GlyR,^{65,66} AK5,⁶⁷ and DPPX6,⁶⁸ and in the intracellular antigen group includes GAD65,⁶⁹ Hu,⁸ amphiphysin,⁷⁰ and Ma2.⁷¹ Viral encephalitis,¹¹ neurosyphilis,¹² Whipple disease,¹³ glioma,¹⁴ ictal changes,⁹ and posterior circulation stroke¹⁵ are among other important diagnostic considerations. Depending on the time of imaging, anti-LGI1 encephalitis might already have presented with hippocampal atrophy, in which case neurodegenerative diseases, including Alzheimer disease,^{72,73} frontotemporal dementia,⁷⁴ and limbic-predominant age-related TDP-43 encephalopathy,⁷⁵ as well as medial temporal sclerosis of other causes, are to be included in the differential diagnosis. Other causes to consider, depending on clinical presentation and other associated signal changes, include metabolic and mitochondrial disorders.⁷⁶

Notably, BG signal abnormalities, encompassing both T2 and T1 hyperintensities and T1 hypointensities, were reported in around 10% of patients (Fig 5). The available number of studies providing information regarding the BG was substantially smaller than that for the MTL. However, these changes can be the sole signal alteration observed on MR imaging and might be unilateral¹⁶ (Fig 1B), suggesting that this brain region deserves detailed attention when suspecting AIE. In fact, LGI1 expression is high in the BG in humans (Fig 6B), and [¹⁸F] fluorodeoxyglucose PET studies have repeatedly shown metabolic alterations in these regions.^{27,39,41} Most important, these lesions can present with diffusion restriction,¹⁶ the cause of which is unknown. Ischemic infarction is thus an important differential diagnosis, and attention to clinical presentation is crucial.

The nature of T1 hyperintensities of the BG is also not yet understood. Underlying causes of T1 relaxation time shortening included blood, fat, high paramagnetic substances such as iron, and high protein content. In anti-LGI1 encephalitis, BG T1-hyperintensities are sometimes preceded by T2-hyperintensities and have been shown to remain for a longer time than the latter before resolving.¹⁶ A putative explanation might be the accumulation of proteins at the site of antibody engagement, which persists after initial inflammatory changes. A parallel explanation has been drawn for T1 pallidal hyperintensities in Creutzfeldt-Jakob disease, where accumulation of prion protein, confirmed at neuropathology, was correlated with this MR imaging signal abnormality.⁷⁷ Signal alterations in the BG have a vast differential diagnosis, which includes toxic and metabolic disorders,⁷⁸ among which hepatic failure and Wilson disease are important

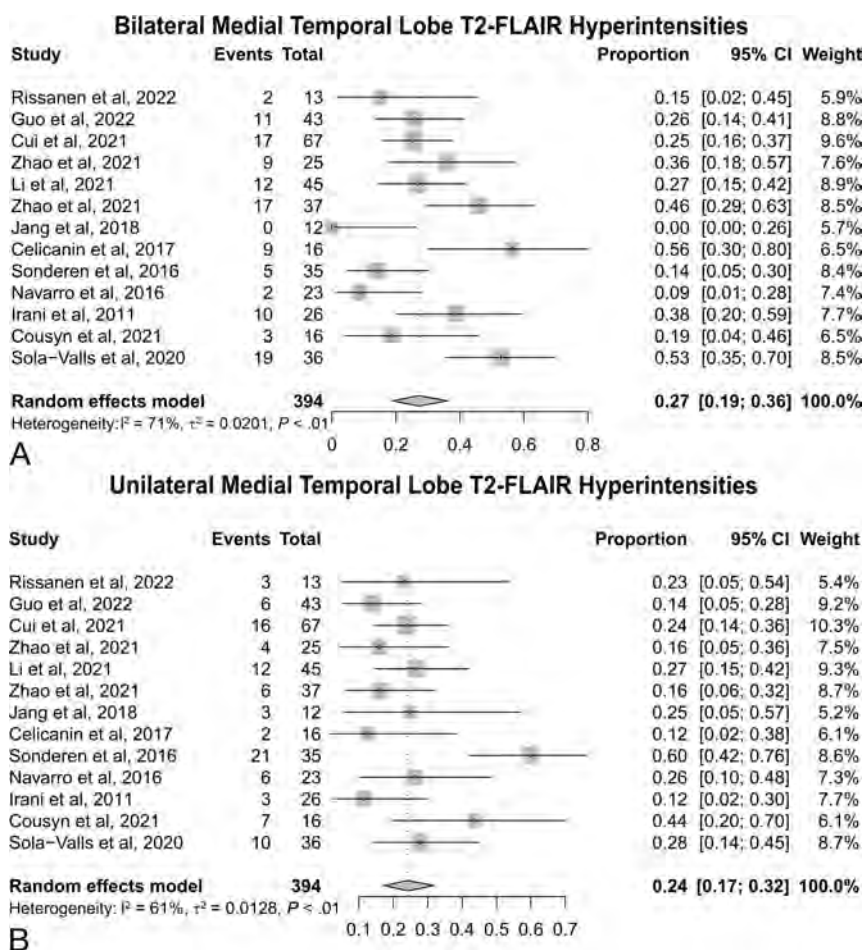


FIG 4. Forest plots showing the prevalence of bilateral T2 FLAIR-MTL hyperintensities (27% of 394 patients in 13 studies) (A) and unilateral MTL T2 FLAIR-MTL hyperintensities (24% of 394 patients in 13 studies) (B).

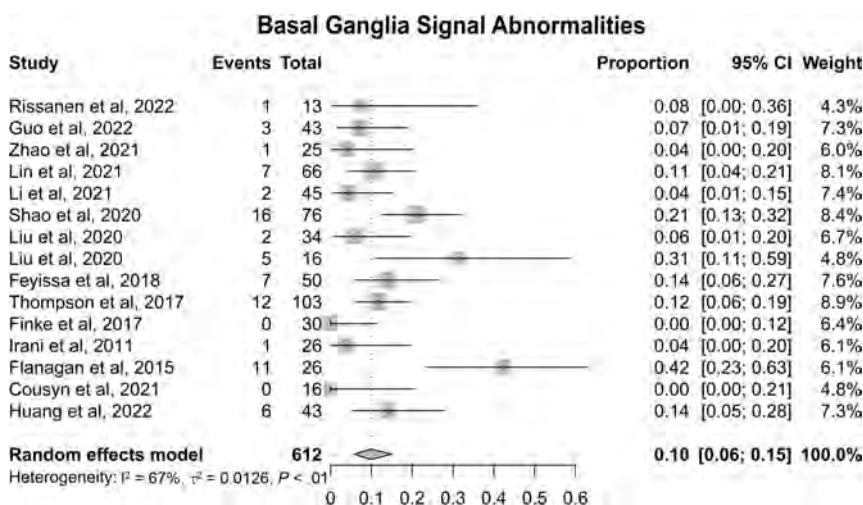


FIG 5. Forest plot showing the prevalence of BG signal abnormalities (T2-FLAIR hyperintensities and T1 hypo- and hyperintensities with 10% of 612 patients having these abnormalities).

considerations, Creutzfeldt-Jakob disease,⁷⁹ other autoimmune encephalitis (eg, CV2/collapsin response mediated protein 5),⁸⁰ viral encephalitis,¹¹ and arterial and venous infarction, among others.⁸¹

Other brain regions were found to be altered in LGI1 encephalitis, namely, the amygdala, insula, cerebellum, and different regions of the neocortex, with signal abnormalities across T1 with gadolinium enhancement, T2 and diffusion MR imaging, as well as leptomeningeal gadolinium enhancement. This finding suggests that LGI1 AIE can present with a widespread variety of signal abnormalities across multiple brain regions and multiple MR imaging sequences. Moreover, the under-reporting of altered signal beyond the MTL indicates that there is a need for further research in systematizing MR imaging signal abnormalities in LGI1 encephalitis across the whole brain.

In the studies that included a follow-up period, 46% of patients went on to develop hippocampal atrophy or mesial temporal sclerosis (Table 2). These results support the concept that anti-LGI1 encephalitis might induce a neurodegenerative process in a large proportion of patients, which might be associated with remaining cognitive deficits.⁸² Detection of these imaging findings by the radiologist in serial scans provides useful information for the clinician.

To assess qualitatively whether MR imaging abnormalities tend to occur at brain regions most enriched for *LGI1* gene expression, we generated a brain map using the publicly available Allen Human Brain Atlas. Regions with the highest expression were the amygdala, hippocampus, and caudate (Fig 6), suggesting that at least partially, the selective appearance of abnormalities on MR imaging might be due to the relative expression of LGI1. The LGI1 protein is expressed at the synapse, where binding presynaptic a disintegrin and metalloprotease domain 23 (ADAM23) and postsynaptic ADAM22 forms a trans-synaptic tether that couples presynaptic voltage-gated potassium channels and postsynaptic AMPA (α -amino-3-hydroxy-5-methyl-4-isoxazolepropionic acid) receptors, thereby regulating synaptic activity.³ Evidence from animal models has shown that patient-derived anti-LGI1 antibodies induce important impairment of synaptic plasticity,^{83,84} neuronal excitability⁸⁵ and memory in rodents.^{83,84} This evidence supports the pathogenicity of the

Table 2: Other MR imaging abnormalities associated with anti-LGI1 encephalitis

	Studies (No.)	Total Subjects (No.)	Proportion
Amygdala T2 hyperintensity	3	94	9 (10%)
Insula T2 hyperintensity	5	153	12 (8%)
Cortical T2 FLAIR hyperintensity ^a	4	79	14 (18%)
Cortical with diffusion restriction ^a	3	85	2 (2%)
Leptomeningeal gadolinium enhancement	2	61	3 (5%)
MTL swelling	4	117	18 (15%)
MTL atrophy ^b	7	353	55 (16%)
MTL with gadolinium enhancement	2	151	5 (3%)
MTL atrophy or mesial temporal sclerosis on follow-up	6	154	71 (46%)
BG atrophy	2	102	3 (3%)

^a Excluding MTL and insula.

^b The time of the MR imaging relative to symptom initiation was not available.

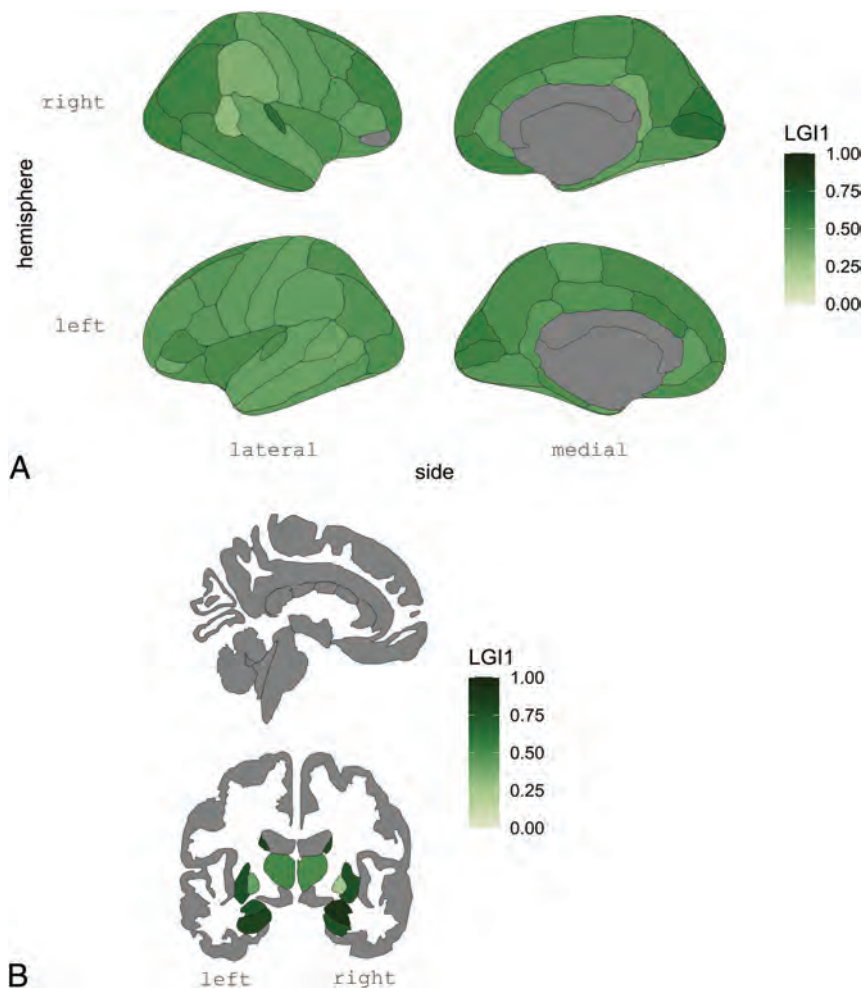


FIG 6. *LGI1* gene expression in the cortical (A) and subcortical (B) regions derived from the Allen Human Brain Atlas. In this figure, *LGI1* gene expression is shown to be higher in the MTLs and BG, concordant with the main MR imaging signal abnormality findings, suggesting that regional brain susceptibility in anti-LGI1 encephalitis might be mediated by the relative levels of brain regional expression of this gene.

antibody and the hypothesis that higher expression of the target antigen might be a contributing factor to explain brain regional susceptibility in these diseases. The accessibility of the antibodies to these brain regions is also a putative contributing

express the *LGI1* gene at high levels, thus lending support to the hypothesis that the regions affected by autoimmunity might be at least partially determined by the expression levels of the target protein.

factor. Many patients presenting without MR imaging signal abnormalities suggests that only in certain cases is the underlying pathophysiologic mechanism capable of generating a detectable change on MR imaging. The reasons are still to be explored. PET imaging approaches might unravel promising biologic markers of disease activity in the acute phase.⁸⁶

While these results provide the first estimate of neuroimaging signal abnormalities reported in the literature for LGI1 encephalitis, this study has important limitations. Even though MR imaging signal abnormality is likely to be present at the time of symptom onset, we were unable to report any analysis on this parameter. Moreover, neuroimaging findings were not the main outcome in most studies. While we did not find any clinical modifiers on the prevalence of these neuroimaging findings, not all studies provided data for all subjects who underwent MR imaging. More research is needed to establish whether signal abnormalities on MR imaging correlate with clinical presentation or other auxiliary tests. Finally, the specific MR imaging sequence parameters and magnetic field strength of the scanner were not taken into account in the analyses.

Most important, a considerable number of studies were excluded due to incomplete reporting on MR imaging data (Fig 2). These results lead us to highlight the need to include detailed MR imaging descriptions in a disease that can present with a variety of signal abnormalities across various MR imaging sequences.

CONCLUSIONS

This study presents a first approach to estimate the main findings of anti-LGI1 AIE on MR imaging and underlines the importance of considering this diagnosis in the context of unilateral signal abnormalities of the MTL, while also calling for detailed attention to the BG with suspicion of this disease. Most interesting, these regions

ACKNOWLEDGMENTS

We thank Dr Alexandra Rodrigues from the Neuroradiology Department of Centro Hospitalar Universitário de São José for her valuable input.

Disclosure forms provided by the authors are available with the full text and PDF of this article at www.ajnr.org.

REFERENCES

- Hébert J, Riche B, Vogrig A, et al. **Epidemiology of paraneoplastic neurologic syndromes and autoimmune encephalitis in France.** *Neurol Neuroimmunol Neuroinflamm* 2020;7:e883 CrossRef Medline
- Irani SR, Alexander S, Waters P, et al. **Antibodies to Kv1 potassium channel-complex proteins leucine-rich, glioma inactivated 1 protein and contactin-associated protein-2 in limbic encephalitis, Morvan's syndrome and acquired neuromyotonia.** *Brain* 2010;133:2734–48 CrossRef Medline
- Baudin P, Cousyn L, Navarro V. **The LGI1 protein: molecular structure, physiological functions and disruption-related seizures.** *Cell Mol Life Sci* 2021;79:16 CrossRef Medline
- Fels E, Muñoz-Castrillo S, Vogrig A, et al. **Role of LGI1 protein in synaptic transmission: from physiology to pathology.** *Neurobiol Dis* 2021;160:105537 CrossRef Medline
- Bastiaansen AE, van Steenhoven RW, de Bruijn MA, et al. **Autoimmune encephalitis resembling dementia syndromes.** *Neurol Neuroimmunol Neuroinflamm* 2021;8:e1039 CrossRef Medline
- Costa D, Sardoeira A, Carneiro P, et al. **Autoimmune encephalitis: suspicion in clinical practice and mimics.** *J Neuroimmunol* 2022;365:577824 CrossRef Medline
- Graus F, Titulaer MJ, Balu R, et al. **A clinical approach to diagnosis of autoimmune encephalitis.** *Lancet Neurol* 2016;15:391–404 CrossRef Medline
- Kelley BP, Patel SC, Marin HL, et al. **Autoimmune encephalitis: pathophysiology and imaging review of an overlooked diagnosis.** *AJNR Am J Neuroradiol* 2017;38:1070–78 CrossRef Medline
- Alves IS, Coutinho AM, Vieira AP, et al. **Imaging aspects of the hippocampus.** *Radiographics* 2022;42:822–40 CrossRef Medline
- Kim SE, Lee BI, Shin KJ, et al. **Characteristics of seizure-induced signal changes on MRI in patients with first seizures.** *Seizure* 2017;48:62–68 CrossRef Medline
- Ramli NM, Bae YJ. **Structured imaging approach for viral encephalitis.** *Neuroimaging Clin N Am* 2023;33:43–56 CrossRef Medline
- Abdelrahman KT, Santamaria DD, Rakocevic G. **Pearls and oysters: neurosyphilis presenting as mesial temporal encephalitis.** *Neurology* 2012;79:e206–08 CrossRef Medline
- Black DF, Aksamit AJ, Morris JM. **MR imaging of central nervous system Whipple disease: a 15-year review.** *AJNR Am J Neuroradiol* 2010;31:1493–97 CrossRef Medline
- Zoccarato M, Vallengia S, Zuliani L, et al. **Conventional brain MRI features distinguishing limbic encephalitis from mesial temporal glioma.** *Neuroradiology* 2019;61:853–60 CrossRef Medline
- Salerno A, Strambo D, Nannoni S, et al. **Patterns of ischemic posterior circulation strokes: a clinical, anatomical, and radiological review.** *Int J Stroke* 2022;17:714–22 CrossRef Medline
- Flanagan EP, Kotsenas AL, Britton JW, et al. **Basal ganglia T1 hyperintensity in LGI1-autoantibody faciobrachial dystonic seizures.** *Neurol Neuroimmunol Neuroinflamm* 2015;2:e161 CrossRef Medline
- Dalmau J, Graus F. **Antibody-mediated encephalitis.** *N Engl J Med* 2018;378:840–51 CrossRef Medline
- Moher D, Liberati A, Tetzlaff J, et al; PRISMA Group. **Preferred reporting items for systematic reviews and meta-analyses: the PRISMA statement.** *PLoS Med* 2009;6:e1000097 CrossRef Medline
- Hoy D, Brooks P, Woolf A, et al. **Assessing risk of bias in prevalence studies: modification of an existing tool and evidence of interrater agreement.** *J Clin Epidemiol* 2012;65:934–39 CrossRef Medline
- Hawrylycz MJ, Lein ES, Guillozet-Bongaarts AL, et al. **An anatomically comprehensive atlas of the adult human brain transcriptome.** *Nature* 2012;489:391–99 CrossRef Medline
- Arnatkeviciute A, Fulcher BD, Fornito A. **A practical guide to linking brain-wide gene expression and neuroimaging data.** *NeuroImage* 2019;189:353–67 CrossRef Medline
- Quackenbush J. **Microarray data normalization and transformation.** *Nat Genet* 2002;32(Suppl):496–501 CrossRef Medline
- Hawrylycz M, Miller JA, Menon V, et al. **Canonical genetic signatures of the adult human brain.** *Nat Neurosci* 2015;18:1832–44 CrossRef Medline
- Fulcher BD, Little MA, Jones NS. **Highly comparative time-series analysis: the empirical structure of time series and their methods.** *J R Soc Interface* 2013;10:20130048 CrossRef Medline
- Mowinckel AM, Vidal-Piñero D. **Visualization of brain statistics with R packages ggseg and ggseg3d.** *Advances in Methods and Practices in Psychological Science* 2020;3:466–83 CrossRef
- Guo K, Liu X, Lin J, et al. **Clinical characteristics, long-term functional outcomes and relapse of anti-LGI1/Caspr2 encephalitis: a prospective cohort study in Western China.** *Ther Adv Neurol Disord* 2022;15:17562864211073203 CrossRef Medline
- Rissanen E, Carter K, Cicero S, et al. **Cortical and subcortical dysmetabolism are dynamic markers of clinical disability and course in anti-LGI1 encephalitis.** *Neurol Neuroimmunol Neuroinflamm* 2022;9:e1136 CrossRef Medline
- Yang M, Lian Y. **Clinical features and early recognition of 242 cases of autoimmune encephalitis.** *Front Neurol* 2021;12:803752 CrossRef Medline
- Cui L, Boltze J, Zhang Y. **Positive LGI1 antibodies in CSF and relapse relate to worse outcome in anti-LGI1 encephalitis.** *Front Immunol* 2021;12:772096 CrossRef Medline
- Nissen MS, Ryding M, Nilsson AC, et al. **CSF-neurofilament light chain levels in NMDAR and LGI1 encephalitis: a national cohort study.** *Front Immunol* 2021;12:719432 CrossRef Medline
- Zhao X, Zhao S, Chen Y, et al. **Subcortical hypermetabolism associated with cortical hypometabolism is a common metabolic pattern in patients with anti-leucine-rich glioma-inactivated 1 antibody encephalitis.** *Front Immunol* 2021;12:672846 CrossRef Medline
- Chen W, Wang M, Gao L, et al. **Neurofunctional outcomes in patients with anti-leucine-rich glioma inactivated 1 encephalitis.** *Acta Neurol Scand* 2021;144:632–39 CrossRef Medline
- Lin N, Liu Q, Chen J, et al. **Long-term seizure outcomes in patients with anti-leucine-rich glioma-inactivated 1 encephalitis.** *Epilepsy Behav* 2021;122:108159 CrossRef Medline
- Li TR, Zhang YD, Wang Q, et al. **Clinical characteristics and long-term prognosis of anti-LGI1 encephalitis: a single-center cohort study in Beijing, China.** *Front Neurol* 2021;12:674368 CrossRef Medline
- Lardeux P, Fourier A, Peter E, et al. **Core cerebrospinal fluid biomarker profile in anti-LGI1 encephalitis.** *J Neurol* 2022;269:377–88 CrossRef Medline
- Muñoz-Castrillo S, Haesebaert J, Thomas L, et al. **Clinical and prognostic value of immunogenetic characteristics in anti-LGI1 encephalitis.** *Neurol Neuroimmunol Neuroinflamm* 2021;8:e974 CrossRef Medline
- Zhao Q, Sun L, Zhao D, et al. **Clinical features of anti-leucine-rich glioma-inactivated 1 encephalitis in northeast China.** *Clin Neurol Neurosurg* 2021;203:106542 CrossRef Medline
- Shao X, Fan S, Luo H, et al. **Brain magnetic resonance imaging characteristics of anti-leucine-rich glioma-inactivated 1 encephalitis and their clinical relevance: a single-center study in China.** *Front Neurol* 2020;11:618109 CrossRef Medline
- Liu X, Shan W, Zhao X, et al. **The clinical value of ¹⁸F-FDG-PET in autoimmune encephalitis associated with LGI1 antibody.** *Front Neurol* 2020;11:418 CrossRef Medline
- Liu X, Han Y, Yang L, et al. **The exploration of the spectrum of motor manifestations of anti-LGI1 encephalitis beyond FBDS.** *Seizure* 2020;76:22–27 CrossRef Medline

41. Jang Y, Lee ST, Bae JY, et al. **LGI1 expression and human brain asymmetry: insights from patients with LGI1-antibody encephalitis.** *J Neuroinflammation* 2018;15:279 CrossRef Medline
42. Feyissa AM, Lamb C, Pittock SJ, et al. **Antiepileptic drug therapy in autoimmune epilepsy associated with antibodies targeting the leucine-rich glioma-inactivated protein 1.** *Epilepsia Open* 2018;3:348–56 CrossRef Medline
43. Thompson J, Bi M, Murchison AG, et al; Faciobrachial Dystonic Seizures Study Group. **The importance of early immunotherapy in patients with faciobrachial dystonic seizures.** *Brain* 2017;141:348–56 CrossRef Medline
44. Celicanin M, Blaabjerg M, Maersk-Møller C, et al. **Autoimmune encephalitis associated with voltage-gated potassium channels-complex and leucine-rich glioma-inactivated 1 antibodies: a national cohort study.** *Eur J Neurol* 2017;24:999–1005 CrossRef Medline
45. Kim TJ, Lee ST, Moon J, et al. **Anti-LGI1 encephalitis is associated with unique HLA subtypes.** *Ann Neurol* 2017;81:183–92 CrossRef Medline
46. Finke C, Prüss H, Heine J, et al. **Evaluation of cognitive deficits and structural hippocampal damage in encephalitis with leucine-rich, glioma-inactivated 1 antibodies.** *JAMA Neurol* 2017;74:50–59 CrossRef Medline
47. van Sonderen A, Thijs RD, Coenders EC, et al. **Anti-LGI1 encephalitis: clinical syndrome and long-term follow-up.** *Neurology* 2016;87:1449–56 CrossRef Medline
48. Navarro V, Kas A, Apartis E, et al; collaborators. **Motor cortex and hippocampus are the two main cortical targets in LGI1-antibody encephalitis.** *Brain* 2016;139:1079–93 CrossRef Medline
49. Irani SR, Michell AW, Lang B, et al. **Faciobrachial dystonic seizures precede LGI1 antibody limbic encephalitis.** *Ann Neurol* 2011;69:892–900 CrossRef Medline
50. Gadoth A, Pittock SJ, Dubey D, et al. **Expanded phenotypes and outcomes among 256 LGI1/CASPR2-IgG-positive patients.** *Ann Neurol* 2017;82:79–92 CrossRef Medline
51. Cousyn L, Lambrecq V, Houot M, et al. **Seizures in autoimmune encephalitis: specific features based on a systematic comparative study.** *Epileptic Disord* 2021;23:879–92 CrossRef Medline
52. Kambadja B, Marion H, Cousyn L, et al. **When should we test patients with epilepsy for autoimmune antibodies? Results from a French retrospective single center study.** *J Neurol* 2022;269:3109–3118 CrossRef Medline
53. Sola-Valls N, Ariño H, Escudero D, et al. **Telemedicine assessment of long-term cognitive and functional status in anti-leucine-rich, glioma-inactivated 1 encephalitis.** *Neurol Neuroimmunol Neuroinflamm* 2019;7:e652 CrossRef Medline
54. Huang X, Fan C, Gao L, et al. **Clinical features, immunotherapy, and outcomes of anti-leucine-rich glioma-inactivated-1 encephalitis.** *J Neuropsychiatry Clin Neurosci* 2022;34:141–48 CrossRef Medline
55. Teng Y, Li T, Yang Z, et al. **Clinical features and therapeutic effects of anti-leucine-rich glioma inactivated 1 encephalitis: a systematic review.** *Front Neurol* 2021;12:791014 CrossRef Medline
56. Zhang T, Duan Y, Ye J, et al. **Brain MRI characteristics of patients with anti-N-methyl-D-aspartate receptor encephalitis and their associations with 2-year clinical outcome.** *AJNR Am J Neuroradiol* 2018;39:824–29 CrossRef Medline
57. Joubert B, Saint-Martin M, Noraz N, et al. **Characterization of a subtype of autoimmune encephalitis with anti-contactin-associated protein-like 2 antibodies in the cerebrospinal fluid, prominent limbic symptoms, and seizures.** *JAMA Neurol* 2016;73:1115–24 CrossRef Medline
58. Moura J, Samões R, Cardoso M, et al. **Distinct phenotypes in a cohort of anti-CASPR2 associated neurological syndromes.** *Clin Neurol Neurosurg* 2023;234:107994 CrossRef Medline
59. Zhu F, Shan W, Lv R, et al. **Clinical characteristics of anti-GABA-B receptor encephalitis.** *Front Neurol* 2020;11:403 CrossRef Medline
60. Höftberger R, Titulaer MJ, Sabater L, et al. **Encephalitis and GABAB receptor antibodies: novel findings in a new case series of 20 patients.** *Neurology* 2013;81:1500–06 CrossRef Medline
61. Gresa-Arribas N, Planagumà J, Petit-Pedrol M, et al. **Human neu-rexin-3 α antibodies associate with encephalitis and alter synapse development.** *Neurology* 2016;86:2235–42 CrossRef Medline
62. Höftberger R, van Sonderen A, Leypoldt F, et al. **Encephalitis and AMPA receptor antibodies: novel findings in a case series of 22 patients.** *Neurology* 2015;84:2403–12 CrossRef Medline
63. Joubert B, Kerschen P, Zekeridou A, et al. **Clinical spectrum of encephalitis associated with antibodies against the α -amino-3-hydroxy-5-methyl-4-isoxazolepropionic acid receptor: case series and review of the literature.** *JAMA Neurol* 2015;72:1163–69 CrossRef Medline
64. Spatola M, Sabater L, Planagumà J, et al. **Encephalitis with mGluR5 antibodies: symptoms and antibody effects.** *Neurology* 2018;90:e1964–72 CrossRef Medline
65. Carvajal-González A, Leite MI, Waters P, et al. **Glycine receptor antibodies in PERM and related syndromes: characteristics, clinical features and outcomes.** *Brain* 2014;137:2178–92 CrossRef Medline
66. Swayne A, Tjoa L, Broadley S, et al. **Antiglycine receptor antibody related disease: a case series and literature review.** *Eur J Neurol* 2018;25:1290–98 CrossRef Medline
67. Muñiz-Castrillo S, Hedou JJ, Ambati A, et al. **Distinctive clinical presentation and pathogenic specificities of anti-AK5 encephalitis.** *Brain* 2021;144:2709–21 CrossRef Medline
68. Xiao J, Fu PC, Li ZJ. **Clinical and imaging analysis to evaluate the response of patients with anti-DPPX encephalitis to immunotherapy.** *BMC Neurol* 2022;22:129 CrossRef Medline
69. Fredriksen JR, Carr CM, Koeller KK, et al. **MRI findings in glutamic acid decarboxylase associated autoimmune epilepsy.** *Neuroradiology* 2018;60:239–45 CrossRef Medline
70. Sun Y, Qin X, Huang D, et al. **Anti-amphiphysin encephalitis: expanding the clinical spectrum.** *Front Immunol* 2023;14:1084883 CrossRef Medline
71. Dalmau J, Graus F, Villarejo A, et al. **Clinical analysis of anti-Ma2-associated encephalitis.** *Brain* 2004;127:1831–44 CrossRef Medline
72. Quintas-Neves M, Teylan MA, Morais-Ribeiro R, et al. **Divergent magnetic resonance imaging atrophy patterns in Alzheimer's disease and primary age-related tauopathy.** *Neurobiol Aging* 2022;117:1–11 CrossRef Medline
73. Pinho J, Almeida FC, Araújo JM, et al. **Sex-specific patterns of cerebral atrophy and enlarged perivascular spaces in patients with cerebral amyloid angiopathy and dementia.** *AJNR Am J Neuroradiol* 2023;44:792–98 CrossRef Medline
74. Preiß D, Billette OV, Schneider A, et al. **The atrophy pattern in Alzheimer-related PPA is more widespread than that of the frontotemporal lobar degeneration associated variants.** *NeuroImage Clin* 2019;24:101994 CrossRef Medline
75. Nelson PT, Dickson DW, Trojanowski JQ, et al. **Limbic-predominant age-related TDP-43 encephalopathy (LATE): consensus working group report.** *Brain* 2019;142:1503–27 CrossRef Medline
76. Eran A, Hodes A, Izbudak I. **Bilateral temporal lobe disease: looking beyond herpes encephalitis.** *Insights Imaging* 2016;7:265–74 CrossRef Medline
77. de Priester JA, Jansen GH, de Kruijk JR, et al. **New MRI findings in Creutzfeldt-Jakob disease: high signal in the globus pallidus on T1-weighted images.** *Neuroradiology* 1999;41:265–68 CrossRef Medline
78. de Oliveira AM, Paulino MV, Vieira AP, et al. **Imaging patterns of toxic and metabolic brain disorders.** *Radiographics* 2019;39:1672–95 CrossRef Medline
79. Fragoso DC, Gonçalves Filho AL, Pacheco FT, et al. **Imaging of Creutzfeldt-Jakob disease: imaging patterns and their differential diagnosis.** *Radiographics* 2017;37:234–57 CrossRef Medline
80. Vakrakou A, Constantinides VC, Velonakis G, et al. **Paraneoplastic basal ganglia encephalitis associated with anti-CV2/CRMP-5 and anti-Yo antibodies in a patient with non-small-cell lung cancer.** *Neurol Sci* 2020;41:2649–51 CrossRef Medline

81. Hegde AN, Mohan S, Lath N, et al. **Differential diagnosis for bilateral abnormalities of the basal ganglia and thalamus.** *Radiographics* 2011;31:5–30 CrossRef Medline
82. Miller TD, Chong TT, Aimola Davies AM, et al. **Focal CA3 hippocampal subfield atrophy following LGI1 VGKC-complex antibody limbic encephalitis.** *Brain* 2017;140:1212–19 CrossRef Medline
83. Petit-Pedrol M, Sell J, Planagumà J, et al. **LGI1 antibodies alter Kv1.1 and AMPA receptors changing synaptic excitability, plasticity and memory.** *Brain* 2018;141:3144–59 CrossRef Medline
84. Ramberger M, Berretta A, Tan JM, et al. **Distinctive binding properties of human monoclonal LGI1 autoantibodies determine pathogenic mechanisms.** *Brain* 2020;143:1731–45 CrossRef Medline
85. Kornau HC, Kreye J, Stumpf A, et al. **Human cerebrospinal fluid monoclonal lgi1 autoantibodies increase neuronal excitability.** *Ann Neurol* 2020;87:405–18 CrossRef Medline
86. Sadaghiani MS, Roman S, Diaz-Arias LA, et al. **Comparison of quantitative FDG-PET and MRI in anti-LGI1 autoimmune encephalitis.** *Neuroradiology* 2023;65:1225–38 CrossRef Medline

Shift Volumes

What great discussions have been sparked by a recent *American Journal of Neuroradiology* article from Ivanovic et al.¹ We used this article in a recent neuroradiology journal club at Emory University, and it came up during the 2024 Stanford Radiology Improvement Summit, February 22–23, 2024, Stanford, California. I would like to share some thoughts that came up during these events.

The initial reaction to the article is one of surprise and disbelief. There is a certain audacity in stating that 19–26 cross-sectional imaging studies per neuroradiologist per day are associated with lower error rates. In the current practice environment, it seems impossible to imagine putting a specific number to it, or is it?

Have we been slowly conditioned to tackle increasing volumes across the years? How much of our ability to manage higher volumes is related to cutting corners, such as skipping the medical chart review, looking at fewer priors, scrolling faster, relying on trainee initial reads and reporting, worrying less about catching incidental findings, and taking a narrower approach informed by the clinical context rather than a comprehensive interpretation?

It may be good to have this number out there when it comes to negotiating for more FTEs. However, most practices find that there are currently not enough radiologists in the recruiting pool. Unable to hire up, we are becoming creative in tackling high clinical demands in other ways. The discussions I participated in listed several interventions, real and theoretic: Schedule shifts to match volumes, accept backlogs, shut down scanners/decrease outpatient imaging volumes to match radiologist reading capacity, allow radiologists to stay within certain limits (hours of work, work relative value units), call backup readers to jump in for an hourly fee, further increase radiologists' efficiency by eliminating noninterpretive tasks and "efficiency rounding," and reduce the number of images in a study.

Most important, we need to make up our own rules and approaches within our practices or larger organizations. Regulators have no business regulating how we serve our patients, and the American College of Radiology has no interest in prescribing volume caps for radiologists. If errors become a costly issue, payors and malpractice insurers may develop an opinion, but there is no evidence of this issue now. Maybe the use of radiology-pathology correlations, second reads, or future artificial intelligence (AI) applications can help us get data that inform our true error rates in radiology and the impact those errors have on our patients.

Using daily quotas can result in a race to the bottom. Nobody wants that. Some radiologists can safely read more studies, others less. We need a solution for managing high volumes in the safest way possible. AI applications are evolving but are not quite to a point at which they reduce our workload considerably. This is a wake-up call, and yes, we can!

Disclosure forms provided by the authors are available with the full text and PDF of this article at www.ajnr.org.

REFERENCE

- Ivanovic V, Broadhead K, Chang YM, et al. **Shift volume directly impacts neuroradiology error rate at a large academic medical center: the case for volume limits.** *AJNR Am J Neuroradiol* 2024;45:374–78 CrossRef Medline

 **Nadja Kadom**

Department of Radiology
Children's Healthcare of Atlanta
Atlanta, Georgia

Department of Radiology and Imaging Sciences
Emory School of Medicine
Atlanta, Georgia

<http://dx.doi.org/10.3174/ajnr.A8259>

CPT Codes for Quantitative MRI of the Brain: What It Means for Neuroradiology

Quantitative volumetric postprocessing tools for brain MR imaging studies (QMRI) offer valuable adjunctive information through baseline analysis and longitudinal tracking of a variety of neurologic conditions, including dementia, MS, traumatic brain injury, neuro-oncology, and epilepsy. The novel information provided can assist radiologists and enhance the value of MR imaging while reducing subjectivity.

New Current Procedural Terminology (CPT) Category III codes 0865T and 0866T for quantitative analysis of brain MR examinations came into effect on January 1, 2024. These new CPT codes are vendor-neutral, and applicable to any artificial intelligence (AI) algorithm that quantitatively assesses brain volumetry and lesions. Code 0865T is used when diagnostic brain MR imaging is not performed during the same session, and code 0866T is used when diagnostic brain MR imaging is performed. These new codes represent recognition of QMRI as a clinically impactful diagnostic tool and may help establish reimbursement for comprehensive analysis of brain volumetry as well as for lesion identification, characterization, and quantification.

The new codes establish the definition of QMRI in the CPT code set, provide a mechanism for tracking, and give non-CMS payers an opportunity to establish payment pathways. Reimbursement determination for Category III codes is made by each payer and is not guaranteed.¹ Use of these new codes is an important factor in demonstrating the treatment-guiding value of quantitative MR imaging techniques to payers and may result in the codes achieving Category I status in the future.

An example of the clinical utility of QMRI is in MS, in which new or enlarging brain lesions on MR imaging are a biomarker of both disease activity and treatment response. Accurate quantitation is essential to guide treatment decisions because clinical guidelines recommend treatment change if there is progressive active disease since this is a predictor of long-term disability. Furthermore, MS is associated with brain volume loss, which correlates with cognitive impairment and disability and can be difficult to discern without quantification tools.

Likewise, QMRI is now expected to play a larger role in the dementia imaging pathway. The availability of disease-modifying therapies shifts the role of MR imaging from simply seeking

“treatable” causes of cognitive impairment to assisting in the identification of patients with volumetric changes that might indicate early Alzheimer disease. Baseline MR imaging is critical for identifying patients with potential contraindications to amyloid-mobilizing therapy. For those on therapy, expanded opportunities exist for QMRI to add objective longitudinal analysis of hippocampal and entorhinal cortical volumetric parameters, which can serve as a useful subclinical marker for treatment response. Brain MR imaging surveillance is required in patients undergoing amyloid-mobilizing therapies for detection, grading, and longitudinal tracking of potential adverse effects of therapy, namely amyloid-related imaging abnormalities (ARIA), an area in which AI-fueled QMRI solutions could also play an important role in the future.²

Quantitative analysis tools enhance the value of imaging examinations, while reducing reader bias and improving report standardization. Consistent and correct application of these new vendor-neutral Category III codes will demonstrate the ongoing usage rates of QMRI in clinical practice, provide opportunities to demonstrate how these tools improve patient outcomes, and one hopes, facilitate conversion to appropriate reimbursement.

Disclosure forms provided by the authors are available with the full text and PDF of this article at www.ajnr.org.

REFERENCES

1. Wu G, Segovis C, Nicola L, et al. **Current reimbursement landscape of AI.** *J Am Coll Radiol* 2023;20:957–61 CrossRef Medline
2. Bash S, Tanenbaum LN. **Alzheimer disease imaging in the era of anti-amyloid treatment.** *Applied Radiol* 2023;52:16–23 CrossRef

© S. Bash
© L.N. Tanenbaum
RadNet Inc
Radnet.com

C. Segovis
Emory University School of Medicine
Atlanta, Georgia

© M. Chen
MD Anderson Cancer Center
Houston, Texas

<http://dx.doi.org/10.3174/ajnr.A8286>

Correspondence on “Antithrombotic Treatment after Carotid Stenting in Patients with Concomitant Atrial Fibrillation”

We read with interest the excellent work by Pardo-Galiana et al,¹ which compared the safety and efficacy of the combination of direct oral anticoagulants and a P2Y₁₂ inhibitor with 2 other antithrombotic regimens after carotid artery stent placement in patients with atrial fibrillation. The results indicated that a regimen of direct oral anticoagulants plus a P2Y₁₂ inhibitor might confer a good safety profile with significantly lower rates of bleeding and optimal efficacy. However, we noticed that dual antiplatelet therapy (DAPT) was administered for only 1–3 months after stent implantation in the background and purpose, and patients in the DAPT group received DAPT for only 1 month before switching to aspirin alone. Few studies have reported DAPT for only 1 month after stent placement, and several randomized controlled trials have reported DAPT (aspirin 100 mg, plus clopidogrel 75 mg, daily) for 90 days in patients with symptomatic internal carotid artery stenosis who underwent carotid stent placement.^{2,3}

On the other hand, the assessment methods of stent thrombosis or restenosis in this study were not as rigorous or different as previously.⁴ To be precise, in-stent restenosis was defined as >50% stenosis by DSA or CTA at 6 months or 1 year within or immediately adjacent (within 5 mm) of the treated segment after interventional treatment of intracranial atherosclerotic disease.⁴ Carotid sonography can only detect the stenosis of the extracranial segment of the ICA, and is not suitable for the intracranial segment. Moreover, the short follow-up time (on days 1 and 30) is far from what is generally accepted (6 months or 1 year). Of course, there is no doubt that this retrospective study by Pardo-Galiana et al¹ has preliminarily confirmed that the combination of direct oral

anticoagulants plus clopidogrel during the first month resulted in a lower risk of a bleeding event, with no increment of thromboembolic events. Further randomized studies are expected to provide more information on this.

Disclosure forms provided by the authors are available with the full text and PDF of this article at www.ajnr.org.

REFERENCES

1. Pardo-Galiana B, Medina-Rodriguez M, Millan-Vazquez M, et al. **Antithrombotic treatment after carotid stenting in patients with concomitant atrial fibrillation.** *AJNR Am J Neuroradiol* 2022;43:727–30 CrossRef Medline
2. Gao P, Wang T, Wang D; CASSISS Trial Investigators, et al. **Effect of stenting plus medical therapy vs medical therapy alone on risk of stroke and death in patients with symptomatic intracranial stenosis: the CASSISS Randomized Clinical Trial.** *JAMA* 2022;328:534–42 CrossRef Medline
3. Chimowitz MI, Lynn MJ, Derdeyn CP; SAMMPRIS Trial Investigators, et al. **Stenting versus aggressive medical therapy for intracranial arterial stenosis.** *N Engl J Med* 2011;365:993–1003 CrossRef Medline
4. Peng G, Zhang Y, Miao Z. **Incidence and risk factors of in-stent restenosis for symptomatic intracranial atherosclerotic stenosis: a systematic review and meta-analysis.** *AJNR Am J Neuroradiol* 2020;41:1447–52 CrossRef Medline

Hailong Zhong

 Aihua Liu

Beijing Neurosurgical Institute,
Beijing Tiantan Hospital,
Capital Medical University,
Beijing, China

<http://dx.doi.org/10.3174/ajnr.A8130>

REPLY:

First, we would like to thank Hailong Zhong and Aihua Liu for taking the time to read and review our work. We are pleased that they found it of interest. Following their comments, we would like to clarify that all patients included in our study underwent extracranial carotid artery stent placement (CAS). Therefore, patients with intracranial atherosclerotic stenosis were excluded from the study because their management is different from that of extracranial stenosis. Regarding the antiplatelet regimen used in our cohort, we followed our local protocol, which is in line with the European Vascular Surgery Society Guidelines that recommend dual antiplatelet therapy during at least 4–6 weeks after extracranial CAS.¹ In addition, before switching clopidogrel to aspirin, we assessed the stent patency using carotid Doppler ultrasound (US) at 30 days from CAS.

Related to carotid surveillance after CAS, as mentioned, carotid US accurately defined residual stenosis of $\geq 20\%$, in-stent restenosis of $\geq 50\%$, and high-grade in-stent restenosis in patients with extracranial CAS.² The velocity peak systolic threshold we established to define in-stent restenosis was ≥ 300 cm/s in restenosis of $\geq 70\%$, as previously described.² Finally, the reason we focused on the first month of follow-up exclusively was to assess the rate of in-stent thrombosis rather than long-term restenosis. Therefore, we monitored the patency of the stent immediately af-

ter CAS and during the first month. This first month is also when the bleeding risk increases related to dual antiplatelet therapy to prevent in-stent thrombosis and oral anticoagulation to prevent systemic embolisms/stroke. Nevertheless, we agree that further information regarding stent patency at 6 months or 1 year would be interesting and would have enriched the work. We thank you for your comments, which we will take into consideration for coming investigations.

REFERENCES

1. Naylor R, Rantner B, Ancetti S, et al. **Editor's Choice: European Society for Vascular Surgery (ESVS) 2023 Clinical Practice Guidelines on the Management of Atherosclerotic Carotid and Vertebral Artery Disease.** *Eur J Vasc Endovasc Surg* 2023;65:7–111 CrossRef Medline
2. Lal BK, Hobson RW, Tofighi B, et al. **Duplex ultrasound velocity criteria for the stented carotid artery.** *J Vasc Surg* 2008;47:63–73 CrossRef Medline

Medina-Rodríguez Manuel

Moniche Francisco

Stroke Unit, Department of Neurology
University Hospital Virgen del Rocío
Seville, Spain

Institute of Biomedicine of Seville
IBiS/Hospital Universitario Virgen del Rocío/CSIC/Universidad de Sevilla
Seville, Spain

<http://dx.doi.org/10.3174/ajnr.A8341>

A Note of Caution Regarding Single-Arm 1p or 19q Deletion in *IDH*-Mutant Gliomas

In their article entitled “Radiogenomics Provides Insights into Gliomas Demonstrating Single-Arm 1p or 19q Deletion,” Lasocki et al¹ reported that *IDH*-mutant gliomas with a single-arm deletion of either 1p or 19q have imaging features and clinical outcomes similar to those of astrocytoma *IDH*-mutant. These important results support the current World Health Organization classification of *IDH*-mutant gliomas, in particular its requirement for detecting deletions of both chromosome arms 1p and 19q for establishing a diagnosis of oligodendroglioma *IDH*-mutant and 1p/19q codeleted.

The authors correctly point out that molecular testing for 1p/19q codeletion is occasionally erroneous. In a prior publication, we reported 6 *IDH*-mutant gliomas that were initially misclassified to 1p/19q codeletion status with fluorescence in situ hybridization (FISH).² FISH is a widely used technique for 1p/19q testing and was among the techniques used by Lasocki et al.¹ We discovered these 6 cases due to a discordance between the FISH result and neuroimaging features. Interestingly, 3 of these 6 cases were initially diagnosed as astrocytoma *IDH*-mutant on the basis of 1p unideletion on FISH but were ultimately discovered to be 1p/19q codeleted (ie, oligodendrogliomas) on the basis of subsequent testing with a high-resolution chromosomal microarray assay (see Table 2 in Patel et al²). In these 3 cases, FISH had failed to detect a 19q deletion that was actually present.

Although such cases are uncommon, they slightly complicate the conclusion of Lasocki et al¹ that their findings provide “reassurance to pathologists and treating clinicians that tumors with 1p- or 19q-unideletion should indeed be considered astrocytomas, rather than having a reason to question the 1p/19q result or repeat testing on a different part of the tumor.” Their conclusion

seems valid when 1p or 19q unideletion accompanies other biomarkers consistent with astrocytoma *IDH*-mutant (eg, *ATRX* mutation, p53 overexpression, characteristic neuroimaging findings). However, in cases in which compelling discrepancies exist between the presence of 1p or 19q unideletion and other routinely obtained biomarkers, it might be necessary to retest the 1p/19q status with a different molecular assay. Overall then, we entirely agree with Lasocki et al that radiogenomics can play a useful role in glioma diagnostics, both when supporting the molecular/histologic diagnosis and also when contradicting it.

Disclosure forms provided by the authors are available with the full text and PDF of this article at www.ajnr.org.

REFERENCES

1. Lasocki A, Buckland ME, Molinaro T, et al. Radiogenomics provides insights into gliomas demonstrating single-arm 1p or 19q deletion. *AJNR Am J Neuroradiol* 2023;44:1270–74 CrossRef Medline
2. Patel SH, Batchala PP, Mrachek EK, et al. MRI and CT identify isocitrate dehydrogenase (*IDH*)-mutant lower-grade gliomas misclassified to 1p/19q codeletion status with fluorescence in situ hybridization. *Radiology* 2020;294:160–67 CrossRef Medline

©Sohil H. Patel

Department of Radiology and Medical Imaging
University of Virginia Health, Charlottesville, Virginia

M. Beatriz Lopes

Department of Department of Pathology (Neuropathology)
University of Virginia Health, Charlottesville, Virginia

©Eli S. Williams

Department of Department of Pathology (Genomics and Cytogenomics)
University of Virginia Health, Charlottesville, Virginia

<http://dx.doi.org/10.3174/ajnr.A8201>

REPLY:

We would like to thank Patel et al for their insightful comments regarding our research¹ and how it fits in with their own earlier findings.² However, we do not think that the findings of the study that Patel et al have referenced² are at odds with our own, but rather are complementary. While there are similarities across the 2 publications, the research questions have subtle-but-important differences, and examined 2 different potential roles of radiogenomics.

A fundamental difference between our studies is in how the key patient cohort was selected. Patel et al identified tumors with discordance between the imaging features and 1p/19q fluorescence in situ hybridization (FISH) results² on the basis of the premise that radiogenomics can be used to identify tumors in which molecular testing results should be questioned. We wholeheartedly agree with this concept and have previously highlighted this as one of several ways in which radiogenomics can add value for patients.^{3,4} In addition to occasional inaccuracies of the testing methods themselves, histology is also dependent on the quality of the sample. Even sequencing can produce false-negative results if there are few tumor cells in the sample.⁵

In contrast, our study started with the molecular testing diagnosis. We targeted tumors with 1p- or 19q unideletion because we thought that these might have a higher likelihood of a false-negative 1p/19q result.¹ If we had found imaging appearances suggesting 1p/19q codeletion in a substantial portion of our cohort, it might have suggested value in repeating 1p/19q testing for all undeleted tumors. As it turns out, our results suggest that repeat 1p/19q testing is not warranted as a default, but we do not suggest that testing should not be repeated if there is discordance with imaging, because this issue was not assessed in this study. Additionally, we have not implied that the pathologist should consider only 1p/19q results when distinguishing astrocytomas and oligodendrogliomas.

Ultimately, it is clear that both of our groups think that the addition of imaging features has the potential to positively influence patient management, compared with relying solely on histology. We agree that additional testing should be considered when histology and imaging findings are discordant. Furthermore, we suggest that correlating histology with imaging is relevant to not only 1p/19q FISH but also other molecular markers, other molecular testing methods, the determination of histologic grade,⁶ and even the overarching histologic diagnosis of a glioma versus another disease entity. Indeed, such correlation is important across many areas of radiology.

<http://dx.doi.org/10.3174/ajnr.A8347>

REFERENCES

1. Lasocki A, Buckland ME, Molinaro T, et al. **Radiogenomics provides insights into gliomas demonstrating single-arm 1p or 19q deletion.** *AJNR Am J Neuroradiol* 2023;44:1270–74 CrossRef Medline
2. Patel SH, Batchala PP, Mrachek EK, et al. **MRI and CT identify isocitrate dehydrogenase (IDH)-mutant lower-grade gliomas misclassified to 1p/19q codeletion status with fluorescence in situ hybridization.** *Radiology* 2020;294:160–67 CrossRef Medline
3. Lasocki A, Rosenthal MA, Roberts-Thomson SJ, et al. **Neuro-oncology and radiogenomics: time to integrate?** *AJNR Am J Neuroradiol* 2020;41:1982–88 CrossRef Medline
4. Lasocki A, Roberts-Thomson SJ, Gaillard F. **Radiogenomics of adult intracranial gliomas after the 2021 World Health Organisation classification: a review of changes, challenges and opportunities.** *Quant Imaging Med Surg* 2023;13:7572–81 CrossRef Medline
5. Horbinski C. **What do we know about IDH1/2 mutations so far, and how do we use it?** *Acta Neuropathol* 2013;125:621–36 CrossRef Medline
6. Lasocki A, Tsui A, Tacey MA, et al. **MRI grading versus histology: predicting survival of World Health Organization grade II–IV astrocytomas.** *AJNR Am J Neuroradiol* 2015;36:77–83 CrossRef Medline

Arian Lasocki

Department of Cancer Imaging
Peter MacCallum Cancer Centre
Melbourne, Victoria, Australia

Sir Peter MacCallum Department of Oncology
Department of Radiology
The University of Melbourne
Parkville, Victoria, Australia

Michael E. Buckland

Department of Neuropathology
Royal Prince Alfred Hospital
Camperdown, New South Wales, Australia

School of Medical Sciences
University of Sydney
Camperdown, New South Wales, Australia

Frank Gaillard

Department of Radiology
The University of Melbourne
Parkville, Victoria, Australia

Department of Radiology
The Royal Melbourne Hospital
Parkville, Victoria, Australia

Arterial Spin-Labeling Imaging Features of Atypical Cerebral Developmental Venous Anomaly Phenotypes

We read with interest the recent article by Yoo et al.¹ The definition of venous-predominant (vp) AVM used by Yoo et al applies to both type 1 and 2 arterialized developmental venous anomalies (DVAs) as described by Ruiz et al.² These phenotypes are associated with a hyperemic capillary blush in the venous drainage territory of the caput medusae, which is incompatible with the diagnosis of AVM because circulating blood reaching the anomalous venous structures has already crossed a parenchymal capillary bed.² The basis of the hyperemic capillary blush or tissue stain is not fully known. Some authors have attributed it to an adaptive ectasia of postcapillary venules, which enables redistribution of flow toward the hyperplastic collecting vein of the DVA. Nonetheless, the terms “arterialized” and “arteriovenous malformation” are both misleading in this context because arteriovenous shunting is not a feature of these atypical DVA phenotypes.

In their study, Yoo et al¹ retrospectively analyzed patients with DVA or vpDVA who underwent MR imaging with arterial spin-labeling (ASL) sequences and catheter-directed DSA. The authors used DSA to quantify arteriovenous shunting on the basis of the temporal phase in which the lesions were visualized. This approach is fundamentally flawed according to criterion standard diagnostic principles. Although the rate of appearance of a draining vein can be used to quantitatively estimate a shunt when arteriovenous shunting is present, the presence of a shunt is not defined by the rate of appearance of a vein on a temporal scale, rather it is determined by the appearance of a draining vein before the regional capillary blush. If a capillary blush precedes the appearance of the draining vein, then arteriovenous shunting is excluded. In the absence of a true arteriovenous shunt, the rate of appearance of a draining vein is simply a measure of tissue transit time. The findings of the index study, therefore, correlate ASL signal enhancement with tissue transit time, rather than arteriovenous shunting, which is a distinct cause of ASL signal enhancement. We disagree with the authors when they conclude that ASL imaging predicts the amount of arteriovenous shunting. ASL signal enhancement has been found in numerous lesions with increased blood flow but without arteriovenous shunting, including tumors and inflammatory disorders.

In Figs 1 and 2 from the study, it is shown that the vpAVM phenotype is characterized by a hyperemic capillary blush on DSA. This finding definitively excludes arteriovenous shunting and eliminates AVM from the differential diagnosis. Nonetheless, Yoo et al¹ have demonstrated that an atypical DVA with parenchymal hyperemia can be identified on the basis of increased flow-related signal enhancement on properly protocolled ASL imaging studies. Because this subgroup of atypical DVAs has been associated with an increased risk of cerebral hemorrhage, ASL sequences could be helpful in the evaluation of a DVA.

Disclosure forms provided by the authors are available with the full text and PDF of this article at www.ajnr.org.

REFERENCES

1. Yoo DH, Sohn CH, Kang HS, et al. **Arterial spin-labeling MR imaging for the differential diagnosis of venous-predominant AVMs and developmental venous anomalies.** *AJNR Am J Neuroradiol* 2023; 44:916–21 CrossRef Medline
2. Ruiz DS, Yilmaz H, Gailloud P. **Cerebral developmental venous anomalies: current concepts.** *Ann Neurol* 2009;66:271–83 CrossRef Medline

 **Todd Abruzzo**

Barrow Neurological Institute at Phoenix Children's Hospital
Phoenix, Arizona

Department of Child Health
University of Arizona College of Medicine
Phoenix, Arizona

Department of Radiology
Mayo Clinic College of Medicine
Phoenix, Arizona

 **Prakash Muthusami**

Department of Diagnostic Imaging and Interventional Radiology
The Hospital for Sick Children
University of Toronto
Toronto, Ontario, Canada

 **Ferdinand Hui**

Neuroscience Institute
Queen's Medical Center
Honolulu, Hawaii

<http://dx.doi.org/10.3174/ajnr.A8239>

REPLY:

We greatly appreciate and read with interest the opinion by Abruzzo et al. We understand the argument that a venous-predominant AVM (vpAVM) is not a true AVM in that hyperemic capillary blush is observed, suggesting that the parenchymal capillary bed with rapid transit time is involved in the circulation of the lesion. The lack of a definite nidus on DSA also supports their points. However, a number of case reports and series have addressed the resemblance of these lesions to true AVMs based on histologic similarity.^{1,2} Moreover, their angiographic and clinical features (early appearance of draining vein, various symptoms, and hemorrhage) are those of an AVM.

The nature of these lesions is not yet well-understood, and no definite terminology has been established. They are currently addressed with various terms such as atypical developmental venous anomaly (DVA), transitional venous anomaly, arterialized DVA, and DVA with an arteriovenous shunt. Whether AVM or not, the focus of our study was that arterial spin-labeling can distinguish DVA and vpAVM (or atypical DVA) without the patient having to undergo invasive DSA or the use of contrast agent. Because arterial spin-labeling is increasing in availability, we hope that our findings help readers recognize these rare disease entities in routine MR imaging clinical practice.

<http://dx.doi.org/10.3174/ajnr.A8348>

REFERENCES

1. Hirata Y, Matsukado Y, Nagahiro S, et al. **Intracerebral venous angioma with arterial blood supply: a mixed angioma.** *Surg Neurol* 1986;25:227–32 CrossRef Medline
2. Im SH, Han MH, Kwon BJ, et al. **Venous-predominant parenchymal arteriovenous malformation: a rare subtype with a venous drainage pattern mimicking developmental venous anomaly.** *J Neurosurg* 2008;108:1142–47 CrossRef Medline

Dong Hyun Yoo

Chul-Ho Sohn

Department of Radiology
Seoul National University Hospital
Seoul National University College of Medicine
Seoul, Korea

Hyun-Seung Kang

Department of Neurosurgery
Seoul National University Hospital
Seoul National University College of Medicine
Seoul, Korea

Young Dae Cho

Department of Radiology
Seoul National University Hospital
Seoul National University College of Medicine
Seoul, Korea

Kang Min Kim

Department of Neurosurgery
Seoul National University Hospital
Seoul National University College of Medicine
Seoul, Korea

Regarding “Central Vein Sign in Multiple Sclerosis: A Comparison Study of the Diagnostic Performance of 3T versus 7T MRI”

I appreciate the work of Okromelidze et al¹ on the “Central Vein Sign in Multiple Sclerosis: A Comparison Study of the Diagnostic Performance of 3T versus 7T MRI.” Their study uses the largest 7T MR imaging cohort, demonstrated excellent MS differentiation with 3T SWI, 7T SWI, and 7T T2*WI. Optimal thresholds of 40%, 15%, and 12% for 7T T2*WI, 7T SWI, and 3T SWI, respectively, yielded 100% accuracy, sensitivity, and specificity, with areas under the curve of 1.0 at 7T and 96.0% accuracy, 93.4% sensitivity, and 100% specificity at 3T. However, several factors may have influenced the reported performance metrics.

The authors included lesions without size limitations. They justified including smaller lesions by stating that histopathologically small lesions also have central veins. However, the North American Imaging in MS Cooperative² (<https://www.naimscooperative.org/>) recommends the exclusion of lesions of <3 mm. Considering that the control group mostly comprises lesions of presumed vascular origin and typical MS lesions are >3 mm, lesion size is a potential confounder here. Moreover, they reported that the total number of lesions in the control group is higher (1088 control versus 903 for MS), even though the number of patients is notably lower (39 control versus 61 for MS). This discrepancy could be due to the inclusion of small lesions of vascular origin, in which the evaluation of the central vein sign (CVS) is difficult. Also, larger lesions are more likely to incidentally harbor veins. Reporting the median average lesion diameter for each group would help clarify this issue I suspect it is significantly smaller in the control group in this case.

Another potential confounder is location. In the MS group, a significant number (340/930) of lesions were located in the periventricular area, as expected. In the control group, most lesions were in the subcortical area (675/1088). Periventricular lesions display the highest prevalence of central veins, and this could be

elucidated by increased concentration of parenchymal veins in periventricular regions, particularly at 7T,² increasing risk of false positivity. As lesions progress toward the periphery, the proportion of cases positive for the CVS decreases, owing to reduced vein size, making detection more challenging. Even though the percentage of CVS presence is higher in MS when each location is evaluated separately, in Table 3, this could still be influenced by the average lesion diameter.

Additionally, Table 2 displays discrepancies in total lesion numbers between groups. I believe that the control and MS summations are erroneously swapped.

As the use of 7T increases, the CVS is also gaining popularity. It is imperative to determine whether the observed findings stem from the CVS itself or are influenced by a lack of standardization. Making adjustments for potential confounders is crucial to ensure precise threshold determination and enhance diagnostic utility.

Disclosure forms provided by the authors are available with the full text and PDF of this article at www.ajnr.org.

REFERENCES

1. Okromelidze L, Patel V, Singh RB, et al. **Central vein sign in multiple sclerosis: a comparison study of the diagnostic performance of 3T versus 7T MRI.** *AJNR Am J Neuroradiol* 2023;45:76–81 CrossRef Medline
2. Sati P, Oh J, Constable RT, et al; NAIMS Cooperative. **The central vein sign and its clinical evaluation for the diagnosis of multiple sclerosis: a consensus statement from the North American Imaging in Multiple Sclerosis Cooperative.** *Nat Rev Neurol* 2016;12:714–22 CrossRef Medline

Onur Tuncer

Department of Radiology
Yeditepe University
Istanbul, Turkey

<http://dx.doi.org/10.3174/ajnr.A8260>

REPLY:

We would like to express our gratitude to the authors for their appraisal of our recent article.¹ As correctly pointed out, we made the decision to include all lesions irrespective of size, which contradicts the recommended guidelines of the North American Imaging in MS Cooperative (<https://www.naimscooperative.org/>). The stipulated size criteria are based on subjective opinions rather than rigorous scientific validation. The size limitation is an arbitrary restriction intended to enhance specificity at the expense of reduced sensitivity due to inherent imaging limitations at a lower field strength. It is crucial to emphasize that these size criteria have mostly been investigated at standard field strengths without validation of their impact on diagnostic performance at ultra-high-field MR imaging.

Use of these criteria can pose challenges because it can lead to an overestimation of the predictive value in which enrollment is restricted by lesion size, thereby excluding patients with small lesions that may exhibit the central vein sign (CVS) at histology or 7T MR imaging. Al-Louzi et al² used ex vivo 7T MR imaging and histology to demonstrate that lesions with false-negative MR imaging findings for the CVS had a mean maximum dimension of <3 mm, showing that the absence of the CVS on standard MR imaging is partly technical rather than a purely pathophysiologic feature. It has also been demonstrated that adjusting the lesion size cutoff results in a compromise between specificity and sensitivity.² Hence, it is firmly established that the imposition of such artificial constraints will diminish specificity in accurately diagnosing MS using the CVS and may not be suitable at ultra-high-field MR imaging in which a small CVS can be detected more reliably. Undoubtedly, our predictive value of the CVS in the 3T data is anticipated to be lower than that of studies applying size constraints, but our data also reveal that this reduction in sensitivity and increase in specificity are artificially induced when evaluated on corresponding 7T images (as discussed below). Our findings are additionally supported by Tallantyre et al,³ who also did not apply the size criteria at 3T and 7T and reported 100% sensitivity and specificity for the 7T CVS. Their results further demonstrate that 7T T2* identified the CVS in >80% of lesions with a volume of <50 mm³.³

Next, the author also focused on the prevalence and probability of lesion characteristics. The distribution of lesions will differ

among cohorts with MS and those without due to the known pathophysiology of these lesions, but periventricular lesions are not a requirement for MS. Kilsdonk et al⁴ have demonstrated with 7T MR imaging that restricting lesions to the deep white matter improves specificity from 88% to 94% but significantly reduces sensitivity from 100% to 81%. Furthermore, we found that 6.6% (4/61) of patients with MS did not have a periventricular lesion, yet they had the CVS in at least 2 small subcortical lesions on 7T MR imaging, with 92.3% (12/13) of these lesions having the CVS. If we were to apply the aforementioned logic and constraints to just these 4 cases, our sensitivity would decrease from 100% to 93.4%.

In conclusion, because our results, along with those of others, demonstrate the exceptional sensitivity and specificity of 7T MR imaging without the need to impose constraints on lesion size, it would be illogical to apply artificial constraints to 7T imaging in an attempt to increase specificity, which is already at 100%.³ While we acknowledge that size constraints may improve specificity in lower-field-strength MR imaging at the expense of false-negative results, our findings suggest that these constraints are likely unnecessary at ultra-high-field MR imaging.

REFERENCES

1. Okromelidze L, Patel V, Singh RB, et al. **Central vein sign in multiple sclerosis: a comparison study of the diagnostic performance of 3T versus 7T MRI.** *AJNR Am J Neuroradiol* 2023;45:76–81 CrossRef Medline
2. Al-Louzi O, Manukyan S, Donadieu M, et al. **Lesion size and shape in central vein sign assessment for multiple sclerosis diagnosis: an in vivo and postmortem MRI study.** *Mult Scler* 2022;28:1891–902 CrossRef Medline
3. Tallantyre EC, Morgan PS, Dixon JE, et al. **A comparison of 3T and 7T in the detection of small parenchymal veins within MS lesions.** *Invest Radiol* 2009;44:491–94 CrossRef Medline
4. Kilsdonk ID, Wattjes MP, Lopez-Soriano A, et al. **Improved differentiation between MS and vascular brain lesions using FLAIR* at 7 Tesla.** *Eur Radiol* 2014;24:841–49 CrossRef Medline

L. Okromelidze

V. Patel

E.H. Middlebrooks

Department of Radiology

Mayo Clinic

Jacksonville, Florida

<http://dx.doi.org/10.3174/ajnr.A8267>